DOCTORAL THESIS

OCEANIC LASER-INDUCED BREAKDOWN SPECTROSCOPY. DEVELOPMENT AND APPLICATION FOR THE ANALYSIS OF SUBMERGED SOLIDS

Marina López Claros

Supervisors: J. Javier Laserna Vázquez & Francisco J. Fortes Román

UNIVERSIDAD DE MÁLAGA
Facultad de Ciencias
Doctoral Programme: Química Avanzada, Preparación y Caracterización de Materiales

Málaga 2017

Doctoral Thesis

UNIVERSIDAD DE MÁLAGA

OCEANIC LASER-INDUCED BREAKDOWN SPECTROSCOPY. DEVELOPMENT AND APPLICATION FOR THE ANALYSIS OF SUBMERGED SOLIDS

by

MARINA LÓPEZ CLAROS

Research supervisors: José Javier Laserna Vázquez and Francisco Javier Fortes Román

Doctoral programme

Química Avanzada, Preparación y Caracterización de Materiales

Facultad de Ciencias

Universidad de Málaga

Málaga, España

2017

AUTOR: Marina López Claros

http://orcid.org/0000-0003-0819-8931

EDITA: Publicaciones y Divulgación Científica. Universidad de Málaga

OCEANIC LASER-INDUCED BREAKDOWN SPECTROSCOPY. DEVELOPMENT AND APPLICATION FOR THE ANALYSIS OF SUBMERGED SOLIDS

por **MARINA LÓPEZ CLAROS**

José Javier Laserna Vázquez

Catedrático de Universidad

Departamento de Química Analítica

Universidad de Málaga

Francisco Javier Fortes Román

Doctor en Química

Departamento de Química Analítica

Universidad de Málaga

Memoria de Tesis presentada para optar al grado de Doctor en Química

MARINA LÓPEZ CLAROS

Málaga, Abril 2017

JOSÉ JAVIER LASERNA VÁZQUEZ, Catedrático de Química Analítica de la Facultad de Ciencias de la Universidad de Málaga y **FRANCISCO JAVIER FORTES ROMÁN**, Doctor en Química por la Universidad de Málaga

CERTIFICAN:

Que **Dña. MARINA LÓPEZ CLAROS** ha realizado la presente Tesis Doctoral titulada **"OCEANIC LASER-INDUCED BREAKDOWN SPECTROSCOPY (LIBS). DEVELOPMENT AND APPLICATION FOR THE ANALYSIS OF SUBMERGED SOLIDS"** bajo su dirección en el Laboratorio Láser del Departamento de Química Analítica de la Universidad de Málaga y autorizan su presentación para optar al grado de Doctor en Química.

Y para que así conste a los efectos oportunos,
firman la presente en Málaga, Abril de 2017

Prof. José Javier Laserna Vázquez

Dr. Francisco Javier Fortes Román

AGRADECIMIENTOS

Como estudiante de doctorado el sacrificio y la constancia hasta concluir mis estudios no solo se deben a mi único esfuerzo, sino también a esas personas que con su apoyo me motivaron hasta lograr este proyecto con su paciencia y en especial su ánimo. Mi más sincero agradecimiento a todas aquellas personas e instituciones que, de una u otra forma, han hecho posible la realización de esta memoria.

En primer lugar, quiero dar las gracias a mis directores de tesis. A Javier Laserna por la confianza depositada en mí así como permitirme crecer como científica apoyándome con los recursos técnicos y humanos y con sus directrices para desarrollar este trabajo en el Laboratorio Láser de la Universidad de Málaga. Además de enriquecerme de su amplia experiencia como científico y mostrarme la visión real del mundo de la investigación. A Fco. Javier Fortes por guiarme con absoluta dedicación y entrega en este trabajo transmitiéndome su potencial científico y entusiasmo cada día. En especial me gustaría agradecerle toda la confianza depositada en mi, sus sabios consejos que sin duda me han ayudado a superar los baches del camino, y como no a su gran calidad humana.

A José Miguel Vadillo agradecerle su ayuda y guía en mis primeros pasos en el mundo de investigación y por abrirme la puerta para el desarrollo de esta tesis.

A la Consejería de Economía, Innovación y Ciencia y Empleo, Secretaría General de Universidades, Investigación y Tecnología de la Junta de Andalucía que a través de los proyectos de investigación de excelencia me han brindado el soporte económico con la contratación como personal investigador en formación (PIF) con el proyecto P11-FQM-7193 y con el cual ha sido posible realizar esta Tesis doctoral. Particularmente también me gustaría agradecer la oportunidad que facilita este tipo de contratación a tomar contacto directo en materia docente, sin duda resultó una enriquecedora y grata experiencia. A la Universidad de Málaga y a los Servicios Centrales de Investigación en particular por los medios dispuestos a nuestro alcance, desde los servicios de limpieza y seguridad hasta las técnicas de análisis más avanzadas.

El desarrollo de esta memoria no habría sido posible sin la colaboración del personal de diversas instituciones a las cuales me gustaría agradecer su asesoramiento y trabajo. A Carmen García Rivera, Milagros Alzaga, Josefa Martí, Nuria Rodríguez y Aurora Higueras del Centro de Arqueología Subacuática del Instituto Andaluz de Patrimonio Histórico por aportar el punto de vista arqueológico dándole un sentido práctico a la investigación realizada, así como por el suministro del material de estudio. Además me gustaría prolongar este agradecimiento resaltando su esfuerzo y compromiso en las campañas de medida llevadas a cabo en yacimientos arqueológicos sumergidos reales. Por supuesto quiero hacer extensible este agradecimiento a todos los participantes de las dos campañas de medidas realizadas: Ignacio Entralla y Luis Pellejero (buzos profesionales), Raúl Expósito (técnico de audio y video), Fco. Javier Fortes, Salvador Guirado, Patricia Lucena y Javier Laserna (personal científico de UMALaserLab), Carlos Barbero y su tripulación del barco pesquero Tridacna; y Manual de Alba y su tripulación de Cabo Roche. Por otro lado, debo manifestar mi profundo agradecimiento a Juan Antonio y Jesús del Taller de Mecánico de la

UMA por su asesoramiento y ayuda para hacer realidad aquellas ideas que compusieron la cámara de altas presiones, así como un gran número de piezas del analizador AQUALAS. Y a Paco Prado por asesorarnos siempre sobre la mejor solución a adoptar en aquellos aspectos relacionados con la hidráulica y la alta presión. Al servicio de microscopía de la UMA compuesto por Goyo, Adolfo y David por su amabilidad y enseñanzas.

Al Consiglio Nazionalle delle Ricerche-Istituto di Nanotecnologia (CNR- NANOTEC) e l'Università degli Studi di Bari Aldo Moro (UNIBA) d'Italia, per offrirmi la possibilità di lavorare durante il mio soggiorno di ricerca nel grupo del Prof. Alessandro De Giacomo. Vorrei ringraziare in modo particulare al Prof. Alessandro De Giacomo per l'accoglienza e per avermi fatto sentire parte del suo gruppo di ricerca, ed insieme a Marcella dell'Aglio e Rosalba Gaudiuso per trasmettermi l'entusiasmo, l'impegno e gli insegnamenti sulla ricerca di questa Tesi sulla valutazione della LIBS in profondità dell'acqua alta. Non posso fare a meno di ringraziare anche i miei colleghi di laboratorio en Bari. Tra tutti vorrei ringraziare in particolare a Gabriele Valenza, e Can Koral per la sua gentilezza ed per essere sempre disposto ad aiutarmi, e anche tutti i ricercatori del CNR che sono stati sempre molto gentili.

A mis compañeros de laboratorio los cuales han sido un gran apoyo durante este recorrido y que siempre recordaré con especial cariño. Todos han contribuido de una u otra manera en este proyecto, por ello quiero mostrar mi agradecimiento a todos con los que he ido coincidiendo en este camino. A mi predecesor Salvador Guirado por transmitirme todo tus conocimientos, amistad, ayuda y divertidos momentos en mis primeros pasos en el *Team Aqualas*. A Inma y Jorge por brindarme su amistad, experiencia y enriquecerme con buenos momentos. A Ángel por compartir su particular e interesante filosofía de vida. A Luisa, Javier Ruiz, José Miguel, Patricia, Carmen, Belén e Irene por estar siempre dispuestos a brindarme su ayuda. A Xavi y Tomás sus consejos y el dedicarme siempre un hueco (aunque estén hasta arriba) para ayudarme y escucharme. A Pablo y David su amistad y gran compañerismo. Además Pablo, nunca olvidaré aquel agosto sacando datos como locos para las JAI. Por supuesto no me olvido de Samara y Fran, los reservo con especial cariño para el final. Gracias Samara simplemente por ser tú, por brindarme tu ayuda, bondad y cariño y por hacer más llevadero estos duros últimos meses sacándome siempre unas risas; me llevo una gran amiga. A Fran para ti no tengo palabras, papel ni tinta suficiente para agradecerle todo lo que has hecho por mí, tus enseñanzas, tu confianza depositada cuando ni yo misma la tenía, y tu apoyo, especialmente durante tu ausencia que para mí no fue tal. Gracias por tu calidad profesional y humana. A todos, gracias por crear tan buen ambiente de trabajo y por estar ahí siempre que os he necesitado.

A mis amigos externos al mundo científico también les guardo unas palabras de agradecimiento por su interés en mis proyectos en especial a Fran, Charo y Miriam; y el grupo de arquitectos por el mundo. No me olvido de mi Valenciana Lidia. Gracias por los buenos ratos.

También con todo el cariño agradecer a mi familia su incondicional apoyo. A mis padres Joaquín y Paqui, gracias por la educación que me habéis brindado con vuestro esfuerzo, dedicación y cariño; por mostrarme que siempre hay que seguir adelante que así es como se alcanzan las metas. Gracias a todo

eso hoy estoy escribiendo estas letras. A mi hermana Laura y Alberto por ser mis más fieles consejeros y estar siempre ahí. A mis sobrinos que los quiero con locura, Álvaro y Adrián por hacerme feliz los ratos que compartimos. A mi hermano Joaquín y Cristina por su cariño y apoyo. A los que se marcharon durante este camino pero que tan presentes están cada día. A Guillermo y Conchi, Cristina y Carlos y Carlitos por su confianza y afecto.

Por último a ti Luis, mi estructura de hormigón armado, sin duda este trabajo en el fondo es íntegramente tuyo. Por estar a mi lado en todo momento, por ser mi mejor amigo y el mayor de mis críticos, por tu infinita paciencia, confianza y ayuda. Por no dejarme caer y enseñarme a ver desde otra óptica.

"*Si yo pudiera enumerar cuánto debo a mis grandes antecesores y contemporáneos, no me quedaría mucho en propiedad.*"

Johann W. Goethe

A mi Familia

A Luis

Table of Contents

CONTENTS

Spanish Summary

Cumpliendo con el REGLAMENTO DE LOS ESTUDIOS DE DOCTORADO DE LA UNIVERSIDAD DE MÁLAGA y por el hecho de que la presente Memoria de Tesis Doctoral está íntegramente redactada en inglés, la siguiente sección incluye un resumen de la misma en español.

Resumen de la Tesis Doctoral

Actualmente, la caracterización del patrimonio cultural sumergido se ha convertido en una de las áreas de mayor interés en arqueología. El motivo principal es la cantidad de información histórica que contienen los restos que permanecen hundidos, no sólo en las profundidades de mares y océanos, donde se encuentran la mayoría de estos yacimientos, sino también en otras localizaciones como ríos, lagos o pantanos. Cada yacimiento arqueológico es una puerta abierta al pasado, donde cada dato averiguado sobre un objeto es un paso más hacia el conocimiento de su propia historia. En este sentido su localización en combinación con los registros documentales de la época y junto al conocimiento de su composición química pueden ser una información vital para situar la procedencia espacio-temporal o para entender la tecnologías constructivas de la época. Un ejemplo de ello se encuentra en el análisis de los forros de barcos hundidos para los cuales a lo largo de los siglos se ha ido modificando el material base, así como, el material de defensa de las naves, donde los cañones podían ser fabricados en hierro o bronce según el periodo histórico. Por todo ello, es imprescindible estudiar, proteger y conservar los bienes sumergidos los cuales se encuentran sometidos a la continua agresión del medio.

Las técnicas analíticas clásicas suelen requerir el traslado de las piezas hasta el laboratorio para estudiar su composición, sin embargo, esto no siempre es posible. Algunas veces no se puede extraer el objeto de su yacimiento simplemente por cuestiones logísticas, por ejemplo debido a su tamaño. En otras ocasiones, la causa puede tener su origen en la legislación, o bien estar contraindicada para la integridad del objeto. Los materiales presentes en el propio yacimiento se encuentran en equilibrio químico con su entorno, lo que evita su deterioro. Tras su extracción, las piezas fuera del agua comienzan a oxidarse debido al oxígeno del aire y a los electrolitos que puede llevar ocluidos en su interior. Impedir este proceso es complejo, caro y puede llevar varios meses de trabajo. De esta forma, el análisis in-situ de los objetos suele ser la única alternativa en muchos casos. Además, es importante indicar que la propia disposición del objeto en el contexto del yacimiento puede proporcionarnos información sobre el mismo. Por ello, la *Organización de las Naciones Unidas para la Educación y la Cultura* (UNESCO), en la Convención para la protección del patrimonio cultural sumergido, considera la conservación in-situ del patrimonio cultural como *"la opción prioritaria antes de autorizar o emprender actividades dirigidas a ese patrimonio".*

Por tanto se plantea un reto analítico que es caracterizar los restos en los yacimientos subacuáticos sin extraerlos de su ubicación original. A pesar de esta demanda, no existen muchas técnicas analíticas disponibles para llevar a cabo el análisis químico in-situ, en realidad, sólo aquellas basadas en la tecnología láser son capaces de afrontar este reto (por ejemplo Raman, LIF y LIBS). En este sentido l*a espectroscopía de formación de plasma inducidos por láser* (LIBS), combina prácticamente todos los requisitos deseables

para este tipo de aplicación. Entre sus características, se pueden destacar su potencial para realizar análisis *in-situ* en un rango ilimitado de materiales, su capacidad de detección atómica simultánea y multi-elemental sin necesidad de preparar la muestra previamente, y la posibilidad de su implementación en equipos portátiles y de detección a distancias remotas.

Tras el problema planteado, los trabajos realizados en esta tesis doctoral han sido enfocados a sumar un granito de arena más en la implementación de la técnica LIBS para el reconocimiento e identificación in-situ de materiales sumergidos en yacimientos arqueológicos reales. En concreto, la investigación llevada a cabo puede englobarse en dos áreas diferenciadas por la aproximación de la técnica al medio marino. Por un lado, se plantea una configuración de acceso remoto al yacimiento arqueológico sumergido utilizando un sistema portátil en el cual el análisis se realiza en contacto con la muestra guiando el láser al objeto a través de una fibra óptica. En este contexto, el primer bloque de la presente Tesis Doctoral se centra en la evaluación de las capacidades de análisis, estabilidad y robustez del prototipo de acceso remoto (desarrollado por la Universidad de Málaga), así como en la optimización de los parámetros operacionales del mismo. Además, se ha diseñado un método de clasificación que permite discriminar in situ las piezas desconocidas hallas en el fondo del mar en función de su naturaleza. El segundo bloque se ha encaminado en la evaluación de la implementación hipotética de la técnica al medio marino utilizando un vehículo de operación remota (ROV) en el cual el análisis se realice a distancia. En este contexto se presentan unos estudios preliminares utilizando una configuración de excitación de doble pulso. Concretamente, se evalúa el efecto de la profundidad de análisis sobre cuestiones fundamentales enfocadas en el fenómeno formación del plasma así como de post-formación del plasma (generación de burbuja de cavitación), además de la evaluación de la influencia de distintos parámetros operaciones sobre la señal espectral.

A continuación se resumen los resultados más relevantes de la investigación desarrollada, diferenciándose los dos bloques de contenidos anteriormente mencionados.

Bloque 1: Aproximación de la técnica LIBS para la identificación de materiales arqueológicos sumergidos basado en una configuración remota de análisis en contacto con la muestra.

Sistema experimental

En este bloque el sistema experimental utilizado fue un novedoso instrumento llamado *AQUALAS 2.0* (desarrollado por la Universidad de Málaga) basado en el guiado del haz láser a través de una fibra óptica hasta la superficie del material de interés. Éste fue especialmente diseñado para el análisis químico remoto de materiales sumergidos.

El prototipo consta de dos partes bien definidas: una sonda de muestreo y un módulo principal, interconectadas por medio de un umbilical de 50 metros de longitud. La unidad principal contiene el módulo óptico, donde se realiza el acoplamiento láser-fibra, el módulo de adquisición de datos y la fuente de alimentación del láser. Las dimensiones del prototipo son de 81 x 86 x 126 cm.

El módulo óptico consiste en una estructura de metacrilato especialmente adaptada para prevenir la deposición de aerosoles marinos sobre los componentes ópticos del sistema. Este módulo también contiene la fuente de excitación láser así como todos los componentes ópticos para realizar tanto el acoplamiento láser-fibra como la detección del plasma procedente de la superficie de la muestra. El haz láser es transmitido a través de 55 metros de fibra óptica protegidos en el interior de un umbilical que conecta la sonda de análisis con el módulo óptico. En el extremo final de la fibra óptica, el haz láser es enfocado sobre la superficie del material mediante un sistema óptico incorporado en el interior de la sonda LIBS de análisis. El umbilical también suministra un flujo constante de gas al interior de la sonda, para eliminar el agua de la superficie del material creando una interfase gas-sólido que facilita el análisis LIBS bajo agua.

Una vez generado el plasma sobre la superficie del material, la luz se transmite a través de la misma fibra óptica para regresar al módulo óptico, donde es guiada hacia el módulo de adquisición de datos a través de un sistema óptico de colección. El módulo de adquisición de datos, instalado en la unidad principal, consta de un espectrómetro, un convertidor de video y un ordenador. Un generador de pulsos y retrasos que controla externamente el sistema. El espectrómetro utilizado es un Czerny-Turner que tiene una red de difracción de 1200 líneas/mm y una resolución espectral de 0.1-0.2 nm/pixel en el rango espectral de 300-550 nm.

El equipo también dispone de un módulo auxiliar para su total autonomía en los trabajos de campo. Este módulo contiene un compresor de aire, un estabilizador de corriente y un generador externo de corriente que dota al equipo de siete horas de autonomía de trabajo.

Por otro lado, este instrumento puede ser configurado en dos modos de excitación diferente tanto en pulso-simple convencional (SP-LIBS) como en múltiples pulsos (MP-LIBS). La configuración MP-LIBS permite introducir una mayor radiación láser a través de la fibra óptica aumentando de tal modo las

prestaciones del equipo en términos de energía. De hecho, esta última será la empleada en los trabajos que se indican en este bloque.

Además de esto, es importante mencionar la forma de actuación del prototipo en un entorno real de análisis de un yacimiento arqueológico sumergido. En primer lugar, debe realizarse una prospección previa por personal cualificado y autorizado, que en nuestro caso pertenecen al *Centro de Arqueología Subacuática* (CAS). Siguiendo los protocolos establecidos para minimizar el riesgo de dañar las piezas arqueológicas, eliminan la capa de concreción de la superficie de las muestras. Seguidamente, el instrumento AQUALAS 2.0 se transporta hasta el puerto más cercano al yacimiento y de aquí se despliega en una embarcación auxiliar que nos desplaza al entorno del yacimiento. En este punto, un buzo profesional portando la sonda de análisis se dirige a las inmediaciones donde se sitúa el material de interés.

- **Capacidades, estabilidad y robustez del equipo AQUALAS 2.0 para el análisis de sólidos sumergidos y caracterización química submarina de aceros galvanizados.**

Una primera investigación para evaluar la estabilidad y robustez del equipo AQUALAS 2.0 en el ambiente marino fue realizada utilizando como escenario la bahía de Málaga. La muestra seleccionada para la secuencia de experimentos fue un bronce certificado para el cual se seleccionó la línea de Cu a 521.82 nm.

En primer lugar, se evalúo el despliegue del cable umbilical que contiene en su interior la fibra óptica. Los 50 m de cable se encuentra enrollados en un soporte en el cual la posible tensión acumulada podría afectar al suministro de energía a través de la fibra óptica. Se comprobó que la intensidad de la señal espectral se mantuvo prácticamente constante con el despliegue de la sonda en el rango de trabajo de 0-50 m y la variabilidad de la señal obtenida fue por debajo del 14%. Además, la energía promedio de 500 pulsos en cada trayecto de 10 m de despliegue de la sonda indicó una alta estabilidad con una energía promedio de 42.6 mJ pulso $^{-1}$ y una variabilidad del 2%.

Atendiendo a los resultados mencionados anteriormente, la estabilidad del sistema LIBS es muy satisfactoria. En este sentido, un daño hipotético de la fibra óptica puede ser el único punto débil de nuestro prototipo. Por lo tanto, con el objetivo de evaluar la robustez del acoplamiento de láser a la fibra el sistema LIBS se trasladó a lo largo de un camino adoquinado de 500 m. Los espectros LIBS registraron a cada 100 m muestran una intensidad promedio prácticamente constante en 35.000 cuenta alcanzando una desviación estándar relativa menor del 10% en todos los casos, esto confirman la robustez del acoplamiento de láser a la fibra.

En relación con esto resultados, la estabilidad probada y robustez del sistema LIBS remoto garantizan la fiabilidad de los datos adquiridos en condiciones severas (es decir, en un entorno marino) durante una campaña de campo.

Por otro lado, es importante destacar que el análisis de los materiales sumergidos es un área de aplicación de creciente interés, especialmente en el sector industrial donde, para asegurar la fiable protección

a la corrosión, el espesor del recubrimiento tiene que ser mantenido constante en un rango de tolerancia. En este sentido, y bajo el mismo escenario de trabajo, la capacidad del equipo para analizar y determinar espesores de capa en materiales sumergidos se evaluó. Para este estudio se utilizó un conjunto de 5 muestras de aceros galvanizados con diferentes espesores de recubrimiento comprendidos en el rango de 3.2 a 11.2 µm. Las muestras fueron analizadas en el mar y se registró tanto la emisión de las líneas de Zn (I) a 472.21nm como de Fe (I) 438.35 nm del recubrimiento y sustrato, respectivamente. Además este estudio se realizó utilizando una configura de excitación de MP para dos valores de duración del pulso láser principal de 22 y 30 ns. Se observó que el número de pulsos necesarios para agotar completamente la capa de recubrimiento fue menor para la duración de pulso más larga, 30 ns. Utilizando la derivada del perfil de intensidad y en base al criterio descrito en bibliografía de $P_{0.5}$, se calculó la tasa de ablación media (AAR) para ambas anchos de pulso en una muestra de espesor de recubrimiento de 11.2 µm. Los resultados mostraron una AAR de 172 nm pulso^{-1} y 254 nm pulso^{-1} para el ancho de pulso de 22 ns y 30 ns, respectivamente. Por tanto, se observó que al utilizar una duración de pulso más larga $P_{0.5}$ decrece y por consiguiente la AAR aumenta en comparación a una duración de pulso corta. Este hecho puede ser debido a que a mayor duración del impulso principal en la secuencia de multipulsos favorece el calentamiento y la fusión de la muestra. De esta forma se facilita la ablación de la superficie de la muestra por el resto de los pulsos de la secuencia. Por otro lado, con el objetivo de cuantificar el límite de exactitud y precisión de los perfiles obtenidos, se calculó la resolución en profundad (ΔZ) para la muestra de espesor 3.2 µm usando ambos anchos de pulso. Se obtuvo un ΔZ de 2.8 µm y 2.2 µm para 22 ns y 30 ns, respectivamente. Se pudo concluir que una caracterización más rápido y con una mejor resolución del perfil se obtiene al utilizar una duración de pulso mayor.

Además de esto, con el fin de determinar el espesor de un recubrimiento de Zn desconocido, se construyó una curva de calibrado correlacionando el número de pulsos para llegar a la interfase Zn-Fe con el espesor de la capa. La calibración se realizó para los dos valores de duraciones de pulso. En ambos casos, la correlación entre ambas variables fue excelente obteniéndose un coeficiente de correlación lineal (R^2) de 0.99. Estos resultados muestran el potencial de la tecnología a distancia-LIBS para la estimación del espesor de recubrimiento de una muestra de acero galvanizado desconocido.

- **Optimización de parámetros operacionales del equipo AQUALAS 2.0: influencia de la presión de salida y composición química del gas de purga sobre la señal LIBS.**

Nuestro instrumento remoto basado en una configuración de guiado de haz láser por fibra óptica, como se comentó, se constituye por una sonda de LIBS sumergible en el que a través de un cordón umbilical se suministra un gas de protección o gas de purga. De hecho, el uso del gas de purga es clave para expulsar el agua de la superficie de la muestra y crea una interfaz entre la muestra y la sonda de sólido a gas en lugar de sólido a líquido. Este hecho, es ideal para el análisis LIBS bajo el agua ya que la gran atenuación que produce ésta sobre la radiación de 1064 nm evitaría la deposición de una dosis suficiente de energía sobre la posición de análisis. De este modo, en comparación con una interfase sólido-líquido, se mejora la eficiencia

de ablación. Por otra parte, el gas de purga se utiliza para impedir la entrada de agua en la sonda LIBS. En este caso, debe tenerse en cuenta que la diferencia de presión (ΔP) entre el interior (P_{int}) y fuera de la sonda (P_{ext}) debe ser superior o al menos a 1 bar.

Además de estos usos comentados, se decidió estudiar el empleo del gas de purga con el objetivo de mejorar las prestaciones y el rendimiento analítico del prototipo. Como es conocido en literatura, las propiedades del gas circundante al plasma influencian severamente en la respuesta espectroscópica. En este sentido, se optó por evaluar tanto la influencia del ΔP como la composición química de este gas circundante. En particular, estos estudios se enfocaron con la proyección de mejorar la detección de muestras de carácter cerámica. Este tipo de materiales son muy comúnmente hallados en los yacimientos arqueológicos sumergidos, sin embargo, el análisis en tales condiciones puede ser complejo debido a su naturaleza altamente porosa y quebradiza.

- **Influencia del diferencial de presión del gas de purga sobre la señal LIBS**

La influencia del diferencial de presión del gas de purga a la salida de la sonda LIBS se evaluó en las líneas de emisión de Ca (I) a 422,6 nm, Fe (I) a 438,3 nm y Ti (I) at 498,1 nm de una muestra de origen cerámico. En este experimento se fue aumentando ΔP en intervalos de 0.5 bar en un rango comprendido entre 1 a 4 bar. Se observó que para las tres líneas de emisión la intensidad disminuye a medida que ΔP aumenta. Este hecho se podría atribuir a un posible proceso de apantallamiento del plasma. Cuando la presión del medio aumenta, el plasma se confina sobre la superficie de la muestra. En este caso, una mayor densidad de especies se encuentra en el plasma por unidad de volumen produciendo un efecto de "*protección*"-"*apantallante*" del plasma más acusado a medida que aumenta el confinamiento. Debido a esto, la radiación láser que llega a la superficie de la muestra se reduce y por lo tanto se obtiene una disminución en la señal de LIBS. Este efecto de "protección" del plasma se pudo contrastar calculando la densidad electrónica del mismo (N_e). Como era de esperar, se obtuvo una mayor densidad de especies en el plasma cuando ΔP = 4 bar (N_e $1.09 \cdot 10^{19}$ cm^{-3}) y se encuentra más confinado éste en comparación con el valor de N_e obtenido para ΔP = 1bar (N_e $0.5\ 10^{19}$ cm^{-3}). Por tanto, en el caso particular evaluado de material cerámico, el ΔP debe establecerse en el mínimo posible para evitar el apantallamiento del plasma y mejorar de esta forma la caracterización química de la cerámica durante el análisis in situ en un yacimiento arqueológico bajo el agua.

- **Influencia de la composición química del gas de purga sobre la señal LIBS**

La influencia de la composición química de gas de purga también se evaluó con el objetivo de mejorar la sensibilidad analítica en muestras cerámicas. Este experimento se llevó a cabo utilizando diversos gases ambiente tales como aire, CO_2, He y Ar manteniendo contante ΔP 3 bar. Las líneas de emisión seleccionadas fueron Ca (I) a 422,6 nm, como representación de elementos mayoritarios, y Fe (I) a 438,3 nm, para los elementos minoritarios de la muestra. La intensidad de emisión de Ca y Fe mayores se obtuvo

utilizando como gas de purga Ar. Para el resto de los gases, la intensidad fue disminuyendo siguiendo la secuencia de He > Aire > CO_2. Por otra parte, la intensidad de fondo también fue estudiada encontrándose la menor contribución usando He en comparación con Ar, aire y CO_2. Así como, la relación señal ruido (SNR) de los espectros en la que se obtuvo la misma secuencia que para el parámetro de intensidad Ar > He > Aire > CO_2.

Los comportamientos descritos se pueden atribuir a los parámetros del plasma tales como la temperatura electrónica (T_e) y la densidad (N_e) las cuales están influenciadas por las propiedades del gas circundante a la muestra. En general, plasmas con alta T_e (energéticos), producen una mayor emisión alcanzando intensidades en los espectros LIBS altas. Por tanto, ambos parámetros fueron calculados para los cuatro gases. Como se esperaba, una T_e mayor se obtuvo utilizando una atmósfera de Ar con respecto al aire, CO_2 y He. Además, también se obtuvo una gran densidad de electrones con Ar que explica la intensidad de fondo mayor debido a la influencia de la radiación continua. Incluso se observó que los tránsitos con diferenciales energéticos mayores son favorecidos con este gas. Por otra parte, es importante mencionar el caso del gas He. Es conocido en bibliografía el carácter del gas para producir plasmas fríos y de baja N_e, coincidente a nuestros resultados experimentales expuestos. Sin embargo, con este gas se alcanzó la segunda intensidad de emisión más alta. Este hecho puede estar asociado con una menor contribución de la radiación del continuo con respecto al resto de los gases estudiados.

A raíz de los resultados expuestos, la sustitución de aire como gas de purga, de uso común para una campaña de campo, por argón se presenta como una alternativa para aumentar la sensibilidad analítica de los equipos AQUALAS 2.0 en materiales cerámicos. Sin embargo, a pesar de los beneficios que produce Ar en la respuesta analítica, otro factor debe tenerse en cuenta como es su costo. Para una campaña de campo es fácil y accesible emplear aire utilizando un compresor. En contraste Ar debe ser transportado en un contenedor previamente suministrado por un distribuidor. Por lo tanto, con el fin de reducir el costo de análisis y mantener una buena calidad espectral, se decidió llevar a cabo un estudio con mezclas de diferentes proporciones de Ar y aire. Se observó un aumento neto de intensidad cuando el porcentaje en Ar es en aumento. A partir de una mezcla de 50% de los gases la tendencia obtenida para ambos elementos Ca (mayoritario) y Fe (minoritario) fue moderadamente creciente. Además de esto, se alcanza una menor desviación estándar y RSD utilizando bajos porcentajes de Ar. A la vista de estos resultados, se decidió que la mejor alternativa para una campaña de campo podría ser una mezcla de 50% de los gases porque mantiene un compromiso favorable entre costo y la respuesta analítica.

Por otra parte, los beneficios que reporta Ar sobre la intensidad de emisión también se chequearon en materiales arqueológicos con carácter metálico y aleado. De igual forma que en cerámicas, la intensidad obtenida usando Ar fue más elevada que con el empleo de aire.

Tras la optimización de trabajo descrita en este apartado, el equipo AQUALAS 2.0 fue trasladado al Centro de Arqueología Subacuática (CAS) de Cádiz con el objetivo de analizar un conjunto de muestras pertenecientes a 6 pecios de las costa andaluza que se encontraban sumergidas en tanques desaladores en fase de estabilización. En el anexo 2 se puede encontrar los resultados obtenidos.

- **Identificación y clasificación espectral submarina de los restos de un naufragio situado en aguas de San Pedro de Alcántara (bahía de Málaga)**

LIBS en el entorno marino es una tecnología en desarrollo que ofrece ventajas únicas sobre los métodos tradicionales. No sólo ofrece la composición de líquidos con alta fiabilidad; sino que también proporciona la composición elemental de sólidos con poco o ninguna manipulación del usuario. Debido a esta ventaja LIBS se ha utilizado como una herramienta para la inspección de los materiales en arqueología subacuática, donde el conocimiento de la composición química puede proporcionar pistas valiosas sobre el origen de los materiales en naufragios y edificios sumergidos. Sin embargo, dada la gran diversidad de composición, las diferencias de textura y alteración de la superficie del patrimonio cultural sumergido, el uso de algoritmos estadísticos avanzados se manifiesta casi de forma esencial para el reconocimiento y clasificación de los hallazgos subacuáticos. En este sentido, se intentó dotar el instrumento LIBS AQUALAS 2.0 con una herramienta de procesado de datos que permita evaluar la inspección del naufragio de una forma fácil y rápida. Esta nueva herramienta se diseñó para ordenar las lecturas obtenidas por el sistema LIBS cuando se inspeccionan piezas desconocidas que se encuentran en el fondo del mar de tal forma que se asigna su composición elemental a uno de los grupos de materiales comunes, previamente descrito, que se encuentran en un yacimiento arqueológico sumergido.

- **Diseño y evaluación de un método de clasificación para objetos arqueológicos sumergidos basado en el análisis discriminante**

Para el reconocimiento y clasificación de los objetos hallados en el entorno subacuático con el instrumento AQUALAS 2.0 se utilizó la herramienta del *Análisis Lineal Discriminante* (LDA) para generar un modelo de algoritmo supervisado. De forma conceptual, con LDA se evalúa los pesos relativos de las variables originales descritas para la discriminación de grupo y la puntuación de la separación entre múltiples clases. Después, el modelo predice la probabilidad de que una muestra desconocida pertenezca a cada clase propuesta en el modelo.

Para desarrollar el método de clasificación, se estudió primero un conjunto de treinta y ocho objetos recogidos de varios naufragios. Para simular las condiciones experimentales de un entorno submarino, las muestras se sumergieron y se analizaron en un tanque de agua en nuestro laboratorio utilizando como gas de purga argón a 5 bar. Debido a la gran variedad de muestras utilizadas en este estudio, los objetos se dividieron en diferentes grupos para el análisis quimiométrico, tales como: aleaciones de bronce (10), piezas metálicas (18), cerámica (5) y mármoles (5). Los espectros LIBS fueron adquiridos en el rango espectral de 350-550 nm, se promedió la respuesta de 50 pulsos láser y se repitió la operación dos veces más en posiciones adyacentes en la muestra. Posteriormente, la intensidad promedio se normalizó a la unidad. Sin embargo, todo el espectro de LIBS no se consideró como datos de entrada para el modelo sino que se redujo de manera significativa a 10 variables espectrales. Se seleccionaron aquellas líneas de emisión

características de los grupos de materiales descritos para el método tales como: Cu (I) 510,55 nm, Zn (I) 481,05 nm, Sn (I) 452,47 nm, Pb (I) 405,78 nm, Fe (I) 438,35 nm, Ca (I) 422,67 nm, Mg (I) 517,26 nm, Si (I) 390,55 nm, Sr (I) 407,61 nm y Ti (I) 498,17 nm. Las funciones discriminantes obtenidas fueron:

$$F_1 = 2.7\ I_{Cu} + 2.4\ I_{Zn} + 22.8\ I_{Sn} + 0.8\ I_{Pb} + 2.7\ I_{Fe} - 7.2\ I_{Ca} - 1.2\ I_{Mg} - 3.8\ I_{Sr} - 6.0\ I_{Si+Ti} + 0.59$$

$$F_2 = 1.8\ I_{Cu} + 3.8\ I_{Zn} + 24.8\ I_{Sn} - 0.2\ I_{Pb} - 0.8\ I_{Fe} - 2.5\ I_{Ca} - 1.8\ I_{Mg} - 1.5\ I_{Sr} + 9.4\ I_{Si+Ti} - 2.0$$

Donde I_m es la intensidad normalizada de cada línea de emisión. Además en ambos casos se obtuvieron una buena correlación canónica 0,98 y 0.91 respectivamente. Así como, los valores de lambda de Wilk de tratamiento estadístico (0,0013 y 0,03), sugieren que las variables seleccionadas para el análisis discriminante lineal eran apropiadas para la discriminación de la muestra.

Previo al trabajo de campo, se decidió evaluar el método de clasificación en laboratorio con un set de muestras diferentes al de entrenamiento. El conjunto de prueba seleccionado está compuesto por 4 forros de barcos. Estas muestras son de un alto interés arqueológico ya que según la composición elemental pueden arrojar información sobre la época de construcción del barco y el origen. De hecho, en base a la composición elemental y la ayuda del material bibliográfico del personal arqueólogo, se detectó una clara evolución de la composición de los revestimientos de barco que podrían estar relacionados con un período de la historia o incluso con el país de su fabricación. Respecto al método de clasificación propuesto, fue realmente eficaz incluyendo cada muestra en el grupo correcto; tres forros metálicos y una aleación de bronce.

- **Identificación y clasificación de los objetos del naufragio de San Pedro de Alcántara, campaña de campo**

Los restos de un naufragio que yace en aguas de San Pedro de Alcántara, zona de la bahía de Málaga, se estudiaron utilizando el analizador remoto AQUALAS 2.0. El protocolo de actuación seguido para esta campaña de campo fue el mismo descrito en la primera sección del este bloque resumen. Además, las muestras halladas se analizaron utilizando las misma metodología que la descrita para la construcción del modelo de clasificación (gas de purga argón a 5 bar, secuencia de 50 pulso realizando tres repeticiones en zonas adyacentes y rango espectral de análisis de 350-550 nm).

Durante las dos jornadas de análisis se hallaron un gran número de objetos arqueológicos los cuales fueron clasificados de manera inequívoca en cada uno de los grupos que previamente se habían definido en el método. Los objetos se identificaron correctamente como cuatro aleaciones de bronce, ocho fragmentos de cerámica, siete piezas metálicas y cuatro mármoles. Entre ellas, los objetos formaban parte del material de defensa del barco, tales como cañones y balas para los mismos, así como piezas propias de la indumentaria de la tripulación como botones de chaquetas y hebillas de cinturón. En cuanto a los fragmentos cerámicos se cree su uso para contenedor de almacenaje tales como vasijas.

Tras la satisfactoria evaluación del equipo AQUALAS 2.0 con la nueva herramienta de clasificación se logra un paso más hacia delante permitiendo la adquisición de un conjunto coherente de datos del espectro que puede ser tratada por un software basado en el análisis lineal discriminante para asignar la identidad química del objeto. La información así recopilada proporciona valiosos datos sobre la identidad de naufragios localizados en aguas costeras.

Profundidad máxima de alcance con el sistema AQUALAS 2.0

Como se indica en la primera sección el equipo AQUALAS 2.0 se configuró para trabajar en dos modalidades de excitación, tanto en SP como MP. Con la configuración de MP se logró mejorar el rendimiento del instrumento en términos de energía de transmisión a través de la fibra óptica. Sin embargo, se entiende que la limitación analítica del instrumento en relación a la profundidad máxima de trabajo estará sujeta al porcentaje de transmisión de energía en función de la longitud de la fibra óptica. Por tanto, se quiso conocer de forma semi-experimental la profundidad máxima de análisis que se lograría con este sistema experimental. Esta estimación fue posible calcularla atendiendo a las especificaciones de la fibra óptica utilizada, la transmisión teórica para 1m de fibra para la radiación 1064 nm es del 99.4%. De forma teórica es posible esbozar una tendencia de porcentaje de transmisión para una irradiancia máxima umbral de 2.5 GW/ cm^2. Así como de forma experimental pudo calcularse la curva de tendencia de atenuación para los valores de transmisión medido experimentalmente a 1, 5, 10 y 55 metros de longitud de la fibra. Por otro lado, conociendo la irradiancia umbral de formación del plasma para el objeto de interés, fue posible estimar la profundidad máxima a la que puede desarrollarse el análisis de esa muestra resultando de un valor de 260 m para muestras de origen metálico y de 130 m para aquellas de carácter cerámico o rocoso. Sin embargo, debe anotarse que para tal estudio no se tuvo en cuenta la atenuación de la luz de plasma que regresa a través de la misma fibra óptica y por tanto en la práctica la distancia antes mencionada se reduciría aún más.

Bloque 2: Aproximación de la técnica LIBS para la identificación de materiales sólidos sumergidos basado en una configuración de análisis a distancia.

Como se ha descrito hasta este punto, el empleo de un equipo remoto basado en el guiado del haz láser por fibra óptica, como es el prototipo propuesto por la Universidad de Málaga, es una alternativa novedosa y eficaz para resolver el problema analítico de determinación de objetos arqueológicos sumergidos sin extraerlos de su entorno. Sin embargo, la profundidad máxima que se podría alcanzar para llevar a cabo el análisis está limitada a la energía láser de entrada a la fibra óptica y al porcentaje de la transmisión de la luz. No obstante, LIBS no tiene límites en el horizonte y gracias a los continuos avances en la reducción del tamaño y peso de los componentes; junto con el aumento de la capacidad tecnológica de láser, espectrógrafos y detectores permite desarrollar vehículos operados a distancia que integran el sistema LIBS sumergible con acceso a distancia a la muestra a través del agua (standoff). Esta alternativa es muy prometedora desde el punto de vista de la investigación del océano a alta profundidad aunque presenta una alta complejidad en el diseño y manejo del equipo y hasta la investigación adicional requerida. En este sentido, la validación previa en laboratorio de LIBS como técnica viable para la detección química de objetos arqueológicos sumergidos sometidos a altas presión se hace primordial. Esto es así debido a la importante cantidad de tiempo necesario para el desarrollo de estos nuevos sensores capaces de trabajar en el contexto oceánico.

Es importante mencionar que bajo las condiciones de trabajo de una configuración de análisis a distancia el haz láser interacciona con la muestra a través de una interfase líquida. Este tipo de análisis LIBS a 1 bar de presión ha sido estudiado ampliamente y se conoce que los principales mecanismos responsables de la formación de plasma son los mismos que ocurren durante la ablación en gas. Brevemente se indica que la secuencia del proceso se inicia con la ablación del material por el láser y la siguiente formación del plasma inducido por el mismo. Debido a su rápida expansión se genera una onda de choque (SW). Si debe tenerse en cuenta que las diferencias entre la formación de plasma en un entorno gaseoso y dentro de un líquido están relacionadas con el confinamiento del plasma y la producción del efecto de cavitación. Éste último es debido a que el plasma inducido por láser con una alta temperatura transfiere una cantidad significativa de su energía interna al líquido circundante, por lo tanto una capa de vapor se produce en todo el volumen de plasma. La capa de vapor se convierte en una burbuja de cavitación que se expande y colapsa en una escala de tiempo del orden de cientos de microsegundos. Por consiguiente, debido al confinamiento del plasma por el medio líquido casi incompresible y a la rápida transferencia de su energía al líquido circundante hacen que los plasmas en líquido sean más pequeños que los generados en gas. Como consecuencia, su vida útil es significativamente más corta. En cuanto a la capacidad analítica LIBS en agua está limitada a esta fuerte interacción entre el plasma y el líquido circundante que hace que la respuesta del

espectro de emisión aparezca dominada por la radiación del continuo. Sin embargo la configuración de excitación con doble pulso se presenta como una alternativa para mejorar la intensidad de emisión. Brevemente, en este caso, el primer pulso láser produce la burbuja de cavitación mientras que el segundo pulso ablaciona la muestra y re-excita el plasma dentro de la burbuja logrando una mayor emisión del plasma.

En base a estos conocimientos, en este bloque de investigación se pretendió evaluar la viabilidad de LIBS para un análisis en agua a distancia utilizando una configuración de excitación de doble pulso donde se persiguió alcanzar una profundidad de análisis superior a los 50 m. En este caso, la presión hidrostática del medio inducida por la profundidad jugará un papel importante en la formación del plasma, en la generación de la burbuja de cavitación y consecuentemente en la respuesta LIBS. Todo ello junto con la evaluación de distintos parámetros operacionales como la longitud de onda del láser, la energía de los pulsos, la configuración de colección, entre otros, fue evaluado y se detallará en los apartados siguientes. Aunque previamente para desarrollar esta investigación fue necesario simular las condiciones reales de análisis en el contexto de aguas profundas. Con este propósito, en primera instancia se diseñó y construyó una cámara para inducir presiones elevadas hasta el orden de 400 bares.

Diseño y construcción de una cámara de simulación de altas presiones

Para evaluar en laboratorio el potencial de LIBS en el entorno de profundidad oceánica se diseñó y construyó una cámara de simulación de altas presiones. Para su construcción el material seleccionado fue el acero inoxidable. Este material fue elegido para evitar el deterioro por el agua y por su excelente resistencia a la presión y el desgaste. Sus dimensiones son 130 x 135x 115 mm y tiene una capacidad de 80 ml. El prototipo, es de forma cilíndrica y se compone de siete puertos: cinco laterales, uno superior y otro situado en parte posterior de la cámara. El número de accesos diseñados fue elegido con el fin de aumentar la versatilidad para el sistema de configuración de excitación y colección, así como para proporcionar un acceso visual amplio del interior de la cámara. A continuación se describe brevemente los componentes y la función de los distintos puertos de acceso.

- **Puertos laterales**

Cuatro de los cinco puertos laterales se destinaron a la función de enfoque del haz láser sobre la muestra y a la colección de la señal LIBS así como a la visualización del interior de la cámara. El sellado y la estanqueidad del agua en estos 4 puertos se resolvió con un sistema formado por una junta tórica - ventana de zafiro - junta tórica, todo ello ajustado con una pieza cilíndrica de cierre con 6 tornillos. Además se debe indicar que esta última pieza cilíndrica está perforada en la parte central para permitir el acceso óptico a través de la ventana de zafiro.

El restante puerto lateral se diseñó como acceso de entrada del agua a la cámara. Éste es conectado a través de una canalización de acero inoxidable a una bomba que se encarga de suministrar el agua hacia el interior de la cámara. En este caso el sistema de cierre del puerto está constituido por una

junta tórica y un cilindro de apriete. La perforación central de la pieza cilíndrica fue torneada para conectar con una unión de conector 1/4" BSP con una tuerca hexagonal con la canalización metálica.

- **Puerto trasero**

La salida del agua de la cámara se lleva a cabo por el puerto trasero de ésta. Este puerto tiene dos funciones principales. En primer lugar la función de seguridad, desde el que se controla el exceso de presión dentro de la cámara por una limitadora de presión conectada en la salida del puerto. En segundo lugar, junto con la entrada de agua, permite la circulación del agua que hace más fácil la eliminación de las partículas generadas después de la ablación con el láser.

- **Puerto superior**

Este se utiliza como sistema de porta-muestra. En el cilindro de cierre de la cámara, en la parte interna, se ajusta una pieza de acero inoxidable torneada cuya función es posicionar la muestra en su interior. Además esta pieza está ajustada en un sistema de guía que permite desplazarse en la posición axial en un rango de 20 mm, esto es una gran ventaja para ajustar la posición focal. El sellado y estanqueidad en este puerto se consigue de nuevo utilizando una junta y un cilindro de cierre.

Una vez diseñada y construida la cámara, algunos parámetros relacionados con el control y manejo de la misma fueron evaluados. Un factor clave que influye en las mediciones es la atenuación de la luz a través del medio de propagación, en nuestro caso, el agua y las ventanas de zafiro. Por otra parte, hay que señalar que la distancia focal de una lente en agua se hace más largo que en el aire, debido al mayor índice de refracción de éste último. Por lo tanto, fue necesaria una evaluación previa de las condiciones de enfoque para resolver el factor geométrico. Para llevar a cabo estos experimentos se construyó un recipiente de metacrilato; sus dimensiones son de 160 mm de largo, 180 mm de ancho y 110 mm de altura.

Como se indica, debido a la absorción del agua, sólo una fracción de la energía incidente llega a la superficie de la muestra. Aunque, bajo nuestras condiciones experimentales y con una longitud de onda de 532 nm, solamente una atenuación de un 2% se midió en un camino óptico de agua de 14 cm. Sin embargo; si se consideran las componentes ópticas, la atenuación alcanza un valor del 30%. La radiación 532 nm en promedio resultó de una atenuación de 2,14% por centímetro de camino óptico (considerando los componentes ópticos y la ruta bajo el agua), o en otras palabras, -0.11 dB cm^{-1}. Además, con el objetivo de seleccionar la longitud de onda que menor atenuación produzca, este experimento se llevó a cabo con la radiación láser a 1064 nm. Si ambos resultados se comparan, a 532 nm el valor de atenuación es relativamente bajo en contraste con la correspondiente a 1064 nm, que fue de -0.66 dB cm^{-1}. Bajo estas circunstancias se decidió trabajar a 532 nm en futuros experimentos.

El cambio que se produce de la distancia focal en agua también se consideró ya que ésta se hace mayor debido a un cambio en el índice de refracción del medio y en consecuencia se requiere un ajuste

cuidadoso de las condiciones de foco del haz láser en función de la trayectoria interior de la cámara. Se evaluó un set de lente con una distancia focal nominal en aire comprendida entre 30 y 150 mm. Como era de esperar en agua aumentó las respectivas distancias de enfoque. Tras este estudio y considerando la trayectoria óptica en el interior de la cámara (distancia entre la ventana de zafiro hasta la posición central donde se posiciona el porta-muestra, 95 mm), se decidió utilizar una lente plano convexa con una distancia focal teoria de 75 mm.

Por último, debe indicarse que la cámara de propio diseño se sometió a un test de certificación por personal cualificado resultando apta para trabajar hasta una presión máxima de 400 bar de presión. Este certificado puede comprobarse dirigiéndose al anexo 1.

- **Efecto de la presión hidrostática del medio:**

El trabajo presentado en esta sección, es el resultado de una estancia de investigación pre-doctoral llevada a cabo en el laboratorio del *Consiglio Nazionalle del Ricerche-Istituto di Nanotecnologia* (CNR-NANOTEC) y de la *Università degli studi di Bari Aldo Moro* (UNIBA) Italia; bajo la supervisión del Prof. Alessandro De Giacomo.

- **En el proceso de ablación y las características físicas de la pluma del plasma.**

Con el fin de evaluar el efecto de la presión hidrostática del agua sobre las características físicas del plasma generado por un pulso láser de 270 mJ sobre una muestra de aluminio, se tomaron imágenes usando la técnica de shadowgrafía en diferentes momentos de la irradiación con láser. Las imágenes fueron adquiridas en los primeros microsegundos después del pulso láser realizándose el experimento bajo tres condiciones de presión diferentes 30, 90 y 120 bar. Las imágenes mostraron claramente un efecto de confinamiento en el plasma debido a la presión de líquido. Sin embargo, se observó un menor confinamiento en el plasma en el caso de 120 bar, si es comparado con el producido a 90 bar. Este hecho pudo atribuirse, como consecuencia del empuje del plasma en expansión, a que el líquido circundante puede estar en condiciones supercríticas. En esta condición, el agua se caracteriza por tener una menor viscosidad y baja tensión superficial. Por esta razón parece menos confinado el plasma a 120 bar.

Por otro lado, aunque se observó que la presión externa afecta notablemente a la dinámica del plasma inducido por láser, el proceso de ablación no se espera que sea dependiente de ésta. Esto es así, ya que la presión inicial del plasma es del orden de los Mbar y en consecuencia en el rango de presión en el que se realizó este experimento cabría esperar que fuese despreciable el efecto de la presión externa. Además, se observó que la SW (que es causada por la rápida expansión del material ablacionado con láser dentro de una geometría confinada) presentó una velocidad de expansión y una forma geométrica similar en todo el rango de presión estudiada, confirman que el empuje inicial debido al desglose es casi el mismo en todas las presiones externas investigadas.

- **En la expansión de la burbuja de cavitación.**

Como se comentó al inicio, el plasma inducido por láser libera energía al líquido circundante y genera una fina capa de vapor en la frontera del plasma que se convierte en una burbuja de cavitación. Se estudió, con fines comparativos, las dimensiones y la forma de la burbuja de vapor que se forma después del primer pulso láser usando diferentes valores de presión hidrostática del medio con la misma configuración experimental. Se utilizó la técnica de shadowgrafía adquiriendo imágenes a diferentes tiempos de retardo. En primer lugar el estudio se realizó a presión de 1bar observándose que la evolución temporal del tamaño de la burbuja se caracteriza por una etapa de expansión, un máximo y una etapa de compresión. Se obtuvo el tamaño máximo de la burbuja a 250 μs donde presentó una geometría de hemisferio. A partir de este punto, ya que la máxima presión de expansión dentro de la burbuja es menor que la externa, la burbuja empieza a reducirse. Como consecuencia, el tamaño de la burbuja va disminuyendo hasta 950 μs.

A continuación, se fue aumentando la presión hidrostática del medio y se estudió la evolución temporal de la burbuja de cavitación como función de la presión externa (30, 90 y 120 bar). Los resultados de las imágenes de shadowgrafía mostraron que el tamaño de la burbuja observada en un tiempo de retardo más largo fue significativamente más pequeño al aumentar la presión del agua. Además se detectó que en la fase inicial, la velocidad de expansión de ésta fue similar al menos a 30 y 90 bar donde se pudo vislumbrar perfectamente la burbuja. Esto indicó que en la primera fase de expansión el efecto de la presión hidrostática fue insignificante. A partir de este punto, la evolución del proceso de expansión dinámica divergió para las diferentes presiones. La expansión máxima de la burbuja se produjo a los 15, 10 y 7 μs para 30, 90 y 120 bar, respectivamente. Así como el colapso a los 28, 17 y 9 μs. En este sentido, se detectó que un aumento de la presión hidrostática influye en la expansión y enfriamiento de la burbuja de vapor, que conduce a una disminución del tamaño de la burbuja y la vida útil. Respecto a la forma de la burbuja, esta tendió a distorsionarse en la dirección *x* e *y* asumiendo una forma elipsoidal.

Por otra parte, se observó una burbuja secundaria justo después del colapso como consecuencia al rápido aumento de la temperatura y la presión interna de la burbuja. La forma de esta segunda burbuja de cavitación cambió nuevamente, ya que ahora está constituida tanto por el vapor de agua como por parte de las nanopartículas producidas por la ablación láser expulsadas en líquido. Además, con el aumento de la presión del medio la velocidad de colapso también aumentó conduciendo a una re-expansión de la burbuja más pronunciada y se observó un desplazamiento de la burbuja con respecto a la posición de la muestra.

- **En el doble pulso en LIBS.**

En base a esta descripción general, para la optimización del retraso entre pulso en una configuración de excitación de DP en agua debían esperarse mejores resultados para un retraso en el cual la burbuja inducida por el primer pulso esté en su fase de máxima expansión donde la condiciones de presión serán más favorables. Además, como fue observado y contrastado en bibliografía, como consecuencia de la

formación de nanopartículas (NP) con el primer pulso, durante el comienzo de la expansión de la burbuja y en la fase de colapso (momento en el cual las NPs se concentran en frente de la muestra), una parte consistente del segundo pulso láser interactúa con este material generando un plasma secundario. Este plasma se produce a una cierta distancia de la muestra y previene parcialmente la ablación de la misma por el segundo pulso. Por el contrario en el máximo de expansión de la burbuja, siendo el volumen de la burbuja más grande, la concentración de NPs alcanzará su mínimo produciéndose en menor medida este efecto. Por tanto, especialmente durante DP-LIBS a alta presión, cuando el volumen de la burbuja es menor, el efecto apantallante de las partículas producidas por el primer pulso debe ser considerado con precaución en la optimización de la señal LIBS.

La evaluación de retraso entre pulsos óptimo para diferentes valores de presión hidrostática del medio (30, 90 y 120 bar) se llevó a cabo utilizando una energía de 150 mJ y 270 mJ para el primer y segundo pulso, respectivamente. El área del pico de emisión a 396.15 nm en una muestra de aluminio se evaluó en función del retardo entre pulso en un rango comprendido entre 5 y 40 μs. La tendencia de esta área de la línea de emisión a su vez se comparó con la dinámica de la burbuja de cavitación en el mismo rango temporal. Los resultados indicaron que la intensidad máxima de emisión en cada caso se alcanzó para el retardo entre pulso que correspondían con la máxima expansión de la burbuja de cavitación. Sin embargo, a medida que aumentó la presión del medio la intensidad de emisión también se vio disminuida.

Por otro lado a la vista de los espectros resultantes es interesante mencionar que, en el rango espectral estudiado (350-420 nm), mientras las líneas de emisión atómica aparecen absorbidas en el continuo, las líneas iónicas mostraron un carácter típico a los espectros de emisión óptica. Estos resultados pudieron ser debidos a dos razones: I) el predominio del continuo en los espectros puede atribuirse al efecto de alta densidad de Debye Hückel debido al alto valor de la densidad del número de electrones en la etapa inicial de la expansión del plasma. En esta condición la recombinación radiactiva es la principal fuente de radiación en el plasma y en el caso específico del medio líquido de alta presión, como consecuencia del fuerte efecto de confinamiento, este fenómeno puede ser muy marcado. Sin embargo este efecto sobre la limitación de nivel depende de la energía de ionización de las especies. En el caso de los iones, ya que tienen mucha mayor energía de ionización que los átomos, se pueden ver menos afectadas por los efectos de alta densidad. II) es razonable suponer que, como consecuencia de la disminución de la densidad del número de electrones a lo largo de los ejes de propagación, en la región externa del plasma la limitación de Debye-Hückel en los niveles electrónicos no se produce, sin embargo se podría observar una autoabsorción en el continuo de emisión en esta zona periférica. Esto es causado por una transferencia rápida de energía térmica desde el plasma al medio ambiente circundante que hace que la zona periférica se enfríe antes que el interior del plasma. En esta situación se puede producir una absorción de la radiación emitida del núcleo del plasma por las especies de la periferia. Estas observaciones podrían sugerir que los iones de emisión provienen de la parte interna del plasma y por ello no presenta esa absorción en la radiación de continuo mientras que las transiciones atómicas aparecen como picos absorbidos en el continuo. Por otro lado, se observó que la cantidad de información espectral disminuye al aumentar la presión de trabajo. De hecho, a

altas presiones la burbuja es incapaz de alcanzar la presión de saturación porque la alta presión externa hace que el vapor dentro de la burbuja de cavitación se condense. Esta consideración sugiere que el plasma es cada vez más confinado a medida que aumenta la presión del líquido y, en consecuencia, que la principal contribución a los espectros es la radiación continuo. Los efectos de recombinación y alta densidad se vuelven tan severos con una presión creciente que a 120 bar incluso los picos iónicos desaparecen del espectro.

Evaluación del efecto de la presión hidrostática del medio sobre parámetros operacionales en el análisis LIBS bajo agua

En esta sección experimental se utilizó una lámina de hierro como muestra de análisis. Se establecieron las condiciones óptimas de retraso de adquisición (300 ns), la ventana de adquisición de datos (8 µs) así como el retraso entre pulsos (125 µs y 11 µs; a 1 bar y 25 bar respectivamente).

- **Energía de los pulsos láser**

El efecto de la energía de ambos pulsos láser se evaluó con el objetivo de obtener la mayor intensidad de emisión en el caso de una muestra de hierro sumergida en agua. El experimento se realizó a 1 bar de presión con la intención de simplificar el estudio. En primer lugar la intensidad de emisión de Fe (I) a 330.57 nm se midió variando la energía del primer pulso láser (E_1) en un rango comprendido entre 36 y 160 mJ manteniendo constante la energía del segundo pulso láser (E_2) a 215 mJ. Los resultados mostraron que la evolución de la relación señal fondo (SBR) en función del retraso entre pulso, en rango comprendido 0 y 500 µs, fue dependiente de la energía del primer pulso. Se obtuvo una mayor SBR en aquellos casos donde la E_1 fue mayor. Además se detectó que cuando la mayor E_1 se aplica, el intervalo de valores de retraso entre pulsos donde se observan un mayor valor de SBR es más amplio. Estos resultados pueden ser debidos a que un primer plasma más energético se induce a un mayor valor de E_1 así como se induciría una burbuja de cavitación con un tiempo de vida más larga en la cual la expansión máxima de la burbuja se mantiene más tiempo.

Por otro lado, la intensidad de emisión de Fe (I) a 330.57 nm se midió variando E_2 en un rango comprendido entre 7 y 215 mJ manteniendo constante la energía de E_1 a 60 mJ. En este caso, un incremento en la intensidad de emisión se observó hasta alcanzar un valor de E_2 de 50 mJ. Por encima de éste se disminuye gradualmente la intensidad de Fe. Este hecho, fue asociado a un efecto de *apantallamiento* del propio plasma.

Tras los resultados expuestos se pudo concluir que la mejor condición de energía para la configuración de impulsos duales está sometida a dos aspectos: I) la necesidad de utilizar un retardo entre pulsos más largo, en cuyo caso E_1 debe ser la máxima energía posible. II) el efecto de apantallamiento del plasma, E_2 debe ser superior a un cierto valor umbral energético mínimo (nuestro experimento E_2 7 mJ a 1 bar) para observar la mejora del DP pero sin rebasar el valor umbral óptimo, en nuestro caso 50 mJ.

- **Configuración de colección**

En esta sección se estudió la configuración de colección en la cual la señal de emisión de Fe (I) a 330.57 nm recogida es más intensa. Se seleccionaron tres configuraciones de trabajo: coaxial a la trayectoria de excitación, ortogonal y a 45º. Los resultados indicaron que la mayor intensidad colectada fue con una configuración en coaxial. Este hecho pudo ser debido a que una sección menor de la luz de emisión del plasma se recoge a 45º y 90º; sin embargo, la totalidad del plasma se enfoca en la fibra óptica usando una configuración de colección en coaxial,

Este experimento se realizó también aumentando la E_2 a 215 mJ. En este caso la configuración de colección a 45º fue con la que se obtuvo el mayor valor de intensidad de emisión, aunque no consiguió igualar la intensidad alcanzada en la configuración coaxial a menos E_2. Estos resultados pudieron ser debidos al efecto de apantallamiento del plasma siendo más acusado para la colección en coaxial.

Pudo concluirse que la mejor señal de LIBS se alcanza utilizando un bajo valor energético para E_2 y una configuración colección coaxial.

- **Influencia de la temperatura del agua sobre la señal LIBS**

La influencia de la temperatura del agua sobre la intensidad de emisión en los espectros LIBS se evaluó en el rango comprendido entre 5 a 30 ºC. Se observó una disminución de la intensidad registrada con el descenso de la temperatura. Este resultado pudo ser atribuido al hecho de que las características del plasma generado con una configuración de DP-LIBS son fuertemente dependientes de la evolución de las burbujas de cavitación inducida por el primer pulso. De hecho, es plausible que las variaciones en las propiedades del agua afectarán a la dinámica de cavitación y expansión de burbujas y, en consecuencia, a la emisión de señal. Con el descenso de la temperatura la densidad y viscosidad del agua aumenta y por tanto esto pudo inducir una ralentización en la expansión de la burbuja y aumento en el tiempo necesario para alcanzar su radio máximo. Por tanto, a un retardo entre pulsos fijo el segundo impulso no interactúa con el sólido en la expansión máxima de la burbuja por lo que la mejora de la señal debida a DP-LIBS pudo ser menos efectiva. Por otro lado, esta disminución en la intensidad observada pudo ser atribuida en cierta medida también al costo energético invertido para calentar la muestra siendo más acusado con el descenso de la temperatura del agua. A pesar del decrecimiento en intensidad, los resultados obtenidos a 25 bar son bastante prometedores y sugieren la posibilidad de análisis de LIBS al menos a 250 metros de profundidad ya que a esta presión la temperatura del agua es de alrededor de 20 ºC.

- **Influencia de la alta presión en la señal LIBS. Efecto matriz.**

El objetivo que se persiguió en esta sección experimental fue evaluar la influencia de la presión hidrostática del medio sobre el comportamiento de las diferentes especies que constituyen el plasma. Para ello se seleccionaron dos muestras de bronces las cuales fueron sometidas a una presión comprendida entre 1 a 60 bar. En ambos bronces las líneas de emisión utilizadas fueron Cu (521.82 nm), Pb (405.78 nm) y Zn

(481.05 nm). Tras la adquisición de los espectros se pudieron hacer varias observaciones. En primer lugar un ensanchamiento en las líneas de emisión se detectó a medida que la presión del medio incrementaba. Este hecho pudo ser una consecuencia del efecto de confinamiento del plasma y las colisiones que se producen en el volumen confinado cerca de la muestra. Por otro lado, se estudió el retraso entre pulsos óptimo donde la intensidad de emisión es máxima para los distintos valores de presión. Se observó que para las distintas especies del plasma las condiciones de retraso entre pulso eran las misma. Sin embargo, es importante señalar que a medida que se aumentó la presión del medio la intensidad de emisión de Zn y Pb fue aumentando con respecto al Cu. Este comportamiento fue atribuido a una *ablación preferencia*l (efecto matriz) de la muestra debida a un posible efecto apantallante del plasma quedando éste enriquecido en aquellas especies más volátiles. Con el incremento de la presión del medio, la densidad de electrones aumenta con el confinamiento del plasma y en consecuencia el efecto apantallante es más acusado. Bajo estas circunstancias, la energía del láser que llega a la muestra es atenuada observándose un plasma de menor temperatura. Este hecho indica que el plasma es menos estequiométrico favoreciéndose por tanto una ablación preferencial en las especies más volátiles tales como el Pb y el Zn.

Los resultados obtenidos en este segundo bloque de tesis en el que se realizó una evaluación preliminar sobre la operatividad de la técnica LIBS para realizar análisis a distancia en muestras sólidas sumergidas en agua fueron bastante prometedores. Estos sugieren la posibilidad de integrar la técnica en un vehículo operado remotamente (ROV) abriendo una puerta en la investigación del patrimonio cultural sumergido a altas profundidades. Sin embargo, en esta Tesis doctoral solo se aporta un pequeño grano de arena, aún queda una gran labor de investigación futura en esta área de aplicación de LIBS. El potencial de la técnica podría continuar evaluándose con otras posibles configuraciones de excitación como por ejemplo en el uso de multipulsos; o incluso estudiar la posibilidad de aumentar la distancia de análisis entre la muestra y el sistema LIBS, a la ya presentada en esta tesis.

Objectives

Nowadays, the characterisation of underwater cultural heritage has become one of the most interesting areas of archaeology. The Mediterranean Sea is rich in archaeological wrecks due to storms, accidents and naval battles since prehistoric times. Only in the south of Spain, several hundreds of underwater archaeological sites are localized and distributed along the Andalusian coast. The historical and cultural values and the significant economic impact of these findings make the existence of control mechanisms necessary to assist in the preservation of the cultural heritage.

Chemical information extracted from raw materials used in ancient times and the technology employed in the production of archeological objects turns fundamental for a better understanding of historic events. Underwater sites are dynamic and susceptible to change due to marine environment in such a way that artefacts and structures may be uncovered beneath sediments, chemically altered or even destroyed under the severe conditions of the seabed. Discovery of pieces such as amphoras and cannons in their archeological context could indicate the age and nationality of the shipwreck. Nevertheless, sometimes extracting the archeological material from the marine environment is not practical due to the size of the sample, or is not permitted by the legislation or preservation practices. In fact, the *United Nations Educational, Scientific and Cultural Organization* (UNESCO) in article 2 point 5 of the Convention for the protection of underwater cultural heritage considers the in-situ conservation of Cultural Heritage as "*the first option before allowing or engaging in any activities directed at this heritage*". In these cases, the in-situ analysis (in the same place where the archaeological materials were discovered) turns into the only alternative to obtain the chemical composition information of the submerged archaeological object.

Nowadays, laser-induced breakdown spectroscopy (LIBS) provides a new solution for this problem since it combines many of the required features for this application including multi-elemental information, no sample preparation, unlimited range of material capability and real time analysis. In fact, for oceanography, it could be possible to use several alternatives/configurations: i) a remote-LIBS instrument based on the transmission of laser radiation using an optical fiber cable; and ii) a standoff-LIBS instrument that involves the delivery of a focused laser pulse toward the distant target through the aqueous media and then the transmission of the light emitted by the laser-induced plasma back to the detection system. Both alternatives are highly challenging and will be described in detail along this Doctoral Thesis. According to this, the present memory is divided in two main parts: Part I (Chapters 4-6) that focuses on the alternative of a remote-LIBS system capable of perform LIBS analysis in real archaeological sites up to 50 meters depth; and Part II (Chapters 7-8) that evaluates (in laboratory) the feasibility of a standoff instrument for LIBS analysis in the deep ocean, paying special attention to the influence of the oceanic pressure on signal emission.

The overall objectives for this Doctoral Thesis are the following:

- To expand the application range of LIBS to the inspection, identification and diagnosis of pieces located in underwater archaeological sites.
- To increase knowledge of underwater LIBS measurement.

Part I. A remote LIBS instrument based on a fiber optic cable to deliver the laser beam energy will be developed and adapted to the marine environment. This approach gives the possibility of a LIBS analysis in situations where the sample of interest is not directly accessible. In fact, in a range of 50 m deep we could cover most of the underwater archeological sites of practical interest. The specific objectives for this Part of the Doctoral Thesis are:

- To evaluate the stability and robustness, as well as the adaptation to marine environment of a remote LIBS instrument based on the transmission of laser radiation through an optical fiber cable.
- To optimize the operational conditions required to obtain, in extreme conditions, useful analytical data to identify and preserve the submerged culture heritage.
- To design, build and evaluate a discriminating method that allows the sorting of the most common objects that may be find in a shipwreck.
- Subsea spectral identification of shipwreck objects using the remote LIBS instrument.

Part II. For an underwater application, a LIBS sensor capable of performing real time analysis at a distance from the sample of interest would be a significant advancement over current oceanographic technology. The main objective of this Part is to evaluate the feasibility to design, in a space of reduced dimensions, a standoff LIBS (ST-LIBS) system to analyze the samples of interest at different depths. The specific objectives in this Part are:

- To design and build a high-pressure chamber that allows to simulate in laboratory the deep ocean conditions.
- To explore the effect of hydrostatic pressure on fundamental aspect for plasma formation and phenomena post-plasma formation on submerged solid samples.
- To evaluate the double pulse LIBS configuration as a possibility for the analysis of submerged solid samples.
- To study the effect of hydrostatic pressure on LIBS signal.
- To check and optimize the operational parameters such as wavelength, energy pulses and collection geometry using DP-LIBS on submerged solid samples.

Chapter 1. Underwater archaeology

1. What is underwater archaeology?

Historically, the first attempts of adaptation to the underwater medium can be traced to around 3.500 years ago. Interest in this medium arises in parallel to the eagerness to recover valuable objects, ship repairs, submarine warfare or fishing and gathering.

Etymologically, archaeology comes from the Greek "*archayus*" and "*logo*", treatise or science of antiquity. Within historic and cultural heritage, which refers to the remains and relics of humanity's past, archaeological heritage is defined, in short, *as the material cultural elements of past eras of human beings*, the study of which will allow us to know the distant past. Currently, its specific character as a historical science is categorised as part of history, a humanistic science par excellence with the same standing as physics or chemistry enjoy in the field of natural sciences [1].

Scientifically and in terms of methodology there is no difference between land and underwater, submarine, maritime or nautical archaeology… however the study objective of each of these "branches" will differ with regard to the origin of archaeological structures or materials: underwater (saltwater and freshwater), submarine (only saltwater), nautical (man-made instruments and boats, whatever their origin) or maritime (which includes all related cultural samples, from ethnographic traditions, artistic representations, architecture, etc.). Water as a physical medium will chemically and biologically affect different archaeological objects in different ways to how they are affected on land, affecting both their development over the centuries and their recovery and future conservation. And, of course, it involves adaptation to a different medium for the archaeologist, who will require specific means and techniques to access and work in the water.

2. Importance of underwater cultural heritage

Nowadays, the characterisation of underwater cultural heritage has become one of the most interesting areas of archaeology. The reason for this is the sheer quantity of historical information contained in archaeological remains that have sunk to the depths of seas and oceans where most of these sites are found, as well as in other locations such as rivers, lakes and swamps. Archaeologists hope not only to find the remains of sunk ships (shipwrecks), but can also find remains of other civilisations (buildings, utensils, ceramics, etc.) that have been covered by water as the years have passed.

Each archaeological site is an open door to the past. Their location, in combination with the documentary records of the time and their identification, will allow us to know, for example, what occurred with some of these vessels that had been reported missing while transporting valuable cargos or during battle. In addition to their historic and cultural value, we must also add the economic impact of these sites, both due to their tourist interest and because they are often valuable pieces for collectors on account of their age. The latter aspect is what makes them a continual target for treasure looters. The most accessible sites are usually looted by scuba divers who are unaware of the damage they are causing. However, of

more concern is the activity of treasure hunting organisations, which often have sophisticated technology to locate and plunder these underwater sites.

Land archaeological assets enjoy an extraordinarily effective legal protection system, being considered "public domain assets", and therefore are not subject to trade or private appropriation and by obligation are destined for public use. Underwater archaeological assets, on the other hand, have taken much longer to be protected in this way. They have traditionally been considered "hidden treasures" and they were governed by the rule of possession (they belonged to the people who found them). Fortunately, with the UNESCO Convention [2] on underwater heritage, which came into force in 2009, the vision was achieved of this heritage as assets of general interest to societies, States, Nations and the whole of Humanity. It sets out principles such as the prohibition of the commercial exploitation of underwater heritage and particularly the preference for "in situ" conservation of these types of archaeological remains.

In this context, we should mention the well-known case of the *American company Odyssey Marine Exploration*. In May 2007, the company announced the discovery of a shipwreck loaded with gold and silver coins, which was later discovered to be the Spanish warship *Nuestra Señora de las Mercedes.* It was sunk by a cannon shot from English ships near the coasts of the Algarve in Portugal at the Battle of Cape of St. Mary, on 5 October 1804. The American company brought the treasure to the surface in an act riddled with malicious attempts to avoid showing that it was from the Spanish frigate. As known, after intense months of legal conflicts, the authorities ruled in favour of Spain, making the company Odyssey return the loot and pay 1 million dollars to the Spanish State for legal costs. The coins, of little financial value but great archaeological importance, were returned to Spain on 25 February 2012. The great repercussion of this case at the national level was a turning point in the social awareness of the protection of underwater heritage, droving forward measures for the conservation, restoration and dissemination of these assets. This important work, supported by the Spanish ministry of culture, as well as guaranteeing compliance with the agreements of the UNESCO *Convention and the National Plan for the Protection of Underwater Archaeological Heritage*, is carried out by the following institutions [3] (see Figure 1):

- *Centro de Arqueología Subacuática de Cádiz (CAS)*
- *Museo Nacional de Arqueología Subacuática (ARQUA)*
- *Centre d'Arqueologia Subaquàtica de la Comunitat Valenciana (CASCV)*
- *Centre d'Arqueologia Subaquàtica de Catalunya (CASC)*
- *The Group of Research Excellence URBS. CONAI+D*

Figure 1. Spanish institutions responsible for the protection of underwater cultural heritage.

The work of these institutions is enabling the registration of hundreds of shipwrecks, which are objects of study framed against a rich historic diversity extending chronologically from the Neolithic settlement of *La Draga,* dated at 5200 BC, submerged in the Lake of Banyoles (Girona), to 19th century vessels such as the *Isabella*, an English brig shipwrecked due to a storm in 1855 at Benalmádena beach (Málaga) while it was transporting a shipment of marble sculptures from Genoa to India. There are also Phoenician ships such as those found at the beaches of Mazarrón and Bajo de la Campana (Murcia) [4], Greek ships located at Cala Sant Vicenç (Pollença, Mallorca) [5], and various Roman shipwrecks such as *Culip IV* and *VIII* (Girona) [6] or the *Bon Ferrer* shipwreck at La Vila Joiosa beach (Valencia) [7]. We must also remember the medieval ship *Culip VI*, among others.

This historic imprint on the Spanish coast is merely due to its outstanding geographic location as a passageway for innumerable commercial and military routes. Ancient and modern-day commercial and navigation routes have been determined by natural currents and winds that allow the use of sails, which encouraged visits to these coasts, particularly the areas of Levante and Andalucía, by the Greeks and Phoenicians from the 7th century BC. Later came the Carthaginians (from modern-day Tunisia), who would establish their capital in Quart-Hadast (Cartagena), conquered in 209 BC by the Roman Republic. During the 6th century AD, Spain's coasts were the protagonist in the entry of the Byzantine Empire, which again used the city of Cartagena as the capital of its empire. Another invasion, by the Muslims through northern Africa from the start of the 8th century AD until the 13th century, would lead Spain's history to the Reconquista (reconquest) of these territories by the Christian Kingdoms of Castilla and Aragón, the

beginning of the Spanish Empire and its subsequent expansion across all of Europe and the Conquest and Colonisation of the Americas and the Pacific. The various territorial modifications led to the Modern State, up to today.

In addition to this circulation of civilisation and the naval tradition in Spain, this great quantity of archaeological remains is no more than the result of accidents and storms, to a great extent augmented by the difficulty of the rocky terrain of the coast. As was the case, for example, with *El Triunfante*, a warship that fought against the French Republic and was shipwrecked on the Gulf of Roses (Girona) on 5 January 1795 amidst a terrifying storm. Another reason for ships sinking were the naval battles that they witnessed. One case to highlight is the Battle of Trafalgar, which took place on 21 October 1805 where almost fifteen ships of the French–Spanish coalition were sunk near Cape Trafalgar in battle against the British Navy. Some of these ships have been located on the coasts of Cádiz and studied; this is the case of *Bucentaure* [8], the flagship of the French-Spanish Navy, and *Fogueaux* [9].

Research at each of the underwater archaeological sites entails arduous work, not only due to a working environment that is hostile to humans, but also due to the difficulty of searching for and locating them. It is necessary to highlight that the reality of an underwater site is usually quite far removed from the idyllic image that a sunk ship might have at first sight. Typically, it is not even possible to distinguish between the remains of the site and the environment itself, since the remains eventually become integrated into the landscape due to the action of time and the continuous deposition of sediments, as we can observe in Figure 2. It is normal to find layers of limestone or iron deposits on the surface of the pieces. Limestone deposits originate mainly in the shells of molluscs that are deposited on the surface of objects, while iron is usually from the rust present in the object itself or in nearby iron objects. Therefore, it is not easy to visually discover a site only by diving in the vicinity.

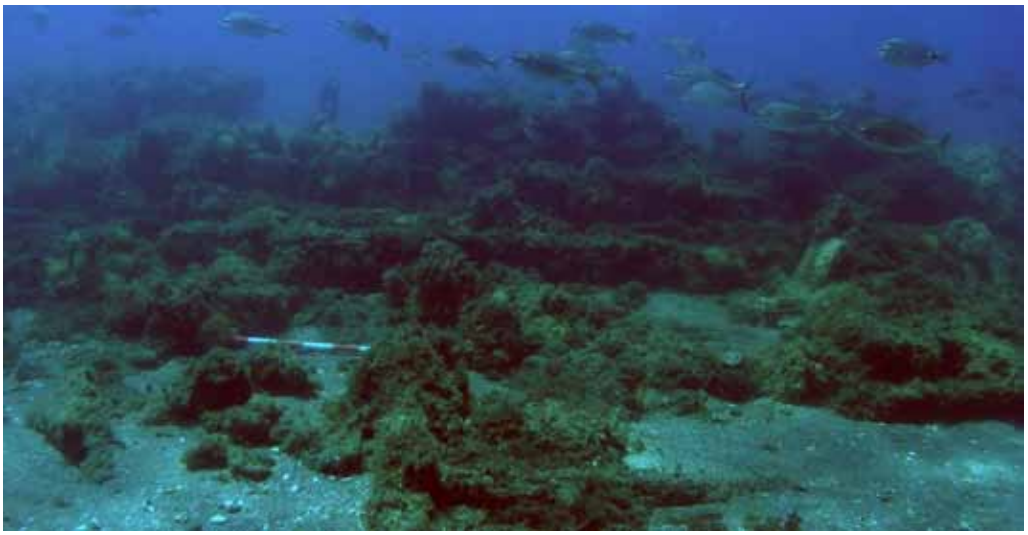

Figure 2. Underwater archaeological site located in San Pedro de Alcántara (Málaga).

3. Phases of research. Underwater prospecting and excavation

The scientific method that will govern this discipline will be the same as for all archaeology: the systematic study of elements belonging to the material culture of human beings throughout their existence and which, in this case and due to various circumstances, are saturated with water, submerged in seas, rivers, lakes, swamps, etc., affecting their chemical structure in a certain way.

This method consists of studying materials, architecture and zones through certain techniques that briefly list its different stages. These stages are: prior study and documenting, applying the hypothetico-deductive method based on previous knowledge; visual prospecting and geophysical methods to delineate areas of archaeological presence; excavation itself, which will require the support of auxiliary sciences such as topography, biology, geology, restoration, statistics, forensic medicine, soil analysis, etc. And finally the historical knowledge to undertake the work with guarantees of proper documentation and contextualisation.

Of course, the sea bed and water make these tasks extremely difficult, particularly the prior location of sites. As mentioned above, archaeological remains are integrated into the landscape due to the action of time and continuous deposition of sediments. Generally, search operations are carried out from a research boat that incorporates study equipment such as sonar detectors, magnetometers or remotely operated vehicles (ROV).

Prospecting

Following the location of the site and documentation on the historic event to be researched, the first stage of prospecting is undertaken with the intention of limiting the work area and locating at the bed the main centres of material accumulation. The aim of this first approach is to identify historical periods and the origin of remains.

This prospecting is visual and is carried out by diver archaeologists who create search routes with the help of guide threads, wires or ropes extended in straight single lines or distributed in parallel, forming streets, a similar system to that used in land prospecting of large sites (see Figure 3A). Another method would also be to hook a rope to a weight and, once stretched, turn it around this weight, which will act as an axis with the divers distributed along its length (known as a circular search: see Figure 3B), amongst other methods.

Excavation

The next stage will be the subdivision into grids of the whole study area defined in the prospecting and the start of its excavation, applying the *Harris method* [10] (see Figure 4). This method consists of adding a fourth dimension to the archaeological studies, the dimension of time, through the superimposing

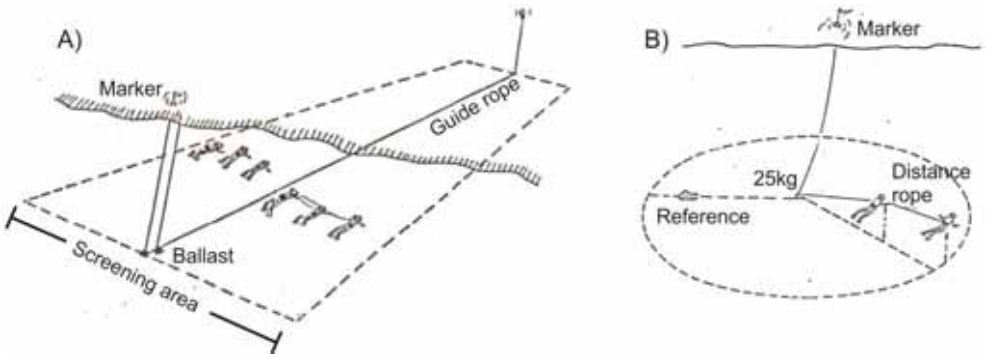

Figure 3. Traditional search scheme by A) linear and B) circular prospecting.

of layers. Each layer corresponds to a different age or period; therefore, we can date objects according to the layer where they are found. Furthermore, all of the grids are added, documenting each of its stages with archaeological field drawing, photography and techniques such as photogrammetry, where possible. The tools used will differ from those used on land, these being the classic pickaxes, shovels and hoes, which are replaced with suckers and suction hoses (see Figure 5) connected at the surface with a compressor that expels pressurised water or air. The materials thus extracted from the sea bed may be raised to the surface with the help of different sized balloons (see Figure 6).

The objects extracted require special treatment with the help of beds and moulds manufactured underwater from the piece itself using with products such as expanded polyurethane or epoxy resins to

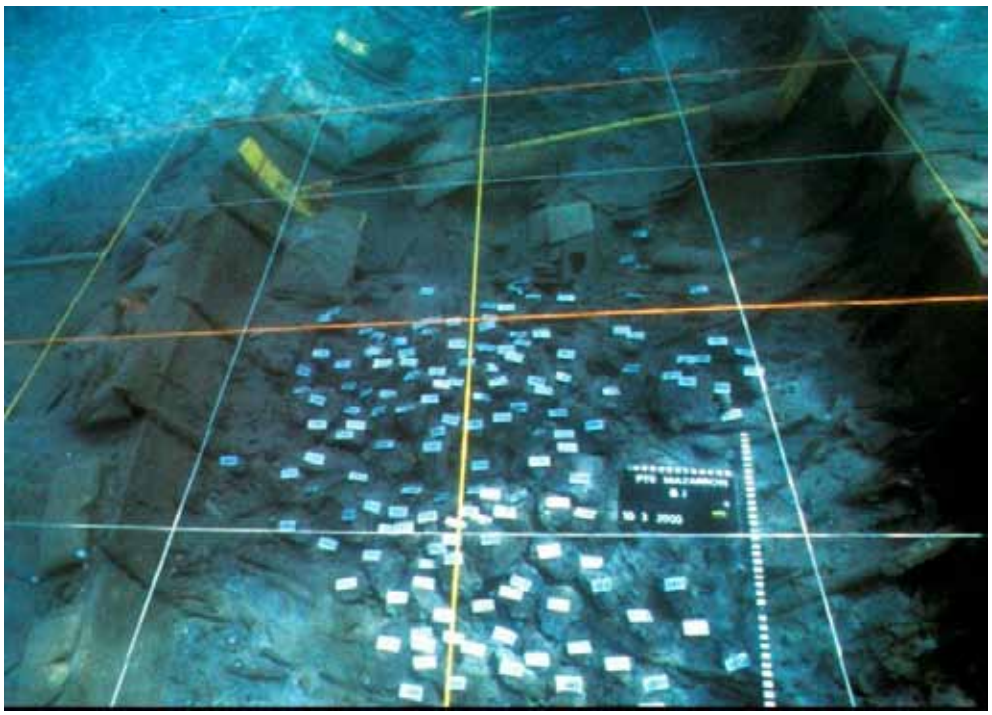

Figure 4. Archaeological grid. Provided by [11].

Figure 5. Excavation with suction hoses. Provided by [12].

manufacture moulds in-situ [13]. It is not possible to move an object from its site for logistic reasons, for example due to its size. At other times, the cause may originate in legislation or it may be contraindicated for the whole object. The materials present at the site itself are in chemical balance with their surroundings, preventing their deterioration. Out of water, they begin to rust due to oxygen in the air and electrolytes they may carry occluded inside them. This entails a serious problem for the researcher, since the information that they can obtain is simply through the visual analysis of the object.

Figure 6. Removing heavy load with balloon. Provided by [12].

4. Objective. In situ analysis of archaeological material submerged

The materials that we can find on an archaeological site can be very diverse in nature, from the skeleton of the boat to the crew's clothing. In general, the structure and the lining/sheathing usually appear (see Figure 7). There will also be pieces related to the goods that it transported, as well as pots and amphoras (see Figure 8). Navigation and pulley apparatus, as well as objects typical of life on board (see Figure 9). Defence equipment such as cannons and ammunition (see Figure 10).

Each piece of information learned about an archaeological object is another step towards knowing our own history. In this regard, knowledge about its chemical composition may be vital for locating the space-time origin or for understanding the technology used in its construction. An example of this is found in the analysis of ships' sheathing, since the base material has continually been modified over the centuries. The modality of covering the wooden hull boats with structural elements had already appeared since the time of the Phoenicians. However, in the 15th Century a change was observed in the base sheathing materials to lead introduced by Portuguese and Spanish manufacturers its use was extended until the 17th Century. Then in the 18 th Century, lead-based sheathing was substituted first by copper and then by copper-based alloys [14]. This also occurs with ships' defensive equipment, where the cannons may have been manufactured in iron or bronze according to the period of history. Likewise, the composition of cannonballs also provides very valuable information, with the analysis of their minor components indicating the type of smelting involved [15]. The elements of the pigments of the ceramic material can speak about how they were made.

Figure 7. Phoenician ship found in La Isla beach (Murcia). Photographic file ARQUA.

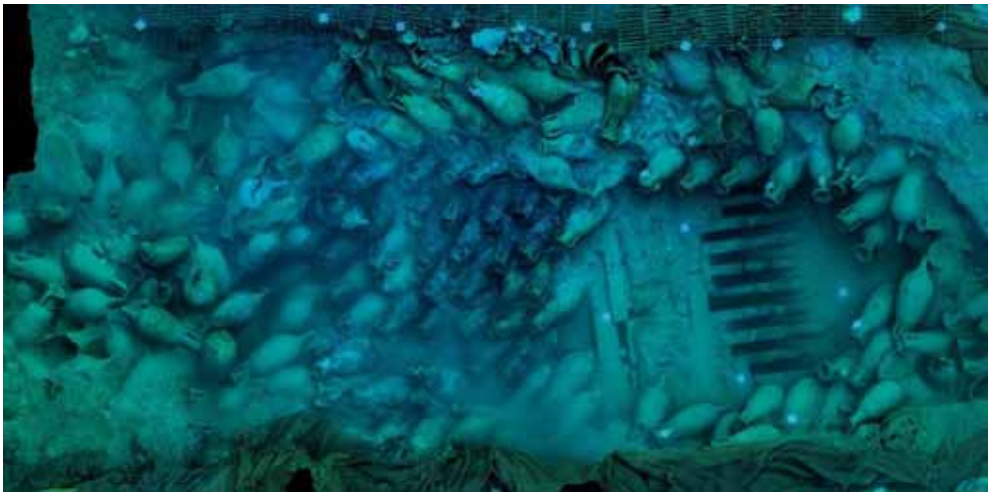

Figure 8. Roman amphorae from the shipwreck of Bou Ferrer in Vile Joiosa (Valencia). Photographic file Universidad de Alicante.

However, the classic analytical techniques usually require transferring the piece to the laboratory to study its composition. As we mentioned, this is not possible in many cases, with studies being limited exclusively to the in-situ analysis of objects. Furthermore, but just as important, it is necessary to bear in mind that the arrangement of the object in the context of the site can provide us with information about it. As such, the United Nations Educational, Scientific and Cultural Organization (UNESCO) [2] in its Convention for the protection of underwater cultural heritage considers the in-situ conservation of Cultural Heritage as "first option before allowing or engaging in any activities directed at this heritage".

Figure 9. Buttons and buckles from the shipwreck of San Pedro de Alcántara (Málaga). Photographic file CAS.

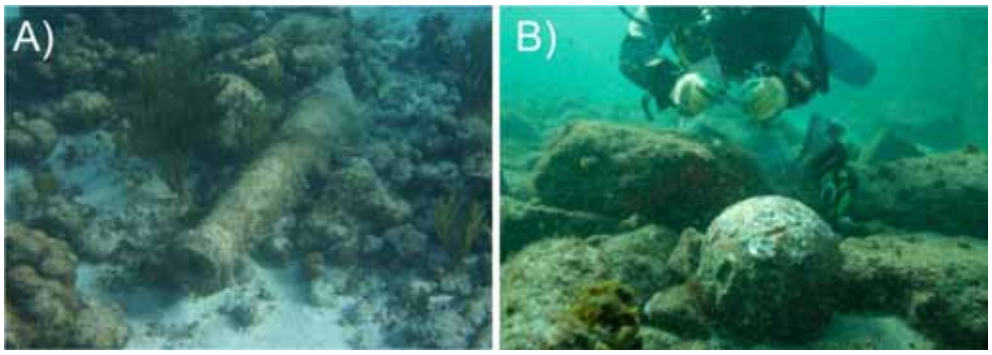

Figure 10. A) Cannon, photographic file ABC newspaper; B) Canon ball, photographic file The National Geographic.

Therefore, an analytical challenge arises: characterising the remains in underwater sites without extracting them from their original location. In spite of this demand, no many analytical techniques are available for this task. Indeed, only those based in laser technology are encouraged for this purpose. Thus, *Raman spectroscopy* have proven to be useful for the analysis of submerged objects [16]. An example is the work of S.N. White et al. [17] in which Raman is used in order to determine the chemical composition of minerals on the seafloor. In addition to this, Raman has been recently employed to study the geochemistry of hydrothermal vents and cold seep fluids at deep-ocean [18]. Also, the continuous efforts of the laser application laboratory in ENEA (Frascati, Rome) for the design and development of instruments based in *Laser Induced Fluoresces* (LIF) for in-situ measurements underwater must be mentioned here [19]. However, although Raman and LIF could be applied in this field, no atomic information is provided. Nowadays, *Laser-Induced Breakdown Spectroscopy* (LIBS) provides a new solution for this analytical challenge. In the last few years, LIBS has emerged as an analytical technique with an important potential for using in archaeology [20, 21] and oceanography applications [22]. Specifically, LIBS is the only one capable of providing the in-situ elemental composition sought. Therefore, the development of tools based on the LIBS technique may be the solution to the problem.

5. References

1. X. Nieto, M. Cau, Arqueologia Nàutica Mediterrània; Monografies del CASC 9, Museu d'Arqueologia de Catalunya, Barcelona, 2009.
2. UNESCO, Convention on the protection of the underwater cultural heritage, Paris, 2001.
3. Subdirección General de Museos, Museo Nacional de Arqueología Subacuática, ARQUA, Ruta del Patrimonio Arqueológico Marítimo de España y Portugal, Instituciones y Museos; Bañuls Impresores, S.L.; 2008 (España).

4. A. Mederos Martin, L. A. Ruiz Cabrero, The Phoenician wreck of the Bajo de la Campana (Murcia, Spain) and the Phoenician trade of the North African ivory, Zephyrvs 57 (2004), 263-281.
5. X. Nieto, M. Santos, El vaixell grec arcaic de Cala Sant Vicenç, Monografies del CASC 7, Museu d'Arqueologia de Catalunya, Barcelona, 2008.
6. X. Nieto, A. Jover, P. Izquierdo, A. M Puig, A. Alaminos, A. Martin, M Pujol, H. Palou, S. Colomer, Excavacions arqueològiques subaquàtiques a Cala Culip 2, Monografies del CASC 9, Museu d'Arqueologia de Catalunya, Barcelona, 1989.
7. C. De Juan, F. Cibechini, E. Vento, El pecio romano Bou Ferrer, un velero de comercio naufragado en la costa de La Vila Joiosa. I Congreso Nacional de Arqueología Subacuática. Cartagena 2013. Online: http://museoarqua.mcu.es/web/uploads/ficheros/becjpecio.pdf
8. C. Zambrano. M. Bethencourt, Conservación y registro arqueológico en el yacimiento submarino Bucentaure II de la Caleta. Cádiz, Boletín del Instituto Andaluz del Patrimonio Histórico, Sevilla (2001), 83-90.
9. N. E. Rodriguez Mariscal, E. Rieth, M. Izaguirre; Investigación en el pecio de camposoto: hacia la identificación del navío francés Fougueux. Revista ph, Instituto Andaluz del Patrimonio Histórico 75 (2010), 94-107.
10. . E. C. Harris, Principios de Estratigrafía Arqueológica; Editorial Crítica S.A, 1991, Barcelona.
11. C. León Amores, "Metodología de la Arqueología Subacuática", Monte Buceiro, 9 (2003), 118-122.
12. J. Rodríguez Iborra, La carta arqueológica subacuática del litoral de la región de Murcia: actualización metodológica y documental; Trabajo fin de máster, Universidad de Murcia 2012.
13. C. León Amores, La conservación del material arqueológico subacuático, Revista Monte Buciero 9 (2003), 110-125.
14. M. Bethencourt, A. Bocalandro, J. Romero-Pastor, Datación de pecios de los siglos XVIII y XIX a través de la caracterización de los forros de cobre, IV Congreso Latinoamericano de Conservación y Restauración del Metal, Madrid (13-17 September 2011), Madrid: Secretaría General Técnica, Ministerio de Educación, Cultura y Deporte; Grupo Español de Conservación, 2011, 51-62.
15. M. E. Medina, A. López, H. G. Svoboda, H. De Rosa; Caracterización microestructural de piezas de fundición de hierro de un navío mercante español del siglo XVIII; XII Congreso Binacional de Metalurgia y Materiales; Valparaiso (Chile) Universidad Técnica Federico Santa Maria (22-26 October 2012), Universidad Técnica Federico Santa María, 2012.
16. X. Zhang, W. J. Kirkwood, P. M. Walz, E. T. Peltzer, P.G. Brewer, A Review of Advances in Deep-Ocean Raman Spectroscopy, Appl. Spectrosc. 66 (2012), 237–249.
17. S. N. White, R. M. Dunk, E. T. Peltzer, J. J. Freeman, P. G. Brewer, In situ Raman analyses of deep-sea hydrothermal and cold seep systems (Gorda Ridge and Hydrate Ridge), Geochem. Geophys. Geosyst. 7 (2006) Q05023.
18. X. Zhang, Z. Dua, R. Zheng, Z. Luan, F. Qi, K. Cheng, B. Wang, W. Ye, X. Liu, Chao Lian, Changan Chen, Jinjia Guo, Ying Li, J. Yana, Development of a new deep-sea hybrid Raman insertion probe and

its application to the geochemistry of hydrothermal vent and cold seep fluids, Deep. Res. Part I in press.

19. R. Fantoni, R. Barbini, F. Colao, D. Ferrante, L. Fiorani, A. Palucci, In: Integration of two lidar fluorosensor payloads in submarine ROV and flying UAV platforms, EARSeL eProc. 3 (2004), 43–53.
20. A. Giakoumaki, K. Melessanaki, D. Anglos, Laser-induced breakdown spectroscopy (LIBS) in archaeological science-applications and prospects, Anal. Bioanal. Chem. 387 (2007), 749–760.
21. F.J. Fortes, M. Cortés, M.D. Simón, L.M. Cabalín, J.J. Laserna, Chronocultural sorting of archaeological bronze objects using laser-induced breakdown spectrometry, Anal. Chim. Acta 554 (2005), 136–143.
22. B. Thornton, T. Takahashi, T. Sato, T. Sakka, A. Tamura, A. Matsumoto, T. Nozaki, T. Ohki, K. Ohki, Development of a deep-sea laser-induced breakdown spectrometer for in situ multi-element chemical analysis, Deep. Res. Part I 95 (2015), 20–36.

Chapter 2. Laser-induced breakdown spectroscopy: fundamental and application

1. Fundamentals of LIBS

1.1. Overview

Laser-induced breakdown spectroscopy (LIBS) is a type of atomic emission spectroscopy that was first reported in the literature in 1962 [1]. This technique is based on the detection and analysis of the spectrally resolved optical emissions of atoms, ions and small molecules present in plasmas generated by the pulsed laser ablation of samples [2]. LIBS exhibits several distinctive capabilities that have contributed to its fast expansion in numerous areas of applied chemistry and physics. Among them, it does not need any treatment of samples and that no limitation is presented for what concerns the typology of the state of the matter solids, liquids, and gases. In addition, LIBS presents a huge potential to perform simultaneous multielemental detection, fast analytical response and real-time monitoring of the elemental composition of samples. In fact, only optical access to the target is required. The possibility of design field deployable instruments and its handiness to operate at remote distances [3] permit the use of LIBS to real-world application.

The origin of LIBS in some ways is parallelto the development of the laser, nearly 50 years ago when the pulsed ruby laser was invented by Maiman [4]. For many years "*the laser was a solution searching for a problem"*. It had to generate its own applications. A couple of years after Maiman works, a first publication presented by Brech and Cross [1] revealed the powerful tool of laser as a spectral source. They vaporized metallic and non-metallic materials using a ruby laser, then the vapours were analysed with an electrical spark. This study is considered to be the beginning of the LIBS itself; though the laser-induced plasma was not produced directly. Interest in the LIBS started to grow when the lasers, with improved Q-switches technology, induced the plasma directly by the beam without the assistant electrode excitation. First steps of LIBS were in the field of surface analysis [5] and to examine metallic samples [6] using a monopulse. Later, laser radiation was also focussed in air [7] and in water [8]. More pioneering works were based on the laser-matter interaction [9], plasma diagnostics [10] and temporally gated detection [11]. Nevertheless, despite its promising start, the expansion of LIBS as analytical technique was slowed down over many years because of its limitations as quantitative method.

In 1980s, a renewed interest in LIBS was achieved with the introduction of two works based on the time integrated (Loree and Radziemski, 1981) [12] and time-resolved (Radziemski and Loree, 1981) [13] analysis of gases. The temporal detection of the plasma radiation, as well as, the evasion of the continuum emission of the LIP leads to the improvement in the signal-to-noise ratio and subsequently to the improvement of the limits of detection (LOD). Since then, LIBS has been in continuous advance, not only on the gaining of more knowledge about its performance but also addressing a lot of real analytical challenges. In order to improve the sensitivity and selectivity of the technique, a part of the research has been focused to evaluate different experimental configuration for the excitation [14]. Thus, the use of a double-pulse

configuration (DP-LIBS) [15], and the delivering of multi-pulses excitation (MP-LIBS), [16] has been considered.

From the 90's to the present day, due to the ongoing need for analytical methods increasingly more demanding, LIBS has been advancing significantly in developments in its instrumental components. LIBS technology is currently undergoing transformation from a bench top analytical technique into a viable tool for field measurements. The advances in optical configurations (such as fiber optics, beam optics and telescopes) for guiding and collecting the plasma light have resulted in instrument design differing from those normally used in laboratory. Furthermore, continuous advances in reducing the size and weight while increasing the capabilities of lasers, spectrographs and detectors make possible the development of compact and rugged instrumentation [17]. In this connection, some LIBS approaches have been able to develop such as *remote LIBS system* (the laser and/or the signal are transmitted through a fiber optic cable) or *standoff* (both the laser and the signal are transmitted along an open path configuration). These sensors have been constructed with the goal of analyzing distant targets in environments where physical access is not possible or may present a risk to the operator.

Nowadays, the effective deployment and implementation as crowning of the technology has been evidenced with its flexibility and adaptability to a huge variety of environments since the surface of Mars [18-20] until deep ocean exploration [21, 22]. And also, the technological advances are reflected on its usage for a wide range of new and interesting applications in extreme and hostile environments such as industry [23], homeland security [24-25], geology [26], biomedicine [27] and cultural heritage [28]. The current research in LIBS is focused towards the starting-up and the development of laser-based analytical applications [14], but also on the knowing, the understanding, and the unveiling of the fundamental aspects of the ablation physical process and the chemistry of the plasma [29, 30].

Along the following sections, although briefly, a description on the most basic aspects of LIBS will be provided.

1.2. Laser–matter interaction and plasma formation

Interaction of a focused laser beam with matter is a complex and not yet fully understood phenomenon, which is still under intensive investigation. These difficulties arise from the many parameters conditioning the process, which can be related to the laser (i.e. wavelength, energy and pulse length) or the sample under inspection (related to material properties, microestructure, morphology and presence of defects) [31]. The process starts with a high power laser pulse that is tightly focused onto the target surface. The irradiation absorbed in the focal spot can lead to a rapid local heating and intense evaporation, followed by a mass removal process called *ablation*. During this process, a wide variety of phenomena including rapid local heating, melting and intense evaporation is involved. Then, the evaporated material expands as a plume above the sample surface, and because of the high temperature, a *plasma* is formed. This plasma

contains electrons, ions, and neutral as well as excited species of the ablated matter, whose light emission constitutes the analytical signal measured by LIBS [2]. Figure 1 depicts a brief survey of some of the numerous phenomena and complicated processes involved during laser-matter interaction and the ensuing target ablation.

A description of all processes following the laser-matter interaction will be discussed in the next subsections. It must be noted that mechanisms will be described for the general case of ns-LIBS.

- **Laser energy absorption and ablation process**

The first step in plasma formation is the absorption of laser energy by the target material. First instance, when a large amount of laser energy is focused on the matter, the absorbed photons lead to theproduction of electrons with a certain amount of kinetic energy. If the electron densities is very high (Ne>10^{17} cm^{-3}), electron-electron collisions dominate over electron-matter collisions and electrons begin tobehave collectively and thermalize each other. Thermal equilibrium among electrons is reached when they transfer their kinetic energy to the matter via recombination and phonon generation. Consequently, a

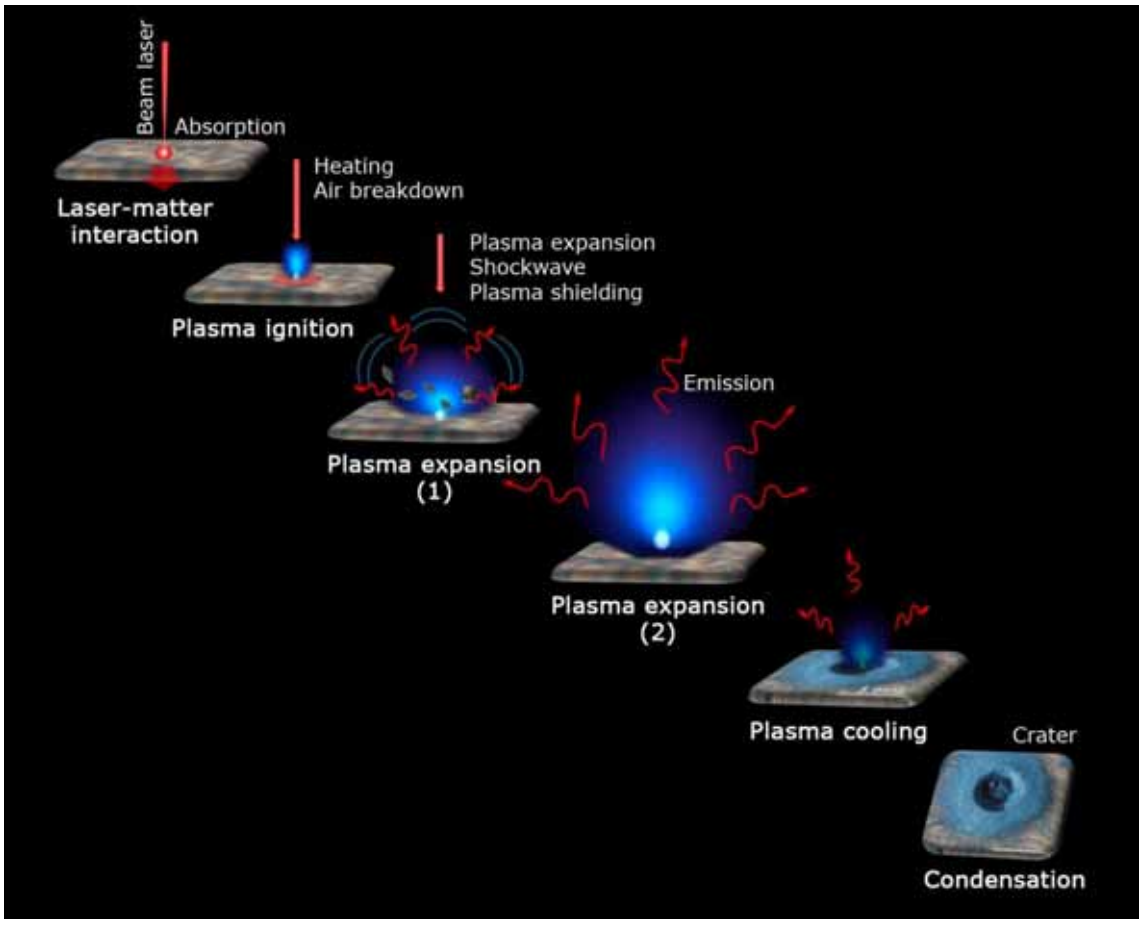

Figure 1. Chronological sequence of the main phenomena that occur during laser-assisted ablation process.

wide variety of thermal phenomena such as a rapid local heating, melting and intense evaporation are caused. Therefore, a sequence of phase transitions occur: from solid to liquid, and from liquid to vapor [32]. After that, as the laser radiation continue, the sputter target material is gasified and ionized, thus leading to the formation of the plasma containing electrons, ions, and neutral as well as excited species of the ablated matter.

- **Plasma ignition**

The ignition of laser-initiated plasmas begins with the gas breakdown by the tightly focused laser pulse. Breakdown itself is not a single and well-defined phenomenon, but a complex body of processes initiated by *multi-photon ionization* (MPI) and propagated by *cascade (or avalanche) ionization* [33]. These sequences of events may be schematized as follows:

$$A + nhv \longrightarrow A^{+} + e^{-} \qquad (1)$$

$$A + e^{-} \longrightarrow A^{+} + 2e^{-} \qquad (2)$$

where *A* is an atom and $A^{+}$is a single charged atom, *n* is the number of photons, *h* is the Planck´s constant, $e^{-}$is an electron and *v* is the frequency of radiation.

The plasma formation begins by *MPI* process (1) whereby atoms and molecules absorb enough photons to ionize, while they release free electrons. From the incoming radiation the high density of generated electrons gains energy. Consequently, the transference of energy from electrons to other atoms from the sample occurs, and the process progresses by *avalanche ionization* or *cascade ionization* (2) [34].

Another phenomenon that must be taken into account is the so called *Coulomb explosion*. It consists in the expulsion of ions after electrons have been removed from the target by MPI. If the extracted electrons are not replaced immediately by others, coming from the surrounding solid, a surface charge develops and consequently the ions in the lattice experience a strong repulsion. If this electrostatic repulsion is able to overcome the lattice bonding energy, ions are ejected from the sample surface to recover neutrality. Due to its electrostatic nature, *Coulomb explosion* is unlikely to emerge during laser ablation of conductive materials [35]. However, this process is substantial for the ablation of dielectrics and semiconductors [36].

The prevalence or the co-presence of the various mechanisms responsible for the breakdown is closely dependent on features of both the irradiated target and the ablation laser (pulse duration and wavelength). There is no a clear separation between the different regimes. A set of generalities may be pointed out according to the nature of the samples and the properties of the radiation. *Thermal processes* and *cascade ionization* dominate in the case of ablation of conductive targets irradiated with long wavelengths and long pulses. In contrast, *multi-photon phenomena* and *Coulomb explosion* are associated to ultra-short pulses, short wavelengths, and high irradiances and are more frequent for dielectric materials.

- **Plasma expansion**

Once the plasma plume has been created, it is directly ejected outward expanding into the surrounding ambient. The direction is in opposite to the propagation of the laser pulses. The plasma expands into the background gas and strongly interacts with it. Since the laser pulse may still present during the early stage of the plasma expansion, a part of the pulse energy stimulate the heating and the ionization of the vapor, while the other fraction continues toward the sample surface [37]. The interaction between the plasma and the laser pulse leads the so-called *laser-supported absorption waves* (LSAWs) that dominates the propagation of the plasma into the surrounding atmosphere. According to experimental parameters, such as, chiefly, the laser fluence and buffer gas pressure, three types of LSAWs regimes, schematized in Figure 2, can be differentiated [37-38]:

Laser-supported combustion waves (LSCWs). It is generated at relatively low fluence levels.The shock front is located ahead of the absorption zone which is coupled to the plasma which is in turn in contact with the target surface. Despite that the shock wave enlarges the gas density, pressure, and temperature, the region of post-shock gas continues to be transparent to the laser radiation. Thus, a residual laser beam energy is efficiently absorbed by the front edge of the plasma while propagates into the shocked gas. The main mechanism causing LSCW propagation is the radiative transfer from the hot plasma to the cool high-pressure gas created in the shock wave.

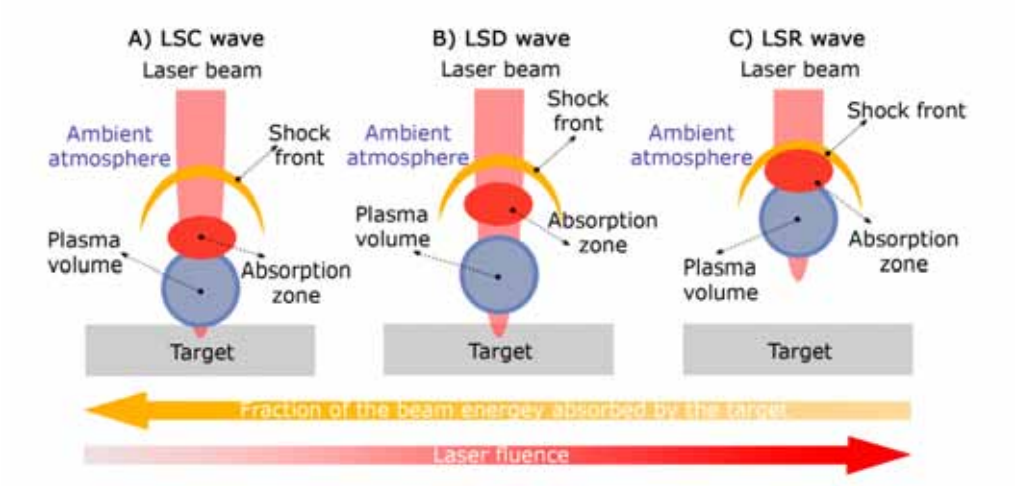

Figure 2. Schematic overview of the structures of A) laser-supported combustion (*LSC*), B) laser-supported detonation (*LSD*), and C) laser-supported radiation (*LSR*) waves expanding into a surrounding ambient at atmospheric pressure. This figure has been adapted from a similar one featured in the reference 38.

- Laser-supported detonation waves (LSDWs). It is generated at intermediate fluence. The absorption zone is located slightly behind the shock front and the plasma is detached from the absorption zone and target surface. The laser energy is absorbed in the post-shock gas zone and the plasma volume is heated isometrically, that is, the absorption zone reaches a pressure, temperature, and density higher than the vapor gas placed just above the sample. Thereby, the shock front enhances efficiently and a great thrust is imparted to the target surface. Thus, the expansion of the LSDW is governed by such absorption mechanism.
- Laser-supported radiation waves (LSRWs). It is generated at very high fluence. The temperature of plasma radiation become very high and coupling of the absorption zone and plasma volume takes place. Consequently, a large fraction of the incident laser radiation is absorbed and prevented from being delivered to the target surface.

Differences among these models are related to the velocity, pressure and the effect of the radial expansion on the subsequent plasma evolution, arise to the different propagation mechanisms of absorbing front into the cool transparent atmosphere.

During its early lifetime stage, the plasma is weakly ionized and therefore is transparent to laser radiation. However, when the electron density is increased during the expansion or a high power density is employed, an optically dense plasma could be obtained. In fact, the surface of the plasma plume may be shielded, which prevents that the tailing part of the laser pulse reaches the sample surface. This phenomenon is named*shielding effect*. This plasma shielding does not only changes the actual energy flux received by the matter but also causes a reheating of the plasma itself. This effect is commonly produced in the case of nanosecond laser pulses, however is not evidenced for ultrafast (pico- and femtosecond) laser pulses, because the total temporal length of the pulse impacts the target before plasma formation [39-41].

Three principal mechanisms that may contribute to the plasma shielding are *inverse bremsstrahlung* (IB)*, photoionization* (PI) *and Mie absorption* [42].

- The IB process involves the absorption of photons by free electrons moving through the electric field of an ion or less likely by a neutral atom.
- The PI is described by the absorption of a photon into a neutral atom, which becomes ionized.
- The Mie absorption involves the absorption of light induced by small clusters or particle generated by the condensation of a supersaturated vapour.

- **Decay and emission of the plasma**

The plasma is highly ionized. These conditions give rise to an intense continuum emission which dominates the spectral response in the first instance. The continuous spectrum of radiation is attributed to Bremsstrahlung and recombination radiation processes [43]. During the Bremsstrahlung process, photons are emitted due to the transition of free-state to free-state contributed by free electrons and ions accelerated or decelerated through collisions. Nevertheless, during the recombination event, free electrons are captured to be bound-state by ions in electron-ion collision and neutral atoms and molecules are created; thus excessive energy is emitted in the form of electromagnetic radiation. As the plasma evolves, it cools off, the temperature and electron density is decreased sufficiently during this process; background continuous intensity decays more rapidly than the spectral lines. Hence, conventional spectral measurements should be registered after some hundreds of nanoseconds delayed from the incidence of the laser pulse onto the target. The spectroscopic analysis of the optical emissions from spectral lines provides qualitative and quantitative information on the elemental composition of the sample as well as on the temperature and particle density of the plasma itself [30].

- **Condensation**

After the extinction of plasma, the complete removal of the material leads to a negligible residual microcrater on the target as the most evident physical sequel of the whole ablation process [44]. Generally, the dominating species leaving the target surface are atoms and ions; beside also the material plume is consisting of particles. These smaller particles are generated after the plasma expansion. In this time, the plasma is gradually cooling down, thus leading to the nucleation and condensation of the vapour atoms, which results on the formation of nanoparticles and growth toward clusters. Other route of particles formation (in this case causes a larger size) take place during the plasma expansion into the ambient. These particles are expected to be created by direct mass ejection as a consequence of different mechanisms (photomechanical fracture, liquid splashing …) depending on the material nature.

1.3. Factor affecting laser ablation and laser induced plasma formation

As exemplified in Figure 3, the nature and characteristics of laser-induced plasmas are strongly affected by the laser operating conditions, such as laser *wavelength* (λ), *pulse duratio*n (τ), and *energy* (E). At the same time, the *surrounding media*, not only in composition but also in pressure, plays a critical role since it is the medium where the plasma evolves. The nature of the probed material also conditions the absorption of the laser pulse/ energy. Next, through some brief information, the main impacts of these parameters will be described.

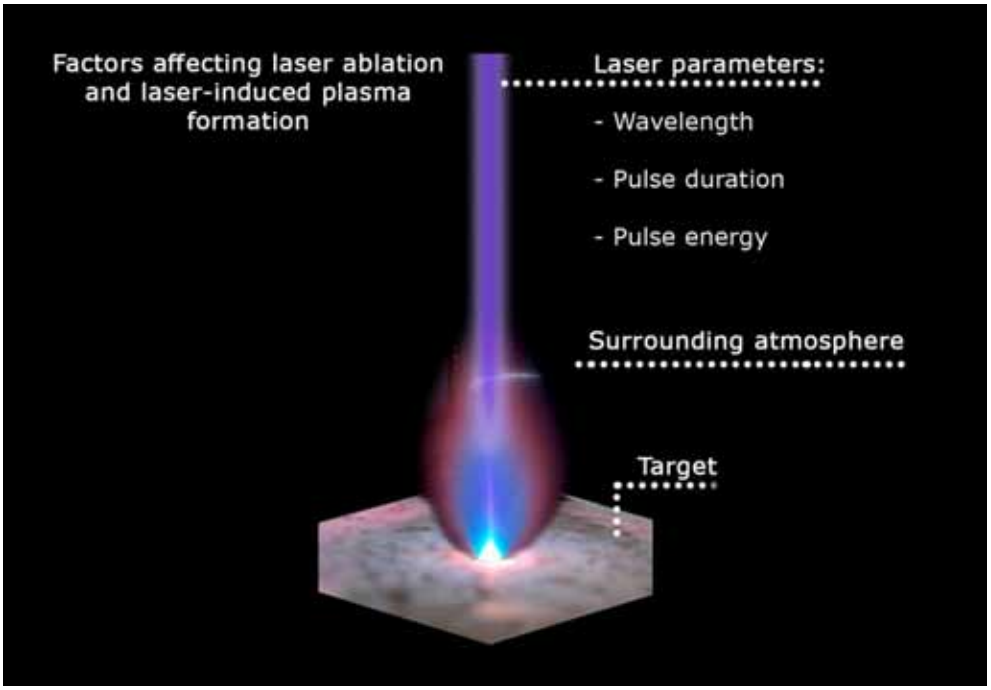

Figure 3. Pictorical summary of the variables affecting the laser ablation and laser-induced plasma.

1.3.1. Influence of laser parameters on the laser induced plasma

The laser parameters are important variables affecting plasma characteristics. In general, the wavelength of the laser radiation will determine the available coupling within the electronic, or vibrational, states in the sample. During this coupling, the material is heated to a particular temperature depending on the mechanism of interaction of the laser pulse with that, and the onset of ablation (either thermal orphotochemical) occurs if the fluence is above a minimum threshold. After the plasma plume is formed, its density may obstruct entirely or partially the laser radiation (plasma shielding), depending on the laser wavelength and pulse length. Thus, only a percentage of energy is transferred from the laser pulseto the target. For a better understanding, effects of laser parameters on the plasma have been separated as follows [2].

- **Laser wavelength**

As mentioned before, laser wavelength plays an important role on plasma generation, laser-plasma coupling, plasma expansion dynamics and confinement, plasma properties and crater generation [45]. A large variety of laser wavelengths ranging from ultra-violet to near infrared passing through the visible can be used. The effect of wavelength on laser-matter interaction has been evaluated both experimentally [46-48] and theoretically [49-50].

Differences in absorption rate between radiations lead to different propagation behaviour of the produced plasma. In line with this, it is important to mention Ma et al. works. They have investigated the ablation of alluminum targets in one-bar Ar background usingnanosecond UV (355 nm) or IR (1064 nm) laser pulses [51]. As indicate such reference, while for UV ablation the background gas is principally evacuated by the expansion of the vapor plume, for IR ablation the background gas is effectively mixed to the ejected vapor. In fact, higher electron temperature (T_e) and density (N_e)are observed for UV ablation than for IR ablation. These parameters confirm a hotter, confined Al plasma for UV ablation, whereas for IR ablation, a larger axially extended Al vapor plume with a better homogeneity is observed. Thus, while a large λ (IR - 1064 nm) produces larger axially extended plasmas, a short λ (UV - 266 nm) generates plasmas much more confined.

- **Laser pulse duration**

Laser pulse duration is a key important parameter in essential changes in the produced plasma due to the different rate of energy deposition and the variable mechanisms of energy redistribution and dissipation within the material. Indeed, interaction of *nanosecond (ns) pulses* with materials is substantially different from those of *femtosecond (fs) pulses* since the rate of energy deposition is significantly shorter in this last instance [2]. In the case of nanosecond (ns) pulses the laser−plasma interaction during the plasma evolution plays an important role. While the leading edge of the laser pulse produces the plasma, the remaining part of the pulse overheats the ejecting plume instead of interacting with the sample. As consequently, a preferential ablation may be done attributed to different rates of volatilization or atomization processes of the elements that constitute the sample [52]. Thus, the plume may be enriched in the most easily vaporizable species. In contrast, in ultrafast laser pulses (pico- and femtosecond) this effect is not observed because last part of pulse arrives so quickly that the plasma is not ignited yet. As this respect, it is important to comment that using ns pulse, plasma plume exhibits two different regions, a high radiation intensity region behind the expanding plasma front and other bright spot located just above the sample surface [53-54]. In the case of ultrashort laser pulses, the phenomenon of distinguishable zone is not observed. In spite of this, a non uniform distribution of intensity regions at the plume may be also evidenced in function of the irradiated material and at the very beginning of ablation. However, in such circumstances obeys to a different causes; the size of the ablated material [55-56].

The effect of laser pulse duration has been also evaluated in sample submerged in water [57]. These authors concluded that long ns pulses are more favorable for this LIBS application due to the relatively slow heating of the plasma. This fact causes a larger and less-dense plume, and, therefore, fairly intense and less broadened emission lines. Also, a weaker continuum has been observed.

- **Laser pulse energy**

Last but not less important, the laser pulse energy (E) is also an influential parameter that alters the ablation and plasma formation. In fact, for LIBS, the energy per unit area that can be delivered to the target is more important than the absolute value of E. Two magnitudes are interchangeably used to describe the energetic regime for laser ablation: *fluence* (energy per unit area, J cm^{-2}) and *irradiance* (power per unit area, GW cm^{-2}). Both are referred to the total laser pulse energy deposited on the target surface per unit of area [58]. The disparity between the two terms is that irradiance includes the laser pulse duration whilst the fluence is a time-integrated measurement of the applied energy. The experimental determination of both parameters requires a judicious estimation of the spot size over which the laser beam is focused. However, any modification on these parameters influences on the amount of ablated mass and, consequently, on the produced plasma plume. The raise of these variables influences on plasma morphology and dynamics. At low irradiance, the lower ablation rates lead to plasmas with less energy, so its expansion in the radial direction prevails over that in the longitudinal direction, so the plume core remains "attached" to the sample surface. In contrast, at high irradiance, the plume, containing more ablated matter and having higher internal energy, is capable of pushing the surrounding air far enough in front of itself in order to expand into a hemispherical shape [59]. In turn, an increase is detected for T_e and N_e with the raise of the irradiance [60].

1.3.2 Influence of ambient gas on the laser induced plasma

As a result of the sample evaporation, the plasma expands at supersonic velocity toward the surrounding atmosphere in front of the target. The interaction of the plume with the ambient gas is a complex gas dynamic process due to the sequence of new physical processes, including deceleration, thermalization of the ablated species, interpenetration of gas components into the plasma, radiative recombination, formation of shock waves, and clustering. Consequently, atmosphere surrounding is also of major relevance for plasma properties and the dynamics. But not only it composition also the pressure under which such plume is evolving.

In general, a decreasing of density and temperature of plasma is larger when the pressure decreases because expansion of the plasma becomes faster, thus resulting in faster cooling. Some works have evaluated the effect of gas pressure over emission intensity [61-63]. A decrease of emission intensity of the plasma with raising pressure has been observed. It is justified from the fact that, under low pressure, the plume interacts less strongly with ambient molecules (less transfer of part of the energy to them), decreasing the number of recombining ions. In contrast, when the ambient gas prevents its expansion, recombination processes proceed faster since energy exchange between particles inside the plume becomes more efficient limiting the emitting species.

It is important to mention the particular case when the plasma evolution takes place in water [34]. Once the plasma is formed, it evolves similarly to what happens in gaseous background, namely, it expands supersonically, driving a shock wave in the surrounding environment, and extinguishes after a given time. However, the water compressibility is several orders of magnitude lower than that of air, which causes the plasma to be severely confined and, consequently, the rate of recombination phenomena to increase strongly. Thus, the plasma persistence is reduced to a few hundred nanoseconds and the emission spectra appear to be dominated by a black body-like broad continuum, due to the radiative recombination and, more limitedly, to the Bremsstrahlung emission [64].

Moreover, the effects of distinct background atmospheres on the dynamics of the generated plasmas have been intensely studied [65]. Changes in the vaporized amount by plasma shielding, changes in plasma temperature by the absorption of laser radiation, and changes in the plasma expansion. All this aspect related at the same time with the properties of gas affect the intensity of LIBSemission [66].

Respect to plasma properties, it is determined that low temperatures and electron densities result in plasmas generated in He atmosphere, whereas high temperatures and electron densities are attained for plasmas in Ar ambient. In this line, a study of temporal data [67] using Ar and He concludes that Ar ambient led to slow decay of both electron density and plasma temperature, whereas He gas caused a fast decay in both parameters. As explained in [68], the differences between values and their ensuing decay of electron density and temperature of plasmas in Ar compared to He is argued on the basis of the thermal conductivity. In addition, considering the ionization potencial of Ar (15.76 eV) and He(24.58 eV); the lower the ionization potential, the higher the electron density and the plasma temperature, and slower their corresponding decays [69].

On the other hand, the influence of composition of the background gas on the amount of material ablated as well as the diameters and depths of craters has been studied [70]. A deeper and wider crater was obtained in He compared to Ar atmosphere. This fact seems to be due to the plasma shielding. Thus, the heating of the background gas by inverse Bremsstrahlung is less effective for He, thereby leading to lowest plasma shielding and most amount of ablated material.

1.3.3. Influence of target on the laser induced plasma

Doubtlessly, variation of plasma parameters for samples at different states of matter –solid, liquid and gas– is more than obvious because of the different energy thresholds required to its particular breakdown. The type and nature of the analyzed material plays a crucial role to the ablation process. For materials at the same state but prepared under differing forms, namely, nanopowder, pressed powder pellets, and sintered ceramics; strong differences on plume plasma dynamics are also found as well as particles ejected from the irradiated material [71]. Also, in this direction of influence of sample structure, the ablated mass is in inverse proportion with hardness of surface of sample [72]. In addition to this, due to the

differences on chemical and physical properties of materials, a matrix effect on the laser-induced plasma plume parameters is evidenced. As expected, the larger the differences on materials properties, the higher the variation of their respective plasma parameters [73].

1.4. Parameters for plasma characterization

Once the plasma plume is produced, there are some physical parameters such as the T_e, the N_e and the atom and ion number densities that allow its characterization. Knowledge of these parameters is vital to understand the dissociation, atomization, ionization, and excitation processes occurring in the plasma and helpful in utilizing the plasma to maximize analytical potential of LIBS.

The description of the plasma state and the evaluation of its essential physical parameters are strictly connected to the concept of thermodynamic equilibrium. As explained by Hahn and Omenetto in [29], for a plasma to be in complete thermodynamic equilibrium, all processes should be in balance and characterized by a single temperature. Therefore, the process of excitation of atoms by collisions with electrons is equal to the reverse deactivation process, collisional ionization is equal to three-body collisional recombination, and radiation emitted is equal to the radiation absorbed. However, when the energy losses by radiative processes is smaller than that involved in collisions between species that govern transitions and chemical reactions, the local thermodynamic equilibrium (LTE) is reached [29, 74]. For satisfying this condition a sufficiently high electron density has to be reached. In the LIBS literature, the most popular criterion usually invoked as a proof of the existence of LTE in the plasma is the *McWhirter criterion*. However, this criterion is known to be a necessary but not a sufficient condition to ensure LTE. The *McWhirter criterion* allows calculating the critical N_e for which the plasma is within LTE using the following equation [32, 75]:

$$N_e \geq 1.6 \times 10^{12} T^{1/2} (\Delta E)^3 cm^{-3} \quad [\text{Eq. } 2.1]$$

where T is the plasma temperature (K) and ΔE is the higher energy difference (eV) of the levels whose populations are given by LTE conditions. This approach assumes that the collisional rates are at least ten times the radiative rates within the plasma. The critical electron density for LIBS plasmas is usually estimated in the range of 10^{15}–10^{16} cm^{-3}.

- **Plasma temperature**

A general approach to determine the plasma temperature is the so-called Saha-Boltzmann plot method [76]. For plasma in LTE, the Boltzmann's law relates the total density N (T) of a neutral atom or ion to the population of an excited level [77-78], as expressed in equation 2.2:

$$ln\left[\frac{\lambda_{mn} I_{mn}}{A_{mn} g_m}\right] = -\frac{E_m}{k\, T_e} + \ln(\text{hcN}) \quad [\text{Eq. } 2.2]$$

where $\lambda_{mn}$is the wavelength of the transition lines, $I_{mn}$is the integrated line intensity of the transition involving an upper level (m) and a lower level (n), A_{mn} (s^{-1}) is the transition probability, g_m (s^{-1}) is the statistical weight, and E_m (eV) is the excited upper level energy. T_e (K) and k ($eV \cdot K^{-1}$) are the electron temperature and the Boltzmann's constant, respectively; h (J·s) is the Planck's constant, c ($m \cdot s^{-1}$) is the speed of light and $N(T)$ (m^{-3}) is the total number density.

By plotting the left hand side term vs. E_m, the plasma temperature is obtained from the slope of the straight line. Depending on both the LIBS operational conditions and the sample nature, the range of plasma temperatures may broadly change but values from 6000 K to 15000 K are characteristically reached [30].

- **Electron density**

Another important parameter for plasma characterization is the electron density. Among the optical emission spectroscopic methods proposed, the broadening of emission lines due to the *Stark effect* has been the most widely used. This effect is due to the collisional processes between the emitting atoms and electrons and ions, resulting in a broadening of the line and a shift of the peak wavelength. This effect is considered the dominant broadening when compared with other mechanisms due to collisions with neutral atoms (i.e., resonance and Van der Waals broadenings) [30]. Then, full width at half maximum (FWHM) of the stark broadening lines $\Delta\lambda_{1/2}$, is related to the electron density and for lines of singly ionized ions is given by the following equation [79]:

$$\Delta\lambda_{1/2} = 2W \times \left(\frac{N_e}{10^{16}}\right) nm \quad [\text{Eq. } 2.3]$$

where N_e is the electron number density (cm^{-3}) and the coefficient W is the electron impact parameter.

2. LIBS configuration

The most basic and typical configuration of LIBS to obtain a fast emission response of the analytes is the single-pulse (SP) LIBS approach [80]. Despite of this configuration is successfully for depth profile and spatial resolution analysis, there are several concerns with SP ablation when LIBS is required for some analytical solutions. It is related with the small quantity of ablated mass that consequently induces weak emission intensity, poor measurement reproducibility, and the fractionation related to crater formation. In order to improve the deficiency of LIBS the use of other configurations based on several controlled laser pulses (double-pulse and multi-pulse) but keeping the flexibility of one-step LIBS, have been also explored.

As far as double-pulse configuration is concerned generally, the first pulse yields a laser induced plasma that is essentially equivalent to that in single-pulse LIBS, with a comparable ablation plume, composition, temperature, electron density, and decay rate. The second pulse is typically fired after an inter-

pulse delay (Δt) up to tens of microseconds that ablates additional material and produces a dual-pulse LIP with vastly different physical properties. The mechanisms responsible for the increased emissions were described by Scaffidi [81] and Babushok [15]. Moreover, whatever the delay time between pulses, DP configuration can operate under different geometries. Figure 4 exemplifies four possible arrangements of how the two delivered pulses can be combined [15].

- Collinear (4A): the two laser beam are coaxial. This configuration is popular because it is the most practical pulse alignment for remote, on-site, in situ, and on-line analyses [82].
- Cross-beam (4B): one of the laser beam interact at a certain angle with respect to the sample surface [15].
- Orthogonal (4C, 4D): involve two synchronized laser pulses aligned perpendicularly to each other. However, at these instances, the order in which the two laser pulses are arranged in time leads to different effects on laser ablation. In Figure 4C, the so-called *re-heating,* the first pulse is used to ablate mass from the sample surface while the second pulse is applied to re-heat such ablated mass. And when the first pulse, delivered parallel to the target surface, is focused above the target to generate the air plasma, while the second pulse focuses perpendicularly to the target surface for ablation is called *pre-ablation*, 4D [83, 84].

Regardless of DP configurations, emission signals are significantly enhanced, thereby leading to a higher analytical sensitivity [70]. It is due to a more efficient ablation, keeping the energy of plasma for longer times, which turns in a higher ionization degree and in a more stable signal. On the other hand, ascompared to SP, it has a much larger versatility using different beam geometries, pulse width and laser beam wavelength [85-88].

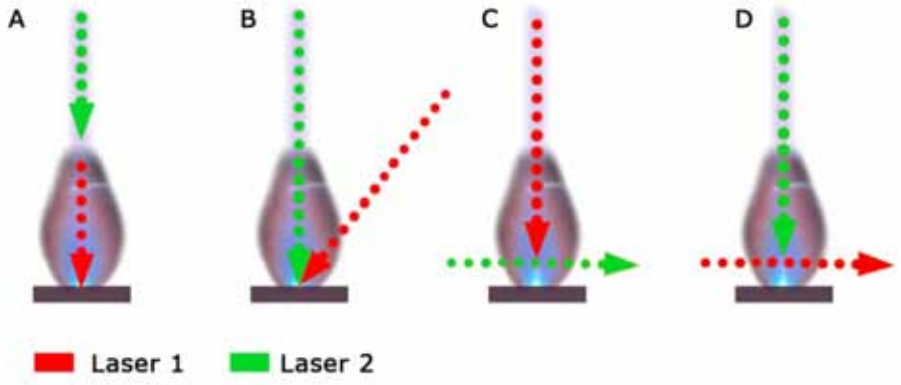

Figure 4. Schematic diagrams of double-pulse LIBS geometries: A) collinear, B) cross-beam, C) orthogonal re-heating, D) orthogonal pre-ablation.

It is important to mention that the original purpose of DP-LIBS was the improvement of the observed signal in an attempt to increase the analytical sensitivity. However, the advantages of this approach and their combined and multiple optical configurations lead also to improvements in LIBS applications such as underwater analysis which would not be feasible without the benefits of double-pulse excitation. This topic will be explained more extensively in section LIBS in liquid.

Another alternative is the multi pulse excitation or MP-LIBS (more than two sequential pulses) that have been also investigated in order to improve the analytical performance of LIBS.MP configuration consists in a laser bursts containing a variable number of pulses with different duration and separated by distinct inter-pulse gaps [89]. Analytical figures of merit are significantly improved with MP respect to those of SP or DP LIBS. The enhancement in MP-LIBS is caused by the increased material ablation but also because the reheated plume provides long excitation. As a conclusion, MP-LIBS causes a lower breakdown threshold and consequently an improvement in the ablation efficiency. This ablation rate increases as the pulse number increases and the pulse-to-pulse temporal distance within the pulse train decreases [90-91].

3. LIBS approach

Sometimes an in situ analysis is needed in those applications where access to the sample is difficult or in situations that may severely affect the human health of the operator. Moreover, it is also necessary in those cases where the material cannot be transported to the lab due to the size of material or to avoids possible risks to the pieces. As a result of this demand, LIBS has been received a particular attention, as it combines many of the required features in a field-portable technology such as rapid analysis with no sample preparation, a realtime response and an inherent high sensitivity. In the last few years, continuous advances in reducing the size and weight while increasing the performance of lasers, spectrographs, and detectors make possible the development of compact and rugged instrumentation. In especial, the use of fiber lasers, compact spectrometers, and fiber optics for guiding the plasma emission offers greater flexibility while reducing the risk of instrument failure. All these aspects has led to a rapid evolution of LIBS analytical equipment. [17]

In addition, the flexibility of these systems has allowed them to adapt to changing operational scenarios, thereby enabling the use of hand-held portable as well as distant analyzers. Fortes et al. have reported a complete review of the variety of such developed instruments, as well as their different applications [17]. In this work, these instruments capable of performing in-situ analysis are clearly classified as: portable sensors or sensors for distant objects.

Figure 5 exemplifies the different operational LIBS approaches of these field-portable technologies. The most relevant design features and particular qualities relating to each system will be briefly described below.

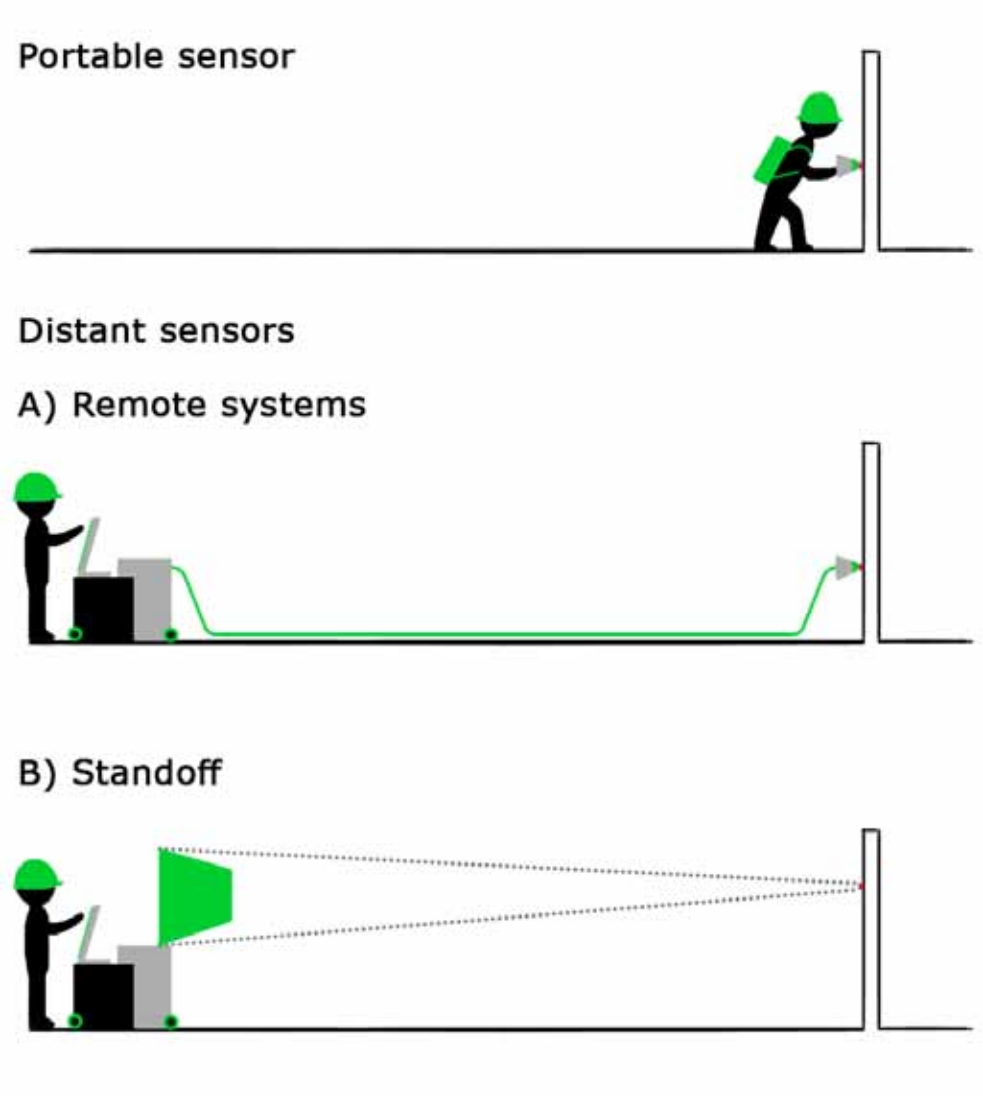

Figure 5. Operational approaches of the field-portable sensing LIBS systems.

3.1. Portable sensors

This category includes all those configurations in which both the operator and the LIBS sensor are located next to the sample. In the majority of works reported in the literature, the laser used is a Nd:YAG working at 1064 nm due to the proven reliability and ruggedness of solid-state lasers and also for size requirements. However, each particular application will be determine the type of detector required, and thespectral range used. Despite that designs can be varied, in general, the overall system involves the laser power supply, a main unit that consists of a specially adapted backpack and encloses the spectrometer and the computer components, and a hand-held probe that houses in the laser head together with the focusing and collection optics arrangements [92-93]. An external power supply may provide autonomy of several hours to the sensor, thereby permitting its transportation to anywhere.

This configuration has been successfully utilized in a variety of application such as geo-chemical analysis of karstic formations [92-94], determination of lead in road sediment [95], chemical imaging ofhistorical buildings [93], oil spill residues [96], detection of indoor biological hazards samples [97] or using a double pulse configuration [98].

3.2. Sensors for distant objects

There are particular scenarios in which a LIBS measurement at a certain distance is needed, e.g. when there is a hostile environment (potential risk in handling the sample to be analyzed) and/or there is a restricted physical access up to the material. At these circumstances, LIBS is usually performed remotely (via a controlled displacement of the sensing platform), or at standoff distance (where the sensing platform and the target are physically separated by distances up to several tens of meters).

- **Remote systems**

In the remote system, the laser and the signal are transmitted through a fiber-optic cable. The fiber optical materials provide a new method for plasma light collection and it is also possible to transmit the laser energy through the same fiber. At the end of the fiber, the laser beam is focused onto the sample surface by an appropriate optical configuration. Furthermore, within this approach, there exists two working possibilities: first, the use of a unique fiber optic cable capable of transmitting the laser energy andcollect the optical emission from the luminous plasma plume and to conduct it to the spectrometerfor analysis; second,the employment of an individual fiber optic cable for each specific process, the launch and the collection.

The remote LIBS analyzers provide solutions to a wide variety of analytical problems. However per each particular application the instrument will be adapted to a maximum distance reached for the instrument as well as the optical system for laser focusing at the output end of the fiber.

The majority of application with this approach has been directed towards environment monitoring [99]. It has also been investigated LIBS remote for the determination of contaminants in solids [100, 101]. Other applications include, for example, materials analysis in nuclear reactors [102], and determining minority components in systems alloys [103]. It is important to add, as will be explained in the next chapters; it is possible today to obtain the chemical composition of objects in an underwater archaeological site, which may be found submerged up to tens of meters depth [21, 104].

- **Standoff**

In a standoff configuration both the laser radiation delivered up to a target located at several meters distance and the returning light from the induced plasma are transmitted through a "transparent"

atmosphere in an open-path configuration [105]. Normally, the transmission medium is air, although recently it has demonstrated the viability of standoff LIBS (ST-LIBS) to carry out analysis of solids submerged in water [106].

The solutions of ST-LIBS to a large field of applications as analytical demands and technology evolves, have promoted this approach. Some of theseare suggests as detection of explosives [107,108], planetary exploration [109, 110] and ocean mining analysis [111], among others. Despite of variety of applications, thisapproach implies great complexity. Beyond the restriction on the specifications of the instrumental components entailed, the circumstances associated to the "transparent" atmosphere through which the light propagates contribute to raise difficulties [112].

4. Applications

4.1. General overview

The total number of fields in which LIBS finds application are increasing steadily every year and there are also major applications for which the analytical features of LIBS seems to fit the requirements perfectly. Generally speaking, in the, e.g., space exploration or cultural-heritage fields LIBS is used mostly because it can do things that other techniques cannot do; whereas in industry LIBS is used more and more because it does things better than other techniques.In a graphical manner, a summary of instances for which LIBS has been susceptible of being considered is projected in Figure 6. The following sub-sections give a brief, commented overview of some representative applications.

4.1.1. Cultural Heritage

The use of LIBS in the archeological and cultural-heritage field offers particular benefits. It is a rapid and portable technique. In addition to this, it is an in-situ, non-contact, and nearly nondestructive, and these are all important features in the case of precious art items (paintings, antique jewelry, pottery, etc.) kept in museums or art collections. Laser ablation can be used for cleaning artworks and also qualitative analytical applications are most abundant in this field.

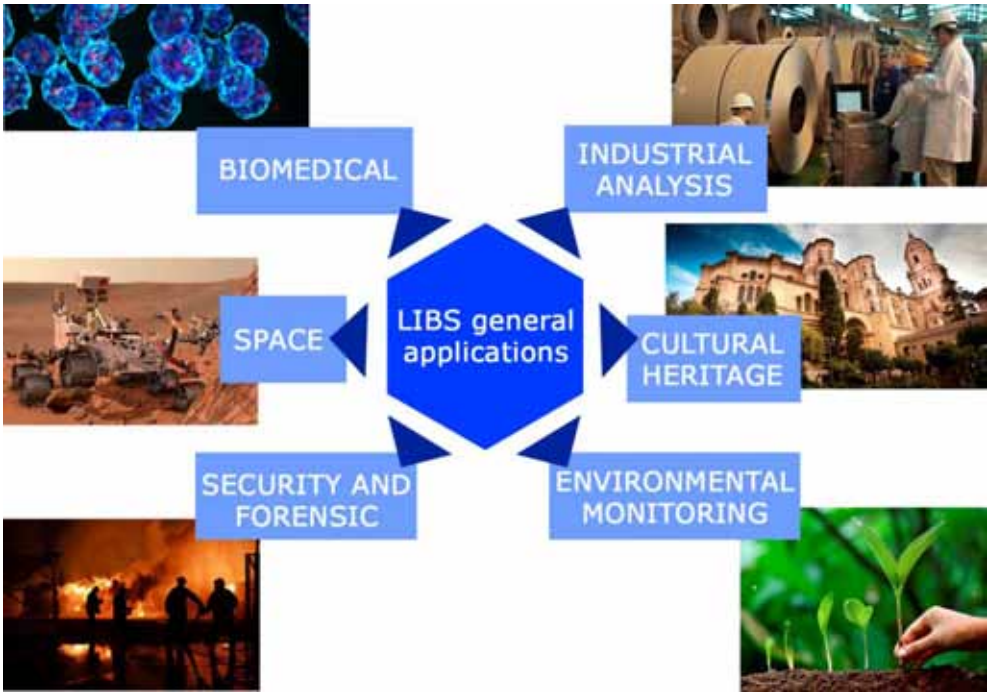

Figure 6. Main LIBS applications.

One of the most important problems in this area arises from the fact that most of these pieces are structured in different layers. LIBS (preserving the sample integrity) is capable of describing the surface and subsurface composition of a material. This capability is largely advantageous when attempting thepaintings from the archeological area of Pompeii [113] or chemical analysis of multilayered painted surfaces [114]. In addition to this, a recent example of this trend is the state-of-the-art combined instrument incorporating optical-coherence tomography and LIBS (OCT-LIBS) [115], which was specifically constructed to aid multilayer pigment identification in paintings.

Recently an increasingly popular topic is the study of the origin or the age of archeological construction materials [116]. The use of multivariate statistical methods, mainly PCA, DA, or SIMCA, in such studies is becomingmore usual to improve their accuracy. Also is frequent in literature the analysis by LIBS of archaeologic bone and teeth; these studies have tended to investigate the degradation and/or diagenesis processes of such artefacts [117].

Although LIBS is already an established technique in this area, studies that compare LIBS results with those produced by standard instruments, for example EDS, LA-TOFMS, and XRF, are still frequent [118]. The comparisons are generally positive for LIBS, and the studies always mention that an added benefit of LIBS is that it can be made portable. In this way the use of standoff LIBS is suggested as a further development [119]. Transport of the artwork to the laboratory is eliminated, thus reducing the total analysis time and the risk of irreversible damage to the object.

4.1.2. Industrial analysis

LIBS has been extensively investigated for industrial process control, especially in the steel making industry. The most important applications in this field include characterization of hot and molten metals, analysis of slag, classification of metals and alloys, sorting of steel parts or online measurement of coating thickness and composition [120]. Robustness, stability, reliability, analysis speed, and operational availability are important performance characteristics that make LIBS an important tool in the factory.

On the other hand, the application of LIBS to control process of precious metal recovery and recycling has been also evaluated [121]. The results have been successful demonstrating that LIBS can be considered as a viable alternative to ICP-OES and XRF for the determination of recovered precious metals. Moreover, LIBS together with discriminant function analysis (DFA) has been utilized for identification and classification of six groups of the most used polymers in manufacturing and packaging of materials [122].

4.1.3. Environmental monitoring

The atmospheric aerosols, soils and slurries constitute the environmental workspace most affected by heavy and toxic metals from many anthropogenic sources. Thus, a huge interest has focused on the in situ semiquantitative and quantitative characterization of these metals. LIBS has been effectively evaluated to analyze toxic metals [28, 123]

On the other hand, detection of micronutrients (Fe, Cu, Mn, Zn, B, Mo, Ni, and Cl) and macronutrients (N, P, K, Ca, Mg, S) is also an important area in which LIBS seems a suitable in situ and real-time technique. When the nutrients are not present in appropriate concentration levels in soils could play a decisive role in plant nutrition and can affect crop yields [124, 125]. In addition to this, an interesting application of LIBS has focused on the investigation of the metal accumulation in vegetal tissues [126]. Galiová et al. demonstrated the capability of LIBS for mapping Ag and Cu distribution directly in plant leaves of Helianthus Annuus L [127].

Another important area in which LIBS has been extensively used is in situ monitoring of gas and particle emissions (heavy metals) originating from exhaust stacks, incinerators, industry, foundries, etc. Approaches reported in the literature indicated that these studies can be carried out by analyzing the particles deposited on a filter or directly by analyzing the cloud constituting aerosols [128]. However, indirect analysis appears to be significantly more efficient than direct analysis [129].

4.1.4. Security and forensic

In the security field has been studied extensively the explosive detection and their residues, as well as, other military applications [25]. In last year, a considerable amount of literature has been published in

this topic, some review are indicated to provide further information [130, 131].

The main advantages of LIBS that make it really interesting for these applications are quickness of analysis, potential field portability, the ability to provide characteristic spectral fingerprint information for classification and/or identification purposes, and, last but not least, the potential for the investigation of dangerous materials from a safe distance and/or in safe microscopic quantities. However, one of the main challenges in these applications is minimizing the effect imposed by surrounding atmosphere and the deposit substrate (e.g. organic, metallic, or polymer) that could contribute to the signal of N, C and O. First studies aimed to discrimanate among organic compounds were reported in 2001 [132]. In these works atmospheres of He and Ar were used to displace air, causing an increase in sensitivity. Most recently, a series of studies investigated the elimination of the effects imposed by the substrate and conditions used in LIBS analysis on the success of classification [133, 134]. The discrimination capabilities and robustness of a range of multivariate chemometric methods were also tested.

LIBS has also been tested in a variety of other forensic investigations including fraud detection of a variety of industrial products [135], document discrimination [136], the study of human remains [137] or of samples taken from suspects [138] and soil fingerprinting [139]. The success of all these applications heavily relies on the performance of the multivariate chemometric methods used.

4.1.5. Biomedical

The beneficial use of LIBS when applied in biomedical field has been also outlined [140]. This is an important core of recent application. Just to cite some examples, the information contained in LIBS spectra has been used to differentiate types of tissue samples from chicken brain, lung, spleen, liver, kidney and skeletal muscle [141]. LIBS has been also used to diagnose the state of human teeth through the characterization of the elemental composition of their healthy and infected parts [142]. Furthermore, the application of LIBS for in situ quantitative estimation of elemental constituents distributed in different parts of renal- and urinary-calculus obtained directly from patients by surgery [143] as well as to differentiate live pathogens (B. anthracis Sterne) strains, live vaccines (F. tularensis) strains, and UV-killed hantavirus strains on substrates has been also evaluated [144]. In addition to this, the most important area to highlight is the in vitro possibilities and its effectiveness for the identification of both breast and colorectal cancer from frozen human tissues as well as determining the disease grade and severity have been also outlined [145].

In general, medical results published so far promise the development of novel LIBS-based clinical and point-of-care diagnostic instruments in the near future.

4.1.6. Space exploration

The space exploration is an exotic LIBS application that highlights the versatility of the method. The application of LIBS to Mars exploration is closely related to its capability for standoff analysis and mainly focused on the identification and discrimination of minerals.

Since 1990s, the viability of LIBS for planetary exploration has been studied. However, it was not until 2004 when the efforts of the LIBS community in the field of planetary exploration were recognized when a new LIBS instrument was selected for the mobile NASA Mars Science Laboratory (MSL) rover. The Chemistry and Camera instrument named ChemCam, is one of 11 science instruments onboard NASA's 2011 MSL rover named Curiosity. The main objective of ChemCam is determining elemental compositions of geological samples (rocks and soils) on another planet at distances from 2 to 9 m [18, 19]. Furthermore ChemCam supports MSL with 5 capabilities: I) remote active removal of surface dust and coatings or weathering rinds from rocks to determine their underlying composition through depth profiling; II) image of the targeted area to place the LIBS analysis in a geological context; III) a remote classification of rock and soil characteristics; IV) passive spectroscopy over the 240–905 nm range; and V) quantitative elemental compositions including light elements like hydrogen and some elements to which LIBS is uniquely sensitive (e.g., Li, Be, Rb, Sr, Ba, B, C, N, and O).

ChemCam optimization was not an easy task and several papers were published about it [146, 147]. First results of preliminary analysis of LIBS indicated that the spectrum is consistent with basalt, which is known from previous missions to be abundant on Mars. In addition to this, one of the findings of the ChemCam instrument along the Curiosity rover traverse on the Martian soil chemistry at the submillimeter scale has been the identification of two principal soil types: a fine-grained mafic type and a locally derived, coarse-grained felsic type [148].

4.2. LIBS in liquids

The work presented in this Thesis lies in expanding the LIBS application area in a new environment unapproachable until now: submarine. Therefore, basic principles of plasma formation in this ambient are explained below.

4.2.1. Basic principles

In previous sections, laser-induced breakdown has been described in the case of solid targets in air, but it is a general phenomenon that can occur as well in liquids, as has been extensively reviewed in [29, 149]. However, due to peculiar structure of water, below the breakdown threshold, many phenomena can take place, including non-linear effects, molecule orientation and liquid contraction, electron hydration,

laser filamentation and white light generation; as De Giacomo et al. [34]. The main effects when a laser beam interacts with bulk water below the breakdown threshold comprise: coherent scattering (stimulated Raman and/or Brillouin scattering), self-focusing, medium heating, and production of quasi-free electrons by photolysis [150, 151]. But at higher irradiances, the multi-photon excitation, inverse Bremsstrahlung and electron-impact ionization can indeed produce the breakdown of the medium, equal at what described in the case of solid samples [152]. Also, in the case of a laser pulse is focused on a target through a liquid, the main mechanisms responsible for the plasma formations are the same occurring during ablation in gas [34]. A difference can be indicated, the breakdown thresholds of liquids are usually higher than those of solids, because the cross section of laser absorption is lower in less dense media and the probability of initiating the plasma formation by multi-photon ionization decreases consequently.

Once the plasma is created, it expands supersonically, driving a shock wave in the surrounding environment, and extinguishes after a given time. Nevertheless, due to the high density and nearly incompressible character of water in comparison with air it causes a severe plasma confinement. Consequently, the rate of recombination phenomena increase strongly. Thus, the plasma persistence is reduced to a few hundred nanoseconds. An extremely important post-breakdown phenomenon is induced by this fast release of energy to the water, namely, the formation of a *cavitation bubble* [149, 153]. The high-temperature of a laser-induced plasma transfers a significant amount of its internal energy to the surrounding liquid, thus a layer of vapour is produced around the plasma volume. This vapour expands almost adiabatically, causing a growth of a cavity containing both the vapour and the diffused gas [152]. During the growth of the cavitationbubble, the pressure inside decreases both due to the volume enlargement and vapour condensation across the interface. In the maximum volume of bubble cavity expansion, the temperature inside approaches that of the surrounding liquid while the pressure is reduced at saturated vapour pressure (0.0233 bar for water vapour), much lower than that of the liquid [154]. In that point, the bubble begins to shrink, the inner pressure and temperature increase again until the rate of condensation cannot offset the volumetric reduction. The timescale in which the bubble expands and then collapses is on the order of hundreds microseconds, thus, order of magnitudes longer than the plasma duration itself [64, 155]. The maximum determined bubble radius is in the order of a few millimetres and it depends on laser pulse characteristics such as wavelength, output energy and focusing condition, pulse duration and the external pressure [34]. It is important to note that in last fast phase of the bubble collapse a rapid increase of the inside gas temperature and pressure, giving rise to a second shock–wave and to the re-expansion of the cavity. Some oscillations of the bubble cavity may continue for many cycles of expansion and collapse [154, 156].These temporal trends of pressure and temperature of the vapour in the bubble itself and the cavitation bubble evolution have been extensively investigated through spectroscopy and shadowgraph experiments, as well as through theoretical models (see [149] and references therein). Figure 7 (taken from Lazic et al. work [156]) shows a sequence of shadowgraph images in which the different phases of cavitation bubble evolution mentioned are represented.

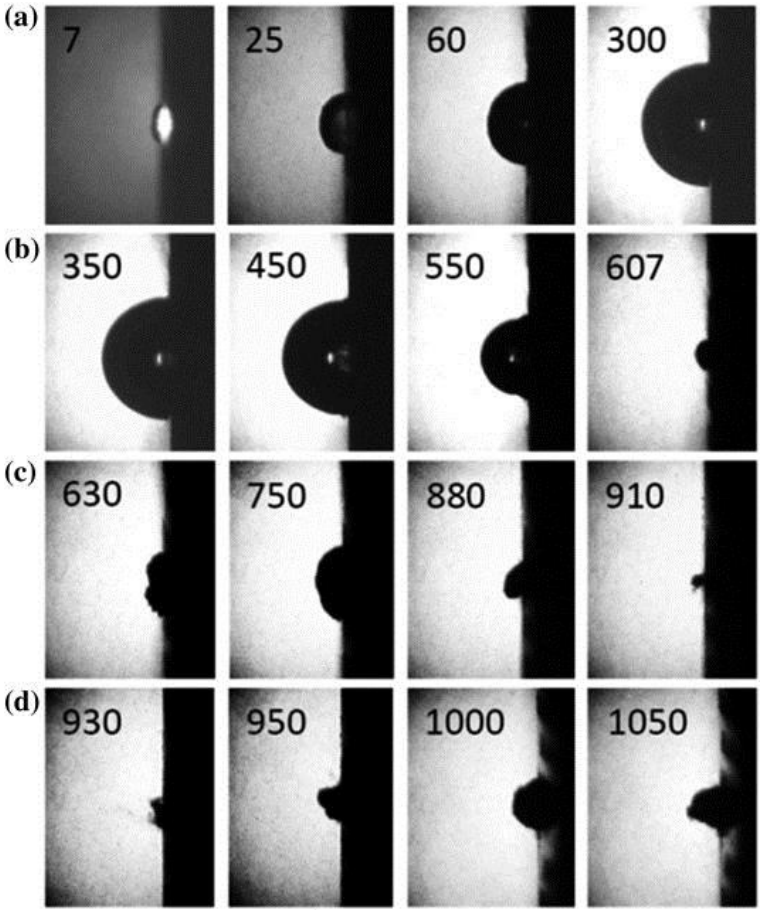

Figure 7. Bubble evolution at different delays (in μs) from the ablative laser pulse: A) first expansion; B) first collapse; C) second rebound; D) third rebound (Figure from reference 156).

It is important to mention that the differences to plasma formation process inside a liquid are related with the plasma confinement and the production ofcavitation effect. i.e. the vapor bubble. Regarding LIBS analytical capability in liquid environment, this strong interaction between the plasma and the surrounding liquid makes the emission spectra appear to be dominated by broad continuum. It is due to the radiative recombination and, more limitedly, to the Bremsstrahlung emission more pronounced than gas media [64].

An additional complication that should be taken into account when pursuing in situ analysis of seawater or submerged objects is the effect of hydrostatic pressure on the LIBS signal, which becomes more and more severe upon increasing the depth. In this case, the confinement effects and quenching of plasma are even more pronounced than in liquids at atmospheric pressure, and the LIBS signal is degraded accordingly. Lawrence-snyder et al. and Michel have addressed this aspect in a series of papers in which LIBS is applied to pressurized solutions, with the aim of testing the technique as an in situ chemical sensor for deep ocean hydrothermal vents [157-160]. Other author such as Sakka and co-workers have focused the effect of hydrostatic pressure in bulk liquids [161] and even for immersed solid target [162]. But in this

case, authors use an alternative to common SP configuration. In such worksa long-duration nanosecond laser is used. A significant improves the quality of SP-LIBS spectra at high pressure is observed.

In spite of these drawbacks and of its relatively low sensitivity compared to routine analytical techniques for liquids analysis, some features unique to LIBS have pushed research toward specific applications requiring in situ and non contact analyses of aqueous solutions as well as submergedsolid samples. In the specific case of aqueous solution, some single pulse (SP) alternative approaches have been proposed. It is mostly tackled avoiding the consequences of the liquid confinement. The most traditional approach is focusing the laser on the liquid surface, also with some specific precautions to limit splashing of the liquid and formation of aerosols over the liquid surface [163 and references therein]. Other possible solutions such as laser focusing on the surface of a vertically flowing liquid stream or formation of a liquid jet [163]; spraying to form micro-droplets [164, 165]; nebulization of the liquid into aerosols [166] have been evaluated. In all last approaches, the purpose was to eliminate the direct interaction of the plasma with the liquid and allowing it to expand in a gaseous environment. On other way, in the case of submerged solid samples, an interesting alternative that also avoids the expansion of bubble in liquid environment is using a gas flow that removes water from the surface to be analyzed. In such case, it is not necessary to create a cavitation bubble, but the gas purge flow supplied is responsible for removing the water from the sample surface to condition a solid-gas interface. Thus, all the disadvantages of working in a solid-liquid interface are avoided [21]. First LIBS underwater measures using a gas flow were reported by Beddows and colleagues in 2002 [167].

Nevertheless, sometimes these mentioned approaches are not possible to apply due to the analysis is necessary to carry in liquid media, in such way a growing interest have pushed research focusing in different excitation configuration. In this meaning, due to relatively low-boiling of water, the most efficient approach is probably the Double Pulse (DP) excitation. Since it was first proposed in 1984 [168] it has been successfully exploited not only in bulk liquids but also for the analysis of submerged targets. Next section discusin more detail the DP excitation approach to underwater application.

4.2.2. LIBS excitation configurations inside liquids

Emission intensity of the plasma produced inside liquids is generally lower than in gaseous environment due to several factors such as: absorption by the medium both of the laser and plasma radiation and their scattering on suspended particles and micro-bubbles, a fast plasma quenching in the dense medium and laser beam shielding by the high density plasma [34, 153]. On the other hand, the ablation rate inside liquids is higher due to major mechanical scavenging [169], however, the LIBS signal at equivalent laser excitation is significantly lower than in sample-gas interface. Furthermore, the spectral lines are strongly broadened and the continuum emission is very intense because of the high electron density

[34]. As results of these effects, a relatively poor signal in SP LIBS measurements is obtained, thus hindering the detection of minor and/or trace elements of the sample [149].

Under this circumstance and in order to improve the deficiency of LIBS in liquid, the uses of other configurations based on several controlled laser pulses (double-pulse and multi-pulse) have been suggested. In such cases, the first laser pulse produces a cavitation bubble, while the successive pulse ablates the sample and induced a second plasma inside the bubble. Considering that the duration of LIP in the bubble is of a few microseconds, while the life-time of the bubble is in the order of a few hundreds microseconds, the plasma obtained by the second pulse can be considered as expanding in a stationary environment induced by the first laser pulse [64, 170]. As explained in [149], this assumption will depend on the bubble expansion rate. Generally a more efficience second plasma is achieved in a re-excitation moment around the maximum expansion of bubble, in contrast to the initial stage of expansion and final stage of collapse, when the rate at which the bubble changes its parameters is high. Thus, it is not surprising that the most important parameter in the case of DP configuration in liquid environment is the interpulse delay time between pulses. In fact, adjusting the inter-pulse delay between the laser pulses, it is possible to select the bubble conditions where the laser induced plasma expands achieving an emission enhancement. In Figure 8, taken from reference [149], this influence of delay time between the lasers pulses associated to LIBS emission can be observed. They indicate that such experiment was carried on Ti sample submerged in water acquiring five time-integrated DP-LIBS spectra at the same delay time but at

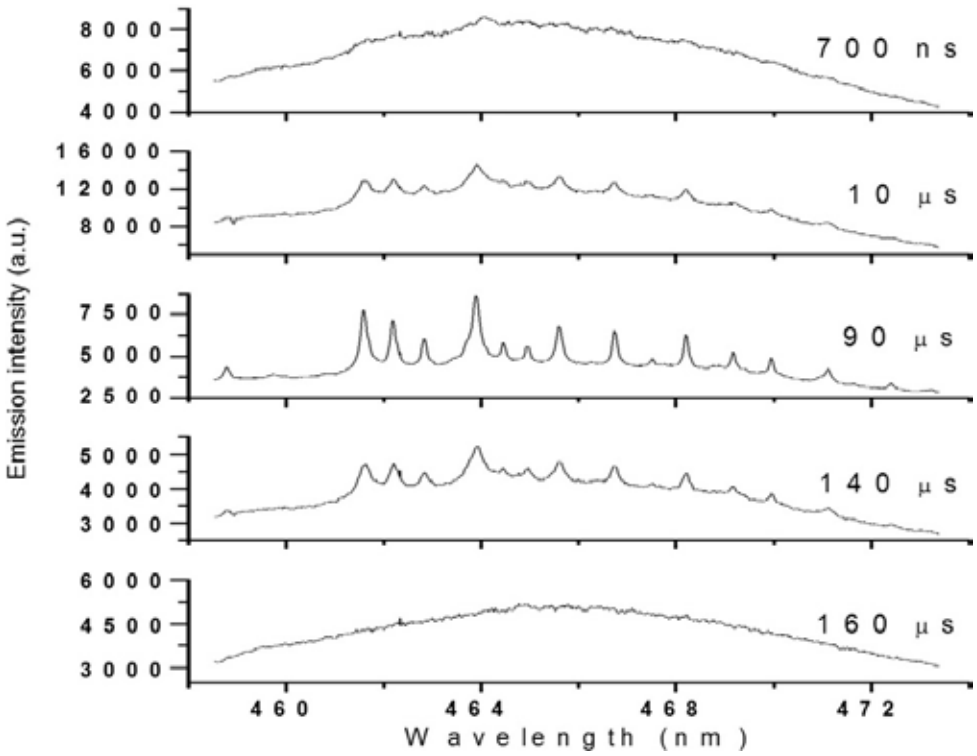

Figure 8. DP-LIBS emission spectra of Ti in water at different interpulse delays (Nd:YAG 7 ns ablation lasers: 1st pulse=532 nm, fuence=0.51 J/cm^2; 2nd=532 nm, fuence=6 J/cm^2). (Figure from reference 149).

different interpulse delays. As they explained, using an interpulse delay too short (Δt = 700 ns) or too long (Δt = 160 μs) does not produce an improvement in LIBS signal, both spectra are similar to using a SP configuration. However, for an interpulse delay of 90 μs, that corresponds to the maximum expansion of the cavitation bubble when the plasma expands in the bubble, an increase of the spectral resolution and enhancement in LIBS signal is observed.

In conclusion, the above discussion has pointed the importance of selecting the appropriate delay between the two pulses for underwater application. The time delay yielding the maximum expansion is more suitable for enhancing the emission spectrum sensitivity. In this direction as it is detailed in literature [153], using a DP optimized configuration, for some elements directly analyzed from bulk waters have been achieved detection limits below 1 ppm, and in order of 100 ppm for different elements from submerged metallic samples.

It is important to note that as commented in last section, an increase of the hydrostatic liquid pressures leads to a smaller radius and to a shorter lifetime of the cavitation bubble [157-160]. Thus, the interpulse delay optimization in DP laser excitation becomes even more critical, moving to shorter intervals the optimum value. The corresponding inner bubble pressure and temperature are higher and the conditions approach those of the SP laser excitation. This causes the second plasma to expand in andinteract with a gaseous environment whose conditions become less and less favourable for the emission of well-resolved spectra. For these reasons, DP LIBS loses efficiency at high liquid pressures [153, 160]. However, the reference [158] suggests that the pressure range for the LIBS signal enhancement by DP excitation might be achieved by an increase of the first pulse energy or by multi-pulse laser excitation, the both aimed to obtain a larger vapour bubble. Chapters 7 and 8 of this thesis will discuss this topic in greater detail.

Another alternative to improve the capability of LIBS analysis in liquid is the use of a long-duration nanosecond laser source. Recently, Sakka et al. and Takahashi et al. [57, 171-172] evaluated the effect of pulse duration in the laser ablation of a Cu target in water. Shadowgraphy images revealed that long pulses (150 ns) were more favorable for LIBS analysis. Under these conditions, the relatively slow heating of the plume causes a larger and less dense plume, and consequently, the spectral emission shows less broadening and a weaker continuum. Thus, the emission can be fairly intense, and the surface damage is minimized in comparison with a common SP approach.

4.2.3. Applications

Within the broad range of LIBS applications, there are some particular areas specifically for liquids media. In a graphical manner, a summary of liquid environment application in which LIBS has been susceptible of being considered is projected in Figure 9.

In this vein, a short outline of such particular application fields is presented below.

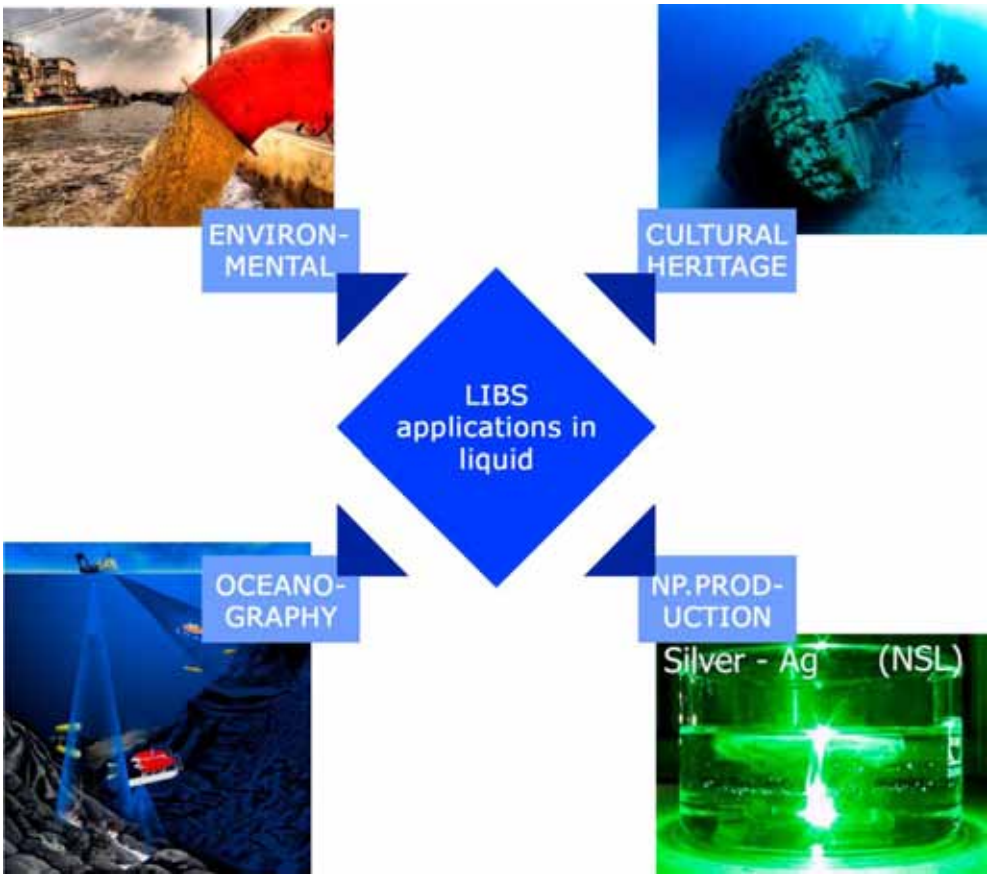

Figure 9. Main applications fields of LIBS in liquid.

- **Environmental**

From the environmental point of view, LIBS in liquid media is particularly interesting with respect to well-established techniques for liquids analysis such as ICP-OES [173] due to the possibility of planning on-site and remote applications dedicated specifically to monitor the concentration of metals in wastewaters from industrial plants and in seawater. As is the case of detection of Cr by a system equipped with a fibre-guided suitable for distances of up to 50 m between measurement system and detection sensor, reaching a limit of detection over 200 ppm [174]. Moreover, De Giacomo et al. have been checked also several elements such as in bulk aqueous solution for Al, Na, Ca and Li in bulk aqueos solutions [64]. However, as discussed in section 4.2.1 focusing a single laser pulse through a liquid bulk does not usually provide suitable analytical signal, but low emission spectra mainly dominated by a continuum background radiation. The technique need to improve in this aspect. Despite of this, several alternatives has been employed to detect the elements composition of wastewater samples. For example, Hussain and Gondal [175] have developed a LIBS system for the analysis of Ca, Mg, P, Si, Fe, Na, and K in wastewater from a dairy product plant. They focused the beam laser on the liquid surface contained in a suitably designed cell. This approach using a relatively high energy laser pulses (100 mJ) provided accurate analytical results that were

in good agreement with those obtained with ICP-OES. A liquid jet configuration to detect Cr in wastewater from electroplating industries was used by Rai et al. [176]. In this case energy pulses of 120 mJ were focused just below the surface of a solution stream from a Teflon nozzle to produce a plasma at its front surface. LIBS results obtained were in good agreement with atomic absorption spectrometry data. Rai et al. [177] also explored the effect of additional elements like Cd and Co in the Cr contaminated water. Limit of detection (LOD) for Cr was determined to be 1.1, 1.5, and 2.0 ppm in unitary, binary, and tertiary matrix, respectively. Furthermore, a similar configuration was also evaluated for the analysis of toxic metals Pb and Cd in aqueous solutions by Sadegh et al. [178].

- **Cultural heritage**

In the past decade, LIBS has become a valuable analytical tool for *cultural heritage.* The combination of main features to LIBS such as no sample preparation, minimally destructive, fast analytical response, depth profiling analysis, and the capability for in situ analysis; makes it a very attractive technique for the characterization and conservation of archeological samples, artworks, and other important materials [28].

A particular interest is growing in the in situ characterization of archeological materials from the marine environment. The possibility of obtaining some information about the findings would be of primary importance prior to planning recovery activities and taking decisions about whether the object should be moved or not. Certainly, extraction of submarine assets is quite often not practical and/or not permitted, thus making the development of analytical technology for submersed material a particularly appealing activity. In this way, a first approximation was carried out by De Giacomo et al. group [179]. A bronze standards immersed in seawater were analyzed in a home-made cuvette with two collinear laser pulses focused through the liquid bulk. The quantitative analysis was obtained with the calibration line method and gave satisfactory results, as compared to similar ones performed in air. A progress continued was observed in Lazic et al. work [180], in which using a similar approach, a qualitative analysis was successful and allowed for the material recognition for a wide range of materials potentially could be find in the undersea archaeological site, such as iron, copper-based alloys, precious alloys, marble and wood. Most recently, Guirado et al. [21] provided a new solution for this working area and demonstrated for the first time the analysis of submarine archeological materials using a remote LIBS instrument. The mode of operation relies on a basic LIBS assembly (laser, spectrometer, optics and electronics and control system) operating on the deck of a vessel. The remote LIBS unit is extendable by means of a fiber optic probe that is operated underwater, guided by a trained diver. The laser beam travels through an umbilical cord to the target and also delivers a stream of pressurized air that removes water from the surface to be analyzed. This fact permits to generate and expand the laser-induced plasma in air and not in water that is well known to quench plasma emission. The same fiber optic probe captures the emitted light and transmits it to the detection system. The capabilities of remote LIBS instrument for in situ analysis of underwater archeological

objects was demonstrated onsite a trials on the Mediterranean Sea in which the chemical signatures of ceramic materials, metallic samples, and precious metals were acquired at depths of 30 m. Guirado et al. [104] have also proposed a new prototype base in multi-pulse excitation. This fact improved the performance of the equipment in terms of energy transmitted through the optical fiber, range of analysis (to a depth of 50 m) and variety of samples to be analyzed (i.e. marble, ceramic, concrete etc).

It is important to indicate that the work presented in this thesis seeks to contribute our grain of sand in this interesting area. A huge part of work has been focused on improving the capabilities of the last prototype mentioned. Moreover, some first preliminary studies aimed at evaluating the potential of the technique to increase the range of depth in which an archaeological site could be analyzed have been carried out. In this case two collinear laser pulses focused through the liquid configuration had been used.

- **Oceanography**

An interesting application, in first instance proposed by Lawrence-Snyder et al. and Michel et al. [157-160], is the use of LIBS as a chemical sensor at high liquid pressures simulating oceanic depths. They dedicated a series of papers with the aim of testing the technique as an in situ sensor for identification of hydrothermal vents. Clearly the quenching and confinement effects are in this case even more pronounced than in liquids at atmospheric pressure, limiting the lifetime of the bubble itself and the temporal windows when the analysis can be pursued, consequently, the LIBS signal is degraded. Despite of this, due to the hydrothermal vent, whose emitted fluids can be observed only in situ, because irreversible changes would occur if they were moved from underwater to a common laboratory; LIBS in the cavitation bubble appears as the only possible choice for the analysis. Authors evaluated the optimal experimental conditions for LIBS detection of five critical elements (Na, Ca, Mn, Mg, K), such as delay between the laser pulses, background pressure, pulse energies and acquisition gate time. Studies were performed up to 270 bar. On the other hand, the use of a long-duration nanosecond laser source has been reported as significant improves the quality of SP-LIBS spectra [21], even for immersed solid targets [162] for oceanography application. Based on these studies, the University of Tokyo incorporated a long-pulse laser in a cylindrical probe mounted in the articulate arm of a remotely operated vehicle (ROV) [111]. This prototype was tested for close-contact multielemental analysis of both seawater and mineral deposits at depths of over 1000 meters.

- **Nanoparticle production**

One of the most studied and innovative applications of laser-induced plasmas in liquid environment are addressed to the generation of nanoparticles (NPs) by laser ablation of submerged solid samples [181]. It is due to conceptual and instrumental intrinsic simplicity of liquid phase-pulsed laser ablation (LP-PLA) shares with LIBS, because it virtually requires only a laser source and a reaction vessel where the submerged target is irradiated. Furthermore, if the employed liquid is water, NPs can be directly obtained in

a safe, environmentally friendly, biologically compatible and cheap solvent. Different kinds of NPs have already been obtained and also an evaluation of the experimental parameter such as pulse duration, wavelength and repetiton frequency as well as liquid pressure have carried out. A wide range of material have been produced from colloidal solutions of noble metals [182] and metal oxides [183] to carbon nanotubes [184], nanodiamonds [185], and other carbon-based materials, also in various organic solvents [186]. In addition to this it important to note that the extreme conditions reached in the cavitation bubble, has a capital importance in driving the process of NPs production. In particular close to its collapse phase are believed to be responsible for the ejection of material from the target and formation of the colloidal dispersion. In such way, the interaction of the plasma with the liquid could be for example to promote functionalization of the metal nanoparticles ablated in suitable solvents. And also, the pressurized solution effect has been evaluated [184].

5. References

1. F. Brech, L. Cross, Optical microemission stimulated by a ruby laser, Appl. Spectrosc. 16 (1962), 59-64.
2. F. J. Fortes, J. Moros, P. Lucena, L. M. Cabalín, J. J. Laserna, Laser-induced breakdown spectroscopy, Anal. Chem. 85 (2013), 640–669.
3. D. A. Cremers, R. C. Chinni, Laser-induced breakdown spectroscopy—capabilities and limitations, Appl. Spectrosc. Rev. 44 (2009), 457–506.
4. T. H. Maiman, Stimulated optical radiation in ruby, Nature 187 (1960), 493–494.
5. J. Debras Guédon, N. Liodec, De l'utilisation du faisceau d'un amplificateur a ondes lumineuses par émission induite de rayonnement (laser á rubis), comme source énergetique pour l'excitation des spectres d'émission des elements, C.R. Acad. Sci. 257 (1963), 3336–3339.
6. E. F. Runge, R. W. Minck, F. R. Bryan, Spectrochemical analysis using a pulsed laser source, Spectrochim. Acta 20 (1964), 733–735.
7. P. D. Maker, R. W. Terhune, C. M. Savage, Optical third harmonic generation, Proceedings of the 3rd International Conference on Quantum Electronics, Paris, Columbia University Press, New York 2(1964), 1559.
8. A. A. Buzukov, Y. A. Popov, V. S. Teslenko, Experimental study of explosion caused by focusing monopulse laser radiation in water, Zhurnal Prikladnoi Makhaniki i Tekhnicheskoi Fiziki 10 (1969), 17–22.
9. J. F. Ready, Development of plume of material vaporized by giant-pulse laser, Appl. Phys. Lett. 3 (1963), 11-13.
10. E. Archbold, T. P. Hughes, Electron temperature in a laser heated plasma, Nature 204 (1964), 670-670.

11. E. Archbold, D. W. Harper, T. P. Hughes, Time resolved spectroscopy of laser-generated microplasmas, British J. Appl. Phys.15 (1964), 1321-1327
12. T. R. Loree, L. J. Radziemski, Laser-induced breakdown spectroscopy: time-integrated applications, Plasma Chem. Plasma Proc. 1 (1981), 271–280.
13. L. J. Radziemski T. R. Loree, Laser-induced breakdown spectroscopy: time-resolved spectrochemical applications, Plasma Chem. Plasma Proc. 1 (1981), 281–293.
14. D. W. Hahn, N. Omenetto, Laser-Induced Breakdown Spectroscopy (LIBS), Part II: Review of Instrumental and Methodological Approaches to Material Analysis and Applications to Different Fields, Appl. Spectrosc.66 (2012), 347-419.
15. V. I. Babushok, F .C. De Lucia, Jr., J. L. Gottfried, C. A. Munson, A. W. Miziolek, Double pulse laser ablation and plasma: Laser induced breakdown spectroscopy signal enhancement, Spectrochim. Acta Part B 61 (2006), 999–1014.
16. L. M. Cabalín, A. González, V. Lazic, J. J. Laserna, Deep ablation and depth profiling by laser-induced breakdown spectroscopy (LIBS) employing multi-pulse laser excitation: Application to galvanized steel, Appl. Spectrosc. 65 (2011), 797–805.
17. F. J. Fortes, J.J. Laserna, The development of fieldable laser-induced breakdown spectrometer: No limits on the horizon, Spectrochim. Acta Part B 65 (2010), 975–990.
18. R. C. Wiens, S. Maurice, The ChemCam Team, The ChemCam instrument suite on the Mars Science Laboratory (MSL) rover: Body unit and combined system tests, Space Sci. Rev. 170 (2012), 167–227.
19. S. Maurice, R. C. Wiens, The ChemCam Team, The ChemCam instrument suite on the Mars Science Laboratory (MSL) rover: Science objectives and mast unit description, Space Sci. Rev. 170 (2012), 95–166.
20. R. C. Wiens, S. Maurice, The ChemCam Team, The ChemCam instrument suite on the Mars Science Laboratory rover Curiosity: remote sensing by laser-induced plasmas, Geochem. News 145 (2011), 41–48.
21. S. Guirado, F.J. Fortes, V. Lazic, J.J. Laserna, Chemical analysis of archeological materials in submarine environments using laser-induced breakdown spectroscopy, On-site trials in the Mediterranean Sea. Spectrochim. Acta B 74–75 (2012), 137–143.
22. B. Thornton, T. Takahashi, T. Sato, T. Sakka, A. Tamura, A. Matsumoto, T. Nozaki, T. Ohki, K. Ohki, Development of a deep- sea laser-induced breakdown spectrometer for in situ multi-element chemical analysis, Deep-Sea Research I 95(2015), 20–36.
23. R. Noll, C. Fricke-Begemann, M. Brunk, S. Connemann, C. Meinhardt, M. Scharun, V. Sturm, J. Makowe, C. Gehlen, Laser-induced breakdown spectroscopy expands into industrial applications, Spectrochim. Acta Part B 93 (2014), 41–51.

24. Q. Q. Wang, K. Liu, H. Zhao, C.H. Ge, Z.W. Huang, Detection of explosives with laser-induced breakdown spectroscopy, Front. Phys. 7 (2012), 701–707.
25. J. L. Gottfried, F. C. De Lucia Jr., C. A. Munson, A. W. Miziolek, Laser-induced breakdown spectroscopy for detection of explosives residues: A review of recent advances, challenges, and future prospects, Anal. Bioanal. Chem. 395 (2009), 283–300.
26. R. S. Harmon, J. Remus, N. J. McMillan, C. McManus, L. Collins, J. L. Gottfried, F.C. De Lucia Jr., A. W. Miziolek, LIBS analysis of geomaterials: Geochemical fingerprinting for the rapid analysis and discrimination of minerals, Appl. Geochem. 24 (2009), 1125–1141.
27. V. K. Singh, A. K. Rai, Prospects for laser-induced breakdown spectroscopy for biomedical applications: A review, Lasers Med. Sci. 26 (2011), 673–687.
28. R. Gaudiuso, M. Dell'Aglio, O. de Pascale, G. S. Senesi, A. de Giacomo, Laser-induced breakdown spectroscopy for elemental analysis in environmental, cultural heritage and space applications: A review of methods and results, Sensors 10 (2010), 7434–7468.
29. D.W. Hahn, N. Omenetto, Laser-induced breakdown spectroscopy (LIBS), part I: Review of basic diagnostics and plasma particle interactions: Still-challenging issues within the analytical plasma community, Appl. Spectrosc. 64 (2010), 335–366.
30. C. Aragón, J.A. Aguilera, Characterization of laser induced plasmas by optical emission spectroscopy: a review of experiments and methods, Spectrochim. Acta Part B 63 (2008), 893-916.
31. Y.I. Lee, K. Song, J. Sneddon, Laser-induced breakdown spectroscopy, Nova Science Publishers, Huntington (2000).
32. A.W. Miziolek, V. Palleschi, I. Schechter, Laser-induced breakdown spectroscopy (LIBS), fundamentals and applications, Cambridge University Press, New York (2006).
33. D.E. Cremers, L. J. Radziemski, Handbook of Laser-Induced Breakdown Spectroscopy, John Wiley & Sons, New York (2006).
34. A. De Giacomo, M. Dell'Aglio, R. Gaudiuso, S. Amoruso, O. De Pascale, Effects of the background environment on formation, evolution and emission spectra of laser-induced plasmas, Spectrochim. Acta Part B 78 (2012), 1–19.
35. L.V. Zhigilei, Z. Lin, D.S. Ivanov, Atomistic modeling of short pulse laser ablation of metals: connections between melting, spallation, and phase explosion, J. Phys. Chem. C 113 (2009), 11892–11906.
36. N.M. Bulgakova, R. Stoian, A. Rosenfeld, I.V. Hertel, W. Marine, E.E.B. Campbell, A general continuum approach to describe fast electronic transport in pulsed laser irradiated materials: the problem of Coulomb explosion, Appl. Phys. A 81 (2005), 345–356.
37. J. Yu, Q. Ma, V. Motto-Ros, W. Lei, X. Wang, X. Bai, Generation and expansion of laser-induced plasma as a spectroscopic emission source, Front. Phys. 7 (2012), 649–669.

38. D. D. Vallejo, Spectroscopic investigations of plasma emission induced during laser material processing, epubli GmbH, Berlin (2014).
39. X. Mao, W. Chan, M. Caetano, M.A. Shannon, R.E. Russo, Preferential vaporization and plasma shielding during nano-second laser ablation, Appl. Surf. Sci. 96–98 (1996), 126–130.
40. J.A. Aguilera, C. Aragón, F. Peñalba, Plasma shielding effect in laser ablation of metallic samples and its influence on LIBS analysis, Appl. Surf. Sci. 127–129 (1998), 309–314.
41. X. Mao, A.C. Ciocan, R.E. Russo, Preferential vaporization during laser ablation inductively coupled plasma atomic emission spectroscopy, Appl. Spectrosc. 52 (1998), 913–918.
42. R. Rozman, I. Grabec, E. Govekar, Influence of absorption mechanisms on laser-induced plasma plume, Appl. Surf. Sci. 254 (2008), 3295–3305.
43. G. Bekefi, Radiation processes in plasmas, John Wiley & Sons, New Jersey (1966).
44. Y. Zhou, B. Wu, S. Tao, A. Forsman, Y. Gao, Physical mechanism of silicon ablation with long nanosecond laser pulses at 1064 nm through time-resolved observation, Appl. Surf. Sci. 257 (2011), 2886–2890.
45. A. E. Hussein, P. K. Diwakar, S. S. Harilal, A. Hassanein, The role of laser wavelength on plasma generation and expansion of ablation plumes in air, J. Appl. Phys. 113 (2013), 143305.
46. C. Barnett, E. Cahoon, J. R. Almirall, Wavelength dependence on the elemental analysis of glass by laser induced breakdown spectroscopy, Spectrochim. Acta Part B 63 (2008), 1016–1023.
47. N. M. Shaikh, M. S. Kalhoro, A. Hussain, M.A. Baig, Spectroscopic study of a lead plasma produced by the 1064 nm, 532 nm and 355 nm of a Nd:YAG laser, Spectrochim. Acta Part B 88 (2013), 198–202.
48. T. Moscicki, J. Hoffman, Z. Szymanski, The effect of laser wavelength on laser-induced carbon plasma, J. Appl. Phys. 114 (2013), 083306-9.
49. A. Bogaerts, Z. Chen, Effect of laser parameters on laser ablation and laser-induced plasma formation: A numerical modeling investigation, Spectrochim. Acta Part B 60 (2005), 1280–1307.
50. V. Morel, A. Bultel, Theoretical study of the formation mechanism of laser-induced aluminum plasmas using Nd:YAG fundamental, second or third harmonics, Spectrochim. Acta Part B 94–95 (2014), 63–70.
51. Q. Ma, V. Motto-Ros, F. Laye, J. Yu, W. Lei, X. Bai, L. Zheng, H. Zeng, Ultraviolet versus infrared: effects of ablation laser wavelength on the expansion of laser-induced plasma into one-atmosphere argon gas, J. Appl. Phys. 111 (2012), 053301-1–053301-11.
52. B.N. Chichkov, C. Momma, S. Nolte, F. von Alvensleben, A. Tünnermann, Femtosecond, picosecond and nanosecond laser ablation of solids, Appl. Phys. A 63 (1996), 109-115.
53. Y. Zhou, B. Wu, A. Forsman, Time-resolved observation of the plasma induced by laser metal ablation in air at atmospheric pressure, J. Appl. Phys. 108 (2010), 093504-1–093504-7.

54. Y. Zhou, S. Tao, B. Wu, Backward growth of plasma induced by long nanosecond laser pulse ablation, Appl. Phys. Lett. 99 (2011), 051106-1–051106-3.

55. E. Axente, S. Noël, J. Hermann, M. Sentis, I.N. Mihailescu, Subpicosecond laser ablation of copper and fused silica: initiation threshold and plasma expansion, Appl. Surf. Sci. 255 (2009), 9734–9737.

56. R.E. Russo, X.L. Mao, C. Liu, J. González, Laser assisted plasma spectrochemistry: laser ablation, J. Anal. At. Spectrom. 19 (2004), 1084–1089.

57. T. Sakka, S. Masai, K. Fukami, Y.H. Ogata, Spectral profile of atomic emission lines and effects of pulse duration on laser ablation in liquid, Spectrochim. Acta Part B 64 (2009), 981-985.

58. J.D. Ingle, S.R. Crouch, Spectrochemical analysis, Prentice Hall, Englewood Cliffs, USA (1988).

59. M. Cirisan, J.M. Jouvard, L. Lavisse, L. Hallo, R. Oltra, Laser plasma plume structure and dynamics in the ambient air: the early stage of expansion, J. Appl. Phys. 109 (2011), 103301-1–03301-17.

60. S. S. Harilal, C. V. Bindhu, Riju C. Issac, V. P. N. Nampoori, and C. P. G. Vallabhan, Electron density and temperature measurements in a laser produced carbon plasma, J. Appl. Phys. 82 (1997), 2140–2146.

61. A.K. Shuaibov, L.V. Mesarosh, M.P. Chuchman, Features of the formation of a laser flare from aluminum in the presence of a background gas, J. Opt. Technol. 78 (2011), 358-361.

62. M.P. Chuchman, A.K. Shuaibov, L.V. Mesarosh, Effect of air pressure on the spatial and emission characteristics of an aluminum laser torch under subthreshold conditions of ablation, Tech. Phys. 56 (2011), 117-120.

63. D. N. Patel, P. K. Pandey, R. K. Thareja, Stoichiometric investigations of laser-ablated brass plasma, Appl. Opt. 51 (2012), B192−B200.

64. A. De Giacomo, M. Dell'Aglio, O. De Pascale, Single-pulse laser induced plasma spectroscopy in aqueous solution, Appl. Phys. A 79 (2004), 1035–1038.

65. A. J. Effenberger Jr., J. R. Scott, Effect of atmospheric conditions on LIBS spectra, Sensors 10 (2010), 4907–4925.

66. Y. Iida, Effects of atmosphere on laser vaporization an excitation processes of solid samples, Spectrochim. Acta Part B 45 (1990), 1353–1367.

67. J. A. Aguilera, C. A. Aragón, Comparison of the temperatures and electron densities of laser-produced plasmas obtained in air, argon, and helium at atmospheric pressure, Appl. Phys. A Mater. 69 (1999), S475–S478.

68. E. Vors, C. Gallou, L. Salmon, Laser-induced breakdown spectroscopy of carbon in helium and nitrogen at high pressure, Spectrochim. Acta Part B 63 (2008), 1198–1204.

69. X.L. Mao, W.T Chan, M.A Shannon, R.E Russo, Plasma shielding during picosecond laser sampling of solid materials by ablation in He versus Ar atmosphere. J. Appl. Phys. 74 (1993), 4915-4922.

70. W. Sdorra, K. Niemax, Basic investigations for laser microanalysis. III. Application of different buffer gases for laser-produced sample plumes, Microchim. Acta 107 (1992), 319–327.

71. R. Viskup, B. Praher, T. Stehrer, J. Jasik, H. Wolfmeir, E. Arenholz, J.D. Pedarnig, J. Heitz, Plasma plume photography and spectroscopy of Fe–Oxide materials, J. Appl. Surf. Sci. 255 (2009), 5215–5219.

72. T.A. Labutin, A.M. Popov, V.N. Lednev, N.B. Zorov, Correlation between properties of a solid sample and laser-induced plasma parameters, Spectrochim. Acta Part B 64 (2009), 938–949.

73. J.A. Aguilera, C. Aragón, C. Madurga, V. Manrique, Study of matrix effects in laser induced breakdown spectroscopy on metallic samples using plasma characterization by emission spectroscopy, Spectrochim. Acta Part B 64 (2009), 993–998.

74. C. Tendero, C. Tixier, P. Tristant, J. Desmaison, P. Leprince, Atmospheric pressure plasmas: A review, Spectrochim. Acta Part B 61 (2006), 2–30.

75. R. W. P. McWhirter, in: Eds. R.H. Huddlestone, S.L. Leonard, Plasma diagnostic techniques, Academic Press, New York (1965), 201–264.

76. J. A. Aguilera, C. Aragón, Multi-element, Saha–Boltzmann and Boltzmann plots in laser-induced plasmas, Spectrochim. Acta Part B 62 (2007), 378–385.

77. S. Rai, A. K. Rai and S. N. Thakur, Identification of nitrocompounds with LIBS, Appl. Phys. B: Lasers Opt. 91 (2008), 645–650.

78. M. Dong, X. Mao, J. J. González, J. Lu, R. E. Russo, Time-resolved LIBS of atomic and molecular carbon from coal in air, argon and helium, J. Anal. At. Spectrom. 27 (2012), 2066–2075.

79. G. Cristoforetti, E. Tognoni, L. A. Gizzi, Thermodynamic equilibrium states in laser-induced plasmas: From the general case to laser-induced breakdown spectroscopy plasmas, Spectrochim. Acta Part B 90 (2013), 1–22

80. A.P.M. Michel, Review: applications of single-shot laser-induced breakdown spectroscopy, Spectrochim. Acta Part B 65 (2010), 185–191.

81. J. Scaffidi, S.M. Angel, D.A. Cremers, Emission enhancement mechanisms in dual-pulse LIBS, Anal. Chem. 78 (2006), 24-32.

82. V. Piñón, C. Fotakis, G. Nicolas, D. Anglos, Double pulse laser-induced breakdown spectroscopy with femtosecond laser pulses, Spectrochim. Acta Part B 63 (2008), 1006-1010.

83. A. Santagata, D. Spera, G. Albano, R. Teghil, G.P. Parisi, A. De Bonis, P. Villani, Orthogonal fs/ns double-pulse libs for copper-based-alloy analysis, Appl. Phys. A: Mater. Sci. Process. 93 (2008), 929-93

84. S. Choi, M. Oh, Y. Lee, S. Nam, D. Ko, J. Lee, Dynamic effects of a pre-ablation spark in the orthogonal dual-pulse laser induced breakdown spectroscopy, Spectrochim. Acta Part B 64 (2009), 427-435.

85. A. De Giacomo, M. Dell'Aglio, D. Bruno, R. Gaudiuso, O. De Pascale, Experimental and theoretical comparison of single-pulse and double-pulse laser induced breakdown spectroscopy on metallic samples, Spectrochim. Acta Part B 63 (2008), 805–816.

86. V. Piscitelli, M.A. Martínez L., A.J. Fernández C., J.J. González, X.L. Mao, R.E. Russo, Double pulse laser induced breakdown spectroscopy: experimental study of lead emission intensity dependence on the wavelengths and sample matrix, Spectrochim. Acta Part B 64 (2009), 147–154.

87. Y. Lu, V. Zorba, X. Mao, R. Zheng, R.E. Russo, UV fs–ns double-pulse laser induced breakdown spectroscopy for high spatial resolution chemical analysis, J. Anal. At. Spectrom. 28 (2013), 743–748.

88. P.K. Diwakar, S.S Harilal, J.R Freeman, A. Hassanein, Role of laser pre-pulse wavelength and inter-pulse delay on signal enhancement in collinear double-pulse laser-induced breakdown spectroscopy, Spectrochim. Acta Part B 87 (2013), 65–73.

89. N. Jedlinszki, G. Galbács, An evaluation of the analytical performance of collinear multi-pulse laser induced breakdown spectroscopy, Microchem. J. 97 (2011), 255–263.

90. R. Sattmann, V. Sturm, R. Noll, Laser-induced breakdown spectroscopy of steel samples using multiple Q-switch Nd:YAG laser pulses, J. Phys. D Appl. Phys. 28 (1995), 2181–2187.

91. Z. Fu, B. Wu, Y. Gao, Y. Zhou, C. Yu, Experimental study of infrared nanosecond laser ablation of silicon: the multi-pulse enhancement effect, Appl. Surf. Sci. 256 (2010), 2092–2096.

92. J. Cuñat, F.J. Fortes, L.M. Cabalín, F. Carrasco, M.D. Simón, J.J. Laserna, Man-portable laser-induced breakdown spectroscopy system for in situ characterization of karstic formations, Appl. Spectrosc. 62 (2008), 1250–1255.

93. F.J. Fortes, J. Cuñat, L.M. Cabalín, J.J. Laserna, In situ analytical assessment and chemical imaging of historical buildings using a man-portable laser system, Appl. Spectrosc. 61 (2007), 558-564.

94. J. Cuñat, S. Palanco, F. Carrasco, M.D. Simón, J.J. Laserna, Portable instrument and analytical method using laser-induced breakdown spectrometry for in situ characterization of speleothems in karstic caves, J. Anal. At. Spectrom. 20 (2005), 295-300.

95. J. Cuñat, F.J. Fortes, J.J. Laserna, Real time and in situ determination of lead in road sediments using a man-portable laser-induced breakdown spectroscopy analyzer, Anal. Chim. Acta. 633 (2009), 38-42.

96. F.J. Fortes, T. Čtvrtníčková, M.P. Mateo, L.M. Cabalín, G. Nicolas, J.J. Laserna, Spectrochemical study for the in-situ detection of oil spill residues using laser-induced breakdown spectroscopy, Anal. Chim. Acta 683 (2010), 52-57.

97. C.A. Munson, J.L. Gottfried, E.G. Snyder, F.C. DeLucia Jr., B. Gullett, A.W. Miziolek, Detection of indoor biological hazards using the man-portable laser induced breakdown spectrometer, Appl. Opt. 47 (2008), G48-G57.

98. J. Goujon, A. Giakoumaki, V. Piñón, O.Musset, D. Anglos, E. Georgiou, J.P. Boquillon, A compact and portable laser-induced breakdown spectroscopy instrument for single and double pulse applications, Spectrochim. Acta Part B 63 (2008), 1091-1096.

99. B. Bousquet, G. Travaillé, A. Ismaël, L. Canioni, K. Michel-Le Pierrès, E. Brasseur, S. Roy, I. le Hecho, M. Larregieu, S. Tellier, M. Potin-Gautier, T. Boriachon, P. Wazen, A. Diard, S. Belbèze, Development of a mobile system based on laser-induced breakdown spectroscopy and dedicated to in situ analysis of polluted soils, Spectrochim. Acta Part B 63 (2008), 1085-1090.

100. D.A. Cremers, J.E. Barefield II, A.C. Koskelo, Remote elemental analysis by laser-induced breakdown spectroscopy using a fiber-optic cable, Appl. Spectrosc. 49 (1995), 857-860.

101. G.A. Theriault, S. Bodensteiner, S.H. Lieberman, A real-time fiber-optic LBS probe for the in situ delineation of metals in soils, Field Anal. Chem. Technol. 2 (1998), 117-125.

102. A.I. Whitehouse, J. Young, I.M. Botheroyd, S. Lawson, C.P. Evans, J. Wright, Remote material analysis of nuclear power station steam generator tubes by laser-induced breakdown spectroscopy, Spectrochim. Acta Part B 56 (2001), 821-830.

103. A.K. Rai, H. Zhang, F.Y. Yueh, J.P. Singh, A. Weisburg, Parametric study of a fiber optic laser-induced breakdown spectroscopy probe for analysis of aluminum alloys, Spectrochim. Acta Part B 56 (2001), 2371-2383.

104. S. Guirado, F.J. Fortes, J.J. Laserna, Elemental analysis of materials in an underwater archeological shipwreck using a novel remote laser-induced breakdown spectroscopy system, Talanta 137 (2015), 182-188.

105. B. Sallé, P. Mauchien, S. Maurice, Laser-induced breakdown spectroscopy in openpath configuration for the analysis of distant objects, Spectrochim. Acta Part B 62 (2007), 739–768.

106. F.J, Fortes, S. Guirado, A. Metzinger, J.J. Laserna, A study of underwater stand-off laser-induced breakdown spectroscopy for chemical analysis of objects in the deep ocean, J. Anal. At. Spectrom. (2015), 1050-1056.

107. S. Wallin, A. Pettersson, H. Östmark, A. Hobro, Laser-based standoff detection of explosives: a critical review, Anal. Bioanal. Chem. 395 (2009), 259-274.

108. R. González, P. Lucena, L.M. Tobaria, J.J. Laserna, Standoff LIBS detection of explosive residues behind a barrier, J. Anal. At. Spectrom. 24 (2009), 1123-1126.

109. R.M.E. Williams, J.P. Grotzinger, W.E. Dietrich, S. Gupta, D.Y. Sumner, R.C. Wiens, N. Mangold, M.C. Malin, K.S. Edgett, S. Maurice, O. Forni, O. Gasnault, A. Ollila, H.E. Newsom, G. Dromart, M.C. Palucis, R.A. Yingst, R.B. Anderson, K.E. Herkenhoff, S. Le Mouélic, W. Goetz, M.B.

Madsen, A. Koefoed, J.K. Jensen, J.C. Bridges, S.P. Schwenzer, K.W. Lewis, K.M. Stack, D. Rubin, L.C. Kah, J.F. Bell III, J.D. Farmer, R. Sullivan, T. Van Beek, D.L. Blaney, O. Pariser, R.G. Deen, MSL Science Team, Martian fluvial conglomerates at Gale Crater, Science 340 (2013), 1068-1072.

110. N. Melikechi, A. Mezzacappa, A. Cousin, N.L. Lanza and 20 more authors and the MSL Science Team, Correcting for variable laser-target distances of laser-induced breakdown spectroscopy measurements with ChemCam using emission lines of Martian dust spectra, Spectrochim. Acta Part B 96 (2014), 51-60.
111. B. Thornton, T.Takahashi, T.Sato, T.Sakka, A. Tamura, A.Matsumoto, T. Nozaki, T. Ohki, K. Ohki, Development of a deep-sea laser-induced breakdown spectrometer for in situ multi-element chemical analysis, Deep-Sea ResearchI 95 (2015), 20–36
112. J. J. Laserna, R. Fernández-Reyes, R. González, L. Tobaria, P. Lucena, Study on the effect of beam propagation through atmospheric turbulence on standoff nanosecond laser induced breakdown spectroscopy measurements, Opt. Express 17 (2009), 10265–10276.
113. L. Caneve, A. Diamanti, F. Grimaldi, G. Palleschi, V. Spizzichino, F. Valentini, Analysis of fresco by laser induced breakdown spectroscopy, Spectrochim. Acta, Part B65 (2010), 702−706.
114. A. Staicu, I. Apostol, A. Pascu, I. Iordache, V. Damian, M. L. Pascu, Laser induced breakdown spectroscopy stratigraphic characterization of multilayered painted surfaces, Spectrochim. Acta, Part B74−75 (2012), 151−155.
115. E. A. Kaszewska, M. Sylwestrzak, J. Marczak, W. Skrzeczanowski, M. Iwanicka, E. Szmit-Naud, D. Anglos, P. Targowski, Depth-resolved multilayer pigment identification in paintings: combined use of laser-induced breakdown spectroscopy (LIBS) and optical coherence tomography (OCT), Appl Spectrosc 67 (2013), 960–972
116. G. Vitkova, L. Prokes, K. Novotny, P. Porizka, J. Novotny, D. Vsiansky, L. Celko , J. Kaiser, Comparative study on fast classification of brick samples by combination of principal component analysis and linear discriminant analysis using stand-off and table-top laser-induced breakdown spectroscopy, Spectrochim Acta B 101(2014),191–199
117. M. A. Kasem, R.E. Russo, M.A. Harith, Influence of biological degradation and environmental effects on the interpretation of archeological bone samples with laser-induced breakdown spectroscopy,J Anal At Spectrom 26 (2011), 1733–1739.
118. O. Kokkinaki, C. Mihesan, M. Velegrakis, D. Anglos, Comparative study of laser induced breakdown spectroscopy and mass spectrometry for the analysis of cultural heritage materials,J Mol Struct 1044 (2013), 160–166.
119. G. Vitkova, K. Novotny, L. Prokes, A. Hrdlicka, J. Kaiser, J. Novotny, R. Malina, D. Prochazka, Fast identification of biominerals by means of stand-off laser-induced breakdown spectroscopy using linear discriminant analysis and artificial neural networks, Spectrochim Acta B 73 (2012),1–6.

120. J. Ruiz, A. González, L.M. Cabalín, J.J. Laserna, On-line laser-induced breakdown spectroscopy determination of magnesium coating thickness on electrolytically galvanized steel in motion, Appl. Spectrosc. 64 (2010), 1342-1349.
121. S. Legnaioli, G. Lorenzetti, L. Pardini, V. Palleschi, D.M. Diaz Pace, F. Anabitarte Garcia, R. Grassi, F. Sorrentino, G. Carelli, M. Francesconi, F. Francesconi, R. Borgogni, Laser-induced breakdown spectroscopy application to control of the process of precious metal recovery and recycling, Spectrochim. Acta Part B 71-72 (2012), 123-126.
122. M. Banaee, S.H. Tavassoli, Discrimination of polymers by laser induced breakdown spectroscopy together with the DFA method, Polym. Test. 31(2012), 759–764.
123. V.S. Burakov, S.N. Raikov, N.V. Tarasenko, M.V. Belkov, V.V. Kiris, Development of laser induced breakdown spectroscopy method for soil and ecological analysis, J. Appl. Spectrosc. 77 (2010), 595-608.
124. L.C. Trevizan, D. Santos Jr., R.E. Samad, N.D. Vieira Jr., C.S. Nomura, L.C. Nunes, I.A. Rufini, F.J. Krug, Evaluation of laser induced breakdown spectroscopy for the determination of macronutrients in plant materials, Spectrochim. Acta Part B 63 (2008), 1151-1158.
125. L.C. Trevizan, D. Santos Jr., R.E. Samad, N.D. Vieira Jr., L.C. Nunes, I.A. Rufini, F.J. Krug, Evaluation of laser induced breakdown spectroscopy for the determination of micronutrients in plant materials, Spectrochim. Acta Part B 64 (2009), 369-377.
126. S. Krizkova, P. Ryant, O. Krystofova, V. Adam, M. Galiova, M. Beklova, P. Babula, J. Kaiser, K. Novotny, J. Novotny, M. Liska, R. Malina, J. Zehnalek, J. Hubalek, L. Havel, R. Kizek, Multi-instrumental analysis of tissues of sunflower plants treated with silver(I) ions - Plants as bioindicators of environmental pollution, Sensors 8 (2008), 445-463.
127. M. Galiova, J. Kaiser, K. Novotny, J. Novotny, T. Vaculovic, M. Liška, R. Malina, K. Stejskal, V. Adam, R. Kizek, Investigation of heavy-metal accumulation in selected plant samples using laser induced breakdown spectroscopy and laser ablation inductively coupled plasma mass spectrometry Appl. Phys. A: Mater. Sci. Process. 93 (2008), 917−922.
128. K. Park, G. Cho, J.H. Kwak, Development of an aerosol focusing-laser induced breakdown spectroscopy (aerosol focusing-LIBS) for determination of fine and ultrafine metal aerosols, Aerosol Sci. Technol. 43 (2009), 375-386.
129. G. Gallou, J.B. Sirven, C. Dutouquet, O.L. Bihan, E. Frejafon, Aerosols analysis by LIBS for monitoring of air pollution by industrial sources, Aerosol Sci. Tech. 45 (2011), 918-926.
130. J.S. Caygill, F. Davis, S.P.J. Higson, Current trends in explosives detection techniques, Talanta 88 (2012), 14-29.
131. S. Musazzi, U. Perini, Laser-induced Breakdown Spectroscopy, theory and applications; Springer-Verlag, Berlin (2014),349-375.

132. M. Tran, Q. Sun, B.W. Smith, J.D. Winefordner, Determinación of C:H:O:N ratios in solid organic compounds by LIBS, J. Anal. At. Spectrom. 16 (2001), 628-632.
133. F.C. De Lucia, J. L. Gottfried Jr, Classification of explosive residues on organic substrates using laser induced breakdown spectroscopy, Appl Opt 51 (2012), 83–92.
134. I. Gaona, J. Serrano, J. Moros, J. J. Laserna, Range-adaptive standoff recognition of explosive fingerprints on solid surfaces using a supervised learning method and laser-induced breakdown spectroscopy,Anal Chem 86 (2014), 5045–5052.
135. E. Schenk, J.R. Almirall, Elemental analysis of cotton by laser-induced breakdown spectroscopy, Appl Opt 49 (2010), 153–160.
136. A. Kula, R. Wietecha-Posluszny, K. Pasionek, M. Krol, M. Wozniakiewicz, P. Koscielniak, Application of laser induced breakdown spectroscopy to examination of writing inks for forensic purposes, Sci Justice 54 (2014),118–125.
137. S. Moncayo, S. Manzoor, T. Ugidos, F. Navarro-Villoslada, J.O. Caceres, Discrimination of human bodies from bones and teeth remains by laser induced breakdown spectroscopy and neural networks,Spectrochim Acta B 101 (2014), 21–25.
138. M. Bahreini, B. Ashrafkhani, S.H. Tavassoli, Elemental analysis of fingernail of alcoholic and doping subjects by laser-induced breakdown spectroscopy, Appl Phys B Lasers Opt 114 (2014), 439–447.
139. S. C. Jantzi, J.R. Almirall, Elemental analysis of soils using laser ablation inductively coupled plasma mass spectrometry (LAICP-MS) and laser-induced breakdown spectroscopy (LIBS) with multivariate discrimination: tape mounting as an alternative to pellets for small forensic transfer specimens, Appl Spectrosc 68 (2014), 963–974.
140. S. J. Rehse, H. Salimnia, A.W. Miziolek, Laser-induced breakdown spectroscopy (LIBS): an overview of recent progress and future potential for biomedical applications, J. Med. Eng. Technol. 36 (2012), 77–89.
141. F. Y. Yueh, H. Zheng, J.P. Singh, S. Burgess, Preliminary evaluation of laser-induced breakdown spectroscopy for tissue classification, Spectrochim. Acta Part B 64 (2009), 1059–1067.
142. R. K. Thareja, A. K Sharma, S. Shukla, Spectroscopic investigations of carious tooth decay, Med. Eng. Phys. 30 (2008), 1143–1148.
143. J. Anzano, R.J. Lasheras, Strategies for the identification of urinary calculus by laser induced breakdown spectroscopy, Talanta 79 (2009), 352–360.
144. R. A. Multari, D. A. Cremers, M. L. Bostian, Use of laser-induced breakdown spectroscopy for the differentiation of pathogens and viruses on substrates, Appl. Optic. 51 (2012), B57−B64.
145. A. El-Hussein, A.K. Kassem, H. Ismail, M. A. Harith, Exploiting LIBS as a spectrochemical analytical technique in diagnosis of some types of human malignancies, Talanta 82 (2010), 495–501.

146. D. Vaniman, D. Dyar, R. Wiens, A. Ollila, N. Lanza, J. Lasue, J.M. Rhodes, S. Clegg, H. Newsom, Ceramic ChemCam calibration targets on Mars Science Laboratory, Space Sci. Rev. 170 (2012), 229-255.

147. N.L. Lanza, S.M. Clegg, R.C. Wiens, R.E. McInroy, H.E. Newsom, M.D. Deans, Examining natural rock varnish and weathering rinds with laser-induced breakdown spectroscopy for application to ChemCam on Mars, Appl. Opt. 51 (2012), 74-82.

148. P. Y. Meslin, O. Gasnault, O. Forni, S. Schröder, A. Cousin, G. Berger, S. M. Clegg, J. Lasue, S. Maurice, V. Sautter, S. Le Mouélic, R. C. Wiens, C. Fabre, W. Goetz, D. Bish, N. Mangold, B. Ehlmann, N. Lanza, A.M. Harri, R. Anderson, E. Rampe, T.H. McConnochie, P. Pinet, D. Blaney, R. Léveillé, D. Archer, B. Barraclough, S. Bender, D. Blake, J.G. Blank, N. Bridges, B.C. Clark, L. DeFlores, D. Delapp, G. Dromart, M.D. Dyar, M. Fisk, B. Gondet, J. Grotzinger, K. Herkenhoff, J. Johnson, J.L. Lacour, Y. Langevin, L. Leshin, E. Lewin, M.B. Madsen, N. Melikechi, A. Mezzacappa, M.A. Mischna, J.E. Moores, H. Newsom, A. Ollila, R. Perez, N. Renno, J.B. Sirven, R. Tokar, M. de la Torre, L. d'Uston, D. Vaniman, A. Yingst, MSL Science Team, Soil diversity and hydration as observed by ChemCam at Gale Crater, Mars, Science 341 (2013),1238670-1–1238670-10.

149. A. De Giacomo, M. Dell'Aglio, O. De Pascale, M. Capitelli, From single pulse to double pulse ns-Laser Induced Breakdown Spectroscopy under water: elemental analysis of aqueous solutions and submerged solid samples, Spectrochim. Acta Part B 62 (2007), 721–738.

150. J.P. Longtin, C.L. Tien, Efficient laser heating of transparent liquids using multiphoton absorption, Int. J. Heat Mass Transfer. 40/4 (1997), 951–959.

151. R.A. Crowell, D.M. Bartels, Multiphoton Ionization of Liquid Water with 3.0–5.0 eV Photons, J. Phys. Chem. 100 (1996), 17940–17949.

152. K. Kennedy, D.X. Hammer, B.A. Rockwell, Laser induced plasma in aqueous media, Prog. Quant. Electr. 21 (1997), 155–248.

153. S. Musazzi, U. Perini, Laser-induced Breakdown Spectroscopy, theory and applications; Springer-Verlag, Berlin (2014),195-226.

154. I. Akhatov, O. Lindau, A. Topolnikov, R. Mettin, N. Vakhitova, W. Lauterborn, Collapse and rebound of a laser-induced cavitation bubble, Phys.Fluids 13 (2001), 2805-2819.

155. V. Lazic, S. Jovicevic, R. Fantoni, F. Colao, Efficient plasma and bubble generation underwater by an optimized laser excitation and its application for liquid analyses by laser-induced breakdown spectroscopy, Spectrochim. Acta Part B 62 (2007), 1433–1442.

156. V. Lazic, J.J. Laserna, S. Jovicevic, Insights in the laser-induced breakdown spectroscopy signal generation underwater using dual pulse excitation. Part I: Vapor bubble, shockwaves and plasma, Spectrochimica Acta Part B 82 (2013), 42–49.

157. M. Lawrence-Snyder, J. Scaffidi, S.M. Angel, A.D. Chave, Laser-induced breakdown spectroscopy of high-pressure bulk aqueous solutions, Appl. Spectrosc. 60 (2006), 786–790.
158. M. Lawrence-Snyder, J. Scaffidi, S.M. Angel, A.D. Chave, Sequential-pulse laser-induced breakdown spectroscopy of high-pressure bulk aqueous solutions, Appl. Spectrosc. 61 (2007), 171–176.
159. A.P.M. Michel, M. Lawrence-Snyder, S.M. Angel, A.D. Chave, Laser-induced breakdown spectroscopy of bulk aqueous solutions at oceanic pressures: evaluation of key measurement parameters, Appl. Opt. 46 (2007), 2507–2515.
160. A.P.M. Michel, A.D. Chave, Double pulse laser-induced breakdown spectroscopy of bulk aqueous solutions at oceanic pressures: interrelationship of gate delay, pulse energies, interpulse delay, and pressure, Appl. Opt. 47 (2008), 131–143.
161. B. Thornton, T. Sakka, T. Masamura, A. Tamura, T. Takahashi, A. Matsumoto, Long-duration nano-second single pulse lasers for observation of spectra from bulk liquids at high hydrostatic pressures, Spectrochim. Acta, Part B97 (2014), 7–12.
162. B. Thornton, T. Sakka, T. Takahashi, A. Tamura, T. Masamura, A. Matsumoto; Spectroscopic Measurements of Solids Immersed in Water at High Pressure Using a Long-Duration Nanosecond Laser Pulse; Appl. Phys. Express 6 (2013), 082401-4.
163. J.P. Singh, S.N. Thakur, Laser-Induced Breakdown Spectroscopy, Elsevier, USA (2007), 223–254.
164. E.M. Cahoon, J.R. Almirall, Quantitative analysis of liquids from aerosols and microdrops using laser induced breakdown spectroscopy, Anal. Chem. 84 (2012), 2239–2244.
165. J. S. Huang, C. B. Ke, L. S. Huang, K.C. Lin, The correlation between ion production and emission intensity in the laser-induced breakdown spectroscopy of liquid droplets, Spectrochim. Acta Part B 57 (2002), 35–48.
166. S.T. Penin, L.K. Chistyakova, Uranium detection in aerosol particles on emission spectra of a laser plasma, J. Aerosol Sci. 27 (1996), 333–334.
167. D.C.S. Beddows, O. Samek, M. Liska, H.H. Telle, Single-pulse laser-induced breakdown spectroscopy of samples submerged in water using a single-fiber delivery system, Spectrochim. Acta Part B 57 (2002), 1461-1471.
168. D.A. Cremers, L.J. Radziemski, T.R. Loree, Spectrochemical analysis of liquids using the laser spark, Appl. Spectrosc. 38 (1984), 721–729.
169. H.W. Kang, H. Lee, A.J. Welch, Laser ablation in a liquid-confined environment using a nanosecond laser pulse, J. Appl. Phys. 103 (2008), 083101-6
170. A. Casavola, A. De Giacomo, M. Dell'Aglio, F. Taccogna, G. Colonna, O. De Pascale, S. Longo, Experimental investigation and modelling of double pulse laser induced plasma spectroscopy underwater, Spectrochim. Acta Part B 60 (2005), 975–985.

171. T. Sakka, H. Oguchi, S. Masai, K. Hirata, Y.H. Ogata, M. Saeki, H. Ohba, Use of a long-duration ns pulse for efficient emission of spectral lines from the laser ablation plume in water, Appl. Phys. Lett. 88 (2006), 061120-3.
172. T. Takahashi, B. Thornton, T. Sato, T. Ohki, K. Ohki, T. Sakka, Temperature based segmentation for spectral data of laser-induced plasmas for quantitative compositional analysis of brass alloys submerged in water, Spectrochimi. Acta Part B 124 (2016), 87–93.
173. P.Fichet, M. Tabarant, B. Salle, C. Gautier, Comparisons between LIBS and ICP/OES, Anal. Bioanal. Chem.385 (2006), 338-344.
174. S. Koch, W. Garen, M. Muller, W. Neu, Detection of chromium in liquids by laser induced breakdown spectroscopy (LIBS), Appl. Phys. A 79 (2004), 1071-1073.
175. T.Hussain, M.A. Gondal, Detection of Toxic Metals in Waste Water from Dairy Products Plant using Laser Induced Breakdown Spectroscopy, Bull. Environ. Contam. Toxicol. 80 (2008), 561-565.
176. K. Rai, A.K. Rai, LIBS-An Efficient Approach for the Determination of Cr in Industrial Wastewater. J. Hazard. Mater. 150 (2008), 835-838.
177. N. K. Rai, A.K. Rai,A. Kumar, S.N. Thakur, Detection sensitivity of laser-induced breakdown spectroscopy for Cr II in liquid samples. Appl. Opt., 47 (2008), 105–111.
178. M. Sadegh Cheri, S. H. Tavassoli, Quantitative analysis of toxic metals lead and cadmium in water jet by laser-induced breakdown spectroscopy, Appl. Opt. 50 (2011), 1227−1233.
179. A. De Giacomo, M. Dell'Aglio, F. Colao, R. Fantoni, V. Lazic, Double-Pulse LIBS in Bulk Water and on Submerged Bronze Samples, Appl. Surf. Sci., 247 (2005), 157-162.
180. V. Lazic, F. Colao, R. Fantoni, V. Spizzicchin, Recognition of archeological materials underwater by laser induced breakdown spectroscopy, Spectrochimi. Acta Part B 60 (2005), 1014–1024.
181. G.W. Yang, Laser ablation in liquids: applications in the synthesis of nanocrystals, Prog. Mater. Sci. 52 (2007), 648–698.
182. M. Kalyva, G. Bertoni, A. Milionis, R. Cingolani, A. Athanassiou, Tuning of the characteristics of Au nanoparticles produced by solid target laser ablation into water by changing the irradiation parameters, Microsc. Res. Tech. 73 (2010), 937–943.
183. F. Barreca, N. Acacia, S. Spadaro, G. Currò, F. Neri, Tungsten trioxide (WO3−x) nanoparticles prepared by pulsed laser ablation in water, Mater. Chem. Phys. 127 (2011), 197–202.
184. A. De Giacomo, A. De Bonis, M. Dell'Aglio, O. De Pascale, R. Gaudiuso, S. Orlando, A. Santagata, G.S. Senesi, F. Taccogna, R. Teghil, Laser ablation of graphite in water in a range of pressure from 1 to 146 atm using single and double pulse techniques for the production of carbon nanostructures, J. Phys. Chem. C 115 (2011), 5123–5130.

185. D. Amans, A.C. Chenus, G. Ledoux, C. Dujardin, C. Reynaud, O. Sublemontier, K. Masenelli-Varlot, O. Guillois, Nanodiamond synthesis by pulsed laser ablation in liquids, Diam. Relat. Mater. 18 (2009), 177–180.

186. R. Matsutani, T. Kakimoto, H. Tanaka, K. Kojima, Preparation of polyynes by liquid-phase laser ablation using different irradiation target materials and solvents, Carbon 49 (2011), 77–81.

Chapter 3. Experimental

1. Overview

The characterization of underwater cultural heritage has become, over recent years, one of the areas of greatest interest in archaeology [1]. As described in *Chapter 1*, an enormous amount of historical information is stored not only at the deep of seas and oceans, which are the most common archaeological sites, but also in other enclaves such as rivers, lakes, and swamps [2-3]. However, extracting of information from these archaeological sites is not a trivial task. Normally, the remains are hardly visible since they are integrated into the natural surrounding because of their deterioration and of deposition of sediment material as time passes. Furthermore, sometimes the pieces may not be removed from the site due to logistical problems, such as their huge scale. Preserving the integrity of the piece as well as institutional constraints and additional bureaucratic requirements are also some of the reasons why these assets must remain in their current placement. Despite this, while it is essential to study, protect and preserve these assets, the UNESCO [4] considers the in-situ preservation of underwater cultural heritage as "*the first option before allowing or engaging in any activities directed at this heritage*". Thus, the direct analysis of the materials in the same place where they are discovered turns into the only alternative for obtaining information about these objects. Once discovered any remains, the chemical characterization of these pieces in their context may provide clues to identify their origin and to date the wreck.

Despite of analytical demand, only those sensing methods based on laser technology are aimed for the in situ chemical analysis of submerged materials. In fact, as described in *Chapter 2*, Laser-Induced Breakdown Spectroscopy (LIBS) is the only analytical method that combines many of the sought features in the oceanography field including multi-elemental information, no sample preparation, unlimited range of material capability and real time analysis [5]. In this sense, ***what solutions does LIBS propose?*** Several alternatives/configurations are aimed to adapt LIBS technology to the marine environment. Figure 1 schematically represents the two proposed alternatives in this Doctoral Thesis, a) a remote-LIBS instrument based on the transmission of laser radiation using an optical fiber cable operated on board in an auxiliary vessel; and b) a standoff-LIBS instrument that involves the delivery of a focused laser pulse toward the distant target through the aqueous media and then the transmission of the light emitted by the laser-induced plasma back to the detection system.

The present chapter encloses a deep description of the experimental alternatives that have been used to perform the research works, divided in two main parts. In Part I (*Chapters 4-6*),a remote-LIBS instrument, named AQUALAS 2.0, based on the transmission of laser radiation using an optical fiber cable operated on board in an auxiliary vessel. This prototype has been entirely designed, engineered and operatively adapted at the University of Málaga during the last 4 years. A complete description of each of the subsystems integrating AQUALAS 2.0 is also provided in this chapter. Finally, in Part II (*Chapters 7-8*) the effect of oceanic pressure on LIBS is investigated in order to evaluate the possibility of design a standoff-LIBS instrument that involves the delivery of a focused laser pulse toward the distant target through the aqueous. For this purpose, a high-pressure chamber has been constructed.

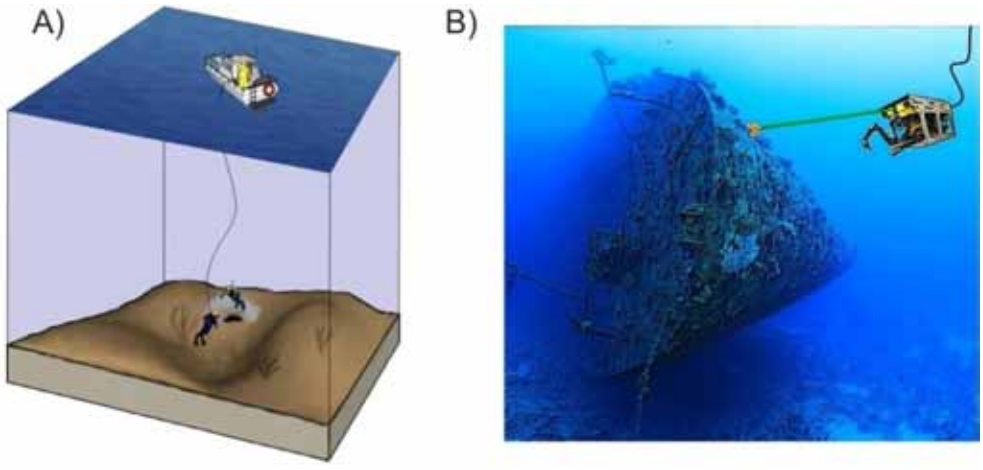

Figure 1. Schematic representation of two alternative configurations to adapt LIBS to the marine environment.

2. Remote LIBS sensor based on fiber optic transmission

The present Partof the Doctoral Thesis describes the prototype *AQUALAS 2.0*, a laser-based sensor specifically designed for the remote chemical analysis of submerged materials. This prototype is a new version of a previous effective device [6], with extended technology that allows performing LIBS analysis using either single- or multipulse- excitation. Furthermore, this advanced sensor is more compact, more robust and with an optical module more accessible, which facilitates maintenance and repair work.

The AQUALAS 2.0 prototype is based on a modular design with three well-defined parts: a main unit, a hand-held probe fitted to an umbilical cable of 50 m length, and an energy supply auxiliary unit. Figure 2 shows the different parts that constitute AQUALAS 2.0. As indicated, the main unit comprises the laser power supply, the optical module for laser–fiber coupling, and the data acquisition module. This main

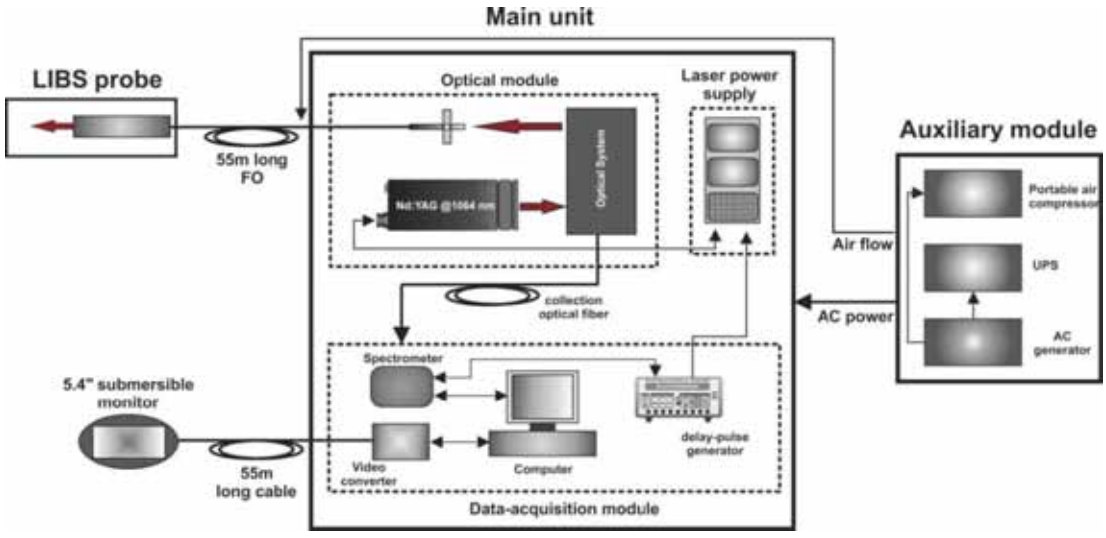

Figure 2. Overview of AQUALAS 2.0.

unit has an overall weight of 150 kg with dimensions of 81 × 86 × 126 cm^3. The technical characteristics of the instrumentation hosted in this unit are detailed in Table 1. Figure 3 shows a pair of photographs of the sensor in its "compact" and "deployed" modes for transportation and operation, respectively.

Along this section, the different systems and integrated subsystems in the prototype will be described according to the actuation hierarchy in the different stages of the analysis process as follows: the optical module, in which the laser-fiber coupling occurs; the transmission of laser radiation and protection gas across the umbilical cord, the LIBS probe, and the data acquisition module, where plasma light is spectroscopically resolved and the analytical information is processed.

2.1. Optical module

The optical module is the key component of the prototype, since it is upon which laser-fiber coupling stage takes place. Figure 4 depicts the layout of the optical components to fit laser radiation to the fiber-optic cable and, in parallel, to gather and to guide the plasma light towards the spectrograph. First, the laser head (Q-switched Nd:YAG laser, Brilliant, Quantel, France, operating at 1064 nm) produces the laser radiation. The laser beam is guided by a 1064 reflecting mirror (M1) and then focused by a plano-convex lens (L1) to the input of the optical fiber. Laser radiation travels through a pierced mirror (M2) with a channel of 5 mm diameter. M2 is positioned at 45º with respect to the propagating axis of the laser radiation. This optical

Table 1. Technical and structural characteristics of the underwater analyzer.

	Description
Dimensions (width x length x height)	86 x 81 x 126 cm
Weight	150 Kg
Opticalfiberlength	50 m
Opticalfiberdiameter	600 µm
Powerconsumption	2300 W
Laser	Q-Switch Nd:YAG(Brilliant, Quantel, France)
Wavelength	1064 nm
Repetitionfrequency	20 Hz
Pulse width	22ns (adjustable 7-40 ns)
Maximumenergy per pulse	400 mJ SP-LIBS
Input maximum energy to optical fiber	85 mJ (FWHM=22ns)
Output maximum energy from optical fiber	65 mJ (FWHM=22ns)
Spectrometer	Czerny-Turner, Avantes, Avaspec-2014, USB2 model
Diffraction grating	Holographic 1200 l/mm
Spectral resolution	0.1-0.2 nm/pixel
Spectral range	300-500 nm

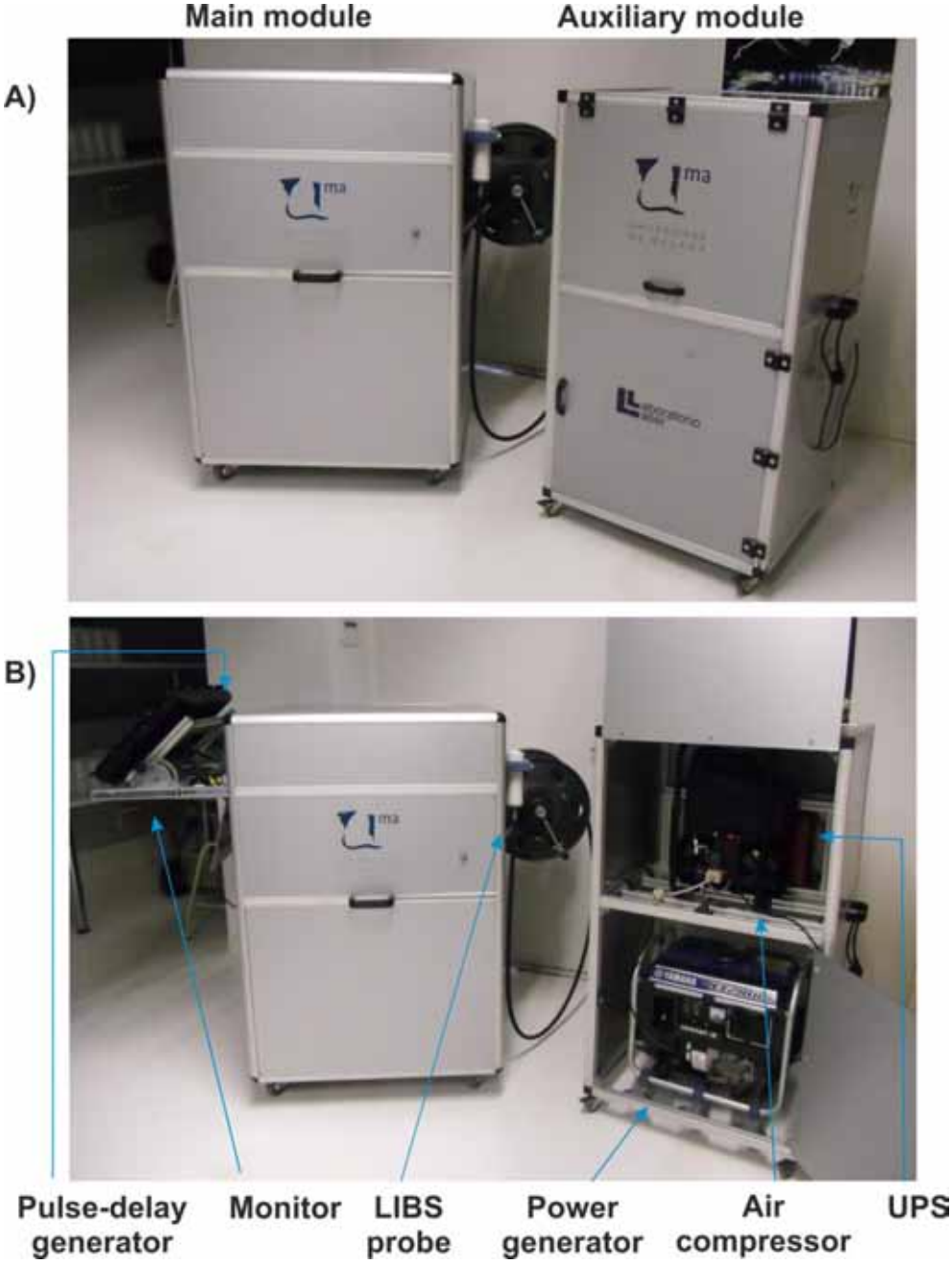

Figure 3. General overview of AQUALAS 2.0 prototype (A) in its "compact" mode for transportation; (B) in its "deployed" mode to operate with.

element is responsible for collecting the light from the plasma generated and sends it to the spectrometer. Before M2, the laser beam was focused by L1, and then is fed into a fiber-optic cable without cladding mounted in a*xyz* stage (all-silica, high-OH, UV-grade fiber, 55 m length, 550 µm core diameter and 0.22 N.A). In this point, the laser beam is transmitted through a 55-m long optical fiber cable sheltered inside an umbilical cord which connects the hand-held probe with the optical module. At the end of the fiber, the hand-held probe

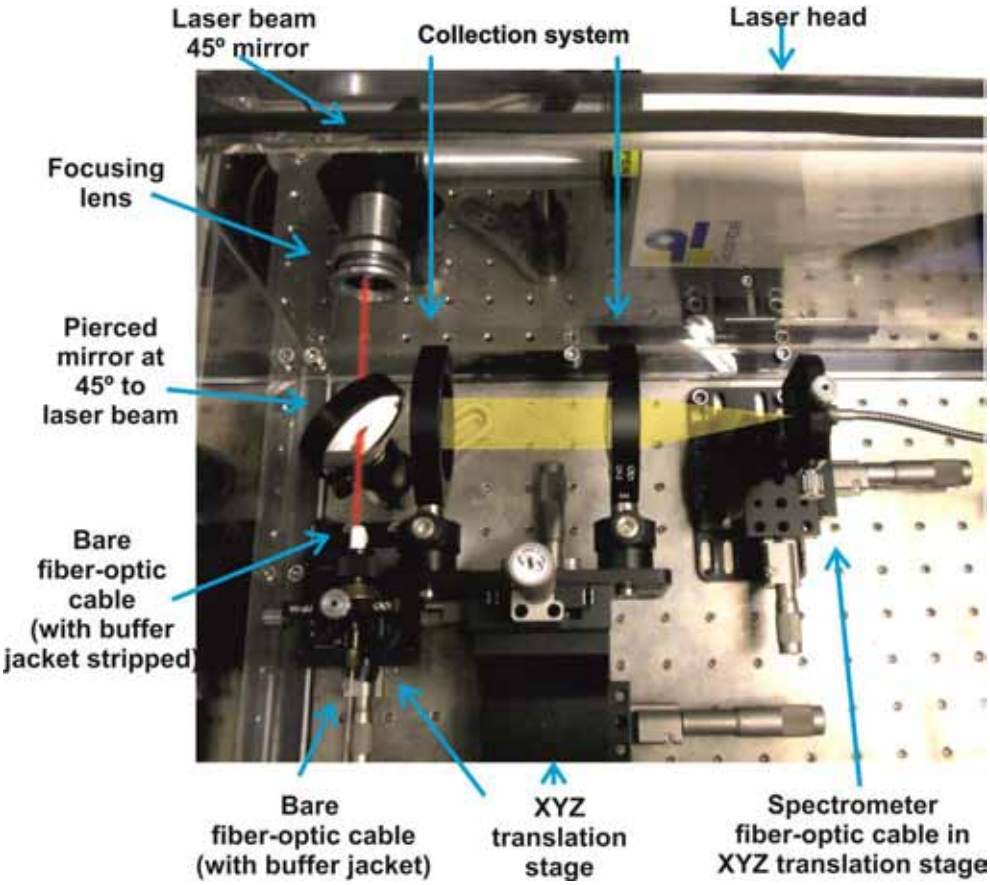

Figure 4. Main components of the optical module.

focuses the laser beam onto the sample surface by an appropriate optical configuration that will be described in the next section. The plasma light is collected and returned through the same optical fiber, reflected from the pierced mirror and then focused by a pair of biconvex lenses (L2 and L3) into the spectrometer fiber-optic cable (2 m length, 600 µm diameter and N.A:0.22). Figure 5 shows a diagram with the sequence described. Furthermore, the characteristic of all optical components are detailed in Table 2. It is important to mention that L1, L2, L3 and the optical fiber support are located over *xy* stages to facilitate the alignment.

Laser head is located over a height adjustable platform. Laser head and all the optical components were assembled on an optical table (44 X 66 X 0.4 cm; M6 drill hole each 2.5 cm). In addition, the optical table was supported by a set of 8 *silentblocks* in order to minimize vibrations on the optical table. A *methacrylate* structure covers the optical set to prevent the deposition of aerosol particles from the marine environment. On the other hand, the laser power supply was fixed on the based structure under the optical table.

A critical component in the optical module is the optical fiber. A correct alignment of the optical fiber is necessary to achieve the maximum performance of the equipment. Furthermore, it is recommended to place the fiber a few millimeters behind the focal point in order to reduce the irradiance deposits on fiber

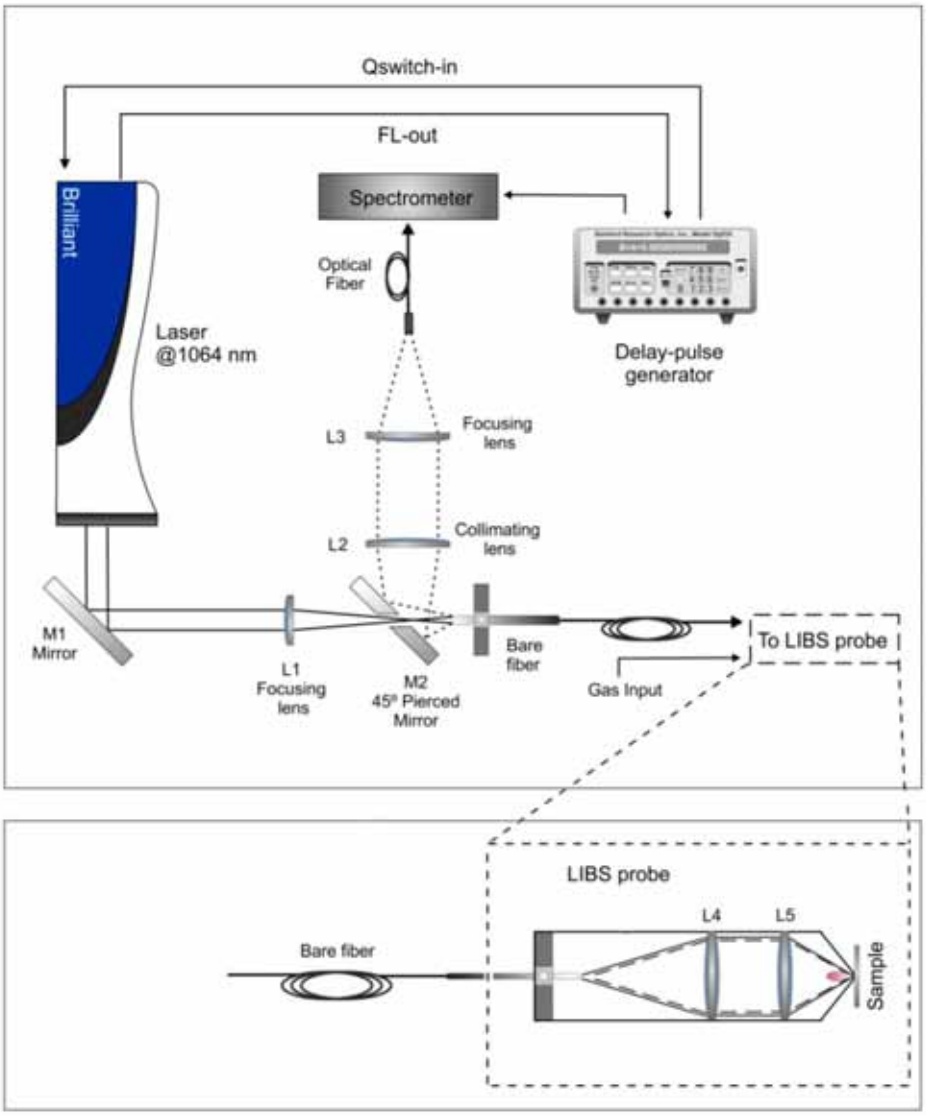

Figure 5. Optical lay-out corresponds to optical module and hand held probe.

end and avoid the risk of rupture. Also, it is also recommended to polish the fiber in order to eliminate possible structural defects; the laser-to-fiber coupling will be more efficient and will prolong the fiber lifetime.

Table 2. Characteristic of all optical components indicated in Figure 5.

Component	Diameter (mm)	Focal length mm)	Features
L1	25.4	100	UVFS bi/cx lens
L2	50.8	100	UVFS pl/cx lens
L3	50.8	100	UVFS pl/cx lens
L4	25.4	40	UVFS bi/cx lens
L5	25.4	25	UVFS bi/cx lens
M1	25.4		Mirror, High energy R >99% @ 1064 nm
M2	50.8		45º Pierce mirror

2.2. Optical fiber, umbilical cord and gas supply protection

The optical fiber used in the system has a core diameter of 550 µm. Its characteristic attenuation curve is shown in Figure 6. It should be taken into account the spectral region in which our spectrometer works, 300-560 nm and the laser wavelength, 1064 nm. As observed, in range of 400-560 nm the attenuation presents a value below 10 dB/km. However, the attenuation increases abruptly at wavelengths lower than 400 nm. The optical fiber is silica and has a high content of hydroxyl group to minimize the effect of solarization. This phenomenon is the appearance of atomic defects due to the action of UV radiation, which causes a loss in efficiency of transmission of radiation through the fiber. The high content of OH groups largely avoids this problem. It should be noticed that sometimes, as mentioned in the previous section, it is unavoidable that the optical fiber can be broken by an excess of energy, poor alignment or fiber degradation. This means that occasionally the fiber should be cut and polished again, consuming a fiber portion. To solve this problem, there are 5 meters of fiber stored inside of the main module, in order to ensure maintenance (Figure 7A). The remaining 50 m are canalized through an umbilical cord (hydraulic hoses with an internal diameter of 5/15"; stainless steel connections at each end and can support up to 350 bar pressure) that is rolled up on an external support of the equipment for its easy deployment and transportation (see Figure 7B).

On the other hand, the umbilical cord also canalizes/supply the protection purge gas during the underwater analysis. The main function of this protection gas is to remove the water from the sample surface and avoid the water enter inside the LIBS probe. In this meaning, it is necessary to take into account that the

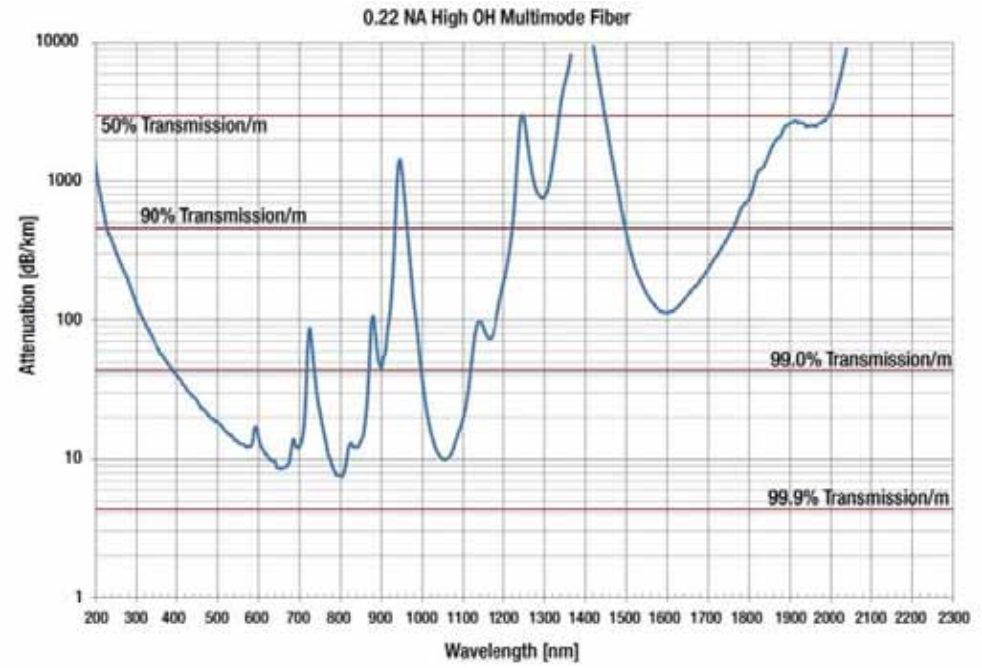

Figure 6. Attenuation of laser radiation through the optical fiber as a function of its wavelength. Source: Thorlabs.

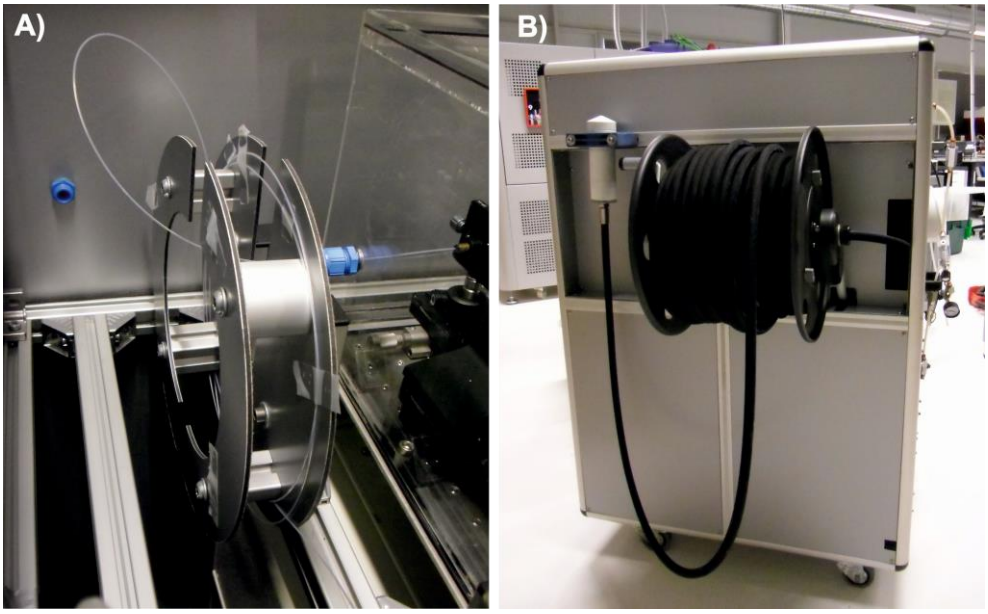

Figure 7. A) optical fiber support to store 5 meters of fiber inside of the main module; B) external support of umbilical cord which canalizes the remaining 50 m of fiber.

difference in pressure between the inside and outside of the LIBS probe must never be less than 1bar. The protection gas input in the system is carried out through an interface that is shown in Figure 8. The gas travels inside of tube (internal diameter of 4 mm) which is attached to a non-return valve through an instant fitting as shown Figure 8A. Before entering into the umbilical, gas passes through a filter in order to remove the humidity

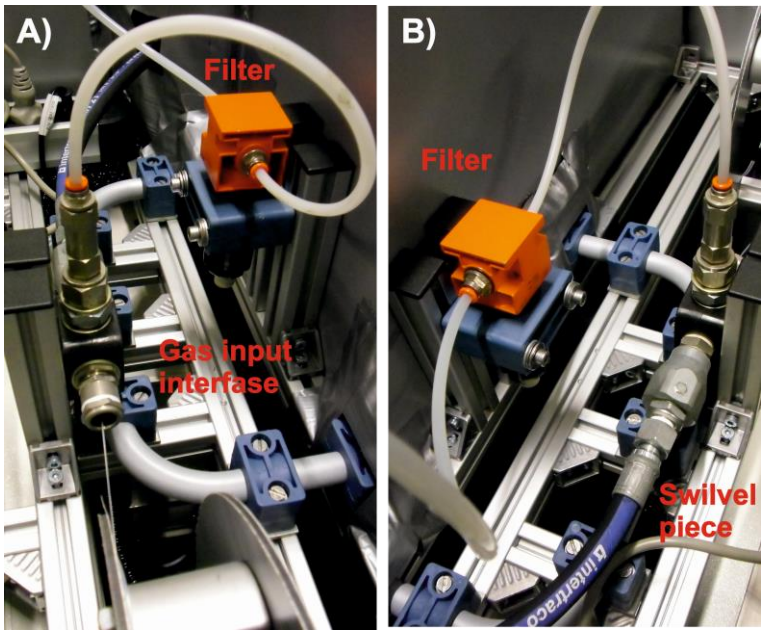

Figure 8.A) general overview of gas input interface and anti-humidity filter; B) swivel piece located between gas input interface and umbilical cord.

of air. Furthermore, between interface and umbilical cord was introduced a swivels as observed in Figure 8B in order to avoid knots rolling and unrolling.

2.3. Hand-held probe

At the end of the fiber, the hand-held probe focuses the laser beam onto the sample surface by an appropriate optical configuration. A photograph of the probe is shown in Figure 9. The optical system in the probe seriously influences the performance of the fiber-based LIBS system. Thus, the optical configuration consisting of a pair of lenses is the most widely used in the literature. Davies et al. [7] and Cremers et al. [8] used a system formed by two identical lenses. In our particular case, after some study, an alternative to this approach was the use of a pair of lenses with different focal length. This configuration has been proposed by several authors [9-11]. The optical system is composed by L4 (collimating): 40 mm focal length and L5 (focusing): 25 mm focal length. The characteristics of the optical components aredetailed inTable 2, included in the section 2.2. As known, the laser radiation is diverged at the end of the optical fiber cable. The use of a collimating lens with longer focal length specifically increases the diameter of the collimated beam, thus reducing the spot size (450 μm) over the sample surface.

A scheme of the different parts that constitute the hand-held probe is represented in Figure 10. Figure 10A shows the external casing of the LIBS probe that was built with ARNITE®. This material polyethyleneterephthalate was chosen for its high dimensional stability and excellent wear resistance. Then, Figure 10B represents a longitudinal cut of LIBS probe where all components are detailed. Additional information and more details are included in Figure 11. A drawing of probe without casing is shown in Figure 10C in which it can be see an internal cylinder constituted by the attached system of the optical fiber (C`) and the optical system (C"). The attached system of the optical fiber has two functions: fixing the optical fiber and canalizing the purge gas flow from the umbilical. It is important to mention that the gas flow travels

Figure 9. Photographic of the hand-held probe.

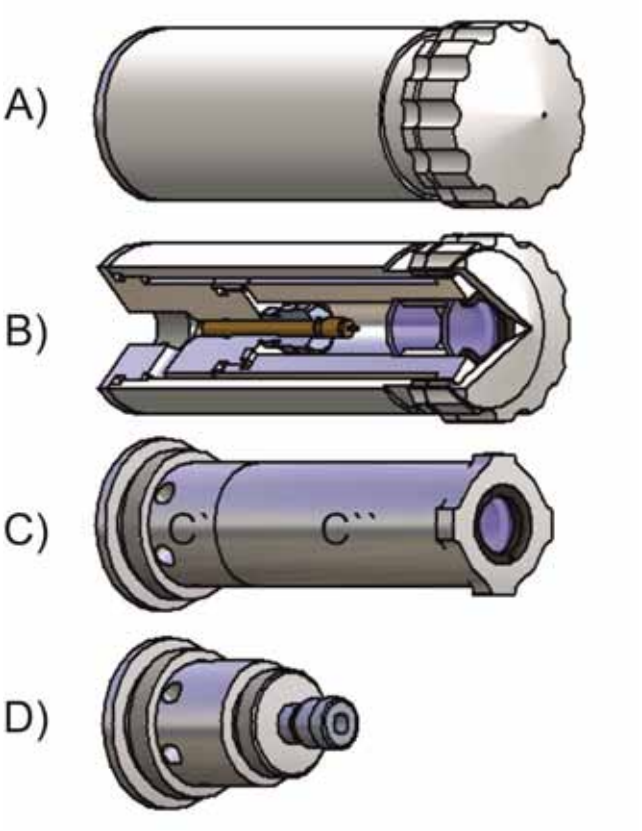

Figure 10. Hand-held LIBS probe. A) external case; B) longitudinal internal section detailing the optical components; C) hand-held LIBS probe without case, C' is the cylinder to attach the optical fiber system, C" is the cylinder to attach the optical components. Image provided by the Machining Service of the University of Málaga.

through the space between the external casing and internal cylinder until a conical end. Then, the gas is canalized by a cone with a hole of 2 mm diameter. This cone allows to adjust the lens-sample distance in order to optimize the focus of the laser radiation on the sample surface. This part of the LIBS probe is in

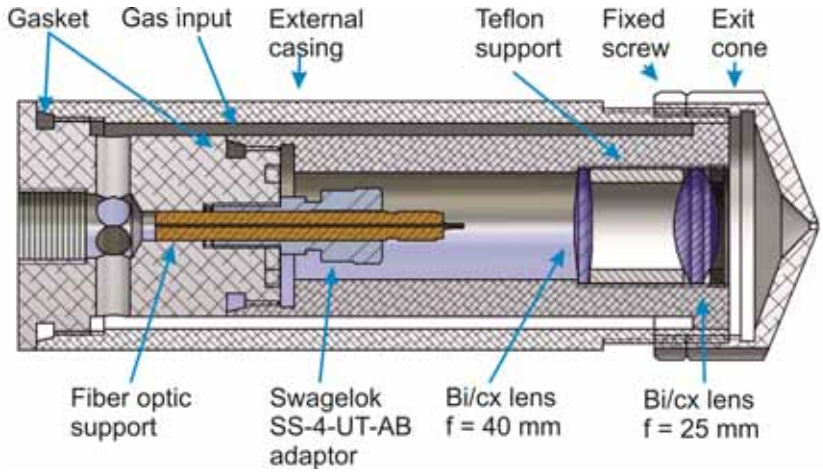

Figure 11. Components details of the hand-held LIBS probe. Image provided by the Machining Service of the University of Málaga.

close-contact with the surface of the sample during the analysis (see Figure 12). Finally, as shown in the optical layout of Figure 5, plasma light is collected and guided to the optical module through the same optical fiber.

2.4. Data acquisition module, spectrometer and results display

Plasma light is collected and guided to the optical module through the same optical fiber. Then, it is focused by a system of two lenses on a collection optical fiber that connects the optical module with the data acquisition module (see Figure 5 and Table 2). The data-acquisition module, consisting of the spectrometer, the video converter and the PC components, was installed in the main unit as shown in Figure 13B. A pulse/delay generator which externally controls the system (Stanford Research Systems DG535 model) and a sun-readable monitor (22 inch) were also configured within this module as is represented in Figure 13A. The spectrometer is a crossed Czerny–Turner design with a holographic diffraction grating of 1200 groove/mm (Avantes, AvaSpec-2014-USB2 model). This configuration provides a spectral resolution of 0.1–0.2 nm/pixel in the spectral range of 300–550 nm. Then the information obtained by the spectrometer is processed in the PC. A data management software was designed in MATLAB for our group in order to process the data at real time.

Regarding the results display, the information is sent to a video converter installed in the PC. This allowsshowing at real-time LIBS spectra simultaneously in both, a 22 inch, sunlight readable monitor installed in the front part of main unit, and in a 5.4 inch submersible monitor specially designed for the diver, and connected to the main unit by a 50-m long cable. Figure 14 shows a LIBS measurement in which the spectrum is observed at real time in the submersible monitor.

Figure 12. Laser-induced plasma during an underwater analysis of a lead sheet.

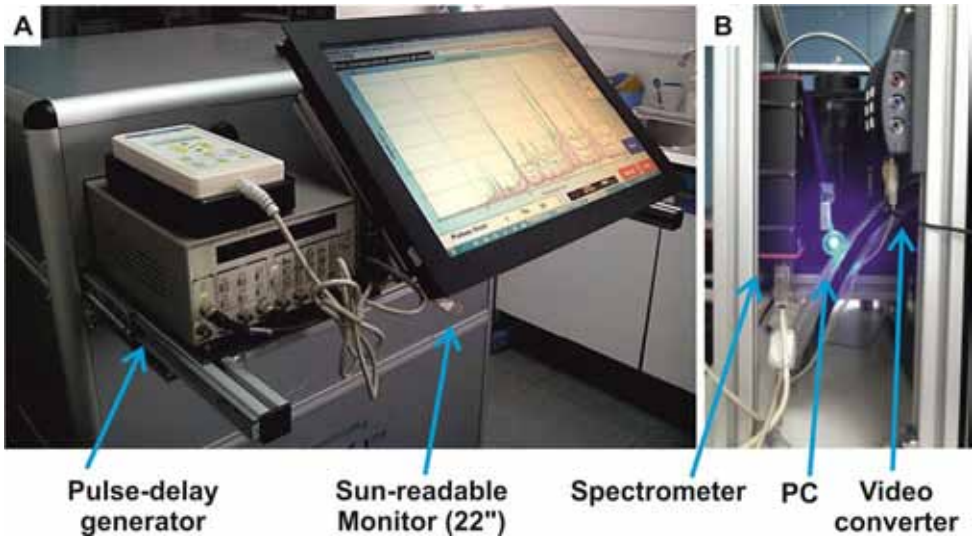

Figure 13. Data acquisition module. A) pulse delay generator and sun-readable monitor; B)spectrometer, PC and video converter.

2.5. Auxiliary module

AQUALAS equipment has a totally energetic autonomous to work in field operation. For this purpose an auxiliary module which provides both power and air flow, required for underwater analysis, was constructed. This module was constructed in a robust structure (123 X 60 X 67 cm^3) and containing an air compressor, an external power generator and uninterruptible power supply (UPS). These components are shown in Figure 15.

The air used like purge gas is obtained cheap, inexhaustible and easily transported through the portable air compressor, which is able to provide up to 8 bar pressure.Problems associated with the transport of helium and argon containers and the high cost of them are solved in this way. The external power generator has inverter technology and 3500W power allowing 8 h of continuous operation of the LIBS instrument without

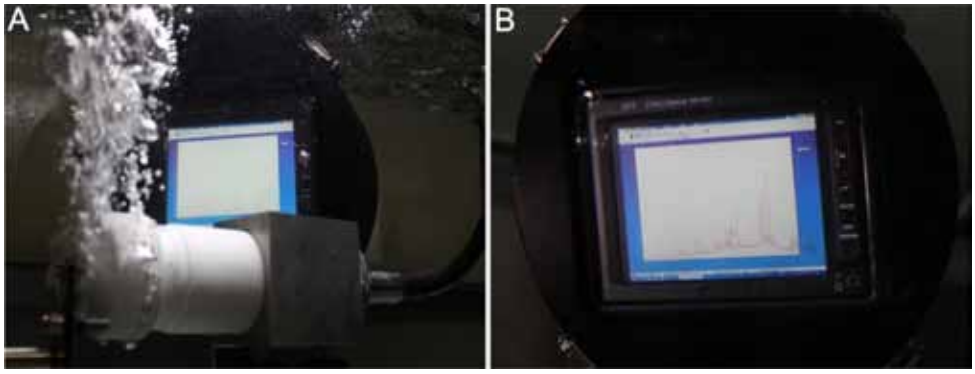

Figure 14.A) LIBS measurement in which the spectrum is observed at real time in the submersible monitor; B) Zoom of submersible monitor.

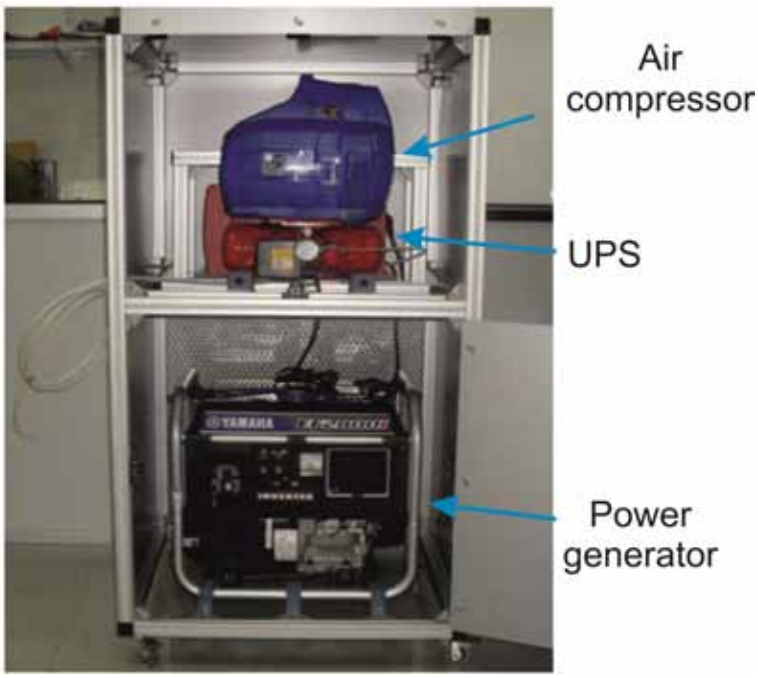

Figure 15.Auxiliary module components. An air compressor and UPS are located up level while the power generator is placed in down level.

refueling. Last, the uninterruptible power supply works with a battery that keeps the power supply to the equipment during 10-15 min, if suddenly the power generator is turned off allowing to extract the LIBS probe of the sea without the water enter into the probe.

2.6. Fiber-based system approach

2.6.1. LIBS excitation configuration

In this section, we will focus on the different LIBS excitation configuration, in order to increase the threshold damage of input laser energy into the optical fiber; and at the same time, achieve an increase the energy transmission. AQUALAS 2.0 was designed integrating both configuration, single pulses (SP) as multi-pulse (MP). First instance, the use of multi-pulse excitation could allow introducing a higher laser radiation through the optical fiber. Briefly, the MP generation and characterization will be described below.

- **Generation and characterization of Multi-pulse**

For a train of multi-pulse (also known as multi-spikes) it is necessary to advance the opening time of the Pockels cell regarding the optimal point of maximum power of the laser by external synchronization thereof with a pulse generator and delays. A temporal scheme of the sequence is represented in Figure 16.This effect, recently reported [12, 13], could be explained by a relatively slow (about 80–100 μs) electronic closing

of the Pockels cell and by its fast opening when the laser resonator is only slightly above the lasing threshold. This allows the population inversion to build up again above the laser threshold during the flash lamp and before the Q-switch (QS) is fully closed. The MP phenomenon occurs only in a certain time, in ourparticular case, when the QS delay is less than 140 µs. It is due to the fact that above this value, the laser becomes stable enough to close the Pockels cell quickly, avoiding the emission of these spikes after the main pulse. When the opening moment of the Pockels cell is progressively before to 140 µs, the time to generatemultiple pulses is increased. Thus, an increase in the number of spikes that constitutes the laser pulse is obtained. The number of spikes varies between 2 and 11. The maximum total duration of the pulse train was over

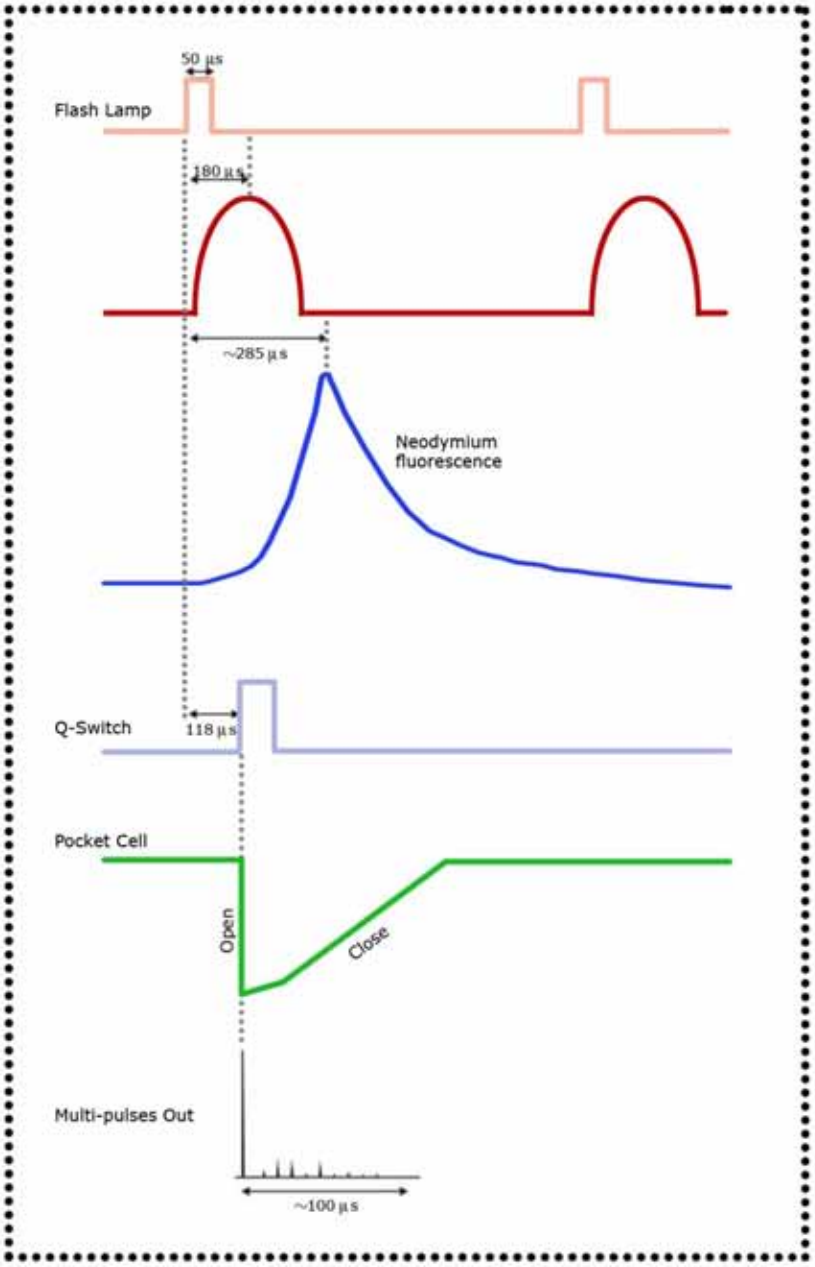

Figure 16. Temporal scheme of multipulse effect generation.

70 µs, and the energy of each spike of the laser burst was stable to 20–30% relative standard deviation (RSD). In addition, the RSD for the pulse ratio (i.e., spike 2 to spike 1, spike 3 to spike 2, and so on) was around 1–2%. In contrast, QS-delay settings beyond 140 µs represent the classic SP regime. Figure 17 shows the monitoring of pulse trace by an oscilloscope (Tektronix DPO 7104) using a photodiode (Thorlabs DET10C) for our working conditions, a pulse of QS-delay 140 µs (case of SP) and a QS-delay 118 µs (MP effect). On the other hand, as explained in Guirado et al. work [12], the pulse width (full-width at half-maximum, FWHM) for the first spike was found to depend on the QS-delay, whereas the pulse width in the remaining spikes was 40 ns. In SP regime, the pulse width was 7 ns. Concluding, the number of spikes, their amplitude and the total pulse energy will be variable for different delays in the opening of the QS shutter of the Nd:YAG laser. It suggests that the QS-delay must be optimizing for each experimental set-up. For AQUALAS 2.0 equipment has been evaluated the FWHM for the first spike and the pulse energy laser in function of Q-switch delayusing a voltage of Flash-lamp (1292 V). The results are represented in Figure 18. The best condition for AQUALAS 2.0 in function of breakdown threshold of optical fiber has been established at 118 µs QS-delay obtaining an energy pulse of 85 mJ and 22 ns pulse duration of first spike.

- **Comparison of optical fiber transmission using multi-pulse sequence and single pulse**

Increased transmitted laser beam energy is almost mandatory for the real time analysis of an underwater object. In the first generation of remote LIBS instruments [6], the damage threshold of the

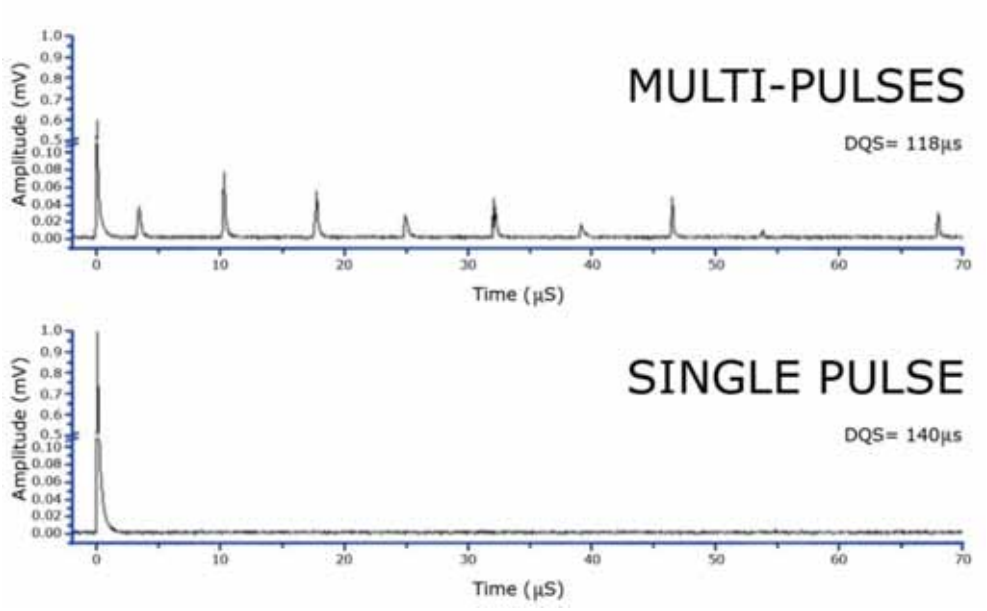

Figure 17. Monitoring of pulse trace by an oscilloscope using a photodiode at a QS-delay 140 µs (SP-LIBS) and a QS-delay 118 µs (MP-LIBS).

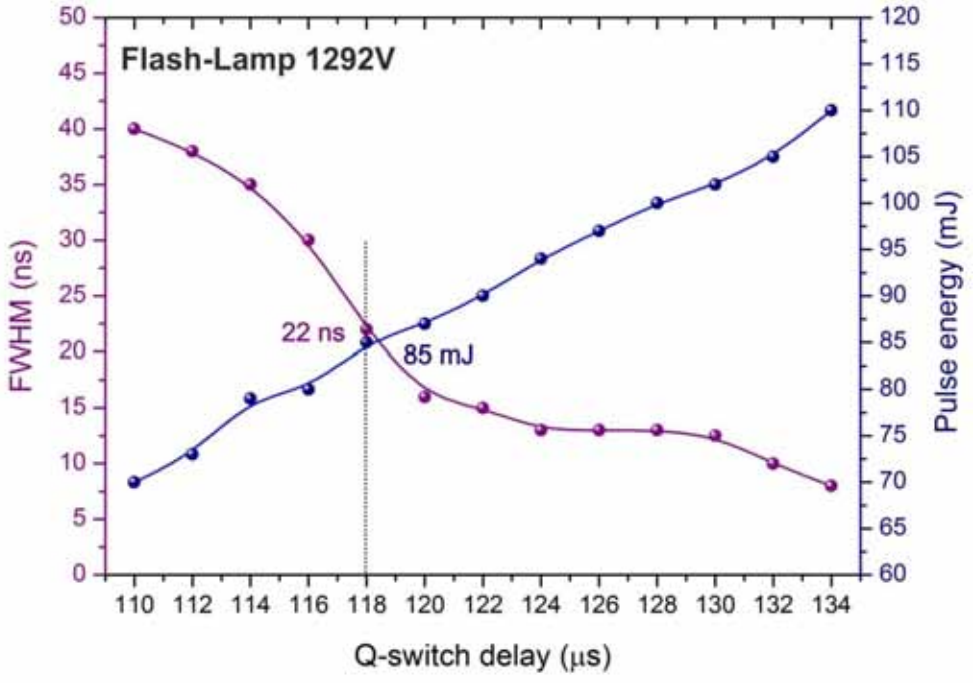

Figure 18. Fist spike characterization in the range of MP effect, FWHM and pulse energy laser for a voltage of flash lamp to 1292 V.

optical fiber (high- OH, UV- grade fiber, 550 μm core diameters) was 30–35 mJ/pulse using a typical 7 ns pulse and SP configuration. The maximum input laser energy did not exceed 32 mJ/pulse which together with a transmission of 50% limited the energy at the target to ca.15 mJ/pulse. This circumstance restricted the variety of samples to be analyzed underwater. However, the second generation of remote LIBS instruments introduced the employment of a multi-pulse excitation scheme; and the maximum laser radiation that can be delivered through the optical fiber is approximately 4-fold larger as compared at SP. In this case, although the characteristics of the optical fiber are the same to that published in [6], the pulse width is 22 ns in the multi-pulse configuration (higher in comparison with SP configuration), facilitating the transmission through the optical fiber up to 74%. Although the 55 m optical fiber cable produces attenuation of the plasma light below 350 nm and may affect the plasma light collection, the transmission in the VIS region is fairly good. The enhancement in the intensity ratio between MP-LIBS and SP-LIBS operating at the same target and irradiance is shown in Figure 19.

2.6.2. Optical fiber LIBS system

Prior to the design and development of prototype AQUALAS 2.0 it was necessary to evaluate the transmission of laser pulses through an optical fiber cable. In this meaning, some factors such as fiber

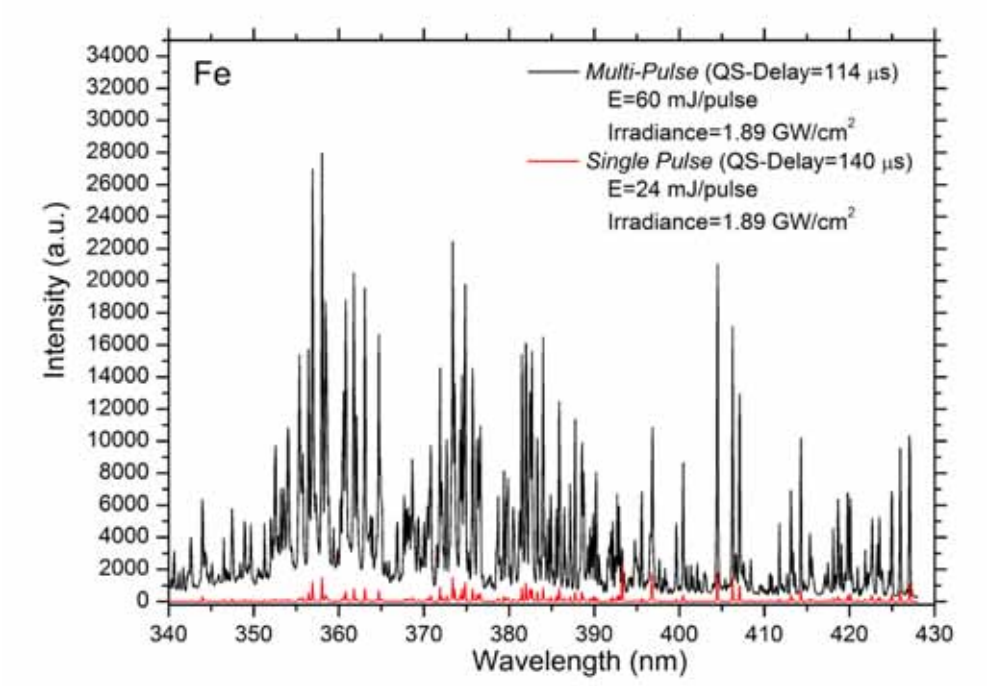

Figure 19.Comparative LIBS spectra between MP-LIBS (QS-delay: 114 μs; Energy: 60 mJ/pulse) and SP-LIBS (QS-delay: 140 μs; Energy: 24mJ/pulse) configurations for an iron-based material. Both spectra were acquired at the same irradiance value, 1.89GW/cm^2. Figure provided by ref 14 with permission of authors.

attenuation, the core diameter and the length of the optical fiber could influence the optical transmission and should be taken into account.In order to evaluate some of these mentioned parameters an experimental setup for guiding the laser pulse through the optical fiber was designed. Figure 20 shows a schematic diagram of the experimental set up where the optical system is composed by a focusing lens L1: 100 mm focal length.

- **Influence of core diameter of the optical fiber on transmission efficiency**

One of the most important aspects in the optical fiber is the amount of laser radiation that can be transmitted. Figure 21 shows the transmission efficiency of laser radiation through an optical fiber cable of 1

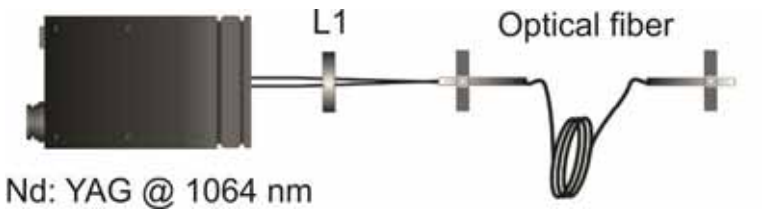

Figure 20. Experimental set-up used in the transmission of laser pulses through an optical fiber.

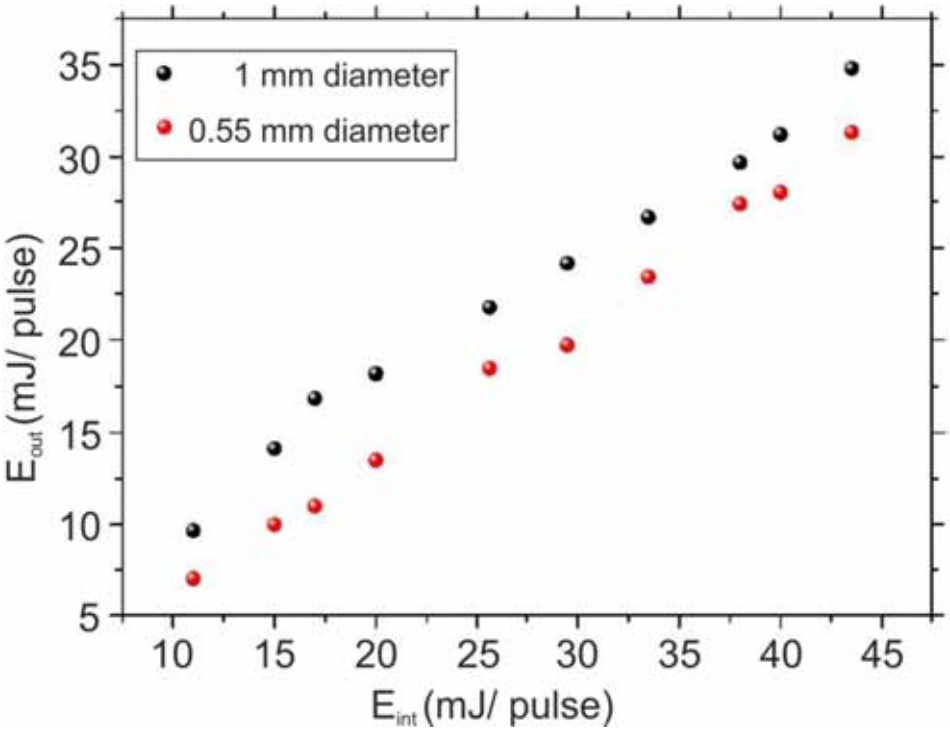

Figure 21. Transmission efficiency of the optical fiber core of 1000 and550 µm.

meter length. In this case, two core diameters at 1000 and 550 µm have been evaluated. The experiment was carried out using a SP configuration varying the input power into the optical fiber in a range from 11 to 45 mJ. Figure 21 shows laser energy values taken at the end of the optical fiber versus the to the input pulse energy. As shown, a linear increase in transmitted energy is observed until an input value of 45 mJ /pulse. Due to the damage threshold of the optical fiber cable for SP configuration, the maximum input power should not exceed 40-50 mJ / pulse.

The results indicated that the transmission efficiency (between the input and output of the fiber) is 80% for fiber core of 1000 µm and 72% for the fiber core of 550 µm. Thus, it is clear that a larger size core improves transmission efficiency. However, this increase is not significant considering the high cost of optical fiber cable core of 1000 µm. Therefore, to prototype development a fiber core of 550 µm was selected.

- **Maximum depth for an optical fiber LIBS system**

As explained in the previous section (2.6.1), in our next generation of underwater LIBS system [14], the employment of a multi-pulse excitation scheme improved the performance of the instrument in terms of energy transmitted through the optical fiber. The maximum depth a fiber-based LIBS system is sketched in Figure 22. The same experimental system, detailed in this section, was utilized but in this case using a MP configuration. As seen, the length of the fiber-based system strongly depends on the transmission of the laser radiation through the optical fiber. Referring to the specifications of the optical fiber used, at the laser

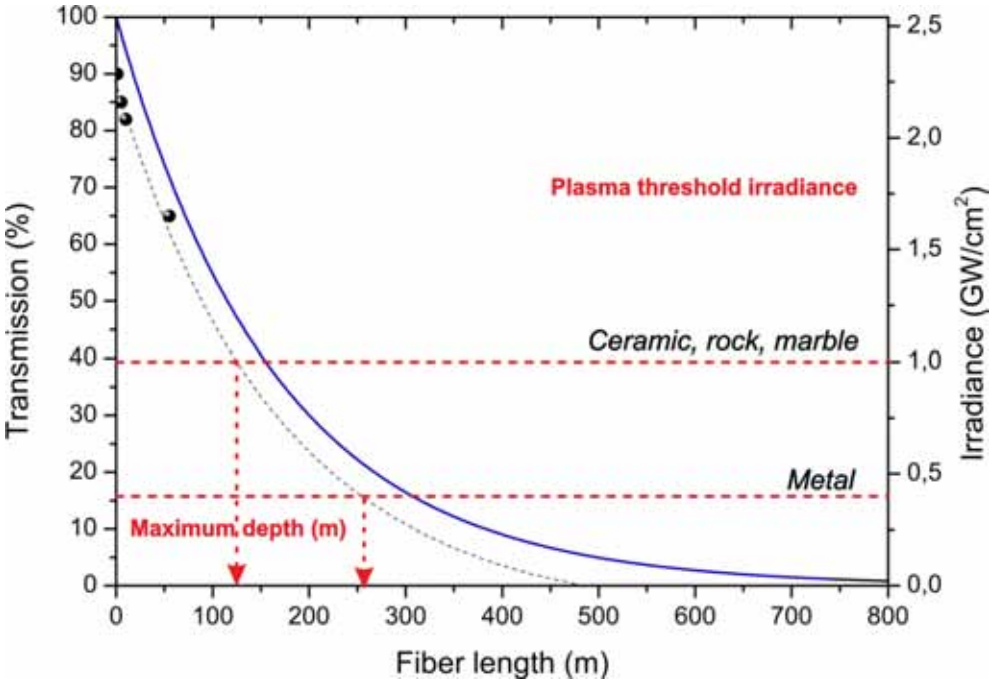

Figure 22. Maximum depth in an optical fiber LIBS system. For MP-LIBs, the input irradiance was 2.4 GW/cm^2. The trend curve (dashed line) for the transmission values experimentally measured at 1, 5, 10 and 55 meters fiber length are also plotted in the graph.

wavelength of 1064 nm, the transmission of 1-m. long optical fiber is 99.4%. The irradiance at the target associated to each energy transmitted is represented in the right axis. In the graph,an input irradiance of 2.4 GW/cm^2 was considered. This irradiance value was just below the damage threshold of the fiber. The trend curve (dashed line) for the transmission values experimentally measured at 1, 5, 10 and 55 meters fiber length is also plotted in the graph. As observed, at the plasma threshold irradiance, it could be possible to perform underwater LIBS analysis of metals (0.4 GW/cm^2 plasma thresholds) at a distance of ca. 260 m. Plasma formation threshold depicted in the graph were experimentally measured in laboratory. When the input energy requirements of the sample grow, as in the case of ceramics, rocks and marble, the maximum distance is substantially reduced. Hence, in the case of ceramics, line corresponding to its plasma formation threshold (1.0 GW/cm^2) cuts the fitting line at approximately 130 m. The same fact occurs for rock and marble materials. However, this analysis does not consider the attenuation of the returning plasma light through the same optical fiber. In practice, aforementioned distance would be further reduced. The results suggested that it could be possible to perform underwater LIBS analysis of metals at a distance of ca. 260 m and 130 m in the case of ceramics.

3. LIBS sensor for distant objects

In this section, an extensive description of the characteristics of each pieces selected to develop a home-made high pressure chamber is presented. In addition to this, the pressure resistance of the

constructed chamber has been evaluated where it was certified its working capacity is up to at least 400 bars of pressure. The influence of the optical path on the laser beam radiation has been also studied in our experimental set-up on the attenuation of light through the environment and the focusing conditions required.

3.1. Design and construction of a high pressure chamber

A laboratory LIBS system was designed to operate in depth ocean experimental conditions. Therefore, a high pressure chamber was required which should reach, at least, a pressure of 300 bar in order to make a simulation. The material selected to build the chamber was stainless steel. This material was chosen to avoid the oxidation by water; and for its excellent wear and pressure resistance. Its dimensions are 135 x 130 x 115 $mm^3$and a capacity of 80 ml. The prototype, of cylindrical shape, consists of water out (P7) and six ports: five laterals ports (P1-P5), an upper port (P6) as observed in different views in Figure 23.

- P3: input for laser beam radiation/coaxial plasma light collection
- P1,P2,P5: visualization and plasma light collection (in a certain angle)
- P4: water in
- P7: water out

The numbers of ports were selected in order to increase the versatility of the high-pressure chamber. A detailed description of the components, functionality and features of the different ports of the chamber are detailing below.

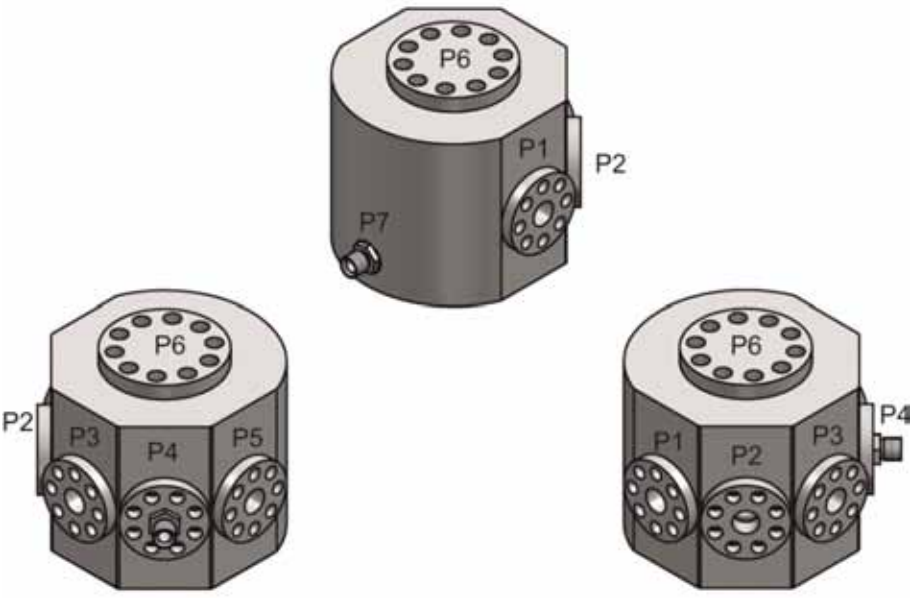

Figure 23.External view of high pressure chamber.

Laterals ports 1, 2, 3 and 5

Ports 1, 2, 3 and 5 were designed identically. Sealing the chamber and watertightness in these ports is achieved using a system of gasket-sapphire window-gasket countersinks in the locking cylinder, as detailed in Figure 24 This set of pieces is adjusted to the chamber with eight M6 screws and a specific washer of pressure. The characteristics of each are described below.

- **Washer support**

Stainless steel piece lathed so that fitting with a gasket in the surface of sapphire window (ϕ22 mm); and another one (ϕ 26 mm) in the lateral contour, as observed in Figure 25.

- **Sapphire window**

The material selected for the windows was sapphire.Sapphire has good qualities for this demanding application that require reliability, strength, a broad transmission range, and low transmitted wavefront distortion at both high and low operating temperatures.Also, it is chemically inert and insoluble to water. In addition to this, it allows see through it providing an optical path view inside the chamber.

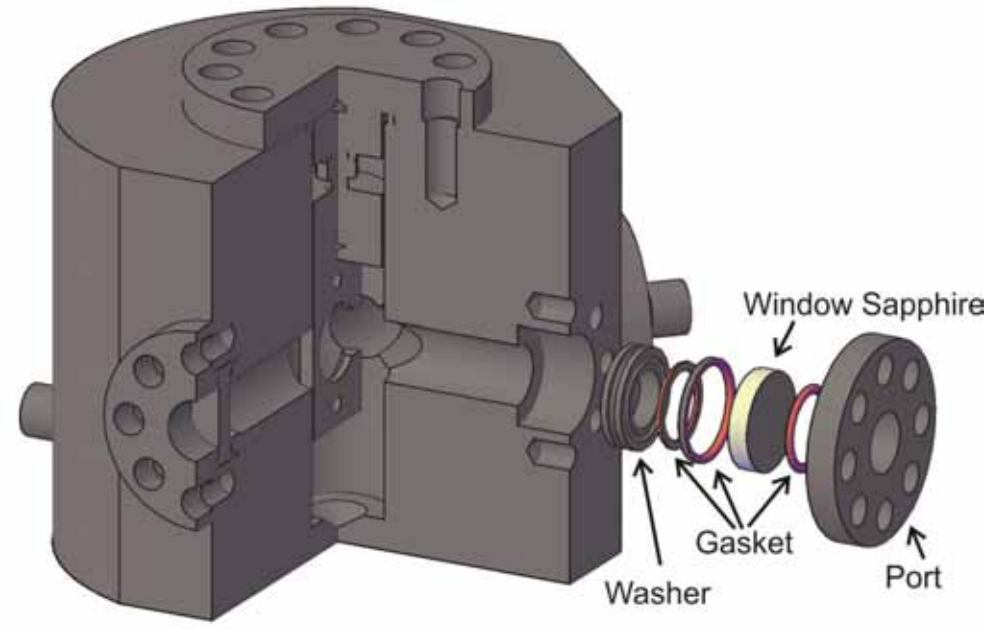

Figure 24. Sealing system chamber for ports 1, 2, 3 and 5.

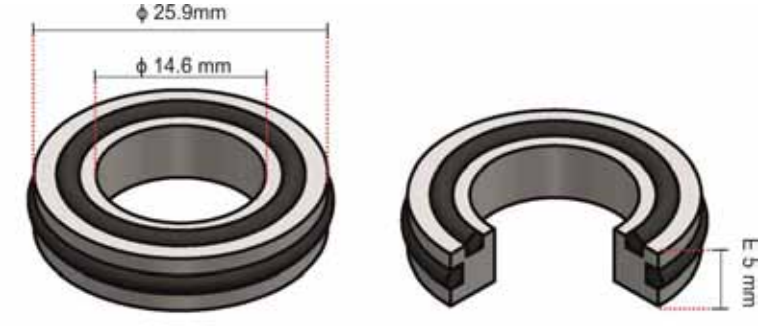

Figure 25. Washer support of stainless steel.

To choose the correct characteristic of the sapphire window, the minimum thickness of a window to withstand a pressure gradient of 300 bar is necessary to calculate. For a circular window, avoiding plastic deformation, the minimum design thickness is indicated by the following expression:

$$t_{min} = \sqrt[2]{K\ x\ p\ x\ D^2 / S}$$

where *K* (0.8) is constant which incorporates a minimum safety factor; *D* is the unsupported diameter; *S* is the apparent elastic limit; and *p* is the pressure differential. After calculations, for a diameter of 25.4 mm, the thickness of the sapphire window should be at least 5 mm.

- **Locking cylinder**

Locking cylinders are circular stainless steel piece with a 51.8 mm diameter and 7.7 mm of thickness. In the middle is drilled with a hole of 16 mm diameter. The piece is pierced with eight holes (M6) with a 9 mm in diameter to screw the locking cylinder to the chamber and to ensure the tightness.

Input water port (P4)

Port 4 was designed to connect the chamber to a high-pressure pump that allows aqueous solutions to flow into the cell and the cell to be pressurized. Sealing the chamber and watertightness in the port is achieved using a gasket and a locking cylinder, as detailed in Figure 26. The locking cylinder, as the rest of port, is a circular stainless steel piece. In the edge of the piece is pierced with eight holes with a diameter of 9 mm to introduce the screws M6. In the middle is pierced with a 16 mm diameter of hole. This hole connects the chamber to pump through a stainless steel tube with 1/4" BSP connection with a hexagonal nut. There are two ferrules inside of nut whose function is to compress the stainless steel tube reaching make a fitting seal.

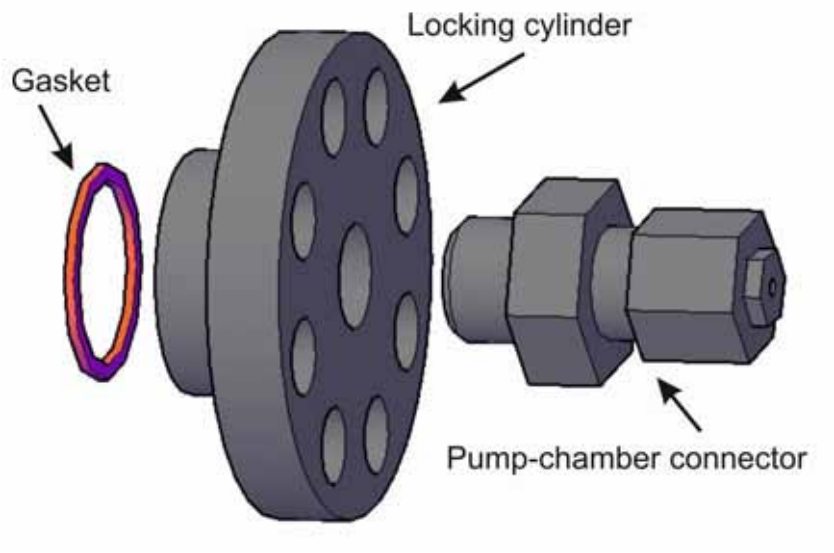

Figure 26. Overview of the water input port.

- **Ouput water port (P7)**

The water output of the chamber is carried out by port 7. It is located in the back to the chamber. It has a hole 12 mm external diameter joined through a fitting steel BSP 1/8-1/4 ", to an adjustable pressure limiter to work among 0 and 400 bars. The port has two main functions. First, safety function is control the pressure excess inside the chamber by the limiter. And second, together with input water port, allows water circulation making easier removal of the particles generated after laser ablation.

- **Sample holder (P6)**

On top of chamber is located port 6. It is constituted by a rectangular stainless steel piece lathed used to support the sample. The target-holder has the possibility of 20 mm axial movement in order to allow us to adjust the distance between the lens and the sample. Sealing and watertightness in this port of chamber is achieved using a gasket and a locking cylinder (ϕ 75.8 mm; E 10 mm). The locking cylinder is adjusted to the chamber with ten M8 screws and a specific washer of pressure. An overview of port 6 is shown in Figure 27.

The high pressure chamber described in this chapter has been tested in order to evaluate its pressure resistance. Certification test was carried out increasing in short steps the pressure inside ofchamber injecting a liquid with a manual pump. The pressure reached inside the chamber was monitored in real time

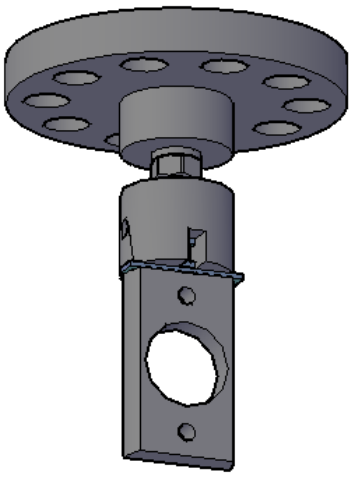

Figure 27. Overview of the target-holder.

in this closed circuit by connecting a pressure manometer (certified up to 400 bar with an error interval of 10 bar) at the outlet of the manual pump as represented in sequence of Figure 28. Figure 28 shows some photographs taken during the resistance test in which is observed the high pressure chamber, the experimental set-up and the operator working, as well as the maximum pressure to which it is was subjected. The results indicated that its working capacity up to at least 400 bars of pressure. The certification report can be read in Appendix 1.

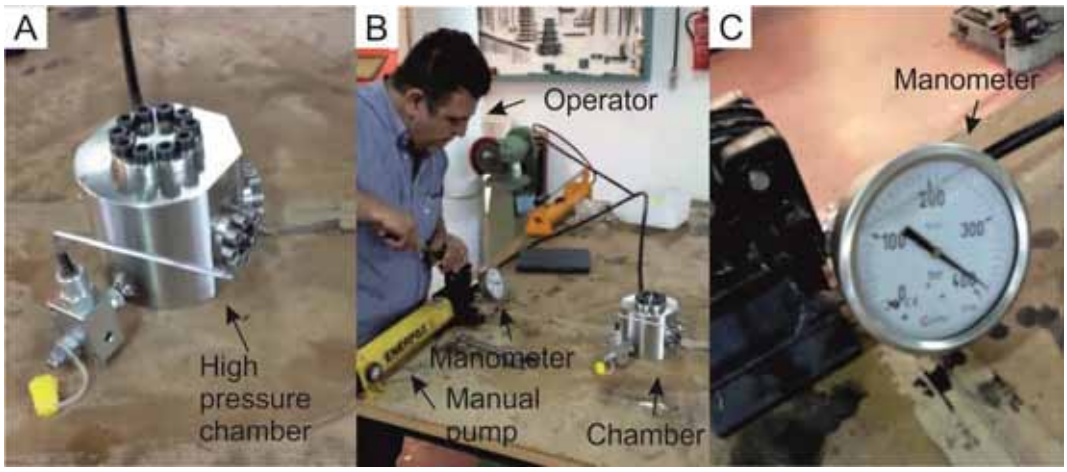

Figure 28. Photographs taken during the pressure resistance test,A) high pressure chamber;B) experimental set-up; C)maximum pressure to which chamber was subjected (400 bar).

3.2. Influence of the optical path on the laser beam radiation

In this particular application, a key factor influencing LIBS measurements is the laser beam attenuation through the environment, in our case, the water and the sapphire windows. Thus, the attenuation percentage of laser radiation due to these components should be evaluated. On the other hand, it should be noted that the focal distance of the lenses in water becomes longer than that in air, due to the higher refractive index of water. Therefore, a previous evaluation of the focal conditions was required to solve geometric factors. To carry out these experiments a water tank was built of PMMA with a wall thickness of 10 mm; its dimensions are 160 mm long, 180 mm cm wide and 110 mm high.

The attenuation of the laser beam by absorption and scattering caused by the particulate matter and by water has been evaluated. Due to water absorption, only a fraction of the incident energy reaches the sample surface. The water absorption coefficient (α) at 532 nm is minimal, 0.00022 cm^{-1}. Under our experimental conditions, only an attenuation of 2% was measured in an underwater optical path of 14 cm due to the presence of particulate matter in water. However, an attenuation of 30% was measured when considered both the optical components and the underwater optical path (laser beam attenuation). The experimental procedure used to measure the attenuation suffered by the laser radiation of under water until the sample is schematised in Figure 29. The energy value was measured at each side the sapphire window

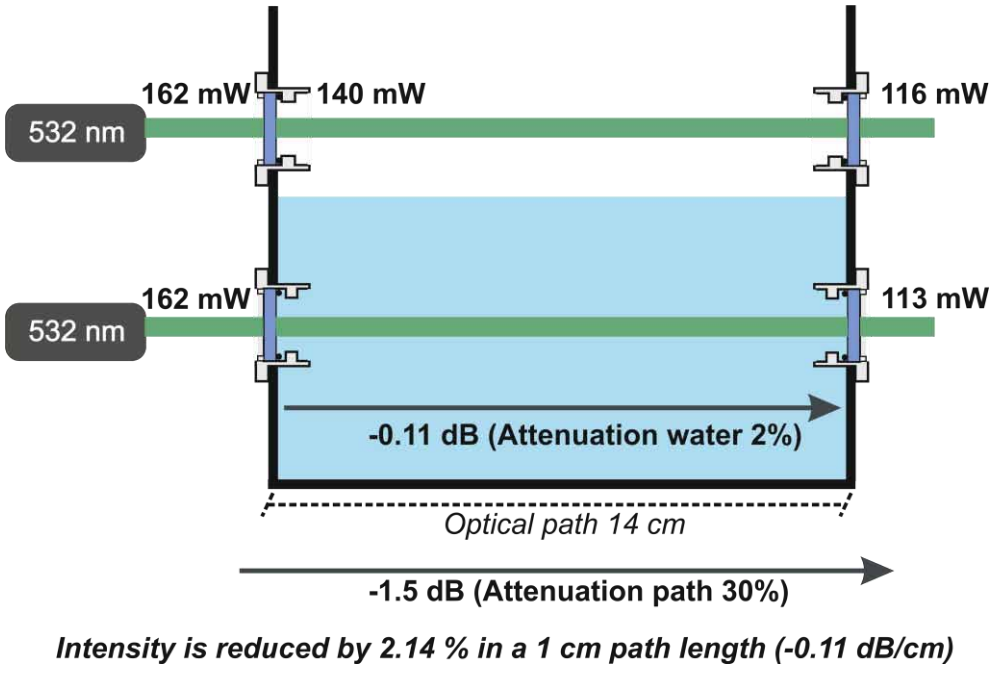

Figure 29. Laser irradiance attenuation measurement at532 nm through optical path.

obtaining an absorption of 14% per each one. Known this value, the energy laser radiation was measured before enter to the container and after, crossing the water and the two windows. Thus, 532 nm radiation inaverage was attenuated 2.14% per cm of optical path (considered the optical components and underwater path), or in other words, -0.11 dB cm^{-1}. Also, this experiment was carried out changing the wavelength to 1064 nm. If both results are compared at 532 nm attenuation value, relatively low, contrasts with the corresponding to 1064 nm, which was -0.66 dB cm^{-1}. Under these circumstance, we decided to work at 532 nm wavelength in future experiments.

Laser radiation is modified as a function of the properties of the propagation medium; a clear example of this is the refractive index. Due to the higher refractive index of water, the focal distance of the lenses in water becomes longer than that in air. Consequently, a careful adjustment of the laser focal conditions is required as a function of the optical path inside water. Figure 30 shows the observed focal distance of a set of lenses with nominal focal distances in the range 30 to 150 mm, in water and air environment. As expected a larger increase of focal distance was obtained in water in comparison with air. This effect is enlarged for lenses with longer focal distance. After that and considering the optical path inside water in our high pressure chamber (sapphire window until central point of the chamber, 95 mm), it is convenient to select a plano convex lens with a nominal focal distance at 75 mm.

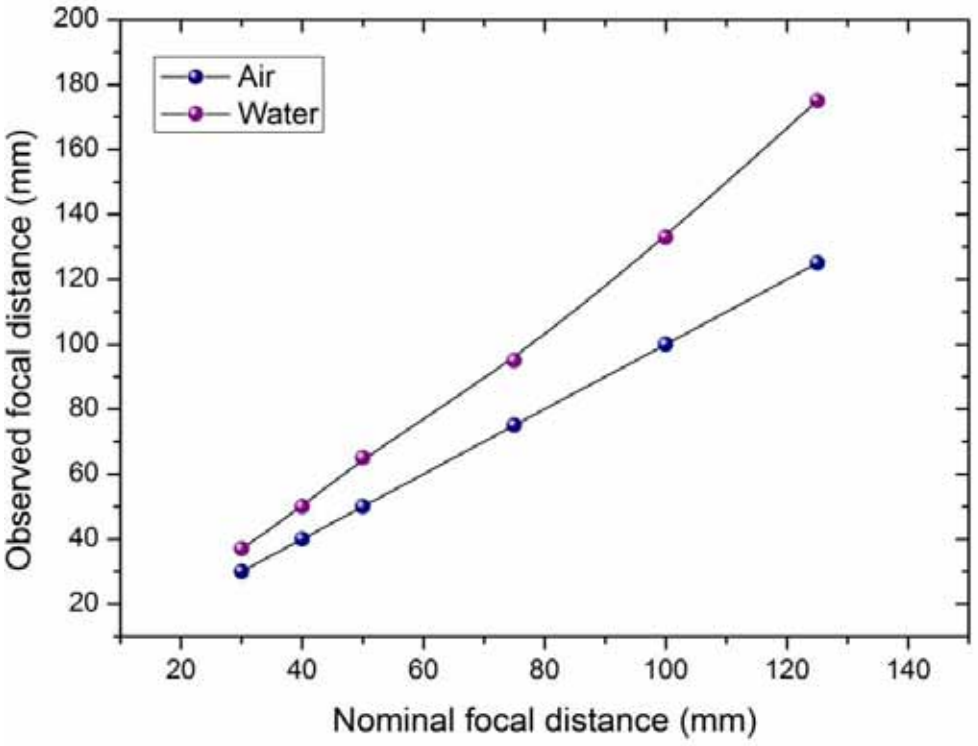

Figure 30. Focal distance lenses as a function of the propagation media, water and air.

4. References

1. A. Bowens; Underwater Archaeology: The NAS Guide to Principles and Practice; 2nd ed., Blackwell 2009, Portsmount, UK.
2. C. Bonifacio, Galeones con Tesoros. Dónde están hundidos, Qué llevaban; Brenes: Muñoz Moya Editores Extremeños, 2008, España.
3. C. León Amores, Buceando en el Pasado. Espasa Calpe, 2009; Madrid.
4. UNESCO, Convention on the Protection of the Underwater Cultural Heritage, 2001, Paris.
5. F.J. Fortes, J.J. Laserna, The development of fieldable laser-induced breakdown spectrometer: no limits on the horizon, Spectrochim. Acta Part B 65 (2010), 975–990.
6. S. Guirado, F. J. Fortes, V. Lazic, J. J. Laserna; Chemical analysis of archeological materials in submarine environments using laser-induced breakdown spectroscopy. On-site trials in the Mediterranean Sea; Spectrochim. Acta Part B 74-75 (2012), 137–143.
7. C. M. Davies, H. H. Telle, D. J. Montgomery, R. E. Corbett, Quantitative analysis using remote laser-induced breakdown spectroscopy (LIBS), Spectrochim. Acta Part B 50 (1995), 1059–1075.
8. D. A. Cremers, J. E. Barefield, A. C. Koskelo, Remote elemental analysis by laser induced breakdown spectroscopy using a fiber-optic cable, Appl. Spectrosc. 49 (1995), 857-860.
9. B. J. Marquardt, S. R. Goode, S. M. Angel; In Situ determination of lead in paint by laser-induced breakdown spectroscopy using a fiber-optic probe; Anal. Chem. 68 (1996), 977-981.
10. A. I. Whitehouse, J. Young, I. M. Botheroyd, S. Lawson, C. P. Evans, J. Wright, Remote material analysis of nuclear power station steam generator tubes by laser-induced breakdown spectroscopy; Spectrochim. Acta Part B 56 (2001), 821–830.
11. A. K. Rai, H. Zhang, F. Y. Yueh, J. P. Singh, A. Weisburg, Parametric study of a fiber-optic laser-induced breakdown spectroscopy probe for analysis of aluminum alloys, Spectrochim. Acta Part B 56 (2001), 2371–2383.
12. S. Guirado, F. J. Fortes, L. M. Cabalín, J. J. Laserna, Effect of Pulse Duration in Multi-Pulse Excitation of Silicon in Laser-Induced Breakdown Spectroscopy (LIBS), Appl. Spectrosc. 68 (2014), 1060–1066.
13. S. Guirado, F. J. Fortes, J. J. Laserna, Multi-pulse excitation for underwater analysis of copper-based alloys using a novel remote laser-induced breakdown spectroscopy system, Appl. Spectrosc. 70 (2016), 618-626.
14. S. Guirado, F. J. Fortes, J. J. Laserna, Elemental analysis of materials in an underwater archeological shipwreck using a novel remote laser-induced breakdown spectroscopy system, Talanta 137 (2015), 182–188.

Chapter 4. Capabilities, stability and robustness of Aqualas system. Underwater chemical characterization of galvanized steel

1. Introduction

Laser-induced breakdown spectroscopy (LIBS) has experienced a growth in interest as a surface analytical method, as revealed by the wide number of LIBS applications found in the bibliography [1-3]. The well-known LIBS attributes (namely multi-elemental detection in a wide variety of matrices, fast analytical response, remote sensing capabilities and analytical figures of acceptable value for most applications) make the technique a suitable alternative for real-world applications even in extreme conditions or hazardous environments that put the technique to the limit [4]. In particular, during the last few years, LIBS has emerged as a new solution for oceanography [5]. Oceanic LIBS technology will take special relevance in the next decades and might be used in applications such as geological and mineralogical exploration, the investigation of underwater cultural heritage, inspection of oil and gas pipelines, and the analysis of alloys and concrete on the seafloor, among others.

In 1984, Cremers and co-workers [6] demonstrated for the first time LIBS analysis inside liquids. The laser–water interaction when a laser pulse is focused into a liquid produces a rapid heating of the liquid followed by its explosive expansion and formation of a gas bubble. As a consequence, the lifetime of the plasma generated is very short, in the order of 100 ns, leading to a relatively poor signal in which the emission is dominated by the continuum component [7]. In an attempt to increase the analytical sensitivity of conventional single-pulse LIBS in submerged solids, some recent experiments [8-10] demonstrated that an enlargement of the laser pulse duration significantly improves the quality of the acquired LIBS spectra. The use of a long-pulse duration lead to an enhancement of the emission lines and to lowering of the continuum level since, before reaching the sample, the later part of the beam is efficiently absorbed by the plume and causes an additional plasma excitation and expansion. However, even though the use of a long-duration ns pulse has been demonstrated as a good solution, the double-pulse configuration is the most widespread alternative in LIBS community. At this point, De Giacomo et al. [11] reviewed the limitations of SP-LIBS and discussed the peculiarities of DP-LIBS as an invaluable analytical tool for the elemental analysis of bulk water and submerged solid samples. In this approach, the first laser pulse produces a gas bubble whereas the second pulse ablates the sample and re-excites the plasma inside the bubble. Recently, in a series of two papers, Lazic et al. [12-13] explained the cavitation bubble formation during laser-water interaction and the dependence of DP-LIBS signal intensity inside liquids on the interpulse delay and how the formation and detection of the secondary plasma are strongly affected by the optical properties of the vapor bubble induced by the first laser pulse.

Another alternative is the use of a gas purge to remove the water from the sample surface and create a gas–sample interface ideal for underwater LIBS analysis without the need to create first the vapor bubble, as in a double-pulse configuration. As compared to a solid–liquid interface, working in a solid–gas environment improves the ablation efficiency since the input energy is not lost in liquid evaporation and it is not absorbed and/or scattered by the liquid and the suspended particles. Based on this concept, in 2002,

Beddows et al. [14] published the first analysis of submerged targets under gas flow. Here, LIBS analysis on steel samples was performed at a 20 meters distance by delivering the laser radiation through an optical fiber cable. In fact, the employment of fiber optics play an increasingly important role in the design and construction of sensors and LIBS measuring systems. Thus, applications including the analysis of ferrous material in a nuclear reactor [15], the determination of minor trace components in different matrices [16, 17] and the determination of pollutants in soils [18,19] have been also addressed in the literature. In general, the maximum distance reached for the instrument as well as the LIBS configuration and the optical system for laser focusing at the output end of the fiber depends on each particular application. In the field of oceanography, in 2012, the first in situ submarine LIBS analysis of solid samples was published by the University of Málaga [20]. An integrated LIBS technology platform for underwater analysis was developed and adapted to the marine environment. A set of metallic materials was analyzed at 30 m deep. Later, the employment of a multi-pulse configuration was raised by the authors as a possibility to increase the laser beam energy transmitted while avoiding the damage of the fiber [21-23]. MP-LIBS operates in a collinear configuration with the advantages of using a single laser source, thus avoiding problems related to the alignment and synchronization between several laser sources. Also, MP-LIBS reduces the dimensions, consumption and equipment costs, which are important in the design of a fieldable LIBS system. With this configuration, the performance of the equipment was improved in terms of energy transmitted through the optical fiber, range of analysis and variety of samples to be analyzed. The improved version of this remote system was tested in a real archaeological shipwreck in the Atlantic coast of Andalucía.

LIBS has no limited horizon and the continuous advances in reducing the size and weight while increasing the capabilities of lasers, spectrographs and detectors make possible the development of compact and rugged instrumentation. Portable systems give greater flexibility and also increase the range of LIBS applications. Thus, sea floor exploration at deep-ocean (2000-3000 meters) could be accomplished by the integration of LIBS technology in a remotely operated vehicle (ROV). Studies concerning the effect of pressure in LIBS analysis inside liquids [24, 25] and the influence of the underwater optical path on the LIBS signal [26] have recently explored the suitability of LIBS for a deep-sea survey.

What is clear is that LIBS is the only available technique for chemical analysis directly inside liquids. To further exploit the inherent advantages of the technology, a mobile fiber-based LIBS platform capable of performing remote measurements in the tens of meters range has been designed. In the present chapter, its performance is discussed on the basis of the spectral response. To check the reliability and reproducibility of the instrument several robustness tests were performed outside the lab. Last, the potential of remote-LIBS technology for the underwater measurements of coating thickness in galvanized steel was also studied.

2. Experimental set-up

2.1. Instrument

The instrument used in this chapter is the remote LIBS system AQUALAS 2.0. A more detailed description of AQUALAS 2.0 has been presented in *Chapter 3*.

2.2. Samples

For field tests, a certified bronze standard (BCR 691) with variable concentration of Cu, As, Sn, Pb, and Zn was used. Also, a set of electrolytically galvanized steel samples, with variable Zn thicknesses in the range between 3.1 and 11.2 μm provided by ThyssenKrupp Stahl (TKS, Dortmund, Germany) was used. These samples were considered reference materials, which allowed construction of calibration curves.

3. Results and discussion

3.1. Stress tests in a marine environment. Stability and robustness of the remote LIBS system.

The main goal of this approach is the possibility of a LIBS analysis in situations where the sample of interest is not directly accessible, i.e. industrial and geological applications, underwater inspection, hazardous environments and in general, areas of contamination by toxic or radioactive material. In *chapter 3*, the design of a robust fiber optic probe for remote sensing by LIBS has been explained. At the same time, it should be pointed out that focusing of the laser radiation into an optical fiber is the most critical issue. The fiber must be mounted on a *xyz* stage and also it should be placed behind the laser focus position to avoid irreversible damage.

A number of experiments were conducted in order to evaluate the stability and robustness of the prototype in a marine environment. Operations were performed outdoor in the Málaga Bay. In a first step, we evaluated the deployment of the 50-m long umbilical cable which was wound round a cylindrical support. The accumulated stress in the spool may affect the laser beam delivery through the optical fiber cable. Thus, LIBS spectra on a bronze sample (78.7% Cu, 8% Pb, 7.2% Sn and 6% Zn) were acquired at different range of analysis depending on the LIBS-probe deployment. Figure 1 shows the influence of the probe deployment on the LIBS signal. The selected spectral line for this study was Cu (I) at 521.82 nm. Each point in the graph represents the average intensity of 5 replicate measurements. As shown, the signal intensity remained virtually constant with the LIBS probe deployment, in the 0-50 meters range. In this range, the average intensities were measured in ca. 38.000 counts (5% RSD). The inset of Figure 1 represents the relative standard deviation (RSD) for each measurement. As noted, in all cases, the signal variability is better than 14% RSD.

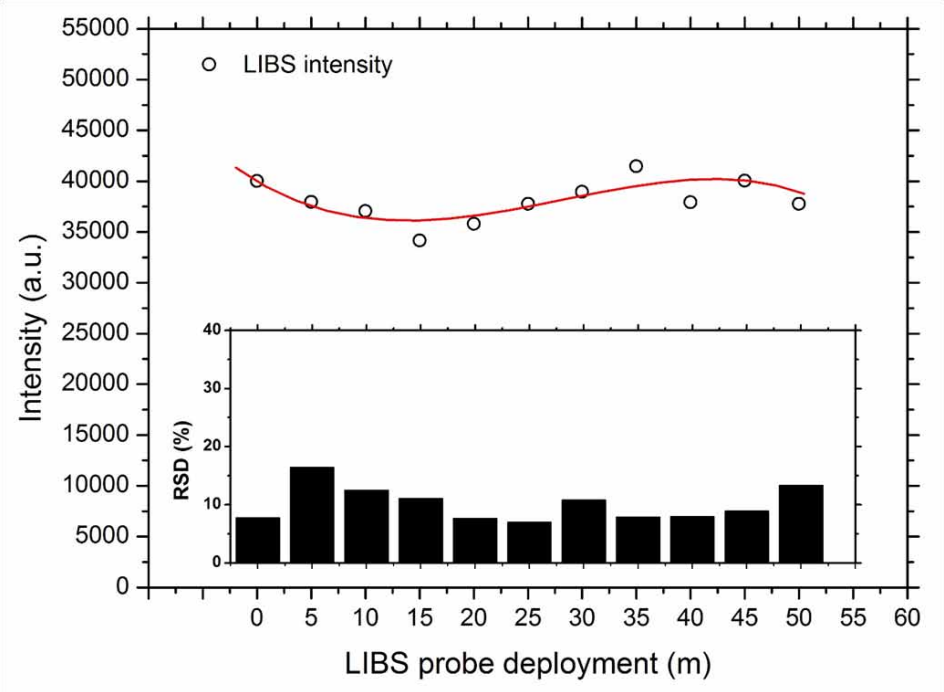

Figure 1. Influence of the probe deployment on LIBS signal. The inset represents the relative standard deviation (RSD) for each measurement in the range 0-50 meters.

Figure 2 depicts the output energy of the LIBS probe as a function of the distance deployed from the instrument, measured with a pyroelectric energy meter. A series of 500 successive laser pulses at a repetition rate of 2 Hz were measured. The energy meter was placed slightly out of focus in order to avoid damage in the sensing head. As shown, the average pulse energies measured remain practically constant with the deployment of the LIBS probe ($RSD_{inter\text{-}range} \sim 2\%$), which means that attenuation of the delivered laser energy is in some way negligible. In this meaning the averaged output energy has been measured in 42.6 mJ $pulse^{-1}$. Furthermore, the pulse-to-pulse fluctuation of the output energy remains more or less static ($RSD_{intra\text{-}range} \sim 0.5\%$) regardless of the deployed distance.

LIBS system stability as function of time was also evaluated. Results are plotted in Figure 3. The selected spectral line for this study was Cu again. Each point in the graph represents the average intensity of 5 replicate measurements on bronze sample. In addition, LIBS spectra were strictly acquired at the same experimental conditions (50 laser shots per replicate; 2 Hz; 1.3 µs acquisition delay; 22 ns pulse width). This study started in 2014 and continues to date. As observed, in the first part of the graph, LIBS signal was in the range 35.000-40.000 a.u. From here, the intensity gradually drops until 30.000 a.u., which may indicate disalignment of the laser-to-fiber coupling. At this point, optical fiber was broken and then was polished again and a smooth adjustment was performed to retrieve the system's performance. Hence, this graph allows the regular monitoring of the LIBS system stability and identifying/diagnosing problems related to the laser-to-fiber coupling.

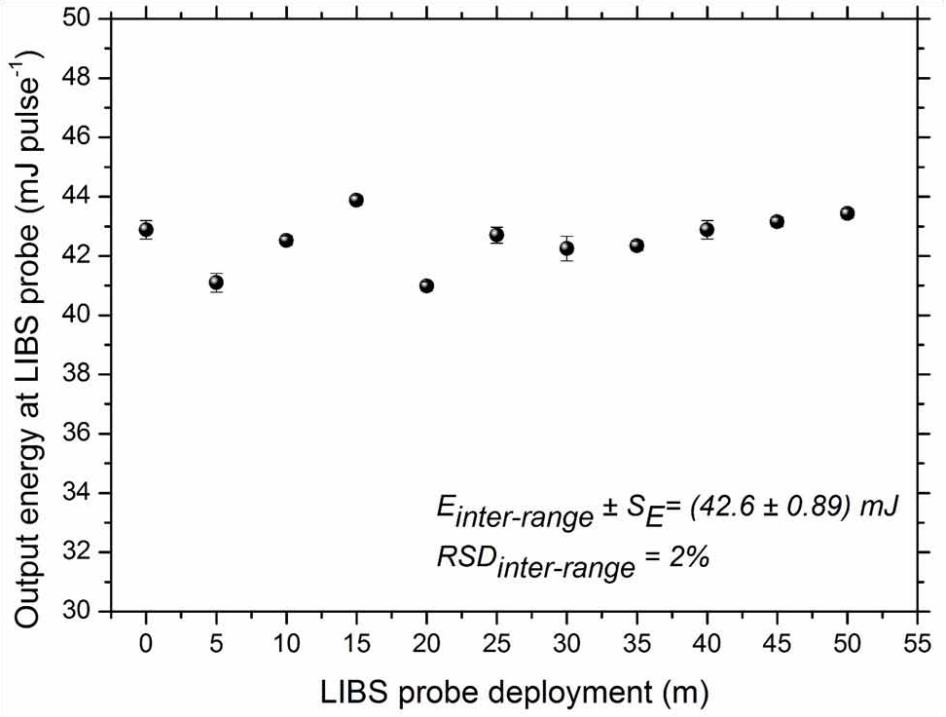

Figure 2. Output energy of the LIBS probe as a function of the distance deployed from the instrument.

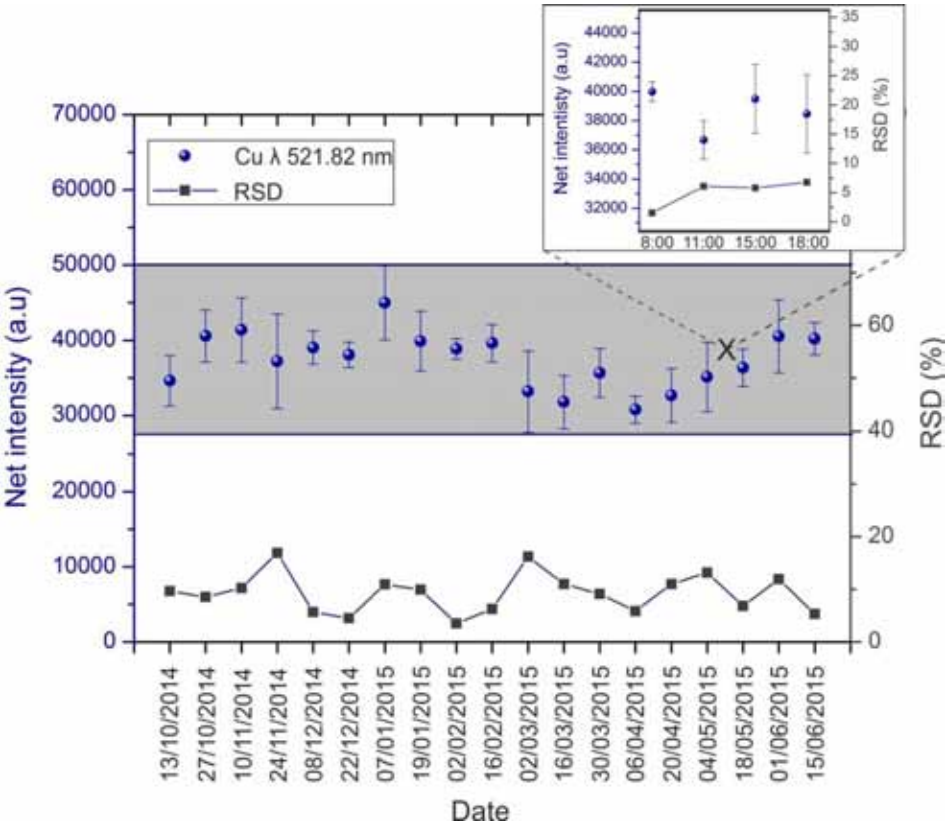

Figure 3. LIBS system stability as a function of time. Each point in the graph represents the average intensity of 5 replicate measurements on a bronze sample (78.7% Cu, 8% Pb, 7.2% Sn and 6% Zn). Experimental conditions: 50 laser shots per replicate; 2 Hz; 1.3 µs acquisition delay; 22 ns pulse width.

Referring to the aforementioned results, the stability of the LIBS system is highly satisfactory, which is particularly relevant especially in a marine environment. In this sense, a hypothetical damage of the optical fiber may be the unique weak point of our prototype. Thus, in another experiment, a stress test was performed with the objective to evaluate the robustness of the laser-to-fiber coupling. LIBS system was moved along a cobblestone road in the access route to the beach in which these tests were performed. The total distance covered in this experiment was 500 meters and LIBS spectra were acquired every 100 meters. The emission line Cu (I) 521.82 nm as function of the distance covered by the prototype is depicted in Figure 4. The calculated RSD values for each test is also plotted in the graph. As shown, the averaged LIBS intensity along the 500 meters was ca. 35.000 counts while the reproducibility in terms of relative standard deviation was, in all cases, better than 10 %. Results obtained confirmed the robustness of the laser-to-fiber coupling even during the displacement of the system in a non-paved road. In relation to this, the proven stability and robustness of the remote LIBS system guarantee the reliability of the data acquired under severe conditions (i.e. in a marine environment) during a field campaign.

3.2. Underwater LIBS analysis of galvanized steel

In the industrial sector, to assure reliable corrosion protection, the coating thickness has to be kept constant over a tolerance range [27]. Underwater depth profiling LIBS analysis, using multi-pulse configuration, of a set of galvanized steel with different coating thicknesses in the range 3.2-11.2 µm was

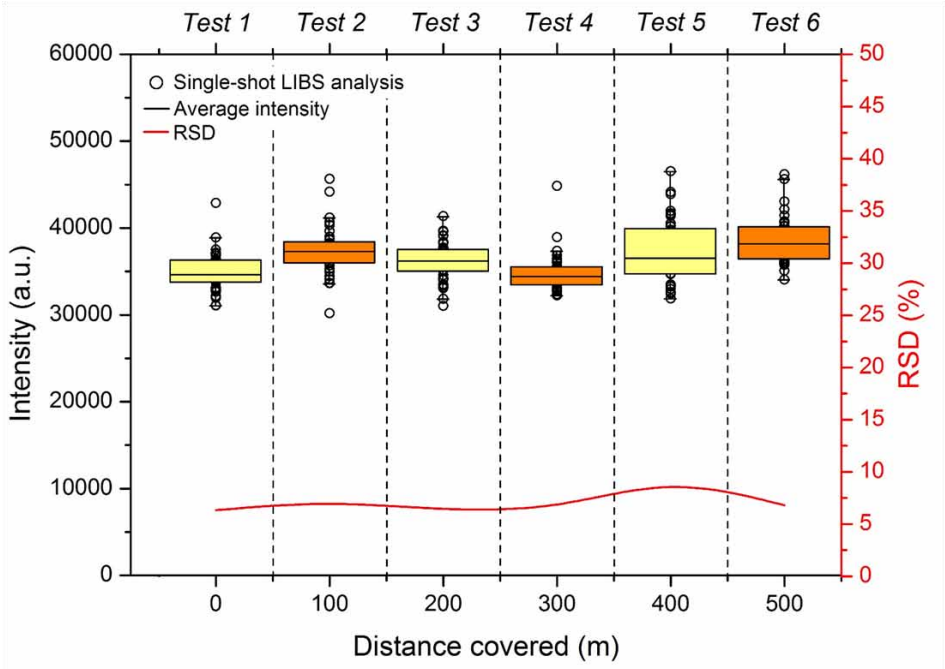

Figure 4. LIBS signal as a function of the distance traveled by the prototype along a non-paved road. The total distance covered in this experiment was 500 meters.

performed. It is worth mentioning that this study was completed in shallow waters during the tests accomplished in the Bay of Málaga. LIBS spectra of galvanized steel were acquired in the 350-550 nm range. Emission lines of Zn (I) 472.21 nm and Fe (I) 438.35 nm were monitored in the coating and the substrate, respectively. Depth information was obtained by tuning the pulse width to 22 ns (QS-delay: 118 µs) and 30 ns (QS-delay: 116µs). The resultant Zn profiles for a coating thickness of 11.2 µm in both instances are plotted in Figure 5. *X-axis* corresponds to the number of laser pulses. For comparative purposes, signal emissions were normalized to unity. As noted, both profiles decay until reaching a value near to zero. The averaged ablation rate (AAR) calculated from the number of pulses corresponding to a normalized intensity value equal to 0.5 (p0.5), that is 50% of the full signal [28]. The inset represents the differentiated profile at each pulse width. As seen, the derivative of the measured LIBS profile exhibit a Gaussian shape and can be also used to elucidate the AAR. The number of pulses to completely deplete the coating layer was lower for the larger pulse duration, 30 ns. Thus, for the coating thickness of 11.2 µm, the AAR was measured in 172 nm pulse-1 and 254 nm pulse-1 for the pulse width of 22 ns and 30 ns, respectively. This fact is could be due to that the pulse duration of the main spike in the sequence promotes the heating and melting of the sample, facilitating the ablation of the sample surface by the rest of the spikes or exciting the material that has been previously ablated by the first pulse. Hence, longer pulses and a greater number of spikes (as is the case of QS-delay: 116µs) could be intensify the ablation of surface [21].

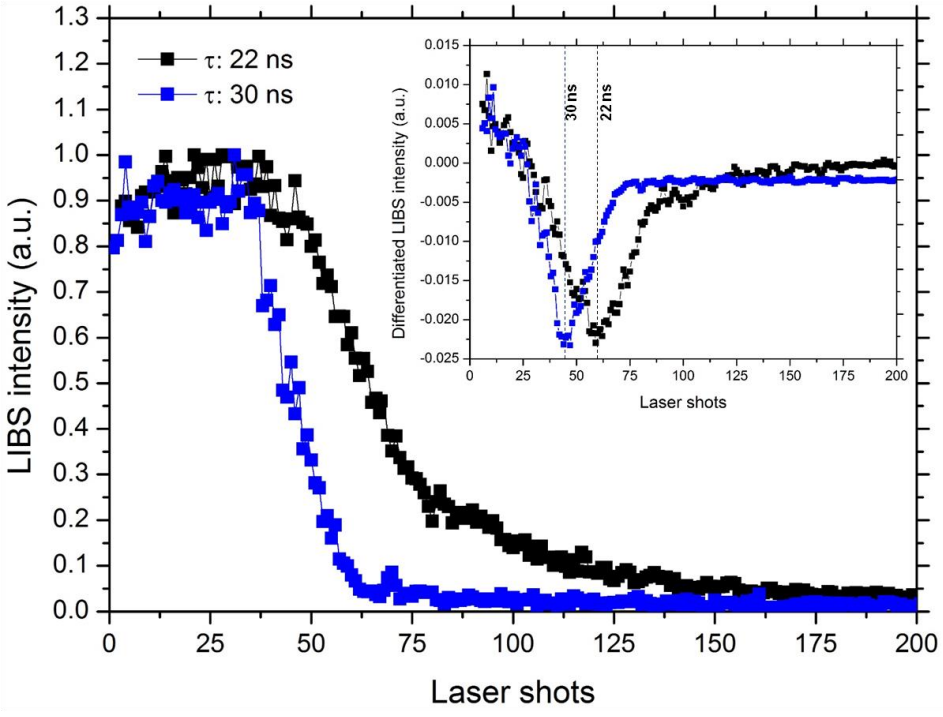

Figure 5. Depth profiles obtained during the underwater LIBS characterization of galvanized steel (coating thickness of 11.2 µm) at 22 ns and 30 ns pulse duration. The inset represents the differentiated LIBS intensity for the Zn profile acquired at both pulse duration. The emission line Zn (I) 472.22 nm was monitored.

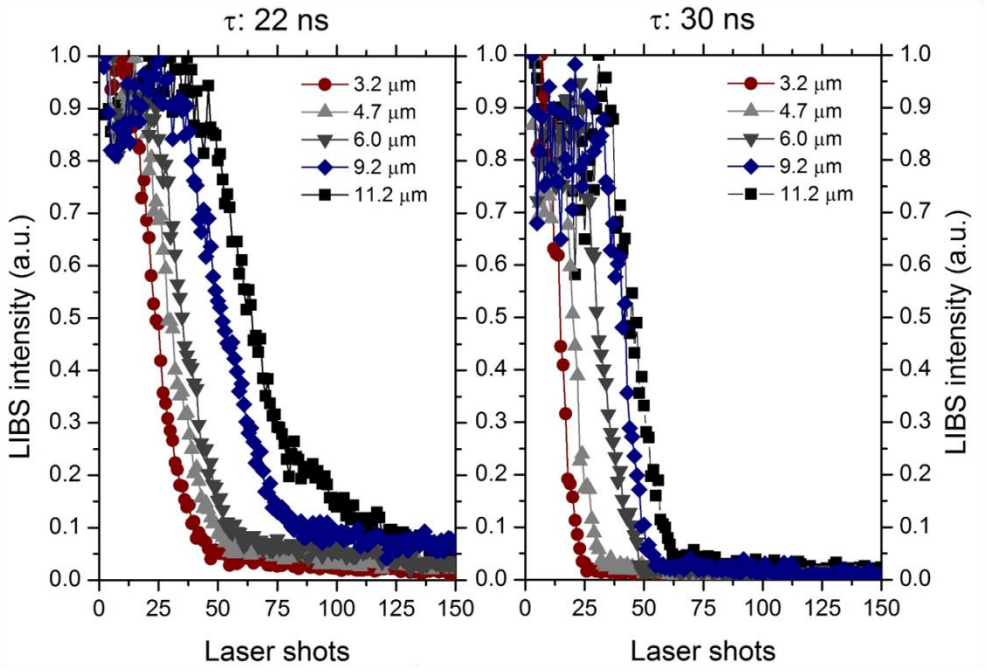

Figure 6. Variation of the Zn profile in a set of commercial galvanized steel (ranging from 3.2 to 11.2 µm) as a function of the laser pulse duration: 22 ns (left) and 30 ns (right).

The rest of the galvanized steels were measured following the same criteria for both pulse widths. Results are plotted in Figure 6. In this graph, the variation of Zn profile as a function of the number of laser pulses is presented. The total laser pulse energy was kept constant for all measurements. Hence, it is clear that the laser irradiance decreases with an increase in pulse duration. As shown, a change in the experimental conditions results in an increase in p0.5 and consequently in a decreases of AAR, as occurs in the left graph, corresponding to 22 ns pulse duration. In contrast, in all the coating thickness measured, p0.5 decreases at 30 ns pulse duration. To establish a correspondence within the laser pulse duration, data were plotted in Figure 7. In this sense, the averaged ablation rates were higher for the larger pulse duration, 30 ns, in all the coating thickness examined. Thus, for 22 ns pulse duration the AAR was measured in the 130-160 nm pulse^{-1} while in the case of 30 ns the AAR was ~250 nm pulse^{-1} in all the examined range.

In addition to this, in order to quantify the limit of accuracy and precision of the profiles obtained, depth resolution (Δz) was calculated for a coating thickness of 3.2 µm in both pulse widths. This parameter is defined as the depth range over which a signal decreases (or increases) by a specified amount when profiling an ideally sharp interface between two media. By convention, the depth resolution corresponds to the depth range over which an 84 to 16% (or 16 to 84%) change in the full signal is measured as explained in ref [28]. Also, such reference indicate that if a change in experimental conditions results in an increase in p0.5 then AAR will decrease, as was observed in Figure 7. In that case, as more points will define the depth profile, and consequently the interface description, an improvement of depth resolution would be expected, that is, as AAR decreases, Δz should decrease too. However, in our experimental conditions Δz was measured in 2.8 µm and 2.2 µm for the pulse width of 22 ns and 30 ns, respectively. It was due to that the

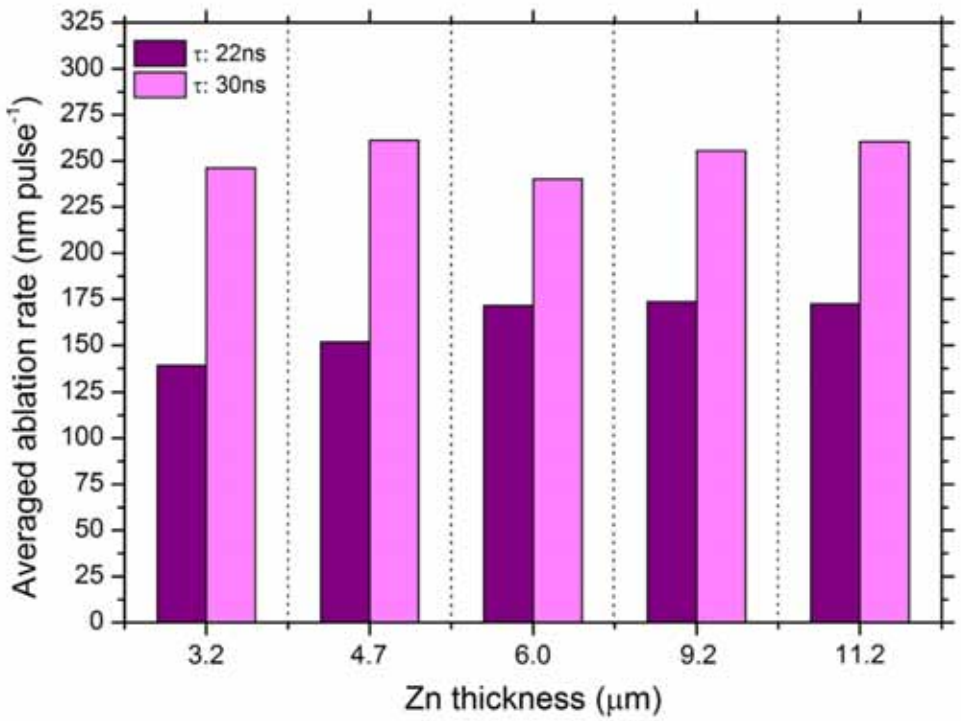

Figure 7. Calculated averaged ablation rate (AAR) as a function of the coating thickness and the laser pulse duration.

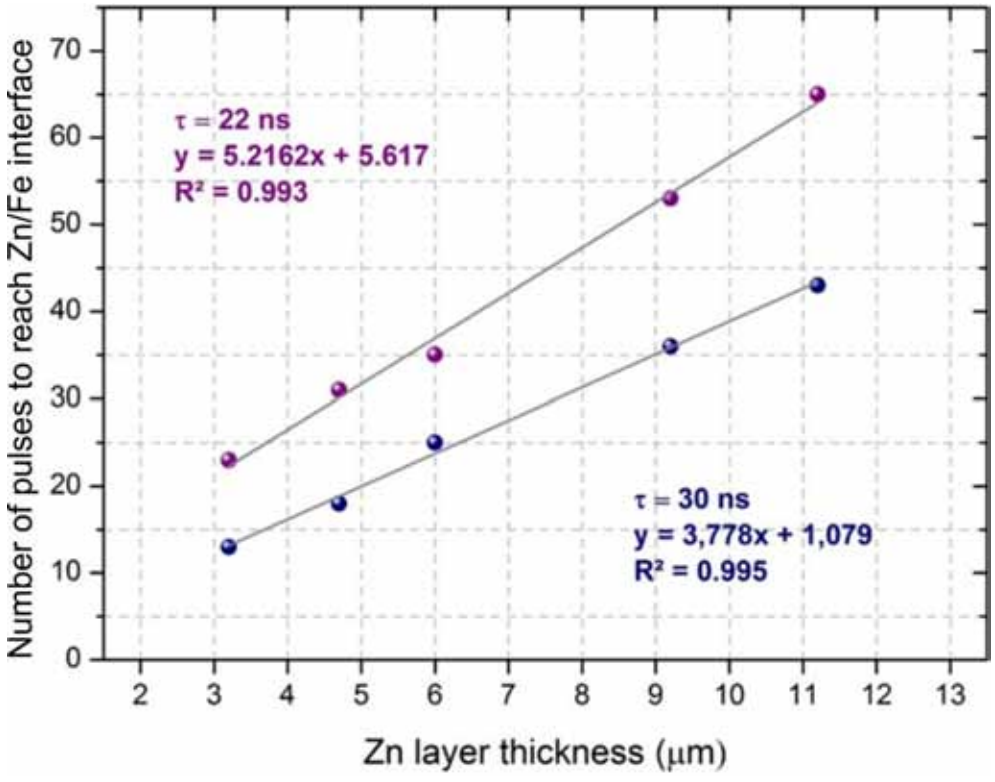

Figure 8: Number of pulses to reach the Zn-Fe interface, $p_{0.5}$, as a function of the coating thickness.

factor Δp (that corresponds to the number of laser shots to reach 84% and 16% of the normalized signal intensity) was changed as a function of the pulse width. In view of the results a faster and well resolved deep characterization is obtained using large pulse duration.

On the other hand, in order to determine the Zn coating thickness, calibration curves were constructed for both pulse durations. In Figure 8, the number of pulses to reach the Zn-Fe interface is plotted as function of the coating thickness. As expected, this value increases with the thickness of the Zn coating. In both cases, the excellent correlation between both variables allows the estimation of the coating thickness of an unknown sample. Thus, the longer the pulse duration, the larger the ablated mass. This result is consistent with that published in [21] and demonstrates the potential of remote-LIBS technology for the underwater measurements of coating thickness in galvanized steel.

4. Conclusions

In this part of the work, underwater characterization of galvanized steel has been accomplished in shallow waters in the Bay of Málaga. Also, a number of experiments were conducted outdoors in order to evaluate the stability and robustness of the Remote-LIBS prototype in a marine environment. Results confirmed the potential of LIBS for underwater measurements, which could be considered as a solution for mining exploration, cultural heritage and the industrial sector, among others.

A stress test was designed with the objective to assess the improvements performed in the remote system. At first, we studied if the accumulated stress in the spool may affect the laser beam delivery through the optical fiber cable. However, signal intensity remained virtually constant with the LIBS probe deployment. In the 0-50 meters range, the averaged output energy was measured in 42.6 mJ pulse^{-1} while the RSDinter-range was approximately 2%. This means that attenuation of the delivered laser energy is in some way negligible and does not depend on the deployment of the LIBS probe.

Also, results obtained confirmed the robustness of the laser-to-fiber coupling even during the displacement of the system in a non-paved road. The total distance covered in this experiment was 500 meters. In relation to this, the proven stability and robustness of the remote LIBS system guarantee the reliability of the data acquired under severe conditions (i.e. in a marine environment) during a field campaign.

During the stress tests, the potential of remote-LIBS technology for the underwater measurements of coating thickness in galvanized steel was demonstrated. A multi-pulse excitation scheme was selected for LIBS analysis. Depth information was obtained by tuning the pulse width to 22 ns and 30 ns. In order to determine the Zn coating thickness, calibration curves were constructed for both pulse durations. Information extracted from depth profiling analysis could be employed for the quality control of the corrosion protection in the industrial sector. The average ablation rate (AAR) was measured in 172 nm pulse^{-1} and

260 nm pulse^{-1} for the pulse width of 22 ns and 30 ns, respectively; and depth resolution (Δz) 2.8 μm and 2.2 μm. Hence, the longer the pulse duration, the larger the ablated mass and depth resolution.

5. References

1. F. J. Fortes, J. Moros, P. Lucena, L. M. Cabalín, J. J. Laserna, Laser-induced breakdown spectroscopy, Anal. Chem. 85 (2013), 640–669.
2. D. W. Hahn, N. Omenetto, Laser-induced breakdown spectroscopy (LIBS), part I: review of basic diagnostics and plasma-particle interactions: still-challenging issues within the analytical plasma community, Appl. Spectrosc. 64 (2010), 335–366.
3. R. E. Russo, X. Mao, J. J. Gonzalez, V. Zorba, J. Yoo; Laser ablation in analytical chemistry, Anal. Chem. 85 (2013), 6162–6177.
4. F. J. Fortes, J. J. Laserna, The development of fieldable laser-induced breakdown spectrometer: No limits on the horizon, Spectrochim. Acta Part B 65 (2010), 975–990.
5. V. Lazic, S. Jovićević, Laser induced breakdown spectroscopy inside liquids: Processes and analytical aspects, Spectrochim. Acta Part B 101 (2014), 288–311.
6. D. A. Cremers, L. J. Radziemski, T. R. Loree, Spectrochemical analysis of liquids using the laser spark, Appl. Spectrosc. 38 (1984), 721–726.
7. B. Charfi, M. A. Harith, Panoramic laser-induced breakdown spectrometry of water, Spectrochim. Acta Part B 57 (2002), 1141–1153.
8. H. Oguchi, T. Sakka, Y.H. Ogata, Effects of pulse duration upon the plume formation by the laser ablation of Cu in water, J. Appl. Phys. 102 (2007), 023306-6.
9. T. Sakka, S. Masai, K. Fukami, Y.H. Ogata, Spectral profile of atomic emission lines and effects of pulse duration on laser ablation in liquid, Spectrochim. Acta Part B 64 (2009), 981–985.
10. T. Sakka, H. Oguchi, S. Masai, K. Hirata, Y.H. Ogata, Use of a long-duration ns pulse for efficient emission of spectral lines from the laser ablation plume in water, Appl. Phys. Lett. 88 (2006), 061120-3.
11. A. De Giacomo, M. Dell'Aglio, O. De Pascale, M. Capitelli, From single pulse to double pulse ns-Laser Induced Breakdown Spectroscopy under water: Elemental analysis of aqueous solutions and submerged solid samples, Spectrochim. Acta Part B 62 (2007), 721–738.
12. V. Lazic, J. J. Laserna, S. Jovicevic, Insights in the laser induced breakdown spectroscopy signal generation underwater using dual pulse excitation — Part II: Plasma emission intensity as a function of interpulse delay, Spectrochim. Acta Part B 82 (2013), 50–59.
13. V. Lazic, J. J. Laserna, S. Jovicevic, Insights in the laser-induced breakdown spectroscopy signal generation underwater using dual pulse excitation — Part I: Vapor bubble, shockwaves and plasma; Spectrochim. Acta Part B 82 (2013), 42–49.

14. D. C. Beddows, O. Samek, M. Liška, H. Telle, Single-pulse laser-induced breakdown spectroscopy of samples submerged in water using a single-fibre light delivery system, Spectrochim. Acta Part B 57 (2002), 1461–1471.
15. A. I. Whitehouse, J. Young, I. M. Botheroyd, S. Lawson, C. P. Evans, J. Wright, Remote material analysis of nuclear power station steam generator tubes by laser-induced breakdown spectroscopy, Spectrochim. Acta Part B 56 (2001), 821–830.
16. A. K. Rai, H. Zhang, F. Y. Yueh, J. P. Singh, A. Weisburg, Parametric study of a fiber-optic laser-induced breakdown spectroscopy probe for analysis of aluminum alloys, Spectrochim. Acta Part B 56 (2001), 2371–2383.
17. B. J. Marquardt, S. R. Goode, S. Michael Angel, In Situ determination of lead in paint by laser-induced breakdown spectroscopy using a fiber-optic probe, Anal. Chem. 68 (1996), 977-981.
18. D. A. Cremers, J. E. Barefield II, A. C. Koskelo, Remote elemental analysis by laser induced breakdown spectroscopy using a fiber-optic cable, Appl. Spectrosc. 49 (1995), 857-860.
19. G. A. Theriault, S. Bodensteiner, S. H. Lieberman, A real-time fiber-optic LIBS probe for the in situ delineation of metals in soils, F. Anal. Chem. Technol. 2 (1998), 117–125.
20. S. Guirado, F. J. Fortes, V. Lazic, J. J. Laserna, Chemical analysis of archeological materials in submarine environments using laser-induced breakdown spectroscopy. On-site trials in the Mediterranean Sea, Spectrochim. Acta Part B 74-75 (2012), 137–143.
21. S. Guirado, F. J. Fortes, L. M. Cabalín, J. J. Laserna, Effect of Pulse Duration in Multi-Pulse Excitation of Silicon in Laser-Induced Breakdown Spectroscopy (LIBS), Appl. Spectrosc. 68 (2014), 1060–1066.
22. S. Guirado, F. J. Fortes, J. J. Laserna, Elemental analysis of materials in an underwater archeological shipwreck using a novel remote laser-induced breakdown spectroscopy system, Talanta 137 (2015), 182-188.
23. S. Guirado, F. J. Fortes, J. J. Laserna, Multi-pulse excitation for underwater analysis of copper-based alloys using a novel remote laser-induced breakdown spectroscopy system, Appl. Spectrosc. 70 (2016), 618-626.
24. B. Thornton, T. Takahashi, T. Sato, T. Sakka, A. Tamura, A. Matsumoto, T. Nozaki, T. Ohki, K. Ohki, Development of a deep-sea laser-induced breakdown spectrometer for in situ multi-element chemical analysis, Deep. Res. Part I. 95 (2015), 20–36.
25. M. Lawrence-Snyder, J .P. Scaffidi, W.F. Pearman, C.M. Gordon, S.M. Angel, Issues in deep ocean collinear double-pulse laser induced breakdown spectroscopy: Dependence of emission intensity and inter-pulse delay on solution pressure, Spectrochim. Acta Part B 99 (2014), 172–178.
26. F. J. Fortes, S. Guirado, a. Metzinger, J. J. Laserna, A study of underwater stand-off laser-induced breakdown spectroscopy for chemical analysis of objects in the deep ocean, J. Anal. At. Spectrom. 30 (2015), 1050–1056.

27. H. Balzer, M. Hoehne, V. Sturm, R. Noll, Online coating thickness measurement and depth profiling of zinc coated sheet steel by laser-induced breakdown spectroscopy, Spectrochim. Acta Part B 60 (2005), 1172–1178.
28. M. P. Mateo, J. M. Vadillo, J. J. Laserna, Irradiance-dependent depth profiling of layered materials using laser-induced plasma spectrometry, J. Anal. At. Spectrom. 16 (2001), 1317–1321.

Chapter 5. Influence of gas on underwater laser-induced breakdown spectroscopy analysis. Application to the cultural heritage field

1. Introduction

Laser-induced breakdown spectroscopy (LIBS) is a popular technique because of its speed, simplicity, and usually inexpensive hardware. Additionally, LIBS requires little or no sample preparation and can provide in situ simultaneous multi-element analysis. Thus, joining the LIBS potential with the improvements of instrumentation development to adapt the technique to field trials with deployable equipment, it is not surprising that this technique is being employed for a wide variety of applications [1, 2]. In particular those that take place in an extreme environment where it is difficult access to the sample or its transport, or represents a risk for the analyst such as the explosive detection [3], submerged cultural heritage [4, 5], space exploration [6, 7] among others. However, LIBS still suffers from relatively poor sensitivity compared to other analytical methods, and this aspect often limits the performance of the technique. In an attempt to increase the analytical capabilities of LIBS, a substantial part of the research interests has been focused on two work areas related to the study of the effect of the sample surrounding gas and the evaluation of different experimental approaches for the sample excitation.

Respect to the sample surrounding gas, it is well known that its properties critically influence the laser-target and laser-plasma couplings as well as the plume de-excitation mechanisms; thus altering the plasma temperature, electron density, mass removal, and plasma shielding. Consequently, the ensuing spectral features of LIBS for chemical analysis will be modified [8-10]. It is particularly manifested in spectral line resolution, emission signal intensity and signal-to-noise ratio (SNR). In this meaning, there is a growing interest not only in evaluating the effect of pressure of surrounding gas; but also in performing experiments under atmospheres with different chemical composition. In spite of the large number of available reports in the literature in where the plasmas are generated using in very different experimental conditions which vary according to the laser used, and the type of samples employed to particularly applications, there is no a definitive study that fully accounts for all of the phenomena occurring in LIBS when the pressure and atmospheric compositions are changed. However, some general aspects respect to signal intensity could be established.

Regarding gas pressure, as explained by Fortes et al. [2], an increase in the plasma intensity when decreasing pressure is observed. It is due to the fact that at high pressures, plasma energy is quickly lost to the surrounding atmosphere by coalitional processes with the gas and therefore the plasma is short lived. In contrast, at low pressures the plasma expands much further into the ambient atmosphere but it is not cooled rapidly by the surrounding species [11, 12]. Hence, lifetime of the emitting species is longer and the integrated emission volume becomes larger. Thus, more light from the laser plasma can be collected, and a higher peak intensity of emission lines is observed. In spite of this, there is a lower limit in the gas pressure below which the plasma confinement seems to be insufficient, thereby leading to a reduced coalitional excitation. In this case, the intensity of the emission signals may drop [13]. In general, as mentioned in [10] the highest signal intensity is observed around 5–10 Torr. However, some researchers have noted that the

optimal pressure is dependent on the gas composition. Thorough studies respect to effect of gas composition such as Ar, He, CO_2 and air on plasma, typically have revealed that the highest overall intensity is observed for Ar buffer gas. This fact is associated to higher plasma temperatures. Löbe et al. [14] and others [9, 15, 16] also noted that this huge temperature is due to thermal properties of the gas, so that at lower thermal conductivity of the gas less heat flow is transferred from the plasma to the buffer gas. Consequently higher temperature and slowest decay is observed [17].

In the second work area, considering different experimental configurations for sample excitation, as Scaffidi et al. [18] and Babushok et al. [19] studies, the use of double pulse (DP) produced an enhancement of emission compared to traditional single pulse. Briefly, it is due to the fact that the first laser pulse affects the sample, and the resulting shock wave displaces the surrounding gas. Then, a second pulse interacts with the material within the first plasma plume, resulting in an enhancement of the LIBS signal. This fact has revolutionized the way in which LIBS measurements were performed, especially in areas related to bulk or liquid analysis [20] in which a huge part of energy of the first laser pulse is inverted to water evaporation. Another alternative, such as multipulse excitation (MP) had been already demonstrated in 1969 by Piepmeier and Malmstadt [21] as a good way to further excite the sample species with a multispike laser pulse. But it was not until over two decades later that publications in this field highlighted the advantages of emission enhancement mechanisms for MP-LIBS to improve the analytical sensibility [22-25].

For our particular application, chemical in-situ characterization in an underwater site to cover around 50 meters deep, the design of a remote LIBS system based in guide by a fiber optic was decided would be the best alternative. In first instance, the prototype developed in University of Málaga utilized a SP configuration [4]. However, LIBS analysis was restricted to metallic samples due to the low energy threshold allowed by the optical fiber. The employment of a multi-pulse configuration was raised by the authors as a possibility to increase the laser beam energy transmitted while avoiding the damage of the fiber. In fact, in this new remote equipment the pulse duration of the main spike in the train of pulses allows introducing a higher laser radiation through the optical fiber and also promotes the heating and melting of the sample, facilitating to the rest of the spikes the ablation of the sample surface or exciting the material that has been previously ablated by the first pulse. With this configuration, the performance of the equipment is improved in terms of: energy transmitted through the optical fiber, range of analysis and variety of samples to be analyzed (i.e., marble, ceramic, concrete, etc.) [5].

In addition to these improvements which have been already implemented in our prototype, the use of a gas purge is also considered not only to prevent the water from entering the analysis probe and remove it creating a solid-gas interface optimum for LIBS analysis; but also to continue improving the performance of the prototype. As mentioned above, the properties of the surrounding gas severely influence the spectroscopy response. Therefore, in this chapter the effect of gas pressure in a range from 2 to 5 bar is evaluated, as well as, the use of different gases such as air, CO_2, He and Ar. In particular, these studies will be focused on improving ceramic samples detection. This kind of materials are very common in submerged

archaeological sites, however, the analysis in such conditions can be complex due to it highly porous nature.

2. Experimental Set-up

2.1. Instrument

The instrument used in this chapter is the remote LIBS system AQUALAS 2.0. A detailed description of AQUALAS 2.0 has been presented in *Chapter 3*.

2.2. Samples

A set of certified standard bronzes materials (BCR 691) with variable concentrations of Cu, As, Sn, Pb, and Zn was used. Ceramic samples have been provided by the *Centro de Arqueología Subacuática of Cádiz* (CAS). Furthermore, variety of real archaeological materials provided by CAS was also characterized in this work. Data were obtained by averaging 50 laser shots at each sample position, after 10 laser shots used for cleaning purposes in the case of bronze, and 20 laser shots in ceramic. Each sample was measured 5 times. In order to simulate real conditions, samples were immersed for LIBS analysis in a water tank of 100 L capacity and 35 x 80 x 41 cm dimensions.

2.3. Submersible LIBS probe. Gas protection

In our fiber-based instrument, the submersible LIBS probe supplies gas to remove the water from the sample surface and creates a gas–sample interface ideal for underwater LIBS analysis. Moreover, for preventing the admittance of water into the LIBS probe, the *pressure difference* (ΔP) between inside (P_{in}) and outside (P_{out}) of the probe must exceed at least 1 bar [4]. In fact, the use of a gas purge is of key importance, especially during real analysis in a marine environment where ΔP decreases when increasing the depth of analysis. Figure 1 shows a schematic diagram of the submersible LIBS probe. As seen, the gas flow coming from the auxiliary module travels through the umbilical cord and exits the probe through the nozzle located at the probe tip.

3. Results and discussion

3.1. Influence of purge gas

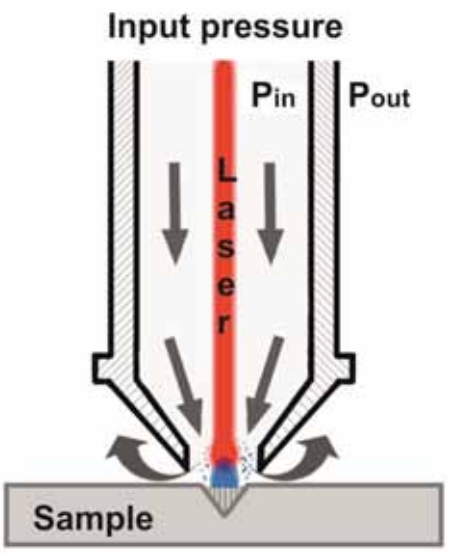

Figure 1. schematic drawing of the process to creating a gas–sample interface.

3.1.1. Influence of the differential of pressure on LIBS signal

In a first experiment, the influence of ΔP on LIBS signal of metallic samples was evaluated. The LIBS signal was acquired by changing the inner pressure in a range from 2 to 5 bar while keeping constant the external pressure of the probe at 1 bar. The results are presented in Figure 2. The emission lines of Cu

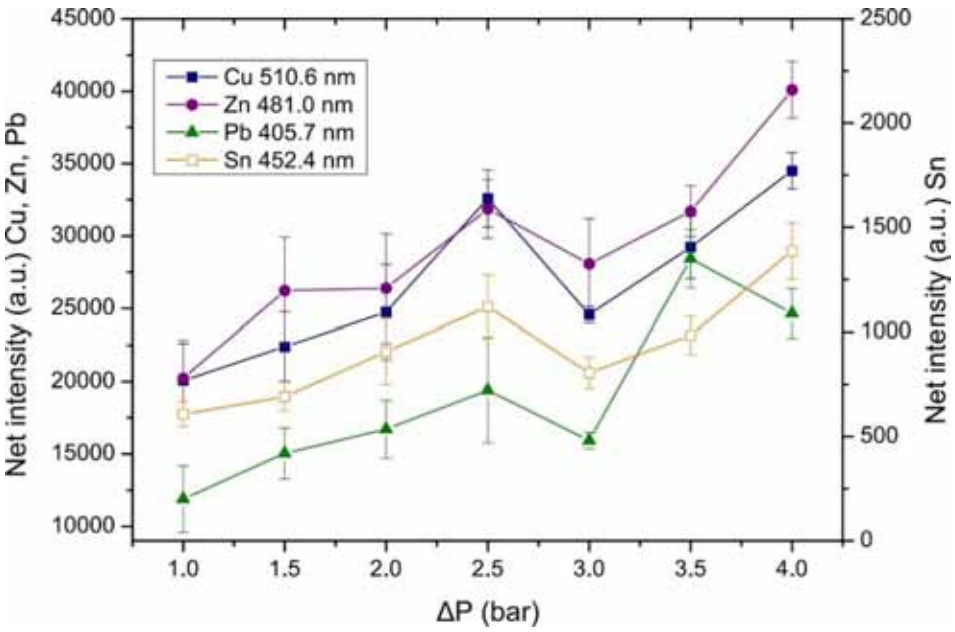

Figure 2. Influence of the pressure difference (ΔP) between inside and outside of the probe in the LIBS signal of Cu (510.6 nm), Zn (481.0), Pb (405.7 nm) and Sn (452.4 nm) on a bronze sample.

(I) at 510.6 nm, Pb (I) at 405.7 nm, Zn (I) at 481 nm and Sn (I) at 452.4 nm are plotted as a function of ΔP. Each point in the graph represents the average of 5 replicate measurements. As shown, the tendency of Cu, Pb, Zn, and Sn is quite similar as function of ΔP, with a gradualy increase of LIBS signal. These results are in good agreement with those reported by Guirado et al. [26]. Thus, the use of multi-pulse excitation mitigates the preferential ablation that typically occurs in bronze materials when using a SP-LIBS configuration.

On the other hand, the effect of the ΔP has not been yet investigated in ceramic. Ceramic materials (e.g., amphoras) are usually discovered in underwater archaeological sites covered by different types of deposits such as calcareous and/or ferrous components. For that reason, the influence of ΔP on the LIBS signal of Ca (I) at 422.6 nm, Fe (I) at 438.3 nm and Ti (I) at 498.1 nm on a ceramic sample is presented in Figure 3. As shown, signal intensity decreased in a similar trend for the three studied elements, namely Ca, Fe and Ti. Also, in the range of ΔP 1-4 bar, the effect observed in ceramics is opposite to that perceived in metallic samples (Figure 2). In fact, at higher ΔP values, 4 bar, a shielding effect [24-27] is observed due to the larger number density of species when the plasma is confined at the sample surface. For this reason, the laser radiation reaching the sample surface is considerably reduced and consequently a decrease in LIBS signal is obtained. In contrast, at lower ΔP, the plasma is less confined and shielding effect is reduced [4]. In this sense, plasma shielding was confirmed by the estimation of the *electron number density* (N_e). This parameter has been determined from *Stark broadening* of the Fe (I) line at 426.04 nm, following the procedure described by Tognoni et al. (*Chapter 3*, Ref. [28]). In summery

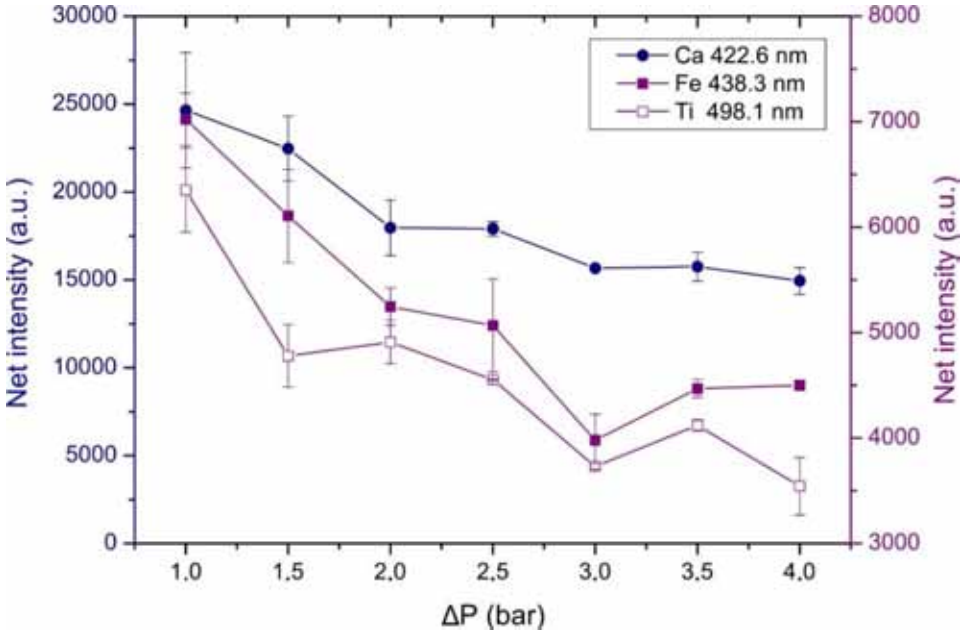

Figure 3. Influence of the pressure difference (ΔP) between inside and outside of the probe in the LIBS signal of Ca (422.6 nm), Fe (438.3 nm) and Ti (498.1 nm) on a ceramic sample.

N_e was derived from the following equation:

$$\Delta\lambda_{1/2} = 2W \times \left(\frac{\mathrm{Ne}}{10^{16}}\right) nm \quad [\mathrm{Eq.\,1}]$$

The Stark broadening, expressed as the FWHM (full width at half maximum) in nanometers, can be obtained in a semi-empirical way by means of:

$$\Delta\lambda_{\mathrm{line}} = \Delta\lambda_{\mathrm{Stark}} + \Delta\lambda_{\mathrm{instrumental}} \quad [\mathrm{Eq.\,2}]$$

for which, $\Delta\lambda_{instrumental}$ is a fixed value equal to 0.14 nm inherent to the Avantes spectrometer used in this case and $\Delta\lambda_{line}$ can be measured directly in the spectra. Other sources of broadening (e. g. Doppler broadening) can be considered negligible [29]. The value of the electron impact half-width (W) depends on the temperature and it can be found tabulated in the literature [30]. The plasma temperature (T_e) was deduced from Boltzmann plot, assuming that plasma is in local thermal equilibrium (LTE) [31] and is calculated from five Fe atomic lines, namely Fe (I) 371.99 nm, Fe (I) 373.48 nm, Fe (I) 373.71 nm, Fe (I) 375.82 nm, Fe (I) 376.37 nm) [29]. According to the Boltzmann plot, T_e was calculated as 11000 K. Using the W value, tabulated for the calculated plasma temperature, N_e can be derived from Eq. (1). N_e values were $1.09 \cdot 10^{19}$ cm^{-3} at ΔP=4 bar and 0.5 10^{19} cm^{-3} at ΔP=1 bar. These values are in agreement with those expected under these environmental conditions. As expected, a higher density of species in the laser plasma is observed when the plasma confinement is more accentuated (ΔP=4 bar). This fact supports our hypothesis that plasma shielding increases for higher ΔP values. In the case of ceramics, a porous and breakable material, the plasma shielding effect is highly accentuated and consequently LIBS signal is considerably reduced. In addition, the use of a purge gas at higher pressure could play a counter-productive role helping to remove a larger amount of particulate material of the sample thus increasing the shielding effect.

Ceramics samples are difficult to analyze in an archaeological site context due to the mentioned characteristics. Thus, the following section is focused in this kind of materials in order to improve the analytical sensitivity.

3.1.2. Influence of purge gas type on LIBS signal

The influence of the chemical composition of the purge gas has been evaluated with the purpose to improve the analytical sensitivity on ceramic samples. This experiment was carried out using various ambient gases such as air, CO_2, He and Ar. In all cases ΔP was kept constant at 3 bar. The emission lines of Ca (I) at 422.6 nm and Fe (I) at 438.3 nm were selected for LIBS analysis. Results are plotted in Figure 4A. Each point in the graph is the average of 5 replicates measurements. As shown, the maximum signal intensity was achieved using Ar as purge gas. The obtained values were ~45.000 counts and ~14.500 counts for Ca and Fe, respectively. For the rest of gases, the intensity decreases following the sequence

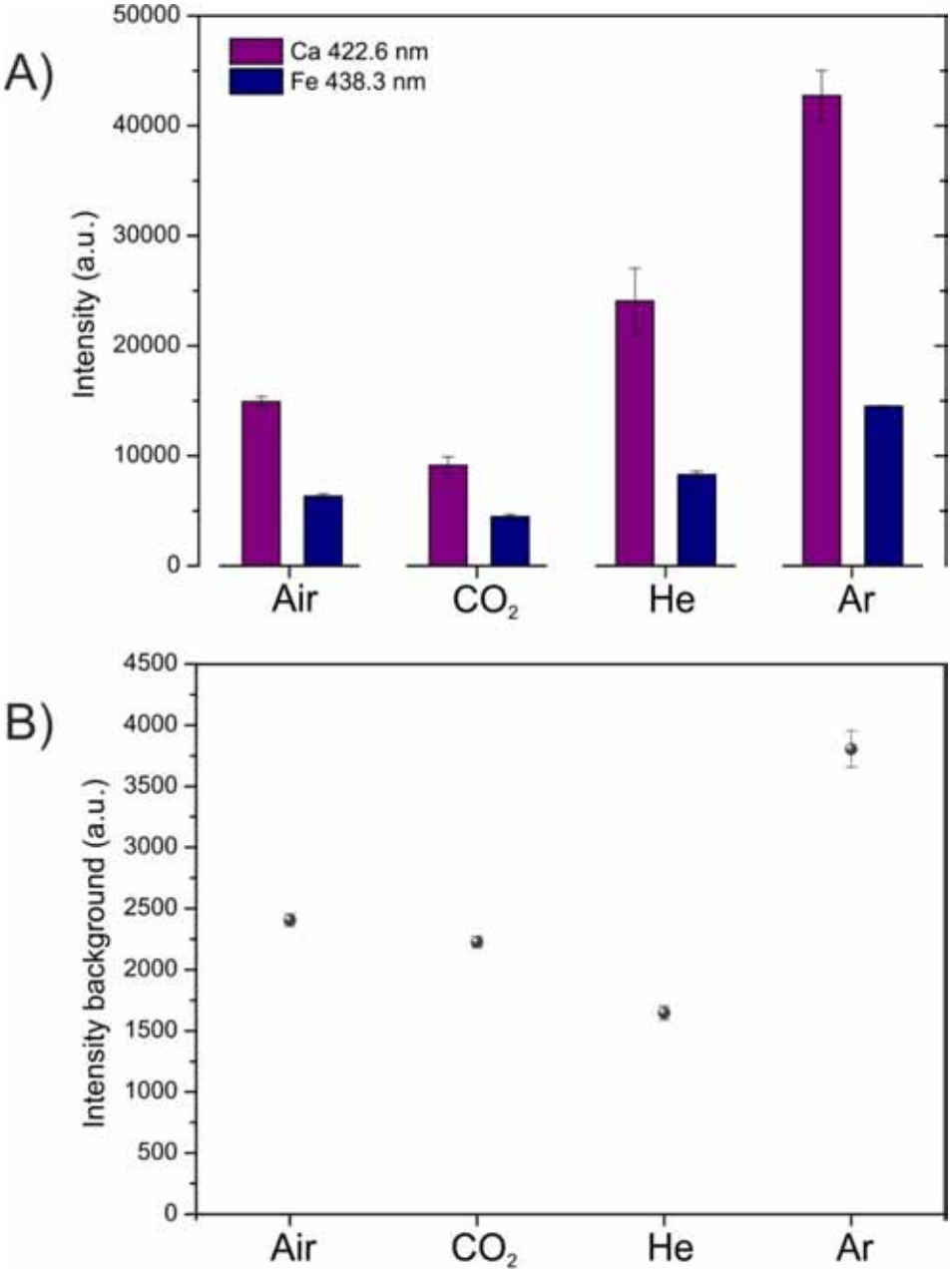

Figure 4. Influence of chemical composition of surrounding atmosphere in A) LIBS intensity signals of Ca (422.6 nm) and Fe (438.3 nm) and B) intensity background.

of He > Air > CO_2. On the other hand, Figure 4B shows the background intensity acquired for the different surrounding ambient gases under study. As seen, background intensity was lower under a He atmosphere compared to Ar, air and CO_2.

Signal and background intensity were both used for determining the analytical quality of a spectrum. In this sense, the signal-to-noise ratio (SNR) was selected as criterion for evaluating and comparing spectra from atmospheric experiments [32]. Thus, in our experiment, for Ca and Fe lines, the signal was calculated at its maximum peak intensity I_{max} after the subtraction of the background I_{bg}, while the

noise was calculated by the standard deviation σ_{bg} of the background emission in the vicinity of the selected emission line. The signal to noise ratio is thus given by:

$$SNR = \frac{I_{max} - I_{bg}}{\sigma_{bg}}$$

Figure 5 shows the calculated SNR values for Ca and Fe lines as a function of purge gas. The trend is similar to that observed in Figure 4A. Thus, the highest SNR for both Ca and Fe was obtained for Ar. Hence, SNR: Ar > He > Air > CO_2. This fact can be attributed to plasma parameters, namely electron temperature (T_e) and electron density (N_e), whose values are influenced by the properties of the surrounding gas. Generally, laser-induced plasmas with higher T_e produce a greater emission [10, 33]. T_e and N_e were calculated for Ar, He, air and CO_2. In the case of T_e, it was deduced from the Boltzmann plot using the same emission lines as section 3.1.1, while *Ne* was determined from the Stark broadening of the Fe (I) line at 426.04 nm (following the procedure described by Tognoni et al. in the previous section).

The calculated T_e and N_e are depicted in Figure 6. As expected, a higher T_e was obtained using Ar atmosphere with respect to He, air and CO_2. This fact is accordance with the hypothesis in which a more energetic plasma produces a higher emission intensity. Furthermore, a huge electron density was also calculated for Ar which explains the higher background intensity due to the influence of continuum radiation. The generation of hotter and more dense plasma under Ar atmosphere, as explained by several authors [8, 9, 16], is due to a low thermal conductivity and a low ionization potential. On the other hand, He must be also underline here. As mentioned in the reports published by Vors et al. [15], Aguilera et al. [17] and Effenberger et al. [8], He produces cooler plasmas with lower N_e. Contrarily to Ar, the characteristic of He is

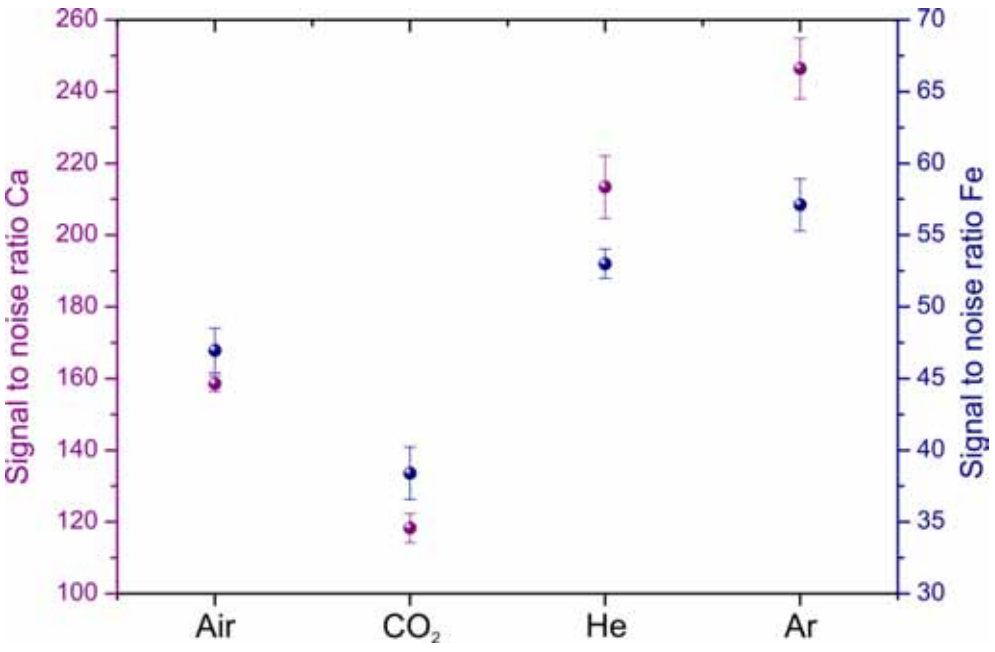

Figure 5. Influence of chemical composition of surrounding atmosphere in signal to noise ratio from of Ca (422.6 nm) and Fe (438.3 nm).

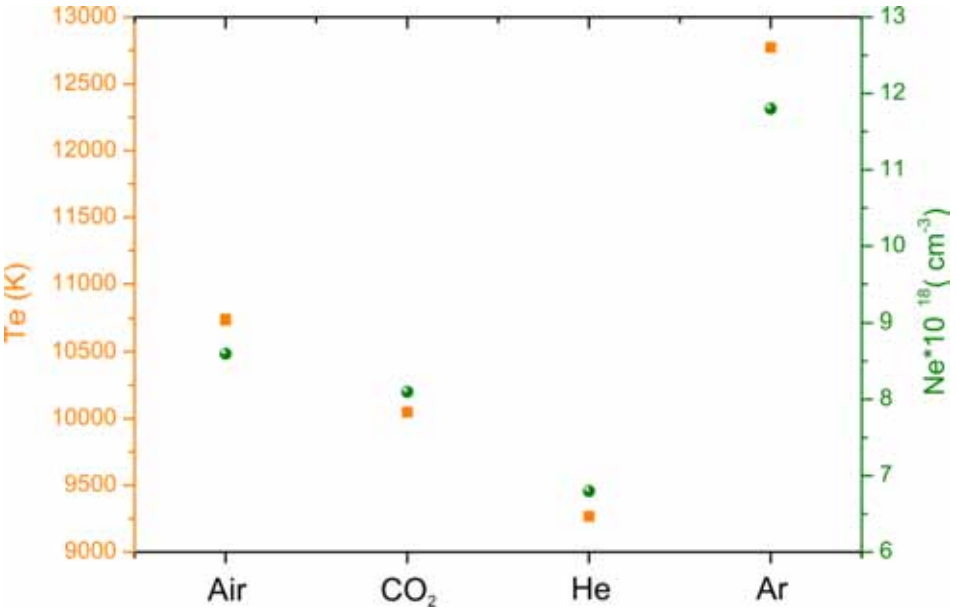

Figure 6. Electron temperature (T_e) and density (N_e) of plasma using different surrounding atmosphere such as air, CO_2, He and Ar.

due to a higher thermal conductivity and ionization potential. However, as observed in Figure. 4, He achieves a higher signal emission intensity and a lower background intensity so consequently, a higher SNR value. Hence, the use of Ar as purge gas achieves an enhancement of LIBS response with respect to CO_2, Air and He. Then, in the following experiment, we evaluate to investigate the potential of using Ar and how it affects the LIBS signal. For this purpose, a ceramic sample was analysed in both air and Ar. The emission lines selected for this study and their energy levels are summarized in Table 1. As observed in Figure. 4, the LIBS signal acquired in Ar atmosphere was larger than in air. In order to quantify the sensitivity advantage, an enhancement factor (υ) has been calculated and plotted in Figure 7 as a function of the energy transition between E_i and E_k for each selected line. This factor was measured as the intensity ratio between Ar and air at each selected line. As shown, the sensitivity advantage of using Ar is more accentuated in those transitions with higher ΔE which is of significant interest especially in minor components.

As a result, for a field measurement, the replacement of air with Ar is presented here as an alternative to increase the analytical sensitivity of the instrument AQUALAS 2.0 for the in-situ characterization of underwater ceramic materials. In this sense, with the aim of visualizing the sensitivity improvement of ceramics during a field campaign, a sequence of 200 laser shots on the same position in a ceramic sample was performed alternating between air and Ar in cycles of 25 laser shots. Results are depicted in Figure 8. As seen, the signal intensity of Ca at 422.6 nm is higher by a factor of 2x when using Ar. Also, the decay of LIBS signal as a function of the number of laser shots is due to the drilling of the sample surface.

Table 1. Energy levels data of atomic emission lines.

Element	λ (nm)	Ei (eV)	Ek (eV)	Element	λ (nm)	Ei (eV)	Ek (eV)
Si (I)	383.2.	2.71	5.94	**Ca (I)**	430.8	1.88	4.76
Fe(I)	404.5	1.48	4.54	**Fe(I)**	438.3	1.48	4.31
Fe(I)	406.3	1.56	4.61	**Fe(I)**	440.5	1.56	4.37
Fe(I)	407.2	1.61	4.65	**Fe(I)**	442.7	0.05	2.85
Fe(I)	427.2	1.48	4.39	**Ti (I)**	498.2	0.85	3.34
Ca (I)	428.3	1.88	4.78	**Ti (I)**	499.1	0.84	3.32
Ca (I)	428.9	1.88	4.77	**Ti (I)**	501.4	0	2.47

However, despite the sensitivity improvement that argon produces, the cost of this gas is a factor to take into account in a field campaign since an air flow is considerably cheaper and readily available from a portable compressor. Thus, in order to reach a compromise between costs and a good analytical response, a comparative study among several mixtures of gases was performed. In this experiment, the emission lines of Ca at 422.6 nm and Fe (I) at 438.3 nm were selected. LIBS intensity as a function of the percentage of Ar in the mixture (0, 25, 50, 75 and 100%) has been plotted in Figure 9. In all measurement, ΔP was kept constant at 3 bar. Each point in the graph represents the average of 5 measurements at each different position. As shown, LIBS intensity increases when the Ar percentage is higher. However, from a

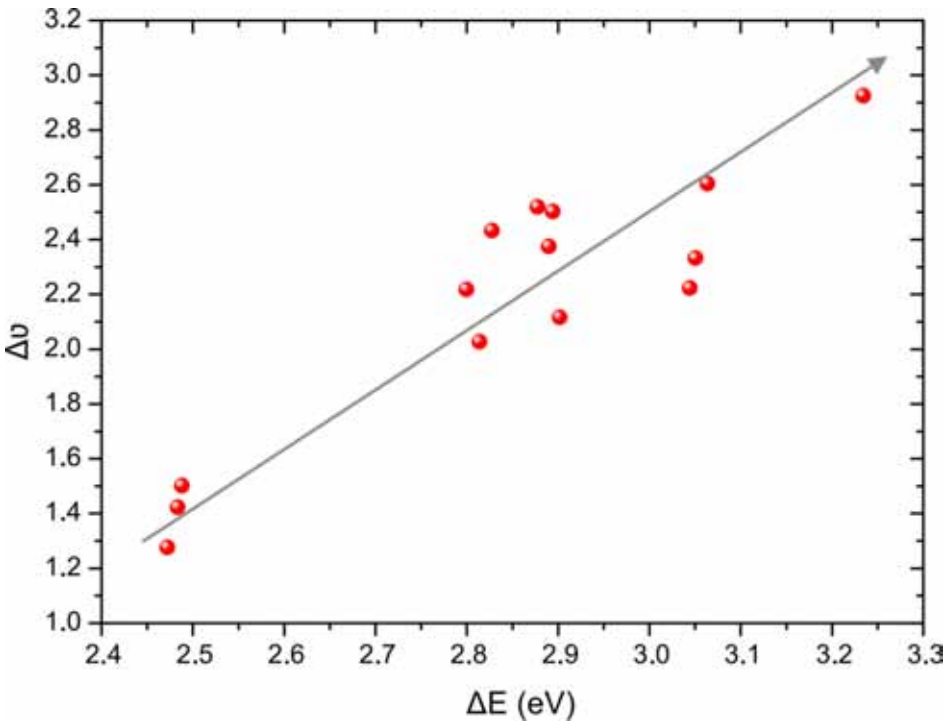

Figure 7. Intensity enhancement factor of Ar respect to air (Δυ) in function of energy difference from distinct transition levels.

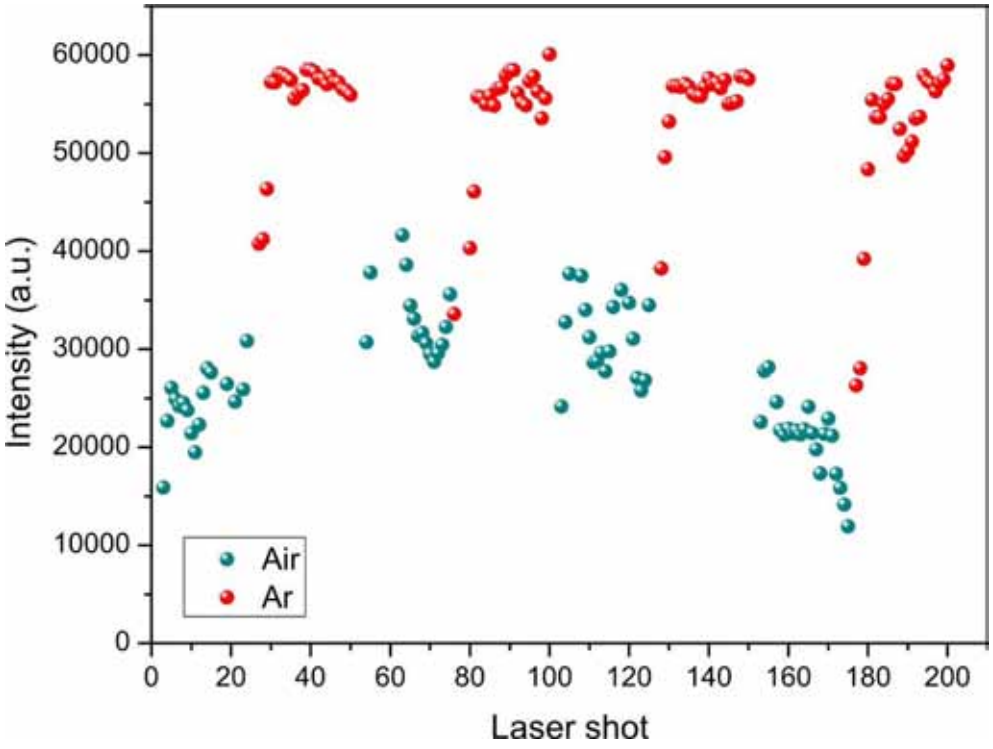

Figure 8. Emission intensity of Ca at 422.6 nm in a sequence of 200 laser shots in a ceramic sample changing at each 25 shot the purge gas between air and argon.

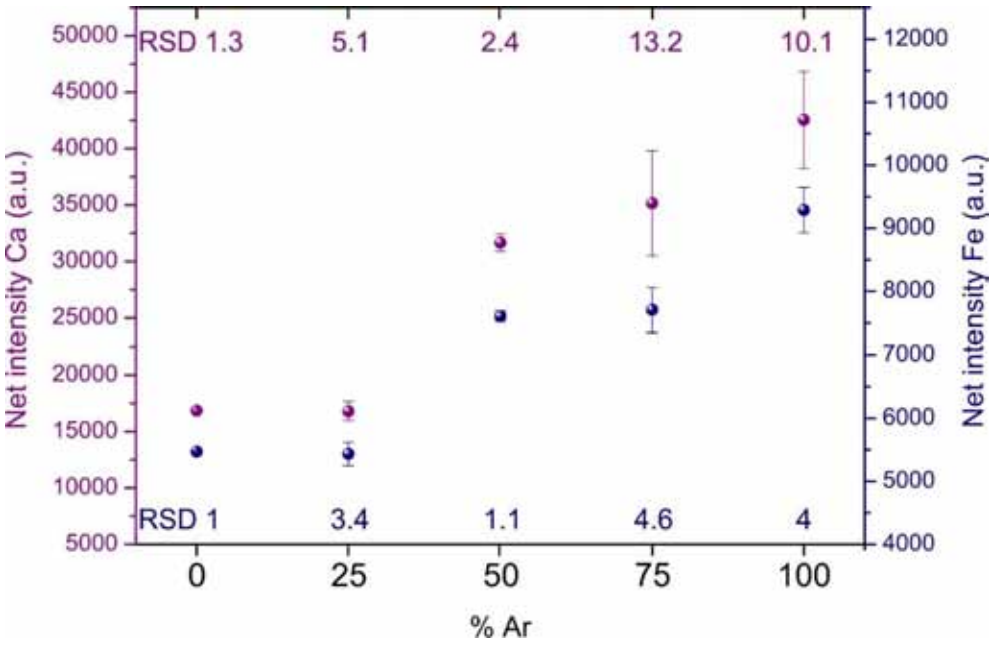

Figure 9. Net intensity signal of Ca (422.6 nm) and Fe (438.3 nm) on a ceramic sample in function of percentage of argon gas.

50% mixture of gases the trend obtained for both Ca and Fe elements is more moderate. In addition to this both, lower deviation and RSD are obtained when a less percentage of Ar is used. In view of these results, it was decided that the best alternative for a field campaign could be a mixture of 50% of gases because it keeps a favourable compromise between cost and analytical response.

3.2. Analysis of archaeological samples

From an archaeological point of view, the development and the improvements in the remote LIBS instrument for the recognition of submersed materials is of great interest in the case that is not immediately recognizable (low visibility conditions or with a higher corrosion degree). In this way, the identification of findings with archaeological value allows the diver to make decisions about the best way to collect or not the sample and its posterior preservation. In this meaning, obtaining good quality LIBS spectra is an essential requisite. However, the analysis in the archaeological site is not trivial and sometimes is quite challenging to achieve a good analytical response due to the rugosity and the grade of deposition of sedimentary layers (concretion) on the sample.

As explained before, in order to increase the intensity of acquired LIBS signal, the use of purge gas plays a key importance role; not only removing the water from the sample surface and creating a gas–sample interface but also regarding to plasma properties. In this sense, a sensitivity improvement was achieved using Ar. In this section, with the purpose to evaluate the capability of our prototype for the

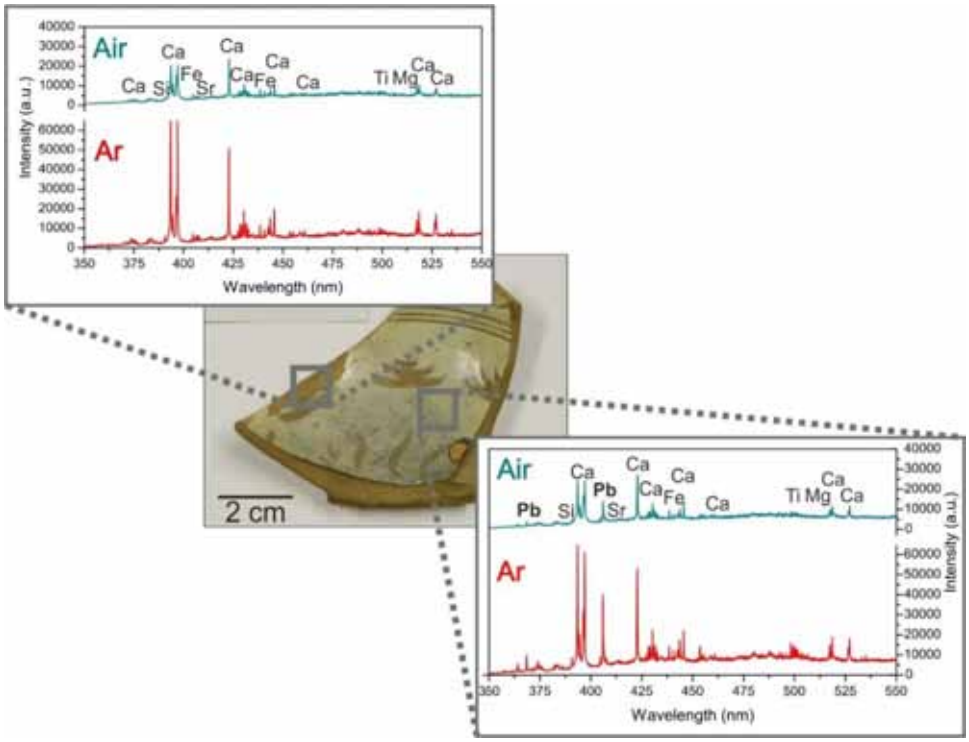

Figure 10. Underwater LIBS spectra obtained in lab of an archaeological pottery using air (in green) and argon (in red). Dark square limited the portion of ceramic without drawing and grey square with drawing.

analysis of real archaeological materials, a set of typical samples which could be found in a shipwreck were inspected using air and Ar gases. The set of samples were provided by the *Centro de Arqueología Subacuática of Cádiz* (CAS). LIBS spectra were acquired in the 350–550 nm range by averaging 25 shots laser on five adjacent positions for each sample in order to obtain a typical spectrum of different materials. The analysis was performed inside a water tank with the purpose of simulating real conditions. The gas flow used was 2 bar (ΔP 1bar). Figure 10 shows an archaeological pottery of Italian origin in which two selected areas were analyzed. As observed, from emission espectra the area delimited by the dark square was composed mainly of quartz (SiO_2), clay (alumina-silicate of Ca and Mg), TiO_2 and iron oxides. However, the spectrum from the zone delimited by grey square shows also lead. This peculiarity could be due to the presence of drawing on this region of the pottery, associating lead with the pigment. Other materials of interest, which can be found at an archaeological site, are related to the arming or defense of the wreck. Figure 11 illustrates the emission lines corresponding to the analysis of a cannon bullet made of iron. On the other hand, a compass utilized for sailing was examined. Figure 12 presents an intense emission from

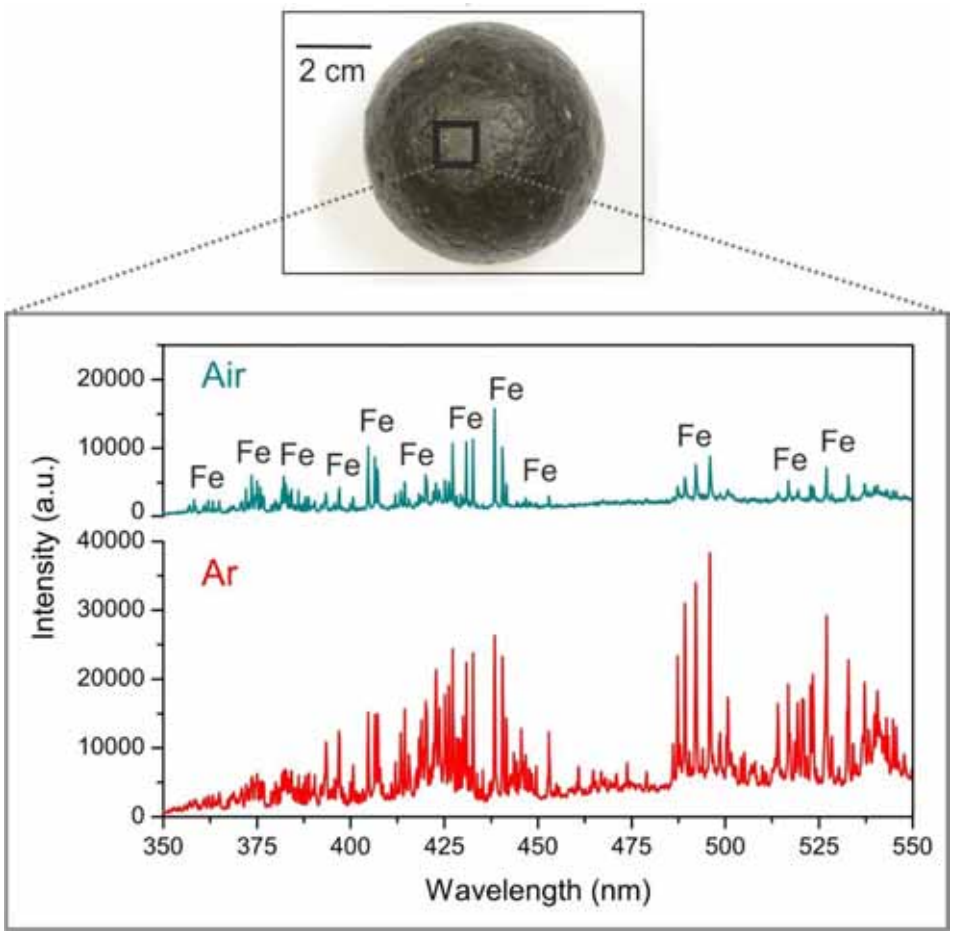

Figure 11. Underwater LIBS spectra obtained in laboratory of a canon bullet using air (green spectrum) and argon (red spectrum).

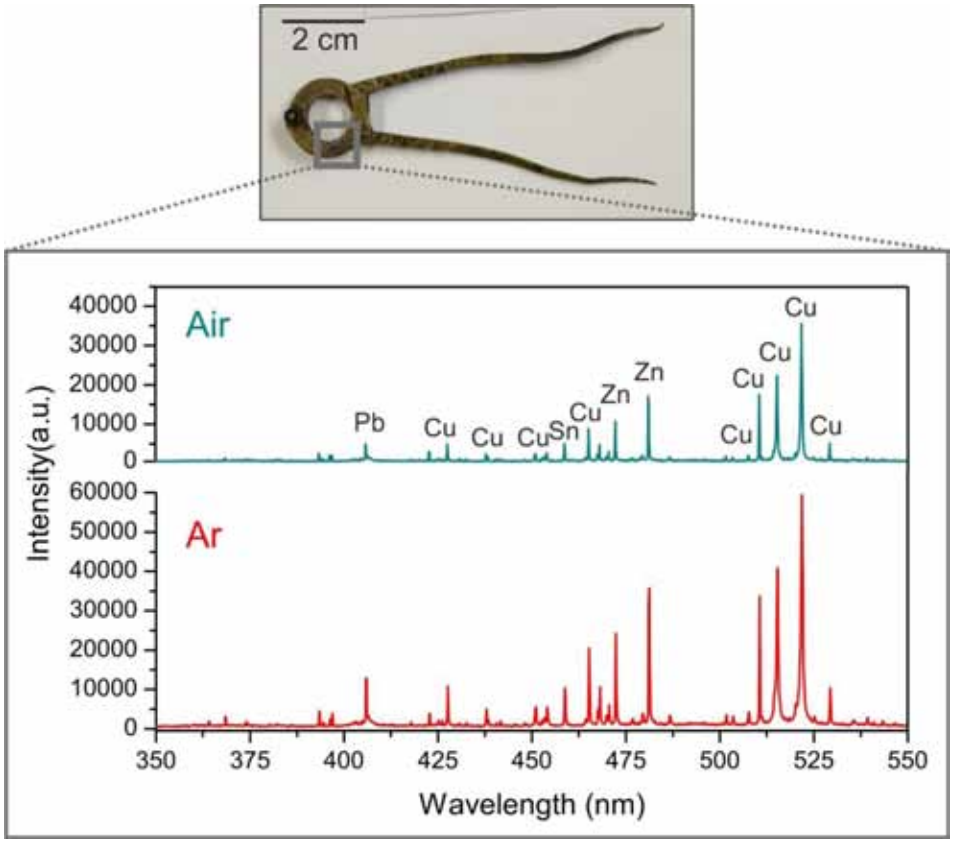

Figure 12. Underwater LIBS spectra obtained in laboratory of a compass utilized in sailing using air (green spectrum) and argon (red spectrum).

Cu, Zn, Pb and Sn elements. By it comparing the analytical response using argon or air observed in the last three figures a clear increase of LIBS signal was achieved with argon gas purge. The improvement of the measure observed is not dependent of the nature material such as ceramics, metals and alloys.

After purge gas optimization presented throughout this chapter, AQUALAS 2.0 was moved to *Centro de Arqueología Subacuática of Cádiz* (CAS) in order to carry out an in-situ analysis of a set of archaeological samples belonging to 6 wrecks located in Andalucía coast. The archaeological pieces under study were placed inside of desalination pools in stabilization phase (treatment that is carried out for its later conservation). The analysis protocol was that described in this chapter using 2 bar of argon. In *Appendix 2* the results of the analyzed pieces can be found.

4. Conclusions

The purge gas can be used not only to prevent the water entry into analysis probe but also to remove the water from the sample surface creating a gas–sample interface optimal for LIBS analysis. In addition to this, in this chapter the purge gas has been evaluated as a tool to improve the analytical

sensitivity of AQUALAS 2.0 equipment in order to increase its performance for analysis in a submerged archaeological site. The studies were focused on ceramic samples since the physical characteristics of this type of material made difficult the LIBS analysis and therefore obtaining its chemical composition. Both nature of purge gas on the sample surface and total gas pressure applied during LIBS analysis have been evaluated. It has been observed that a low pressure of purge gas output through the analysis probe can produce less plasma confinement and, as consequence, the shielding effect is attenuated and the emission intensity from ceramic material is increased. On the other hand, chemical composition of the atmosphere surrounding the sample revealed to have an influence on plasma parameters such as electron temperature and plasma density. Since the emission and background intensity signal as well as SNR were altered. After comparison of the results obtained using Ar, He and CO_2 respect to air (the most common gas employed for analysis with AQUALAS), the best alternative in order to improve the analytical sensitivity of the LIBS prototype was decided to be Ar gas. Moreover, a study mixing different proportions of Ar and air gas was carried out in order to reduce the analysis cost but keeping a good spectral quality. This was achieved with a mixture of 50% of both gases. Last, Ar benefits have been also checked successfully in a set of found archaeological sample such as metals, alloys and ceramics.

5. References

1. F. J. Fortes, J. J. Laserna, The development of fieldable laser-induced breakdown spectrometer: No limits on the horizon, Spectrochimi. Acta Part B 65 (2010), 975–990.
2. F. J. Fortes, J. Moros, P. Lucena, L. M. Cabalín, J. J. Laserna, Laser-induced breakdown spectroscopy, Anal. Chem. 85 (2013), 640–669.
3. J. L Gottfried, F. C. De Lucia, C. A. Munson, A. W. Miziolek, Laser-induced breakdown spectroscopy for detection of explosives residues: a review of recent advances, challenges, and future prospects, Anal. Bioanal. Chem. 395 (2009), 283−300.
4. S. Guirado, F. J. Fortes, V. Lazic, J. J. Laserna, Chemical Analysis of Archeological Materials in Submarine Environments Using Laser-induced Breakdown Spectroscopy, On-site Trials in the Mediterranean Sea. Spectrochim. Acta B Atom. Spectros. 74–75 (2012), 137–143.
5. S. Guirado, F. J. Fortes, J. J. Laserna, Elemental analysis of materials in an underwater archeological shipwreck using a novel remote laser-induced breakdown spectroscopy system, Talanta 137 (2015), 182–188.
6. R. C. Wiens, S. Maurice, B. Barraclough, M. Saccoccio, W. C. Barkley, J. F. Bell III, S. Bender, J. Bernardin, D. Blaney, J. Blank, M. Bouyé, N. Bridges, N. Bultman, P. Caïs, R. C. Clanton, B. Clark, S. Clegg, A. Cousin, D. Cremers, A. Cros, L. DeFlores, D. Delapp, R. Dingler, C. D'Uston, M. D. Dyar, T. Elliott, D. Enemark, C. Fabre, M. Flores, O. Forni, O. Gasnault, T. Hale, C. Hays, K. Herkenhoff, Ed Kan, L. Kirkland, D. Kouach, D. Landis, Y. Langevin, N. Lanza, F. LaRocca, J.

Lasue, J. Latino, D. Limonadi, C. Lindensmith, C. Little, N. Mangold, G. Manhes, P. Mauchien, C. McKay, Ed Miller, J. Mooney, R. V. Morris, L. Morrison, T. Nelson, H. Newsom, A. Ollila, M. Ott, L. Pares, R. Perez, F. Poitrasson, C. Provost, J. W. Reiter, T. Roberts, F. Romero, V. Sautter, S. Salazar, J. J. Simmonds, R. Stiglich, S. Storms, N. Striebig, J.-J. Thocaven, T. Trujillo, M. Ulibarri, D. Vaniman, N. Warner, R. Waterbury, R. Whitaker, J. Witt, B. Wong-Swanson, The ChemCam instrument suite on the Mars Science Laboratory (MSL) rover: Body unit and combined system tests, Space Sci. Rev. 170 (2012), 167–227.

7. http://www.nasa.gov/mission_pages/msl/multimedia/pia16089.html.
8. A. J. Effenberger Jr., J. R. Scott, Effect of atmospheric conditions on LIBS spectra, Sensors 10 (2010), 4907–4925.
9. Y. Iida, Effects of atmosphere on laser vaporization and excitation processes of solid samples. Spectrochim. Acta B 45 (1990), 1353-1367.
10. S. Mussazzi, U. Perini, Laser-induced Breakdown Spectroscopy, theory and applications; Springer-Verlag, Berlin (2014), 91-116.
11. M.P. Chuchman, A.K. Shuaibov, L.V. Mesarosh, Effect of air pressure on the spatial and emission characteristics of an aluminum laser torch under subthreshold conditions of ablation, Tech. Phys. 56 (2011), 117-120.
12. D. N. Patel, P. K. Pandey, R. K. Thareja, Stoichiometric investigations of laser-ablated brass plasma, Appl. Opt. 51 (2012), B192−B200.
13. S. Yalçin, Y. Y. Tsui, R. Fedosejevs, Pressure dependence of emission intensity in femtosecond laser-induced breakdown spectroscopy, J. Anal. At. Spectrom. 19 (2004), 1295–1301.
14. A. Löbe, J. Vrenegor, R. Fleige, V. Sturm, R. Noll, Laser-induced ablation of a steel sample in different ambient gases by use of collinear multiple laser pulse, Anal. Bioanal. Chem. 385 (2006), 326-332.
15. E. Vors, C. Gallou, L. Salmon, Laser-induced breakdown spectroscopy of carbon in helium and nitrogen at high pressure, Spectrochim. Acta Part B 63 (2008), 1198–1204.
16. Y. I. Lee, K. Song, H. K. Cha, J. M. Lee, M. C. Park, G. H. Lee, J. Sneddon, Influence of atmosphere and irradiation wavelength on copper plasma emission induced by excimer and Q-switched Nd:YAG laser ablation, Appl. Spectrosc. 51 (1997), 959–964.
17. J. A. Aguilera, C. Aragon, A comparison of the temperatures and electron densities of laser-produced plasmas obtained in air, argon, and helium at atmospheric pressure. Appl. Phys. A 69 (1999), S475-S478.
18. J. Scaffidi, S. M. Angel, D. A. Cremers, Emission Enhancement Mechanisms in Dual-Pulse LIBS, Anal. Chem. 78 (2006), 24-32.

19. V. I. Babushok, F. C. De Lucia, J. L. Gottfried, C. A. Munson, A. W. Miziolek, Double Pulse Laser Ablation and Plasma: Laser Induced Breakdown Spectroscopy Signal Enhancement, Spectrochim. Acta B 61 (2006), 999-1014.
20. A. De Giacomo, M. Dell'Aglio, O. De Pascale, M. Capitelli, From single pulse to double pulse ns-Laser Induced Breakdown Spectroscopy under water: Elemental analysis of aqueous solutions and submerged solid samples, Spectrochim. Acta Part B 62 (2007), 721–738.
21. E. H. Piepmeier, H. V. Malmstadt, Q-Switched Laser Energy Absorption in the Plume of an Aluminum Alloy, Anal. Chem. 41 (1969), 700-707.
22. R. Sattmann, V. Sturm, R. Noll, Laser-induced breakdown spectroscopy steel samples using multiple Q-Switch Nd:YAG laser pulses, J. Phys. D 28 (1995), 2181–2187.
23. G. Galbács, V. Budavári, Z. Geretovszky, Multi-pulse laser–induced plasma spectroscopy using a single laser source and a compact spectrometer, J. Anal. At. Spectrom. 20 (2005), 974–980.
24. G. Galbács, N. Jedlinszki, K. Herrera, N. Omenetto, B. W. Smith, J. D. Winefordner, A Study of Ablation, Spatial, and Temporal Characteristics of Laser-Induced Plasmas Generated by Multiple Collinear Pulses, Appl. Spectrosc. 64 (2010), 161–172.
25. S. Guirado, F. J. Fortes, L. M. Cabalin, J. J. Laserna, Effect of Pulse Duration in Multi-Pulse Excitation of Silicon in Laser-Induced Breakdown Spectroscopy (LIBS), Appl. Spectrosc. 68 (2014), 1060–1066.
26. S. Guirado, F. J. Fortes, J. J. Laserna, Multi-pulse Excitation for Underwater Analysis of Copper-based Alloys using a Novel Remote Laser-induced Breakdown System, Appl. Spectrosc., 70 (2016), 618–626.
27. J. A. Aguilera, C. Aragón, F. Peñalba, Plasma shielding effect in laser ablation of metallic samples and its influence on LIBS analysis, Appl. Surf. Sci. 127–129 (1998), 309–314.
28. A. W. Miziolek, V. Palleschi, I. Schechter, Laser-Induced Breakdown Spectroscopy (LIBS) Fundamentals and Applications, Cambridge University Press, 2006, Cambridge.
29. L. M. Cabalín, J. J. Laserna. Atomic emission spectroscopy of laser-induced plasmas generated with an annular-shaped laser beam. J. Anal. At. Spectrom. 19 (2004), 445-450.
30. N. Konjevic, A. Lesage, J. R. Fuhr, W. L. Wiese, Experimental Stark Widths and Shifts for Spectral Lines of Neutral and Ionized Atoms (A Critical Review of Selected Data for the Period 1989 Through 2000), J. Phys. Chem. Ref. Data, 31 (2002), 819-927.
31. H. Griem, Plasma Spectroscopy, McGraw-Hill, 1964, New York.
32. N. Farid, S. S. Harilal, H. Ding, A. Hassanein, Emission features and expansion dynamics of nanosecond laser ablation plumes at different ambient pressures, J. Appl. Phys., 115 (2014), 033107-9.
33. W. Sdorra, K. Niemax, Basic investigations for laser microanalysis. III. Application of different buffer gases for laser-produced sample plumes, Microchim. Acta 107 (1992), 319–327.

Chapter 6. Subsea spectral identification of shipwreck objects using laser-induced breakdown spectroscopy and linear discriminant analysis

1. Introduction

Underwater cultural heritage is a rich source of information and a window to the past. In fact, the presence of specific elements (either greater or lesser percentage) in an archaeological material, namely *chemical fingerprints*, is of great interest for a better understanding of its age, provenance and manufacturing technology. Discovery of amphoras, cannons and metallic artefacts in their archaeological context could provide further information concerning the age and nationality of a shipwreck [1]. However, the severe conditions of the marine environment change the appearance of the underwater sites and distorts the idyllic image of the shipwreck until blending with the surroundings. Hence, artefacts and structures may be uncovered beneath sediments, chemically altered or even destroyed.

Recent advances in electronic engineering, underwater robotics and novel systems for processing and image recognition make localization of underwater archaeological sites much easier than in past. However, underwater archaeology still requires the development of screening techniques for the in-situ recognition of findings. A restricted number of laser-based techniques (e. g. Raman, LIBS and LIF) have proven to be useful for this purpose [2-4]. Specifically, LIBS as the technique really appreciated as is the unique that could provide atomic information from the spectral signature of underwater objects [5, 6]. Additionally, LIBS combines valuable attributes specially demanded in cultural heritage preservation and investigation [7, 8]. It's worth mentioning that underwater LIBS analysis is not a trivial task and several research groups have proposed different alternatives for improving LIBS sensitivity inside liquids [9-11]. In this sense, the dual pulse excitations being the most common approach proposed in the literature [12-14]. However, problems related to the use of two laser sources, the precise alignment needed and synchronization in data acquisition are obstacles for its implementation in field analysis [15, 16]. The instrumental development was further investigated until 2012 when Guirado et al. [17] published the first in-situ undersea LIBS analysis of solid materials, at a depth of 30 meters, using a fiber-based LIBS system. Later, a new generation of LIBS instruments based on transmission of a collinear sequence of multi-pulses through the optical fiber cable was proposed by the same authors to improve the performance of the technology [18, 19]. An archaeological shipwreck situated 17 meters deep was inspected using this approach [20].

In subaquatic archaeology, quantitative information turns crucial for planning restoration/conservation activities and taking decisions about whether the object should be moved from the underwater site or not. Nevertheless, LIBS strongly depends on matrix effects, pulse to pulse fluctuations, plasma-solid interactions, among other factors. In this sense, a broad number of fundamental studies have been reported to overcome the so-called fractionation effect [21-24]. Certain procedures such as internal standardization, background normalization, calibration-free analysis and the use of a double-pulse configuration has been explored so far for quantitative analysis of submersed materials. Most recently, Guirado et al. [25] evaluated the use of multi-pulse (MP) excitation as an effective solution to mitigate the

fractionation effects observed in LIBS analysis of copper-based alloys. MP-LIBS also prevents the effect of ambient pressure on LIBS signal, thus demonstrating the feasibility of LIBS for quantitative analysis of bronze materials in a real underwater site.

In such a scenario, development of spectral libraries and data processing algorithms also improve the capability of LIBS for field measurements. Hence, from an archaeological point of view, both qualitative and quantitative information extracts compositional evidence that together with the use of chemometric methods may identify specific materials which could be related to ancient manufacturing or production processes [26]. A number of statistical methods including linear and rank correlation, principal component analysis (PCA), partial least-squares discriminant analysis (PLS-DA) and soft independent modeling of class analogy (SIMCA), among others have proved to group and classify ancient artefacts in archaeometric analysis [27]. In this work, a classification method is evaluated for the identification of chemical fingerprints in shipwrecks. A variety of archaeological objects has been previously characterized in laboratory using essentially the same operational conditions than those found undersea in order to ensure the effectiveness of the method during the recognition process in the site. Moreover, a set of sheathings from different shipwrecks were analyzed with the objective to perform a chronocultural sorting of these structural pieces. Based on this procedure, findings from the shipwreck of *San Pedro de Alcántara* (Málaga, Spain) were directly classified into metallic alloys, ceramics, rocks or marbles.

2. Materials and methods

The instrument used in this chapter is the remote LIBS system AQUALAS 2.0. A more detailed description of AQUALAS 2.0 has been presented in *Chapter 3*.

3. Results and discussion

3.1. Classification method for archaeological artefacts

Given the great compositional diversity, textural differences and surface alteration of the submersed cultural heritage, the use of advanced statistical algorithms is essential for the recognition and sorting of underwater findings. For this purpose, linear discriminant analysis (LDA) was used to generate a classification model from which unknown samples will be predicted in site on the basis of their LIBS response. As a supervised algorithm, a LDA model based on the spectra acquired from a set of known archaeological samples was constructed. LDA evaluates the relative weights of the original variables for group discrimination and score the separation between multiple classes [28-30]. Afterwards, the model predicts the probability that an unknown sample belongs to each class.

A set of thirty-eight objects collected from several archaeological shipwrecks was first studied. To simulate the experimental conditions of a subsea environment, samples were immersed and analyzed in a water tank in our laboratory. Because of the large variety of samples used in this study, objects were divided into different groups for chemometric analysis, i.e. bronze-alloys (10 samples), metallic pieces (18 samples), ceramics (5 samples) and marbles (5 samples). LIBS spectra were acquired in the 350-550 nm spectral range and their intensities normalized to unity for comparative purposes. Data were acquired by averaging the response of 50 laser shots on three adjacent positions for each sample. However, the whole LIBS spectra were not considered as input data so the initial information based on 2048 data points was significantly reduced to 10 spectral variables. The selected variables were Cu (I) 510.55 nm, Zn (I) 481.05 nm, Sn (I) 452.47 nm, Pb (I) 405.78 nm, Fe (I) 438.35 nm, Ca (I) 422.67 nm, Mg (I) 517.26 nm, Si (I) 390.55 nm, Sr (I) 407.61 nm and Ti (I) 498.17 nm. In addition, the presence of Ca, Mg, Si and Ti in metallic samples is associated to the deposition of sedimentary material on the sample surface. The experimental condition are summarized in Table 1. The first discriminant function has the expression:

$$F1 = 2.7 \cdot I_{Cu} + 2.4 \cdot I_{Zn} + 22.8 \cdot I_{Sn} + 0.8 \cdot I_{Pb} + 2.7 \cdot I_{Fe} - 7.2 \cdot I_{Ca} - 1.2 \cdot I_{Mg} - 3.8 \cdot I_{Sr} - 6.0 \cdot I_{Si+Ti} + 0.59$$

where I_n is the intensity of each element line. This function has an excellent canonical correlation, 0.98, that is its relative ability to discriminate amongst the groups. The second function is:

$$F2 = 1.8 \cdot I_{Cu} + 3.8 \cdot I_{Zn} + 24.8 \cdot I_{Sn} - 0.2 \cdot I_{Pb} - 0.8 \cdot I_{Fe} + 2.5 \cdot I_{Ca} - 1.8 \cdot I_{Mg} - 1.5 \cdot I_{Sr} + 9.4 \cdot I_{Si+Ti} - 2.0$$

Table 1. Experimental condition.

	Description
Protection gas	*Argon*
Pressure difference	*4*
Pulse width	*30 ns*
Laser frequency	*2 Hz*
Irradiance	*1.2 GW/ cm²*
Average	*50 pulses*
Delay time acquisition	*1 μs*

which also exhibits a good canonical correlation (0.91). Nevertheless, the statistics treatment scores *Wilk's lambda* values of 0.0013 for F_1 and 0.03 for F_2, which suggest that the variables selected for the linear discriminant analysis are appropriate for sample discrimination. Both functions also have a very high significance level of *Chi-square* statistics, 201 and 106 for F_1 and F_2, respectively.

The coefficients associated to different elements calculated by the software for discriminant functions give information about the relative contribution of each spectral line to the separation of groups. Thus, large coefficient values, such as those associated to *Sn* or *Si+Ti* spectral lines, contribute to a larger extent to group discrimination. For instance, tin is present in alloys whereas it is virtually absent in metals, ceramics and marbles. The software then assigns a large coefficient to this element to enable the separation of alloys from the other groups. Similarly, *Si* and *Ti* help in the separation of ceramics. Since the lines of these elements in the selected spectral window are weak, the intensities were summed to allow a better separation.

Positive and negative coefficients also contribute to separation among groups. The LDA software assigns positive coefficients to the alloying elements in bronzes and metallic pieces; in contrast, negative coefficients characterize strongly dissimilar materials such as ceramics and marbles.

The classification functions generated by the proposed model were validated with the *training* set of samples. Table 2 summarizes the classification of each sample based on the proposed model. It's worth mentioning that all samples were identified without exceptions. A scatter plot of the first two discriminant functions is presented in Figure 1. As shown, samples are separated in four classes or groups attending to

Table 2. Prediction groups membership for training set samples. ID sample is constitutes by a letter and two numbers as follows: the letter represents the type of sample (A: copper based alloy M: metal, C: ceramic, B: marble), the first number corresponds to the shipwreck (I: Delta II, II Delta III) and the second to a number in the group classified.

ID	Prediction group membership (%)					ID	Prediction group membership (%)				
	Alloy	Metal	Ceramic	Marble	Total		Alloy	Metal	Ceramic	Marble	Total
AII1	100	0	0	0	100	MI12	0	100	0	0	100
AII2	100	0	0	0	100	MI13	0	100	0	0	100
AI1	100	0	0	0	100	MI14	0	100	0	0	100
AI2	100	0	0	0	100	MI15	0	100	0	0	100
AI3	100	0	0	0	100	MI16	0	100	0	0	100
AII3	100	0	0	0	100	MI17	0	100	0	0	100
AII4	99.4	0.6	0	0	100	MII9	0	100	0	0	100
AII5	100	0	0	0	100	MI18	0	100	0	0	100
AI4	99.9	0.1	0	0	100	MII10	4.2	95.8	0	0	100
AII6	94.7	5.3	0	0	100	CI19	0	0	100	0	100
MII7	3.3	96.7	0	0	100	CI20	0	0	100	0	100
MII8	0	100	0	0	100	CI21	0	0	100	0	100
MI5	0	100	0	0	100	CI22	0	0	100	0	100
MI6	0	100	0	0	100	CI23	0	0	100	0	100
MI7	0	100	0	0	100	B1	0	0	0	100	100
MI8	0	100	0	0	100	B2	0	0	0	100	100
MI9	0	100	0	0	100	B3	0	0	0	100	100
MI10	0	100	0	0	100	B4	0	0	0.2	99.8	100
MI11	0	100	0	0	100	B5	0	0	0	100	100

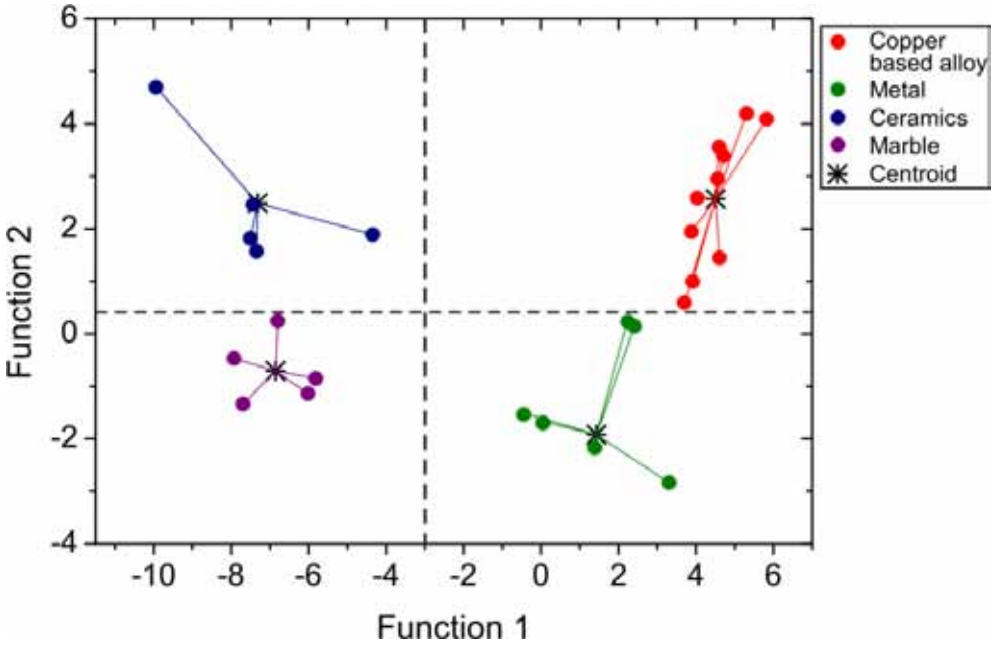

Figure 1. Scatter plot of the first two canonical discriminant functions containing the four groups defined in the method.

the type of material previously described in the "supervised" model. Bronze alloys and metallic pieces are grouped in the right-hand side of the graph, whereas ceramics and marbles are grouped in the second and third quadrant of the scatter graph, respectively. The centroid of each group is also marked in the graph. The model has been checked in our laboratory with a set of sheathings simulating the experimental conditions of a subsea environment. Furthermore, it has been tested during the underwater inspection of the wreck of *San Pedro de Alcántara*.

3.2. Chronological sorting of metallic sheathings

Since the Phoenician times, the use of sheathings in wooded-hulled vessels has been extensively tested to prevent wood degradation by the action of seawater, bivalve molluscs and algae. Sheathings were also used to improve the operability of the boat. The type of sheathing has evolved with time so the knowledge of elemental composition of this kind of samples makes it possible the assignment of the manufacturing period and provides clues to uncover the ship's origin [31].

A set of sheathing pieces belonging to different shipwrecks were analyzed in a water tank in an attempt to provide information about the geographical origin of the shipwreck that could help us to understand its historical context. In addition, this set of four samples will be used to evaluate in laboratory our chemometric model. Samples were found in the underwater archaeological sites of "*Delta I*" (XVII Century, Spanish), "*Delta II*" (XVI Century, Italian), "*Mercante de San Sebastian*" (XVIII Century, Spanish)

and "*Fougueaux*" (XVIII Century, French). A chronocultural sorting of the sheathings analyzed by LIBS is presented in Figure 2. The main emission lines are labeled in the spectra. As seen, the squares limit the timeline in two periods, depending on the sheathing composition. Thus, lead-based sheathings were early introduced in the XV Century in Portuguese and Spanish arsenals and its use was extended until the XVII Century [31]. This fact is easily observed in the sheathings belonging to *Delta I* and *Delta II*, as revealed by the LIBS spectra sketched in the figure. In the XVIII Century, lead-based sheathings were substituted first by copper and then by copper-based alloys. As shown in Figure 2 the LIBS spectra of *Mercante de San Sebastian* and *Fougueaux* in chronological order. In addition, the presence of minor components such as zinc, iron or lead, as observed in the spectrum corresponding to the *Fougueaux*, could indicate its country of origin. Hence, it exists a clear evolution of the sheathing's composition from lead to copper based alloys that could be related to a period of history or even to the country of manufacture of the shipwreck.

On the other hand, the intensity of emission lines of this set of sheathings has been used to check in laboratory our LDA model proposed in section 3.1 using samples different to the training set. In this case, the discriminant functions (*F1* and *F2*) have been able to assign successfully the samples as metallic sheatings corresponding to *Delta I*, *Delta II* and *Mercante de San Sebastian* and a bronze-alloy as part of the *Fougueaux.*

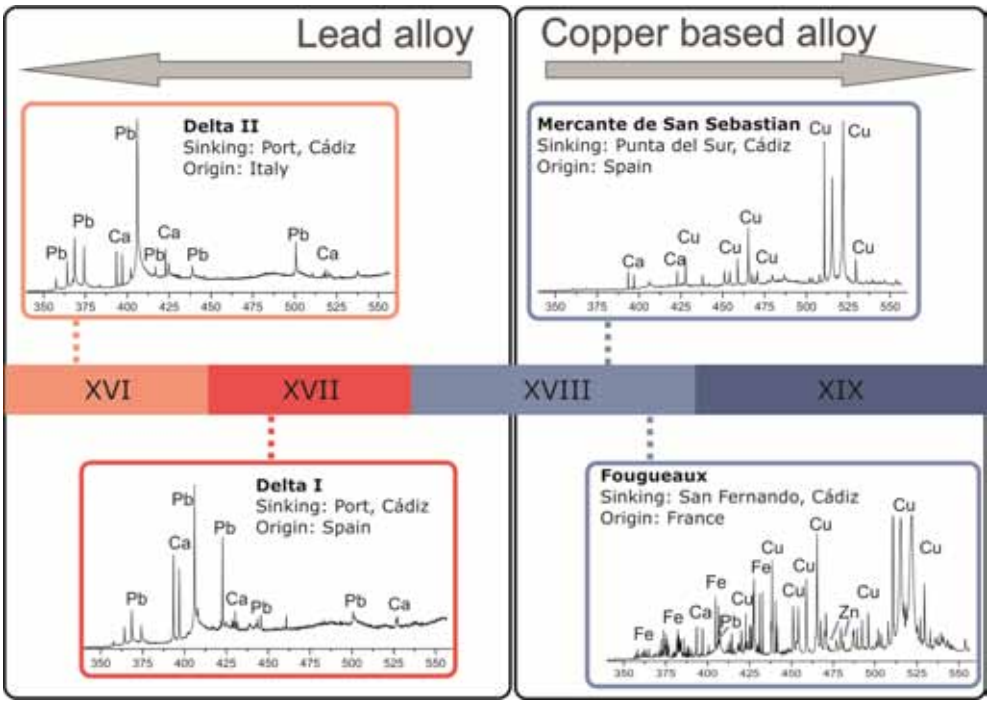

Figure 2. Chronocultural sorting of sheathing's composition from lead to copper based alloys. The main emission lines are labeled in the spectra.

3.3. Identification of objects in shipwrecks. The wreck of *San Pedro de Alcántara*

The wreck of San Pedro de Alcántara, located in the South of Spain, was discovered 10 m deep over a sandy bottom area. The wreck presents a military-structure type with a beam of 60 m, 10-12 m of breadth. The structure of the boat is covered by sediments, calcareous deposits and marine algae. Prior to the LIBS measurement campaign, a site survey was accomplished by the archaeologists from the Centro de Arqueología Subacuática (CAS) who located archaeological pieces from the remains of the wreck and removed the concretion layer from the sample surface.

The LIBS instrument was deployed on the vessel's board while a diver operated the LIBS probe in the sea bottom. Figure 3 shows a sequence of different stage of the *San Pedro de Alcántara* campaign. It is

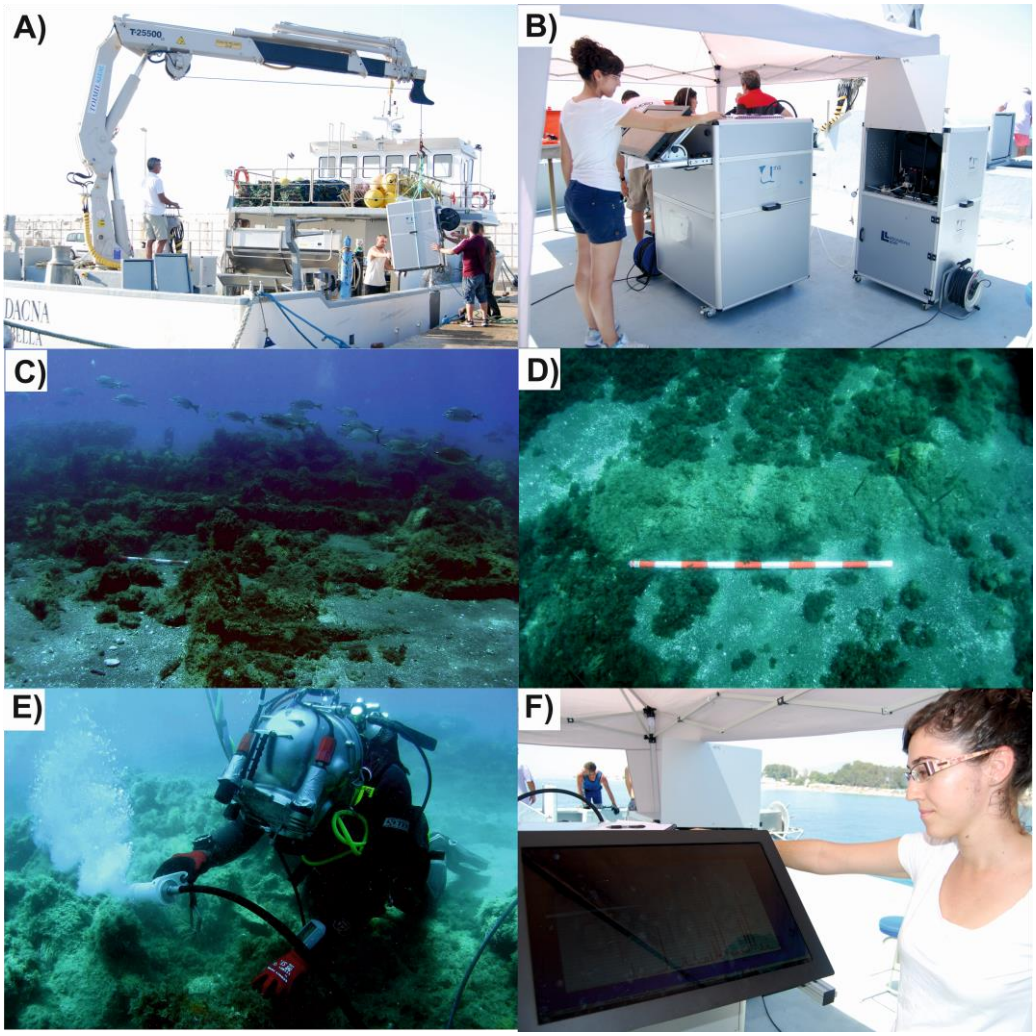

Figure 3. Pictures taken during the field campaign in the shipwreck of San Pedro de Alcántara. A) Equipment deployment; B) operators working from the deck; C) structure of the shipwreck, D) Cannon; E) diver operating the LIBS probe; F) LIBS results.

observed the deployment of the equipment on vessel's board, operators working from the deck, the archaeological site and the material found in it. As a diver operating the LIBS probe and the spectra results. The input pressure for underwater analysis was set to 5 bars, the maximum pressure supported by the system. Given the high alteration degree of the samples inspected, we decided to use argon as a purge gas, which provided a larger LIBS intensity when compared to air. The influence of argon as protection gas on the LIBS signal of an archaeological ceramic is presented in Figure 4. The main emission lines are labeled in the spectra. As shown, the use of argon increased the signal 4-fold for the emission line of Ca (I) at 422.67 nm when compared to air. Although metallic objects also benefit from the use of Ar, this observation is especially noticeable in ceramics.

A large number of archaeological objects were discovered and analyzed by LIBS during the survey. To assign the typical spectrum of a material and in order to ensure the reproducibility of the results,

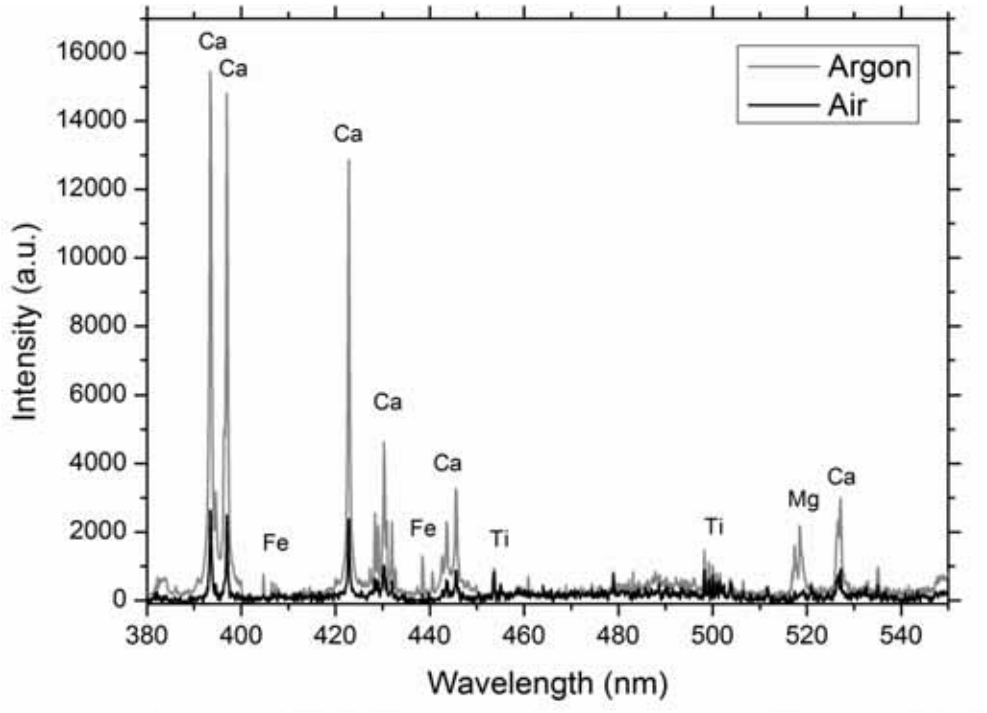

Figure 4: Comparison of the influence of air and argon gas protection on the LIBS signal of an archaeological ceramic. The main emission lines are labeled in the spectra.

data were acquired by averaging the response of 50 laser shots on three adjacent positions for each sample. The analysis was carried out at the same experimental conditions as the classification method developed in section 3.1. are summarized in Table 1. Then, acquired spectral intensities were normalized to unity for comparative purposes. Each object exhibits a distinctive chemical that was introduced in the classification method developed in *section 3.1.* From the canonical discriminant functions described there the unknown findings from the wreck were grouped into several categories easily. Figure 5 presents the classification of the set of unknown objects. As shown, samples from the subsea archaeological site were unequivocally classified in each of the aforementioned groups. The scatter points (in grey color) from the set of samples employed for modeling the classification method are also plotted in the graph. Results for the unknown samples classification are summarized in Table 3. Objects were correctly identified as four bronze alloys, eight ceramic fragments, seven metallic pieces and four marbles.

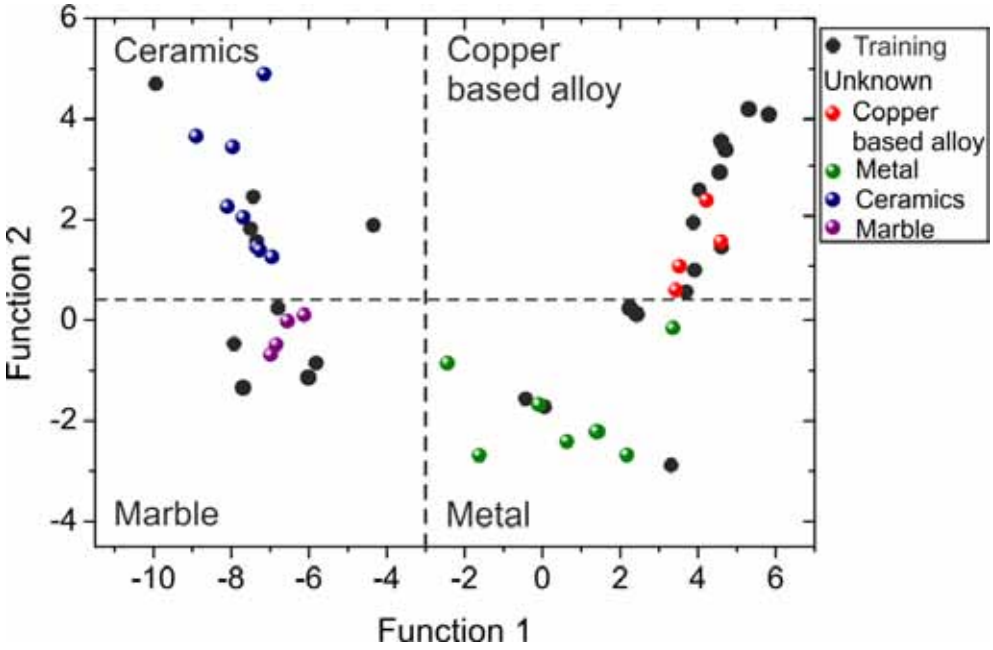

Figure 5. Classification scatter plot of the first two canonical discriminant functions of modeling developed. The scatter points in grey color corresponds to the set of samples employed for modeling the classification method and colored spheres represents the set of unknown objects.

Table 3. Prediction groups membership for unknown samples. ID sample is constitutes by a letter represents the type of sample (A: copper based alloy M: metal, C: ceramic, B: marble) and a number in the group classified.

ID	Prediction group membership (%)					ID	Prediction group membership (%)				
	Alloy	Metal	Ceramic	Marble	Total		Alloy	Metal	Ceramic	Marble	Total
A1	100	0	0	0	100	C4	0	0	100	0	100
A2	100	0	0	0	100	C5	0	0	100	0	100
A3	100	0	0	0	100	C6	0	0	100	0	100
A4	99.4	0.6	0	0	100	C7	0	0	100	0	100
M1	0	100	0	0	100	C8	0	0	100	0	100
M2	0	91.2	0	8.8	100	M8	0	100	0	0	100
M3	0	100	0	0	100	M9	0	100	0	0	100
M4	0	100	0	0	100	M10	13	87	0	0	100
M5	0	100	0	0	100	A5	88.7	11.3	0	0	100
M6	0	100	0	0	100	B1	0	0	0.5	99.5	100
M7	0	100	0	0	100	B2	0	0	0	100	100
C1	0	0	100	0	100	B3	0	0	0	100	100
C2	0	0	100	0	100	B4	0	0	0	100	100
C3	0	0	100	0	100						

Figure 6 shows a drawing top view of the shipwreck in which the bow is oriented to the northwest position and the aft, to the southeast. The drawing describes the state of conservation of the wreck, where the shipwreck structure is observed, as well as the way is distributed along the site. The locations of the archaeological pieces are also indicated. Chemical composition of each object is detailed as a bar graph inset. As shown, various types of samples were identified as defense material such as two iron cannons (M2, M4) and a cannon bullet (M3) composed of iron with manganese as a minor constituent. On the other hand, pieces of crew clothing present a chemical composition based on copper alloy with zinc in the case of jacquet button (A2) and zinc-lead in the case of the belt buckle (A4). Regarding to ceramic fragments, in general, are constituted by calcium, magnesium, aluminum, iron, silicon, strontium and titanium; although pieces C3, C5 and C7 also contained lead. Some unidentified pieces show a variable chemical composition such as metals copper-lead (A3) alloy, and copper-zinc-lead (A1) alloy; and lead (M1, M7) or iron (M5, M6) metals. Figure 7 shows all team members who took part in the campaign.

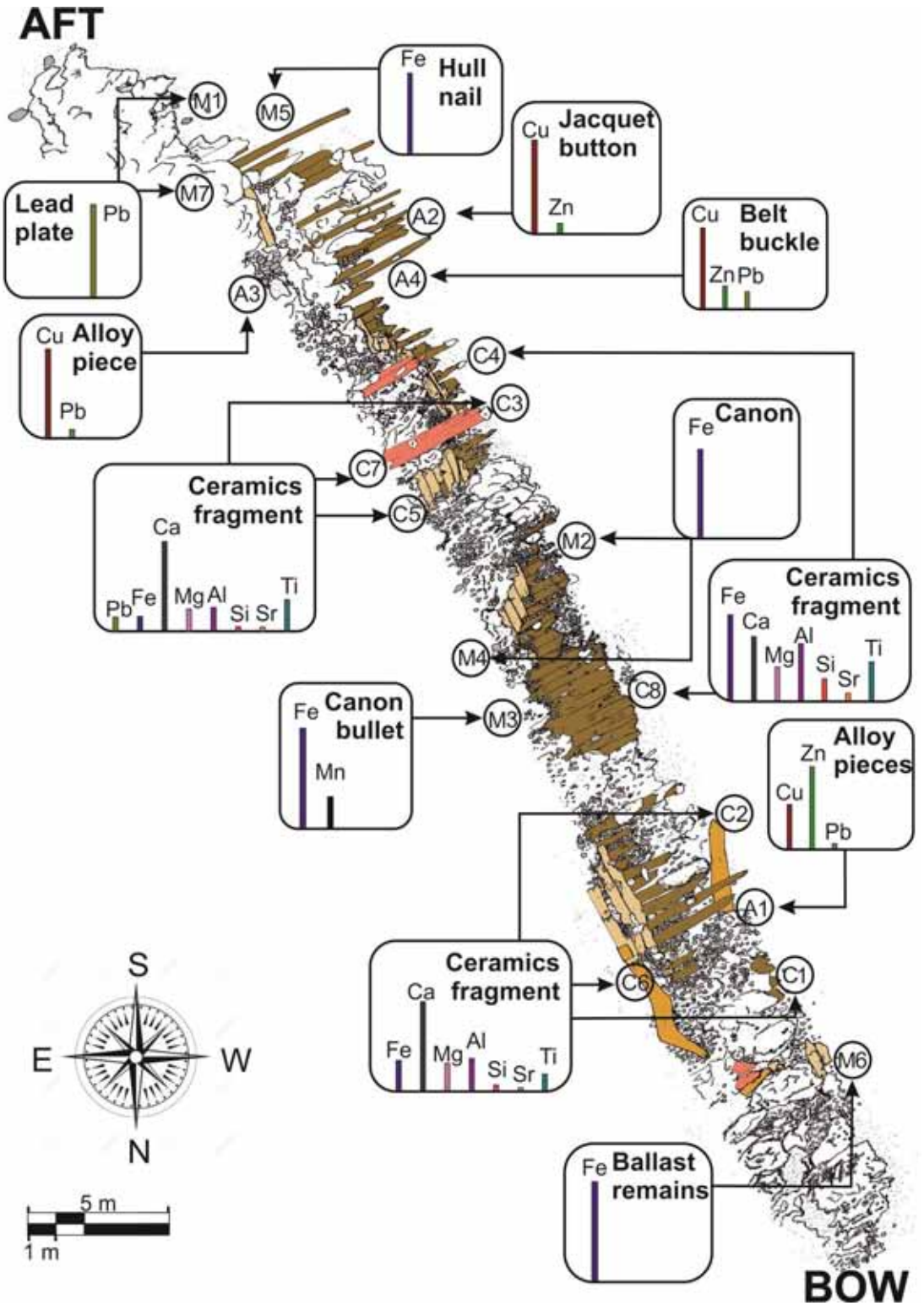

Figure 6. Schematic drawing of the shipwreck. The inset bar diagrams represent the chemical composition of each object and the locations of the archaeological findings.

Figura 7. Team members who taken part in San Pedro de Alcántara campaing. From left to right top row S. Guirado and F.J. Fortes (researcher from UMALaserLab), R. Exposito (audio team), J. Martí, M. Alzaga, N. Rodríguez (archeologists from CAS), C. Barbero (ship's captain), R. Liste and D. López (crew) and J.J. Laserna (Main researcher from UMALaserLab). From left to right bottom row L. Pellejero (support of diver), A. Higueras (archeologists from CAS), I. Entralla (professional diver) and M. López (researcher from UMALaserLab).

4. Conclusions.

Using a LIBS sensor deployed on a small vessel, a hand-held probe was submersed by a diver to the shipwreck of *San Pedro de Alcántara* located in the South of Spain over the Mediterranean Sea. LIBS data from a variety of objects found in the wreck were collected, logged and accurately geo-positioned for post survey analysis. In addition to metallic objects, refractory materials such as rocks and ceramics were analyzed. Although algae and calcareous deposits had to be removed from the sample surface before the analysis, the LIBS system constitutes a significant step forward, allowing the acquisition of a consistent set of spectral data that can be treated by a software based on linear discriminant analysis for assigning the chemical identity of the object. The information thus gathered provides valuable data on the identity of shipwrecks located in coastal waters.

5. References

1. C. Pearson, Conservation of marine archaeological objects, Butterworth & Co. Ltd. 1987, London.
2. X. Zhang, W. J. Kirkwood, P. M. Walz, E. T. Peltzer, P.G. Brewer, A Review of Advances in Deep-Ocean Raman Spectroscopy, Appl. Spectrosc. 66 (2012), 237–249.
3. B. Thornton, T. Takahashi, T. Sato, T. Sakka, A. Tamura, A. Matsumoto, T. Nozaki, T. Ohki, K. Ohki, Development of a deep-sea laser-induced breakdown spectrometer for in situ multi-element chemical analysis, Deep. Res. Part I 95 (2015), 20–36.
4. R. Fantoni, R. Barbini, F. Colao, D. Ferrante, L. Fiorani, A. Palucci, In: Integration of two lidar fluorosensor payloads in submarine ROV and flying UAV platforms, EARSeL eProc., 3 (2004), 43–53.
5. F. J. Fortes, J. Moros, P. Lucena, L. M. Cabalín, J. J. Laserna, Laser-induced breakdown spectroscopy, Anal. Chem. 85 (2013), 640–669.
6. R. E. Russo, X. Mao, J. J. Gonzalez, V. Zorba, J. Yoo, Laser ablation in analytical chemistry, Anal. Chem. 85 (2013), 6162–6177.
7. A. Giakoumaki, K. Melessanaki, D. Anglos, Laser-induced breakdown spectroscopy (LIBS) in archaeological science - applications and prospects, Anal. Bioanal. Chem. 387 (2007), 749-760.
8. V. Spizzichino, R. Fantoni, LIBS in archaeometry: A review of its application and future perspectives, Spectrochim. Acta Part B 99 (2014), 201-209.
9. V. Lazic, F. Colao, R. Fantoni, V. Spizzicchino, Recognition of archeological materials underwater by laser induced breakdown spectroscopy, Spectrochim. Acta Part B 60 (2005), 1014–1024.
10. V. Lazic, S. Jovićević, Laser induced breakdown spectroscopy inside liquids: Processes and analytical aspects, Spectrochim. Acta Part B 101 (2014), 288–311.
11. T. Sakka, H. Oguchi, S. Masai, K. Hirata, Y. H. Ogata, Use of a long-duration ns pulse for efficient emission of spectral lines from the laser ablation plume in water, Appl. Phys. Lett. 88 (2006), 061120-4.
12. V. Lazic, J. J. Laserna, S. Jovicevic, Insights in the laser induced breakdown spectroscopy signal generation underwater using dual pulse excitation — Part II: Plasma emission intensity as a function of interpulse delay, Spectrochim. Acta Part B 82 (2013), 50–59.
13. V. Lazic, J. J. Laserna, S. Jovicevic, Insights in the laser-induced breakdown spectroscopy signal generation underwater using dual pulse excitation — Part I: Vapor bubble, shockwaves and plasma, Spectrochim. Acta Part B 82 (2013), 42–49.
14. A. De Giacomo, M. Dell'Aglio, O. De Pascale, M. Capitelli, From single pulse to double pulse ns-Laser Induced Breakdown Spectroscopy under water: Elemental analysis of aqueous solutions and submerged solid samples, Spectrochim. Acta Part B 62 (2007), 721–738.
15. F. J. Fortes, J. J. Laserna, The development of fieldable laser-induced breakdown spectrometer: No limits on the horizon, Spectrochim. Acta Part B 65 (2010), 975–990.

16. F. J. Fortes, S. Guirado, A. Metzinger, J. J. Laserna, A study of underwater stand-off laser-induced breakdown spectroscopy for chemical analysis of objects in the deep ocean, J. Anal. At. Spectrom. 30 (2015), 1050–1056.
17. S. Guirado, F. J. Fortes, V. Lazic, J. J. Laserna, Chemical analysis of archeological materials in submarine environments using laser-induced breakdown spectroscopy. On-site trials in the Mediterranean Sea, Spectrochim. Acta Part B 74-75 (2012), 137–143.
18. L. M. Cabalín, A. González, V. Lazic, J. J. Laserna, Deep ablation and depth profiling by laser-induced breakdown spectroscopy (LIBS) employing multi-pulse laser excitation: Application to galvanized steel. Appl. Spectrosc. 65 (2011), 797-805.
19. S. Guirado, F. J. Fortes, L. M. Cabalín, J. J. Laserna, Effect of Pulse Duration in Multi-Pulse Excitation of Silicon in Laser-Induced Breakdown Spectroscopy (LIBS), Appl. Spectrosc. 68 (2014), 1060–1066.
20. S. Guirado, F. J. Fortes, J. J. Laserna, Elemental analysis of materials in an underwater archeological shipwreck using a novel remote laser-induced breakdown spectroscopy system, Talanta 137 (2015), 182-188.
21. R. Fantoni, L. Caneve, F. Colao, L. Fornarini, V. Lazic, V. Spizzichino, Methodologies for laboratory laser induced breakdown spectroscopy semi-quantitative and quantitative analysis - a review, Spectrochim. Acta Part B 63 (2008), 1097–1108.
22. A. De Giacomo, M. Dell'Aglio, A. Casavola, G. Colonna, O. De Pascale, M. Capitelli, Elemental chemical analysis of submerged targets by double-pulse laser-induced breakdown spectroscopy, Anal. Bioanal. Chem. 385 (2006), 303–311.
23. S. Almaviva, R. Fantoni, L. Caneve, F. Colao, L. Fornarini, A. Santagata, R. Teghil, Use of ns and fs pulse excitation in laser-induced breakdown spectroscopy to improve its analytical performances: A case study on quaternary bronze alloys, Spectrochim. Acta B 99 (2014), 185–192.
24. E. Tognoni, G. Cristoforetti, S. Legnaioli, V. Palleschi, Calibration-free laser-induced breakdown spectroscopy: State of the art, Spectrochim. Acta Part B 65 (2010), 1-14.
25. S. Guirado, F. J. Fortes, J. J. Laserna, Multi-pulse excitation for underwater analysis of copper-based alloys using a novel remote laser-induced breakdown spectroscopy system, Appl. Spectrosc. 70 (2016), 618-626.
26. M. J. Baxter, "Exploratory Multivariate Analysis in Archaeology", Edinburgh University Press, Edinburgh, 1994.
27. M. Corsi, G. Cristoforetti, M. Giuffrida, M. Hidalgo, S. Legnaioli, L. Masotti, V. Palleschi, A. Salvetti, E. Tognoni, C. Vallebona, A. Zanini, Archaeometric analysis of ancient copper artefacts by laser-induced breakdown spectroscopy technique, Microchim Acta 152 (2005), 105-111.
28. J. B. Sirven, B. Sallé, P. Mauchien, J. L. Lacour, S. Maurice, G. Manhès, Feasibility study of rock identification at the surface of Mars by remote laser-induced breakdown spectroscopy and three chemometric methods, J. Anal. At. Spectrom. 22 (2007), 1471.

29. J. L. Gottfried, R. S. Harmon, F. C. De Lucia, A. W. Miziolek, Multivariate analysis of laser-induced breakdown spectroscopy chemical signatures for geomaterial classification, Spectrochim. Acta Part B 64 (2009), 1009–1019.
30. F. Colao, R. Fantoni, P. Ortiz, M.A. Vazquez, J.M. Martin, R. Ortiz, N. Idris, Quarry identification of historical building materials by means of LIBS XRF and chemometric analysis, Spectrochim. Acta Part B 65 (2010), 688-694.
31. M. Bethencourt, A. Bocalandro and J. Romero-Pastor, Datación de pecios de los siglos XVIII y XIX a través de la caracterización de los forros de cobre, IV Congreso Latinoamericano de Conservación y Restauración del Metal, Madrid (13-17 September 2011). Madrid: Secretaría General Técnica, Ministerio de Educación, Cultura y Deporte; Grupo Español de Conservación, 2011, 51-62.

Chapter 7. Double pulse laser induced breakdown spectroscopy of a solid in water: effect of hydrostatic pressure on laser induced plasma, cavitation bubble and emission spectra

1. Introduction

Laser-Induced Breakdown Spectroscopy (LIBS) has emerged in the last decade as a promising solution for deep sea exploration [1-5]. Deep ocean is one of the most challenging and inaccessible environments of the planet, making it difficult to investigate not only the physical, chemical, and biological conditions on the seafloor; but also in areas such as water pollution, cultural heritage, hydrothermal vents , mining and geological exploitation [6-10]. This study aims to provide insight on the fundamental aspects of DP-LIBS that could be useful for developing new chemical sensors for oceanographic surveys [11]. The capabilities of laser-based tools can be useful for experimental campaigns in these extreme conditions. In particular, LIBS combines many of the required features for these applications, i.e. multielemental information, no sample preparation, unlimited range of material capability and real time analysis. Moreover, the experimental setup adaptable to automation makes LIBS a good candidate for non-contact sensing [12-15]. The advance of lasers, spectrograph and detector technology has provided support for integrating remote-operated submersible LIBS systems with stand-off access to the sample [1]. Nevertheless, the actual realization of such systems is really complex both to design and to handle, thus requiring further research efforts. It follows that a significant amount of time is required for developing new sensors for oceanography, such as LIBS, as well as comparing it with other approaches in order to identify which is the most suitable technique viable for the chemical detection of solids submerged in water at high pressures.

Evaluation of LIBS analysis of liquids was investigated for the first time in 1984 by Cremers and co-workers [15]. In this paper, the laser pulse was focused into a bulk liquid, producing its rapid heating at the focal point, followed by an explosive expansion and formation of a gas bubble. Since then, a large number of studies has been conducted with the aim to clarify the different processes involved during the laser–water interaction, including the plasma and vapour bubble formation and the induced shock wave propagation, and to optimize approaches for the optical emission collection [16-20]. In order to obtain an optimum LIBS signal, different excitation approaches have been evaluated. For instance, single pulse excitation has been intensively studied, although, as a consequence of the nearly incompressible fluid medium, the generated plasma has a very short persistence, leading to a poor signal to noise ratio. De Giacomo et al. [21-23], and other authors such as Lazic et al. [24,25] and Rifaiet al. [26] have discussed the limitations of this approach for the analysis of liquids and investigated the potential advantages of the Double Pulse (DP-) LIBS. Briefly, in DP-LIBS, the first laser pulse produces a water vapour bubble whereas the second one, fired at an optimal interpulse delay with respect to the first one, induces a second plasma inside the previously formed bubble. The second laser-induced plasma expands in a gas environment, so that its emission spectra result comparable to those of a plasma induced in air, in terms of persistence, resolution and signal-to-noise ratio. For all these reasons, DP-LIBS represents a powerful tool for the elemental analysis of bulk water and submerged solid samples. In any case, the application of DP-LIBS in oceanography still requires a deep study of the phenomena induced by the laser ablation process in water at high pressure.

In the last decade, the suitability of LIBS for laboratory characterization of bulk liquids at high pressure has been explored [7, 27, 28]. Several experimental parameters have been monitored, such as pulse energy focusing geometry and liquid pressure, so to try and make up for the observed decrease of the LIBS signal with increasing pressure. The same authors have employed a double-pulse approach in order to improve LIBS capability [2]. However, the features of plasmas and cavitation bubbles generated at a given interpulse delay are strongly affected by the water pressure. For example, despite the use of DP, a negligible signal enhancement has been obtained at static pressures above 100 bar [29]. This suggests that DP is not necessarily helpful for applications in bulk liquids. On the other hand, it has been reported by Thornton et al. that the use of a long-duration nanosecond laser pulse (150 ns) can significantly improve the quality of SP-LIBS spectra [30], as well as the capability to analyze submerged solid targets with single pulses [31-32]. With this regards, the quality of DP approach still needs further studies in order to evaluate the full range of its benefits over other possible experimental strategies.

Most recently, the effect of water pressure on submersed solid targets has been fully investigated for surveying the laser ablation performed in water during nanoparticle production. As observed in[33],the plasma duration and degree of confinement, as well as the cavitation bubble evolution, that are dependent on the external liquid pressure, can strongly affect both the yield and structure of the produced particles (carbon nanostructures in the mentioned paper). With this in mind, the present study was focused on the fundamental aspects of the generation of single- and double pulse- laser-induced plasmas, as well as the evolution of the cavitation bubble due to the first laser pulse. We used optical emission spectroscopy for plasma characterization and shadowgraph for bubble dynamics study, for investigating the above mentioned parameters as functions of the pressure used. For DP-LIBS, we employed the collinear configuration. We focused our attention on the effects brought by the liquid pressure on the spectroscopic analysis of submerged solid targets, which we investigated characterizing the DP-LIBS spectra as functions of pressure and optimizing the interpulse delay in terms of signal-to-noise ratio.

The work presented in this chapter is the result of a pre-doctoral research stay carried out inthe laboratory of *Consiglio Nazionalle delle Ricerche-Istituto di Nanotecnologia* (CNR- NANOTEC) and the U*niversità degli Studi di Bari Aldo Moro* (UNIBA)-Bari, Italy; under the supervision of Prof. Alessandro De Giacomo.

2. Experimental Set-up

Figure 1 presents a schematic diagram of the experimental setup employed in this work. Here, a two delayed laser pulses (Nd:YAG laser @532 nm, 10 Hz, 5 ns pulse duration, Quanta System, PILS-GIANT) were focused by an appropriate optical configuration on a metallic sample placed inside a stainless-steel chamber x filled with distilled water. The experiments were carried out at different pressures, up to 120

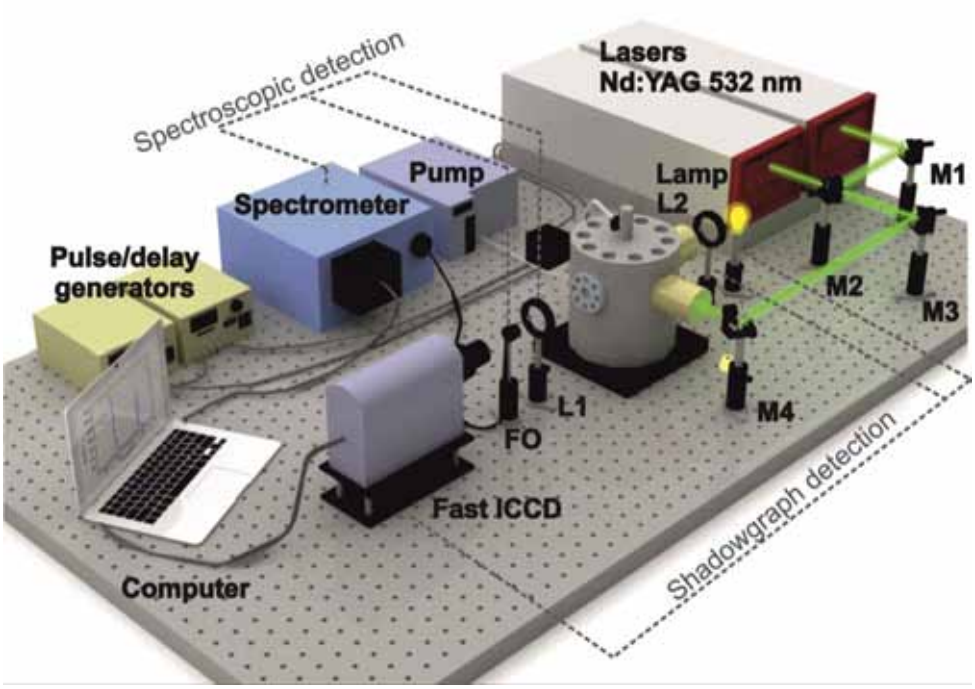

Figure 1.Experimental set-up. M1, M2 and M3 mirrors; M2 dichroic mirror; L1 collimating lens; L2 lens; FO fiber optic. Dashed lines show the two different detection systems, one for OES measurements and the other for shadowgraph images.

bar. The energy of the two lasers beams was set at 150 and 270 mJ, respectively. The system was externally synchronized using a delay and pulse generator (Stanford inc. DG 535). For this study, a collinear double pulse configuration was used, i.e., both laser pulses were focused on the sample surface by a quartz biconvex lens (5 cm focal length) held in a spacer tube placed in front of the target. The chamber was equipped with a rotating target holder, in order to limit drilling effects on the sample surface. A 10 mm axial movement for fine adjustments of the focal distance was also possible by means of a micrometric screw. The chamber was a stainless steel cylinder with a perpendicular aperture for the laser beam entrance, sealed with a sapphire optical window with 532/1064 nm antireflection coating and equipped with spacer tubes enabling adjustment of the lens-to-target distance. The high-pressure chamber is equipped with several extra ports, each provided with sapphire optical windows, for the acquisition of spectra and shadowgraph images. The water outflow was controlled by a micrometric valve that could be either kept closed to seal the chamber or opened to produce a regime of controlled flux. The pressure was created by a HPLC pump (Shimadzu LC-20AT Prominence) which could work in two modes (constant pressure or constant flux) in a pressure range 1-250 bar, in steps of 1 bar.

For spectroscopic experiments, the plasma emitted light was collected at 90º with respect to the laser beam, through the dedicated sapphire optical window, by a 10 cm quartz lens placed outside the chamber. The plasma light was focused onto the entrance slit of a monochromator through an optical fiber cable. The spectroscopic system consisted of a spectrograph (JobinYvon TRIAX 550) with a grating of 1200

grooves mm^{-1} and an ICCD detector (JobinYvon i3000) which was controlled and synchronized by a pulse/delay generator (Stanford inc. DG 535). All the emission spectra were acquired with 10 accumulations and 5 averages to optimize the signal-to-noise ratio. The employed acquisition time parameters (with respect to the second laser pulse) were: delay time of 0 ns and 50 ns; and gate width of 10 μs and 100 ns for the used Al and Ti target, respectively.

The shadowgraph set-up for studying the cavitation bubble dynamics consisted of a continuous white light source, a set of lenses to reduce light divergence, a fast Camera (Andor i-Star, DH334T-18F-E3) with a tele-objective to acquire the bubble profile and a pulse generator to synchronize the laser pulses with the camera. The bubble shadow was collected through a sapphire window at 90º with respect to the laser pulse direction. During the acquisition of shadowgraph images, the target holder was stopped in order to avoid formation of bubbles along the optical path, which would affect the acquisition. Furthermore, to minimize drilling of the sample surface, the target was turned after the acquisition of each shadowgraph image. Also in these studies the repetition rate of laser pulses was 10 Hz. The shadowgraph images of the laser-induced bubble and shockwave were acquired by using the kinetic mode of the ICCD, with a gate width of 1 μs and of 200 ns respectively. The shadowgraph images of the plasma were acquired by using the kinetic mode of the ICCD, with a gate width of 500 ns.

3. Results and discussion

3.1. Underwater laser-induced plasmas

The main mechanisms responsible for the plasma formation are the same occurring during ablation in gas. Briefly, the sequence of the process starts with the laser ablation and the laser induced plasma (LIP) production. Due to its fast expansion, a shock wave (SW) is generated. It is important to note that the differences between plasma formation in a gaseous environment and inside a liquid are related to the plasma confinement and the onset of cavitation effects, i.e. the vapor bubble formation. Due to the confinement of the plasma by the nearly incompressible liquid medium and to the fast transfer of energy from the plasma to the surrounding liquid, the plumes generated under water are smaller than those generated in gas. As a consequence, the plasma persistence is significantly shorter, ending typically few microseconds after the laser irradiation [27-29].

In order to evaluate the effect of underwater environmental pressure over the physical characteristics of the generated plumes, we acquired shadowgraph images at different delays after laser irradiation. Figure 2 depicts results obtained for an aluminum target and acquired few microseconds after the first laser pulse at three different pressures: 30, 90 and 120 bar. The images clearly show the confinement effect of the liquid on the plasma. For instance, the plasma at 90 bar is smaller than the corresponding one at 30 bar. In the case of 120 bar it should be considered that, as a consequence of the

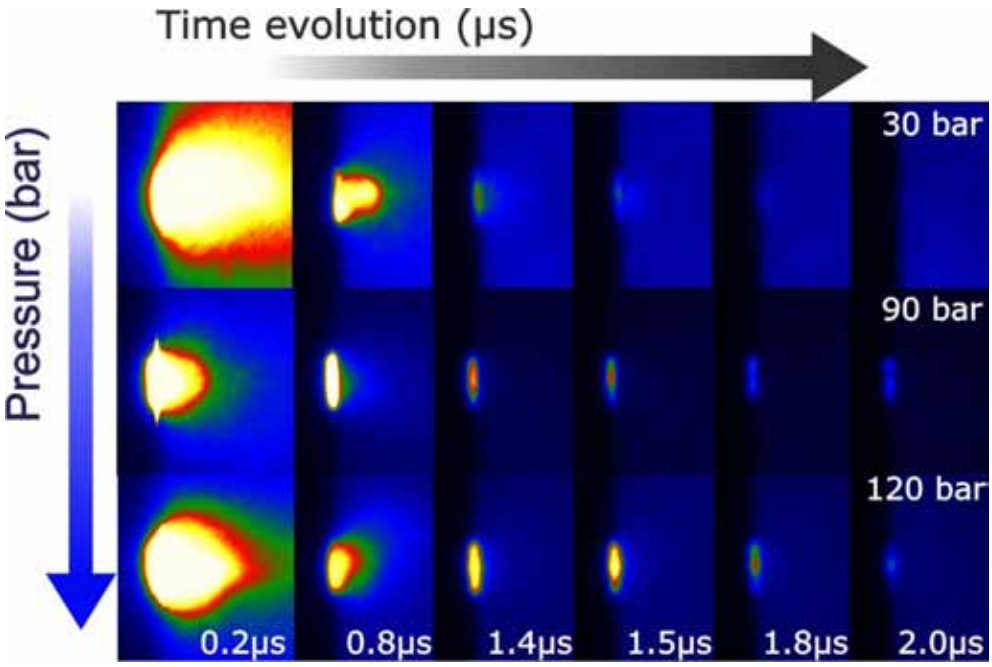

Figure 2.Plasma shadowgraphy images after the first laser pulse at different delays. The aluminum target was submerged in water at 30, 90 and 120 bar.

thrust of the expanding plasma, the surrounding liquid can reach supercritical conditions [34]**.** Under these circumstances, water is characterized by lower viscosity and surface tension, thus the plasma appears less confined than at 90 bar. In general, the strong confinement induced by the nearly uncompressible liquid and the steep decrease of the ionization degree and temperature due to the fast transfer of energy to the surrounding medium, cause the plasma species to rearrange in particles of nanometric size. This produces a colloidal solution in front of the sample that may affect the shot-to-shot reproducibility of LIBS measurements [33]. Although the external pressure noticeably affects the LIP dynamics, the ablation process itself is not expected to depend on the external pressure [33-35] as a consequence of the conditions at the early stages of expansion. In fact, in this case, the ablated matter reaches a number density close to that of the sample in the solid phase and an electronic temperature of about 10000 K. In these conditions, the initial plasma pressure is in the order of tens of Mbar and consequently, as it is reported in [35-38], by considering the range of pressures used in this work, the external pressure at the initial stage of LIP expansion can be neglected. Therefore, even if the plasma volume is reduced and its shape is changed by the water pressure increase, the plasma parameters (temperature and electron density) hold similar values. As mentioned above, after plasma formation, a SW is generated. The shockwave is caused by the rapid expansion of the laser-ablated material into the surrounding liquid, which generates a sharp, high pressure impulse that expands outwards from the focal point of the laser. It is reasonable to expect that, in the range of external pressures employed in this work, the characteristics of the SW produced by the LIP expansion do not vary greatly. The outward SW driven in the surrounding liquid by the plasma expansion was directly investigated by shadowgraphy experiments.

Figure 3A shows images of the SW propagation as a function of the delay time at 30 and 120 bar. The relative position of the shockwave at each delay is also labelled in the picture. As shown, the size and volume of the SW is similar in both cases. From here, the maximum distance travelled by the front of the shockwave is plotted in Figure 3B. Data were acquired at different water pressure: 1, 30, 60, 90 and 120 bar. Additionally, the inset shows the velocity of the shockwave at each pressure. In the first 10 μs, the SW propagation velocity is in the order of the speed of sound in water, around 1500 m s^{-1}, for each value of pressure. It is well known that, when external pressure increases, the propagation of the SW should vary of

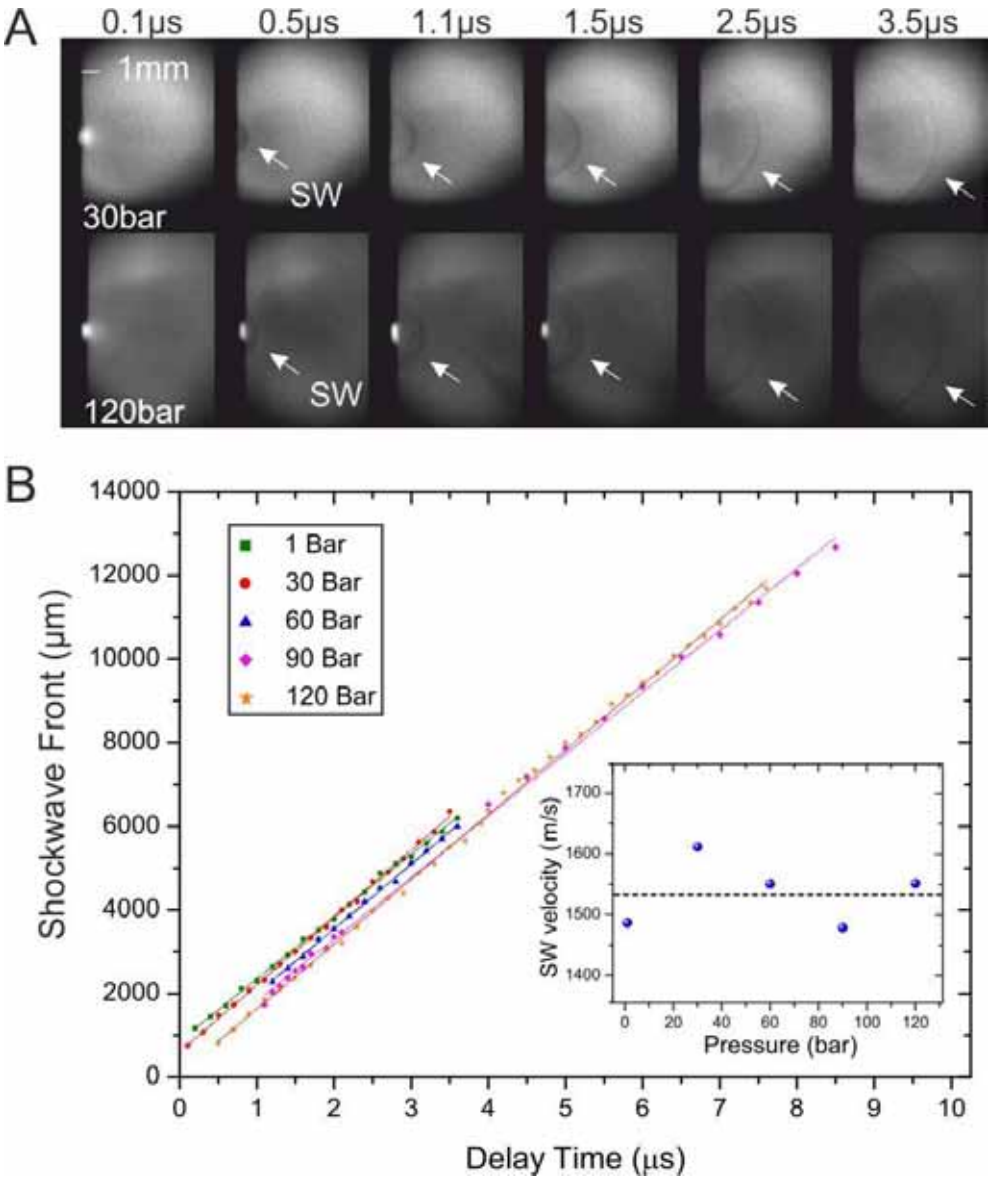

Figure 3.Time-resolved shadowgraph images of shockwave front, at atmospheric pressure and 120 bar. (a) Laser focused on an Al in water at 1, 30, 90 and 120 bar of pressure; (b) shockwave front space vs delay time plot. Graphical inset shockwave velocity vs environment pressure plot.

a few tens of units, but as a consequence of the experimental uncertainty of our measurement, we are not able to clearly appreciate this difference. Nevertheless, such similar values of the SW propagation velocity confirm that the initial thrust due to the breakdown is almost the same at all the external pressures investigated in the present work.

3.2. Effect of hydrostatic pressure on the cavitation bubble expansion

The plasma induced by a laser shot releases its energy to the surrounding liquid and generates a thin vapour layer at the border of the plasma, which evolves into a cavitation bubble. The behaviour of a cavitation bubble induced by laser ablation in water at 1 bar has been already investigated [23, 24]. For comparative purposes, we used fast shadowgraph to study the dimensions and shape of the vapour bubble formed after the first laser pulse at different pressures. Frames acquired at different delay times at a pressure of 1 bar are shown in Figure 4. The temporal evolution of the bubble size is characterized by three stages: first, the expansion stage; then, the stage of maximum expansion; and finally the compression/collapse stage. At 1 bar, the bubble expansion was well discerned even at 2 μs from the laser pulse ,whereas the maximum bubble size was observed at 250 μs. In this stage, the shape of the bubble is a hemisphere [39]. Afterwards, at the maximum expansion, the pressure inside the bubble is lower than the external one, and consequently the bubble starts to shrink. Thus, the size decreases until 950 μs. At the collapse stage, a rapid increase of the gas temperature and pressure inside the bubble produces a re-expansion of the cavitation bubble. Additionally, if enough energy is accumulated in the bubble, its oscillations can continue for many cycles of both expansion and collapse [24].

The temporal evolution of the cavitation bubble has been studied as a function of the external pressure (30, 90 and 120 bar). Results are depicted in Figure 5. The size of the cavitation bubbles observed at a longer delay time was significantly smaller by increasing the water pressure. Also, Figure 5 shows that, regardless of pressure, a cavitation bubble starts to appear during the early stage of the processes. Thus,

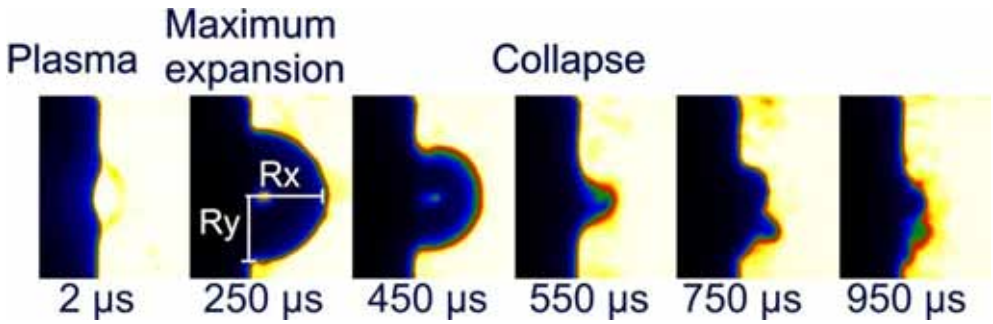

Figure 4. Time-resolved shadowgrams of the laser-induced cavitation bubble on an Al sample submerged in water at 1barr.

the initial expansion velocity along the *x*-direction was similar for the three studied cases, that is around 40 m/s. This observation reveals that the effect of hydrostatic pressure is negligible during the early stage of the expansion process [40]. Beyond this point, the evolution of the dynamic expansion process diverges for the different pressures. At 120 bar, the cavitation bubble could not be discerned at early times. The maximum bubble expansion occurs at 15, 10 and 7 μs for 30, 90 and 120 bar, respectively, whereas the collapse was observed at 28, 17 and 9 μs, again depending on hydrostatic pressure. The velocities calculated at the collapse stage were 30, 70 and 90 m/s at 30, 90 and 120 bar, respectively [40]. Thus, a pressure increase influences the expansion and cooling of the vapour bubble, leading to a decrease of the bubble size and lifetime, as it can be observed in Figure 5. We considered the volume instead of the radius to estimate the bubble size, in order to take into account that hydrostatic pressure can distort the bubble shape. In fact, due to the external pressure, the bubble expands differently along the *x* and *y* directions, thus assuming an ellipsoidal shape [41-42]. The observed variations of bubble size and lifetime are in good agreement with those found in [43], where a range of pressures up to 50 bar was evaluated.

In Figure 5, a secondary bubble can be observed. This is assumed to be produced by the rapid increase of both the internal temperature and pressure of the cavitation occurring bubble just after its collapse. After rebounding, the bubble shape changes again, because it is now constituted by both water

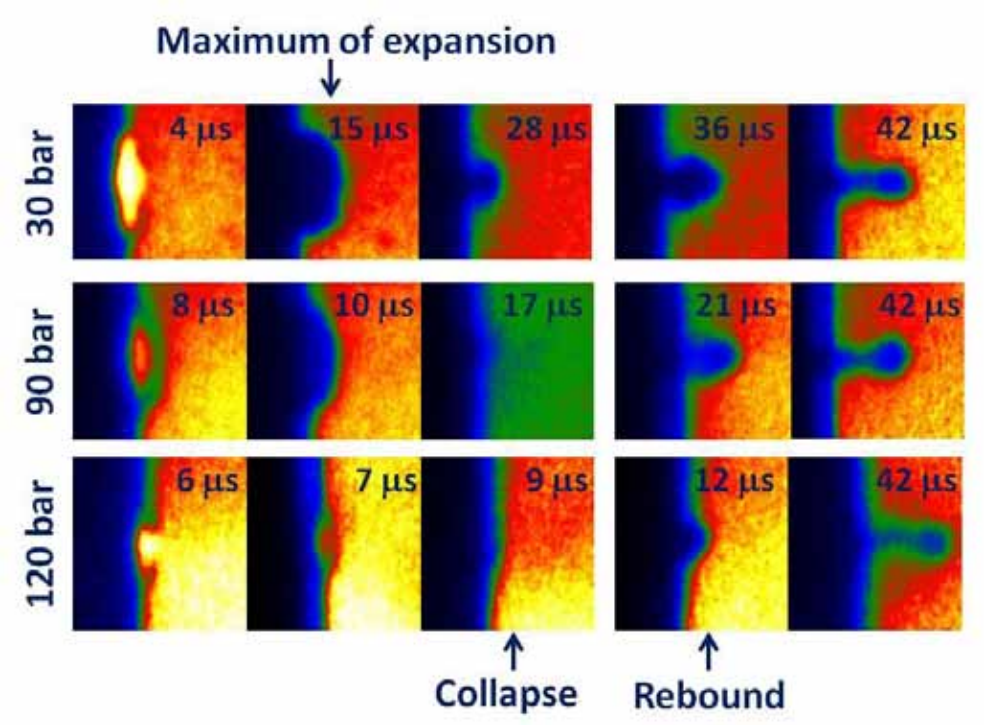

Figure 5. Representative time-resolved shadowgraphy images of the bubble induced by a single laser pulse at different water pressures (30, 90 and 120 bar, respectively). The images were acquired at various delay times with a gate width of 500 ns.

vapour and the nanomaterials produced during the cooling down of the plasma [44]. By increasing the water pressure, the collapse velocity along the *x*-direction also increases and a pronounced bubble rebound followed by its displacement with respect to the target surface takes place. On the contrary, at atmospheric pressure, the rebound phase can be observed according to the initial laser energy, but is not accompanied by any displacement of the bubble with respect to the target position.

3.3. Double pulse LIBS underwater at high pressure

Keeping in mind the general description of the laser-induced bubble at different pressures, DP-LIBS underwater requires a careful optimization of the interpulse delay. In agreement with the conclusions of a previous work [22] performed at atmospheric pressure, the optimum interpulse delay time could be expected to match the maximum expansion of the bubble. In such a situation, the plasma produced by the second pulse expands in a cavitation bubble with more favourable pressure conditions than those at the initial stage of the bubble expansion or the final stage of the bubble collapse. It has recently been observed that, in these initial and final stages, a significant part of the energy of the second laser pulse is spent in the interaction with the NPs generated by the first laser pulse [39]. This causes the breakdown of the just formed NPs and, accordingly, the production of a secondary plasma. Hence, the secondary plasma is generated at a distance from the target and it partially prevents the second laser pulse from ablating the sample. On the contrary, at the maximum of the bubble expansion, that is when its volume is the largest, the NP concentration in the bubble reaches its minimum and this shielding effect occurs to a lesser extent. As an example, Figure 6 shows the effect of the plasma produced by the second laser pulse within the bubble generated by the first laser pulse. The interpulse delay time was set at the maximum bubble expansion, 250 μs at atmospheric pressure. Therefore, the presence of NPs must be taken into account,

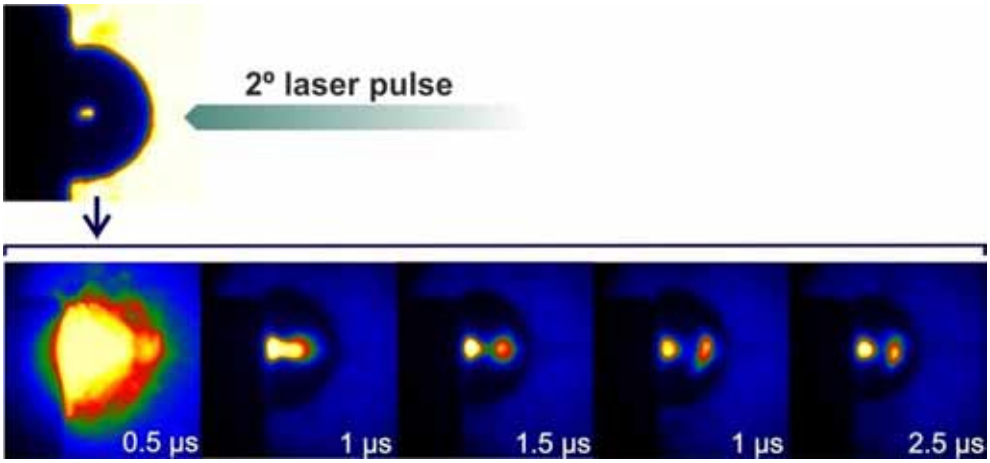

Figure 6.Plasma shadowgraphy images of the effect produced by the second pulse on the NPs generated by the first laser pulse. Interpulse delay:250 μs, pressure: 1 bar.

especially when DP-LIBS is performed at high external liquid pressures. In these conditions, the bubble volume is smaller and the NP concentration higher than at atmospheric pressure. Figure 7 shows some of the images of the second laser-induced plasma, taken at several interpulse delay times at the representative water pressures of 30 and 90 bar. The interpulse delay times used in this experiment were chosen in correspondence with the maximum of the bubble expansion. The images of the plasma induced by the second laser pulse were compared with those produced by the first one. The plasma aspect ratios (R_x/R_y) on the left of Figure 7 clearly indicate that the second plasma induced inside the first bubble has a more spherical shape. A rigorous treatment of the aspect ratio reported in Figure 7 would require to take into account the image distortion due to the shape of the induced cavity around the plasma. Nonetheless, for the scope of the present discussion we suppose that, as the plasma fills up completely the cavitation bubble during the expansion, this effect may be reasonably neglected.

On the other hand, from the spectroscopic point of view, and contrary to what observed at atmospheric conditions [33], emission spectra at high pressure are characterized by self-absorbed lines on the continuum radiation. This is shown in Figure 8 for titanium spectra acquired at 30 bar. The predominance of the continuum spectra in the LIP can be ascribed to the Debye-Hückel's high density

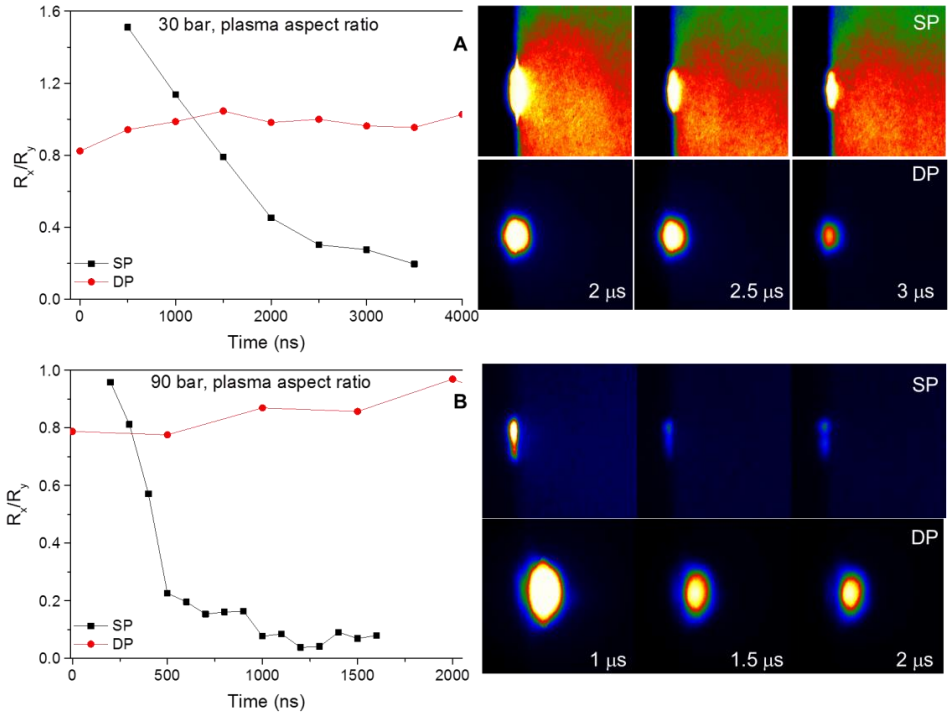

Figure 7.Comparison between the plasma shapes produced by the first laser pulse and the second laser pulse at two representative water pressure values: A) 30 bar and B) 90 bar. The temporal trend of the plasma aspect ratios and the plasma shadowgraphy images are reported on the left and right hand side, respectively.

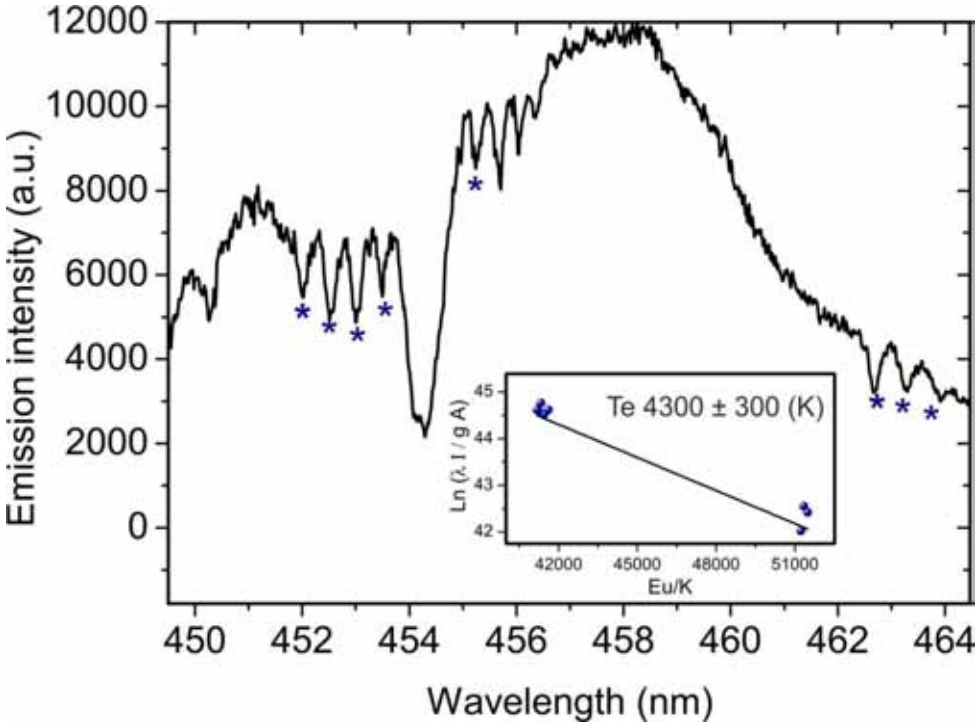

Figure 8.Spectrum of DP-LIBS of Ti in water at 30 bar together with a graphical inset of the corresponding Boltzmann plot.

effect on the cut-off of excited levels due to the high value of the electron number density at the initial stage of the plasma expansion [45]. In this condition, the radiative recombination is the main source of radiation in the plasma and in the specific case of a high pressure liquid medium this phenomenon is particularly effective [33] due to strong confinement. Therefore, as electron number density decreases along the propagation axis, it is reasonable to suppose that, in the external region of the LIP, the Debye-Hückel's limitation of available electronic levels does not occur anymore. Although the initial temperature of the front head of the plasma is very high, the fast transfer of thermal energy from the plasma to the surrounding environment causes the peripheral zone to cool down sooner than the plasma interior and thus the occurrence of self-absorption of the continuum radiation. This effect is very similar to Fraunhofer absorption observed in the spectra of stars and it has been reported in a previous work dealing with DP-LIBS in sea-water, where sodium lines appeared reabsorbed on the continuous Ti-LIP spectrum [23].

In order to exploit the self-absorbed lines for analytical purposes, it is important to check that their intensity is proportional to the total number density of the ablated species, which can be investigated by their atomic energy distribution function. If the distribution has a Boltzmann form, it means that the peak intensities are almost completely absorbed on the continuum, and, through the Boltzmann relation, this implies that the intensity of the single line is proportional to the total number density of the ablated species. The inset of Figure 8 shows the corresponding Boltzmann plot. The absorbed lines have a Boltzmann

distribution which suggests the possible use of such signals for analytical purposes. Moreover, as it has been already demonstrated by Sakka et al. [46], the width of the self-reversed lines can also be used for determining the local electron density, which in this case results to be around 10^{18} cm^{-3} and represents the electron number density in the plasma zone where the species are absorbing the continuum radiation.

In order to optimize the DP-LIBS signal, the emission intensity observed during the Al-target ablation performed at different pressures was investigated. Figure 9shows the absorbed area of the transition of Al (I) at 396.15 nm as a function of the interpulse delay at different water pressures. In order to show the correlation between plasma emission intensity and bubble dynamics, the bubble volume is also reported in the figure. As expected, the maximum intensity was detected at the interpulse delay of maximum bubble expansion. As an example, Figure 10 shows the Al spectra as functions of interpulse delay with a liquid pressure of 30 bar. It is worth noting that, while atomic transitions appear as absorbed peaks on the continuum, ionic transitions appear as typical emission lines. This can be due to two reasons: i) in Debye Hückel's theory the effect on the limitation of the allowed levels depends on the ionization energy of the

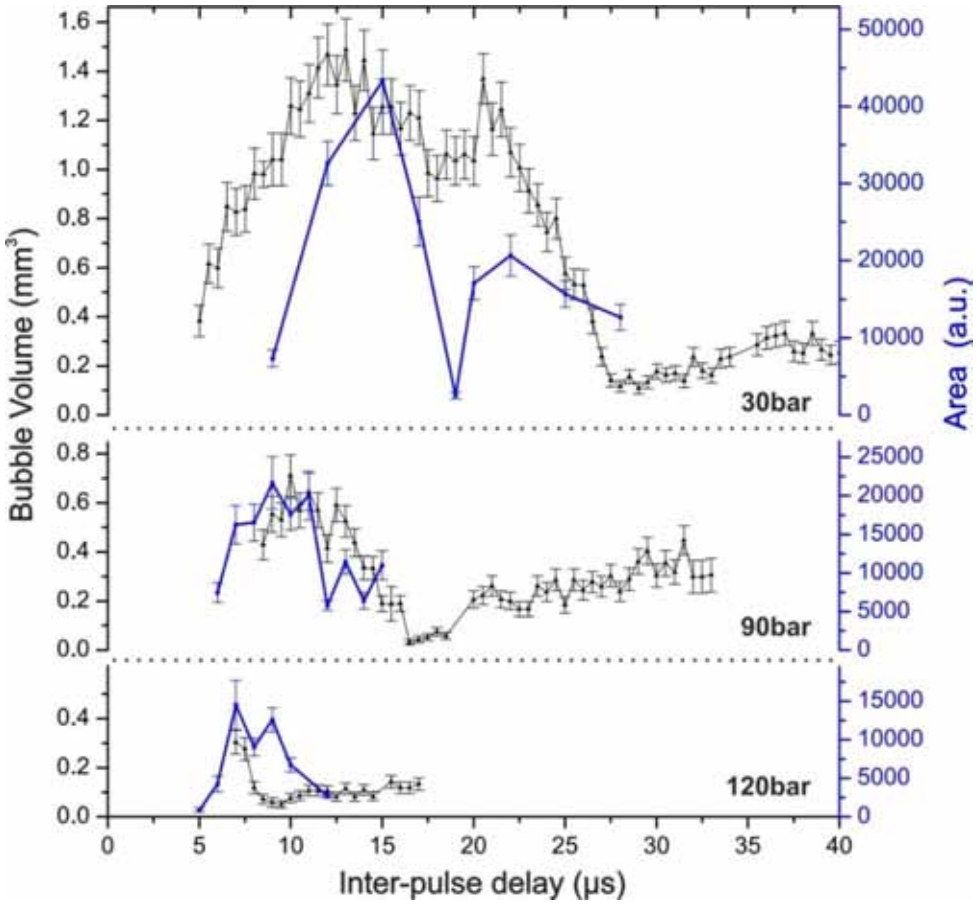

Figure 9.Comparison between the laser-induced bubble volumes and the corresponding area of the DP-LIBS signal of Al (I) at 396.15nm as functions of the interpulse delay at three different pressure values (30, 90 and 120 bar).

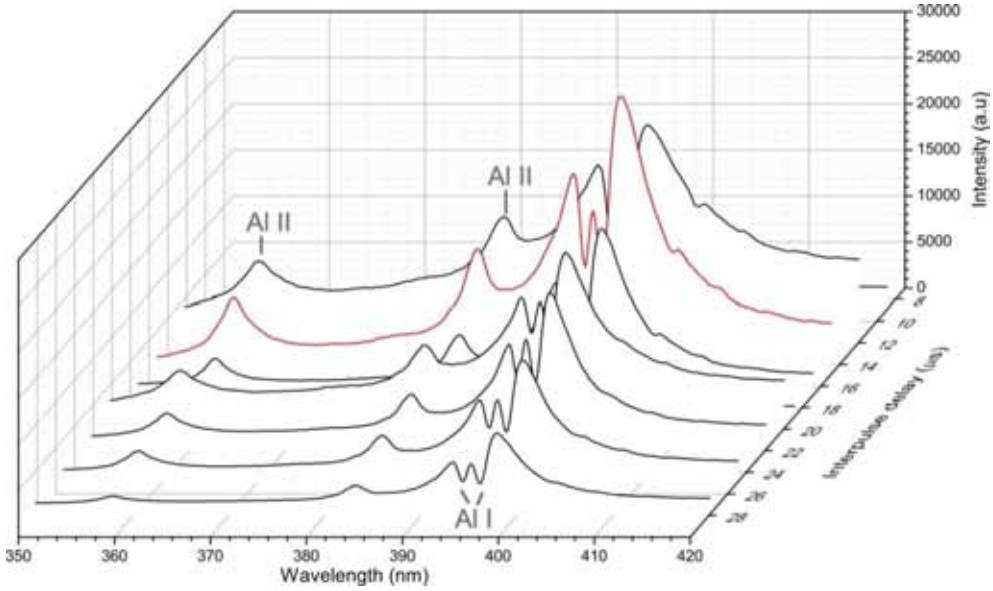

Figure 10.DP-LIBS spectra of Al in water at 30 bar as a function of the interpulse delay.

species. Ions have much higher ionization energy than atoms, thus they are less affected by high electron density effects and their excited levels become available before those of the atoms; ii) ion emission comes from the inner part of the plasma and therefore it does not undergo to Fraunhofer-like absorption effects.

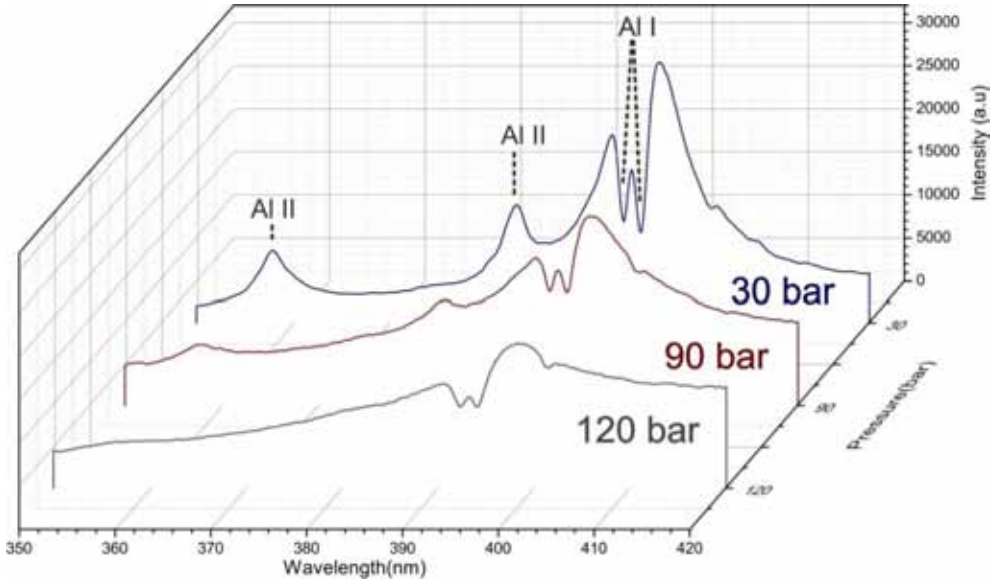

Figure 11.DP-LIBS spectra of Al in water at three different pressures (30, 90 and 120 bar) acquired at the best interpulse delay (15, 10 and 7 μs, respectively).

Figure 11 reports the Al spectra acquired at the best interpulse delay for three different pressures. This figure clearly shows that the amount of spectral information decreases by increasing the working pressure. Indeed, at high pressures the bubble expansion is unable to reach the saturation pressure (i.e. the equilibrium condition with the surrounding liquid [33]), because the high external pressure causes the vapor inside the cavitation bubble to condense. This consideration suggests that the plasma is more and more confined as the liquid pressure increases and, consequently, that the main contribution to spectra is continuum radiation rather than spontaneous emission. Recombination and high density effects become so severe with increasing pressure that at 120 bar even ionic peaks disappear from the spectrum.

4. Conclusions

Time-resolved optical emission spectroscopy and shadowgraph were used to investigate single-pulse bubble formation and double-pulse plasma emission in collinear DP-LIBS of aluminium submerged in water at pressure up to 120 bar. Plasma persistence and cavitation bubble size and lifetime were observed to considerably decrease upon increase of hydrostatic pressure, and the optimum interpulse delay decreased accordingly. Furthermore, as a result of the reduced dimensions and lifetime of the cavitation bubble, also the DP-LIBS emission enhancement decreased by increasing the applied pressure. Finally, we observed that, as a consequence of the fast decrease of temperature in the peripheral regions of the plasma, atomic transitions appear as absorption peaks on the continuum radiation. The intensity of these absorbed spectral lines resulted proportional to the total number density of the ablated species and their atomic energy distribution function had a Boltzmann form. This implies that the peak intensities are almost completely absorbed on the continuum, suggesting that the use of these spectra for elemental analysis with conventional methodologies is still feasible.

5. References

1. B. Thornton, T. Takahashi, T. Sato, T. Sakka, A. Tamura, A. Matsumoto, T. Nozaki, T. Ohki, K. Ohki, Development of a deep-sea laser-induced breakdown spectrometer for in situ multi-element chemical analysis; Deep-Sea Research I 95 (2015) 20–36.
2. A. P. M. Michel, A. D. Chave, Double pulse laser-induced breakdown spectroscopy of bulk aqueous solutions at oceanic pressures: interrelationship of gate delay, pulse energies, interpulse delay, and pressure; Appl. Opt. 47 (2008) 131−143.
3. F. J. Fortes, J. Moros, P. Lucena, L. M. Cabalín, J. J. Laserna, Laser-Induced Breakdown Spectroscopy, Anal. Chem., 85 (2013) 640–669.

4. D.W. Hahn, N. Omenetto, Laser-Induced Breakdown Spectroscopy (LIBS), Part II: Review of Instrumental and Methodological Approaches to Material Analysis and Applications to Different fields; Appl. Spectrosc., 66 (2012) 347– 419.
5. S. Guirado, F. J. Fortes, J. J. Laserna, Elemental analysis of materials in an underwater archeological shipwreck using a novel remote laser-induced breakdown spectroscopy system, Talanta 137 (2015) 182-188.
6. S. Koch, W. Garen, M. Muller, W. Neu, Detection of chromium in liquids by laser induced breakdown spectroscopy (LIBS), Appl. Phys. A 79 (2004) 1071-1073.
7. M. Lawrence-Snyder, J. Scaffidi, S. M. Angel, A. P. M. Michel, A. D. Chave, Laser-Induced Breakdown Spectroscopy of High-Pressure Bulk Aqueous Solutions, Appl. Spectrosc. 60 (2006) 786-790.
8. V. E. McKelvey, Subsea Mineral Resources, Mineral and Petroleum Resources of the Ocean, U.S. Geological Survey Bullletin 1689-A, 1986.
9. Y. Nakajima, B. Thornton, Application of Laser-Induced Breakdown Spectroscopy for In-situ Measurement of Metal Grade for Seafloor Mineral Processing. Oceans 2015 - MTS/IEEE Washington, 1-6.
10. S. Guirado, F. J. Fortes, V. Lazic, J. J. Laserna, Chemical analysis of archeological materials in submarine environments using laser-induced breakdown spectroscopy. On-site trials in the Mediterranean Sea, Spectrochim. Acta Part B 74–75 (2012) 137-143.
11. R. D. Prien, The future of chemical in situ sensors, Mar. Chem. 107 (2007) 422–432.
12. S. Palanco, J. M. Baena, J. J. Laserna, Open-path laser-induced spectrometry for remote analytical measurements on solid surfaces, Spectrochim. Acta Part B 57/3 (2002) 591–599.
13. F. J. Fortes, J. Cuñat, L. M. Cabalín, J. J. Laserna, In situ analytical assessment and chemical imaging of historical buildings using a man-portable laser system, Appl. Spectrosc. 61 (2007) 558–564.
14. I. Gaona, P. Lucena, J. Moros, F. J. Fortes, S. Guirado, J. Serrano, J. J. Laserna, Evaluating the use of Standoff LIBS in architectural heritage: surveying the Cathedral of Málaga, *J. Anal. At. Spectrom.,* 28 (2013) 810 – 820.
15. D. A. Cremers, L. J. Radziemski, T. R. Loree, Spectrochemical Analysis of Liquids Using the Laser Spark, Appl. Spectrosc. 38 (1984) 721–726.
16. M. A. Harith, V. Palleschi, A. Salvetti, D. P. Singh, M. Vaselli, G. V. Dreiden, Y. I. Ostrovsky, I. V. Semenova, Dynamics of laser-driven shock waves in water J. Appl. Phys. 66 (1989), 5194–5197.
17. F. Fama, M. A. Harith, V. Palleschi, A. Salvetti, D. P. Singh, M. Vaselli, G. V. Dreiden, Y. I. Ostrovsky , I. V. Semenova, Hydrodynamics of laser-produced shock waves in water: Reflection and transmission measurements, J. Appl. Phys. 69 (1991) 1660–1665.

18. V. Lazic, S. Jovicevic, M. Carpanese, Laser induced bubbles inside liquids: Transient optical properties and effects on a beam propagation, Appl. Phys. Lett. 101 (2012) 054101-4.
19. V. Lazic, S. Jovićević, Laser induced breakdown spectroscopy inside liquids: processes and analytical aspects, Spectrochim. Acta Part B 101 (2014) 288-311.
20. T. Sakka, A. Tamura, A. Matsumoto, K. Fukami, N. Nishi, B. Thornton, Effects of pulse width on nascent laser-induced bubbles for underwater laser-induced breakdown spectroscopy, Spectrochimica Acta Part B 97 (2014) 94-98
21. A. De Giacomo, M. Dell'Aglio, O. De Pascale, M. Capitelli, From single pulse to double pulse ns-laser induced breakdown spectroscopy under water: elemental analysis of aqueous solutions and submerged solid samples, Spectrochim. Acta Part B 62 (2007) 721–738.
22. A. Casavola, A. De Giacomo, M. Dell'Aglio, F. Taccogna, G. Colonna, O. De Pascale, S. Longo, Experimental investigation and modelling of double pulse laser induced plasma spectroscopy under water, Spectrochim. Acta, Part B 60 (2005) 975–985
23. A. De Giacomo, M. Dell'Aglio, F. Colao, R. Fantoni, V. Lazic, Double-pulse LIBS in water bulk and on submerged bronze samples, Appl. Surf. Sci. 247 (2005) 157–162.
24. V. Lazic, J. J. Laserna, S. Jovicevic, Insights in the laser-induced breakdown spectroscopy signal generation underwater using dual pulse excitation, Part I: Vapor bubble, shockwaves and plasma, Spectrochim. Acta Part B 82 (2013) 42–49.
25. V. Lazic, J.J. Laserna, S. Jovicevic, Insights in the laser-induced breakdown spectroscopy signal generation underwater using dual pulse excitation, Part II: Plasma emission intensity as a function of interpulse delay, Spectrochim. Acta Part B 82 (2013) 50–59.
26. S. Rifai, F. Laville, M. Vidal, J. Chaker, Quantitative analysis of metallic traces in water-based liquids by UV-IR double-pulse laser-induced breakdown spectroscopy, J. Anal. At. Spectrom. 27 (2012) 276-283.
27. A. P. M. Michel, A. D. Chave, Single pulse laser-induced breakdown spectroscopy of bulk aqueous solutions at oceanic pressures: interrelationship of gate delay and pulse energy, Appl. Opt., 47 (2008) 122–130.
28. A. P. M. Michel, M. Lawrence-Snyder, S. M. Angel, A. D. Chave, Laser-induced breakdown spectroscopy of bulk aqueous solutions at oceanic pressures: evaluation of key measurement parameters, Appl. Opt. 46 (2007) 2507–2515.
29. M. Lawrence-Snyder, J. Scaffidi, S. M. Angel, A. P. M. Michel, A. D. Chave, Sequential-Pulse Laser-Induced Breakdown Spectroscopy of High-Pressure Bulk Aqueous Solution, Appl. Spectrosc. 61 (2007) 171–176.
30. B. Thornton, T. Sakka, T. Masamura, A. Tamura, T. Takahashi, A. Matsumoto, Long-duration nano-second single pulse lasers for observation of spectra from bulk liquids at high hydrostatic pressures, Spectrochim. Acta, Part B 97 (2014) 7–12.

31. B. Thornton, T. Sakka, T. Takahashi, A. Tamura, T. Masamura, A. Matsumoto, Spectroscopic Measurements of Solids Immersed in Water at High Pressure Using a Long-Duration Nanosecond Laser Pulse, Appl. Phys. Expresss 6 (2013) 08240-4.
32. T. Takahashi, B. Thornton, T. Ura, T. Sakka, Investigation of influence of Hydrostatic Pressure on Double-Pulse Laser-Induced Breakdown Spectroscopy for Analysis of the Composition of Solids Submerged at High Pressures, Appl. Phys. Express 6 (2013) 042403-3.
33. A. De Giacomo, A. De Bonis, M. Dell'Aglio, O. De Pascale, R. Gaudiuso, S. Orlando, A. Santagata, G. S. Senesi, F. Taccogna, R. Teghil, Laser Ablation of Graphite in Water in a Range of Pressure from 1 to 146 atm Using Single and Double Pulse Techniques for the Production of Carbon Nanostructures, J. Phys. Chem. C 115 (2011) 5123–5130.
34. J. Noack, A. Vogel, Laser-Induced Plasma Formation in Water at Nanosecond to Femtosecond Time Scales: Calculation of Thresholds, Absorption Coefficients, and Energy Density, IEEE Journal of quantum electronics, 35 (1999) 1156-1167.
35. B. Thornton, T. Ura, Effects of Pressure on the Optical Emissions Observed from Solids Immersed in Water Using a Single Pulse Laser, Appl. Phys. Exp. 4 (2011) 022702-3.
36. S. M. Angel, J. Bonvallet, M. Lawrence-Snyder, W. F. Pearman, J. Register, Underwater measurements using laser induced breakdown spectroscopy, J. Anal. At. Spectrom. 31 (2016) 328-336.
37. H. Hou, Y. Tian, Y. Li, R. Zheng, Study of pressure effects on laser induced plasma in bulk seawater, J. Anal. At. Spectrom. 29 (2014) 169-175.
38. B. Thornton, T. Takahashi, T. Ura, T. Sakka; Cavity Formation and Material Ablation for Single-Pulse Laser-Ablated Solids Immersed in Water at High Pressure, Appl. Phys. Express 5 (2012) 102402-3
39. M. Dell'Aglio, R. Gaudiuso, R. Elrashedy, O. DePascale, G. Palazzo, A. De Giacomo, Collinear double pulse laser ablation in water for the production of silver nanoparticles, Phys. Chem. Chem. Phys.15 (2013) 20868-20875.
40. M. Dell'Aglio, A. Santagata, G. Valenza, A. De Stradis, A. De Giacomo, Study of the effect of water pressure on plasma and cavitation bubble induced by Pulsed Laser Ablation in Liquid (PLAL) of silver and missed variations of observable NPs features, Chem. Phys. Chem, 2017, DOI: 10.1002/cphc.201601231.
41. N. Takada, T. Nakano, K. Sasaki, Influence of additinal external pressure on optical emission intensity in liquid-phase laser ablation, Appl. Surf. Sci. 255 (2009) 9572-9575.
42. K. Sasaki, T. Nakano, W. Soliman, and N. Takada, Effect of pressurization on the dynamics of a cavitation bubble induced by liquid-phase laser abaltion, Appl. Phys. Express 2 (2009) 046501-3.

43. M. Lawrence-Snyder, J. P. Scaffidi, W. F. Pearman, C. M. Gordon, S. M. Angel, Issues in deep ocean collinear double-pulse laser induced breakdown spectroscopy: Dependence of emission intensity and inter-pulse delay on solution pressure, Spectrochim. Acta Part B 99 (2014) 172–178.
44. M. Dell'Aglio, R. Gaudiuso, O. De Pascale, A. De Giacomo, Mechanisms and processes of pulsed laser ablation in liquids during nanoparticle production, Appl. Surf. Sci. 348 (2015) 4–9.
45. A. De Giacomo, R. Gaudiuso, M. Dell'Aglio, A. Santagata, The role of continuum radiation in laser induced plasma spectroscopy, Spectrochim. Acta Part B 65 (2010) 385–394.
46. T. Sakka, T. Nakajima, Y. H. Ogata, Spatial population distribution of laser ablation species determined by self-reversed emission line profile, J. Appl. Phys. 92 (2002) 2296-2303.

Chapter 8. Effect of high pressure on laser induced breakdown spectroscopy signal for oceanographic applications

1. Introduction

Laser-induced breakdown spectroscopy (LIBS) is well suited for in situ, non-contact and remote multi-elemental analysis since only optical access to the sample is required for analysis. Additionally, no sample preparation is required and the results are obtained in real time [1, 2]. Advantages of LIBS are particularly useful for applications in extreme, hostile, and inaccessible environments such as surveys of nuclear powers plants [3, 4], planetary [5, 6] and deep-sea explorations [7, 8]. In particular, in the field of oceanography, a large number of studies have focused in the chemical determination of seawater or hydrothermal vent fluids composition. For the chemical and biological point of view, the investigation of the involved processes takes a special relevance in marine chemistry and geochemistry and also in the understanding of the hydrothermal vent ecosystems [9-13]. For this purpose, the integration of LIBS technology in the development of chemical sensors with remotely operated vehicle (ROV) is a future perspective for the technique.

LIBS analysis of liquids has been extensively investigated since 1984 [14]. The dynamics and evolution of laser driven shock waves in water was also discussed in earlier reports [15, 16]. In fact, the laser–water interaction when a laser pulse is focused into a liquid produces rapid heating of the liquid followed by its explosive expansion and formation of a gas bubble [17, 18]. As a consequence, the lifetime of the plasma generated is very short leading to a poor signal when using single pulse excitation. De Giacomo et al. [19] discussed the limitations of this approach for the analysis of liquids and the peculiarities of double-pulse (DP-) LIBS as an invaluable analytical tool for the elemental analysis of bulk water and submerged solid samples from both the experimental and theoretical points of view. However, when LIBS is used for in situ marine applications, the pressure effect induced by the depth is a key parameter that should be considered since it significantly influence the plasma expansion. In previous reports [11, 13, 20], the effect of oceanic pressure on a simulated hydrothermal vent fluid was evaluated. For this purpose, studies were performed up to 270 bar and the experimental conditions for LIBS detection were properly optimized. However, the effect of water pressure was only noticeable in a regime of high energy, resulting in a decrease in signal intensity. Later, in an attempt to improve LIBS detection, the employment of a DP approach was also evaluated [12, 21, 22]. Under simulated oceanic conditions, a weaker emission was achieved even in a DP-LIBS configuration, mainly due to a confinement effect of the laser-induced plasma. Thus, no signal enhancement was observed beyond 100 bar for bulk liquids and 146 bar for immersed solids [23]. Most recently, the use of a long-duration pulse >100 ns can yield significant enhancements in signal quality for underwater samples [24, 25]. Well resolved spectra were acquired for both bulk liquids [26] and submerged solids [27] at pressures up to 300 bar. No effect of external pressure was observed using a long-duration laser pulse. Furthermore, based on these studies, the University of Tokyo incorporated a long-duration laser pulse in a cylindrical probe mounted in the articulate arm of a remotely operated vehicle

(ROV) [7]. This prototype was tested for close-contact multielemental analysis of seawater and hydrothermal deposits at approximately 3000 meters depth.

In the last few years, an application area of growing interest is the chemical characterization of the submerged cultural heritage. The first in-situ submarine LIBS analysis of solid samples was published in 2012 by the University of Málaga [28]. The instrument developed for this task consisted of a main unit for laser-fiber coupling and signal detection, and of an underwater probe, interconnected by means of a 40 m long umbilical cord. The system was controlled from a vessel while the LIBS probe was operated by a professional diver. This prototype was tested using a set of archaeological materials for close-contact multielemental analysis at a depth of 30 meters. An improved version for the remote LIBS instrument based on the transmission of a train of pulses through the optical fiber cable was also presented. The capabilities of the system have been demonstrated for inspection of a shipwreck situated at a depth of 17 m in the Atlantic coast of Andalucía [29, 30].

In view of what found in the bibliography, and the potential capabilities of LIBS technology, it would be feasible to design, in a remotely operated vehicle, a standoff LIBS (ST-LIBS) system to analyze the samples of interest at certain distances. Underwater ST-LIBS involves the delivery of a focused laser pulse toward the distant target through the aqueous media and then, the transmission of the light emitted by the laser-induced plasma back to the detection system. In a previous report, the potential of LIBS analysis in an open-path configuration for chemical characterization of archaeological materials [31] was investigated. The experiment was carried out in the laboratory inside a water tank at atmospheric pressure. Based on these preliminary results, the main motivation of this work is to increase the range of analysis. Thus, several experiments have been performed in a high pressure chamber in order to evaluate LIBS response under oceanic pressure. Experimental considerations including the lasers beam energy, the interpulse delay time and the configuration for plasma collection have been evaluated. The effect of water temperature on LIBS signal has been also studied. In addition, the possibility to analyze complex sample of greater archaeological interest such as copper alloys has been also evaluated at different pressure values.

2. Experimental set-up

2.1. Instrument

A laboratory LIBS system was designed to operate with a high-pressure chamber. A schematic diagram of the experimental setup can be seen in Figure 1. The laser source was at 532 nm Q-switched Nd:YAG (10 Hz, 400 mJ pulse^{-1}, 7 ns pulse width) dual pulse laser system (Brilliant Twins, Quantel, France). Both delivered laser beams are spatially overlapped and were directed via two reflecting mirror and a dichroic mirror (with high reflectivity for 532 nm at 45º and transparent to the emission of the plasma), the

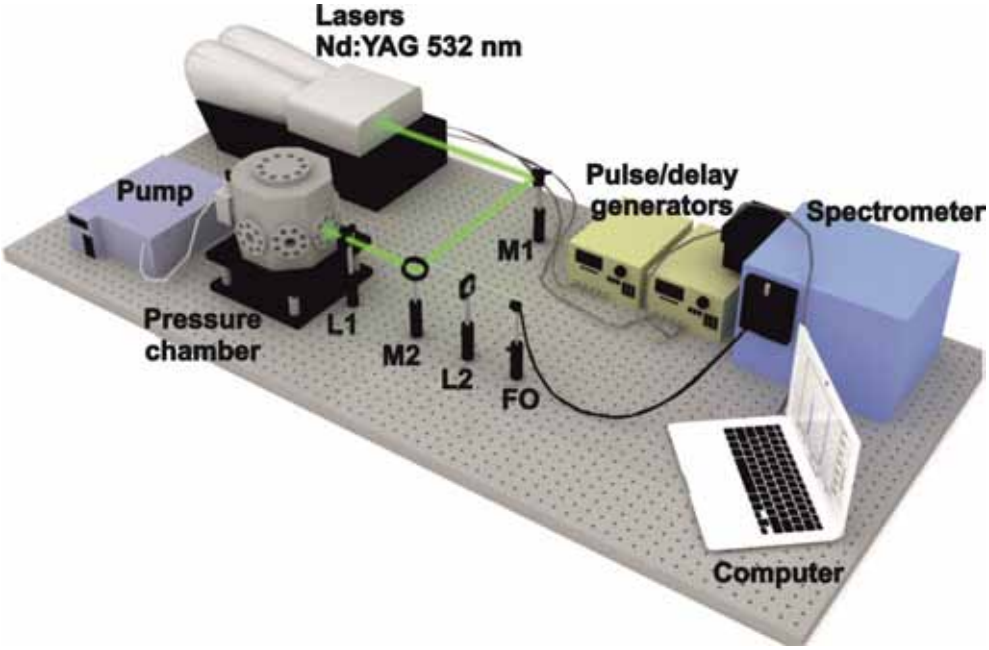

Figure 1: Experimental set-up. M1 mirror; M2 dichroic mirror; L1 focusing lens; L2 collimating lens; FO fiber optic.

latter being placed just before the focusing lens, into the sample surface. In order to simulate the real conditions in a marine environment, samples were placed (perpendicular to the laser beam) inside a high pressure chamber of 80 ml capacity and 135 mm x 130 mm x 115 mm dimensions. The high pressure chamber has been extensively described in *Chapter 3*. The chamber was positioned on three crossed stages which allow precise movement in *xyz directions*. The laser beam was focused onto the sample surface by a BK7 lens, 75 mm focal length and 1 inch diameter. The output energy was variable depending on the experiment, reaching a maximum value of 160 mJ pulse^{-1} for the first laser and 215 mJ pulse^{-1} for the second laser. The repetition rate was set at 10 Hz. Plasma emission was observed along the optical axis through the dichroic mirror and was focused by a plano-convex BK7 lens (100 mm focal length and 2 inch diameter) into the spectrometer with an optical fiber (2 m length, 600 µm diameter, NA 0.22). The spectrometer is Shamrock 303i (Andor Technology) Czerny–Turner scheme (303 mm focal length, f/4, 15 µm slit) fitted with an intensified charge-coupled device (ICCD) detector (1024 x1024 pixel, 26 mm pixel, intensifier tube diameter 25 mm). The gathered light was then spectrally resolved using two diffraction gratings with 1200 groove mm^{-1} blazed at 300 nm and 300 groove mm^{-1} blazed at 500 nm , which provided a spectral window of 40 nm (0.04 nm spectral resolution) and 140 nm (0.14 nm spectral resolution), respectively. Operation of the lasers was externally controlled by a delay and pulse generator (Berkeley Nucleonic model 565-4C) which allows the synchronization of both laser pulses and the control of data acquisition and interpulse delay. The target was moved and the water was changed to avoid the effect of the formation of the suspended particulate. In general, to improve the sensitivity, the signal was integrated for 5 laser shots.

2.2. Samples

Optimization of experimental conditions was performed using a Fe foil (Sigma-Aldrich, 250 mm nominal thickness and purity better than 99.9%). In addition, two certified bronzes standard (BCR 691) with variable concentrations (*Bronze A*: 78.7 % Cu, 7.2 % Sn, 7.9 % Pb, 6 % Zn, 0.2% As; *Bronze B*: 82.7 % Cu, 2.1 % Sn, 0.4 % Pb, 14 % Zn, 0.8 % As) were also used. Data were obtained by averaging 5 laser shots and was measured 10 times in each different position.

3. Results and discussion

Due to the confinement of the plasma by the nearly incompressible liquid medium and to the fast transfer of energy from the plasma to the surrounding liquid, the spectral emission is characterized by a really short duration, leading to a poor signal when using single pulse excitation [32]. In order to increase LIBS performances in liquids, several experimental configurations, mainly based in a sequential excitation approach, has been suggested in the literature [19]. In this approach, the first laser pulse produces a gas bubble whereas the second pulse ablates the sample and re-excites the plasma inside the bubble. Figure 2 presents a comparative LIBS spectra of a bronze sample in both single pulse and double pulse configuration taken underwater. As observed, no signal emission was collected in single-pulse excitation,

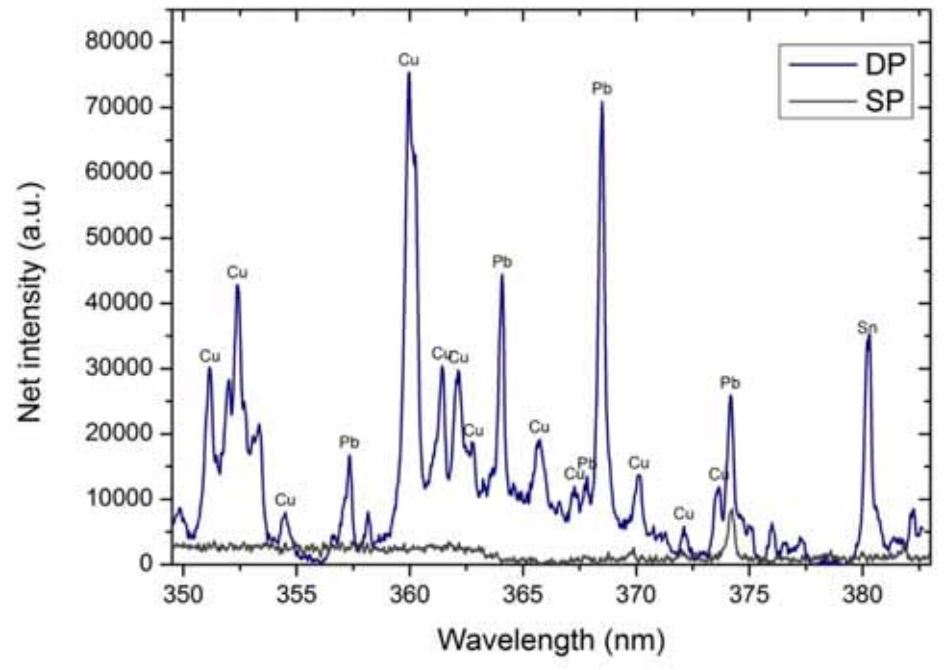

Figure 2. Comparison of LIBS spectra of bronze sample taken after single (Laser energy 216 mJ, gate width 500 ns, delay time acquisition 15 ns) and dual pulse (First laser energy 160 mJ, second laser energy 216 mJ, gate width 8 μs, delay time acquisition 100 ns, interpulse delay time 100 μs) excitation.

while the spectra collected after the second pulse shows the characteristic emission lines of the sample. However, as seen in *chapter 7*, the enhancement of signal intensity will be correlate to the moment of maximum expansion of the bubble induced by the first laser pulse. Thus, optimization of temporal conditions is almost critical. On the other hand, some operational parameters such as laser pulse energy, the configuration of the collection system as well as the effect of water temperature on signal emission take a special relevance in the LIBS application for oceanography.

3.1. Underwater DP LIBS of solid samples. Optimization of temporal conditions

Figure 3 shows the temporal evolution of an iron target submerged in water at atmospheric pressure. In order to improve the signal to noise ratio (SNR), emission spectra were averaged over five laser shots. Initially, the typical high background spectral, which is essentially due to mechanisms involving free electrons (inverse Bremsstrahlung, radiative recombination, photo-ionization) [32] prevails. Several tens of nanoseconds after the laser pulse arrives, spectral lines start to be more clearly defined from the spectral continuum. Here the electron number density is still very high and the spectral lines are broadened by the Stark effect due to electron collisions [33]. For the remaining part of the expansion, the spectral characteristics are governed by the decreasing electron number density, and consequently the spectral lines become smaller and narrower. Optimization of the acquisition delay was based on the signal to noise ratio. Results are plotted in Figure 4. The emission line of Fe (I) at 330.57 nm was selected. As shown, the maximum signal to noise ratio, approximately 60 (a.u.), was acquired at 300 ns.

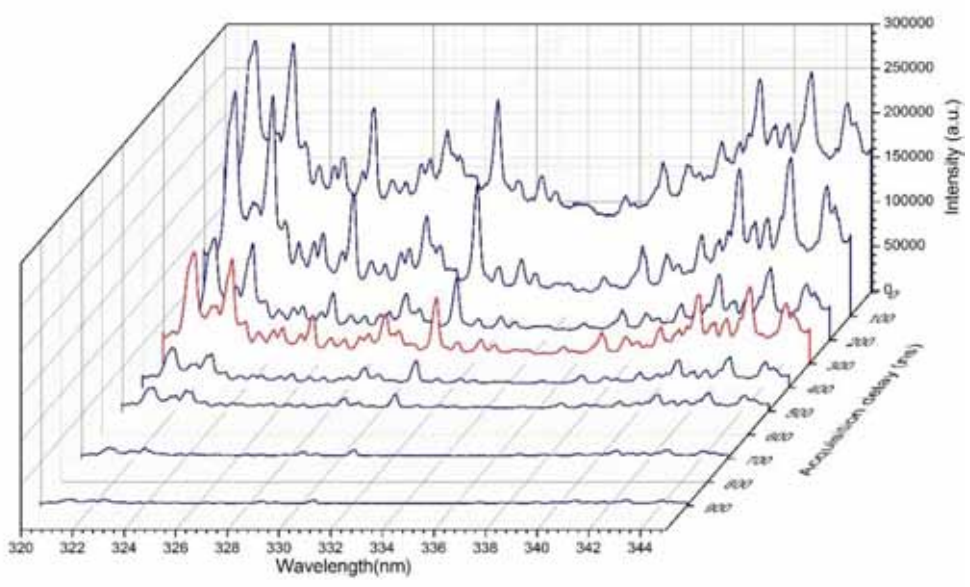

Figure 3. Emission spectrum of iron in water at different delay time after the second laser pulse. Gate width 200 ns and interpulse delay time 100 μs. The selected value at 300 ns is in red.

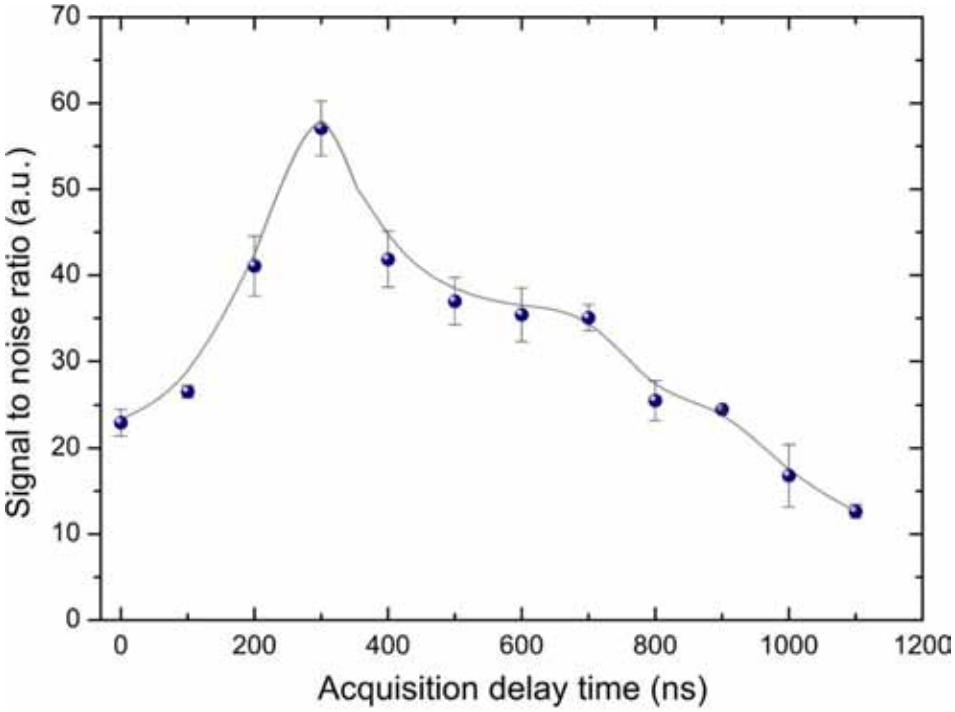

Figure 4. Signal to noise ratio of iron at 330.57 nm in water at different delay times after the second laser pulse. Gate width 200 ns and interpulse delay time 100 μs.

In this experiment, the signal to background ratio was studied as a function of the interpulse delay time (Δt). As observed in Figure 5, a more intense and well resolved signal was acquired at Δt 125 μs, that will be coincident at the maximum bubble expansion created by the first laser pulse. This fact was explained in detail in *Chapter 7* and also is in good agreement with those found in a previous report [34]. In the present study, spectra were acquired in the temporal range between 25 to 400 μs. As revealed by the LIBS spectra appearing in the inset of Figure 5, the selection of the optimum interpulse delay time is critical and have a significant influence over the spectral resolution and the analytical quality of LIBS spectra. The inset of Figure 5 shows that the signal-to-background ratio is higher at the optimum Δt, 125 μs, when compared to 25 and 400 μs, at the beginning and the collapse of the bubble expansion, respectively.

However, signal enhancement observed at atmospheric pressure does not correspond to an increase in the water pressure. Figure 6 compares the temporal evolution of the laser-induced plasma in iron, in both 1 and 25 bar. As shown, both pressures present a similar trend although the acquired emission spectra are higher at atmospheric pressure. Also, signal intensity initially increases with Δt at a similar rate. The emission line Fe (I) at 330.57 nm was selected. Nevertheless, the plasma lifetime is considerably reduced when increasing the water pressure. In this sense, the optimum interpulse delay time (Δt_{opt}) decreases rapidly from 125 μs at 1 bar, to 11 μs at 25 bar. For this experiment, the employed energy was 60 mJ pulse^{-1} for the first laser pulse and 92 mJ pulse^{-1} for the second laser pulse. Furthermore, results obtained are in good agreement with those described in *Chapter 7*, in which an increase in water pressure

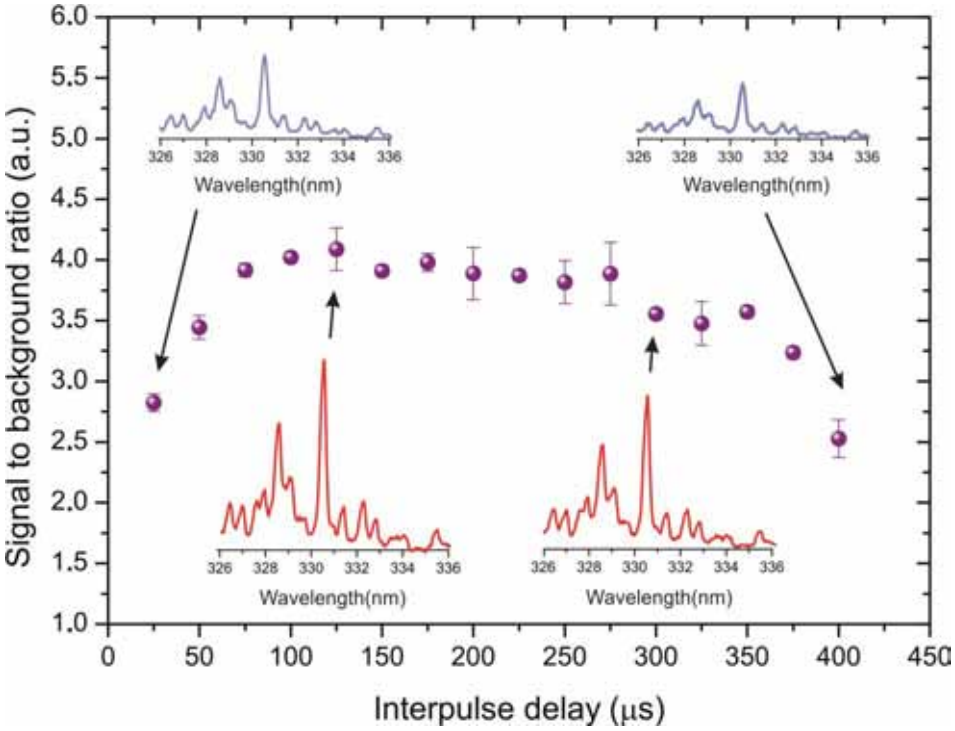

Figure 5. Signal to background ratio of Fe (I) at 330.57nm as a function of the interpulse delay time (Δt). Spectra inset correspond to interpulse delay 25 and 400μs in blue; 125 and 300 μs in red. E_1 61 mJ, E_2 215 mJ, gate width 8 μs, delay time acquisition 300 ns.

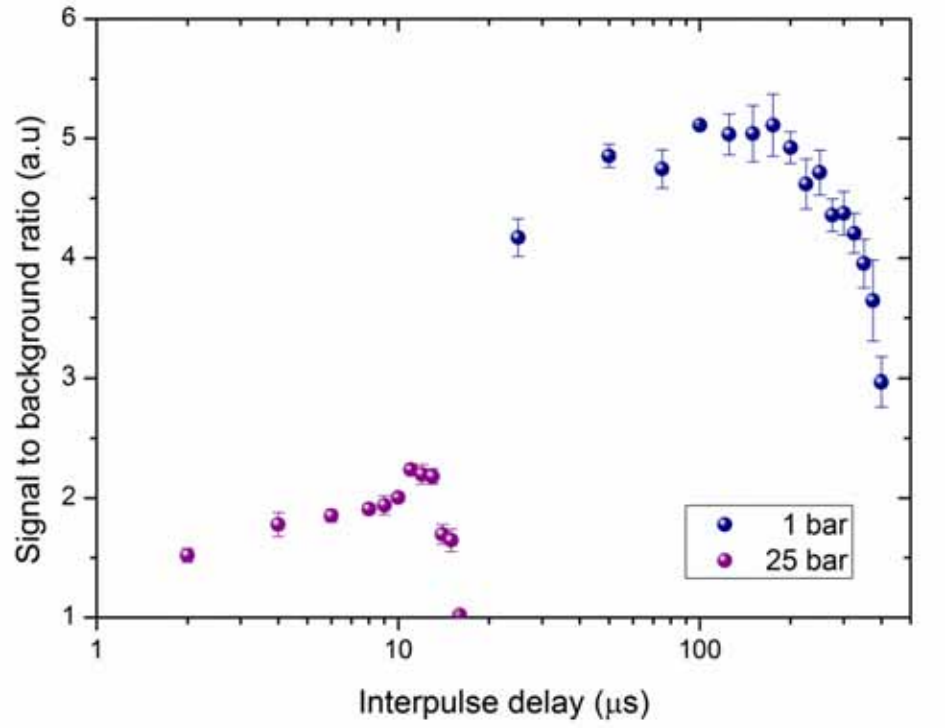

Figure 6. Signal to background ratio of Fe (I) at 330.57nm as a function of the interpulse delay time (Δt) at two different pressures. E_1 60 mJ, E_2 92 mJ, gate width 8 μs, delay time acquisition 300 ns.

(1–120 bar) caused a significant decrease in the maximum bubble size and bubble lifetime. Thus, the optimum interpulse delay, coincident with the maximum bubble expansion in which is observed the maximum emission intensity, was reached at shorter interpulse delay. Furthermore, these trends also are coincident with previous reports [22, 34].

3.2. Underwater DP LIBS of solid samples. Influence of laser energy

Once optimized the temporal conditions for underwater DP-LIBS, the next step was to evaluate the influence of laser beam energy on LIBS signal. At this point, in the case of iron, the optimum temporal conditions are: Δt, 125 μs at 1 bar and 11 μs at 25 bar; gate delay (t_d), 300 ns; and the integration time 8 μs.

In order to simplify the study, the experiment was initially performed at atmospheric pressure. The emission line Fe (I) 330.57 nm was used for this purpose. In a first step, the energy of the first laser pulse (E_1) was evaluated in the range 36-162 mJ pulse^{-1} while the energy of the second laser pulse (E_2) was kept constant at 215 mJ pulse^{-1}. Each point in the graph results from the averaged of ten spectra. Results are depicted in Figure 7. The signal to background ratio (SBR) is plotted as function of the interpulse delay time in the range from 0 to 500 μs, at different E_1 values. As observed, at higher E_1, 162 mJ pulse^{-1}, the signal to

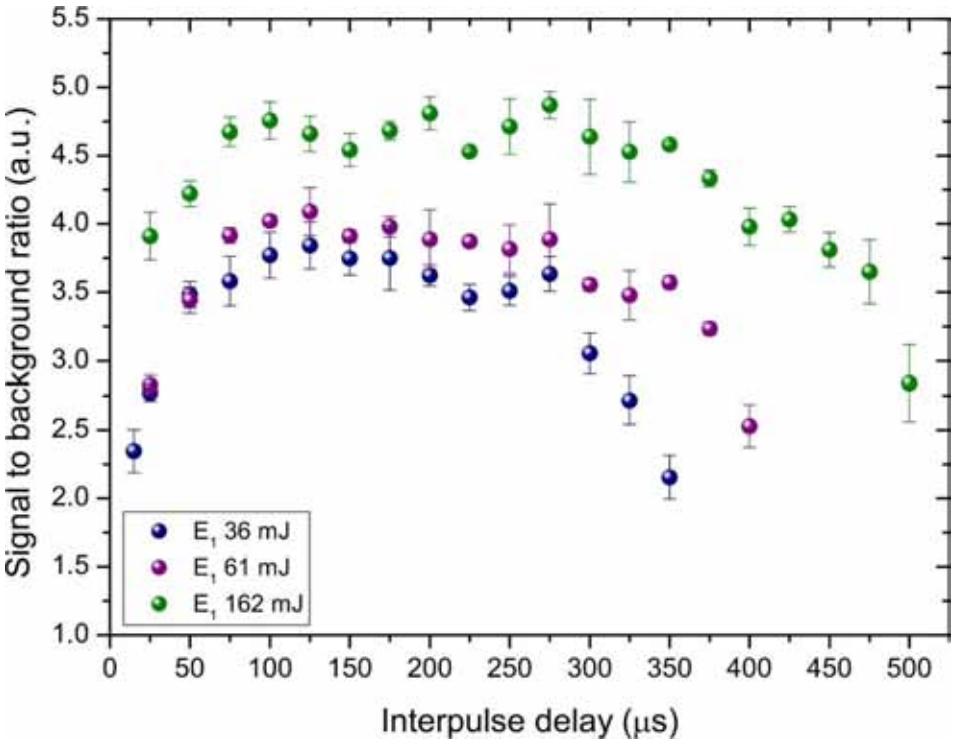

Figure 7. Effect of E_1 on the signal to background ratio of Fe (I) at 330.57nm as a function of the interpulse delay time (Δt) at 1 bar. E_2 was kept constant at 215mJ.

background ratio is larger, probably due to that a more energetic first plasma is induced at higher pulse energy. In addition, the lifetime of the laser-induced plasma is considerably reduced from 162 mJ pulse^{-1} to 36 mJ pulse^{-1}. This fact could be due to that at 162 mJ pulse^{-1} the plasma induced by the first laser pulse produced a longer bubble lifetime in which the maximum bubble expansion is kept for longer time. This hypothesis is in good agreement with the results explained in *Chapter 7*. There, the size of the laser-induced bubble was measured by shadowgraphy and was compared to the emission intensity after the second laser pulse. Thus, it was observed that signal intensity was directly proportional to the bubble volume. Moreover, in *Chapter 7*, the effect of pressure over the bubble lifetime and bubble dynamics was also described.

On the other hand, the effect of E_2 on LIBS signal is shown in Figure 8. For this experiment, E_2 was evaluated in the range 7-215 mJ pulse^{-1} while E_1 was kept constant at 60 mJ pulse^{-1}. As seen, at atmospheric pressure, signal intensity increases until reaching a maximum value at 50 mJ pulse^{-1}. From here, LIBS intensity start to decrease probably due to the plasma shielding effect. Plasma shielding occurs when the plasma itself reduces the transmission of the laser-pulse energy along the beam path like what was observed in previous report [13]. At higher pressure, 25 bar, the behaviour of signal intensity is quite similar. In fact, results depicted here show that the optimization of laser beam energy depends on two aspects: a) E_1 must be set at the maximum energy to provide an increased bubble lifetime, and b) E_2 must be set to a certain value that avoid the plasma shielding effect.

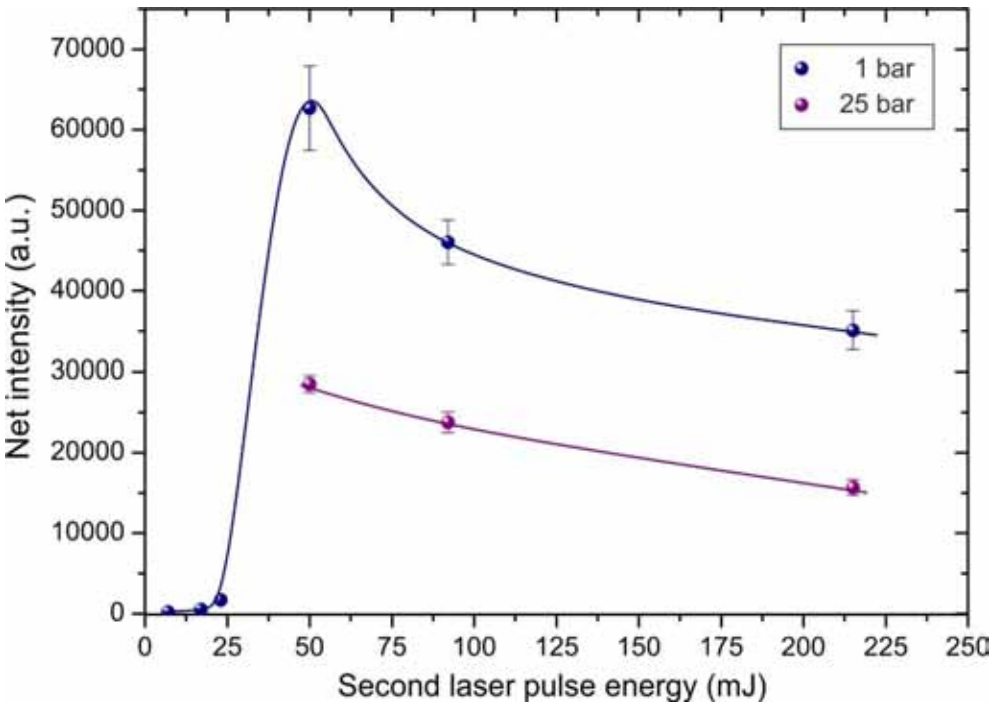

Figure 8. Effect of E_2 on the LIBS signal intensity of Fe (I) at 330.57nm at two different pressures. E_1 was kept constant at 60 mJ. Interpulse delay was fixed at 125 and 11 μs for 1 and 25 bar respectively.

3.3. Influence of plasma light collection geometry

Figure 9 compares the influence of plasma collection geometry on LIBS signal. Several alternatives has been proposed for plasma collection. The schematic diagrams are detailed in Figure 9A. Thus, the optical arrangements for plasma collection were evaluated: i) orthogonal to the incident laser pulse, ii) 45º with respect to the incident laser and iii) coaxial to the incident laser pulse. As described in the *experimental set-up section* of this *Chapter*, the focusing of the laser beam radiation was exactly the same for the three evaluated configurations.

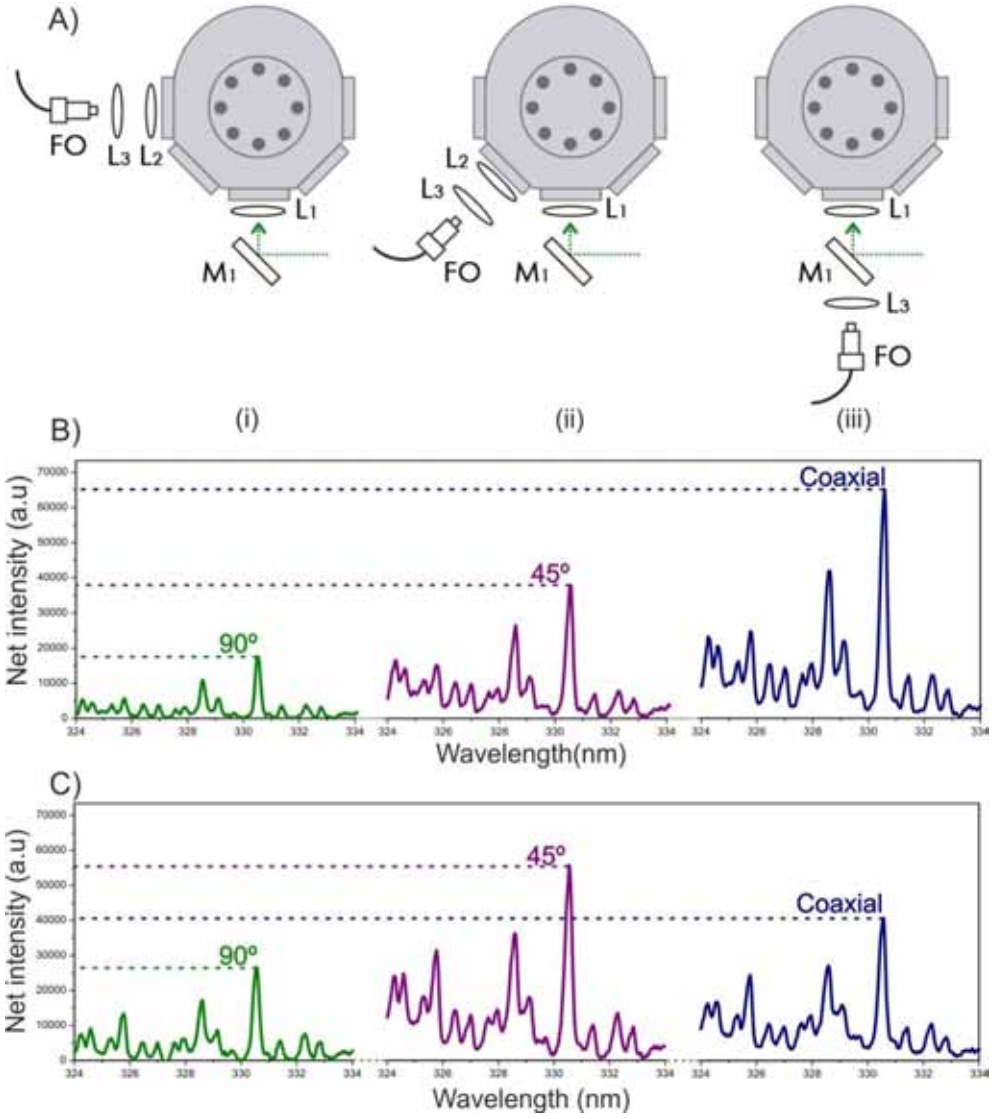

Figure 9. A) Optical collection geometry used. FO fiber optic, M1 is a dichroic mirror, L1 and L2 is a plano-convex lens 75 mm focal length, and L3 is a plano-convex lens 100 mm focal; B) LIBS signal intensity of Fe (I) at 330.57nm at different collection geometry using E_1 60 and E_2 50 mJ; C) LIBS signal intensity of Fe (I) at 330.57nm at different collection geometry E_1 60 and E_2 215 mJ.

Underwater plasmas were performed in iron samples. Figure 9B shows LIBS spectra in the spectral range 324-334 nm for three proposed alternatives at experimental conditions of E_1 60 mJ pulse^{-1}, E_2 50 mJ pulse^{-1} and Δt: 125 µs. The emission line Fe (I) at 330.57 nm was selected for LIBS experiments. Under these conditions, the maximum signal intensity was observed in the coaxial configuration, 65000 counts, in contrast to the 38000 and 17000 counts achieved at 45º and 90º, respectively. This fact could be attributed to that maybe a minor section of plasma light emission is collected at 45º and 90º configuration. However, the plasma is entirely focused in the FO using a coaxial configuration, hence increasing the quality of LIBS signal.

However, when increasing the energy of E_2, the maximum signal intensity was achieved at 45º with respect to the incident laser pulse. The corresponding LIBS spectra are plotted in Figure 9C. In this case, the experimental conditions were E_1 60 mJ pulse^{-1}, E_2 215 mJ pulse^{-1} and Δt: 125 µs. As described in *section 3.2*, a plasma shielding effect was observed at higher E_2 values [13, 34]. Thus, the shielding effect interrupts the light transmission through the optical path in the coaxial configuration. This effect is less pronounced when the plasma light was collected at a certain degree with respect the incident laser pulse, it means 45º and 90º. Nevertheless, best results were achieved using low energy value and a coaxial collection configuration. In view of these results, the design and develop of an oceanographic sensor would be simplified with a coaxial DP LIBS configuration.

3.4. Influence of water temperature on LIBS signal

Figure 10 shows the influence of water temperature on the LIBS signal. For this study, the applied pressure was 1 and 25 bar in a water temperature range of 5 ºC to 30ºC. The selected spectral line for this study was Fe (I) 330.57 nm and the interpulse delay time was set at the optimum for each pressure (1 bar, Δt: 125 µs; 25 bar, Δt: 11 µs). The laser beam energy was E_1: 160 mJ pulse^{-1} and E_2: 215 mJ pulse^{-1}. Water was sequentially cooled in steps of 5 ºC. The water temperature was appropriately homogenized throughout the water volume in order to ensure that the temperature in the vicinity of the sample was the same as the rest of the chamber. Each point in the graph represents the average intensity of 5 replicate measurements. As shown, the signal intensity markedly falls in the range of 15ºC to 20ºC. From here, the slope is quite smooth and the signal gradually decreases up to 5 ºC. This behaviour is similar in both pressures. Hence, results obtained at 25 bar are quite promising and suggest the possibility of LIBS analysis at least at 250 meters deep since at this pressure the water temperature is around 20 ºC [31]. Thus, assuming that in DP-LIBS the plasma features strongly depend on the laser-induced bubble created by the first laser pulse; it is plausible that variations in the properties of water will affect the cavitation dynamics and bubble expansion and consequently the signal emission [35]. In water, the refractive index *n* increases with salinity pressure, with a decrease in temperature. In principle, one might think that a

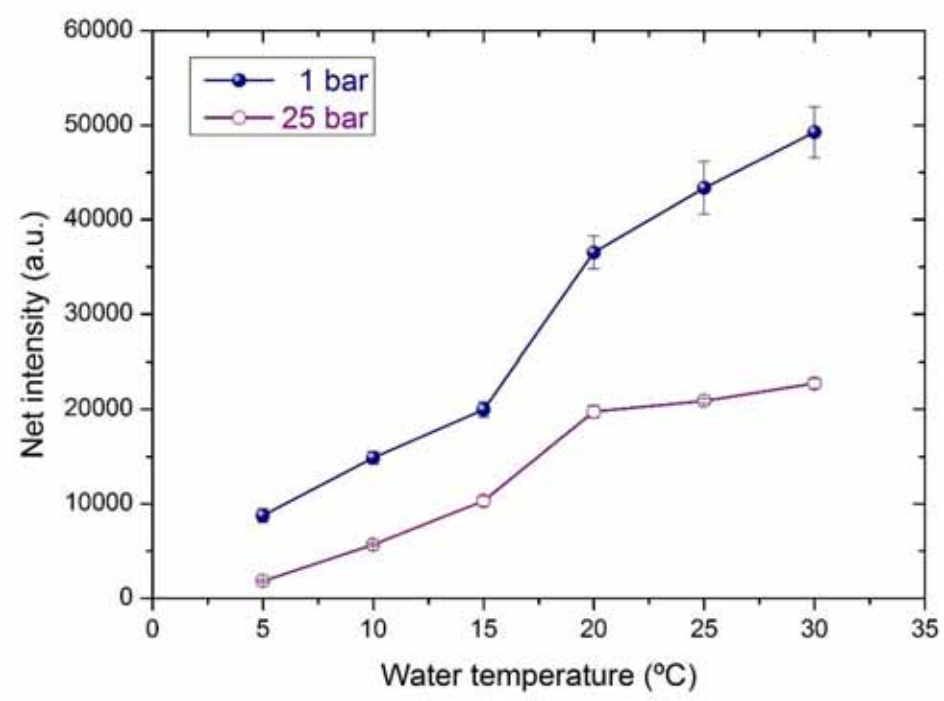

Figure 10. Effect of water temperature on the LIBS signal of Fe (I) at 330.57nm at two different pressures. Interpulse delay was fixed at 125 and 11 μs for 1 and 25 bar respectively and E_1 160 mJ E_2 215 mJ.

change in the refractive index may affect the focal beam conditions, however, at atmospheric pressure *n* is calculated to be 1.333 at 0 ºC and 1.332 at 20 ºC; and at 25 bar 1.333 at 20ºC [36]. Therefore, this change is negligible and reasonably discards this possibility. Other properties of water such as density and viscosity also change with temperature. As shown in Table 1 [37], both parameters are inversely proportional to the temperature. In the range from 15ºC to 5ºC the water density is close to its maximum 0.999 g/cm^3; and the viscosity increases around 34%. These data are compatible with the change in slope observed in Figure 10. The increase in density and viscosity affects the dynamics of the cavitation bubble, slowing down its expansion and increasing the time needed to reach its maximum radius. At a fixed interpulse delay, the second pulse does not interact with the solid at the maximum bubble expansion, so the signal enhancement due to DP-LIBS is less effective, thus explaining the decrease in signal emission with the decrease of water temperature [31].

In addition to this, plasma formation inside liquids lack efficiency because a great percentage of laser energy is expended for liquid vaporization. Thus, only a portion of the incident laser radiation is involved in material ablation. At low water temperature, this effect could be even more pronounced due to the large thermal diffusivity of iron 2.5 x 10^{-5} m^2 s^{-1} [38]. Then, also the decrease in signal emission may be explained to a certain extent by energy cost for heating the sample due to decreasing of the environment temperature.

Table 1. Properties of water such as density and viscosity as function of temperature [37].

Temperature (°C)	Density (g/cm^3)	Viscosity 10^{-3} (Kg/m s)
5	1	1.5182
10	0.9997	1.3059
15	0.9991	1.1375
20	0.9982	1.0016
25	0.997	0.89
30	0.9956	0.7972
35	0.994	0.7191

3.5. Influence of water pressure on LIBS signal. Matrix effect

In situ chemical analysis of submersed materials constitutes a technology area of growing interest. In subaquatic archaeology, metallic objects are the most appreciated due to their shortage and intrinsic heritage value. Knowledge of quantitative elemental composition of this kind of samples makes possible the assignment of the manufacturing period and the classification of the metallic objects. Hence, the chemical composition extracted from a LIBS analysis gives archaeologists additional information to better understand our history. In the particular case of copper-based alloys, the matrix effects of this kind of sample which provides a different plasma behaviour, due to the variation of physical and chemical properties of the elements integrating the matrix and consequently influence the mass ablation rate and other processes occurring in the plasma. The objective of this study was to evaluate the influence of water pressure on matrix effects. For this purpose, two bronze samples were examined in the range 1-60 bar. The laser beams energies were E_1: 160 mJ pulse^{-1} and E_2: 215 mJ pulse^{-1}. LIBS spectra were acquired in the spectral range 380-525 nm. The main emission lines of Cu at 521.82 nm, Pb at 405.78 nm and Zn at 481.05 nm were selected for this study. It must be taken into account that no self-reversal was observed in LIBS spectra. Figure 11 shows a comparative LIBS spectra of a bronze sample at different water pressures, 1 bar and 40 bar. As shown, the species are well identifiable although signal intensity is lower at higher pressure. In addition, the spectra acquired at 40 bar revealed a line width substantially larger than that observed at 1 bar.

Figure 12 shows line broadening of the Zn (I) 481.05 nm as a function of water pressure. As shown, line broadening increases almost a factor of 2.5x when water pressure increases from 1 bar to 60 bar. This fact may be a consequence of confinement effect of plasma and the collisions in the confined volume close to the target [19]. In addition, as described in *Chapter 7*, the dynamics, lifetime and maximum radius of the cavitation bubble remarkably depend on the pressure characteristics. Figure 13 shows that the optimum interpulse delay drops significantly as a function of the water pressure. The optimum interpulse

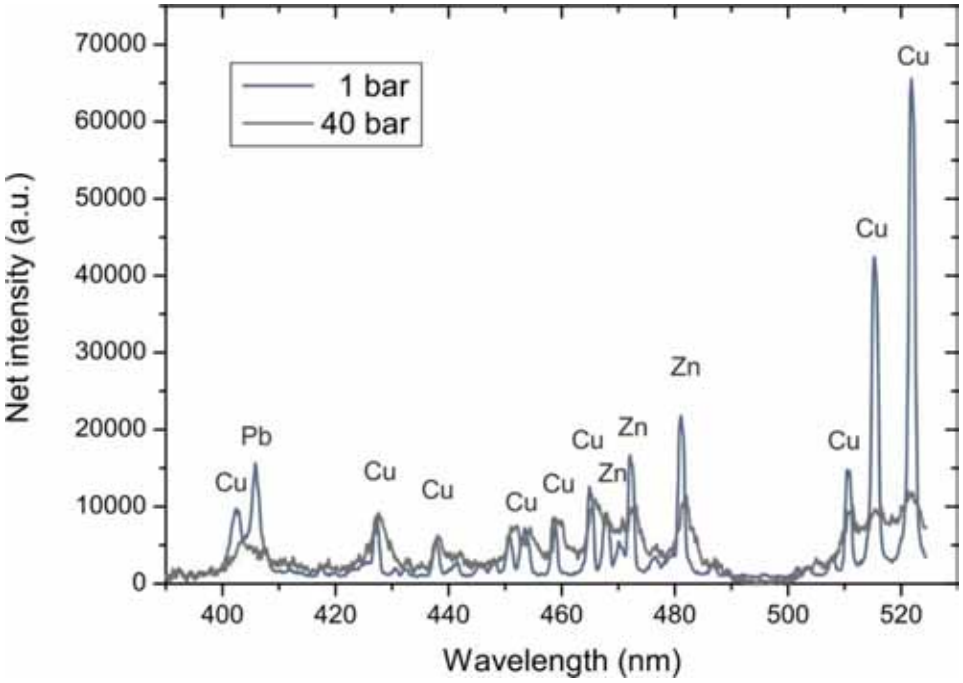

Figure 11. Underwater LIBS spectra of sample bronze B at 1and 40 bar pressure. E_1 160 mJ, E_2 215 mJ, gate width 5 µs, delay time acquisition 200 ns and interpulse delay time 200 µs and 2 µs, respectively.

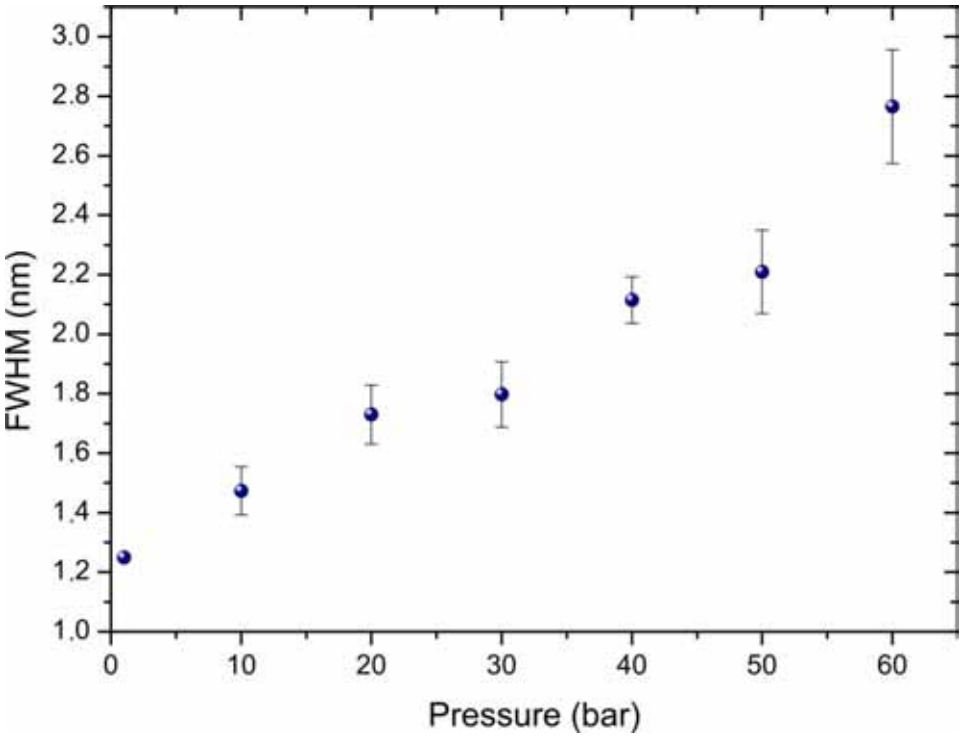

Figure 12. Influence of pressure on the full Width at Half Maximum (FWHM) of the emission line of Zn (I) at 481.05 nm.

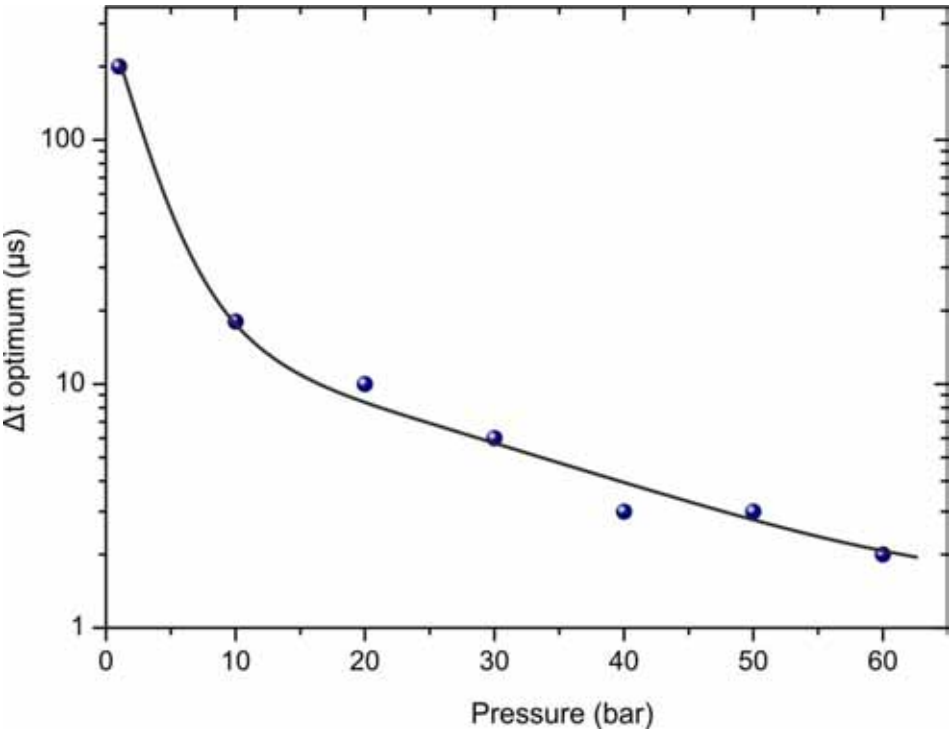

Figure 13. Influence of hydrostatic pressure on the optimum interpulse delay time.

delay falls from 110 μs at 1 bar to approximately 2 μs when the water pressure increases up to 60 bar. For comparative purposes, the signal-to-background ratio (SBR) for the emission lines of Cu and Zn as function of Δt is plotted in Figure 14. Results show that it exits a difference in the SBR values found for Cu and Zn at 1 bar. However, at higher pressure, the measured SBR is almost coincident for both species, Cu and Zn. Based on these results, it seems that (when compared to the atmospheric pressure) exits a fraction effect which provides a different plasma behavior, due to the variation of physical and chemical properties of the elements integrating the matrix and consequently influence the mass ablation rate and other processes occurring in the plasma. In order to elucidate this phenomena, the Zn/Cu and Pb/Cu intensity ratios for the samples *bronze A* and *bronze B* as function of the water pressure has been plotted in Figure 15. The range of pressure was 1-60 bar. In both samples, Figure 15A and Figure 15B, intensity LIBS ratio significantly changes as function of the water pressure. In this sense, at higher pressure, the laser-induced plasma is enriched in Zn and Pb with respect to the Cu content. In fact, as explained above, this behavior can be attributed to matrix effects; it means that a preferential ablation or fractionation of some species in the laser-induced plasma may occur [39].

In fact, a thermal vaporization mechanism characterizes ns- laser ablation and the interaction between the laser pulse and the transient states of the elements in the plume could also evaporate material

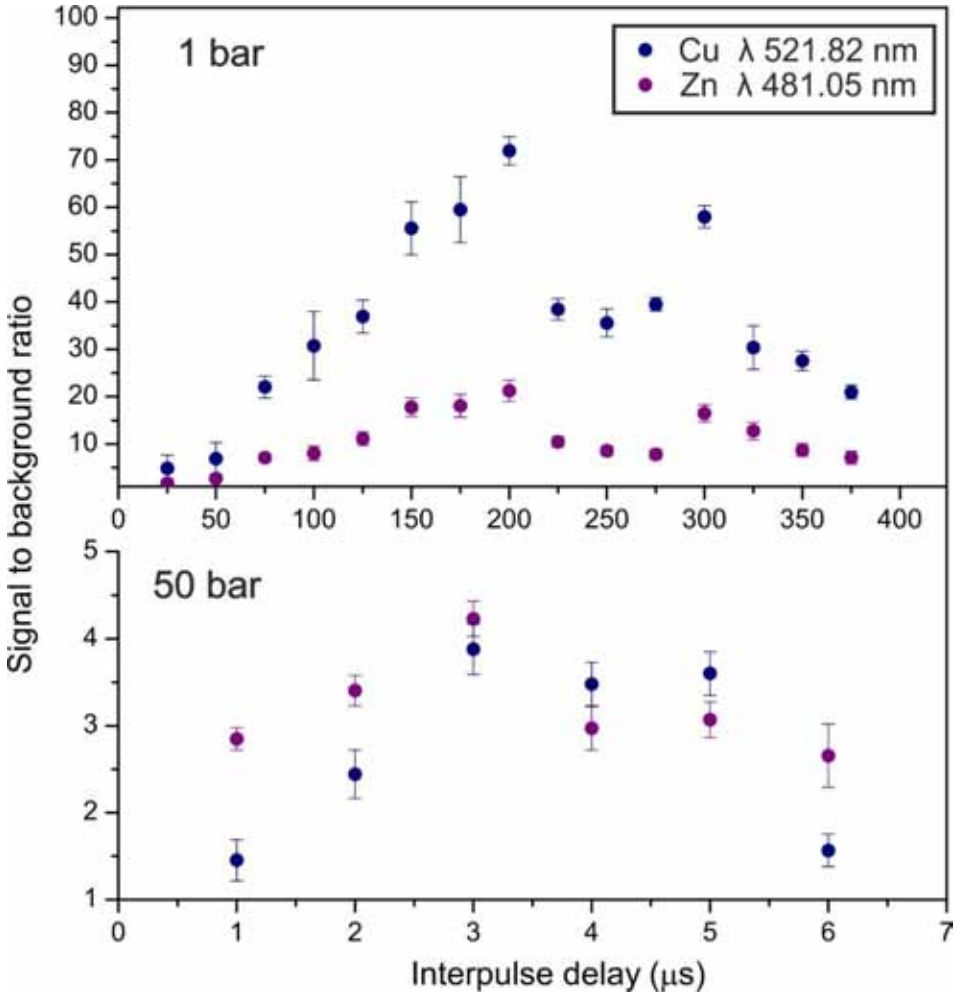

Figure 14. Signal to background ratio of Cu (I) at 521.82 and Zn at 481.05 nm as a function of the interpulse delay time (Δt) at two different pressures.

from the sample surface doing this effect even more pronounced. Due to this constraint, the variation observed in the LIBS intensity ratio may be attributed to different rates of volatilization or atomization processes for Zn (latent heat of vaporization, 1748 J/g; T melting, 420 ºC; T boiling, 907 ºC), Pb (latent heat of vaporization, 862 J/g; T melting, 327 ºC; T boiling, 1740 ºC), and Cu (latent heat of vaporization, 4790 J/g; T melting; 1083 ºC; T boiling, 2595 ºC) in the plume. This effect, which is well documented for copper-based alloys [40, 41] is related to plasma shielding that in our experiment this parameter could be associated to plasma confinement due to the external pressure. In this case, taken into account the thermal properties and the mechanisms of ns-laser ablation, the plume may be enriched in the most easily vaporizable species: Pb and Zn.

As observed in a previous report [31], it is due to the electron density. At higher pressure, the electron density is higher as a result of the compression effect that makes shielding effect more intense.

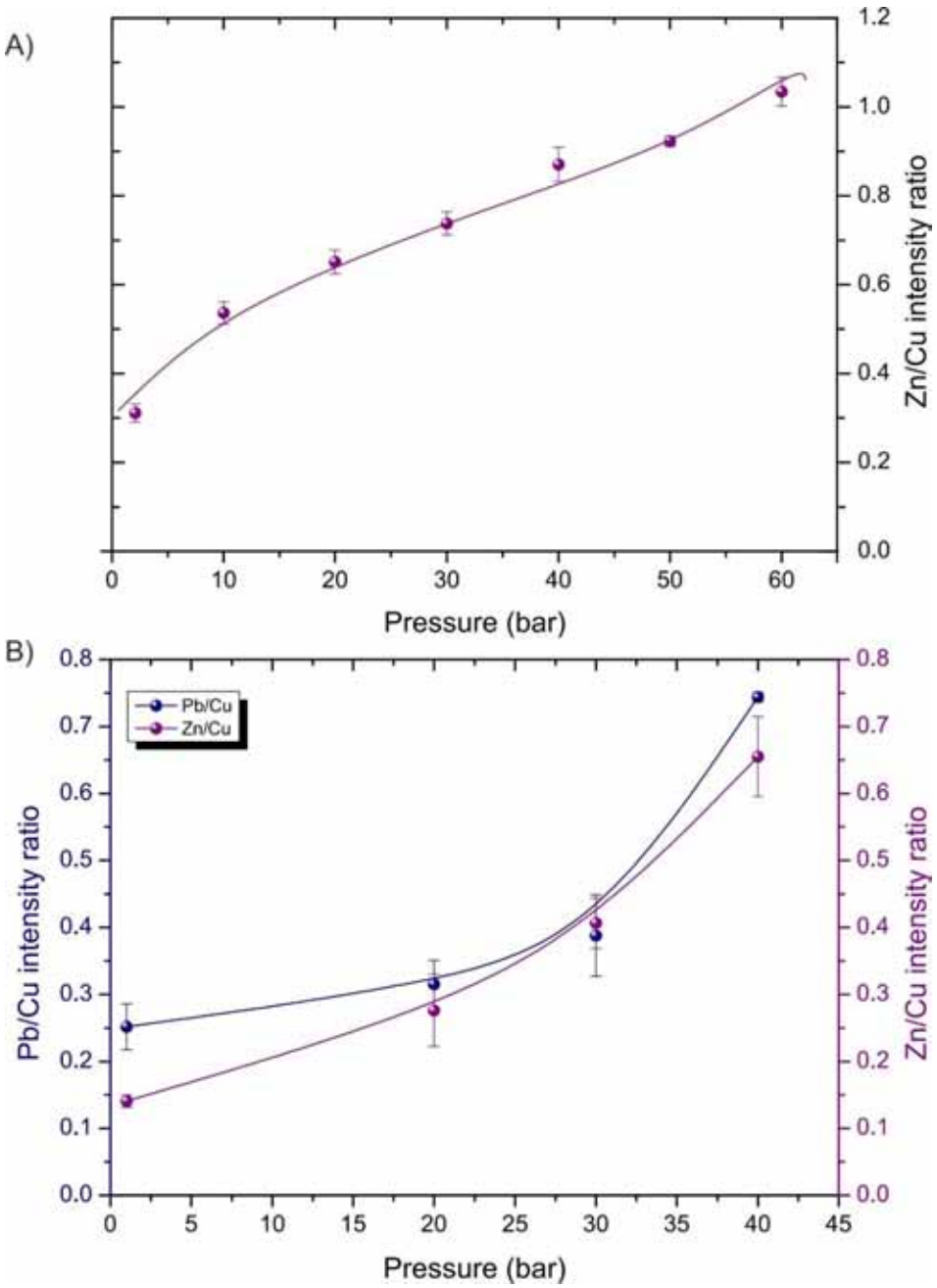

Figure 15. A) Zn/Cu intensity ratio from bronze B and B) Zn/Cu and Pb/Cu intensity ratio from bronze A as function of environment pressure.

Consequently, the laser energy that reaches the sample surface is attenuated inducing less energetic plasma. A decrease of plasma temperature could be expected when hydrostatic pressure increases, as observed in [42]. In our experiment, electron temperature was calculated observing that the plasma temperature change among 12000-10500 K in a pressure range of 1-40 bar. This fact indicates that less stoichiometric plasma was obtained, in such a way matrix effect will be favoured producing a preferential ablation.

4. Conclusions

In this work, LIBS experiments simulated oceanic conditions in order to evaluate the capabilities of this technique for underwater chemical characterization of archaeological materials immersed at higher depth. Experiments performed in a DP-LIBS configuration provided a signal enhancement with respect to SP-LIBS that suggest the possibility of using this approach for underwater LIBS analysis. Experimental parameters including the interpulse delay time (Δt), the acquisition delay and the laser beam energy has been optimized for a better analytical response. Concerning the interpulse delay time, Δt drops significantly as a function of hydrostatic pressure due to a significant decreases in the maximum bubble size and bubble lifetime. Also, the energy of the first laser pulse (E_1) affects to the bubble lifetime and its maximum expansion. Thus, E_1 must be set at the maximum energy to provide an increased bubble lifetime while E_2 should be set to a certain value that avoid the plasma shielding effect.

The influence of plasma collection geometry has been also evaluated. The optical arrangements were: i) orthogonal to the incident laser pulse, ii) 45º with respect to the incident laser and iii) coaxial to the incident laser pulse. Best results were achieved using low energy value and a coaxial collection configuration and indicate that the design and develop of an oceanographic sensor would be simplified with a coaxial DP LIBS configuration.

Concerning the water temperature, results obtained at 25 bar are quite promising and suggest the possibility of LIBS analysis at least at 250 meters deep since at this pressure the water temperature is around 20 ºC. Finally, at higher pressure, it seems that (when compared to the atmospheric pressure) exits a matrix effect which provides a different plasma behaviour, due to the variation of physical and chemical properties of the elements integrating the matrix and consequently influence the mass ablation rate and other processes occurring in the plasma. In this sense, intensity LIBS ratio significantly changes as function of the water pressure and the laser-induced plasma is enriched in Zn and Pb with respect to the Cu content. The results obtained are quite promising and suggest the possibility of integrating LIBS technology into a remotely operated vehicle (ROV). This application could be considered as a new LIBS frontier and open the door for geological/mineralogical exploration, cultural heritage investigation and/or the inspection of oil and gas pipelines in the seafloor.

5. References

1. S. Palanco, J. M. Baena, J. J. Laserna, Open-path laser-induced spectrometry for remote analytical measurements on solid surfaces, Spectrochim. Acta Part B 57 (2002), 591–599.
2. I. Gaona, P. Lucena, J. Moros, F. J. Fortes, S. Guirado, J. Serrano; J. J. Laserna; Evaluating the use of standoff LIBS in architectural heritage: surveying the Cathedral of Málaga; J. Anal. At. Spectrom., 28 (2013), 810.

3. M. Saeki, A. Iwanabe, C. Ito, I. Wakaida, B. Thornton, T. Sakka, H. Ohba, Development of a fiber-coupled laser-induced breakdown spectroscopy instrument for analysis of underwater debris in a nuclear reactor core, J. Nucl. Sci. Technol. 51 (2014), 930–938.
4. A. I. Whitehouse, J. Young, I.M. Botheroyd, S. Lawson, C.P. Evans, J. Wright, Remote material analysis of nuclear power station steam generator tubes by laser-induced breakdown spectroscopy, Spectrochim. Acta Part B 56 (2001), 821–830.
5. B. Sallé, J.-L. Lacour, P. Mauchien, P. Fichet, S. Maurice, G.Manhès, Comparative study of different methodologies for quantitative rock analysis by laser-induced breakdown spectroscopy in a simulated Martian atmosphere, Spectrochim. Acta Part B 61 (2006), 301–313.
6. P.-Y. Meslin, O. Gasnault, O. Forni, et al., Soil diversity and hydration as observed by ChemCam at Gale crater, Mars, Science 341 (2013), 1238670-1-10.
7. B. Thornton, T. Takahashi, T. Sato, T. Sakka, A. Tamura, A. Matsumoto, T. Nozaki, T. Ohki, K. Ohki, Development of a deep-sea laser-induced breakdown spectrometer for in situ multi-element chemical analysis, Deep-Sea Res. I 95 (2015), 20–36.
8. B. Thornton, T. Ura, Effects of pressure on the optical emissions observed from solids immersed in water using a single pulse laser, Appl. Phys. Express 4 (2011), 022702-3.
9. C. van Dover, The ecology of deep-sea hydrothermal vents, Princeton, New Jersey, Princeton University Press, 2000.
10. L. L. Demina, N. G. Holm, S. V. Galkin and A. Y. Lein, Some features of the trace metal biogeochemistry in the deep-sea hydrothermal vent fields (Menez Gwen, Rainbow, Broken Spur at the MAR and 9°50'N at the EPR): A synthesis, J. Mar.Syst., 126 (2013), 94–105.
11. M. Lawrence-Snyder, J. Scaffidi, S.M. Angel, A.P.M. Michel, A. D. Chave, Laser-induced breakdown spectroscopy of high-pressure bulk aqueous solutions, Appl. Spectrosc. 60 (2006), 786–790.
12. M. Lawrence-Snyder, J. Scaffidi, S. M. Angel, A. P. M. Michel, A.D. Chave, Sequential pulse laser-induced breakdown spectroscopy of high-pressure bulk aqueous solutions, Appl. Spectrosc. 61 (2007), 171–176.
13. A. P. M. Michel, M. Lawrence-Snyder, S. M. Angel, A. D. Chave, Laser-induced breakdown spectroscopy of bulk aqueous solutions at oceanic pressures: evaluation of key measurements parameters, Appl. Opt. 46 (2007), 2507–2515.
14. D. A. Cremers, L. J. Radziemski, T. R. Loree, Spectrochemical analysis of liquids using the laser spark, Appl. Spectrosc. 38 (1984), 721–729.
15. M. A. Harith, V. Palleschi, A. Salvetti, D. P. Singh, M. Vaselli, G. V. Dreiden, Y. I. Ostrovsky and I. V. Semenova, Dynamics of laser-driven shock waves in water, J. Appl. Phys., 66 (1989), 5194–5197.

16. F. Fama, M. A. Harith, V. Palleschi, A. Salvetti, D. P. Singh, M. Vaselli, G. V. Dreiden, Y. I. Ostrovsky and I. V. Semenova, Hydrodynamics of laser-produced shock waves in water: Reflection and transmission measurements, J. Appl. Phys. 69 (1991), 1660–1665.
17. V. Lazic, S. Jovicevic, M. Carpanese, Laser induced bubbles inside liquids: Transient optical properties and effects on a beam propagation Appl. Phys. Lett. 101 (2012), 054101-4.
18. V. Lazic, S. Jovicevic,Laser induced breakdown spectroscopy inside liquids: Processes and analytical aspects, Spectrochim. Acta, Part B 101 (2014), 288–311.
19. A. De Giacomo, M. Dell'Aglio, O. De Pascale, M. Capitelli, From single pulse to double pulse ns-Laser Induced Breakdown Spectroscopy under water: Elemental analysis of aquous solutions and submerged solid samples, Spectrochim. Acta, Part B 62 (2007), 721–738.
20. A. P. M. Michel, A. D. Chave, Single pulse laser-induced breakdown spectroscopy of bulk aqueous solutions at oceanic pressures: interrelation ship of gate delay and pulse energy, Appl. Opt., 47 (2008), G122–G130.
21. A. P. M. Michel, A. D. Chave, Double pulse laser-induced breakdown spectroscopy of bulk aqueous solutions at oceanic pressures: interrelationship of gate delay, pulse energies, interpulse delay, and pressure, Appl. Opt., 47 (2008), 131– 143.
22. M. Lawrence-Snyder, J. Scaffidi, W. F. Pearman, C. M. Gordon, S.M. Angel, Issues in deep ocean collinear double-pulse laser induced breakdown spectroscopy: Dependence of emission intensity and inter-pulse delay on solution pressure, Spectrochimi. Acta Part B 99 (2014), 172–178
23. A. De Giacomo, A. De Bonis, M. Dell'Aglio, O. De Pascale, R. Gaudiuso, S. Orlando, A. Santagata, G.S. Senesi, F. Taccogna, R. Teghil, Laser ablation of graphite in water in a range of pressure from 1 to 146 atm using single and double pulse techniques for the production of carbon nanostructures, J. Phys. Chem. C 115 (2011), 5123–5130.
24. T. Sakka, H. Oguchi, S. Masai, K. Hirata, Y.H. Ogata, M. Saeki, H. Ohba, Use of a long duration ns pulse for efficient emission of spectral lines from the laser ablation plume in water, Appl. Phys. Lett. 88 (2006), 061120-3.
25. T. Sakka, A. Tamura, A. Matsumoto, K. Fukami, N. Nishi, B. Thornton, Effects of pulse width on nascent laser-induced bubbles for underwater laser-induced breakdown spectroscopy, Spectrochim. Acta Part B 97 (2014), 94–98.
26. B. Thornton, T. Sakka, T. Masamura, A. Tamura, T. Takahashi, A. Matsumoto, Long duration nano-second single pulse lasers for observation of spectra from bulk liquids at high hydrostatic pressures, Spectrochim. Acta Part B 97 (2014), 7–12.
27. B. Thornton, T. Sakka, T. Takahashi, A. Tamura, T. Masamura, A.Matsumoto, Spectroscopic measurements of solids immersed in water at high pressure using a long-duration nanosecond laser pulse, Appl. Phys. Express 6 (2013), 082401-082404.

28. S. Guirado, F. J. Fortes, V. Lazic, J. J. Laserna, Chemical analysis of archeological materials in submarine environments using laser-induced breakdown spectroscopy, On-site trials in the Mediterranean Sea. Spectrochim. Acta B 74–75 (2012), 137–143.
29. S. Guirado, F. J. Fortes, J. J. Laserna, Elemental analysis of materials in an underwater archeological shipwreck using a novel remote laser-induced breakdown spectroscopy system, Talanta 137 (2015), 182-188.
30. M. López-Claros, F. J. Fortes, J. J. Laserna, Subsea spectral identification of shipwreck objects using laser-Induced breakdown spectroscopy and linear discrimiant analysis, J.Cult. Herit. X (2016), xx-xx (accepted).
31. F. J. Fortes, S. Guirado, A. Metzinger, J. J. Laserna, A study of underwater stand-off laser-induced breakdown spectroscopy for chemical analysis of objects in the deep ocean, J. Anal. At. Spectrom., 30 (2015), 1050–1056.
32. A. De Giacomo, M. Dell'Aglio, R. Gaudiuso, S. Amoruso, O. De Pascale, Effects of the background environment on formation, evolution and emission spectra of laser-induced plasmas, Spectrochimi. Acta Part B 78 (2012), 1–19.
33. A. De Giacomo, Experimental characterization of metallic titanium-laser induced plasma by time and space resolved optical emission spectroscopy, Spectrochim. Acta Part B 58 (2003), 71–83.
34. S. M. Angel, J. Bonvallet, M. Lawrence-Snyder, W. F. Pearman, J. Register, Underwater measurements using laser induced breakdown spectroscopy, J. Anal. At. Spectrom., 31 (2016), 328-336.
35. X. Liu, Y. Hou, X. Liu, J. He, J. Lu, X. Ni, Oscillation characteristics of a laser-induced cavitation bubble in water at different temperatures; Optik, 122 (2011), 1254-1257.
36. A. Thormählen, J. Straub, U. Grugyll, Refractive index of Water and Its Dependence on wavelength, Temperature and Density. J. Phys. Chem., 14 (1985), 933-945.
37. The International Association for the Properties of Water and Steam (IAPWS), http://www.iapws.org/index.html.
38. K. Amponsah-Manager, N. Omenetto, B. W. Smith, I. B. Gornushkin, J. D. Winefordner, Microchip laser ablation of metals: investigation of the ablation process in view of its application to laser-induced breakdown spectroscopy; J. Anal. At. Spectrom., 20 (2005), 544–551.
39. S. Guirado, F. J. Fortes, J. J. Laserna, Multi-pulse Excitation for Underwater Analysis of Copper-based Alloys using a Novel Remote Laser-induced Breakdown System, Appl. Spectros. 70 (2016), 618–626
40. O. V. Borisov, X. L. Mao, R. E. Russo, Effects of crater development on fractionation and signal intensity during laser ablation inductively coupled plasma mass spectrometry, Spectrochim. Acta Part B 55 (2000), 1693–1704.

41. V. Margetic, A. Pakulev, A. Stockhaus, M. Bolshov, K. Niemax, R. Hergenroder, A comparison of nanosecond and femtosecond laser induced plasma spectroscopy of brass samples, Spectrochim. Acta Part B 55 (2000), 1771–1785.
42. T. Takahashi, B. Thornton, T. Ura, Investigation of influence of hydrostatic pressure on Double-Pulse Laser- Induced Breakdown Spectroscopy for Detection of Cu and Zn in submerged solids, Appl. Phys. Express 6 (2013), 042403-03.

Conclusions

The results obtained in this Doctoral Thesis are quite promising and suggest the possibility of integrating LIBS technology in oceanography. This application could be considered as a new LIBS frontier and open the door for geological/mineralogical exploration, cultural heritage investigation and/or the inspection of oil and gas pipelines in the seafloor. In this sense, according to the initially proposed objectives, the results obtained and the individual conclusions presented in the different *Chapters* of this Doctoral Thesis, the following general conclusions can be outlined:

- The capability of LIBS for the on-site recognition and identification of immersed objects has been demonstrated by using a remote LIBS instrument.
- Parametric studies in the laboratory such as gas flow pressure, beam focal conditions and acquisition delay time, among others, were performed to optimize the best conditions for field analysis. In addition, a number of tasks were conducted outdoors in order to evaluate the stability and robustness of the Remote-LIBS prototype in a marine environment.
- Underwater characterization of galvanized steel has been accomplished in shallow waters in the Bay of Málaga. A multi-pulse excitation scheme was selected for LIBS analysis. Depth information was obtained by tuning the pulse width to 22 ns and 30 ns. In order to determine the Zn coating thickness, calibration curves were constructed for both pulse durations. Information extracted from depth profiling analysis could be employed for the quality control of the corrosion protection in the industrial sector.
- The use of a gas of purge (Ar, He) improve the chemical characterization of ceramics during the in-situ analysis in an underwater archeological site. In our prototype, the umbilical cord supply gas to the submersible probe for removing the water and creates a gas–sample interface that improves the ablation efficiency. The influence of gas pressure on the LIBS signal of ceramic has been also studied.
- Results obtained during the measurement campaign performed in the wreck of *San Pedro de Alcántara* confirmed the maturity of the LIBS technique to perform in a marine environment.
- A software based on linear discriminant analysis for in-situ assigning the chemical identity of the object in a real underwater site has been designed. The information thus gathered provides valuable data on the identity of shipwrecks located in coastal waters.
- A high-pressure chamber has been designed and constructed to simulate oceanic conditions in laboratory. The chamber is certified for pressures up to 400 bar.
- The influence of high-pressure over LIBS signal has been evaluated. For this purpose, a coaxial DP-LIBS configuration has been properly optimized. Studies based on fast photography and shadowgraphy images demonstrated that the cavitation bubble expansion is crucial for a better optimization of the temporal conditions. The optimum Δt drops significantly as a function of the pressure. We noted that although the bubble persistence time is considerably larger (a few hundred μs), the duration of the laser-induced plasma is only a few μs.

- In view of the results obtained in this thesis, it would be feasible to design, in a space of reduced dimensions such as a remotely operated vehicle (ROV) a standoff LIBS (ST-LIBS) system to analyze the samples of interest at different distances in the deep ocean.

Appendix 1. High pressure chamber certificate

HIDRAULICA PRADO S.L.
C/ Carabela Nº 20
29006 Málaga
Telf/Fax: 952 33 74 47
C.I.F.: B92862598
www.hidraulicaprado.com
info@hidraulicaprado.com

Certificado de estanqueidad de cámara de altas presiones

Yo, Francisco Gabriel Prado Peñuela con DNI: 33362214-R y gerente de la empresa *HIDRAULICA PRADO S.L.* con C.I.F.: B92862598,

CERTIFICO, que la estanqueidad de la cámara de altas presiones diseñada por el Laboratorio Láser de la Universidad de Málaga ha sido testada satisfactoriamente hasta una presión de trabajo de 400 bares.

Málaga, a 15 de Julio de 2015

HIDRAULICA PRADO SL
C/ CARABELA 20 EL VISO
29006 MALAGA
TF/FAX. 952337447

Fdo.: Francisco Prado

GASLI

CERTIFICADO DE CALIBRACION

Calibration Certificate

CLIENTE /Customer	HIDRAULICA PRADO

PATRON PRIMARIO /Primary Master:	
FABRICANTE/Manufacturer:	DRUCK
TIPO/Type:	DPI605
NÚMERO DE SÉRIE / Serial number:	3709/97-12
DIVISIÓN DE ESCALA/:	0.001
PRECISIÓN / Precision:	0.025% rdg
INCERTIDUMBRE / Uncertainty K=2):	±0.025%rdg

PATRON DE MEDIDA CALIBRADO / Master under test:	
TIPO / Type: "	MANOMETRO
ESCALA / Range:	600 BAR
DIVISION DE ESCALA/ Scale Div.:	10 BAR
CLASE/ Accuracy Class :	+/- 1.6 %
MATRICULA/ Serial # :	34-12

CONDICIONES DE CALIBRACIÓN/ Ambient Conditions:
TEMPERATURA DE MEDICIÓN: 20.05
/Ambient Temperature (°C)
TRAZABILIDAD DE LA CALIBRACIÓN/Traceable with:
INTA nº 24915-24922-24964-24978-25032 del 13-08-10)

PROCEDIMIENTO DE CALIBRACIÓN/ Calibration Procedure
NC 15

	NOMINAL	LECTURA(DPI)	ERROR	% F.S.
CRECIENTE / DECRECIENTE	0	0		
	100	96,688	3,312	0,552
	200	194,782	5,218	0,870
	300	294,325	5,675	0,946
	500	502,078	-2,078	0,346
	500	501,054	-1,054	0,176
	300	293,781	6,219	1,037
	200	193,021	6,979	1,163
	100	93,765	6,235	1,039
	0	0		
DATOS	FONDO ESCALA:	600,0	CLASE:	1,6
	INCERTIDUMBRE:	1,163	MATRICULA	
	HISTERESIS:(% fs)	0,487	ACEPTADO	
	CLASE REAL:	1,163		

GRAFICO

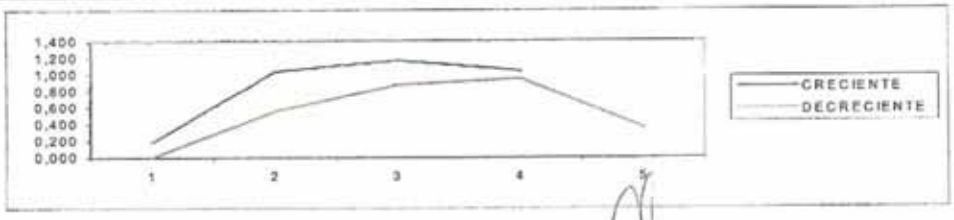

OBSERVACIONES:

FECHA Y FIRMA :

25-04-12
CARLOS BECERRA
RESPONSABLE DE CALIBRACIÓN

CERTIFICADO COMPROBACION

HIDRAULICA PRADO

CERTIFICA LA COMPROBACION DE TODOS LOS COMPONENTES CON UN FACTOR DE SEGURIDAD DE 1.3X LA PRESION DE TRABAJO, CON MANOMETRO PATRON CERTIFICADO Nº 34-12 DE 0-600 BARES.

CERTIFICADO Nº / Certificate #	34-12

GASLI

CERTIFICADO DE CALIBRACION
Calibration Certificate

CLIENTE /Customer	HIDRAULICA PRADO

PATRON PRIMARIO /Primary Master:	
FABRICANTE/Manufacturer:	DRUCK
TIPO/Type:	DPI605
NÚMERO DE SÉRIE / Serial number:	3709/97-12
DIVISIÓN DE ESCALA/:	0.001
PRECISIÓN / Precision:	0.025% rdg
INCERTIDUMBRE / Uncertainty K=2):	±0.025%rdg

PATRON DE MEDIDA CALIBRADO / Master under test:	
TIPO / Type: *	MANOMETRO
ESCALA / Range:	600 BAR
DIVISION DE ESCALA/ Scale Div.:	10 BAR
CLASE/ Accuracy Class :	+/- 1.6 %
MATRICULA/ Serial # :	34-12

CONDICIONES DE CALIBRACIÓN/ Ambient Conditions:
TEMPERATURA DE MEDICIÓN: 20.05
/Ambient Temperature (°C)
TRAZABILIDAD DE LA CALIBRACIÓN/Traceable with:
INTA nº 24915-24922-24964-24978-25032 de(13-08-10)

PROCEDIMIENTO DE CALIBRACIÓN/ Calibration Procedure
NC 15

	NOMINAL	LECTURA(DPI)	ERROR	% F.S.
CRECIENTE / DECREC.	0	0		
	100	96,688	3,312	0,552
	200	194,782	5,218	0,870
	300	294,325	5,675	0,946
	500	502,078	-2,078	0,346
	500	501,054	-1,054	0,176
	300	293,781	6,219	1,037
	200	193,021	6,979	1,163
	100	93,765	6,235	1,039
	0	0		

DATOS				
	FONDO ESCALA:	600,0	CLASE:	1,6
	INCERTIDUMBRE:	1,163	MATRICULA	
	HISTERESIS:(% fs)	0,487	ACEPTADO	
	CLASE REAL:	1,163		

GRAFICO

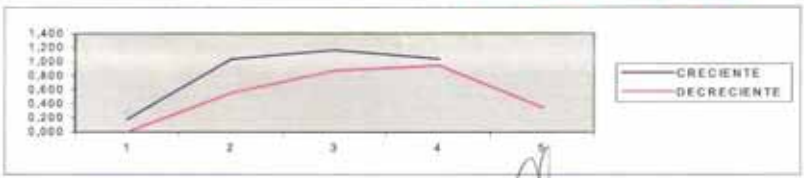

OBSERVACIONES:	FECHA Y FIRMA :
	25-04-12 CARLOS BECERRA RESPONSABLE DE CALIBRACIÓN

Q-014/4 PR7.6.1

Ficha técnica de los componentes principales

- Manguera termoplástica ¼ 700 bares

Mangueras termoplásticas TrAle
Termoplásticas malla metálica
Manguera termoplástica 700 bar

Composición: ·Tubo interior: elastómero de poliester.
·Refuerzo: una o dos mallas de fibra "Aramid" más una malla metálica.
·Cubierta: poliuretano negro.

Temperatura de trabajo: De -40º C a +100º C, limitada a +70º C para aire y fluidos de solución acuosa.

Artículo	DN	Ø in	Ø ext	Presión de trabajo (bar)	Presión de trabajo (psi)	Presión de rotura (bar)	Presión de rotura (psi)	Radio de curvatura (mm)	Peso (kg/m)
	1/4"	6,6	12,7	700	10000	2800	40000	35	0,180

- Válvula de seguridad- limitadora de presión

VÁLVULAS EN LÍNEA
IN-LINE VALVES / VALVES EN LIGNE
LIMITADORAS / RELIEF VALVES / LIMITEURS

LIMITADORAS PANELABLES CUERPO ACERO / *BULKHEAD RELIEF VALVE STEEL BODY*
LIMITEURS SUR TABLEAU CORPS ACIER

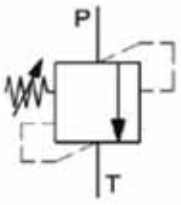

Type	Q (l/min.)		Rang.	
VMP 1/4 L	40	1/4	30...500	500

TABLA DE PRENSADOS PARA CASQUILLOS EN ACERO

(MANGUERAS PTFE Y TERMOPLÁSTICAS)

TABLEAU SERTISSAGE POUR LES JUPES EN ACIER (TUYAUX PTFE ET THERMOPLASTIQUES)
CRIMPING TABLE FOR CARBON STEEL (PTFE AND THERMOPLASTIC HOSES)

TOLERANCIAS DE PRENSADO
Tolérance de sertissage
Crimping tolerances
1/8" - 3/8" : + 0 / - 0,2
1/2" - 2" 1/2 . + 0 / - 0,4
mm

FECHA (date): **feb-15**

MANGUERA/Tuyau/Hose	DN (mm)	3	5	6	8	10	13	16	19		22	25	32	38	50	63
	PULGADAS/Pouces/Inch	**1/8"**	**3/16"**	**1/4"**	**5/16"**	**3/8"**	**1/2"**	**5/8"**	**3/4"**		**7/8"**	**1"**	**1"1/4**	**1"1/2**	**2"**	**2"1/2**
	GALGA	02	03	04	05	06	08	10	12		14	16	20	24	32	40
PTFE FHL	CASQUILLO/Jupe/Ferrule	-	21040	21040	21040	21040	21040	21040	21040		21040	21040	-	-	-	-
M2900...	Φ EXT. CASQUILLO		14	15	17	18	24	28	30		34	36				
	Φ PRENSADO/Sertissage/Crimping		**11,5**	**13**	**13,8**	**15,5**	**20,5**	**23,5**	**27**		**30,5**	**34**				
PTFE FHM (2 Mallas/Tresses/Braids)	CASQUILLO/Jupe/Ferrule	-	-	DI / PF23	DI / PF23	DI /PF23	21040	21040	21040	21012	-	21012	-	-	-	-
M29012...	Φ EXT. CASQUILLO			18	19	22	24	28	30	31,5		40				
	Φ PRENSADO/Sertissage/Crimping			**13,6**	**14,6**	**17,5**	**20,7**	**25,2**	**27**	**27**		**34,5**				
PTFE COARRUGADO/Convoluté/ Convoluted PTFE	CASQUILLO/Jupe/Ferrule	-	-	21041	21041	21041	21041	21041	210411201		-	21041	21041	21041	21041	21041
	Φ EXT. CASQUILLO			16	17	21,5	25	29	32			40	48	55	69	80
M2920...	Φ EXT. MANGUERA/Tuyau/Hose (2)			9,2					25							
(1)	Φ PRENSADO/Sertissage/Crimping			**12,2**	**14**	**16,8**	**20,2**	**24**	**26,7**			**34**	**41**	**48,2**	**60,2**	**74**
SAE 100 R7	CASQUILLO/Jupe/Ferrule	21012	DI / PF23	DI / PF23	DI / PF23	DI / PF23	DI / PF23	21012 / DI23	21012		-	DI23	-	-	-	-
MT07...	Φ EXT. CASQUILLO	13	14	18	19	22	26	29	31,5			40				
	Φ EXT. MANGUERA/Tuyau/Hose (2)	8,4	9,6	12,2	14	16	20,2	24,3	27,6			34				
	Φ PRENSADO/Sertissage/Crimping	**11**	**11,2**	**14,9**	**16,1**	**18,6**	**23**	**26**	**28,4**			**37**				
SAE 100 R8	CASQUILLO/Jupe/Ferrule	-	DI / PF23	DI / PF23	DI / PF23	DI / PF23	DI / PF23	DI23	21012		-	DI23	-	-	-	-
MT08...	Φ EXT. CASQUILLO		14	18	19	22	26	29	31,5			40				
	Φ EXT. MANGUERA/Tuyau/Hose (2)		9,4	11,5	13,3	15,5	19,9	23,4	27			34,2				
	Φ PRENSADO/Sertissage/Crimping		**11,3**	**14,3**	**15,7**	**18,3**	**23**	**26**	**29**			**37**				
ELASTOMERO MALLA METÁLICA	CASQUILLO/Jupe/Ferrule	-	DI / PF23	DI / PF23	DI / PF23	DI / PF23	DI / PF23	21012 / DI23	21012		-	DI23	-	-	-	-
Élastomère 1 tresse metallique/ Metallic braid elastomer	Φ EXT. CASQUILLO		14	18	19	22	26	29	31,5			40				
	Φ EXT. MANGUERA/Tuyau/Hose (2)		9,4	11,7	13,4	15,9	18,4	21,6	25,5			33				
MT09...	Φ PRENSADO/Sertissage/Crimping		**11,3**	**14,5**	**15,8**	**18,5**	**22**	**25**	**28**			**36,5**				
ELASTOMERO MALLA METÁLICA PINTURA	CASQUILLO/Jupe/Ferrule	-	DI / PF23	DI / PF23	21012	DI / PF23	DI / PF23	-	21012		-		-	-	-	-
Élastomère peinture 1 tresse metallique/ Paint metallic braid elastomer	Φ EXT. CASQUILLO		14	18	19	22	26		31,5							
MT099...	Φ PRENSADO/Sertissage/Crimping		**11,3**	**14,5**	**16,5**	**18,4**	**22**		**27,8**							
ELASTOMERO DOBLE MALLA METALICA PINTURA	CASQUILLO/Jupe/Ferrule	-	-	DI / PF1224	DI / PF1224	DI / PF1224	DI / PF1224	-	DI / PF1224		-	DI / PF1224	-	-	-	-
Élastomère peinture 2 tresses metalliques/ Paint metal. braid double elastomer	Φ EXT. CASQUILLO			22	23	26	30		37			46				
MT299...	Φ PRENSADO/Sertissage/Crimping			**17,3**	**19**	**22**	**26**		**30,6**			**41**				
MANGUERA ALTÍSIMA PRESIÓN	CASQUILLO/Jupe/Ferrule	-	-	71012	-	71012	-	-	-		-	-	-	-	-	-
MT700...	Φ EXT. CASQUILLO			20		26										
	Φ EXT. MANGUERA/Tuyau/Hose (2)			12,7		18,7										
	Φ PRENSADO/Sertissage/Crimping			**16,6**		**22,8**										
MANGUERA MINIMEX	CASQUILLO/Jupe/Ferrule	555010100	-	-	-	-	-	-	-		-	-	-	-	-	-
2X5 mm	Φ EXT. CASQUILLO	8														
MT01002	Φ EXT. MANGUERA/Tuyau/Hose (2)	5														
	Φ PRENSADO/Sertissage/Crimping	**7**														

NOTE: Las tablas de prensado i son siempre orientativas / Tableau sertissage DICSA sont toujours indicatifs / Crimping lists of DICSA are allways orientatives.

(1) Los diámetros de prensado de las mangueras PTFE coarrugado, se corresponden con los ensayados para mangueras de nuestro proveedor. Por lo tanto estos diámetros pueden variar dependiendo de la manguera.
Se recomienda, que en diámetros de prensado de 1"1/4, 1"1/2 y 2" se comprueben todos los montajes que se realicen.
(1) Les diamétres de sertissage du PTFE convoluté sont suite aux diamétres de sertissage des tuyaux de notre fornisseur. C'est pourquoi, ces diamétres peuvent changer selon le tuyau. Pour diamétres de sertissage de 1" 1/4, 1" 1/2 et 2", on recommand de verifier tous les montages.
(1) Crimping diameters of convoluted PTFE are according the tests of crimping diameters for hoses of our supplier. Therefore, these diameters can change depending on the hose. For crimping diameters 1" 1/4, 1" 1/2 and 2",it es recommended to check all the assembles.
(2) Los diámetros de prensado han sido validados para estos diámetros exteriores de manguera. Por lo tanto, éstos diámetros pueden variar dependiendo de la manguera. En rojo queda marcada la última modificación realizada.
(2) Les diamétres de sertissage ont été verifiés pour ces diamétres de tuyau. C'est pourquoi, ces diamétres peuvent charger selon le tuyau. Les derniéres modifications sont indiquées en rouge.
(2) Crimping diameters have been validated for these outer diameters of the hoses. Therefore, these diameters can change depending on the hose. The last modification is marked in red.

- Bomba manual

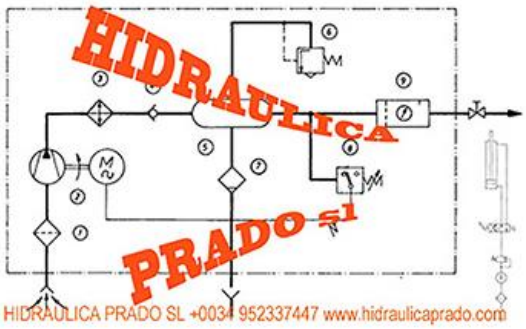

Características

- BM-04, BM-1, BM-2 y BMAP-1
- Son bombas manuales de simple efecto y una velocidad, utilizables de forma fija o portátil, en posición horizontal o vertical. En esta última posición, el cabezal debe situarse hacia abajo.
- Están equipadas con válvulas de sobrepresión, tarada a la presión máxima de trabajo.

Ficha técnica

Metric | Imperial

Referencia	Capacidad de aceite útil (cm3)	Pres. de trabajo (Kg/cm2)	Caudal por embolada (cm3) 1 Etapa	Caudal por embolada (cm3) 2 Etapa	Peso (kg)
BM-04	400	700		2.5	4.25
BM-1	1250				6.7
BM-2	2000				12
BMAP-1	1250	1500		1	7.2

CONSEJERIA DE ECONOMIA, INNOVACION Y CIENCIA
DELEGACIÓN PROVINCIAL DE Malaga

09 JUL. 2012 18936

DECLARACIÓN RESPONSABLE DE EMPRESA DE SERVICIOS EN MATERIA DE SEGURIDAD INDUSTRIAL:
INSTALADORA/REPARADORA DE EQUIPOS A PRESIÓN

1 IDENTIFICACIÓN DEL TITULAR DECLARANTE

NOMBRE Y APELLIDOS O RAZÓN SOCIAL: HIDRAULICA PRADO,S.L.	NOMBRE COMERCIAL: HIDRAULICA PRADO,S.L.	NIF / NIE / CIF: B92862598
DOMICILIO DE ESTABLECIMIENTO DE LA ACTIVIDAD: C/ CARABELA Nº 20.POL.IND. EL VISO		CODIGO POSTAL: 29006
LOCALIDAD: MALAGA	PROVINCIA: MALAGA	PAIS: ESPAÑA
CORREO ELECTRÓNICO: info@hidraulicaprado.com	PÁGINA WEB: www.hidraulicaprado.com	TELÉFONO: 952337447 / FAX: 952337447

2 DATOS DEL REPRESENTANTE (en su caso)

NOMBRE Y APELLIDOS DEL REPRESENTANTE: FRANCISCO G.PRADO PEÑUELA	TELÉFONO: 629454238	NIF / NIE / PASAPORTE: 33362214R

3 NOTIFICACIONES (cumplimentar sólo si es distinto al del titular)

DOMICILIO:		CODIGO POSTAL:
LOCALIDAD:	PROVINCIA:	PAIS:
CORREO ELECTRÓNICO:		FAX:

4 DECLARACIÓN RESPONSABLE

☑ INICIO DE LA ACTIVIDAD ☐ MODIFICACIÓN DE DATOS DE DECLARACIÓN ANTERIOR ☐ CESE TOTAL DE LA ACTIVIDAD

De acuerdo con lo previsto por la ley 21/1992, de 16 de julio, de industria, en su artículo 4 y en su artículo 12, apartados d) y e), y la reglamentación específica relativa a cada actividad en las especialidades, categorías y modalidades enumeradas y declaradas a continuación, y al objeto de que la empresa arriba identificada quede habilitada para el ejercicio de actividades reguladas por los reglamentos de seguridad industrial, según lo previsto en el artículo 4.3 de la ley 21/1992, quien suscribe este documento, **DECLARA:**

1. Que la empresa va a ejercer la actividad en las siguientes categorías, y que así mismo, cumple con todos los requisitos exigidos por el Real decreto 2060/2008, de 12 de diciembre, por el que se aprueba el reglamento de equipos a presión y sus instrucciones técnicas complementarias:

O **EIP-1** ● **EIP-2** O **ERP-1** O **ERP-2**

¿La actividad se limita a utilizar exclusivamente sistemas de unión no permanentes?: O **SI** ● **NO**

Requisitos Específicos

2. Que para cubrir la la responsabilidad civil exigida y derivada del ejercicio de la actividad respecto a daños materiales y personales producidos a terceros, la empresa ha asegurado, mediante póliza de seguro, aval u otra garantía suficiente, las siguientes cantidades:

ENTIDAD ASEGURADORA	CAPITAL ASEGURADO POR SINIESTRO (EUROS)
ALLIANZ	€300.00

3. Que la empresa dispone de las siguientes acreditaciones (sistemas de calidad, de fabricantes, etc):

ISO 1400:2004 Nº MA24444/11 - DISEÑO INDUSTRIAL PROTOTIPOS Y DISPOSITIVOS HIDRAULICOS,NEUMATICOS, Y AUTOMATISMOS.
ISO 9001,2008 - MISMA CERTIFICACION

4. Que dispone de personal contratado con la cualificación requerida reglamentariamente, y de la documentación que lo acredita, para el ejercicio de la actividad:

NOMBRE Y APELLIDOS	Función	NIF / NIE
FRANCISCO GABRIEL PRADO PEÑUELA	Técnico titulado compe	33362214R
	-seleccionar-	
	-seleccionar-	33362214R

CONSEJERÍA DE ECONOMÍA, INNOVACIÓN Y CIENCIA
DELEGACIÓN PROVINCIAL DE Malaga

Que la empresa se encuentra inscrita en el registro de establecimientos industriales de Andalucía con el nº _____, o que no estando inscrita o no estando sus datos convenientemente actualizados, aporta los mismos para su inscripción de oficio.

Nº CUENTA PRINCIPAL DE COTIZACIÓN A LA SEGURIDAD SOCIAL:	29119972296
ACTIVIDAD PRINCIPAL DE LA EMPRESA (descripción)	CNAE-2009
FABRICACION ,REPARACION ,VENTA EQUIPOS HIDRAULICOS Y NEUMATICOS	3312
ACTIVIDAD SECUNDARIA DE LA EMPRESA (descripción)	CNAE-2009
Nº DE TRABAJADORES:	3

6. Que dispone de la siguiente marca del punzón o tenaza para el precintado de válvulas de seguridad: HIDRAULICA PRADO nº1

Requisitos GENERALES:

7. Que como representante de la empresa, dispongo de poder legal suficiente para actuar como tal.
8. Que la empresa que represento dispone de la escritura de constitución de la misma y de sus estatutos, los cuales están debidamente inscritos en el Registro Mercantil o que, como titular de la empresa individual declarada dispongo de la documentación acreditativa de constitución de la misma de índole fiscal y laboral.
9. Que la empresa va a ejercer la actividad en las especialidades, categorías y modalidades enumeradas y declaradas anteriormente, y que así mismo, conoce y cumple con todos los requisitos exigidos por la correspondiente reglamentación de seguridad industrial para el ejercicio de la actividad establecidos en la normativa estatal y autonómica vigente.
10. Que dispone de la documentación acreditativa del cumplimiento de los requisitos y de las otras acreditaciones relacionadas, que presentará inmediatamente a la autoridad competente cuando ésta lo requiera en el ejercicio de sus facultades de inspección, comprobación y control.
11. Que la empresa se compromete a mantener el cumplimiento de los requisitos exigidos durante la vigencia de la actividad, así como a ejercer su actividad cumpliendo los requisitos que se establezcan en los correspondientes reglamentos o normas reguladoras y, en su caso, en las respectivas instrucciones técnicas y ordenes de desarrollo, así como cumpliendo con las disposiciones establecidas por la Comunidad Autónoma donde realice sus actuaciones.
12. Que la dirección de la empresa, declarada anteriormente, constituye la dirección legal a efectos de solicitud de información y de notificación de quejas o reclamaciones por los usuarios y consumidores.
13. Que los datos y manifestaciones que figuran en este documento son ciertos y que la empresa es conocedora de que:
    - La inexactitud, falsedad u omisión, de carácter esencial de los mismos, faculta a la administración competente para declarar el cese de la actividad e inhabilitar temporalmente para el ejercicio de la actividad.
    - La falta de comunicación en el plazo legal o reglamentariamente establecido a la administración competente, de cualquier modificación que supusiera dejar de cumplir los requisitos necesarios anteriormente referidos, podrá suponer, además de las posibles sanciones económicas, la inmediata inhabilitación de la actividad.

Y para que así conste, a los efectos de habilitación para el ejercicio de la actividad en las categorías señaladas, el declarante firma la presente declaración responsable.

En MALAGA a 9 de JULIO de 2012

FIRMA DEL DECLARANTE Y SELLO DE LA EMPRESA

HIDRAULICA PRADO SL
CIF: B92362596
C/ CARABELA 20 EL VISO
29006 MALAGA
FAX: 952337447

Los datos carácter personal contenidos en este impreso podrán ser incluidos en un fichero para su tratamiento por este órgano administrativo como titular responsable del fichero, en el uso de las funciones propias que tiene atribuidas y en el ámbito de sus competencias. Asimismo, se le informa de la posibilidad de ejercer los derechos de acceso, rectificación, cancelación y oposición, todo ello de conformidad con lo dispuesto en el artículo 5 de la Ley Orgánica 15/1999, de Protección de Datos de carácter Personal (BOE nº 298, de 14/12/1999)

Antecedentes

El Laboratorio Láser de la Universidad de Málaga contacta con la empresa HIDRAULICA PRADO S.L. con objeto de certificar una cámara de altas presiones. El material utilizado para su fabricación fue acero inoxidable. El dispositivo, de forma cilíndrica, consta de siete puertos, cinco laterales y uno superior. En la figura 1 se muestran las dimensiones exteriores de la cámara.

Los puertos 1, 2, 3 y 5 están diseñados de igual forma constituidos por un cilindro interior de profundidad 48.7 mm con un diámetro 26.2 mm los primeros 10.7 mm y 16.2 mm los restantes 38 mm. Para conseguir el sellado de la cámara y la estanqueidad del agua en estos puertos se utiliza un sistema de junta tórica, ventana de zafiro y junta tórica encastrada en el cilindro de cierre, tal como se detalla en la figura 2. Todo este conjunto de piezas quedan sujetas a la cámara con ocho tornillos de M6 y arandelas específicas de presión. A continuación se detallan las características de cada una.

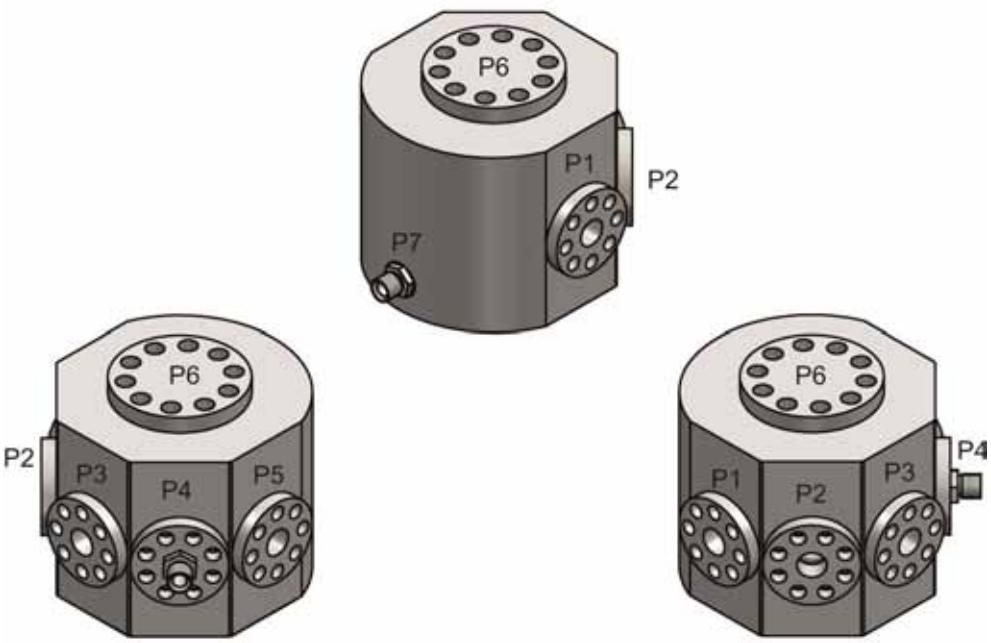

Figura 1: visión externa de la cámara de altas presiones.

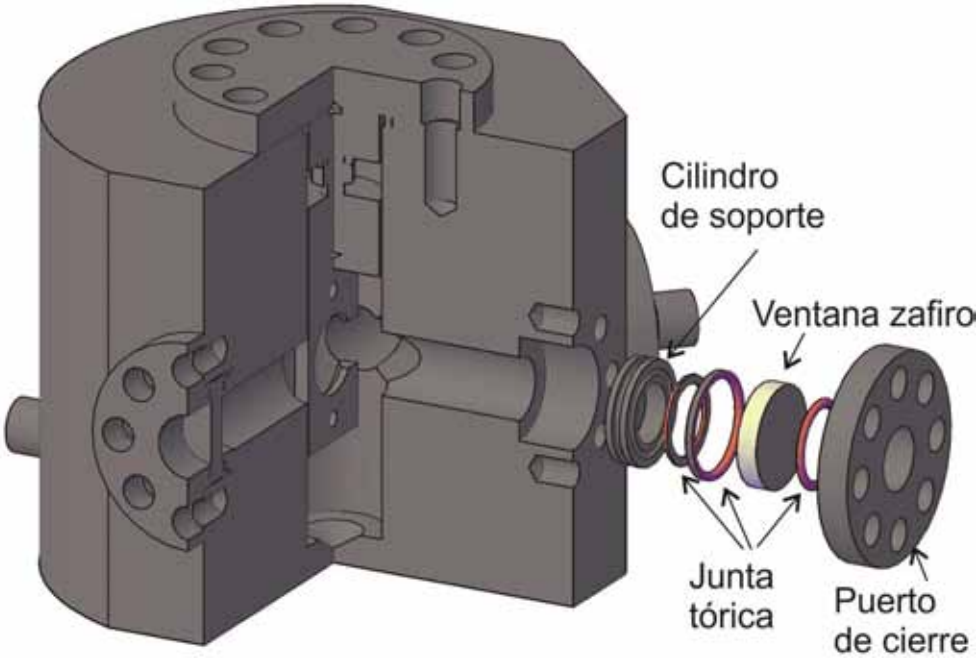

Figura 2: sistema de sellado de la cámara para los puertos 1, 2, 3 y 5.

- Collar de soporte de las juntas tóricas: pieza de acero inoxidable torneada, de tal modo que encaje una junta tórica (ϕ 22 mm) en su superficie y otra (ϕ 26mm) en el contorno lateral como se muestra en la figura 3.

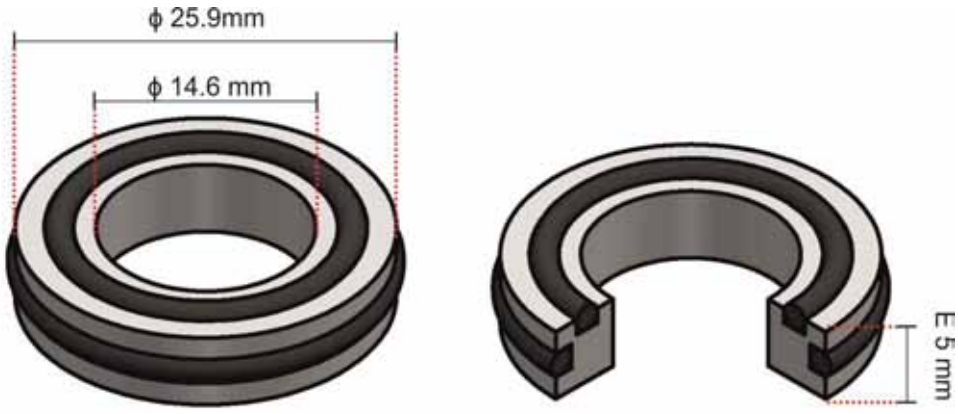

Figura 3: collar de acero inoxidable torneado con hendiduras para hacer de base a la junta tórica.

- Ventana de zafiro: pieza de zafiro ϕ 12.7 mm y E 3.0 mm.

- Cilindro de cierre: pieza circular de acero inoxidable de diámetro 51.8 mm y espesor 7.7 mm perforada en el centro (ϕ 16 mm).

El puerto 4 diseñado para la entrada del agua en la cámara posee un cilindro interior de profundidad 48.7 mm con un diámetro de 26.2 mm los primeros 13 mm y 16.2 mm los restantes 35.7 mm. Como sistema de cierre del puerto se utiliza una pieza cilíndrica (ϕ 51.8 mm y E 7.7 mm) perforada en el centro (ϕ 16 mm) y una junta tórica (ϕ 27 mm) tal como se muestra en la figura 4. De igual forma que en los puertos 1, 2, 3 y 5, las piezas quedan sujetas a la cámara usando ocho tornillos de M6 y arandelas específicas de presión. A continuación, el puerto de cierre está unido a un latiguillo de longitud 1750 mm capaz de soportar 700 bares, por un tapón hembra giratorio TL 1/4" BSP unido a un reductor macho-macho 1/4 -1/4" BSP.

En la parte superior de la cámara se encuentra el puerto 6 mecanizado para la función de porta muestra. Consta de una profundidad de 108 mm de longitud y ϕ 26.5 mm. En el sellado se utiliza una junta de metal buna ϕ 43 mm junto con un cilindro de cierre (ϕ 75.8 mm; E 10 mm) ajustado a la cámara con diez tornillos M8 y arandelas específicas de presión. Unidos por vástago M6 se encuentra el cilindro de cierre con el porta muestra semi-rectangular de acero inoxidable. Ver la figura 5.

La salida del agua de la cámara se realiza por el puerto 7. Es un orificio de 12 mm de diámetro externo unido, a través de un racor de acero BSP 1/8-1/4", a una limitadora de presión regulable entre 0 y 400 bares.

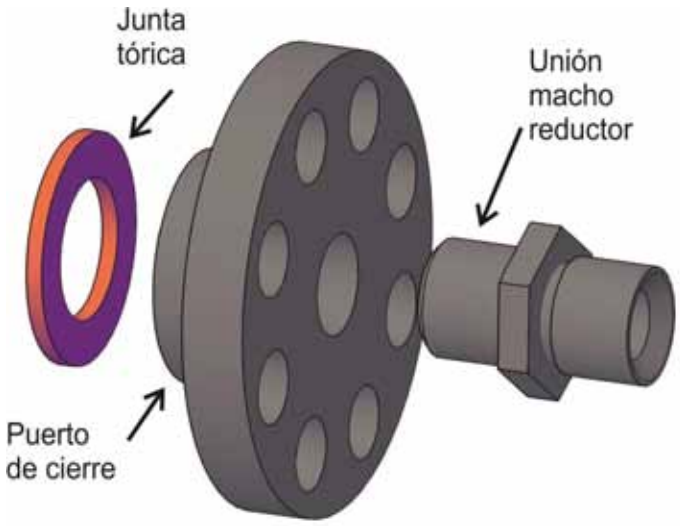

Figura 4. Puerto de entrada de agua.

Figura 5. Porta muestras

Prueba de certificación

La cámara de altas presiones fue sometida a un test de presión para validar su funcionalidad hasta 400 bares. La prueba de certificación consistió en aumentar poco a poco la presión interna en la cámara inyectándole líquido refrigerante con una bomba manual (MEGA, modelo BM-1) tarada a una presión máxima de trabajo de 700 bares. En la salida de la bomba manual de inyección se conectó un manómetro, certificado hasta 400 bares con un intervalo de error de 10 bar, donde se chequeó la presión alcanzada. Se utilizó un látigo de longitud 1750 mm capaz de soportar 700 bares para conducir el líquido refrigerante al interior de la cámara. Ver la figura 6.

Los resultados de la prueba fueron satisfactorios hasta 400 bares de presión.

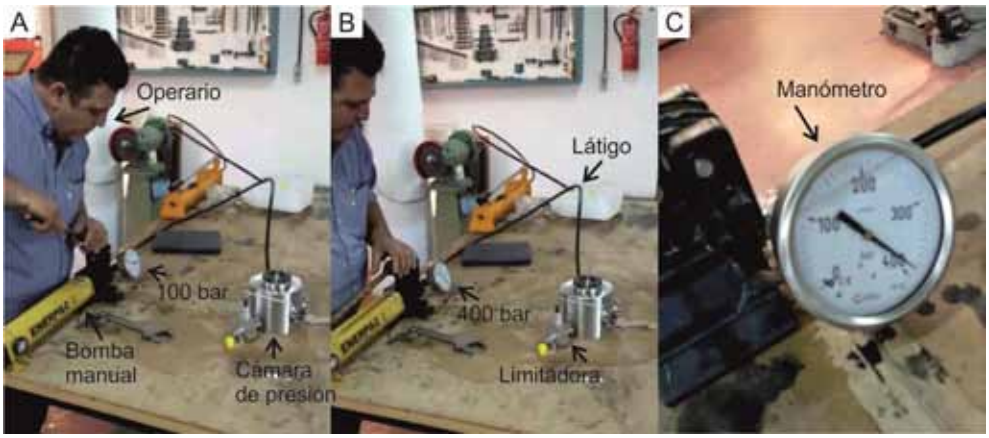

Figura 6. Fotografías del montaje de la prueba de certificación. a) Inicio de la prueba, presión alcanzada 100 bares; b) aumento de la presión hasta 400 bares; c) final de la prueba, presión estable en 400 bares.

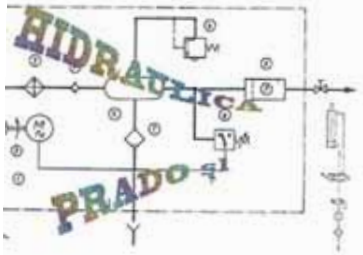

HIDRAULICA PRADO S.L.
C/ Carabela Nº. 20
29006 Málaga
Telf/Fax: 952 33 74 47
C.I.F.: B92862598
www.hidraulicaprado.com
info@hidraulicaprado.com

Certificado de estanqueidad de camara de altas presiones

Cilente : **Universidad de Malaga**

Fecha : Septiembre 2014

Manometro patron : marca Druck

Modelo Dpi 1605

Escala 0.001

Precision 0.025

Hidraulica prado certifica que con manometro patron ha probado la camara de altas presiones

A 300 bares con manometro certificado

Adjuntamos la siguiente documentacion

Certificado calibracion manometro

Certificado instalador autorizado

Certificado Nº 00026

Firmado

Francisco Prado

www.hidraulicaprado.com

Appendix 2. Archaeological samples of Centro de Arqueología subacuática

A set of several archaeological pieces was analyzed in *Centro de Arqueología Subacuática* of Cádiz with AQUALAS 2.0. LIBS spectra were acquired in the 350–550 nm range and data were obtained by averaging 25 shots laser on three adjacent positions for each sample to obtain a typical spectrum of the material. The gas flow used was 2 bar (ΔP 1bar) of Ar. The archaeological pieces under investigation were located inside of desalination pools in stabilization phase (treatment that is realized for its later conservation). This set of pieces is part of the material found in the archaeological sites of Andalucía coast indicated in Figure 1. The result of each of the studied pieces is presented below.

- **Delta II shipwreck**

Delta II is a wood wreck with a beam of 24 m and 7 m of breadth located in container terminal of Cadiz port. Constructive characteristics suggest a Mediterranean origin. Several cannon, cannon bullets and ceramic pieces, as well as a huge part of transported cargo, which is still intact conserved, have been found in this site.

Figure 1. Archaeological sites of Andalucía coast investigated.

Sample i.d: DII.12.272	**Material:** cannon bullet

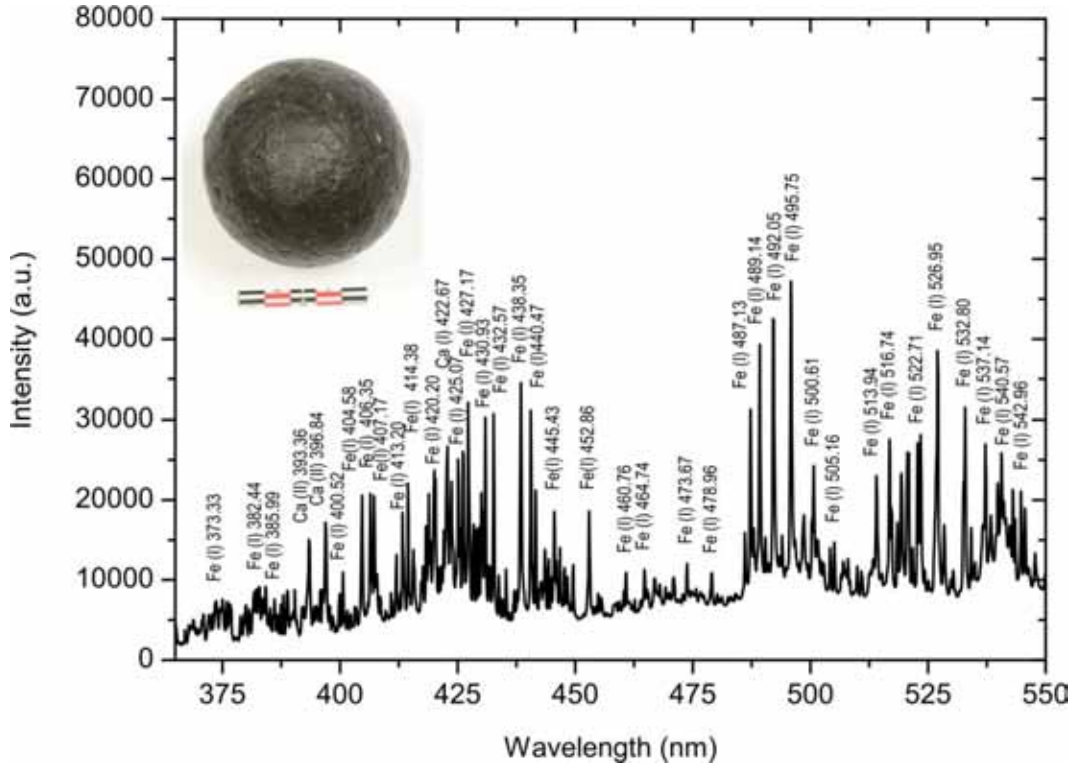

Sample i.d: DII.12.304	**Material:** olive ceramic container

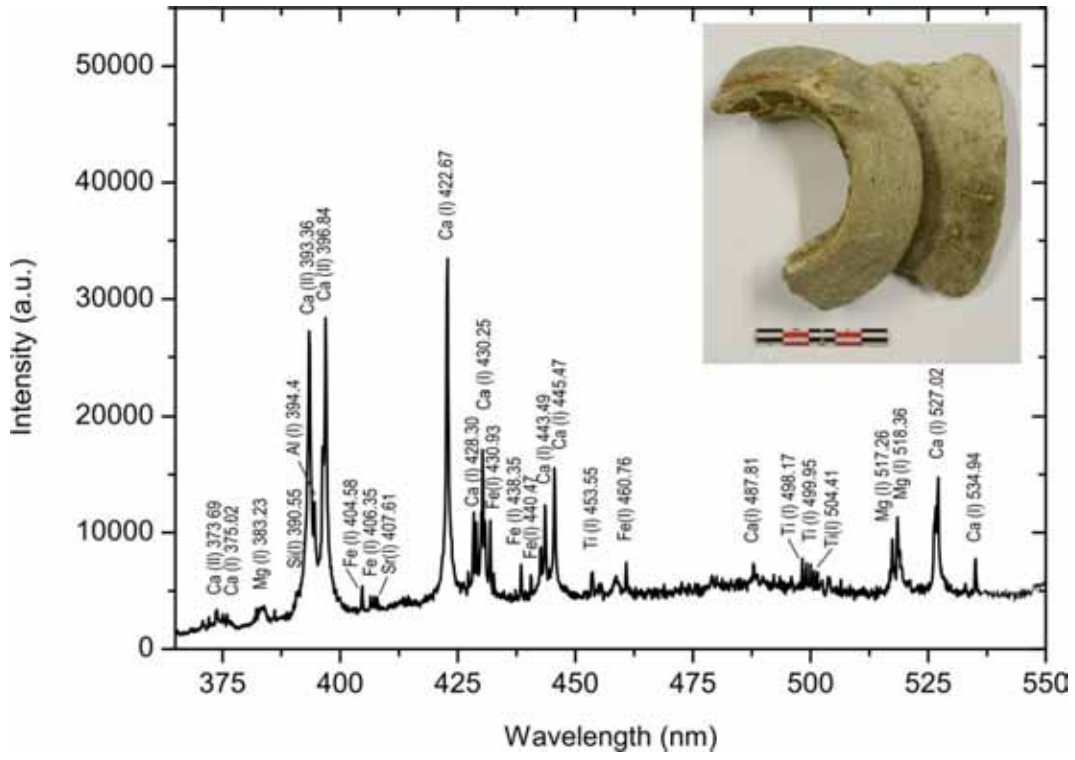

Sample i.d: DII.12.951	**Material:** cannon

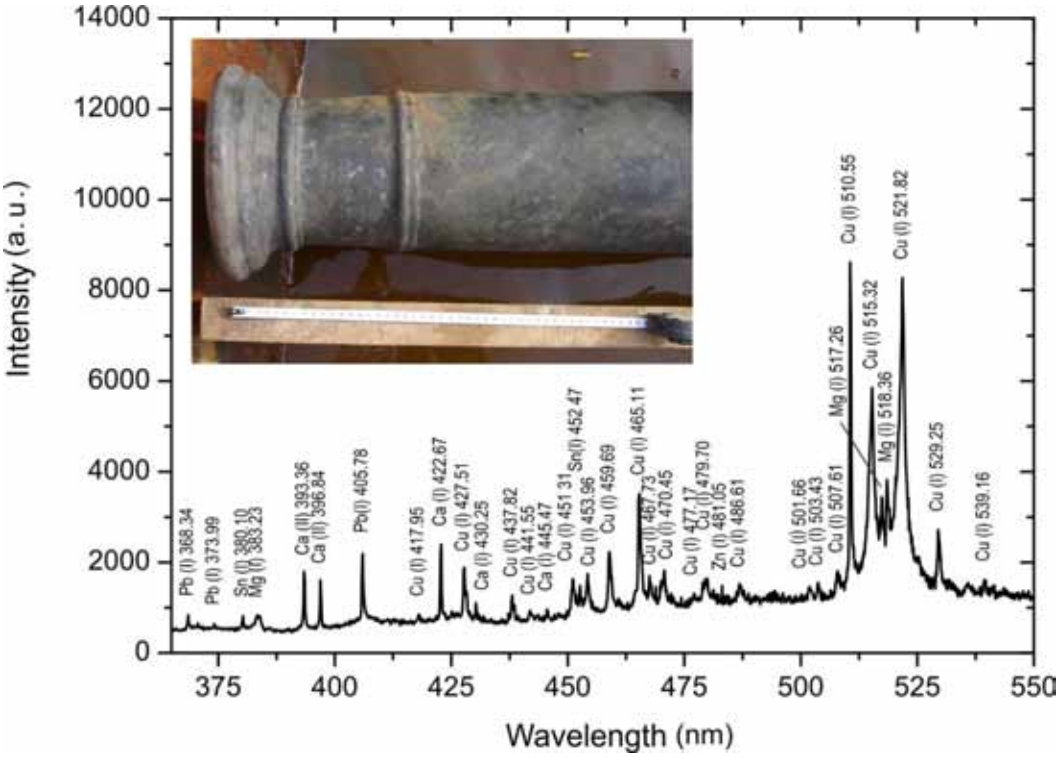

Sample i.d: DII.12.952	**Material:** cannon

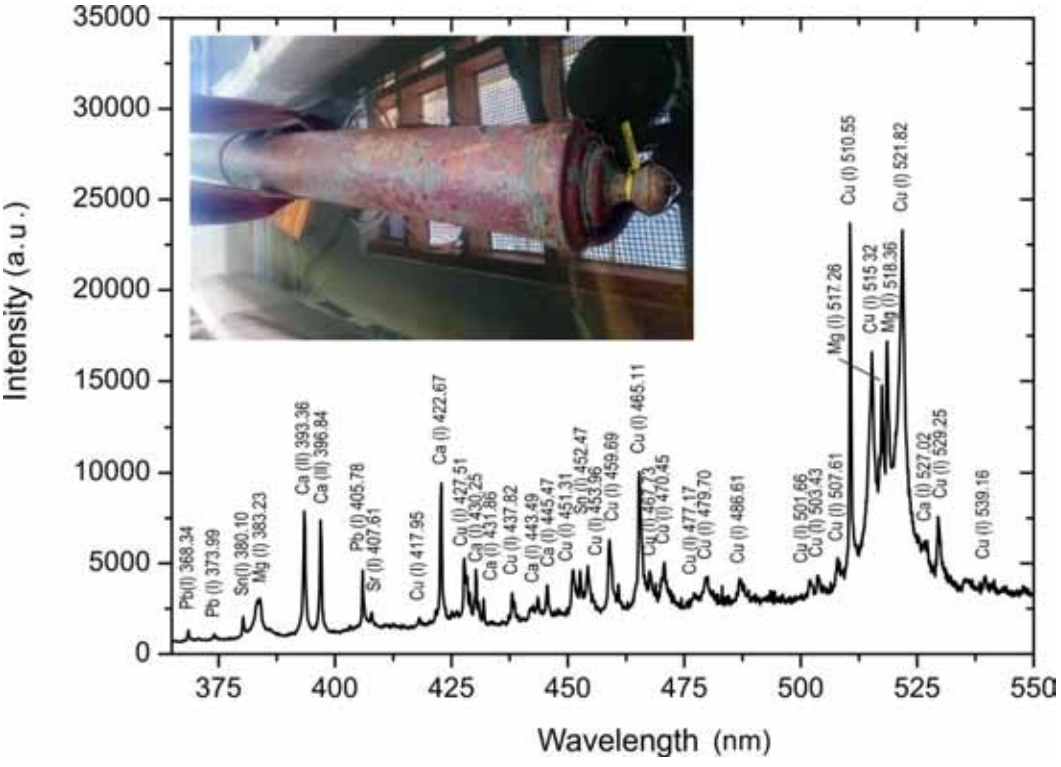

Sample i.d: DII.12.953	**Material:** cannon

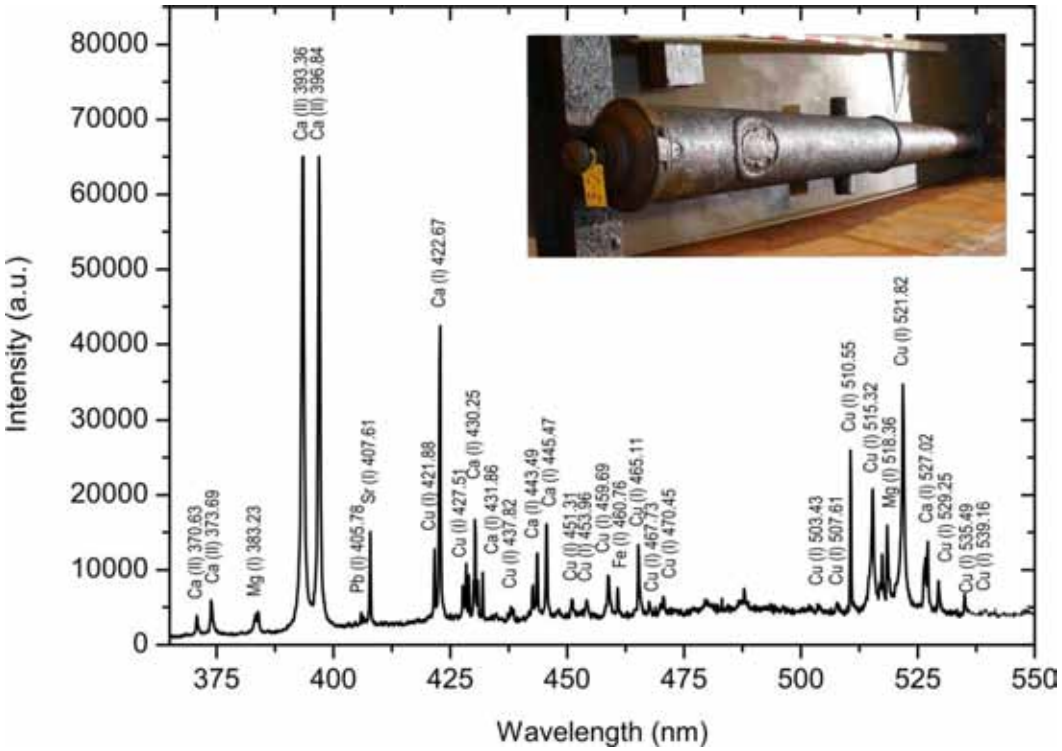

Sample i.d: DII.13.504	**Material:** earthenware pitcher

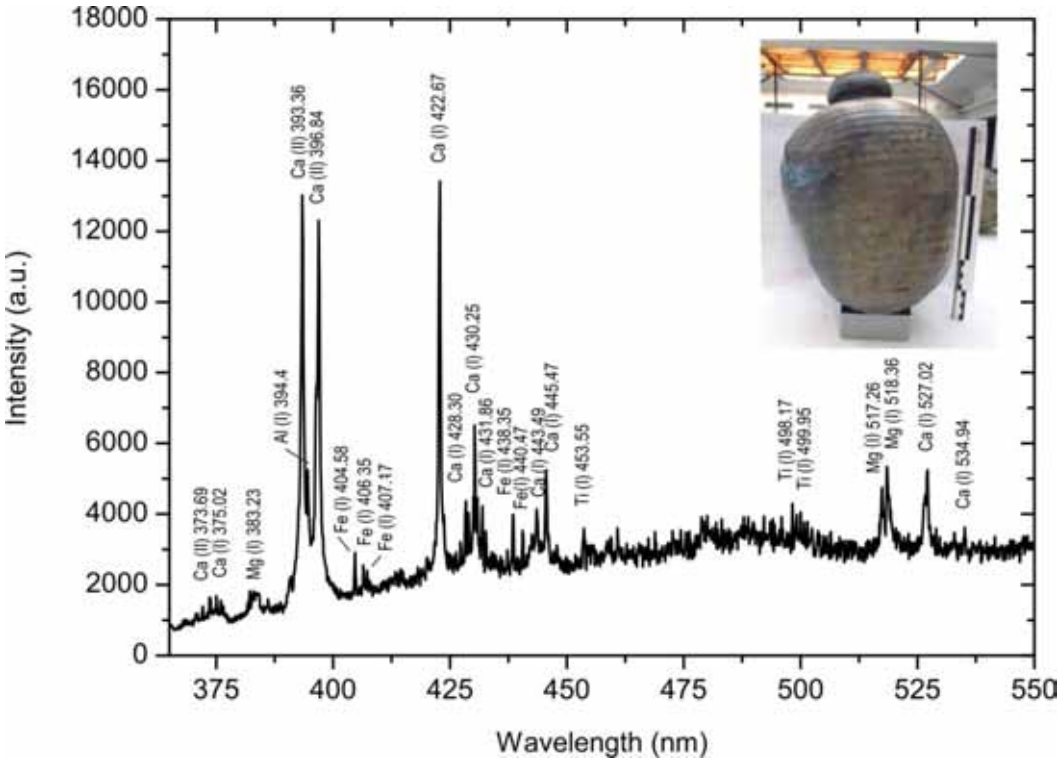

Delta III shipwreck

Delta III corresponds to remains of a wreck of a ship located in container terminal of Cadiz port. Constructive characteristics that it presents as well as the manufacture of the mechanism observed, indicate a Dutch origin and a chronological period around 17th century.

Sample i.d: DIII.541	**Material:** spoon

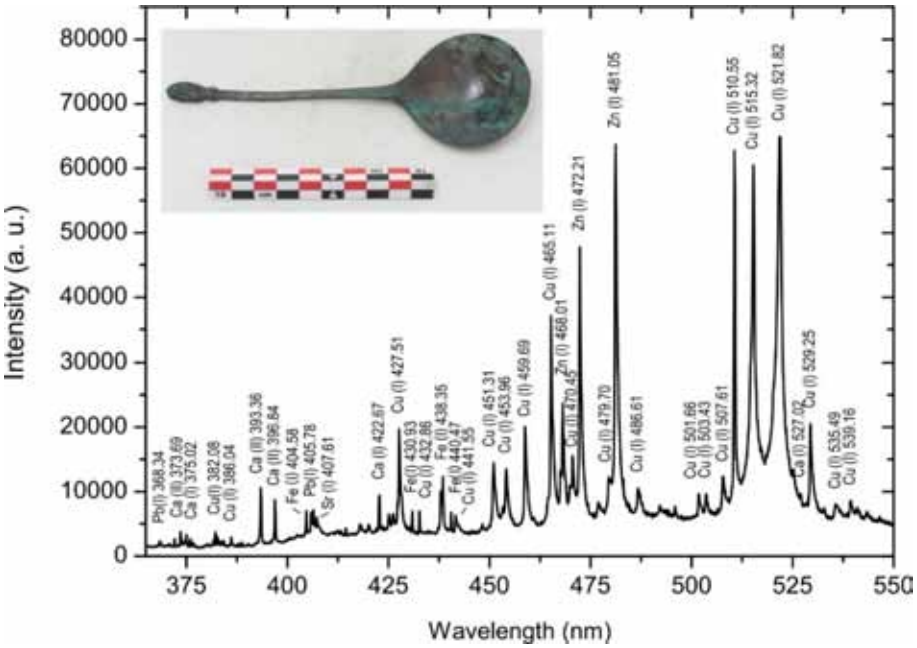

Sample i.d: DIII.605	**Material:** ring

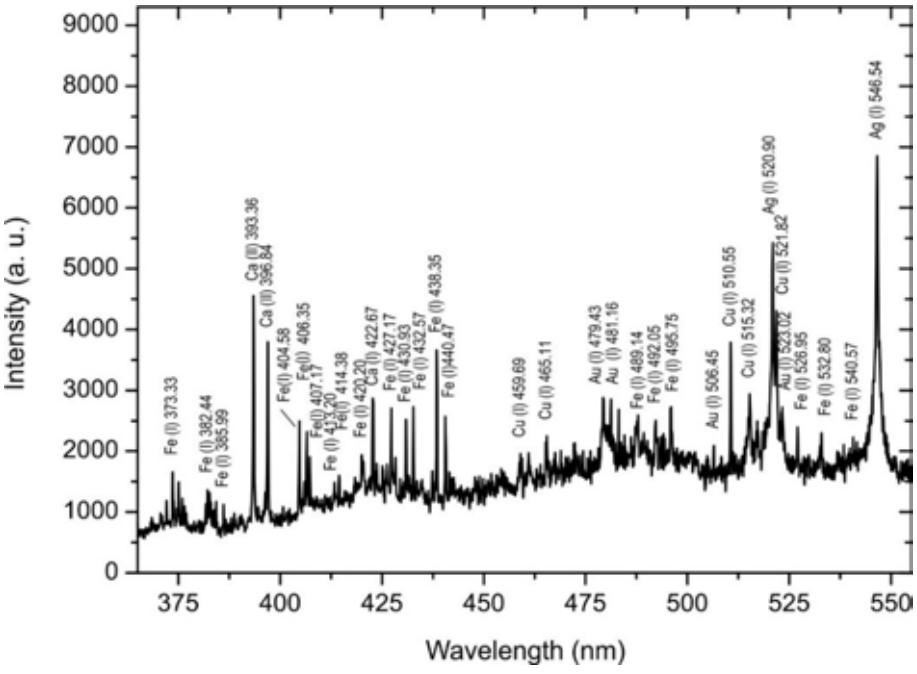

Sample i.d: DIII.838	**Material:** cannon fragment

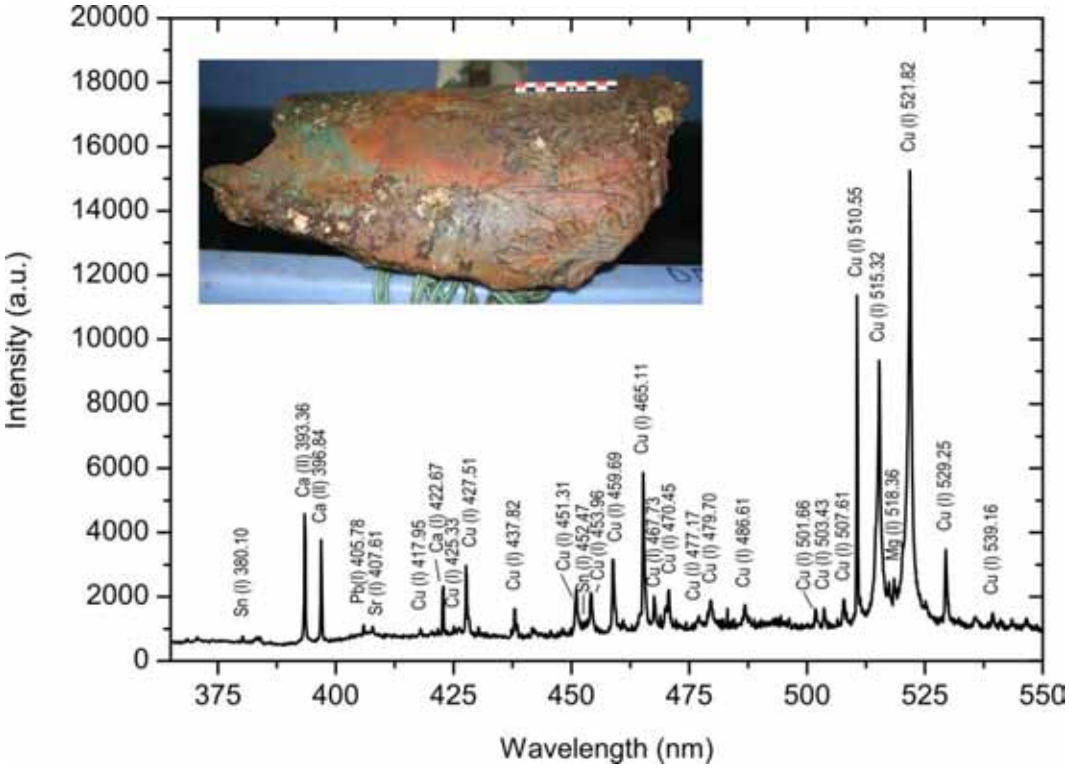

Sample i.d: DIII.839	**Material:** cannon

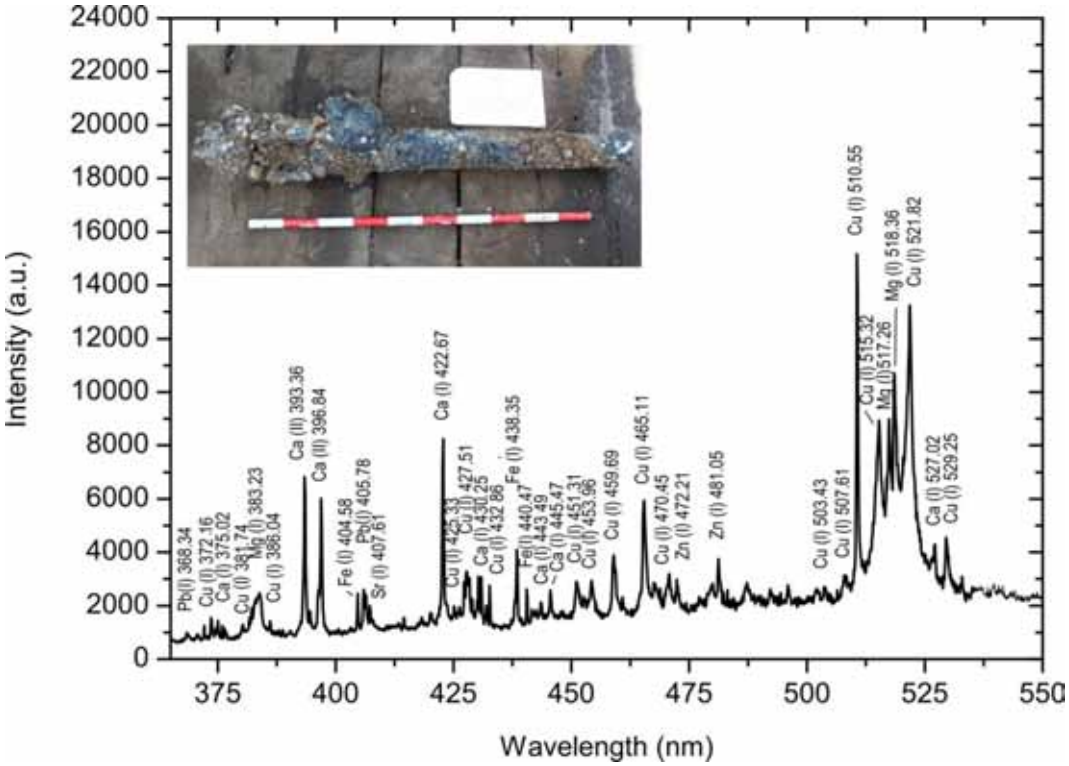

Sample i.d: DIII.14.18	**Material:** cannon bullet

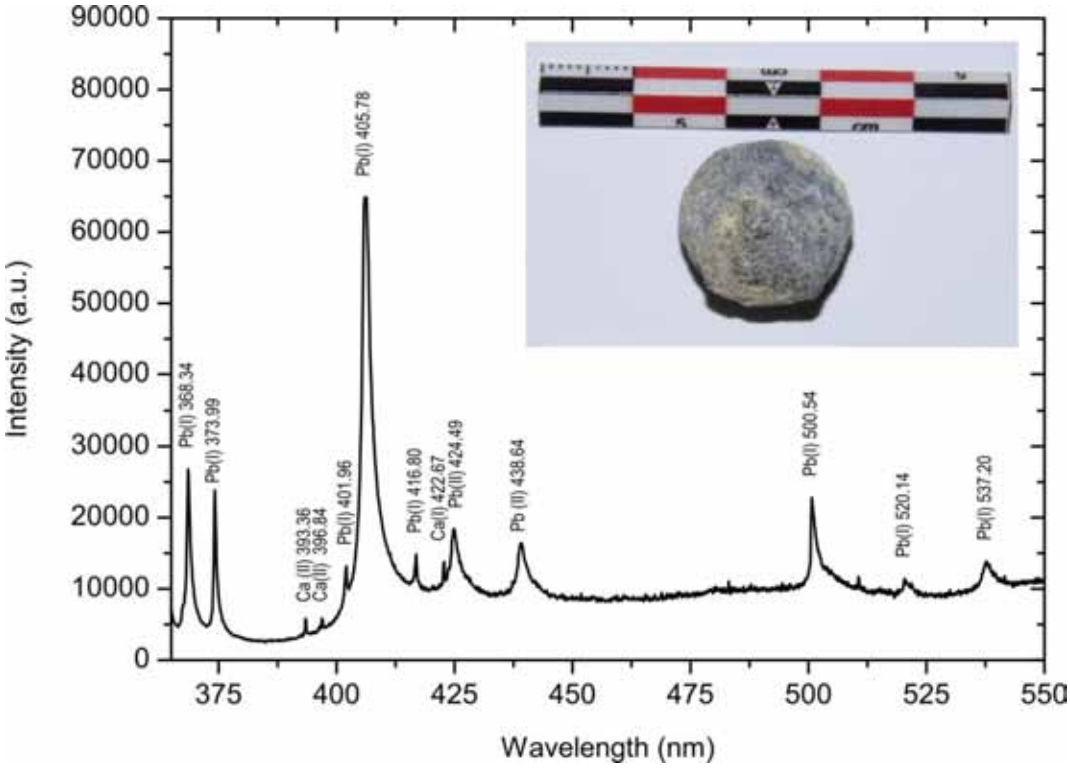

Sample i.d: DIII.14.2	**Material**: cannon load zone

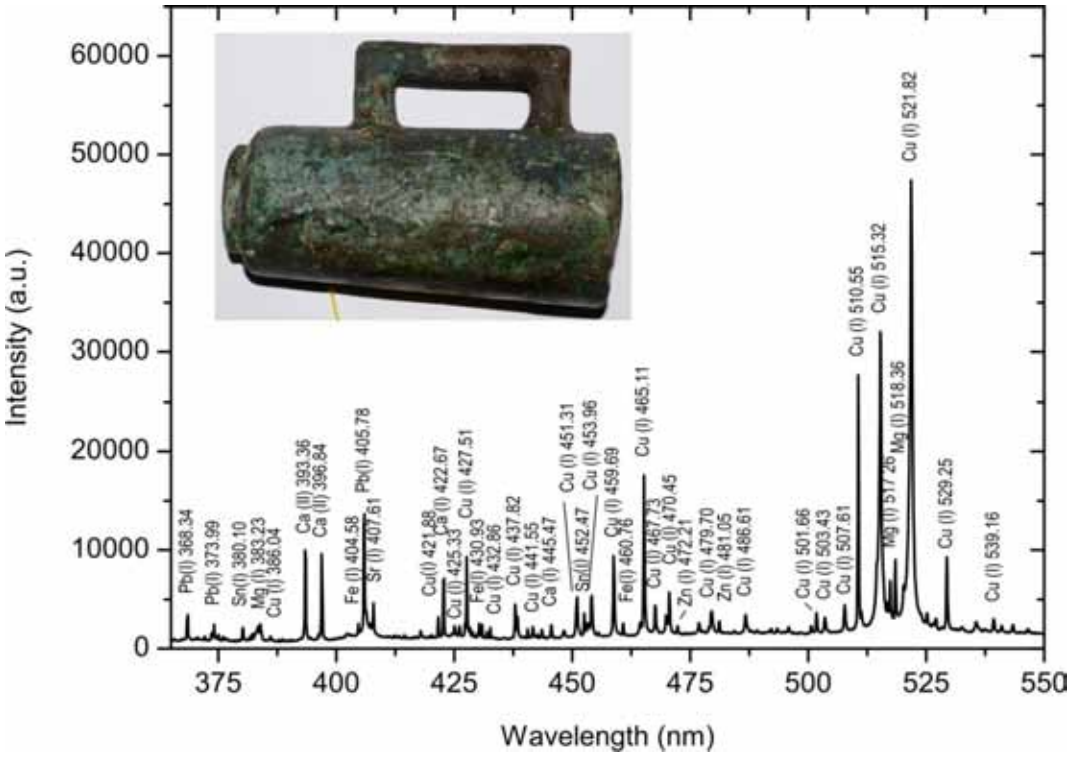

Sample i.d: DIII.SP.19	**Material:** crucible

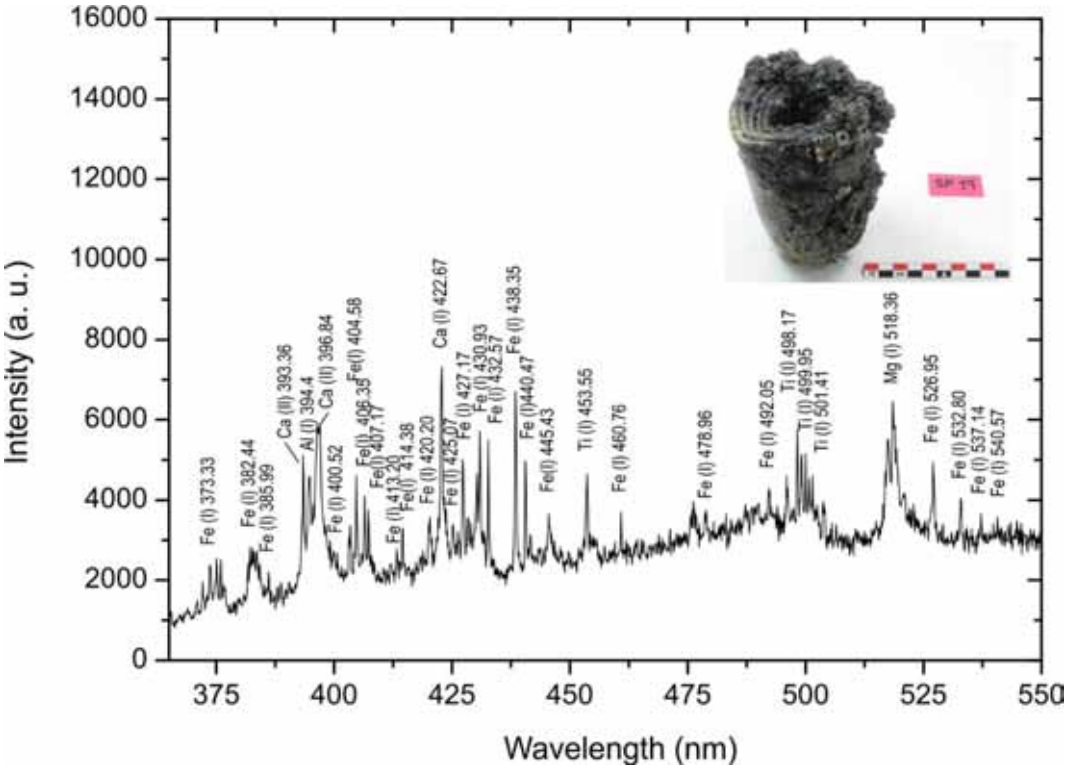

Sample i.d: DIII.SP.116	**Material:** metal band

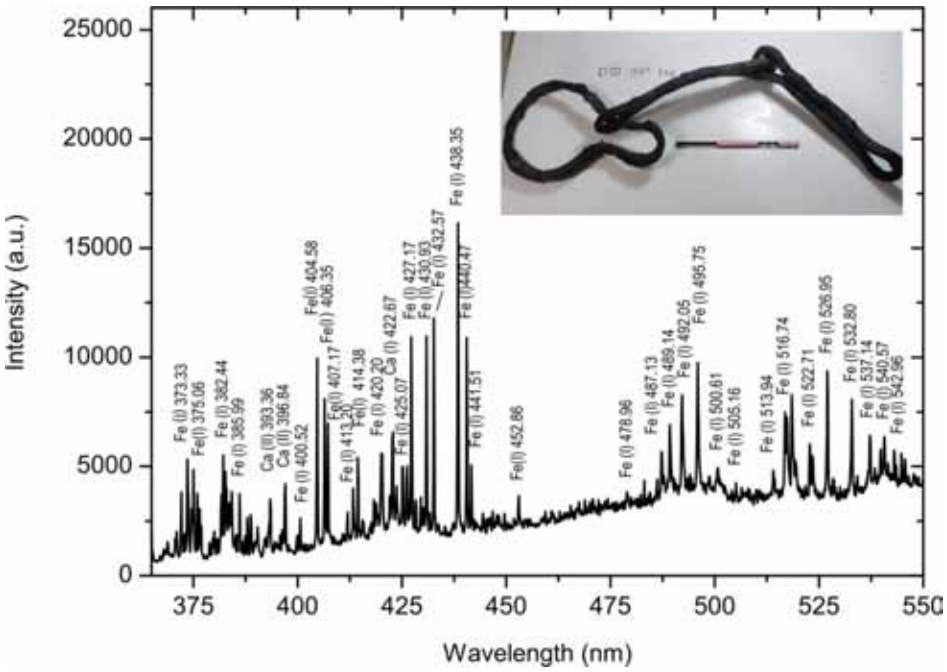

Bajo de San Sebastián shipwreck

The remains of a shipwreck of a medium-sized vessel have been located in the *Bajo de San Sebastián* (Cadiz). On based of the materials found, archaeologists point out that it should be merchant vessel built at the end of 18th century- early 19th century. The merchant was carrying a military cargo in which is highlighted discovery such as sword hilts and artillery pieces. Currently, the ship preserves part of one side.

Sample i.d: MSS. CA-10.02	**Material:** handgun fragment

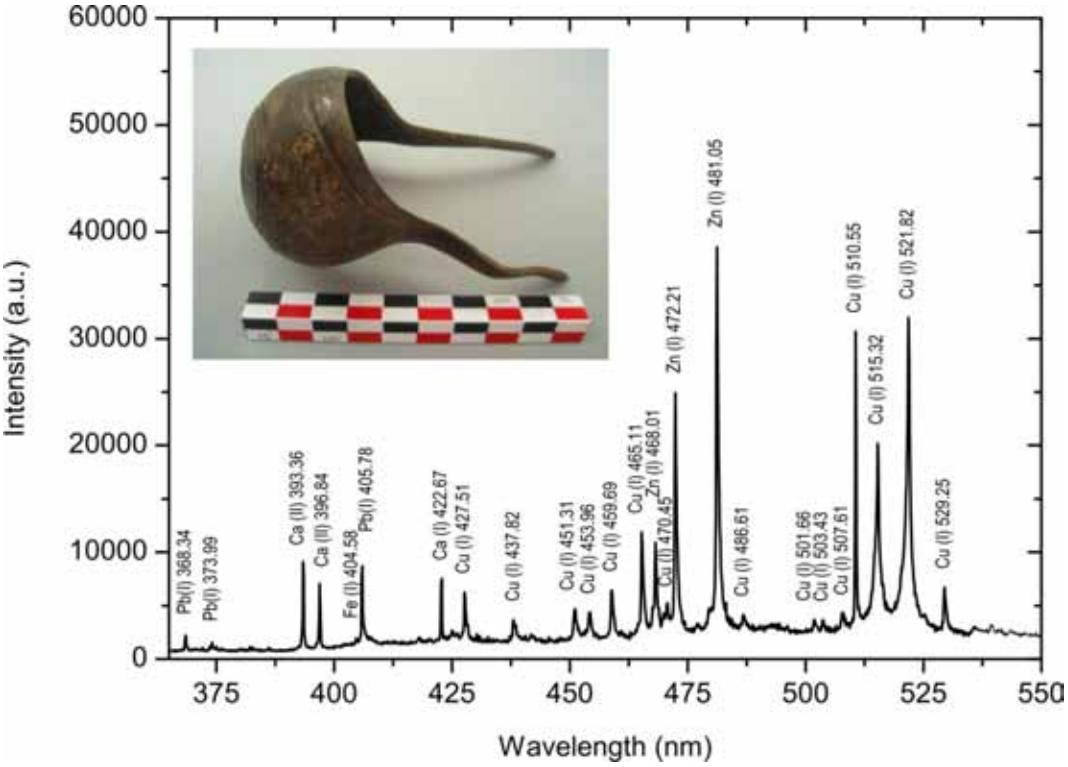

Sample i.d: MSS. CA-10.03-1	**Material:** sabre hilt

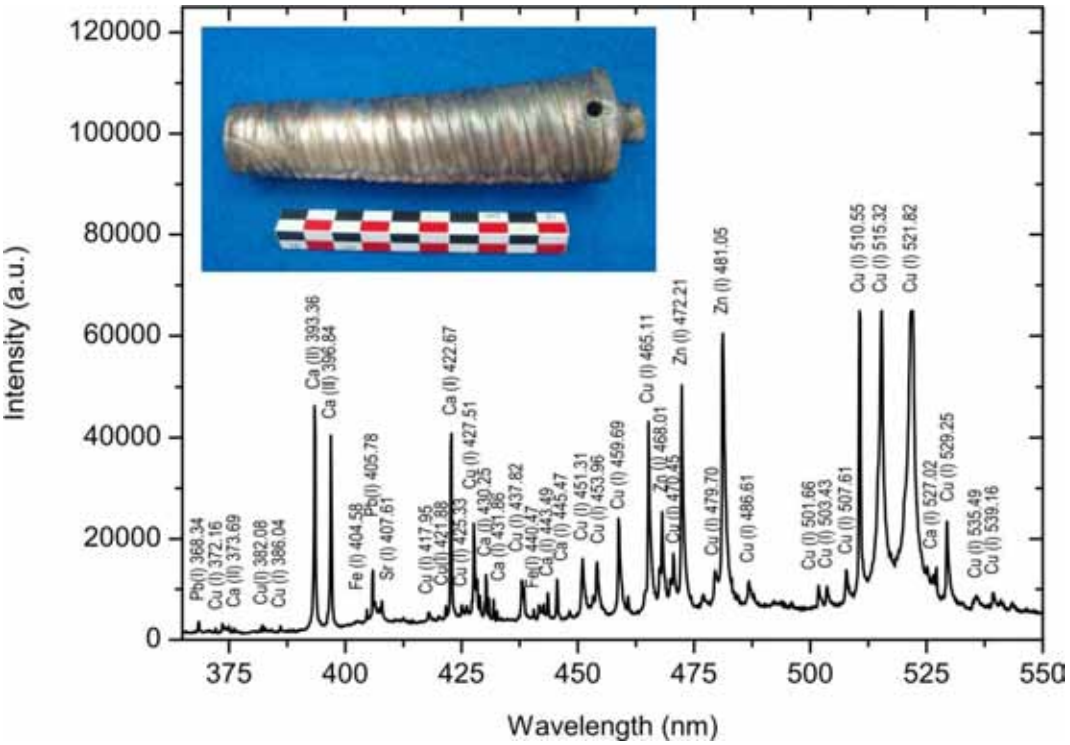

Sample i.d: MSS. CA-10.45	**Material:** rifle fragment

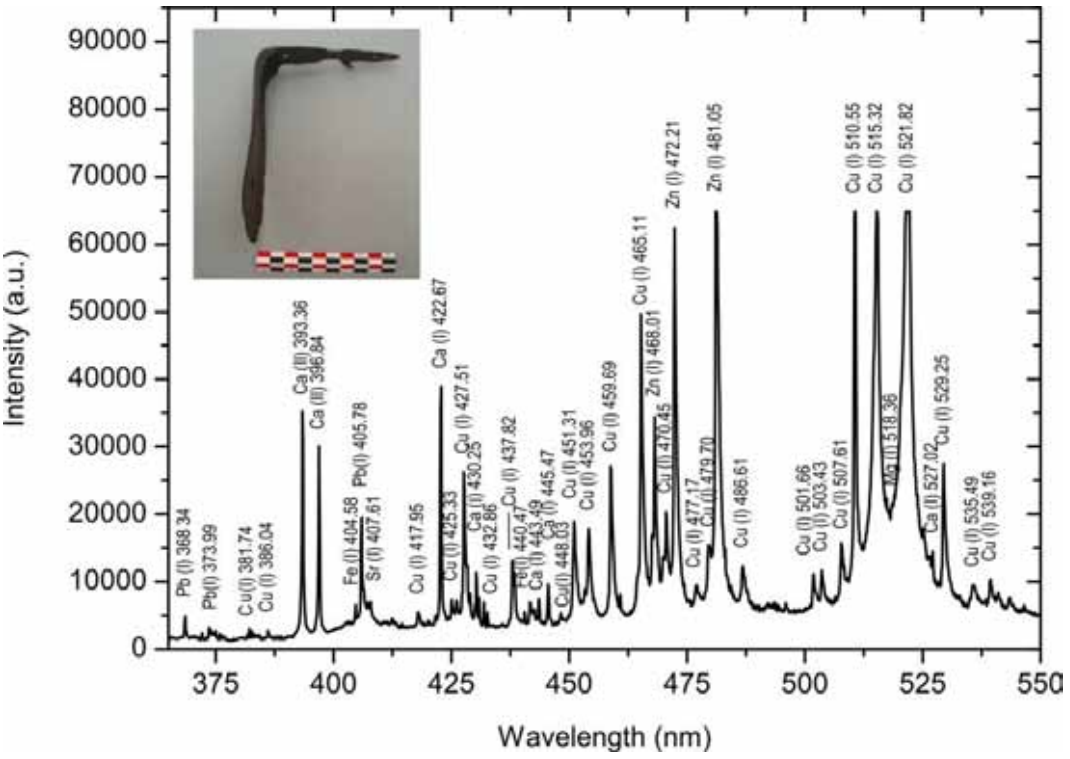

Sample i.d: MSS. CA-10.46	**Material:** hilt

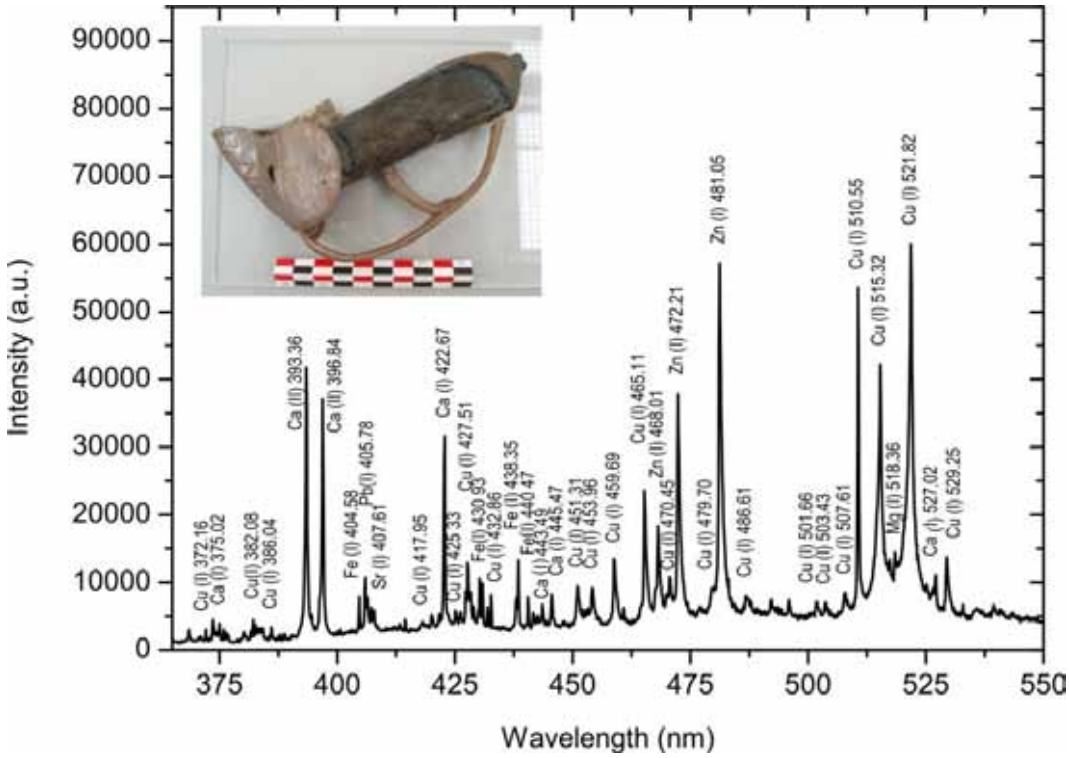

Sample i.d: MSS. CA-10.50	**Material:** arm fragment

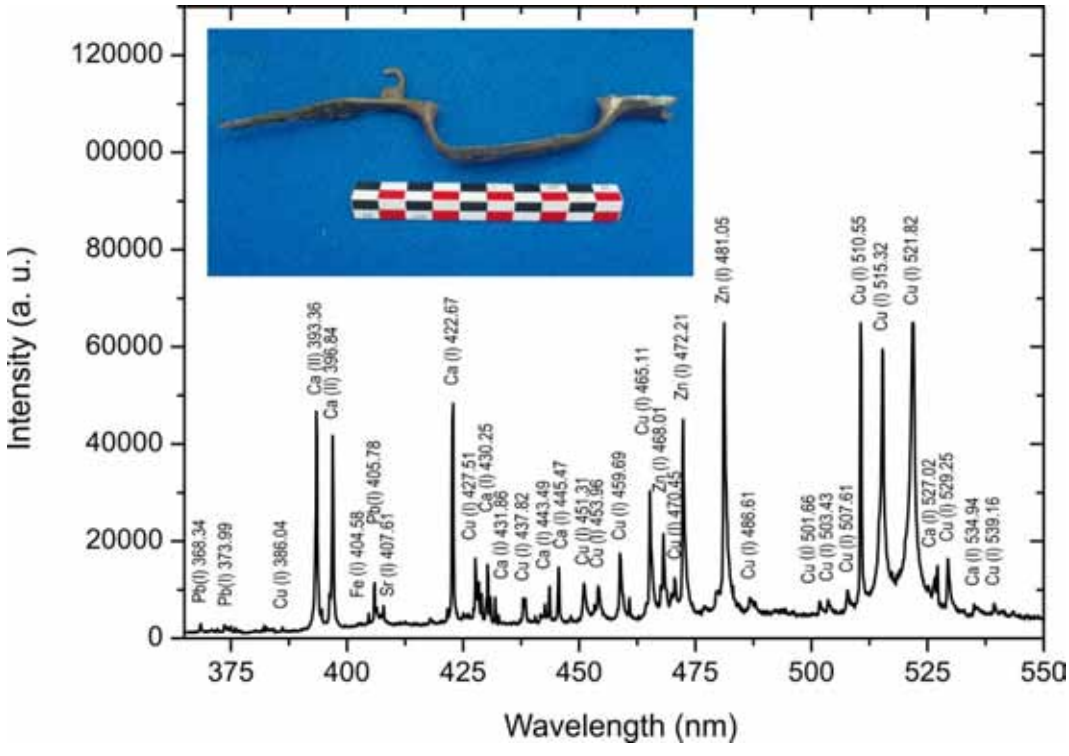

Sample i.d: MSS. CA-11.219	**Material:** sheathing

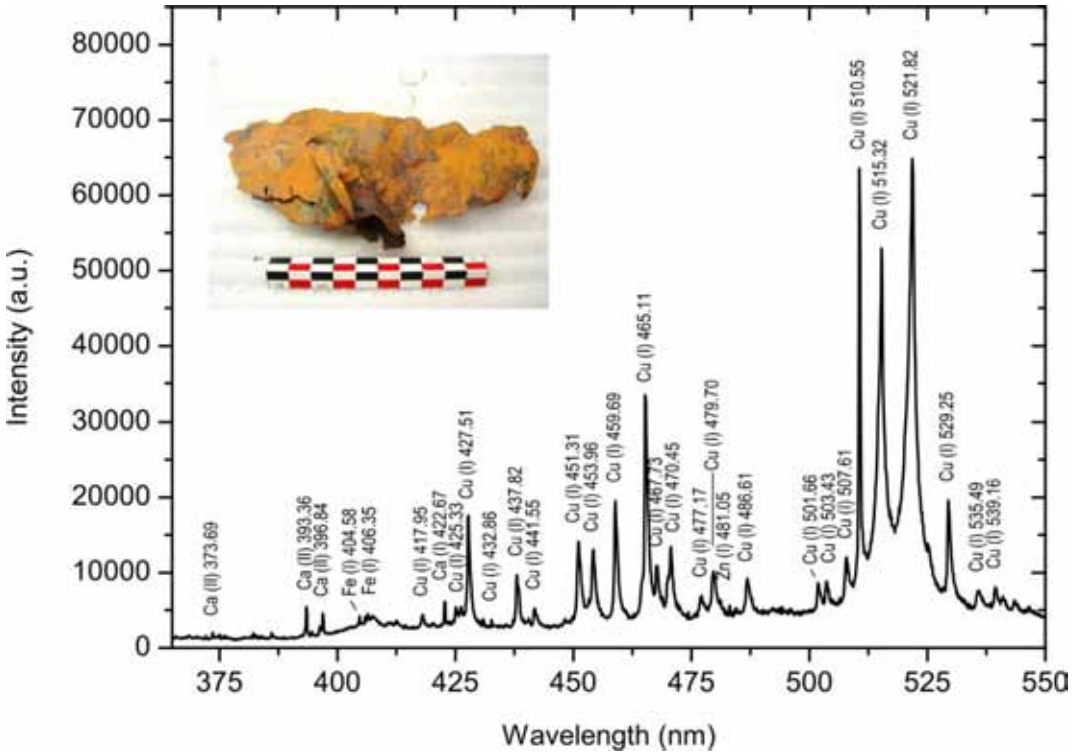

Sample i.d: MSS. CA-11.220	**Material:** sheathing

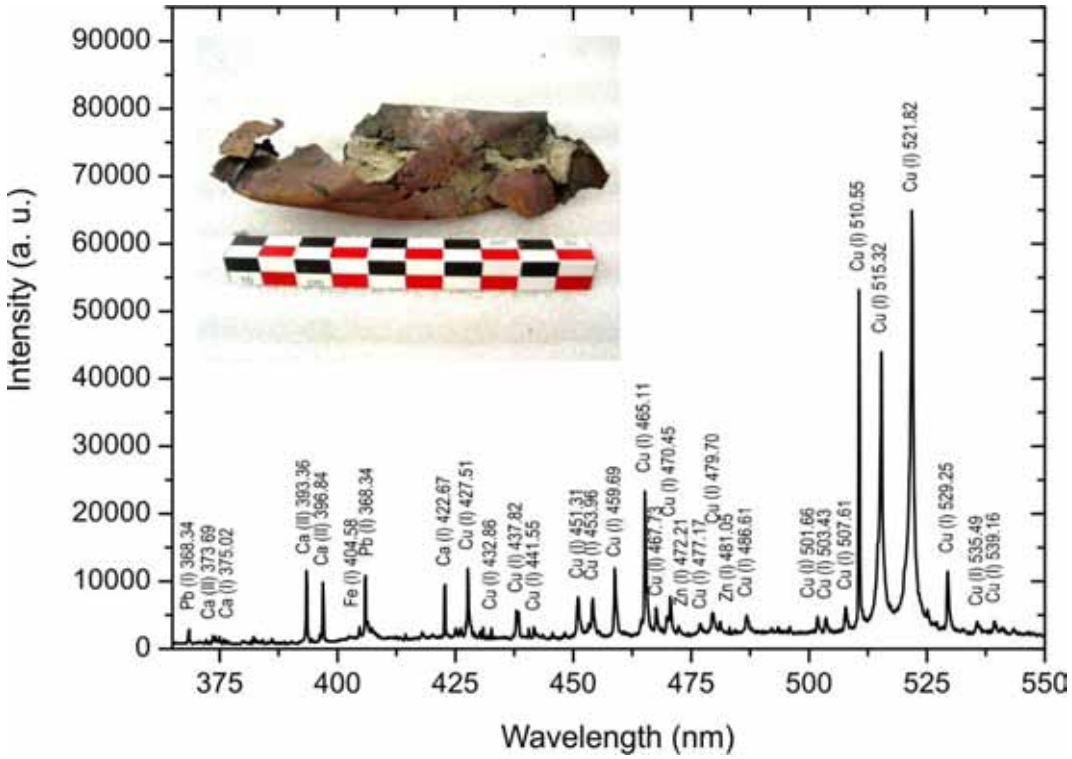

Bucentaure shipwreck

The remains of a shipwreck of a vessel have been located close to *Castillo de San Sebastian*, *Bajo de San Sebastián* (Cadiz). On based of current documentation found, archaeologists point out that it should be the vessel *Bucentaure*. This ship, which was the flag ship of the French–Spanish alliance during the Battle of Trafalgar, sank in the Bay of Cadiz in 1805. There mains of the wreck were discovered in 1949 at 17 m depth and include remarkably well-preserved objects such as cannons.

Sample i.d: BCH.CA-05.14	**Material:** cannon

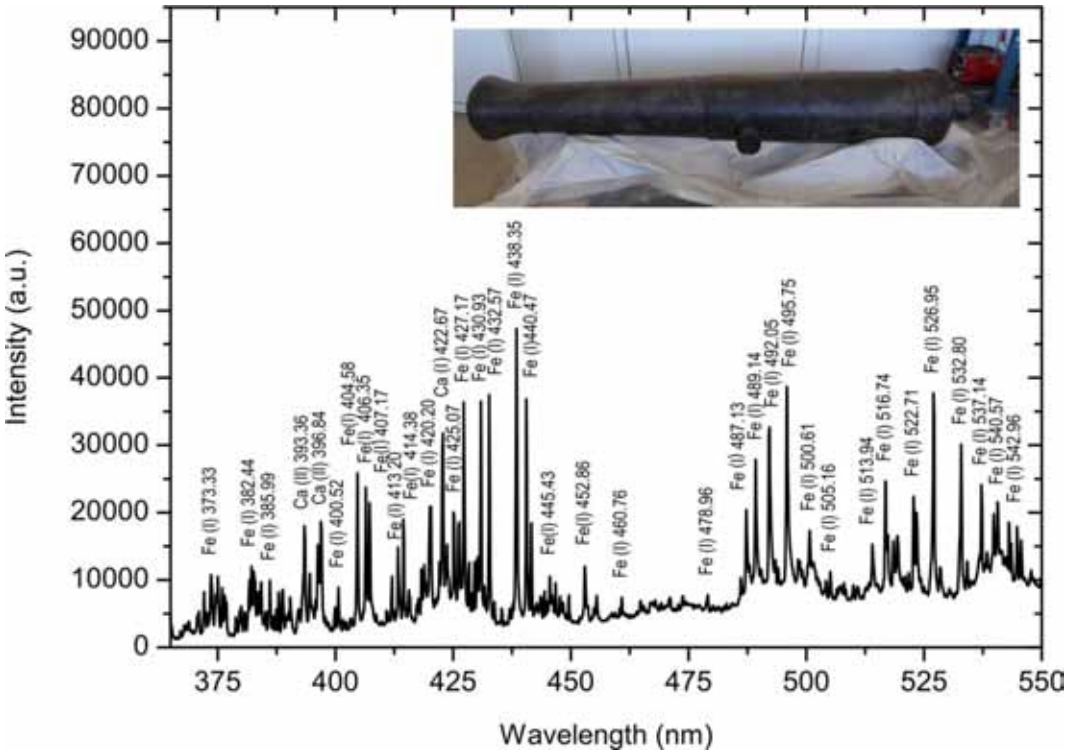

Camposoto shipwreck

The main archaeological remains found in *Camposoto*, *San Fernando* (Cádiz) site, correspond to a ship sank in which a beam of 25 m is preserved. The analysis of constructive system, as well as, its artillery and personal basic tools and military could indicate that is a ship of French origin and its chronological ascription to moments close to the Battle of Trafalgar. On based of this current documentation, archaeologists point out that it should be the French line vessel *Fougueux*. This ship took part of the French–Spanish alliance during the Battle of Trafalgar where it was captured by an English vessel. On the night of October, 22th 1805, *Fougueux* was abandoned after a strong storm erupt being run aground in front of Camposoto beach.

Sample i.d: CAMP.CA-07.33	**Material:** key

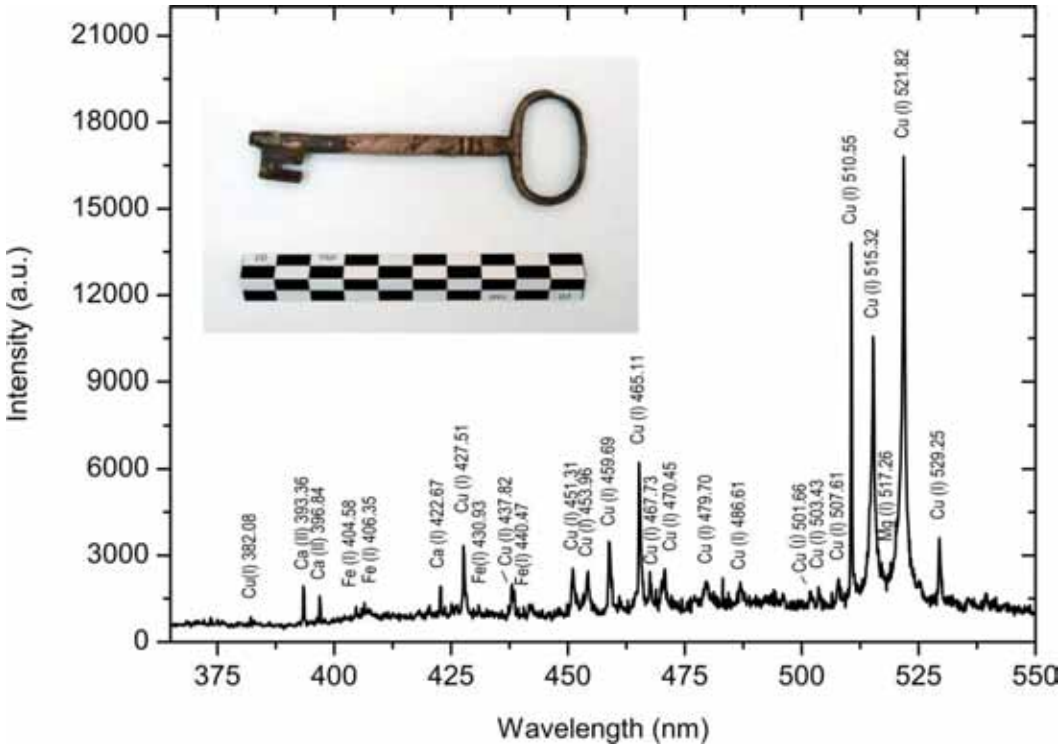

Sample i.d: CAMP.CA-07.44	**Material:** button

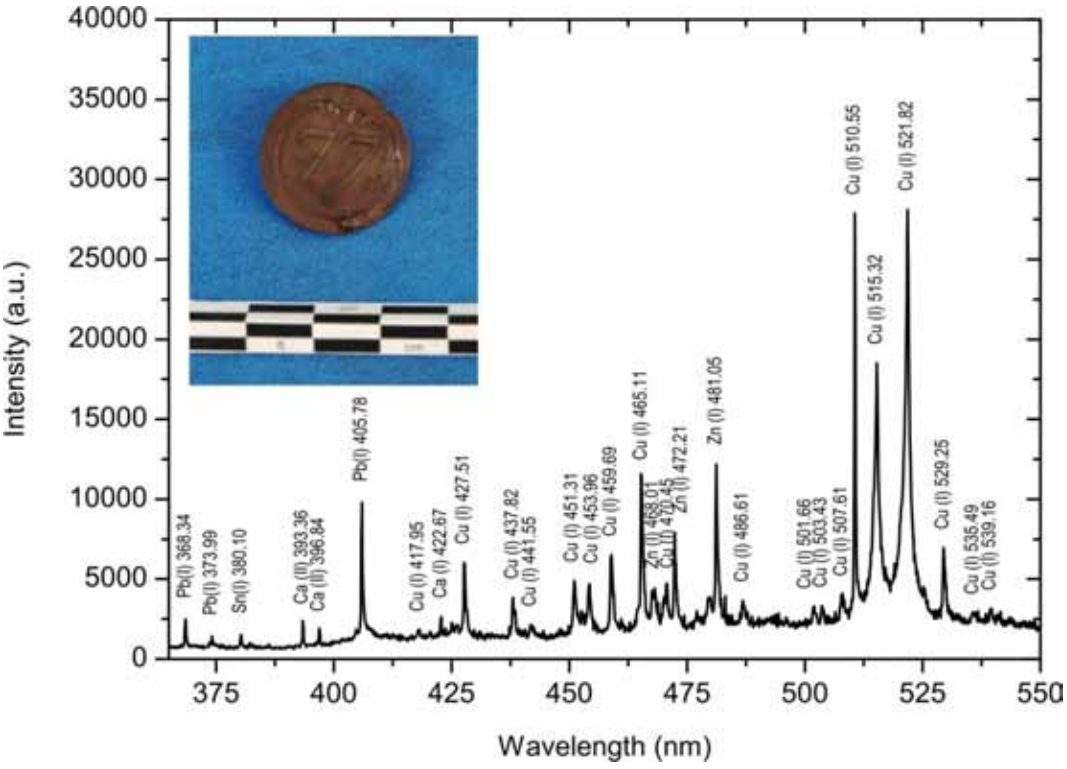

Sample i.d: CAMP.CA-07.59	**Material:** straightedge

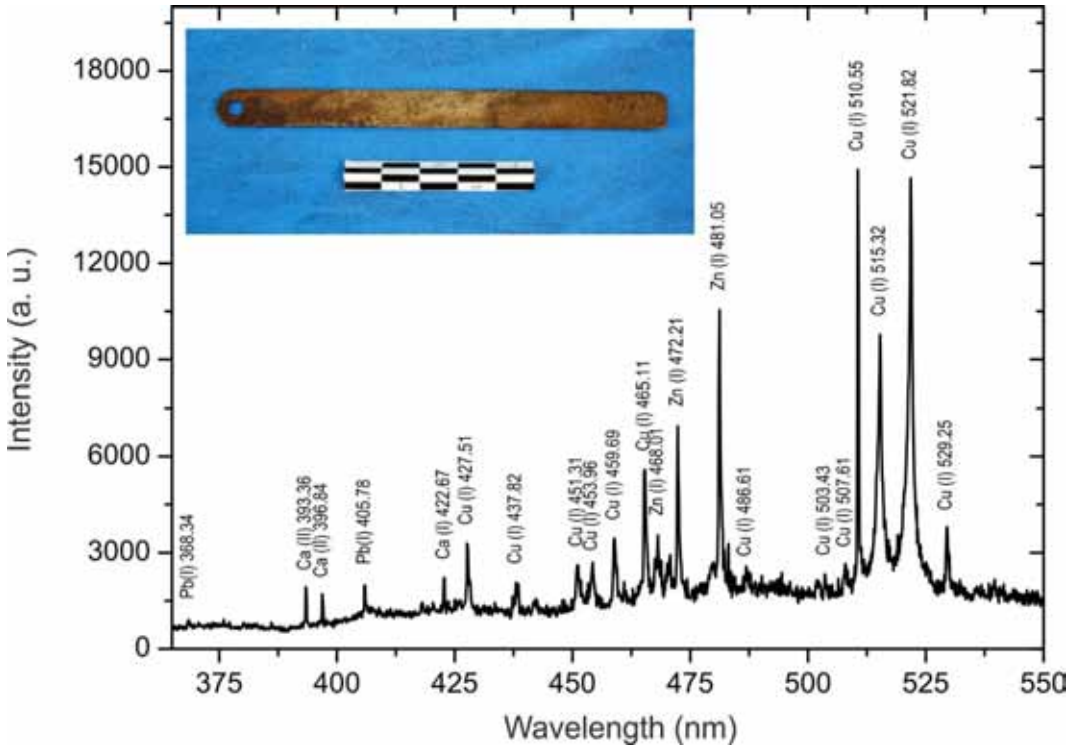

Sample i.d: CAMP.CA-07.81	**Material:** enema

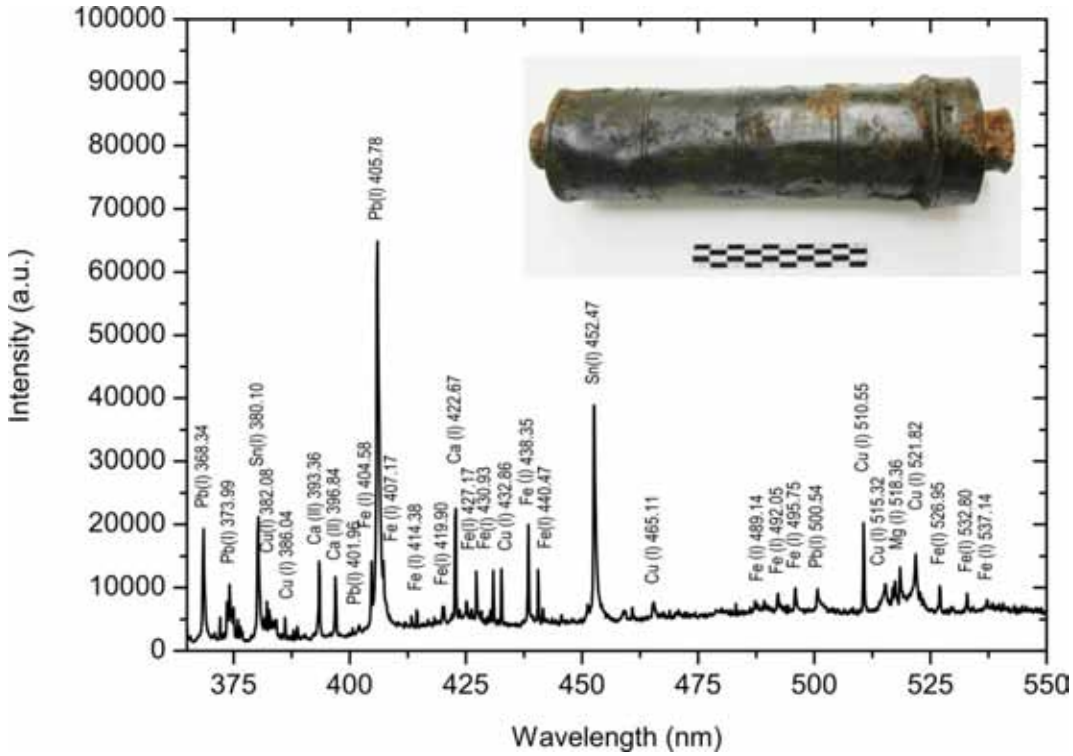

Sample i.d: CAMP.CA-07.96	**Material:** sabre cover

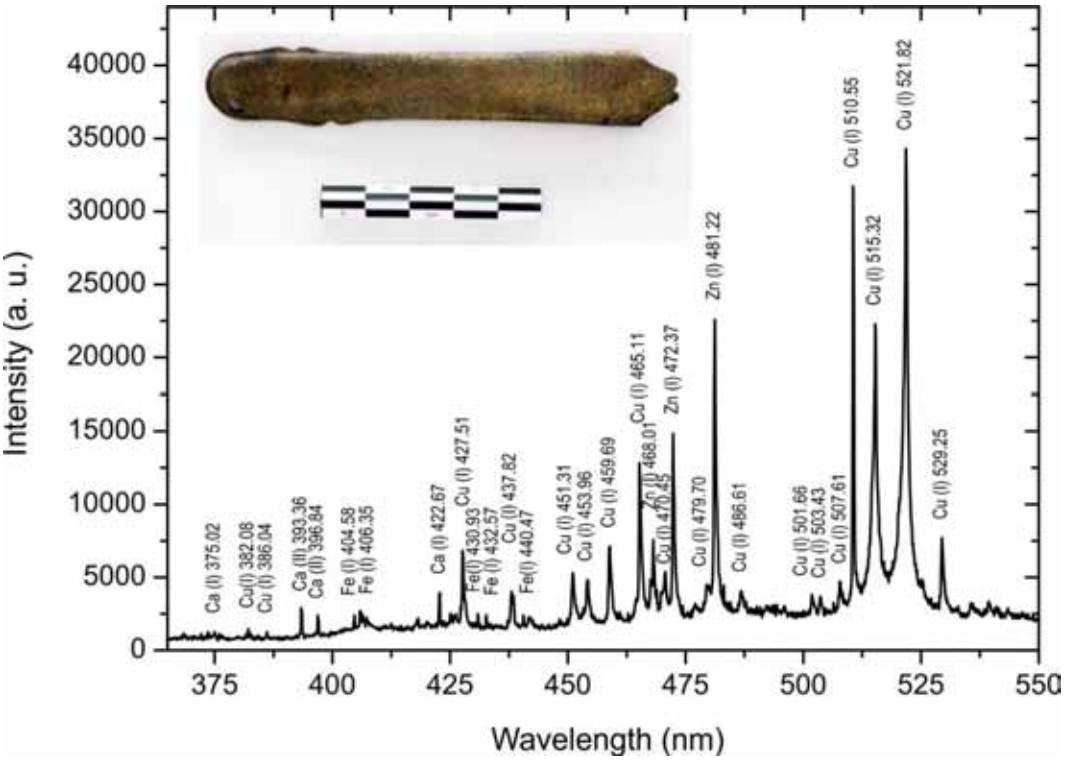

Sample i.d: CAMP.CA-07.109	**Material:** arm fragment

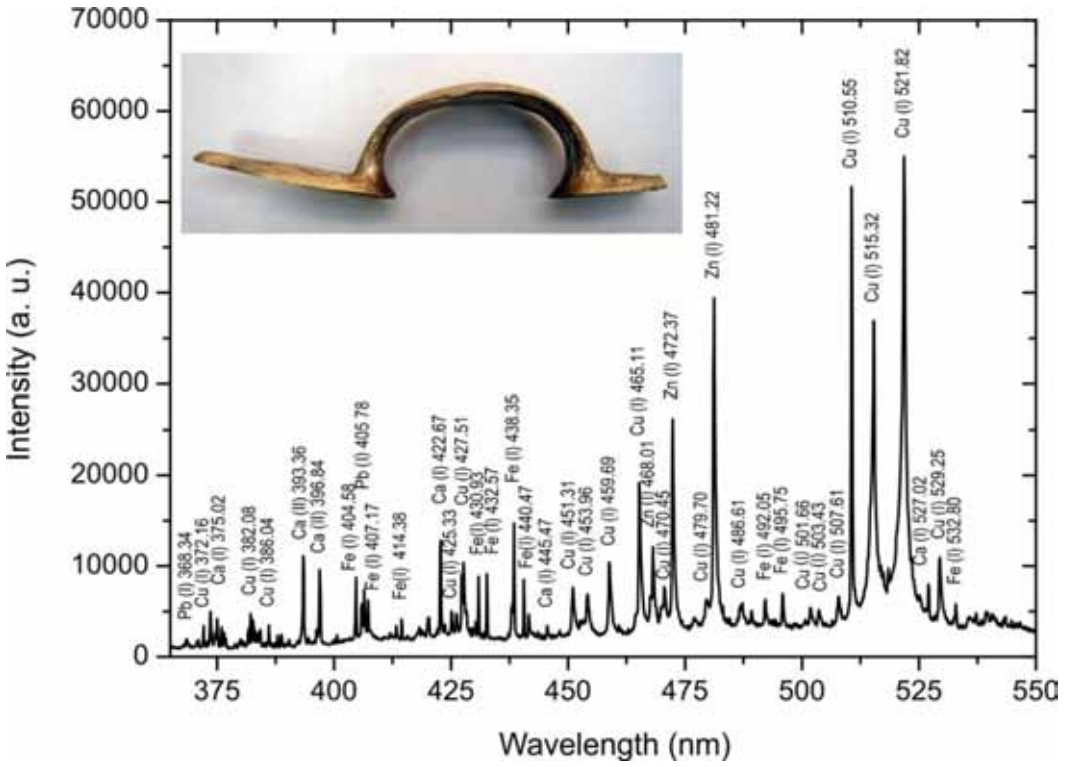

Sample i.d: CAMP.CA-07.136	**Material:** button

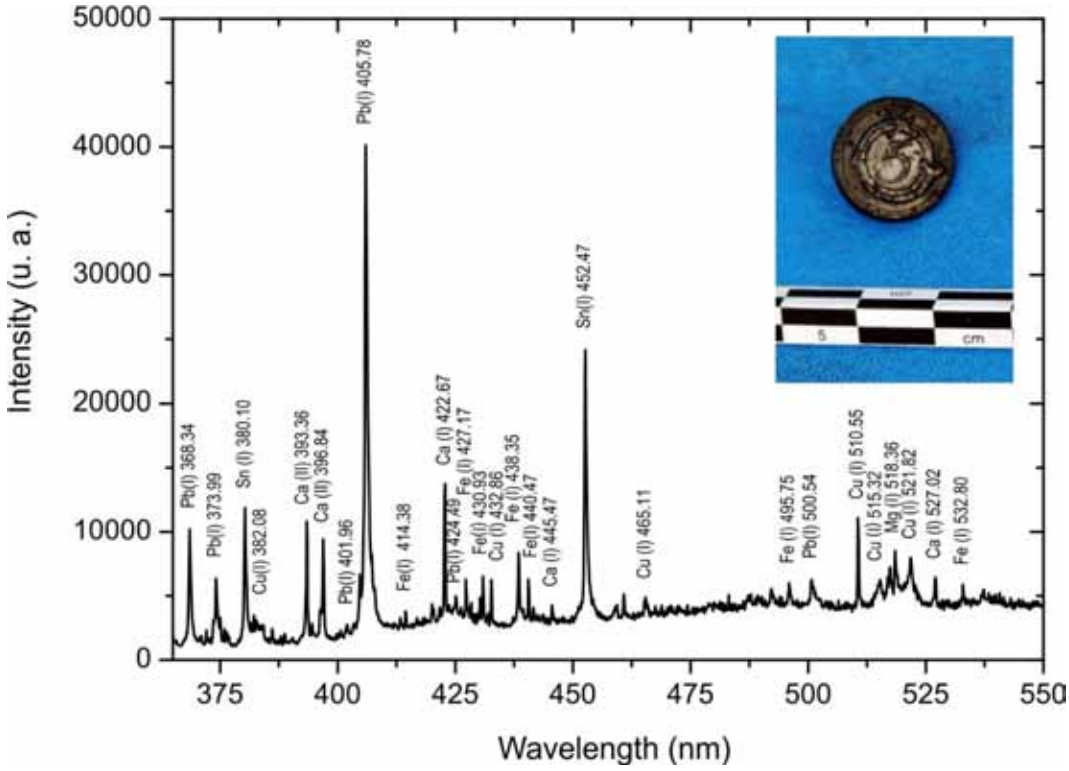

Sample i.d: CAMP.CA-07.137	**Material:** button

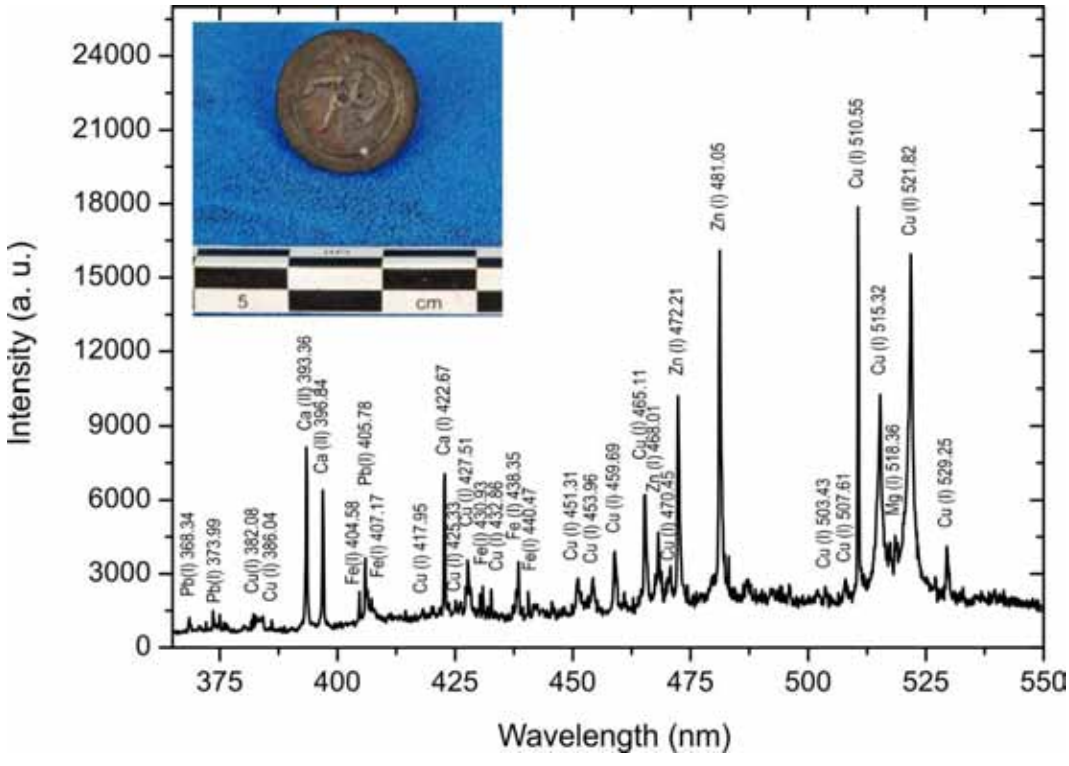

Sample i.d: CAMP.CA-07.147-1	**Material:** republican coin

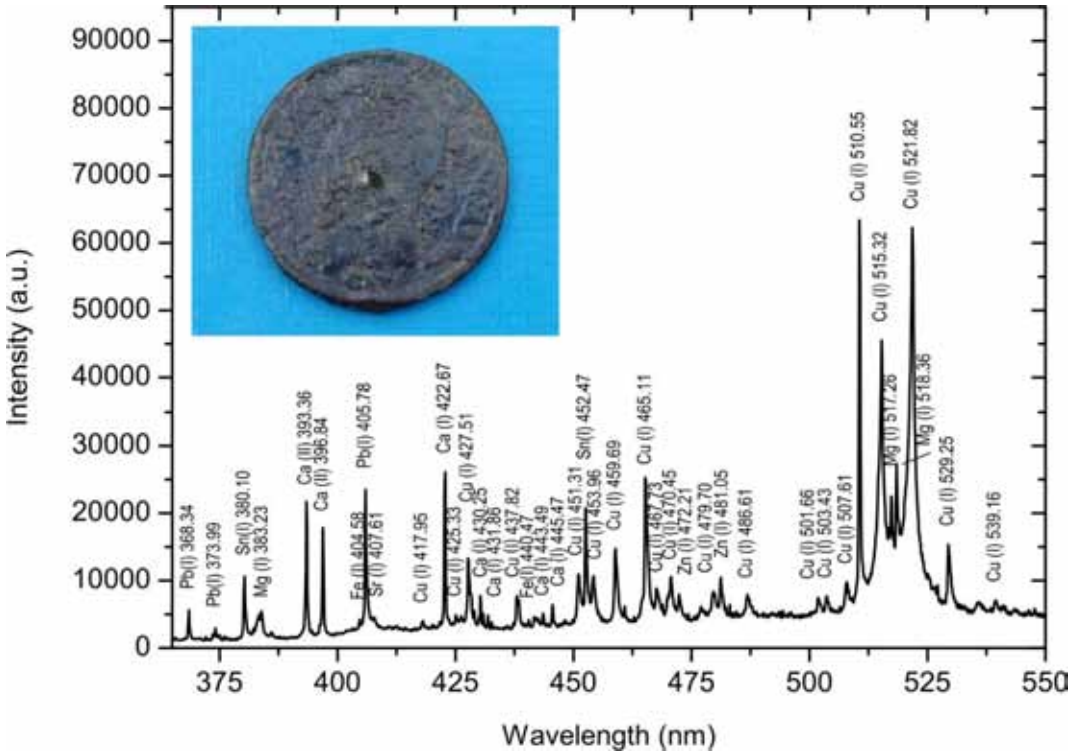

Sample i.d: CAMP.CA-07.147-4	**Material:** monarchical coin

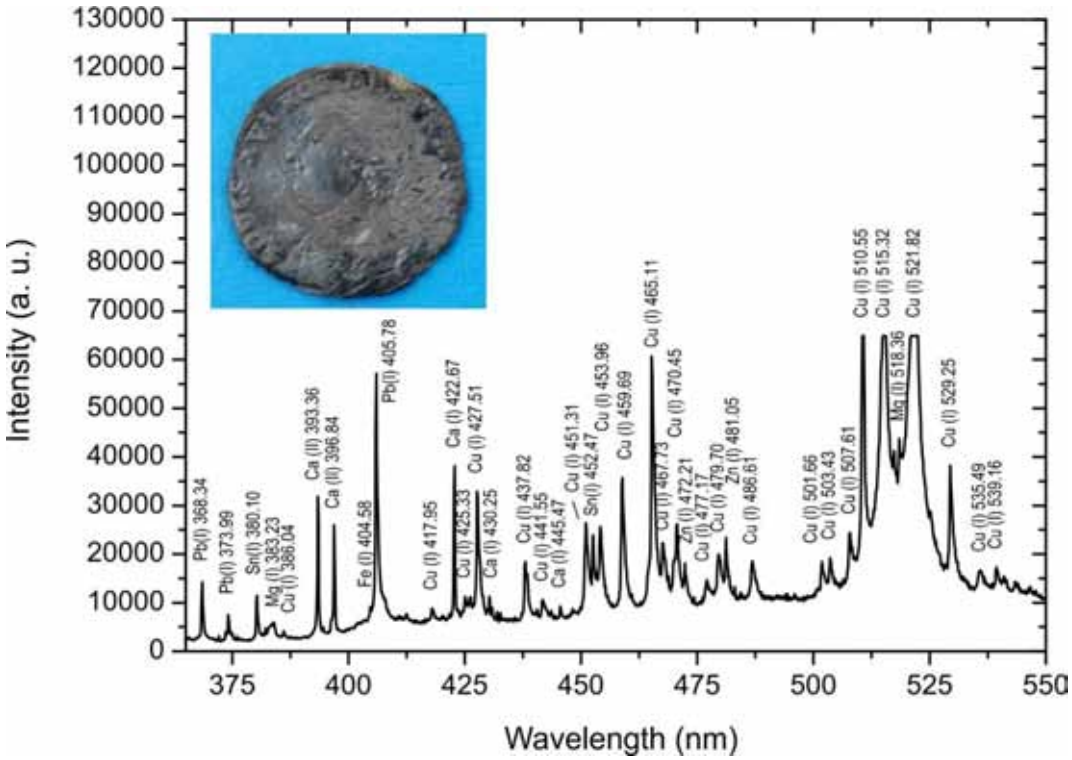

Sample i.d: CAMP.CA-07.149	**Material:** clock

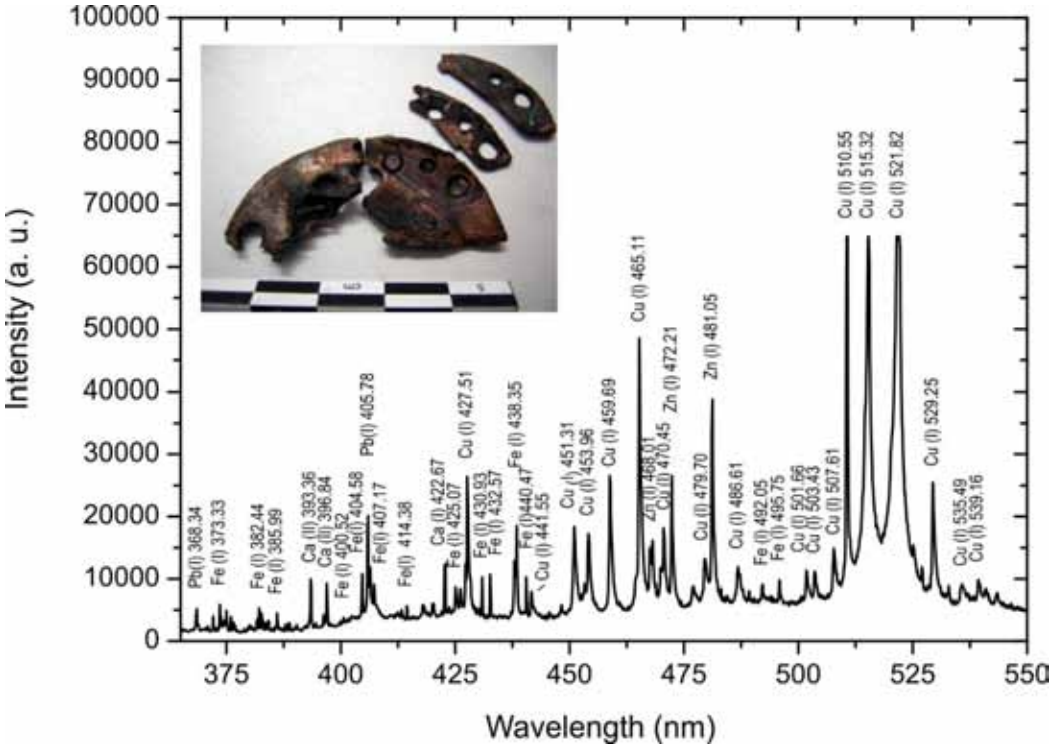

Sample i.d: CAMP.CA-07.171	**Material:** tourniquet

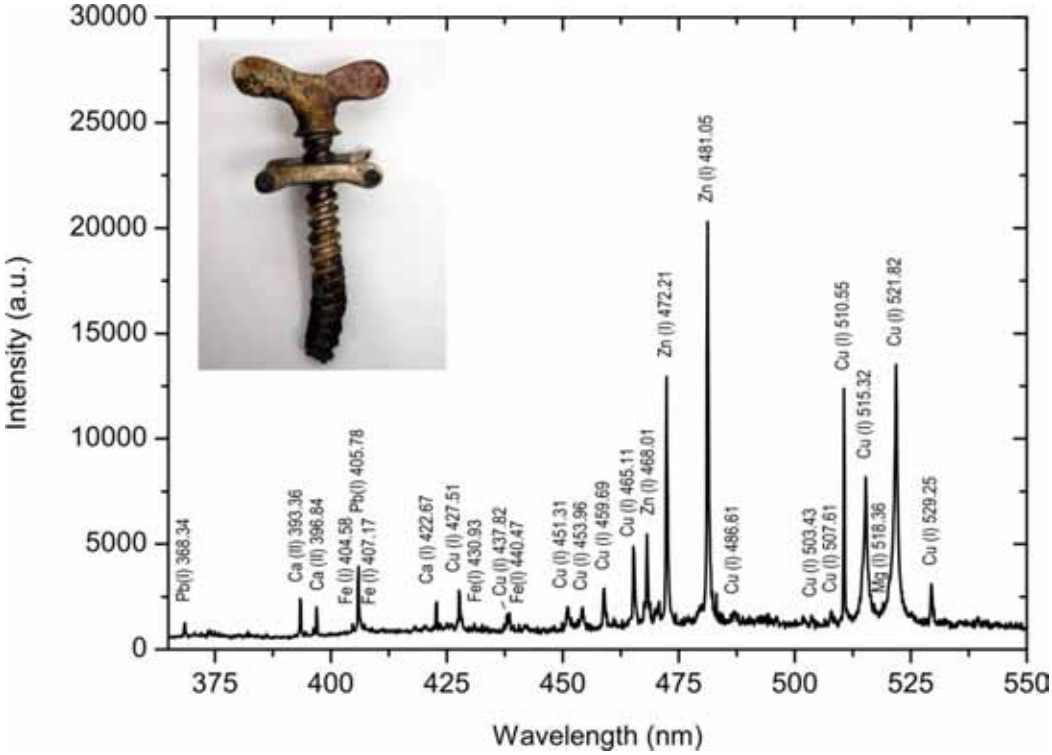

Sample i.d: CAMP.CA-08.20	**Material:** Guinea coin

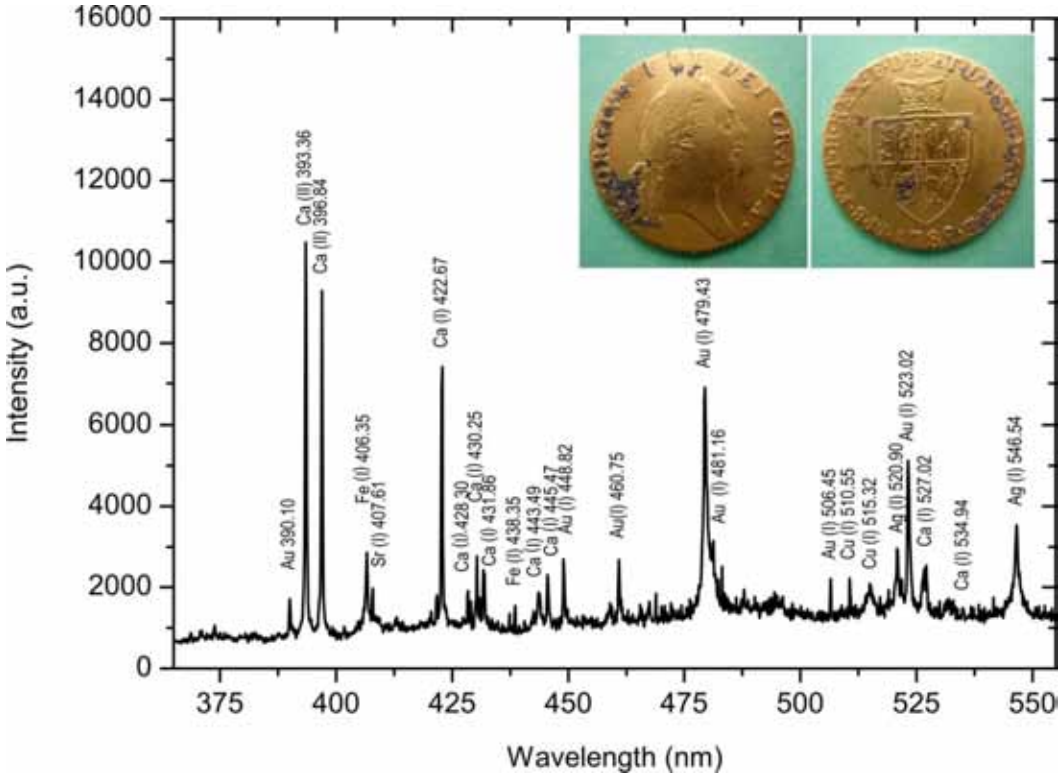

Sample i.d: CAMP.CA-08.23	**Material:** hilt

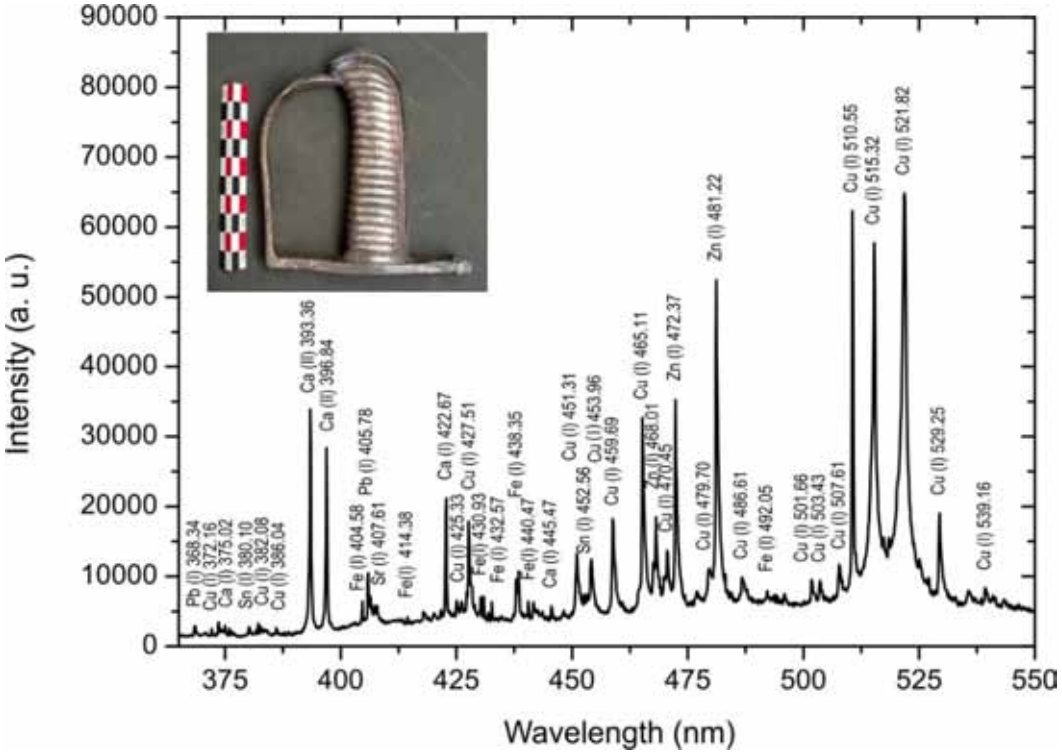

Sample i.d: CAMP.CA-08.67	**Material:** wedge

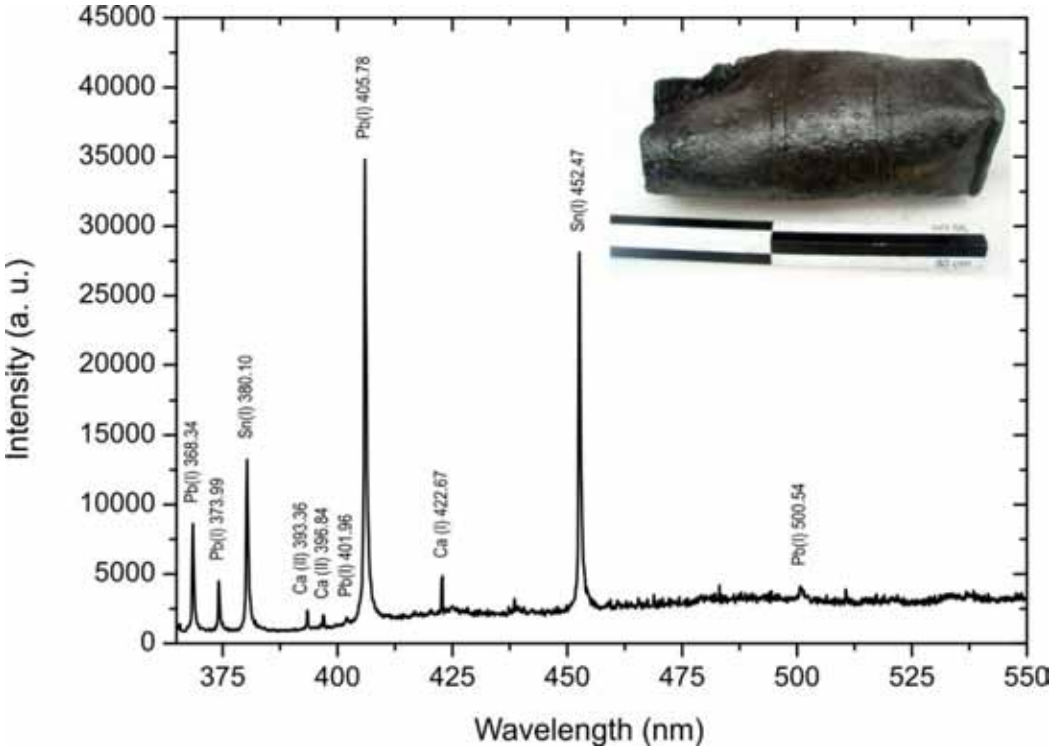

Sample i.d: CAMP.CA-08.73	**Material**: handgun fragment

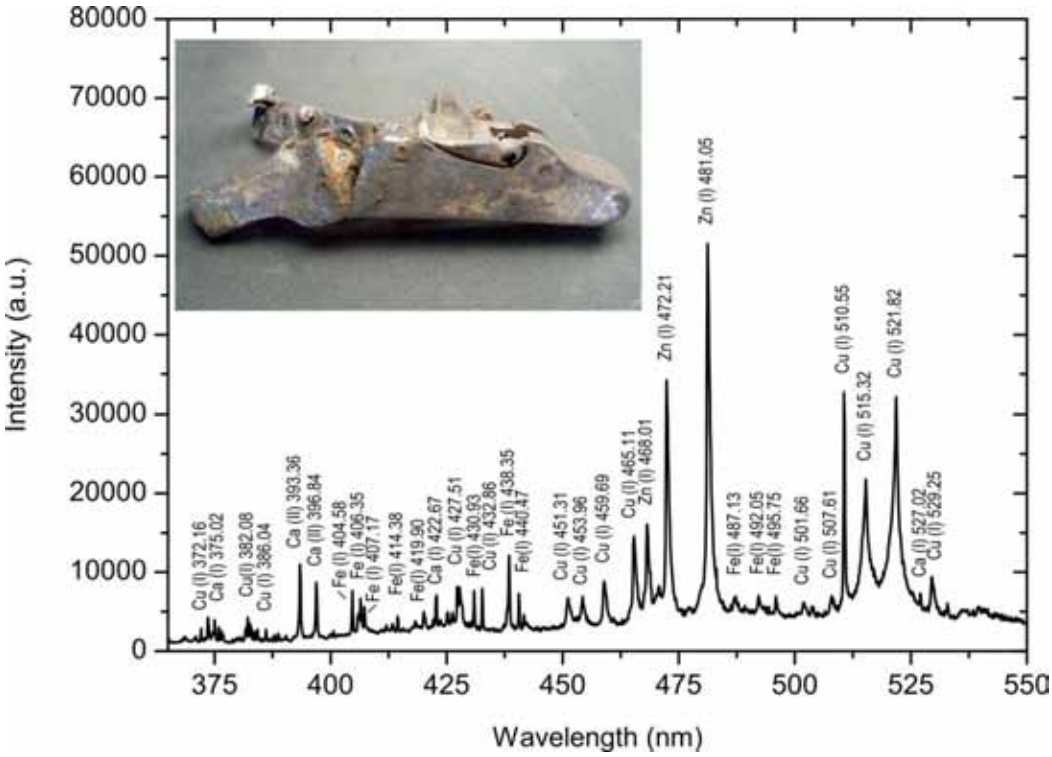

Sotogrande shipwreck

In *Sotogrande*, *San Roque* (Cadiz) lie the remains of a boat of mixed construction that had to be shipwrecked stranding on the beach. The origin of this ship is still unknown. However, the sheathing's ship analysis performed with AQUALAS 2.0 (composed by copper and zinc, see sample STG.CA-16.03), together with constructive structure study revel that it can be a ship of contemporary era built at the end of 19th century- early 20th century .

Sample i.d: STG.CA-14.05	**Material:** bolt

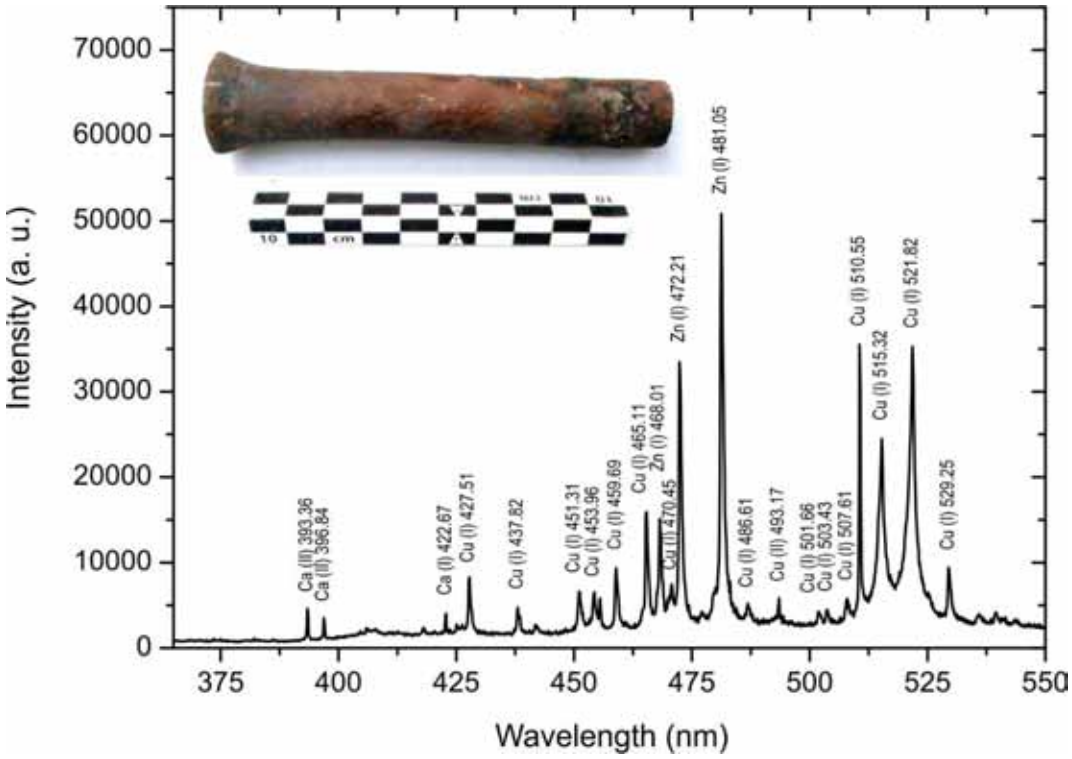

Sample i.d: STG.CA-14.10	**Material:** bolt

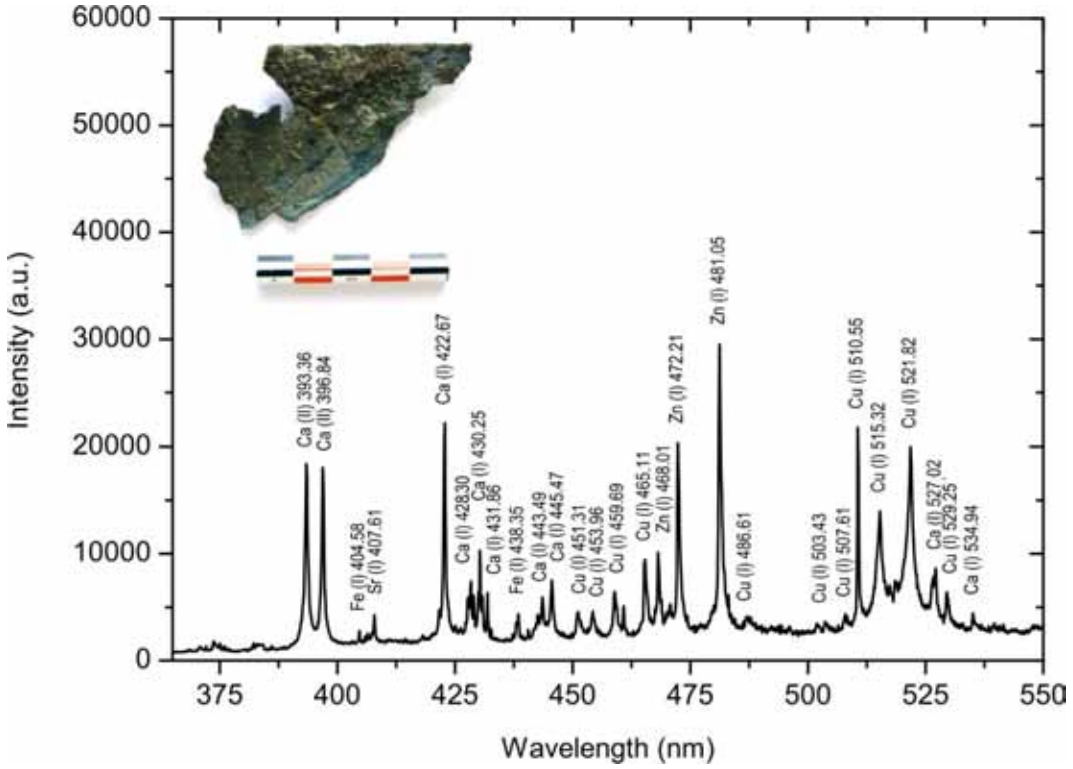

Sample i.d: STG.CA-16.02	**Material:** sheathing

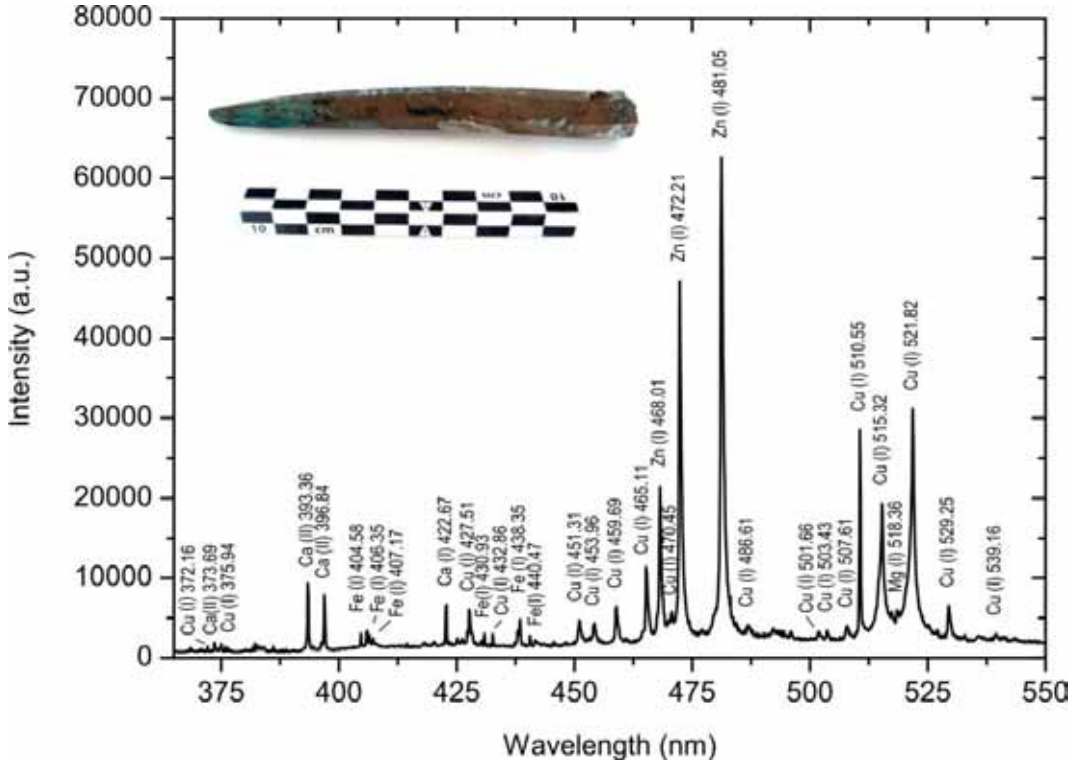

Sample i.d: STG.CA-16.03	**Material:** sheathing

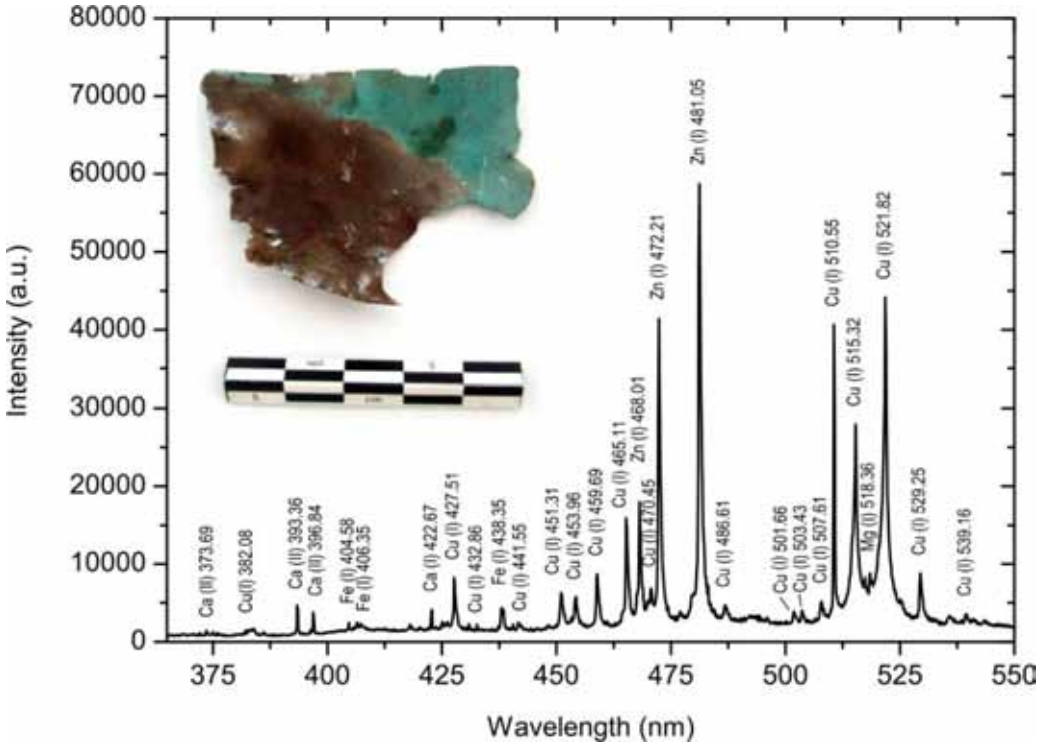

Sample i.d: STG.CA-16.05	**Material:** sheathing

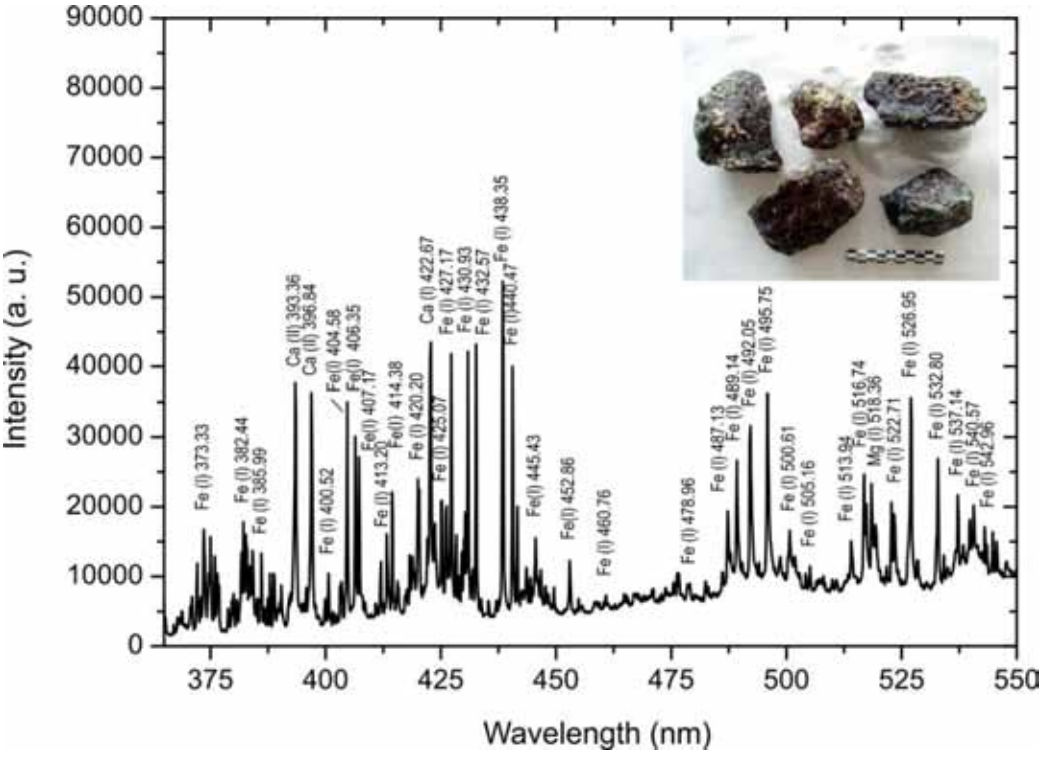

Appendix 3. Publications

PH06
INVESTIGACIÓN

LIBS in cultural heritage: exploration and identification of objects at underwater archaeological sites

Francisco Javier Fortes 01| Marina López-Claros 01| Salvador Guirado 01| Javier Laserna 01|

In this work, the capabilities of LIBS technique for the in-situ recognition and identification of materials in real submerged archaeological sites are discussed. A fiber-optics-based remote instrument was designed for the recognition and identification of archeological assets in underwater archaeological shipwrecks. The LIBS prototype featured both single-pulse (SP-LIBS) and multi-pulse excitation (MP-LIBS). The use of multi-pulse excitation allowed an increased laser beam energy (up to 95 mJ) transmitted through the optical fiber. This excitation mode results in an improved performance of the equipment in terms of extended range of analysis (to a depth of 50 m) and a broader variety of samples to be analyzed (i.e., rocks, marble, ceramics and concrete). Parametric studies in the laboratory such as gas flow pressure, beam focal conditions and angle of incidence, among others, were performed to optimize the best conditions for field analysis. The dependence of LIBS signal with the analysis depth was also studied in a real environment (Bahía de Málaga). Ancient artifacts found in the wreck of *Bucentaure* (Cádiz, Spain) and the wreck of San Pedro de Alcántara (Málaga, Spain) have been characterized and identified. Results obtained in these field trials confirmed the capability of remote LIBS for in-situ analysis of underwater archeological samples.

Keywords
Underwater analysis | Archaeology | Laser-induced breakdown spectroscopy | Intervention | LIBS | Underwater archeological heritage | Cultural heritage | Historical heritage |

LIBS en patrimonio cultural: reconocimiento e identificación de objetos en yacimientos arqueológicos sumergidos

Francisco Javier Fortes 01| Marina López-Claros 01| Salvador Guirado 01| Javier Laserna 01|

En este trabajo se discutirán las capacidades de la técnica LIBS para el reconocimiento e identificación in situ de materiales sumergidos en yacimientos arqueológicos reales. Se ha diseñado un instrumento remoto basado en fibra óptica que permite el reconocimiento e identificación de objetos en este tipo de escenarios. El prototipo desarrollado por la U. de Málaga es capaz de trabajar en dos configuraciones, pulso-simple convencional (SP-LIBS) y excitación multi-pulso (MP-LIBS). El uso de una configuración de multi-pulso permitió aumentar la cantidad de radiación láser (hasta 95 mJ) que puede ser transmitida a través de un cable de fibra óptica. Como consecuencia, se produce una mejora de las prestaciones del equipo, sobre todo en términos de rango de análisis (hasta una profundidad de 50 metros) y variedad de muestras que pueden ser analizadas (por ejemplo, rocas, cerámica, mármol y hormigón). Previamente, se han realizado estudios de parametrización en laboratorio (presión del gas, condiciones focales, ángulo de incidencia…) para alcanzar las mejores condiciones durante las medidas de campo. La dependencia de la señal LIBS con la profundidad de muestreo se estudió en un escenario real. Por otro lado, se caracterizaron e identificaron los objetos arqueológicos encontrados en el pecio del *Bucentaure* (Cádiz) y el pecio de San Pedro de Alcántara (Málaga). Los resultados obtenidos durante estas campañas de medida confirmaron la adaptabilidad de la técnica al ambiente marino y su potencial para analizar objetos arqueológicos en un yacimiento subacuático.

Palabras clave
Análisis subacuático | Arqueología | Espectroscopía de plasmas inducidos por láser | Intervención en el PH | LIBS | Patrimonio arqueológico subacuático | Patrimonio cultural | Patrimonio histórico |

URL <http://www.iaph.es/phinvestigacion/index.php/phinvestigacion/article/view/140>

01| Departamento de Química Analítica, Universidad de Málaga

FORTES, F. J.; LÓPEZ-CLAROS, M.; GURADO, S.; LASERNA, J. (2016)
LIBS in cultural heritage: exploration and identification of objects at underwater archaeological sites
PH Investigación (en línea), n.º 6, junio de 2016, pp. 25-46
<http://www.iaph.es/ph-investigacion/revista.php/ph-investigacion/article-view/1.do>

INTRODUCTION

At present, the characterisation of underwater cultural heritage has become one of the areas of greatest interest in archaeology (BOWEN, 2009). The main reason is the amount of historical information contained in these sunken archaeological remains, not only at the bottom of seas and oceans where the majority of these sites are found, but also at other locations such as rivers, lakes and swamps (BONIFACIO, 2008; LEÓN AMORES, 2009). More specifically, the Mediterranean Sea is home to a large amount of archaeological remains as a result of the storms, accidents and naval battles it has witnessed since Antiquity. In particular, the coast of Andalusia can be considered a privileged enclave where a multitude of sites of archaeological interest can be found. Given its geographical location, the Mediterranean has been utilised throughout history as an area of transit by many commercial and military routes - hence the great interest aroused by maritime archaeology.

Each archaeological site is a valuable source of historical information. We must point out that the reality of an underwater site tends to differ considerably from the ideal image initially presented by a shipwreck. Normally the remains from the site cannot even be distinguished from their surroundings since these remains end up becoming integrated into the landscape due to the effects of time and continuous sediment deposition. The discovery of pieces such as amphorae and cannons, in their archaeological context, could give indications of the age of the shipwreck as well as where it came from. It is essential to study, protect and preserve sunken properties given the constant aggressions they are subjected to. Classic analytical techniques generally require that the piece be taken to the laboratory in order to study its composition. This, however, is not always possible.

Sometimes the object cannot be removed from its site because of logistical issues, such as its size for example. Other times, the reason may be due to legislation or may put the object's integrity in jeopardy. The materials present at the site are in a chemical balance with their surroundings, thus preventing their deterioration. After being removed, the pieces out of water begin to oxidise as a result of the oxygen in the air and the electrolytes that may be occluded in their interior. Preventing this process is complex, costly and could take several months. Thus, the in situ analysis of objects tends to be the only alternative in many cases. Furthermore, but not less important, it is necessary to keep in mind that the position of the object in the context of the site can provide us with information about it. This information would be lost if the object was removed from its environment. Therefore, the United Nations Educational, Scientific and Cultural Organization (UNESCO), under the Convention for the

protection of underwater cultural heritage, states that the preservation in situ of cultural heritage shall be considered as "the first option before allowing or engaging in any activities directed at this heritage" (CONVENTION, 2001).

Despite this principle, not many analytical techniques are available for conducting chemical analyses in situ on underwater archaeological objects. In fact, only those based on laser technology are capable of addressing this challenge. One of these techniques has been Raman spectroscopy, which has been used to determine the chemical composition of minerals present on the sea floor (WHITE; DUNK; PELTZER et al., 2006). Laser-induced fluorescence (LIF) has also been utilised in the development of portable instrumentation for taking underwater measurements (FANTONI; BARBINI; COLAO et al., 2006). However, although the Raman and LIF technologies can be applied in this field, they do not provide atomic information.

Now, laser-induced breakdown spectroscopy (LIBS) provides a new solution to this problem (FORTES; LASERNA, 2010; FORTES; MOROS; LUCENA et al., 2013). The development of technology has helped this technique to become, over recent years, a tool with growing applications for the study and preservation of historical heritage (FORTES; CORTÉS; SIMÓN et al., 2005; GIAKOUMAKI; MELESSANAKI; ANGLOS, 2007; FORTES; CUÑAT; CABALÍN et al., 2007). The LIBS technique reunites practically all of the desired conditions for this type of application, including atomic, multi-elemental information, an unlimited range of materials that can be analysed and real-time results without the need to prepare the sample beforehand. Additionally, both the basic fundamentals of underwater LIBS measurements as well as the measurement principles, instrumentation and most appropriate methodologies have been described in the literature (LAZIC; LASERNA; JOVICEVIC, 2013a; LAZIC; LASERNA; JOVICEVIC, 2013b). The analysis of liquids using LIBS was evaluated for the first time in 1984 (CREMERS; RADZIEMSKI; LOREE, 1984).

The processes resulting from the laser-liquid interaction lead to the emission of a very weak plasma that, while still useful for analytical purposes, presents difficulties associated with the instability of the emission (CHARFI; HARITH, 2002). The analytical capacity of the technique for the analysis of underwater materials improves considerably with double-pulse LIBS systems (DE GIACOMO; DELL'AGLIO; COLAO et al., 2004; DE GIACOMO; DELL'AGLIO; DE PASCALE et al., 2007). With this methodology, emission efficiency substantially improves and the signal is stabilised, achieving an accuracy that leaves a margin of error of only 10-15%. This configuration has been applied for the semi-quantitative analysis

FORTES, F. J.; LÓPEZ-CLAROS, M.; GUIRADO, S.; LASERNA, J. (2016) LIBS in cultural heritage exploration and identification of objects at underwater archaeological sites. ph investigación [en línea], n.º 6, junio de 2016, pp. 25-46 <http://www.iaph.es/phinvestigacion/index.php/phinvestigacion/article/view/140>

06PH INVESTIGACIÓN

FORTES, F. J.; LÓPEZ-CLAROS, M.; GUIRADO, S.; LASERNA, J. (2016)
LIBS in cultural heritage: exploration and identification of objects at underwater archaeological sites
PH Investigación (en línea), n.º 6, junio de 2016, pp. 23-46
<http://www.iaph.es/ph-investigacion/revista/articulo/6/detalle/view.do>

of solid samples and marine sediment. Recently, the capacity of LIBS for the underwater analysis of metal alloys (iron, bronzes and precious alloys) and non-metal samples (rock and wood) has been demonstrated (LAZIC; COLAO; FANTONI et al., 2005). Thus, the analysis of metallic materials is of vital importance since it allows for the identification of the primary metallic constituents in iron, copper, gold and silver alloys, as well as the detection of trace and minor elements of interest for the clarification of sample origins and the identification of manufacturing processes.

However, all of the studies described to date on underwater materials have been carried out in the laboratory. This research study intends to describe the activities conducted as part of the AQUALAS Project, stemming from the need to solve a well-defined problem: chemically characterising the materials present at an underwater archaeological site without removing them from their original location. The following objectives are posed:

> Broaden the range of application of the LIBS technique for the inspection, identification and diagnosis of properties located in underwater archaeological sites.

> Develop a portable underwater material analysis system adapted to the marine environment.

> Study the conditions necessary for the identification and preservation of underwater cultural heritage.

In 2012, the laser laboratory at the University of Málaga published the first underwater LIBS analysis on solid samples (GUIRADO; FORTES; LAZIC et al., 2012). The system consisted of a main unit (where laser-fibre coupling takes place) and a submersible probe, connected by a 40-metre long cord. The prototype was controlled from the deck of a boat while a professional diver operated the submersible LIBS probe. The test was carried out on the Mediterranean Sea at a maximum depth of 30 metres. The system introduces a coaxial flow of gas that eliminates the water from the surface of the sample and generates a solid-gas interface which facilitates the LIBS analysis under water. Although the results were quite satisfactory, the analyses were practically restricted to metallic samples. Subsequently, the same authors considered the possibility of utilising a multi-pulse configuration or, in other words, a sequence of successive laser pulses (GUIRADO; FORTES; CABALÍN et al., 2014). With this configuration, the unit's performance improved in terms of a) laser energy transmitted with the fibre optic, b) range of analysis and c) variety of samples that can be analysed (for example marble, ceramic, concrete...).

FORTES, F. J.; LÓPEZ-CLAROS, M.; GURADO, S.; LASERNA, J. (2016)
LIBS in cultural heritage: exploration and identification of objects at underwater archaeological sites
ph investigación [en línea], n.º 6, junio de 2016, pp. 25-46
<http://www.iaph.es/phinvestigacion/index.php/phinvestigacion/article/view/143>

These improvements made to the prototype have made interventions on underwater archaeological sites possible, such as the shipwreck Bucentaure (GUIRADO; FORTES; LASERNA, 2015) and the shipwreck San Pedro de Alcántara (July, 2015). Throughout this article we will discuss the capacities of the technique for the exploration and identification in situ of underwater materials at real archaeological sites.

MATERIALS AND METHODS

Instrumentation

This section presents a novel instrument that has been specially designed for the remote chemical analysis of underwater materials. This system can be configured for either the conventional single-pulse (SP-LIBS) or the multi-pulse (MP-LIBS). The MP-LIBS configuration makes it possible to introduce greater laser radiation using the fibre optic. Thus, the maximum input energy into the fibre was 95 mJ/pulse that, together with a transmission of 74%, allowed for an energy output of 70 mJ/pulse to be met. This improved instrument performance in terms of energy transmitted via the fibre, range of analysis (up to 50 metres deep) and the variety of samples that could be analysed (marble, ceramic, concrete, rocks...).

The prototype consists of two well-defined parts: a sampling probe and a main unit, interconnected with a 50-metre-long cord. Image 1 gives a general view of the instrument. The main unit contains the optical module where laser-fibre coupling takes place, the data acquisition module and the laser power supply. The total weight of the instrument amounts to about 150 kg and it measures 81x86x126 cm.

The optical module consists of a methacrylate structure specifically adapted to prevent the deposit of marine aerosol on the system's optical components. This module also contains the laser beam source as well as all of the optical components to carry out both laser-fibre coupling and the detection of plasma from the surface of the sample.

The laser beam is transmitted through 55 metres of fibre optic protected inside of a cord that connects the analysis probe with the optical module. At the very end of the fibre optic, the laser beam is focused on the surface of the material using an optical system which is incorporated into the interior of the LIBS analysis probe. The cord also provides a constant flow of gas to the inside of the probe, eliminating the water from the surface of the material and creating a gas-solid interface which facilitates the LIBS analysis under water.

Image 01 |
A general view of the AQUALAS instrument. Photo: all of the images displayed in this article are from UMA LASERLAB unless indicated otherwise

FORTES, F. J.; LÓPEZ-CLAROS, M.; GURRADO, S.; LASERNA, J. (2016)
LIBS in cultural heritage: exploration and identification of objects at underwater archaeological sites
PH Investigación (en línea), n.º 6, junio de 2016, pp. 29-46
<http://www.iaph.es/phinvestigacion/articulo.php?id=investigacion/articulo&view=1>

Once the plasma has been generated on the surface of the material, the light is transmitted via the same fibre optic to return to the optical module where it is guided towards the data acquisition module through an optical collection system. The data acquisition module, installed on the main unit, features a spectrometer, a video converter and a computer. A pulse and delay generator externally controls the system.

The Czerny-Turner spectrometer has a diffraction grating of 1200 lines/mm. With this configuration a spectral resolution of 0.1-0.2 nm/pixel is obtained in addition to a spectral range of 300-550 nm. The time-space acquisition conditions were optimised to obtain the best signal-noise ratio in the LIBS signal.

The tool also features an auxiliary module for its full autonomy during field studies. This module contains an air compressor, a current stabiliser and an external current generator which provides the tool with seven hours of work autonomy.

Materials

In order to evaluate the capacities of the technique and fine-tune the remote LIBS tool, a series of samples were analysed in the laboratory. This collection of objects included ceramic material as well as metal alloys; the majority of the pieces presented a high degree of corrosion and surface roughness.

These samples are summarised in table 1. The experiments were conducted inside a 100-litre tank with water taken directly from the Mediterranean Sea so that the laboratory measurements would resemble (as much as possible) the conditions of a real marine-environment analysis.

In the second phase, in order to demonstrate the potential of the technique, measurement campaigns were designed in real scenarios of interest to the investigation of Andalusian underwater archaeological heritage. Thus, the remains from the Bucentaure (Cádiz, Spain) and the shipwreck of San Pedro de Alcántara (Málaga, Spain) were analysed at depths of 17 and 10 metres, respectively.

In table 2 the samples analysed during the measurement campaigns conducted at these two archaeological sites are described. During the archaeological prospecting work on the shipwreck of San Pedro de Alcántara, the chemical composition of samples of sheathing from different shipwrecks was also analysed.

A description of these samples is summarised in table 3.

Sample	Material	Sample description
#1	Ceramic	Archaeologial ceramics with calcareous concretion
#2	Ceramic	Archaeologial ceramics with ferrous concretion
#3	Iron	Archaeological iron piece
#4	Bronze	Bronze sheet
#5	Bronze	Archaeological bronze
#6	Bronze	Leaded bronze
#7	Bronze	Certified sample bronze (79% Cu, 8% Pb, 7% Sn, 6% Zn)

Table 01 |
Samples analysed in the laboratory as well as during the tests conducted on the Mediterranean Sea (Málaga, Spain) in 2010

Sample	Shipwreck	Material	Sample description
#8	*Bucentaure*	Iron	Piece of iron with calcareous concretion
#9	*Bucentaure*	Iron	Metal box for storing items of jewelry
#10	*Bucentaure*	Iron	Iron cannon with high concretion degree
#11	*Bucentaure*	Copper	copper object with calcareous concretion
#12	*Bucentaure*	Lead	Pieza de plomo
#13	San Pedro Alcántara	Ceramic	Decorated ceramics
#14	San Pedro Alcántara	Ceramic	Ceramic shard indeterminately
#15	San Pedro Alcántara	Ceramic	Fragment of a possible ceramic container
#16	San Pedro Alcántara	Iron	Cannonball
#17	San Pedro Alcántara	Iron	Iron cannon
#18	San Pedro Alcántara	Iron	Iron cannon
#19	San Pedro Alcántara	Iron	Iron piece indeterminately
#20	San Pedro Alcántara	Bronze	Fragment of a buckle
#21	San Pedro Alcántara	Copper	Copper button
#22	San Pedro Alcántara	Copper	Copper fragment indeterminately

Table 02 |
Samples analysed during the tests carried out on the shipwreck *Bucentaure* (Cádiz, Spain) and the shipwreck San Pedro de Alcántara (Málaga, Spain)

sample	Shipwreck	Origin	Sample description
#23	*Bucentaure*	Francia	Cooper sheathing
#24	*Bucentaure*	Francia	Cooper sheathing
#25	*Bajo S. Sebastián*	España	Cooper sheathing
#26	*Bajo S. Sebastián*	España	Cooper sheathing
#27	Delta II	Italia	Cooper sheathing
#28	Delta II	Italia	Cooper sheathing

Table 03 |
Samples of sheathing analysed during the tests carried out on the shipwreck San Pedro de Alcántara (Málaga, Spain)

FORTES, F. J.; LÓPEZ-CLAROS, M.; GUIRADO, S.; LASERNA, J. (2016)
LIBS in cultural heritage: exploration and identification of objects at underwater archaeological sites
ph investigación [en línea], n.º 6, junio de 2016, pp. 25-46
<http://www.iaph.es/phinvestigacion/index.php/phinvestigacion/article/view/140>

06PH INVESTIGACIÓN

FORTES, F. J.; LÓPEZ-CLAROS, M.; GURRADO, S.; LASERNA, J. (2016)
LIBS in cultural heritage: exploration and identification of objects at underwater archaeological sites
PH Investigación (en línea), n.º 6, junio de 2016, pp. 25-46
<http://www.iaph.es/phinvestigacion/articulo.php?id=investigacion/articulo&view=1>

RESULTS AND DISCUSSION

Optimisation of experimental parameters in remote LIBS analysis underwater

A) Effect of the probe operational parameters on the LIBS signal

To achieve the best results provided by the tool, those parameters capable of affecting the quality of the LIBS signal were optimised in the laboratory, such as the lens-sample distance and the angle of incidence of the laser radiation. The parameterisation studies were conducted utilising a certified bronze sample inside of a water tank.

The submersible probe consists of an opening with a 2 mm diameter whose position must be adjusted in order to reach the optimal focus conditions. The probe must be in direct contact with the surface of the sample. In this first test, He was utilised at a pressure of 2 bars as a protective gas. The same sampling protocol was always employed in order to ensure the exactness and precision of the measurements. Each analysis point is the result of averaging 5 measurements, each of which examined with 25 laser pulses. The measurement value is obtained by averaging the last 15 pulses of the series after considering the first 10 cleaning pulses. Image 2 shows the intensity of the Cu (I) 521.96 nm signal as a function of the working distance. A distance of 0 mm means that the sample is located at the focal point of the lens. We can observe how the net intensity of copper reaches its maximum value when the beam is focused 0.5 mm above the surface of the sample (+0.5 mm). Similar behaviour is observed when the focal point is situated 0.5 mm below the surface of the sample (-0.5 mm). In both cases, the LIBS signal quickly decreases as the distance increases since the amount of energy deposited on the surface of the sample is reduced in terms of radiant exposure (J/cm^2). In other words, the same energy per pulse is applied to an increasingly larger surface area as the beam goes out of focus. The operating range is narrow as a consequence of the short focal distance (35 mm) required to focus the laser from the output end of the fibre optic. In light of these results, the working distance was set to 0.5 mm over the surface of the sample.

The impact of the angle of incidence of the laser with regard to the surface of the sample was a parameter that needed to be considered bearing in mind the extreme conditions the diver was subjected to on account of the sea currents. Image 3 shows the impact of the angle of incidence of the laser radiation on the LIBS signal of a bronze sample. As can be observed, the maximum signal is reached when the probe is placed practically normal to the surface (0-10º). When the intensity of the copper is normalised to the background of the spectrum, the LIBS

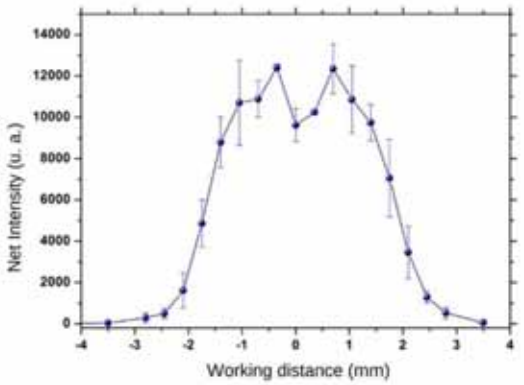

Image 02 |
Intensity of Cu (I) 521.06 nm according to the working distance

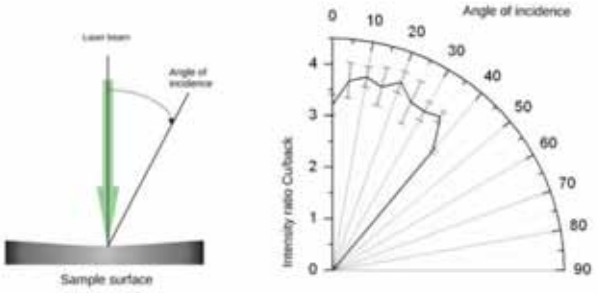

Image 03 |
Relationship between the angle of incidence between the laser radiation and the surface of the sample and the Cu/background intensity

response remains nearly constant in a range between 0º and 40º. However, no signal is observed beyond this angle due to the difficulty involved in collecting the light from plasma under those geometric conditions.

B) Protective gases

The use of a protective gas or a purge gas is key to preventing the entry of water into the inside of the analysis probe. The great diminishing effect that water has on the radiation of 1064 nm would prevent a sufficient amount of energy from being deposited onto the analysis spot. At the same time it hinders the deposit of particles from the sample on the focusing lens. The flow of gas from the auxiliary module travels via the cord and is expelled outside through a hole at the tip of the probe. This flow of gas displaces the water on the surface of the sample and creates a solid-gas interface, thus facilitating the LIBS analysis under water. In this way, in comparison with a solid-

FORTES, F. J.; LÓPEZ-CLAROS, M.; GURADO, S.; LASERNA, J. (2016)
LIBS in cultural heritage: exploration and identification of objects at underwater archaeological sites
ph investigación (en línea), n.º 6, junio de 2016, pp. 25-46
<http://www.iaph.es/phinvestigacion/index.php/phinvestigacion/article/view/149>

FORTES, F. J.; LÓPEZ-CLAROS, M.; GUIRADO, S.; LASERNA, J. (2016)
LIBS in cultural heritage: exploration and identification of objects at underwater archaeological sites
ph investigación (en línea), n.º 6, junio de 2016, pp. 25-46
<http://www.iaph.es/ph-investigacion/articulos.php?id=investigadores/detalle/view/3/>

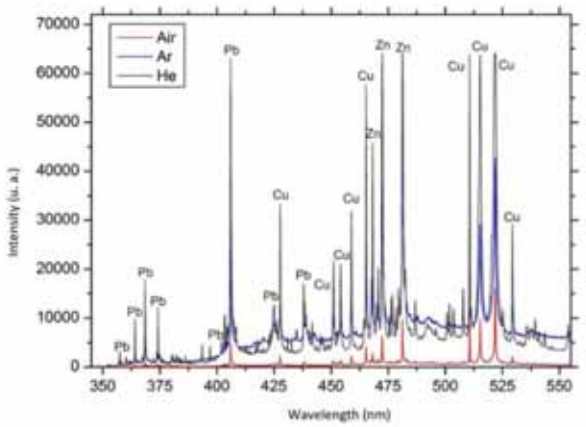

Image 04 |
LIBS spectra (from a sample of bronze) obtained from an environment of air, helium and argon. The main emission lines are labelled on the spectrum

liquid interface, ablation efficiency is improved since the loss of energy which would cause the liquid to heat is prevented.

Additionally, greater plasma emission occurs as a result of the increase in both the temperature and its electron density. This is due to the collisions that occur with the surrounding gas and the ablated material, the electrons and the different species (excited or not) present in the plume. Different gases (Ar, He and air) were evaluated during the analysis of a certified bronze sample. The results are shown in Image 4. As it can observe, the most intense signal was given by He. Nonetheless, no additional information was observed regarding the composition of the sample in comparison with the results obtained using air. Thus, seeing as the air is easily obtained using the portable compressor as well as far less costly, it is logical to utilise this gas for the routine analysis. The use of helium or argon may be useful in some specific applications where increasing signal sensitivity is necessary, for instance for the quantitative analysis of minor elements or during the analysis of ceramic material.

In order to prevent air from entering the inside of the analysis probe, the differential pressure (ΔP) between the interior and exterior of the probe must be greater than 1 bar. Image 5 shows the impact of ΔP on the LIBS signal of Cu (521.96 nm), Pb (405.89 nm) and the background. The intensity of the signal is practically constant when ΔP is among 1 and 3 bars. When ΔP presented higher values, an increase in both the LIBS signal and the background was observed. This point is especially interesting when working at great depths at the bottom of the sea. Additionally, the accuracy of the results was quite satisfactory and the values obtained for the relative standard deviation were among 8-15 %.

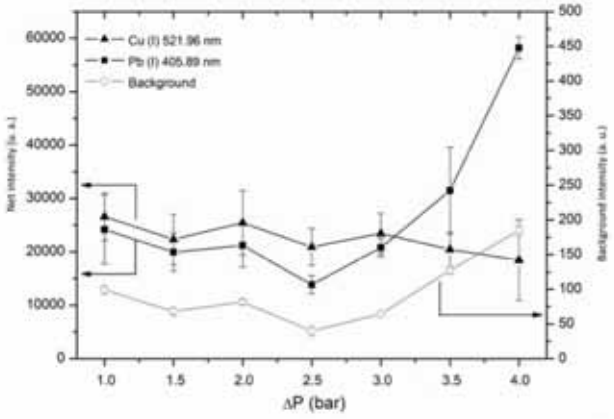

Image 05 |
Impact of the differential pressure (ΔP) –between the interior and exterior of the probe– on the LIBS signal of Cu (521.96 nm), Pb (405.89 nm) and the background intensity.

Underwater chemical characterisation of ceramic objects

The effect of sea water on underwater materials typically results in the deposit of sediment on the surface of the sample. This effect is more severe with metals, even causing oxidation of the object. In underwater archaeology objects must be inspected in situ, especially those materials that present a high degree of surface oxidation. Ceramic materials (amphorae, for example) discovered at archaeological sites are usually found covered by several types of deposits: calcareous and ferrous. In order to demonstrate the capacity of the new tool concerning the underwater chemical characterisation of ceramic objects, several samples presenting these two types of deposits were analysed in the laboratory. The samples were submerged in a water tank in order to simulate real conditions. Image 6 shows the LIBS spectra obtained in each case. Calcareous deposits tend to appear as a heterogeneous, white layer only a few millimetres thick. Its spectral fingerprint corresponds to Ca, Mg and traces of Sr. It must be mentioned that both Mg and Sr tend to replace Ca in calcium carbonate structures. The Fe and Sr emission lines detected around 405 nm could be utilised for the detection of low concentrations of these elements as they are found on an interference-free spectral region of other elements. In addition, the build-up of iron also presents other minor elements such as Ca and Mg, attributed to the build-up of sediment on the oxidised surface of the material. Moreover, due to the heterogeneous nature and the porosity of these materials, we observed an increase in the pulse-pulse fluctuation of the signal measured.

The inherent porosity presented by ceramics favours the obstruction of water in their structures. As was described earlier, the cord directs

35
FORTES, F. J.; LÓPEZ-CLAROS, M.; GURADO, S.; LASERNA, J. (2016)
LIBS in cultural heritage: exploration and identification of objects at underwater archaeological sites
ph investigación (en línea), n.º 6, junio de 2016, pp. 25-46
<http://www.iaph.es/phinvestigacion/index.php/phinvestigacion/article/view/143>

36

FORTES, F. J.; LÓPEZ-CLAROS, M.; GUIRADO, S.; LASERNA, J. (2016)
LIBS in cultural heritage exploration and identification of objects at underwater archaeological sites
ph investigación [en línea], n.º 6, junio de 2016, pp. 25-46
<http://www.iaph.es/phinvestigacion/index.php/phinvestigacion/article/view/140>

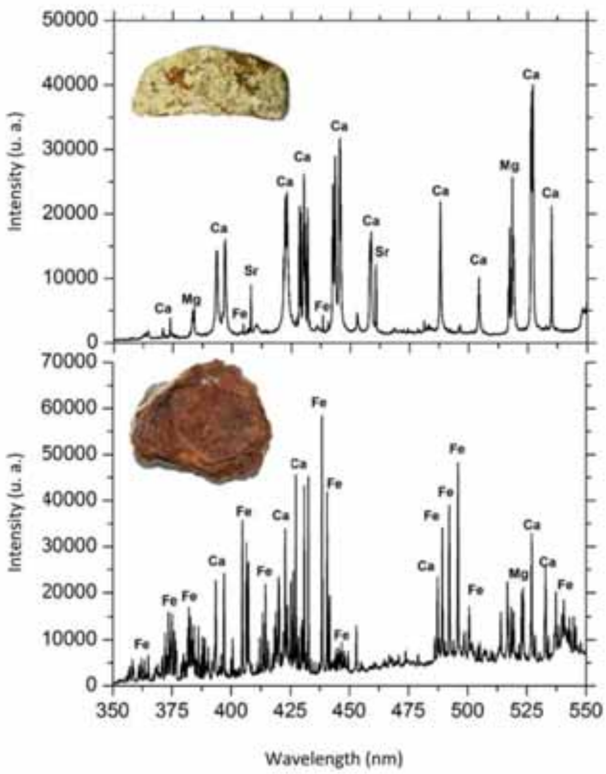

Image 06 |
LIBS spectra of A) calcareous deposit and B) ferrous deposit on a ceramic sample. The main emission lines are labelled on the spectrum

the supply of gas in the probe to remove the water from the surface of the material and create a gas-sample interface that improves ablation efficiency. Image 7, obtained from the literature (GUIRADO; FORTES; LASERNA, 2015), presents the impact of air pressure on the LIBS signal of our ceramic sample. ΔP is the differential pressure between the interior and exterior of the probe. This differential pressure must never be less than 1 in order to correctly prevent water from entering the probe. As we can observe on the graph, while the Ca signal disappears after 25 laser pulses at 1 bar, the intensity of the emission line disappears after almost 60 pulses when the ΔP is increased to 2 and 3 bars. When ΔP = 4 bars, however, the signal is maintained during much more time. This is due to the fact that water molecules are evacuated more efficiently at higher ΔP values, thus facilitating the analysis and consequently the increase in the LIBS signal. In order to improve the chemical characterisation of ceramic materials during a measurement campaign in a real environment conditions, the differential pressure must be set at its maximum value: 5 bars.

PH06
INVESTIGACIÓN

FORTES, F. J.; LÓPEZ-CLAROS, M.; GURADO, S.; LASERNA, J. (2016)
LIBS in cultural heritage: exploration and identification of objects at underwater archaeological sites
ph investigación (en línea), n.º 6, junio de 2016, pp. 25-46
<http://www.iaph.es/phinvestigacion/index.php/phinvestigacion/article/view/143>

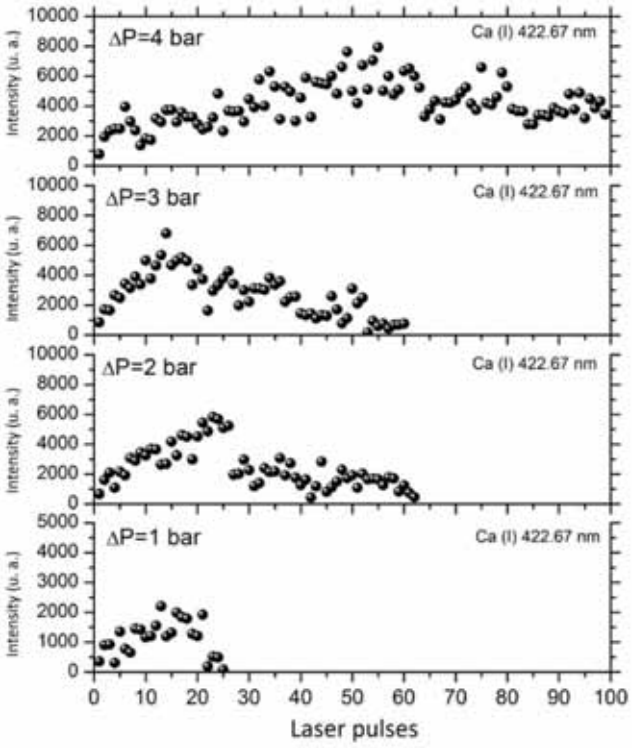

Image 07 |
Impact of air pressure on the intensity of the Ca (I) 422.67 nm signal. ΔP is the differential pressure between the interior and exterior of the analysis probe

Exploration and identification of materials at underwater archaeological sites

The prototype, installed aboard a boat, was controlled by the scientific team while a professional diver operated the analysis probe on the sea floor. The diver was equipped with an audio and video system that allowed for communication with the operators on the boat deck. Furthermore, an assistant diver with a submersible video camera recorded all of the events from the field test. The auxiliary module additionally offered total energy autonomy to the remote LIBS tool.

A) Impact of immersion depth on the LIBS signal

A preliminary test conducted on the Mediterranean Sea in 2010 evaluated the impact of immersion depth on the LIBS signal. In order to reach a depth of 30-35 metres, the boat was anchored approximately a mile off the coast of the Bay of Málaga. At the maximum working depth

FORTES, F. J.; LÓPEZ-CLAROS, M.; GUIRADO, S.; LASERNA, J. (2016)
LIBS in cultural heritage: exploration and identification of objects at underwater archaeological sites
ph investigación (en línea), n.º 6, junio de 2016, pp. 25-46
<http://www.iaph.es/phinvestigacion/issues.php/phinvestigacion/issue/view/140>

(30 metres), the pressure underwater is 4 bars. To ensure a ΔP greater than 1 bar and thus prevent water from entering the probe, air pressure at the tool's point of entry was set to 5 bars. For this study, a leaded bronze was analysed at different depths: 3, 7, 15, 25 and 30 m. The LIBS signal of Pb (I) 405.89 nm and Cu (I) 521.96 nm was measured according to the immersion depth. The results of this study carried out by GUIRADO; FORTES; LAZIC; LASERNA, 2012 are presented in Image 8. We can observe that the Pb LIBS signal progressively decreased as the depth increased, while the Cu signal remained practically the same throughout the range of depth. This distinct behaviour of Cu and Pb with the immersion depth was attributed to a matrix effect; this means that preferential ablation or fractionation of some species can occur in the laser-induced plasma. In fact, given the temporal width (7 ns) and the wavelength (1064 nm) of the laser pulse, this effect is even more pronounced. On the scale of nano-seconds, the interaction between the laser pulse and the transition states of the elements in the plume could also evaporate material on the surface of the sample. For this reason, the variation observed in the LIBS signal could be attributed to a different volatilisation rate or atomisation process for Pb (Latent heat: 862 J/g; Boiling point: 1740ºC) and Cu (Latent heat: 4790 J/g; Boiling point: 2595ºC) in the plume. This effect, which is very well documented for copper alloys, is related to plasma shielding processes and, in this case, said parameter has been found to be associated with ΔP. Thus, the behaviour of the Pb signal with immersion depth could be attributed to the different values of ΔP, as it is the only parameter that changes during the experiment. As was mentioned at the beginning, the supply pressure was 5 bars and, consequently, the ΔP falls from 4 bars to 1 bar as immersion depth increases. When ΔP presented the highest values (3 m deep, ΔP = 4 bars), the plasma is more confined to the surface of the sample. Therefore, the number of species located in the plasma per

Image 08 |
A diver working at a depth of 30 metres. Image taken during the measurement campaign in the Bay of Málaga; on the right, impact of immersion depth on the LIBS signal

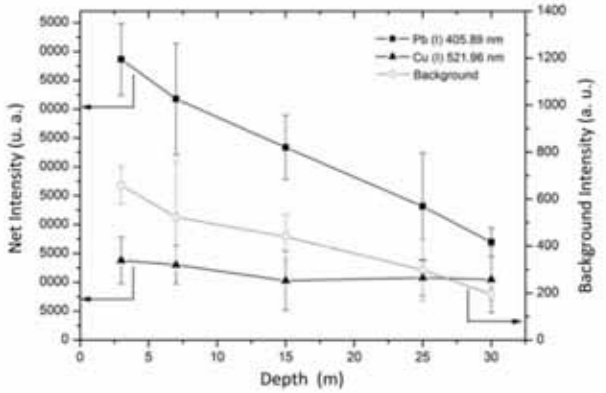

FORTES, F. J.; LÓPEZ-CLAROS, M.; GURRADO, S.; LASERNA, J. (2016)
LIBS in cultural heritage: exploration and identification of objects at underwater archaeological sites
ph investigación (en línea), n.º 6, junio de 2016, pp. 25-46
<http://www.iaph.es/phinvestigacion/index.php/phinvestigacion/article/view/143>

unit volume is larger, producing a greater plasma shielding effect. As a result, the tail of the pulse invests a large part of its energy into heating the plume, thus meaning that the amount of laser radiation that reaches the surface of the sample is lower. Hence, when the tail of the pulse reaches the surface of the material it will only evaporate the species that have low latent heats of vaporisation, or, the Pb (MARGETIC; PAKULEV; STOCKHAUS, 2000). As a result the plume becomes enriched in Pb, thus increasing the number of species that emit this metal. This is the reason why the intensity of Pb on the LIBS spectrum of the material experiences an increase.

The research carried out thus demonstrates that the LIBS technique offers unique possibilities for the study of underwater archaeological heritage located dozens of metres deep.

B) Spectral characterisation of underwater materials

From an archaeological point of view it is very interesting to have access to a remote LIBS instrument which is capable of examining underwater materials, especially under those circumstances in which the object can not be recognised with the naked eye due to low visibility conditions or an artefact's high degree of corrosion. In this regard, the identification of those discoveries that may be of archaeological value helps to make decisions concerning the convenience (or lack thereof) of removing the sample from its site as well as its subsequent preservation.

In this study measurement campaigns were designed in real scenarios of interest to the investigation of Andalusian underwater archaeological heritage in order to demonstrate the potential of the technique. In the first phase a measurement campaign was organised at a real archaeological site in the Bay of Cádiz. This location was chosen for the multitude of sites present along its coasts. The campaign took place from the 9th to 11th of July 2012 and the work group consisted of members from the laser laboratory at the University of Málaga, a group of archaeologists from the Underwater Archaeology Centre (CAS) (Centro de Arqueología Subacuática), professional divers and technical support personnel from the tugboat 'Obama'. The work was planned in collaboration with the CAS in order to study one of the most important vessels that had sunk off the coast of Andalusia. The remains studied corresponded to the Bucentaure, the flagship of the Franco-Spanish Navy during the Battle of Trafalgar which now rests in the Bay of Cádiz at a depth of 17 metres. We must mention that deposits on the surface of the pieces in analysis areas were removed by qualified professionals who are authorised by the CAS and followed standard procedures. This minimised the risk of damage to the archaeological remains during their handling. Likewise, the analysis areas were

sealed upon completion of the analysis to prevent deterioration of the pieces.

Different objects dating back to the late 18th century and the early 19th century were analysed and identified in situ; these included cannons, a rosary (a metal box for storing the rosary bead necklace) and different metal alloys. These materials were analysed in the 350-550 nm spectral range. These studies applied a flow of gas with a supply pressure of 5 bars. To ensure the reproducibility of the results and achieve a LIBS spectrum representative of each material, the data was obtained by averaging 100 laser pulses in 5 adjacent positions on each sample. Image 9 presents the LIBS spectrum of a cannon composed mainly of Fe and in which the presence of other elements such as Ca and Mg was not detected (typically associated with calcareous and ferrous deposits) once the layer of build-up had been eliminated. The layer of corrosion was eliminated locally; thus, the data obtained by LIBS corresponded exclusively to the original material (image 9A). The relative standard deviation (RSD) of the cannon was 30-40%. During the measurements the ferrous sediment deposited on the surface of the cannon was also analysed. However, the intensity of the LIBS signal was lower on the oxidised area than on the clean surface of the cannon. The variability of the signal was much greater on the corroded surface owing to the heterogeneous nature and the porosity of the material. Image 9B shows a photograph of one of the divers identifying the cannon. Other objects were also inspected such as a rosary and a metallic piece (both identified as iron alloys), a piece of copper and a fragment of lead.

The results obtained were quite satisfactory and allowed, for the first time, for the examination and identification of underwater archaeological materials from the real context of the Chapitel site. Nonetheless, following the measurement campaign carried out at the Bay of Cádiz, some areas to be improved upon were detected in the underwater analyser. For that reason some modifications were made to the analyser, mainly affecting its sturdiness, seal and refrigeration, the sampling probe and data processing. Two experimental campaigns were conducted along the shores of the Mediterranean Sea in order to test out the new improvements that had been made. The instrument was accordingly subjected to conditions which pushed it to the limit in order to demonstrate both its strength and solidity during transport and operation as well as the general improvements made following the campaign in the Bay of Cádiz. These improvements were mainly geared towards facilitating its use and increasing its reliability in hostile environments such as the ocean.

The next step in our investigation was the archaeological exploration with LIBS probing of the underwater site of San Pedro de Alcántara. In

FORTES, F. J.; LÓPEZ-CLAROS, M.; GURADO, S.; LASERNA, J. (2016)
LIBS in cultural heritage: exploration and identification of objects at underwater archaeological sites
ph investigación (en línea), n.º 6, junio de 2016, pp. 25-46
<http://www.iaph.es/phinvestigacion/index.php/phinvestigacion/article/view/143>

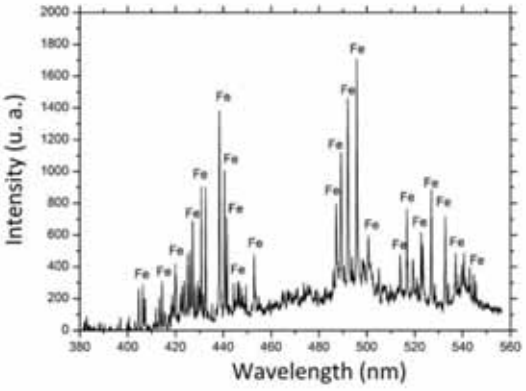

Images 09 (A y B) |
A) LIBS spectrum of an iron cannon recorded during the measurement campaign on the shipwreck Bucentaure and B) Photograph taken during examination of the shipwreck. Photo: IAPH Image Archives.

this case, the remains of a major vessel were studied in which a strong structural design characteristic of military ships stood out. Measuring approximately 60 m long and about 10-12 m wide, this vessel sits on a floor of sand and debris at a depth that varies between 4 and 7 metres. Image 10 gives a panoramic view of the site. Among the artefacts detected at the site we must emphasise the presence of remains from the ship's ballast, pieces of lumber and pulleys, clothing, buttons, buckles and objects from life aboard the ship and defence of the vessel. The campaign took place from the 20th to 23rd of July 2015 and the work group consisted of members from the laser laboratory at the University of Málaga, a group of archaeologists from the Underwater Archaeology Centre (CAS) (Centro de Arqueología Subacuática), professional divers, an advanced audio and sound technical team and technical support staff from the boat 'Tridacna'. In addition, just as with the shipwreck *Bucentaure*, deposits on the surface of the objects in analysis areas were removed by qualified personnel authorised by the CAS who also inspected the shipwreck and located the position of the materials so that the diver could analyse them with the submersible LIBS probe (image 11). These materials were analysed in the 350-550 nm spectral range.

The sampling and data collection protocol was similar to the protocol described above for the Chapitel site (Cádiz, Spain). With regard to the analytic signal, the presence of self-absorbed resonance lines was not observed. Furthermore, the reproducibility of the spectra obtained underwater was more than acceptable in all cases and presented a variability of less than 10%. Only those samples with a high degree of corrosion presented pulse-pulse fluctuations higher than 10% of the RSD. Image 12 shows the LIBS spectra corresponding to the materials analysed underwater. We can observe that the differences among the

Image 10 |
Panoramic view of the site San Pedro de Alcántara (Málaga, Spain). Photo: IAPH Image Archives

Image 11 |
A diver analysing the shipwreck San Pedro de Alcántara with the LIBS probe. Photo: IAPH Image Archives

materials are significant. Image 12A thus shows that the archaeological ceramic studied is mainly composed of Al, Ca, Fe, Si and Ti; this may be correlated with the chemical composition of a type of clayey material. Image 12B presents the analysis corresponding to the sample catalogued as a copper button, for which Cu was primarily detected, along with traces of Ca and Ti, possibly from calcareous sediment. In the cannonball analysed, Image 12C, Fe was mainly detected, although Mn lines were also identified in its composition. In contrast, only iron was detected in the cannon (image 12D).

One of the studies conducted during the archaeological exploration of the shipwreck San Pedro de Alcántara focused on studying the chemical composition of samples of sheathing from different wreckages.

The LIBS analysis is geared towards finding a distinguishing element that makes it possible to correlate the chemical composition with the origin of the shipwreck. The characteristic LIBS spectra are shown in image 13. With regard to the samples from the *Bucentaure*, of French origin, the LIBS spectrum reveals the presence of copper, although in this case it also presents a high concentration of calcium –lines at 393.47 nm, 396.96 nm and 422.79 nm. In the shipwreck *Mercante del bajo de San Sebastián*, of Spanish origin, the LIBS analysis reveals that its sheathing is mainly copper. The shipwreck Delta II is the only Italian wreckage whose sheathing could be analysed. As we can observe in the image, the LIBS spectrum is exclusively composed of lead emission lines, thus ruling out any type of alloy with another chemical element. Although the results obtained could initially establish a correlation between the composition of the material and the origin of the shipwreck, opening up a new line of research, the exclusive analysis of the primary element is not enough to assure this statement, meaning that a more exhaustive study of the minor components is required (BETHENCOURT; BOCALANDRO; ROMERO, 2011).

FORTES, F. J.; LÓPEZ-CLAROS, M.; GURADO, S.; LASERNA, J. (2016)
LIBS in cultural heritage: exploration and identification of objects at underwater archaeological sites
PH investigación (en línea), n.º 6, junio de 2016, pp. 26-46
<http://www.iaph.es/phinvestigacion/index.php/phinvestigacion/article/view/140>

CONCLUSIONS

This research work has demonstrated the potential of laser-induced breakdown spectroscopy (LIBS) for the exploration and identification of archaeological materials at underwater sites. The results obtained during the measurement campaigns confirm the maturity of the technology and its capacity to adapt to the marine environment. Hence, a remote LIBS instrument based on fibre optics and capable of analysing underwater objects at depths of up to 50 metres has been created. The use of a multi-pulse configuration (MP-LIBS) increases the laser radiation transmitted via the fibre optic (74% transmission), thus improving the features of this piece of equipment.

A series of laboratory experiments were conducted with the aim of optimising analysis conditions. In this regard, the LIBS signal is not affected by the angle of incidence in a tolerance range between 0-40º. The use of a purge gas is needed to remove the water from the surface of the sample and generate a solid-gas interface that improves ablation efficiency. The differential pressure must be at least 1 bar in

Image 12 |
Characteristic LIBS spectra of some materials analysed at the site San Pedro de Alcántara: A) ceramic B) copper button C) cannonball and D) iron cannon

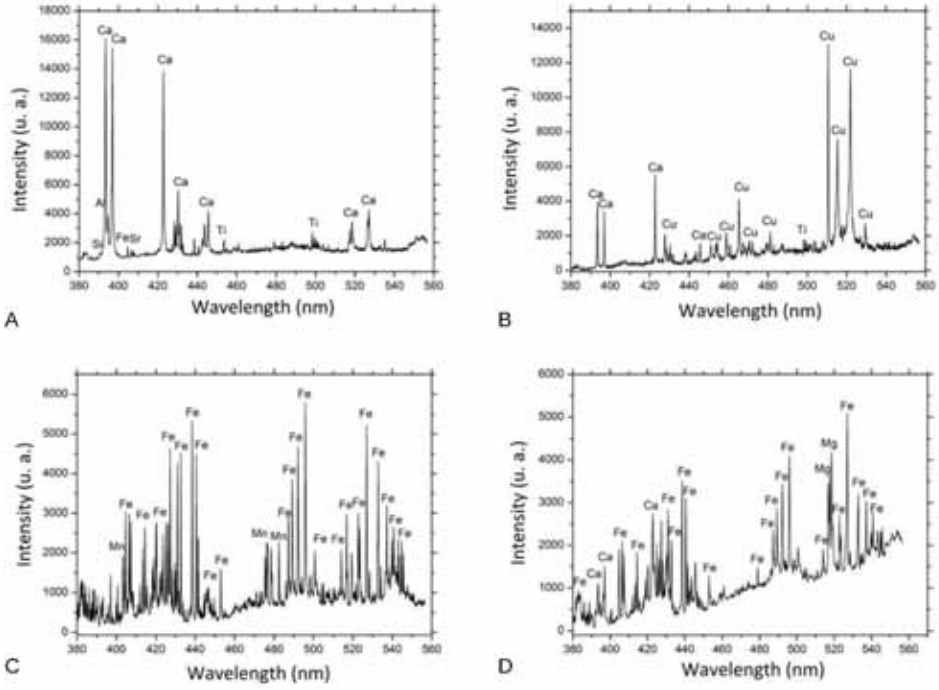

FORTES, F. J.; LÓPEZ-CLAROS, M.; GURRADO, S.; LASERNA, J. (2016)
LIBS in cultural heritage: exploration and identification of objects at underwater archaeological sites
ph investigación (en línea), nº 6, junio de 2016, pp. 29-46
<http://www.iaph.es/ph-investigacion/articulos.php?id=investigadores/articulo&view=1>

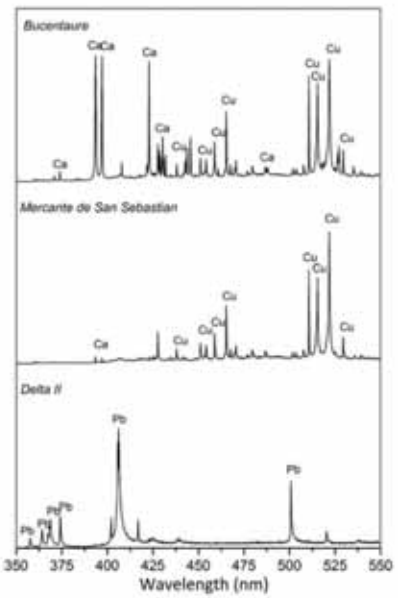

Image 13 |
On the left, LIBS spectra corresponding to sheathing from the *Bucentaure* (France), Mercante de San Sebastián (Spain) and the Delta II (Italy).

On the right and from the top down, a bilge pump wheel from the *Bucentaure*. Photo: IAPH Image Archives; lead sheathing from the shipwreck Delta II. Photo: Tarit Archaeological Management.

order to correctly prevent water from entering the probe. The use of He or Ar considerably improves the LIBS signal.

The results obtained during the measurement campaigns organised at the archaeological sites of Chapitel and San Pedro de Alcántara were quite satisfactory and allowed, for the first time, for the examination and identification of underwater archaeological materials. Ceramic material, marble, bronze alloys, lead fragments and even iron cannons were detected and analysed. Moreover, the chemical composition of samples of sheathing from different shipwrecks was also correlated with the origins of these vessels.

Acknowledgments
This research was funded by the project P11-FQM-7193 (AQUALAS), a joint effort of Instituto Andaluz del Patrimonio Histórico (IAPH)/Centro de Arqueología Subacuática (CAS) and the University of Malaga (UMA). M. Lopez-Claros would like to acknowledge the Consejería de Innovación, Ciencia y Empleo of the Junta de Andalucía for her fellowship.

FORTES, F. J.; LÓPEZ-CLAROS, M.; GUIRADO, S.; LASERNA, J. (2016)
LIBS in cultural heritage: exploration and identification of objects at underwater archaeological sites
ph investigación (en línea), n.º 6, junio de 2016, pp. 25-46
<http://www.iaph.es/phinvestigacion/index.php/phinvestigacion/article/view/1429>

BIBLIOGRAPHY

BETHENCOURT, M.; BOCALANDRO, A.; ROMERO, J. (2011)
Datación de pecios de los siglos XVIII y XIX a través de la caracterización de los forros de cobre. En *IV Congreso Latinoamericano de Conservación y Restauración de Metal, Madrid (13 al 17 de septiembre de 2011)*. Madrid: Secretaría General Técnica, Ministerio de Educación, Cultura y Deporte; Grupo Español de Conservación, 2011, pp. 51-62

BONIFACIO, C. (2008)
Galeones con Tesoros. Dónde están hundidos, Qué llevaban. Brenes (Sevilla): Muñoz Moya Editores Extremeños, 2008

BOWEN, A. (2009)
Underwater Archaeology: The NAS Guide to Principles and Practice. 2nd ed. Portsmounth: Blackwell Publishing, 2009

CHARFI, B.; HARITH, M. A. (2002)
Panoramic laser-induced breakdown spectrometry of water. *Spectrochim. Acta Part B*, vol. 57, 2002, pp. 1141-1153

***CONVENTION** on the Protection of the Underwater Cultural Heritage* (2001). Paris: Unesco, 2001

CREMERS, D. A.; RADZIEMSKI, L. J.; LOREE T. R. (1984)
Spectrochemical analysis of liquids using the laser spark. *Appl. Spectrosc.*, vol. 38, 1984, pp. 721-726

DE GIACOMO, A.; DELL'AGLIO, M.; COLAO, F. et al. (2004)
Double pulse laser produced plasma on metallic target in seawater: basic aspects and analytical approach. *Spectrochim. Acta Part B*, vol. 59, 2004, pp. 1431-1438

DE GIACOMO, A.; DELL'AGLIO, M.; DE PASCALE, O. et al. (2007)
From single pulse to double pulse ns-laser induced breakdown spectroscopy under water: elemental analysis of aqueous solutions and submerged solid samples. *Spectrochim. Acta Part B*, vol. 62, 2007, pp. 721-738

FANTONI, R.; BARBINI, R.; COLAO, F. et al. (2004)
Integration of two lidar fluorosensor payloads in submarine ROV and flying UAV platforms. *EARSeL eProc.*, vol. 3, 2004, pp. 43-53

FORTES, F. J.; CORTÉS, M.; SIMÓN, M. D. et al. (2005)
Chronocultural sorting of archaeological bronze objects using laser-induced breakdown spectrometry. *Anal. Chim. Acta*, vol. 554, 2005, pp. 136-143

FORTES, F. J.; CUÑAT, J.; CABALÍN, L. M. et al. (2007)
In situ analytical assessment and chemical imaging of historical buildings using a man-portable laser system. *Appl. Spectrosc.*, vol. 61, 2007, pp. 558-564

FORTES, F. J.; LASERNA, J. J. (2010)
The development of fieldable laser-induced breakdown spectrometer: no limits on the horizon. *Spectrochim. Acta Part B*, vol. 65, 2010, pp. 975-990

FORTES, F. J.; MOROS, J.; LUCENA, P. et al. (2013)
Laser-induced breakdown spectroscopy. *Anal. Chem.*, vol. 85, 2013, pp. 640-669

GIAKOUMAKI, A.; MELESSANAKI, K.; ANGLOS, D. (2007)
Laser-induced breakdown spectroscopy (LIBS) in archaeological science-applications and prospects. *Anal. Bioanal. Chem.*, vol. 387, 2007, pp. 749-760

GUIRADO, S.; FORTES, F. J.; CABALIN, L. M. et al. (2014)
Effect of Pulse Duration in Multi-Pulse Excitation of Silicon in Laser-Induced Breakdown Spectroscopy (LIBS). *Appl. Spectrosc.*, 2014, vol. 68, pp. 1060-1066

GUIRADO, S.; FORTES, F. J.; LASERNA, J. J. (2015)
Elemental analysis of materials in an underwater archeological shipwreck using a novel remote laser-induced breakdown spectroscopy system. *Talanta*, vol. 137, 2015, pp. 182-188

GUIRADO, S.; FORTES, F. J.; LAZIC, V. et al. (2012)
Chemical analysis of archeological materials in submarine environments using laser-induced breakdown spectroscopy. On-site trials in the Mediterranean Sea. *Spectrochim. Acta, Part B*, vol. 74-75, 2012, pp. 137-143

LAZIC, V.; COLAO, F.; FANTONI, R. et al. (2005)
Recognition of archaeological materials underwater by laser induced breakdown spectroscopy. *Spectrochim. Acta Part B*, vol. 60, 2005, pp. 1014-1024

LAZIC, V.; LASERNA, J. J.; JOVICEVIC, S. (2013a)
Insights in the laser-induced breakdown spectroscopy signal generation underwater using dual pulse excitation. Part I: Vapor bubble, shockwaves and plasma. *Spectrochim. Acta, Part B*, vol. 82, 2013, pp. 42-49

LAZIC, V.; LASERNA, J. J.; JOVICEVIC, S. (2013b)
Insights in the laser-induced breakdown spectroscopy signal generation underwater using dual pulse excitation. Part II: Plasma emission intensity as a function of interpulse delay. *Spectrochim. Acta, Part B*, vol. 82, 2013, pp. 50-59

LEÓN AMORES, C. (2009)
Buceando en el Pasado. Madrid: Espasa Calpe, 2009

MARGETIC, V.; PAKULEV, A.; STOCKHAUS, A. et al. (2000)
A comparison of nanosecond and femtosecond laser induced plasma spectroscopy of brass samples. *Spectrochim. Acta Part B*, vol. 55, 2000, pp. 1771-1785

WHITE, S. N.; DUNK, R. M.; PELTZER, J. J. et al. (2006)
In situ Raman analyses of deep-sea hydrothermal and cold seep systems (Gorda Ridge and Hydrate Ridge). *Geochem, Geophys. Geosyst*, vol. 7, 2006, Q05023

G Model
CULHER 3203 1–7
ARTICLE IN PRESS

Journal of Cultural Heritage xxx (2017) xxx–xxx

Available online at
ScienceDirect
www.sciencedirect.com

Elsevier Masson France
EM|consulte
www.em-consulte.com/en

Original article

Subsea spectral identification of shipwreck objects using laser-induced breakdown spectroscopy and linear discriminantion analysis

M. López-Claros, F.J. Fortes, J.J. Laserna*

Departamento de Química Analítica, Facultad de Ciencias, Universidad de Málaga, Campus de Teatinos s/n, 29071 Málaga, Spain

ARTICLE INFO

Article history:
Received 7 September 2016
Accepted 20 December 2016
Available online xxx

Keywords:
Laser-induced breakdown spectroscopy
LIBS
Underwater analysis
Multi-pulse excitation
Optical fiber
Cultural heritage

ABSTRACT

Underwater LIBS is an evolving technology which offers unique advantages over traditional methods, not only do it offers the composition of liquids with high reliability; it also provides the elemental composition of solids with little or no user manipulation. Because of this advantage LIBS has been used as a tool for inspecting materials in underwater archaeology, where knowledge of the chemical composition may provide valuable clues on the origin of materials in shipwrecks and submerged buildings. This study attempts to provide undersea LIBS instrumentation with the data processing tools intended to make shipwreck inspection surveys easier and faster. The new tool has been designed to sort the readings obtained by a LIBS system when inspecting unknown pieces found in the sea bottom and assign their composition to one of several groups of common materials found in shipwrecks. The tool involves linear discriminant analysis that was first validated in the laboratory with a training set of samples collected from wreckages. Then the method was used in an underwater survey in the Mediterranean Sea to sort the materials found in a shipwreck. In combination with high-definition video recording, this approach can provide an understanding of the materials and a permanent record of the unknown assets, this eliminating the need for underwater archaeologists to make handwritten notes of individual pieces while surveying shipwrecks.

1. Introduction

Underwater cultural heritage is a rich source of information and a window to the past. In fact, the presence of specific elements (either greater or lesser percentage) in an archaeological material, namely *chemical fingerprints*, is of great interest for a better understanding of its age, provenance and manufacturing technology. Discovery of amphoras, cannons and metallic artefacts in their archaeological context could provide further information concerning the age and nationality of a shipwreck [1]. However, the severe conditions of the marine environment change the appearance of the underwater sites and distorts the idyllic image of the shipwreck until blending with the surroundings. Hence, artefacts and structures may be uncovered beneath sediments, chemically altered or even destroyed.

Recent advances in electronic engineering, underwater robotics and novel systems for processing and image recognition make localization of underwater archaeological sites much easier than in past. However, underwater archaeology still requires the development of screening techniques for the in situ recognition of findings. A restricted number of laser-based techniques (i.e. Raman, LIBS and LIF) have proven to be useful for this purpose [2–4]. Specifically, LIBS is really appreciated as is the unique that could provide atomic information from the spectral signature of underwater objects [5,6]. Additionally, LIBS combines valuable attributes (no sample preparation, minimally destructive, fast analytical response and possibility of remote sensing analysis), specially demanded in cultural heritage preservation and investigation [7,8]. It's worth mentioning that underwater LIBS analysis is not a trivial task and several research groups have proposed different alternatives for improving LIBS sensitivity inside liquids [9–11]. In this sense, the dual pulse excitations being the most common approach proposed in the literature [12,13]. However, problems related to the use of two laser sources, the precise alignment needed and synchronization in data acquisition are obstacles for its implementation in field analysis [15,16]. The instrumental development was further investigated until 2012 when Guirado et al. [17] published the first in situ undersea LIBS analysis of solid materials, at a depth of 30 meters,

* Corresponding author. Tel.: +34 951953007.
E-mail address: laserna@uma.es (J.J. Laserna).

http://dx.doi.org/10.1016/j.culher.2016.12.015
1296-2074/

G Model
CULHER 3203 1–7
ARTICLE IN PRESS

using a fiber-based LIBS system. Later, a new generation of LIBS instruments based on transmission of a collinear sequence of multi-pulses through the optical fiber cable was proposed by the same authors to improve the performance of the technology [18,19]. An archaeological shipwreck situated 17 meters deep was inspected using this approach [20].

In subaquatic archaeology, quantitative information turns crucial for planning restoration/conservation activities and taking decisions about whether the object should be moved from the underwater site or not. Nevertheless, LIBS strongly depends on matrix effects, pulse to pulse fluctuations, plasma-solid interactions, among other factors. In this sense, a broad number of fundamental studies have been reported to overcome the so-called fractionation effect [21–24]. Certain procedures such as internal standardization, background normalization, calibration-free analysis and the use of a double-pulse configuration has been explored so far for quantitative analysis of submersed materials. Most recently, Guirado et al. [25] evaluated the use of multi-pulse (MP) excitation as an effective solution to mitigate the fractionation effects observed in LIBS analysis of copper-based alloys. MP-LIBS also prevents the effect of ambient pressure on LIBS signal, thus demonstrating the feasibility of LIBS for quantitative analysis of bronze materials in a real underwater site.

In such a scenario, development of spectral libraries and data processing algorithms also improve the capability of LIBS for field measurements. Hence, from an archaeological point of view, both qualitative and quantitative information extracts compositional evidence that together with the use of chemometric methods may identify specific materials, which could be related to ancient manufacturing or production processes [26]. A number of statistical methods including linear and rank correlation, principal component analysis (PCA), partial least-squares discriminant analysis (PLS-DA) and soft independent modeling of class analogy (SIMCA), among others have proved to group and classify ancient artefacts in archaeometric analysis [27]. In this work, a classification method is evaluated for the identification of chemical fingerprints in shipwrecks. A variety of archaeological objects has been previously characterized in laboratory using essentially the same operational conditions than those found undersea in order to ensure the effectiveness of the method during the recognition process in the site. Moreover, a set of sheathings from different shipwrecks were analyzed with the objective to perform a chronocultural sorting of these structural pieces. Based on this procedure, findings from the shipwreck of *San Pedro de Alcántara* (Malaga, Spain) were directly classified into metallic alloys, ceramics, rocks or marbles.

2. Materials and methods

The remote LIBS instrument and its construction have been described in a recent paper [20] so only a brief description of the instrument is given here. The system consists of two well-defined parts: a hand-held probe and a main unit, interconnected by means of an umbilical cable. The main unit comprises the optical module for laser-fiber coupling, the data acquisition module and the laser power supply.

The optical module consists of a polymethyl methacrylate structure, specially adapted in order to prevent the deposition of particles from the marine environment at the tip of the optical fiber. The module contains the laser head (Q-switched Nd:YAG laser operating at 1064 nm, Brilliant) and all the optical arrangements for launching the laser radiation into the fiber-optic cable (mounted in a *xyz* stage) and collecting the plasma light for the transmission to a spectrograph. The laser beam is transmitted through a 55 m long fiber optic cable that travels inside an umbilical cord, which connects the probe to the optical module. At the end of the fiber, the hand-held probe focuses the laser beam onto the sample surface by an appropriate optical configuration. With this configuration, the spot size was established at 450 μm in diameter.

The same optical fiber is used for light gathering purposes. The plasma light is collected and returned to the optical module, where it is conducted to the data-acquisition module using an optical system used to focus plasma light into the spectrometer fiber-optic cable (2 m length, 600 μm diameter, NA0.22). The data-acquisition module, consisting of the spectrometer, the video converter and the PC components, was installed in the main unit. A pulse/delay generator (which externally controls the system) was also configured within this module. The spectrometer is a crossed Czerny-Turner design with a holographic diffraction grating of 1200 lines mm^{-1} (Avantes, model AvaSpec-2048-USB2). This configuration provides a spectral resolution of 0.1–0.2 nm/pixel in the spectral range of 300-550 nm. AvaSoft software was employed for controlling the spectrometer and for data processing. The acquisition delay was established in 1 μs, which corresponds to the best signal-to-noise ratio (SNR) for the LIBS signal. The irradiance value at sample surface was 1.6 GW cm^{-2}. And all underwater analysis was carried out using 5 bars of argon as a purge gas. The Statgraphics® statistics software package was used for chemometrics analysis.

3. Results and discussion

3.1. Classification method for archaeological artefacts

Given the great compositional diversity, textural differences and surface alteration of the submersed cultural heritage, the use of advanced statistical algorithms is essential for the recognition and sorting of underwater findings. For this purpose, linear discriminant analysis (LDA) was used to generate a classification model from which unknown samples will be predicted in site on the basis of their LIBS response. As a supervised algorithm, a LDA model based on the spectra acquired from a set of known archaeological samples was constructed. LDA evaluates the relative weights of the original variables for group discrimination and score the separation between multiple classes [28–30]. Afterwards, the model predicts the probability that an unknown sample belongs to each class.

A set of thirty-eight objects collected from several archaeological shipwrecks was first studied. To simulate the experimental conditions of a subsea environment, samples were immersed and analyzed in a water tank in our laboratory. Because of the large variety of samples used in this study, objects were divided into different groups for chemometric analysis, i.e. bronze-alloys (10 samples), metallic pieces (18 samples), ceramics (5 samples) and marbles (5 samples). LIBS spectra were acquired in the 350–550 nm spectral range and their intensities normalized to unity for comparative purposes. Data were acquired by averaging the response of 50 laser shots on three adjacent positions for each sample. However, the whole LIBS spectra were not considered as input data so the initial information based in 2048 data points was significantly reduced to 10 spectral varibles. The selected variables were Cu (I) 510.55 nm, Zn (I) 481.05 nm, Sn (I) 452.47 nm, Pb (I) 405.78 nm, Fe (I) 438.35 nm, Ca (I) 422.67 nm, Mg (I) 517.26 nm, Si (I) 390.55 nm, Sr (I) 407.61 nm and Ti (I) 498.17 nm. In addition, the presence of Ca, Mg, Si and Ti in metallic samples is associated to the deposition of sedimentary material on the sample surface. The first discriminant function has the expression:

$$F1 = 2.7 \cdot I_{Cu} + 2.4 \cdot I_{Zn} + 22.8 \cdot I_{Sn} + 0.8 \cdot I_{Pb} + 2.7 \cdot I_{Fe} - 7.2 \cdot I_{Ca} - 1.2 \cdot I_{Mg} - 3.8 \cdot I_{Sr} - 6.0 \cdot I_{Si+Ti} + 0.59$$

G Model
CULHER 32031–7
ARTICLE IN PRESS

Table 1
Prediction groups membership for training set samples. ID sample is constitutes by a letter and two numbers as follows: the letter represents the type of sample (A: copper based alloy M: metal, C: ceramic, B: marble), the first number corresponds to the shipwreck (I: Delta II, II Delta III) and the second to a number in the group classified.

ID	Prediction group membership (%)					ID	Prediction group membership (%)				
	Alloy	Metal	Ceramic	Marble	Total		Alloy	Metal	Ceramic	Marble	Total
AII1	100	0	0	0	100	MI12	0	100	0	0	100
AII2	100	0	0	0	100	MI13	0	100	0	0	100
AI1	100	0	0	0	100	MI14	0	100	0	0	100
AI2	100	0	0	0	100	MI15	0	100	0	0	100
AI3	100	0	0	0	100	MI16	0	100	0	0	100
AII3	100	0	0	0	100	MI17	0	100	0	0	100
AII4	99.4	0.6	0	0	100	MII9	0	100	0	0	100
AII5	100	0	0	0	100	MI18	0	100	0	0	100
AI4	99.9	0.1	0	0	100	MII10	4.2	95.8	0	0	100
AII6	94.7	5.3	0	0	100	CI19	0	0	100	0	100
MII7	3.3	96.7	0	0	100	CI20	0	0	100	0	100
MII8	0	100	0	0	100	CI21	0	0	100	0	100
MI5	0	100	0	0	100	CI22	0	0	100	0	100
MI6	0	100	0	0	100	CI23	0	0	100	0	100
MI7	0	100	0	0	100	B1	0	0	0	100	100
MI8	0	100	0	0	100	B2	0	0	0	100	100
MI9	0	100	0	0	100	B3	0	0	0	100	100
MI10	0	100	0	0	100	B4	0	0	0.2	99.8	100
MI11	0	100	0	0	100	B5	0	0	0	100	100

where I_n is the intensity of each element line. This function has an excellent canonical correlation, 0.98, that is its relative ability to discriminate amongst the groups. The second function is:

$$F2 = 1.8 \cdot I_{Cu} + 3.8 \cdot I_{Zn} + 24.8 \cdot I_{Sn} - 0.2 \cdot I_{Pb} - 0.8 \cdot I_{Fe} + 2.5 \cdot I_{Ca} - 1.8 \cdot I_{Mg} - 1.5 \cdot I_{Sr} + 9.4 \cdot I_{Si+Ti} - 2.0$$

Also, it has a good 0.91 canonical correlation. Nevertheless, the statistics treatment scores Wilk's lambda values of 0.0013 for F_1 and 0.03 for F_2, which suggest that the variables selected for the linear discriminant analysis are appropriate for sample discrimination. Both functions also have a very high significance level of Chi-square statistics, 201 and 106 for F_1 and F_2, respectively.

The classification functions generated by the proposed model were validated with the *training* set of samples. Table 1 summarizes the classification of each sample based on the proposed model. It's worth mentioning that all samples were identified without exceptions. A scatter plot of the first two discriminant functions is presented in Fig. 1. As shown, samples are separated in four classes or groups attending to the type of material previously described in the "supervised" model. Bronze alloys and metallic pieces are grouped in the right-hand side of the graph, whereas ceramics and marbles are grouped in the second and third quadrant of the scatter graph, respectively. The centroid of each group is also marked in the graph. The model will be checked in our laboratory with a set of sheathings simulating the experimental conditions of a subsea environment. Furthermore, it will be tested during the underwater inspection of the wreck of *San Pedro de Alcantara*.

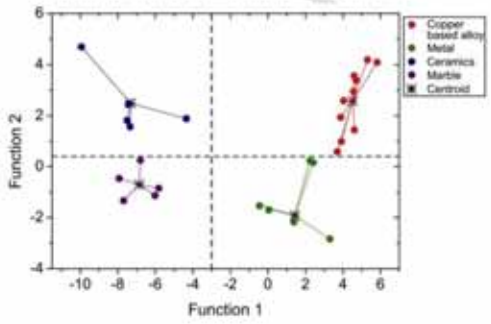

Fig. 1. Scatter plot of the first two canonical discriminant functions containing the four groups defined in the method.

3.2. Chronological sorting of metallic sheathings

Since the Phoenician times, the use of sheathings in wooded-hulled vessels has been extensively tested to prevent wood degradation by the action of seawater, bivalve molluscs and algae. Sheathings were also used to improve the operability of the boat. The type of sheathing has evolved with time so the knowledge of elemental composition of this kind of samples makes it possible the assignment of the manufacturing period and provides clues to uncover the ship's origin [31].

A set of sheathing pieces belonging to different shipwrecks were analyzed in a water tank in an attempt to provide information about the geographical origin of the shipwreck that could be helps us to understand its historical context. In addition, this set of four samples will be use to evaluate our chemometric model. Samples were found in the underwater archaeological sites of "*Delta I*" (XVII Century, Spanish), "*Delta II*" (XVI Century, Italian), "*Mercante de San Sebastian*" (XVIII Century, Spanish) and "*Fougueaux*" (XVIII Century, French). A chronocultural sorting of the sheathings analyzed by LIBS is presented in Fig. 2. The main emission lines are labeled in the spectra. As seen, the squares limit the timeline in two periods, depending on the sheathing composition. Thus, lead-based sheathings were early introduced in the XV Century in Portuguese and Spanish arsenals and its use was extended until the XVII Century [31]. This fact is easily observed in the sheathings belonging to *Delta I* and *Delta II*, as revealed by the LIBS spectra sketched in the figure. In the XVIII Century, lead-based sheathings were substituted first by copper and then by copper-based alloys. As shown in Fig. 2 the LIBS spectra of *Mercante de San Sebastian* and *Fougueaux* in chronological order. In addition, the presence of minor components such as zinc, iron or lead, as observed in the spectrum corresponding to the *Fougueaux*, could indicate its country of origin. Hence, it exists a clear evolution of the sheathing's composition from lead to copper based alloys that could be related to a period of history or even to the country of manufacture of the shipwreck. The classification function was fully effective including each sample to the correct

G Model
CULHER 3203 1–7
ARTICLE IN PRESS
4
M. López-Claros et al. / Journal of Cultural Heritage xxx (2017) xxx–xxx

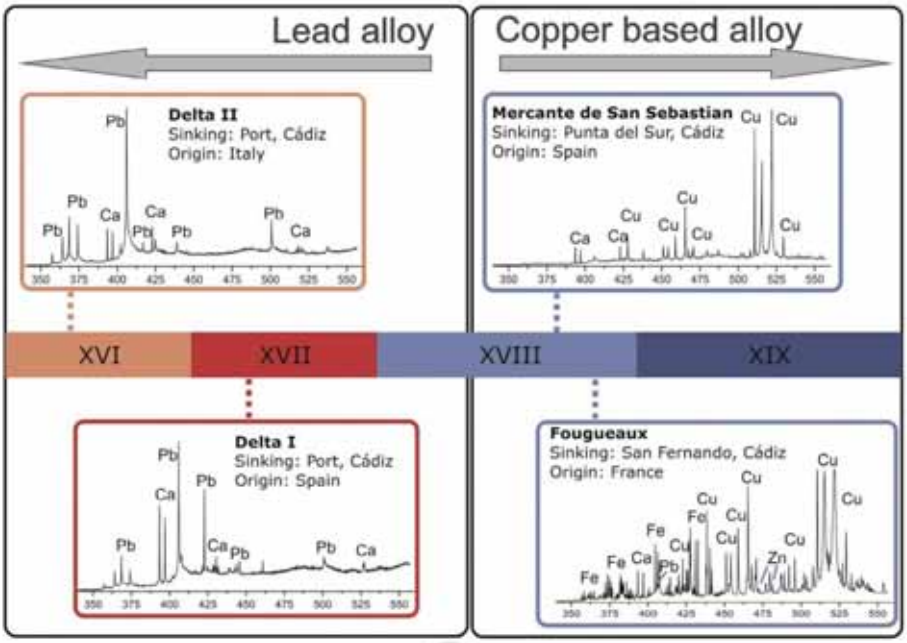

Fig. 2. Chronocultural sorting of evolution of sheathing's composition from lead to copper based alloys. The main emission lines are labeled in the spectra.

group. The sheathing of *Delta I*, *Delta II* and *Mercante de San Sebastian* are metals and the composition of *Fougueaux* corresponds to a bronze alloy.

3.3. *Identification of objects in shipwrecks. The wreck of* San Pedro de Alcantara

The wreck of *San Pedro de Alcantara*, located in the South of Spain, was discovered 10 m deep over a sandy bottom area. The wreck presents a military-structure type with a beam of 60 m, 10–12 m of breadth. The structure of the boat is covered by sediments, calcareous deposits and marine algae. Prior to the LIBS measurement campaign, a site survey was accomplished by the archaeologists from the Centro de Arqueología Subacuática (CAS) who located archaeological pieces from the remains of the wreck and removed the concretion layer from the sample surface.

The LIBS instrument was deployed on the vessel's board while a diver operated the LIBS probe in the sea bottom. The input pressure for underwater analysis was set to 5 bars, the maximum pressure supported by the system. The use of a gas purge is of key importance for preventing the admittance of water into the LIBS probe and create a solid-gas interface for LIBS analysis. Given the high alteration degree of the samples inspected, we decided to use argon as a purge gas, which provided a larger LIBS intensity when compared to air. The influence of argon as protection gas on the LIBS signal of an archaeological ceramic is presented in Fig. 3. The main emission lines are labeled in the spectra. As shown, the use of argon increased the signal 4-fold for the emission line of Ca (I) at 422.67 nm when compared to air. Although metallic objects also benefit from the use of Ar, this observation is especially noticeable in ceramics.

A large number of archaeological objects were discovered and analyzed by LIBS during the survey. Fig. 4 shows parts of the shipwreck and the LIBS probe operated by a diver. To assign the typical

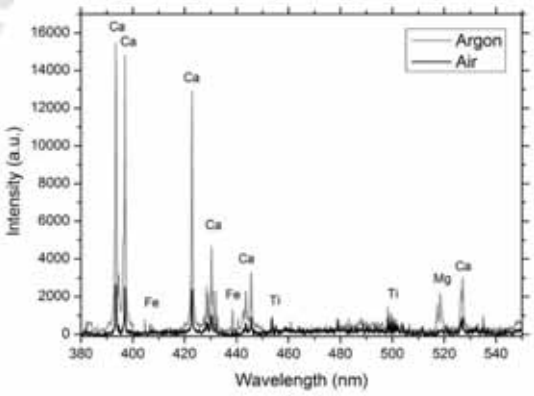

Fig. 3. Comparison of the influence of air and argon gas protection on the LIBS signal of an archaeological ceramic. The main emission lines are labeled in the spectra.

spectrum of a material and in order to ensure the reproducibility of the results, data were acquired by averaging the response of 50 laser shots on three adjacent positions for each sample. Then, acquired spectral intensities were normalized to unity for comparative purposes. Each object exhibits a distinctive chemical that was introduced in the classification method developed in Section 3.1. From the canonical discriminant functions described there, the unknown findings from the wreck were grouped into several categories easily. Fig. 5 presents the classification of the set of unknown objects. As shown, samples from the subsea archaeological site were unequivocally classified in each of the aforementioned

G Model
CULHER 3203 1–7
ARTICLE IN PRESS
M. López-Claros et al. / Journal of Cultural Heritage xxx (2017) xxx–xxx 5

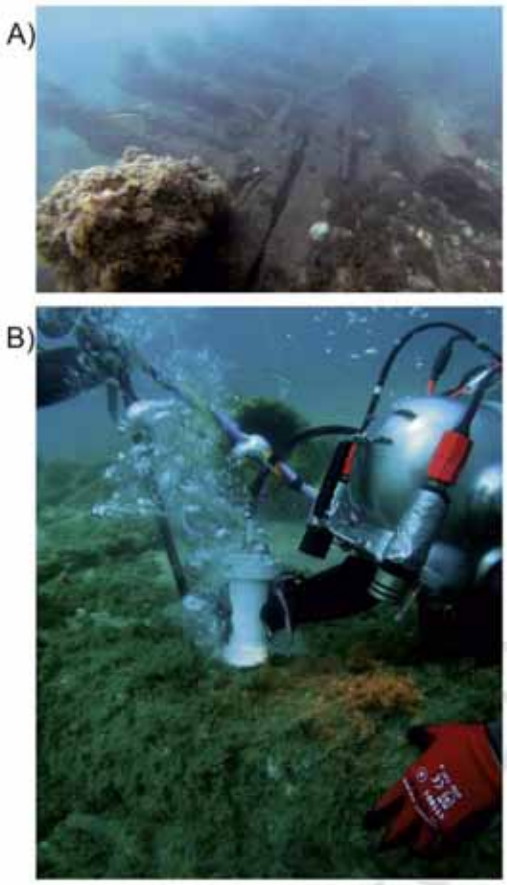

Fig. 4. Photographic detail of the structure of the boat (a), and diver operating the LIBS probe in the wreck of *San Pedro Alcántara* (b).

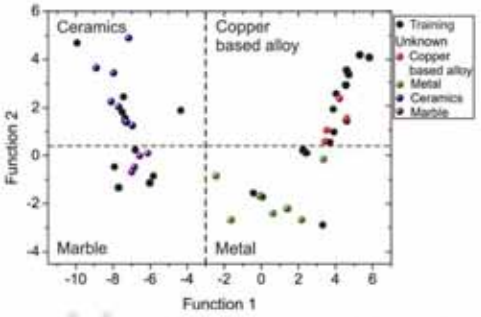

Fig. 5. Classification scatter plot of the first two canonical discriminant functions of modeling developed. The scatter points in grey color corresponds to the set of samples employed for modeling the classification method and colored spheres represents the set of unknown objects.

groups. The scatter points (in grey color) from the set of samples employed for modeling the classification method are also plotted in the graph. Results for the unknown samples classification are summarized in Table 2. Objects were correctly identified as four bronze alloys, eight ceramic fragments, seven metallic pieces and four marbles.

Fig. 6 shows a drawing top view of the shipwreck in which the bow is oriented to the northwest position and the aft, to the southeast. The drawing describes the state of conservation of the wreck, where the shipwreck structure is observed, as well as the way is distributed along the site. The locations of the archaeological pieces are also indicated. Chemical composition of each object is detailed as a bar diagram inset. As shown, various types of samples were identified as defense material such as two iron canons (M2, M4) and a canon bullet (M3) composed of iron with manganese as a minor constituent. On the other hand, pieces of crew clothing present a chemical composition based on copper alloy with zinc in the case of jacquet button (A2) and zinc-lead in the case of the belt buckle (A4). Regarding to ceramic fragments, in general, are constituted by calcium, magnesium, aluminum, iron, silicon, strontium and titanium; although pieces C3, C5 and C7 also contained lead. Some unidentified pieces show a variable chemical composition such as metals copper-lead (A3) alloy, and copper-zinc-lead (A1) alloy; and lead (M1, M7) or iron (M5, M6) metals.

Table 2
Prediction groups membership for unknown samples. ID sample is constitutes by a letter represents the type of sample (A: copper based alloy M: metal, C: ceramic, B: marble) and a number in the group classified.

ID	Prediction group membership (%)					ID	Prediction group membership (%)				
	Alloy	Metal	Ceramic	Marble	Total		Alloy	Metal	Ceramic	Marble	Total
A1	100	0	0	0	100	C4	0	0	100	0	100
A2	100	0	0	0	100	C5	0	0	100	0	100
A3	100	0	0	0	100	C6	0	0	100	0	100
A4	99.4	0.6	0	0	100	C7	0	0	100	0	100
M1	0	100	0	0	100	C8	0	0	100	0	100
M2	0	91.2	0	8.8	100	M8	0	100	0	0	100
M3	0	100	0	0	100	M9	0	100	0	0	100
M4	0	100	0	0	100	M10	13	87	0	0	100
M5	0	100	0	0	100	A5	88.7	11.3	0	0	100
M6	0	100	0	0	100	B1	0	0	0.5	99.5	100
M7	0	100	0	0	100	B2	0	0	0	100	100
C1	0	0	100	0	100	B3	0	0	0	100	100
C2	0	0	100	0	100	B4	0	0	0	100	100
C3	0	0	100	0	100						

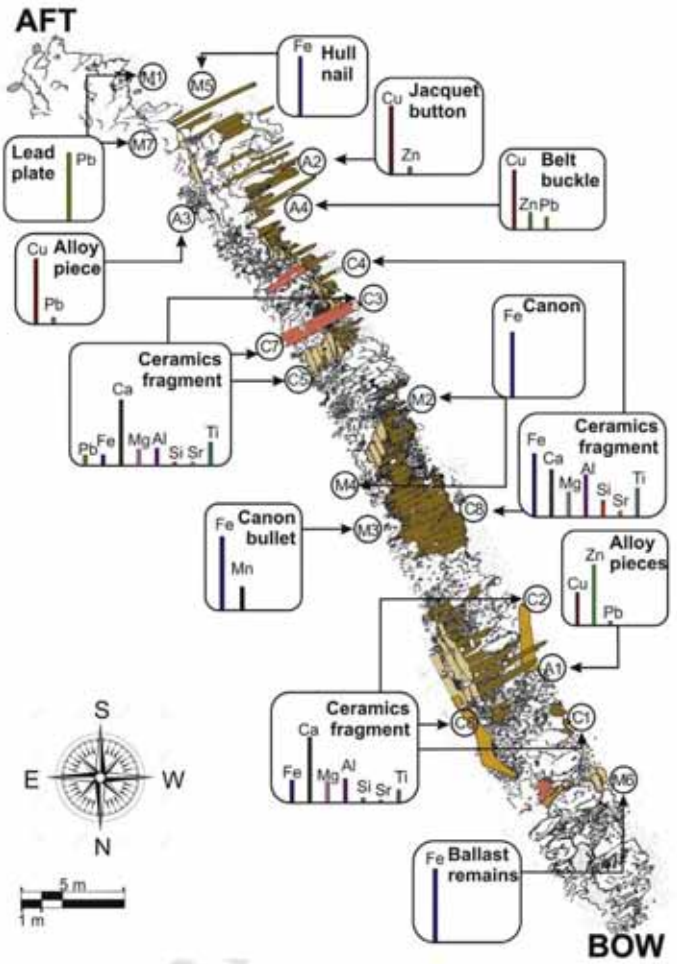

Fig. 6. Schematic drawing of the shipwreck. The inset bar diagrams represent the chemical composition of each object and the locations of the archaeological findings.

4. Conclusions

Using a LIBS sensor deployed on a small vessel, a hand-held probe was submersed by a diver to the shipwreck of San Pedro de Alcantara located in the South of Spain over the Mediterranean Sea. LIBS data from a variety of objects found in the wreck were collected, logged and accurately geo-positioned for post survey analysis. In addition to metallic objects, refractory materials such as rocks and ceramics were analyzed. Although algae and calcareous deposits had to be removed from the sample surface before the analysis, the LIBS system constitutes a significant step forward, allowing the acquisition of a consistent set of spectral data that can be treated by a software based on linear discriminant analysis for assigning the chemical identity of the object. The information thus gathered provides valuable data on the identity of shipwrecks located in coastal waters.

Acknowledgments

This research was funded by Junta de Andalucía, Consejería de Economía, Innovación, Ciencia y Empleo through project P11-FQM-7193 (AQUALAS), a joint effort of Instituto Andaluz del Patrimonio Histórico (IAPH), Centro de Arqueología Subacuática (CAS) and the University of Malaga (UMA). M. Lopez-Claros would like to acknowledge the Consejería de Innovación, Ciencia y Empleo of the Junta de Andalucía for her fellowship. Authors would also like to acknowledge the valuable assistance of Salvador Guirado and at the same time the huge ability to commit, work and peerless

G Model
CULHER 3203 1–7
ARTICLE IN PRESS

dedication of CAS's archaeologists Carmen García Rivera, Milagros Alzaga, Josefa Martí, Nuria Rodríguez and Aurora Higueras-Milena.

References

[1] C. Pearson, Conservation of marine archaeological objects, Butterworth & Co. Ltd, London, 1987.
[2] X. Zhang, W.J. Kirkwood, P.M. Walz, E.T. Peltzer, P.G. Brewer, A review of advances in Deep-Ocean Raman Spectroscopy, Appl. Spectrosc. 66 (2012) 237–249.
[3] B. Thornton, T. Takahashi, T. Sato, T. Sakka, A. Tamura, A. Matsumoto, T. Nozaki, T. Ohki, K. Ohki, Development of a deep-sea laser-induced breakdown spectrometer for in situ multi-element chemical analysis, Deep. Res. Part I 95 (2015) 20–36.
[4] R. Fantoni, R. Barbini, F. Colao, D. Ferrante, L. Fiorani, A. Palucci, Integration of two lidar fluorosensor payloads in submarine ROV and flying UAV platforms, EARSeL eProc. 3 (2004) 43–53.
[5] F.J. Fortes, J. Moros, P. Lucena, L.M. Cabalín, J.J. Laserna, Laser-induced breakdown spectroscopy, Anal. Chem. 85 (2013) 640–669.
[6] R.E. Russo, X. Mao, J.J. González, V. Zorba, J. Yoo, Laser ablation in analytical chemistry, Anal. Chem. 85 (2013) 6162–6177.
[7] A. Giakoumaki, K. Melessanaki, D. Anglos, Laser-induced breakdown spectroscopy (LIBS) in archaeological science – applications and prospects, Anal. Bioanal. Chem. 387 (2007) 749–760.
[8] V. Spizzichino, R. Fantoni, LIBS in archaeometry: a review of its application and future perspectives, Spectrochim. Acta Part B 99 (2014) 201–209.
[9] V. Lazic, F. Colao, R. Fantoni, V. Spizzicchino, Recognition of archeological materials underwater by laser induced breakdown spectroscopy, Spectrochim. Acta Part B 60 (2005) 1014–1024.
[10] V. Lazic, S. Jovićević, Laser induced breakdown spectroscopy inside liquids: processes and analytical aspects, Spectrochim. Acta Part B 101 (2014) 288–311.
[11] T. Sakka, H. Oguchi, S. Masai, K. Hirata, Y.H. Ogata, Use of a long-duration ns pulse for efficient emission of spectral lines from the laser ablation plume in water, Appl. Phys. Lett. 88 (2006) 061120.
[12] V. Lazic, J.J. Laserna, S. Jovicevic, Insights in the laser induced breakdown spectroscopy signal generation underwater using dual pulse excitation – Part II: plasma emission intensity as a function of interpulse delay, Spectrochim. Acta Part B 82 (2013) 50–59.
[13] V. Lazic, J.J. Laserna, S. Jovicevic, Insights in the laser-induced breakdown spectroscopy signal generation underwater using dual pulse excitation – Part I: vapor bubble, shockwaves and plasma, Spectrochim. Acta Part B 82 (2013) 42–49.
[14] A. De Giacomo, M. Dell'Aglio, O. De Pascale, M. Capitelli, From single pulse to double pulse ns-Laser Induced Breakdown Spectroscopy under water: elemental analysis of aqueous solutions and submerged solid samples, Spectrochim. Acta Part B 62 (2007) 721–738.
[15] F.J. Fortes, J.J. Laserna, The development of fieldable laser-induced breakdown spectrometer: no limits on the horizon, Spectrochim. Acta Part B 65 (2010) 975–990.
[16] F.J. Fortes, S. Guirado, A. Metzinger, J.J. Laserna, A study of underwater stand-off laser-induced breakdown spectroscopy for chemical analysis of objects in the deep ocean, J. Anal. At. Spectrom. 30 (2015) 1050–1056.
[17] S. Guirado, F.J. Fortes, V. Lazic, J.J. Laserna, Chemical analysis of archeological materials in submarine environments using laser-induced breakdown spectroscopy. On-site trials in the Mediterranean Sea, Spectrochim. Acta Part B 74–75 (2012) 137–143.
[18] L.M. Caballín, A. González, V. Lazic, J.J. Laserna, Deep ablation and depth profiling by laser-induced breakdown spectroscopy (LIBS) employing multi-pulse laser excitation: application to galvanized steel, Appl. Spectrosc. 65 (2011) 797–805.
[19] S. Guirado, F.J. Fortes, L.M. Caballín, J.J. Laserna, Effect of pulse duration in multi-pulse excitation of silicon in Laser-Induced Breakdown Spectroscopy (LIBS), Appl. Spectrosc. 68 (2014) 1060–1066.
[20] S. Guirado, F.J. Fortes, J.J. Laserna, Elemental analysis of materials in an underwater archeological shipwreck using a novel remote laser-induced breakdown spectroscopy system, Talanta 137 (2015) 182–188.
[21] R. Fantoni, L. Caneve, F. Colao, L. Fornarini, V. Lazic, V. Spizzichino, Methodologies for laboratory laser induced breakdown spectroscopy semi-quantitative and quantitative analysis – a review, Spectrochim. Acta Part B 63 (2008) 1097–1108.
[22] A. De Giacomo, M. Dell'Aglio, A. Casavola, G. Colonna, O. De Pascale, M. Capitelli, Elemental chemical analysis of submerged targets by double-pulse laser-induced breakdown spectroscopy, Anal. Bioanal. Chem. 385 (2006) 303–311.
[23] S. Almaviva, R. Fantoni, L. Caneve, F. Colao, L. Fornarini, A. Santagata, R. Teghil, Use of ns and fs pulse excitation in laser-induced breakdown spectroscopy to improve its analytical performances: a case study on quaternary bronze alloys, Spectrochim. Acta B 99 (2014) 185–192.
[24] E. Tognoni, G. Cristoforetti, S. Legnaioli, V. Palleschi, Calibration-free laser-induced breakdown spectroscopy: state of the art, Spectrochim. Acta Part B 65 (2010) 1–14.
[25] S. Guirado, F.J. Fortes, J.J. Laserna, Multi-pulse excitation for underwater analysis of copper-based alloys using a novel remote laser-induced breakdown spectroscopy system, Appl. Spectrosc. 70 (2016) 618–626.
[26] M.J. Baxter, Exploratory multivariate analysis in archaeology, Edinburgh University Press, Edinburgh, 1994.
[27] M. Corsi, G. Cristoforetti, M. Giuffrida, M. Hidalgo, S. Legnaioli, L. Masotti, V. Palleschi, A. Salvetti, E. Tognoni, C. Vallebona, A. Zanini, Archaeometric analysis of ancient copper artefacts by laser-induced breakdown spectroscopy technique, Microchim Acta 152 (2005) 105–111.
[28] J.B. Sirven, B. Sallé, P. Mauchien, J.L. Lacour, S. Maurice, G. Manhès, Feasibility study of rock identification at the surface of Mars by remote laser-induced breakdown spectroscopy and three chemometric methods, J. Anal. At. Spectrom. 22 (2007) 1471.
[29] J.L. Gottfried, R.S. Harmon, F.C. De Lucia, A.W. Miziolek, Multivariate analysis of laser-induced breakdown spectroscopy chemical signatures for geomaterial classification, Spectrochim. Acta Part B 64 (2009) 1009–1019.
[30] F. Colao, R. Fantoni, P. Ortiz, M.A. Vazquez, J.M. Martin, R. Ortiz, N. Idris, Quarry identification of historical building materials by means of LIBS XRF and chemometric analysis, Spectrochim. Acta Part B 65 (2010) 688–694.
[31] M. Bethencourt, A. Bocalandro, J. Romero-Pastor, Datación de pecios de los siglos XVIII y XIX a través de la caracterización de los forros de cobre, IV Congreso Latinoamericano de Conservación y Restauración del Metal, Madrid (13–17 September 2011), Secretaría General Técnica, Ministerio de Educación, Cultura y Deporte; Grupo Español de Conservación, Madrid, 2011, pp. 51–62.

ARTICLE IN PRESS
SAB-05207; No of Pages 9
Spectrochimica Acta Part B xxx (2017) xxx–xxx
Contents lists available at ScienceDirect
Spectrochimica Acta Part B
journal homepage: www.elsevier.com/locate/sab

Double pulse laser induced breakdown spectroscopy of a solid in water: Effect of hydrostatic pressure on laser induced plasma, cavitation bubble and emission spectra

M. López-Claros [a,*], M. Dell'Aglio [b,*], R. Gaudiuso [c], A. Santagata [d], A. De Giacomo [b,e], F.J. Fortes [a], J.J. Laserna [a]

[a] Department of Analytical Chemistry, Faculty of Sciences, University of Malaga, Campus de Teatinos s/n, 29071 Malaga, Spain
[b] CNR-NANOTEC, Via Amendola 122/D, 70126 Bari, Italy
[c] University of Massachusetts Lowell, Kennedy College of Sciences, 265 Riverside Street, 01854 Lowell, MA, USA
[d] CNR-ISM C.da S. Loja – Zona Industriale, Tito Scalo, 85050 Potenza, Italy
[e] University of Bari, Dipartimento di Chimica, Via Orabona 4, 70125 Bari, Italy

ARTICLE INFO

Article history:
Received 15 December 2016
Received in revised form 9 February 2017
Accepted 13 February 2017
Available online xxxx

Keywords:
Laser-induced breakdown spectroscopy Deep Sea
Double pulse
Cavitation bubble
High pressure

ABSTRACT

There is a growing interest in the development of sensors use in exploration of the deep ocean. Techniques for the chemical analysis of submerged solids are of special interest, as they show promise for subsea mining applications where a rapid sorting of materials found in the sea bottom would improve efficiency. Laser-Induced Breakdown Spectroscopy (LIBS) has demonstrated potential for this application thanks to its unique capability of providing the atomic composition of submerged solids. Here we present a study on the parameters that affect the spectral response of metallic targets in an oceanic pressure environment. Following laser excitation of the solid, the plasma persistence and the cavitation bubble size are considerably reduced as the hydrostatic pressure increases. These effects are of particular concern in dual pulse excitation as reported here, where a careful choice of the interpulse timing is required. Shadowgraphic images of the plasma demonstrate that cavitation bubbles are formed early after the plasma onset and that the effect of hydrostatic pressure is negligible during the early stage of plasma expansion. Contrarily to what is observed at atmospheric pressure, emission spectra observed at high pressures are characterized by self-absorbed atomic lines on continuum radiation resulting from strong radiative recombination in the electron-rich confined environment. This effect is much less evident with ionic lines due to the much higher energy of the levels involved and ionization energy of ions, as well as to the lower extent of absorption effects occurring in the inner part of the plasma, where ionized species are more abundant. As a result of the smaller shorter-lived cavitation bubble, the LIBS intensity enhancement resulting from dual pulse excitation is reduced when the applied pressure increases.

1. Introduction

Laser-induced breakdown spectroscopy (LIBS) has emerged in the last decade as a promising solution for deep sea exploration [1–5]. Deep ocean is one of the most challenging and inaccessible environments of the planet, making it difficult to investigate not only the physical, chemical, and biological conditions on the seafloor; but also in areas such as water pollution, cultural heritage, hydrothermal vents, mining and geological exploitation [6–10]. This study aims to provide insight on the fundamental aspects of DP-LIBS that could be useful for developing new chemical sensors for oceanographic surveys [11]. The capabilities of laser-based tools can be useful for experimental campaigns in these extreme conditions. In particular, LIBS combines many of the required features for these applications, i.e. multielemental information, no sample preparation, unlimited range of material capability and real time analysis. Moreover, the experimental set-up adaptable to automation makes LIBS a good candidate for non-contact sensing [12–15]. The advance of lasers, spectrograph and detector technology has provided support for integrating remote-operated submersible LIBS systems with stand-off access to the sample [1]. Nevertheless, the actual realization of such systems is really complex both to design and to handle, thus requiring further research efforts. It follows that a significant amount of time is required for developing new sensors for oceanography, such as LIBS, as well as comparing it with other approaches in order to identify which is the most suitable technique viable for the chemical detection of solids submerged in water at high pressures.

Evaluation of LIBS analysis of liquids was investigated for the first time in 1984 by Cremers and co-workers [15]. In this report, the laser pulse was focused into a bulk liquid, producing its rapid heating at the

* Corresponding authors.
E-mail addresses: marinalc@uma.es (M. López-Claros), Marcella.dellaglio@nanotec.cnr.it (M. Dell'Aglio).

http://dx.doi.org/10.1016/j.sab.2017.02.010
0584-8547/

focal point, followed by an explosive expansion and formation of a gas bubble. Since then, a large number of studies has been conducted with the aim to clarify the different processes involved during the laser–water interaction, including the plasma and vapor bubble formation and the induced shock wave propagation, and to optimize approaches for the optical emission collection [16–20]. In order to obtain an optimum LIBS signal, different excitation approaches have been evaluated. For instance, single pulse excitation has been intensively studied, although, as a consequence of the nearly incompressible fluid medium, the generated plasma has a very short persistence, leading to a poor signal to noise ratio. De Giacomo et al. [21–23], and other authors such as Lazic and Rifai [24–26] have discussed the limitations of this approach for the analysis of liquids and investigated the potential advantages of the Double Pulse (DP-) LIBS. Briefly, in DP-LIBS, the first laser pulse produces a water vapor bubble whereas the second one, fired at an optimal interpulse delay with respect to the first one, induces a second plasma inside the previously formed bubble. The second laser-induced plasma expands in a gas environment, so that its emission spectra result comparable to those of a plasma induced in air, in terms of persistence, resolution and signal-to-noise ratio. For all these reasons, DP-LIBS represents a powerful tool for the elemental analysis of bulk water and submerged solid samples. In any case, the application of DP-LIBS in oceanography still requires a deep study of the phenomena induced by the laser ablation process in water at high pressure.

In the last decade, the suitability of LIBS for laboratory characterization of bulk liquids at high pressure has been explored [7, 27–28]. Several experimental parameters have been monitored, such as pulse energy focusing geometry and liquid pressure, so to try and make up for the observed decrease of the LIBS signal with increasing pressure. The same authors have employed a double-pulse approach in order to improve LIBS capability [2]. However, the features of plasmas and cavitation bubbles generated at a given interpulse delay are strongly affected by the water pressure. For example, despite the use of DP, a negligible signal enhancement has been obtained at static pressures above 100 bar [29]. This suggests that DP is not necessarily helpful for applications in bulk liquids. On the other hand, it has been reported by Thornton et al. that the use of a long-duration nanosecond laser source (150 ns) can significantly improve the quality of SP-LIBS spectra [30], a s well as the capability to analyze submerged solid targets with single pulses [31–32]. With this regards, the quality of DP approach needs further studies still in order to evaluate the full range of its benefits over other possible experimental strategies.

Most recently, the effect of water pressure on submersed solid targets has been fully investigated for surveying the laser ablation performed in water during nanoparticle production. As observed in [33], the plasma duration and degree of confinement, as well as the cavitation bubble evolution, that are dependent on the external liquid pressure, can strongly affect both the yield and structure of the produced particles (carbon nanostructures in the mentioned paper). With this in mind, the present study was focused on the fundamental aspects of the generation of single- and double pulse- laser-induced plasmas, as well as the evolution of the cavitation bubble due to the first laser pulse. We used optical emission spectroscopy for plasma characterization and shadowgraph for bubble dynamics study, for investigating the above mentioned parameters as functions of the pressure used. For DP-LIBS, we employed the collinear configuration. We focused our attention on the effects brought by the liquid pressure on the spectroscopic analysis of submerged solid targets, which we investigated characterizing the DP-LIBS spectra as functions of pressure and optimizing the interpulse delay in terms of signal-to-noise ratio.

2. Experimental set-up

Fig. 1 presents a schematic diagram of the experimental set-up employed in this work. Here, two delayed laser pulses (Nd:YAG laser @532 nm, 10 Hz, 5 ns pulse duration, Quanta System, PILS-GIANT) were focused by an appropriate optical configuration on a metallic sample placed inside a stainless-steel chamber x filled with distilled water. The experiments were carried out at different pressures, up to 120 bar. The energy of the two laser beams was set at 150 and 270 mJ, respectively. The system was externally synchronized using a delay and pulse generator (Stanford Inc. DG 535). For this study, a collinear double pulse configuration was used, i.e., both laser pulses were focused on the sample surface by a quartz biconvex lens (5 cm focal length) held in a spacer tube placed in front of the target. The chamber was equipped with a rotating target holder, in order to limit drilling effects on the sample surface. A 10 mm axial movement for fine adjustments of the focal distance was also possible by means of a micrometric screw. The chamber was a stainless steel cylinder with a perpendicular aperture for the laser beam entrance, sealed with a sapphire optical window with 532/1064 nm antireflection coating and equipped with spacer tubes enabling adjustment of the lens-to-target distance. The high-pressure chamber is equipped with several extra ports, each provided with sapphire optical windows, for the acquisition of spectra and

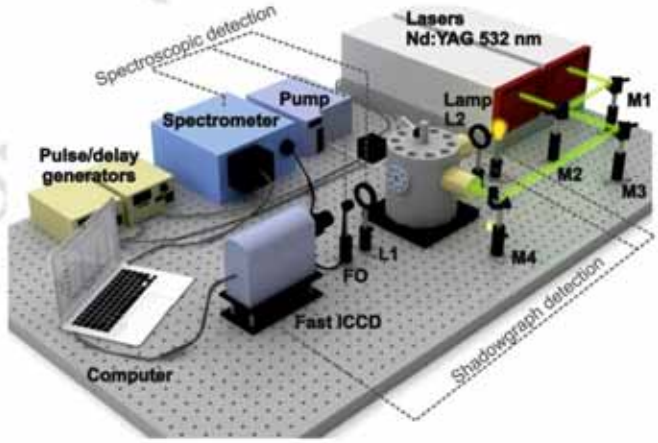

Fig. 1. Experimental set-up. M1, M2 and M3 mirrors; M2 dichroic mirror; L1 collimating lens; L2 lens; FO fiber optic. Dashed lines show the two different detection systems, one for OES measurements and the other for shadowgraph images.

shadowgraph images. The water outflow was controlled by a micrometric valve that could be either kept closed to seal the chamber or opened to produce a regime of controlled flux. The pressure was created by a HPLC pump (Shimadzu LC-20AT Prominence) which could work in two modes (constant pressure or constant flux) in a pressure range 1–250 bar, in steps of 1 bar.

For spectroscopic experiments, the plasma emitting light was collected at 90° with respect to the laser beam, through the dedicated sapphire optical window, by a 10 cm quartz lens placed outside the chamber. The plasma light was focused onto the entrance slit of a mono-chromator through an optical fiber cable. The spectroscopic system consisted of a spectrograph (JobinYvon TRIAX 550) with a grating of1200 grooves mm^{-1} and an ICCD detector (JobinYvon i3000) which was controlled and synchronized by a pulse/delay generator (Stanford inc. DG 535). All the emission spectra were acquired with 10 accumula- tions and 5 averages to optimize the signal-to-noise ratio. The employed acquisition time parameters (with respect to the second laser pulse) were: delay time of 0 ns and 50 ns; and gate width of 10 μs a n d 100 ns for the used Al and Ti target, respectively.

The shadowgraph set-up for studying the cavitation bubble dynamics consisted of a continuous white light source, a set of lenses to reduce light divergence, a fast Camera (Andor i-Star, DH334T-18F-E3) with a tele-objective to acquire the bubble profile and a pulse generator to synchronize the laser pulses with the camera. The bubble shadow was collected through a sapphire window at 90° with respectto the laser pulse direction. During the acquisition of shadowgraph images, the target holder was stopped in order to avoid formation of bubbles along the optical path, which would affect the acquisition. Furthermore, to minimize drilling of the sample surface, the target was turned after the acquisition of each shadowgraph image. Also in these studies the repetition rate of laser pulses was 10 Hz. The shadow- graph images of the laser-induced bubble and shockwave were acquired by using the kinetic mode of the ICCD, with a gate width of 1 μs and of 200 ns respectively. The shadowgraph images of the plasma were acquired by using the kinetic mode of the ICCD, with a gate width of 500 ns.

3. Results and discussion

3.1. Underwater laser-induced plasmas

The main mechanisms responsible for the plasma formation are the same occurring during ablation in gas. Briefly, the sequence of the process starts with the laser ablation and the laser induced plasma (LIP) production. Due to its fast expansion, a shock wave (SW) is generated. It is important to note that the differences between plasma formation in a gaseous environment and inside a liquid are related to the plasma confinement and the onset of cavitation effects, i.e. the vapor bubble formation. Due to the confinement of the plasma by the nearly incompressible liquid medium and to the fast transfer of energy from the plasma to the surrounding liquid, the plumes generated under water are smaller than those generated in gas. As a consequence, the plasma persistence is significantly shorter, ending typically few microseconds after the laser irradiation [27–29].

In order to evaluate the effect of underwater environmental pressure 213 over the physical characteristics of the generated plumes, we acquired 214 shadowgraph images at different delays after laser irradiation. Fig. 2 215 depicts results obtained for an aluminum target and acquired few microseconds after the first laser pulse at three different pressures: 30, 90 and 120 bar. The images clearly show the confinement effect of the liquid on the plasma. For instance, the plasma at 90 bar is smaller than the corresponding one at 30 bar. In the case of 120 bar it should be considered that, as a consequence of the thrust of the expanding plasma, the surrounding liquid can reach supercritical conditions [34]. Under these circumstances, water is characterized by lower viscosity and surface tension, thus the plasma appears less confined than at 90 bar. In general, the strong confinement induced by the nearly uncompressible liquid and the steep decrease of the ionization degree and temperature due to the fast transfer of energy to the surrounding medium, cause the plasma species to rearrange in particles of nanometric size. This produces a colloidal solution in front of the sample that may affect the shot-to-shot reproducibility of LIBS measurements [33]. Although the external pressure noticeably affects the LIP dynamics, the ablation process itself is not expected to depend on the external pressure [33–35] as a consequence of the conditions at the early stages of expansion. In fact, in this case, the ablated matter reaches a number density close to that of the sample in the solid phase and an electronic temperature of about 10,000 K. In these conditions, the initial plasma pressure is in the order of tens of Mbar and consequently, as it is reported in [35–38], by considering the range of pressures used in this work, the external pressure at the initial stage of LIP expansion can be neglected. Therefore, even if the plasma volume is reduced and its shape is changed by the water pressure increase, the plasma parameters (temperature and electron density) hold similar values. As mentioned above, after plasma formation, a SW is generated. The shockwave is

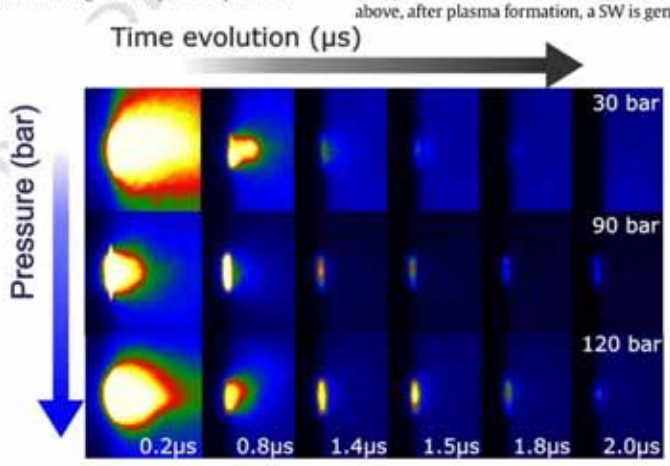

Fig. 2. Plasma shadowgraph images acquired after the first laser pulse at different delays. Al target in water at 30, 90 and 120 bar.

caused by the rapid expansion of the laser-ablated material into the sur- rounding liquid, which generates a sharp, high pressure impulse that expands outwards from the focal point of the laser. It is reasonable to expect that, in the range of external pressures employed in this work, the characteristics of the SW produced by the LIP expansion do not vary greatly. The outward SW driven in the surrounding liquid by the plasma expansion was directly investigated by shadowgraph experiments.

Fig. 3A shows images of the SW propagation as a function of the delay time at 30 and 120 bar. The relative position of the shockwave at each delay is also labeled in the picture. As shown, the size and volume of the SW is similar in both cases. From here, the maximum distance travelled by the front of the shockwave is plotted in Fig. 3B. Data were acquired at different water pressure: 1, 30, 60, 90 and 120 bar. Additionally, the inset shows the velocity of the shockwave at each pressure. In the first 10 μs, the SW propagation velocity is in the order of the speed of sound in water, around 1500 m/s, for each value of pressure. It is well known that, when external pressure increases, the propagation of the SW should vary of a few tens of units, but as a consequence of the experimental uncertainty of our measurement, we are not able to clearly appreciate this difference. Nevertheless, such similar values of the SW propagation velocity confirm that the initial thrust due to the breakdown isalmost the same at all the external pressures investigated in the present work.

3.2. Effect of hydrostatic pressure on the cavitation bubble expansion

The plasma induced by a laser shot releases its energy to the surrounding liquid and generates a thin vapor layer at the border of the plasma, which evolves into a cavitation bubble. The behavior of a cavitation bubble induced by laser ablation in water at 1 bar has been already investigated [23–24]. For comparative purposes, we used fast shadowgraph to study the dimensions and shape of the vapor bubble formed after the first laser pulse at different pressures. Frames acquired at different delay times at a pressure of 1 bar are shown in Fig. 4. The temporal evolution of the bubble size is characterized by three stages: first, the expansion stage; then, the stage of maximum expansion; and finally the compression/collapse stage. At 1 bar, the bubble expansion was well discerned even at 2 μs from the laser pulse, whereas the maximum bubble size was observed at 250 μs. In this stage, the shape of the bubble is a hemisphere [39]. Afterwards, at the maximum expansion, the pressure inside the bubble is lower than the external one, and consequently the bubble starts to shrink. Thus, the size decreases until 950 μs. At the collapse stage, a rapid increase of the gas temperature and pressure inside the bubble produces a re-expansion of the cavitation bubble. Additionally, if enough energy is accumulated in the bubble, its oscillations can continue for many cycles of both expansion and collapse [24].

The temporal evolution of the cavitation bubble has been studied as a function of the external pressure (30, 90 and 120 bar). Results are

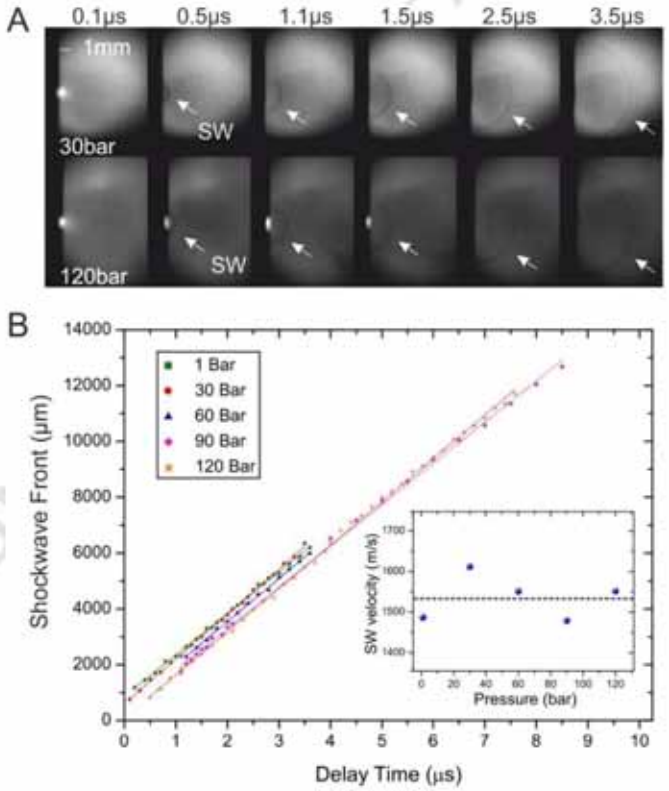

Fig. 3. Time-resolved shadowgraph images of shockwave front, at atmospheric pressure and 120 bar. (A) Laser focused on an Al sample in water at 1, 30, 90 and 120 bar; (B) shockwave front displacement vs delay time plot. Graphical inset: shockwave velocity vs environment pressure plot.

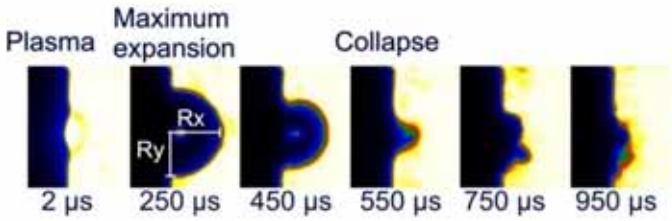

Fig. 4. Time-resolved shadowgraph of the laser-induced cavitation bubble on an aluminum sample submerged in water at 1 bar.

depicted in Fig. 5. The size of the cavitation bubbles observed at a longer delay time was significantly smaller by increasing the water pressure. Also, Fig. 5 shows that, regardless of pressure, a cavitation bubble starts to appear during the early stage of the processes. Thus, the initial expan- sion velocity along the *x*-direction was similar for the three studied cases, that is around 40 m/s. This observation reveals that the effect of hydrostatic pressure is negligible during the early stage of the expansion process [40]. Beyond this point, the evolution of the dynamic expansion process diverges for the different pressures. At 120 bar, the cavitation bubble could not be discerned at early times. The maximum bubble ex- pansion occurs at 15, 10 and 7 µs for 30, 90 and 120 bar, respectively, whereas the collapse was observed at 28, 17 and 9 µs, again depending on hydrostatic pressure. The velocities calculated at the collapse stage were 30, 70 and 90 m/s at 30, 90 and 120 bar, respectively [40]. Thus, a pressure increase influences the expansion and cooling of the vapor bubble, leading to a decrease of the bubble size and lifetime, as it can be observed in Fig. 5. We considered the volume instead of the radius to estimate the bubble size, in order to take into account that hydrostatic pressure can distort the bubble shape. In fact, due to the external pressure, the bubble expands differently along the *x* and *y* directions, thus assuming an ellipsoidal shape [41–42]. The observed variations of bubble size and lifetime are in good agreement with those found in [43], where a range of pressures up to 50 bar was evaluated.

In Fig. 5, a secondary bubble can be observed. This is assumed to be produced by the rapid increase of both the internal temperature and pressure of the cavitation occurring bubble just after its collapse. After rebounding, the bubble shape changes again, because it is now constituted by both water vapor and the nanomaterials produced during the cooling down of the plasma [44]. By increasing the water pressure, the collapse velocity along the *x*-direction also increases and a pronounced bubble rebound followed by its displacement with respect to the target surface takes place. On the contrary, at atmospheric pressure, the rebound phase can be observed according to the initial laser energy, but is not accompanied by any displacement of the bubble with respect to the target position.

3.3. *Double pulse LIBS underwater at high pressure*

Keeping in mind the general description of the laser-induced bubble at different pressures, DP-LIBS underwater requires a careful optimization of the interpulse delay. In agreement with the conclusions of a previous work [22] performed at atmospheric pressure, the optimum interpulse delay time could be expected to match the maximum expansion of the bubble. In such a situation, the plasma produced by the second pulse expands in a cavitation bubble with more favorable pressure conditions than those at the initial stage of the bubble expansion or the

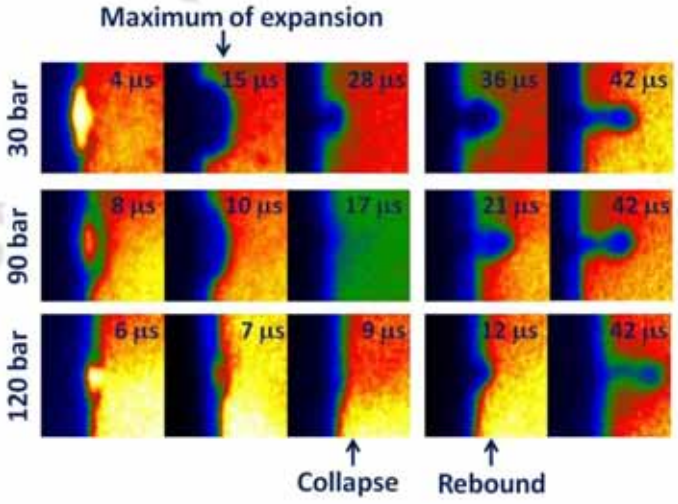

Fig. 5. Representative time-resolved shadowgraph images of bubbles induced by single laser pulses at different water pressures (30, 90 and 120 bar). The images were acquired at various delay times with a gate width of 500 ns.

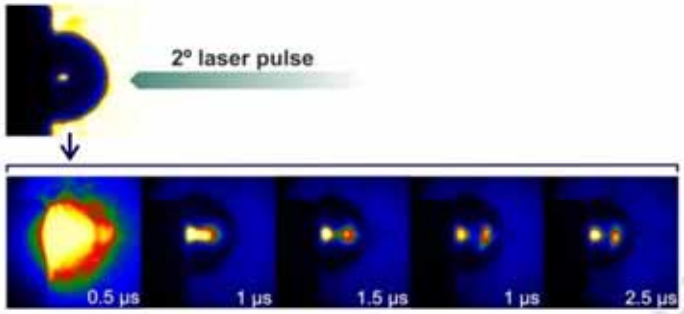

Fig. 6. Plasma shadowgraph images of the effect produced by the second pulse on the NPs generated by the first laser pulse. Interpulse delay: 250 µs, pressure: 1 bar.

final stage of the bubble collapse. It has recently been observed that, in these initial and final stages, a significant part of the energy of the second laser pulse is spent in the interaction with the NPs generated by the first laser pulse [39]. This causes the breakdown of the just formed NPs and, accordingly, the production of a secondary plasma. Hence, the secondary plasma is generated at a distance from the target and it partially prevents the second laser pulse from ablating the sample. On the contrary, at the maximum of the bubble expansion, that is when its volume is the largest, the NP concentration in the bubble reaches its minimum and this shielding effect occurs to a lesser extent. As an example, Fig. 6 shows the effect of the plasma produced by the second laser pulse within the bubble generated by the first laser pulse. The interpulse delay time was set at the maximum bubble expansion, 250 µs at atmospheric pressure. Therefore, the presence of NPs must be taken into account, especially when DP-LIBS is performed at high external liquid pressures. In these conditions, the bubble volume is smaller and the NP concentration higher than at atmospheric pressure. Fig. 7 shows some of the images of the second laser-induced plasma, taken at several interpulse delay times at the representative water pressures of 30 and 90 bar. The interpulse delay times used in this experiment were chosen in correspondence with the maximum of the bubble expansion. The images of the plasma induced by the second laser pulse were compared with those produced by the first one. The plasma aspect ratios (R_x/R_y) on the left of Fig. 7 clearly indicate that the second plasma induced inside the first bubble has a more spherical shape. A rigorous treatment of the aspect ratio reported in Fig. 7 would require to take into account the image distortion due to the shape of the induced cavity around the plasma. Nonetheless, for the scope of the

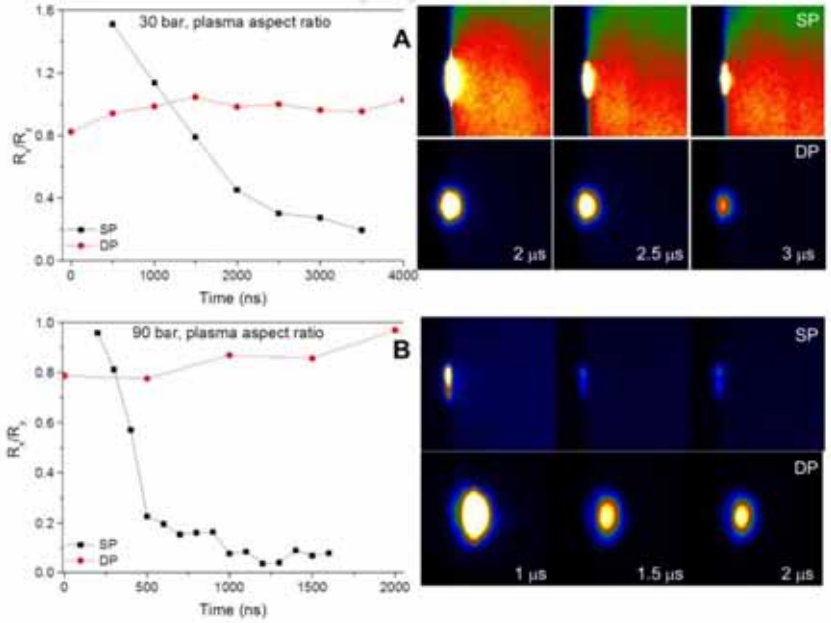

Fig. 7. Comparison between the plasma shapes produced by the first laser pulse and the second laser pulse at two representative water pressure values: A) 30 bar and B) 90 bar. The temporal trend of the plasma aspect ratio and the plasma shadowgraph images are reported on the left and right hand side, respectively.

present discussion we suppose that, as the plasma fills up completely the cavitation bubble during the expansion, this effect may be reasonably neglected.

On the other hand, from the spectroscopic point of view, and contrarily to what is observed at atmospheric conditions [33], emission spectra at high pressure are characterized by self-absorbed lines on the continuum radiation. This is shown in Fig. 8 for titanium spectra acquired at 30 bar. The predominance of the continuum spectra in the LIP can be ascribed to the Debye-Hückel's high density effect on the cut-off of excited levels due to the high value of the electron number density at the initial stage of the plasma expansion [45]. In this condition, the radiative recombination is the main source of radiation in the plasma and in the specific case of a high pressure liquid medium this phenomenon is particularly effective [33] due to strong confinement. Therefore, as electron number density decreases along the propagation axis, it is reasonable to suppose that, in the external region of the LIP, the Debye-Hückel's limitation of available electronic levels does not occur anymore. Although the initial temperature of the front head of the plasma is very high, the fast transfer of thermal energy from the plasma to the surrounding environment causes the peripheral zone to cool down sooner than the plasma interior and thus the occurrence of self- absorption of the continuum radiation. This effect is very similar to Fraunhofer absorption observed in the spectra of stars and it has been reported in a previous work dealing with DP-LIBS in sea-water, where sodium lines appeared reabsorbed on the continuous Ti-LIP spectrum [23].

In order to exploit the self-absorbed lines for analytical purposes, it is important to check that their intensity is proportional to the total number density of the ablated species, which can be investigated by their atomic energy distribution function. If the distribution has a Boltzmann form, it means that the peak intensities are almost completely absorbed on the continuum, and, through the Boltzmann relation, this implies that the intensity of the single line is proportional to the total number density of the ablated species. The inset of Fig. 8 shows the corresponding Boltzmann plot. The absorbed lines have a Boltzmann distribution which suggests the possible use of such signals for analytical purposes. Moreover, as it has been already demonstrated by Sakka et al. [46], the width of the self-reversed lines can also be used for determining the local electron density, which in this case results to be around 10^{18} cm^{-3} and represents the electron number density in the plasma zone where the species are absorbing the continuum radiation.

In order to optimize the DP-LIBS signal, the emission intensity observed during the Al-target ablation performed at different pressures was investigated. Fig. 9 shows the absorbed area of the transition of Al (I) at 396.15 nm as a function of the interpulse delay at different water pressures. In order to show the correlation between plasma

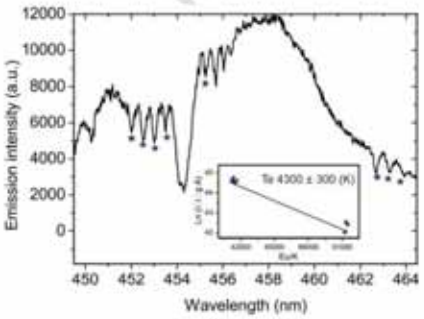

Fig. 8. Spectrum of DP-LIBS of Ti in water at 30 bar together with a graphical inset of the corresponding Boltzmann plot.

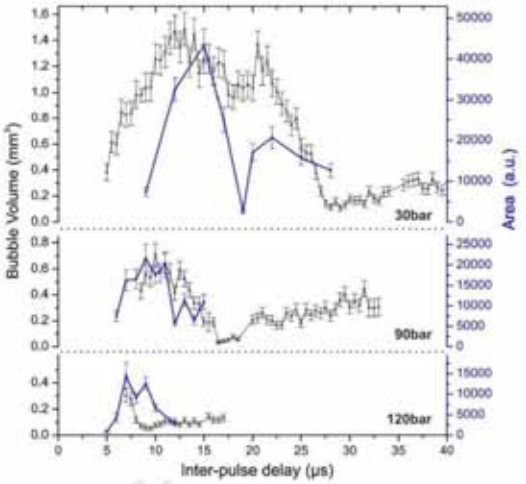

Fig. 9. Comparison between the laser-induced bubble volumes and the corresponding area of the DP-LIBS signal of Al (I) at 396.15 nm as functions of the interpulse delay at three different pressure values (30, 90 and 120 bar).

emission intensity and bubble dynamics, the bubble volume is also reported in the figure. As expected, the maximum intensity was detected at the interpulse delay of maximum bubble expansion. As an example, Fig. 10 shows the Al spectra as functions of interpulse delay with a liquid pressure of 30 bar. It is worth noting that, while atomic transitions appear as absorbed peaks on the continuum, ionic transitions appear as typical emission lines. This can be due to two reasons: i) in Debye Hückel's theory the effect on the limitation of the allowed levels depends on the ionization energy of the species. Ions have much higher ionization energy than atoms, thus they are less affected by high electron density effects and their excited levels become available before those of the atoms; ii) ion emission comes from the inner part of the plasma and therefore it does not undergo to Fraunhofer-like absorption effects.

Fig. 11 reports the Al spectra acquired at the best interpulse delay for three different pressures. This figure clearly shows that the amount of spectral information decreases by increasing the working pressure. Indeed, at high pressures the bubble expansion is unable to reach the saturation pressure (i.e. the equilibrium condition with the surrounding liquid [33]), because the high external pressure causes the vapor inside the cavitation bubble to condense. This consideration suggests that the plasma is more and more confined as the liquid pressure increases and, consequently, that the main contribution to spectra is continuum radiation rather than spontaneous emission. Recombination and high density effects become so severe with increasing pressure that at 120 bar even ionic peaks disappear from the spectrum.

4. Conclusions

Time-resolved optical emission spectroscopy and shadowgraph were used to investigate single-pulse bubble formation and double-pulse plasma emission in collinear DP-LIBS of aluminum submerged in water at pressure up to 120 bar. Plasma persistence and cavitation bubble size and lifetime were observed to considerably decrease upon increase of hydrostatic pressure, and the optimum interpulse delay decreased accordingly. Furthermore, as a result of the reduced dimensions and lifetime of the cavitation bubble, also the DP-LIBS emission enhancement decreased by increasing the applied pressure. Finally, we observed that, as a consequence of the fast decrease of temperature

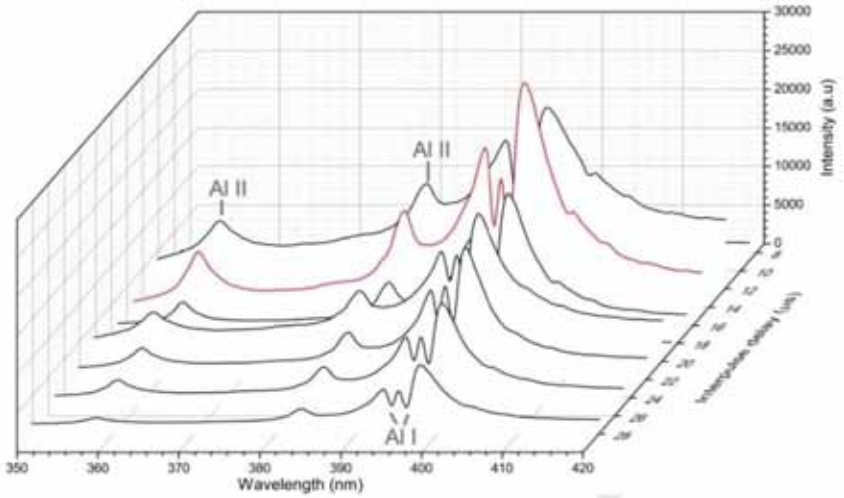

Fig. 10. DP-LIBS spectra of Al in water at 30 bar as functions of the interpulse delay.

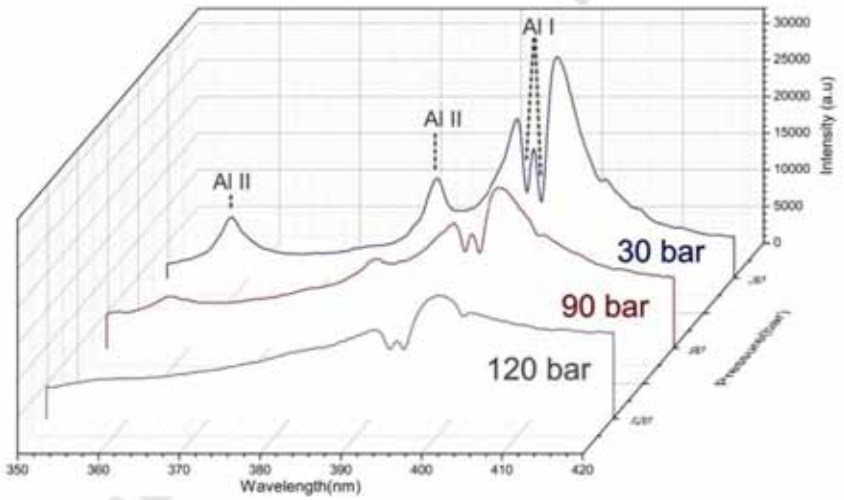

Fig. 11. DP-LIBS spectra of Al in water at three different pressures (30, 90 and 120 bar) acquired at the best interpulse delay (15, 10 and 7 μs, respectively).

in the peripheral regions of the plasma, atomic transitions appear as absorption peaks on the continuum radiation. The intensity of these absorbed spectral lines resulted proportional to the total number density of the ablated species and their atomic energy distribution function had a Boltzmann form. This implies that the peak intensities are almost completely absorbed on the continuum, suggesting that the use of these spectra for elemental analysis with conventional methodologies is still feasible.

Acknowledgments

M. Lopez-Claros would like to acknowledge the Consejería de Innovación, Ciencia y Empleo of the Junta de Andalucía for her fellowship.

References

[1] B. Thornton, T. Takahashi, T. Sato, T. Sakka, A. Tamura, A. Matsumoto, T. Nozaki, T. Ohki, K. Ohki, Development of a deep-sea laser-induced breakdown spectrometer for in situ multi-element chemical analysis, Deep-Sea Res. I 95 (2015) 20–36.
[2] A.P.M. Michel, A.D. Chave, Double pulse laser-induced breakdown spectroscopy of bulk aqueous solutions at oceanic pressures: interrelationship of gate delay, pulse energies, interpulse delay, and pressure, Appl. Opt. 47 (2008) 131–143.
[3] F.J. Fortes, J. Moros, P. Lucena, L.M. Cabalín, J.J. Laserna, Laser-induced breakdown spectroscopy, Anal. Chem. 85 (2013) 640–669.
[4] D.W. Hahn, N. Omenetto, Laser-induced breakdown spectroscopy (LIBS), part II: review of instrumental and methodological approaches to material analysis and applications to different fields, Appl. Spectrosc. 66 (2012) 347–419.
[5] S. Guirado, F.J. Fortes, J.J. Laserna, Elemental analysis of materials in an underwater archeological shipwreck using a novel remote laser-induced breakdown spectroscopy system, Talanta 137 (2015) 182–188.

[6] S. Koch, W. Garen, M. Muller, W. Neu, Detection of chromium in liquids by laser induced breakdown spectroscopy (LIBS), Appl. Phys. A Mater. Sci. Process. 79 (2004) 1071–1073.
[7] M. Lawrence-Snyder, J. Scaffidi, S.M. Angel, A.P.M. Michel, A.D. Chave, Laser-induced breakdown spectroscopy of high-pressure bulk aqueous solutions, Appl. Spectrosc. 60 (2006) 786–790.
[8] V.E. McKelvey, Subsea mineral resources, mineral and petroleum resources of the ocean, U.S. Geol. Surv. Bull. 1689-A (1986).
[9] Y. Nakajima, B. Thornton, Application of Laser-Induced Breakdown Spectroscopy for In-Situ Measurement of Metal Grade for Seafloor Mineral Processing, Oceans, MTS/IEEE Washington 2015, pp. 1–6.
[10] S. Guirado, F.J. Fortes, V. Lazic, J.J. Laserna, Chemical analysis of archeological materials in submarine environments using laser-induced breakdown spectroscopy. On-site trials in the Mediterranean Sea, Spectrochim. Acta Part B 74–75 (2012) 137–143.
[11] R.D. Prien, The future of chemical in situ sensors, Mar. Chem. 107 (2007) 422–432.
[12] S. Palanco, J.M. Baena, J.J. Laserna, Open-path laser-induced spectrometry for remote analytical measurements on solid surfaces, Spectrochim. Acta Part B 57 (3) (2002) 591–599.
[13] F.J. Fortes, J. Cuñat, L.M. Caballín, J.J. Laserna, In situ analytical assessment and chemical imaging of historical buildings using a man-portable laser system, Appl. Spectrosc. 61 (2007) 558–564.
[14] I. Gaona, P. Lucena, J. Moros, F.J. Fortes, S. Guirado, J. Serrano, J.J. Laserna, Evaluating the use of standoff LIBS in architectural heritage: surveying the Cathedral of Málaga, J. Anal. At. Spectrom. 28 (2013) 810–820.
[15] D.A. Cremers, L.J. Radziemski, T.R. Loree, Spectrochemical analysis of liquids using the laser spark, Appl. Spectrosc. 38 (1984) 721–726.
[16] M.A. Harith, V. Palleschi, A. Salvetti, D.P. Singh, M. Vaselli, G.V. Dreiden, Y.I. Ostrovsky, I.V. Semenova, Dynamics of laser-driven shock waves in water, J. Appl. Phys. 66 (1989) 5194–5197.
[17] F. Fama, M.A. Harith, V. Palleschi, A. Salvetti, D.P. Singh, M. Vaselli, G.V. Dreiden, Y.I. Ostrovsky, I.V. Semenova, Hydrodynamics of laser-produced shock waves in water: reflection and transmission measurements, J. Appl. Phys. 69 (1991) 1660–1665.
[18] V. Lazic, S. Jovicevic, M. Carpanese, Laser induced bubbles inside liquids: transient optical properties and effects on a beam propagation, Appl. Phys. Lett. 101 (2012) 054101–054104.
[19] V. Lazic, S. Jovićević, Laser induced breakdown spectroscopy inside liquids: processes and analytical aspects, Spectrochim. Acta Part B 101 (2014) 288–311.
[20] T. Sakka, A. Tamura, A. Matsumoto, K. Fukami, N. Nishi, B. Thornton, Effects of pulse width on nascent laser-induced bubbles for underwater laser-induced breakdown spectroscopy, Spectrochim. Acta Part B 97 (2014) 94–98.
[21] A. De Giacomo, M. Dell'Aglio, O. De Pascale, M. Capitelli, From single pulse to double pulse ns-laser induced breakdown spectroscopy under water: elemental analysis of aqueous solutions and submerged solid samples, Spectrochim. Acta Part B 62 (2007) 721–738.
[22] A. Casavola, A. De Giacomo, M. Dell'Aglio, F. Taccogna, G. Colonna, O. De Pascale, S. Longo, Experimental investigation and modelling of double pulse laser induced plasma spectroscopy under water, Spectrochim. Acta Part B 60 (2005) 975–985.
[23] A. De Giacomo, M. Dell'Aglio, F. Colao, R. Fantoni, V. Lazic, Double-pulse LIBS in water bulk and on submerged bronze samples, Appl. Surf. Sci. 247 (2005) 157–162.
[24] V. Lazic, J.J. Laserna, S. Jovicevic, Insights in the laser-induced breakdown spectroscopy signal generation underwater using dual pulse excitation, part I: vapor bubble, shockwaves and plasma, Spectrochim. Acta Part B 82 (2013) 4 2 –49.
[25] V. Lazic, J.J. Laserna, S. Jovicevic, Insights in the laser-induced breakdown spectroscopy signal generation underwater using dual pulse excitation, part II: plasma emission intensity as a function of interpulse delay, Spectrochim. Acta Part B 82 (2013) 50–59.
[26] S. Rifai, F. Laville, M. Vidal, J. Chaker, Quantitative analysis of metallic traces in water-based liquids by UV-IR double-pulse laser-induced breakdown spectroscopy, J. Anal. At. Spectrom. 27 (2012) 276–283.
[27] A.P.M. Michel, A.D. Chave, Single pulse laser-induced breakdown spectroscopy of bulk aqueous solutions at oceanic pressures: interrelationship of gate delay and pulse energy, Appl. Opt. 47 (2008) 1 2 2 –130.
[28] A.P.M. Michel, M. Lawrence-Snyder, S.M. Angel, A.D. Chave, Laser-induced breakdown spectroscopy of bulk aqueous solutions at oceanic pressures: evaluation of key measurement parameters, Appl. Opt. 46 (2007) 2507–2515.
[29] M. Lawrence-Snyder, J. Scaffidi, S.M. Angel, A.P.M. Michel, A.D. Chave, Sequential-pulse laser-induced breakdown spectroscopy of high-pressure bulk aqueous solution, Appl. Spectrosc. 61 (2007) 171–176.
[30] B. Thornton, T. Sakka, T. Masamura, A. Tamura, T. Takahashi, A. Matsumoto, Long-duration nano-second single pulse lasers for observation of spectra from bulk liquids at high hydrostatic pressures, Spectrochim. Acta Part B 97 (2014) 7–12.
[31] B. Thornton, T. Sakka, T. Takahashi, A. Tamura, T. Masamura, A. Matsumoto, Spectroscopic measurements of solids immersed in water at high pressure using a long-duration nanosecond laser pulse, Appl. Phys. Expresss 6 (2013) 08240–08244.
[32] T. Takahashi, B. Thornton, T. Ura, T. Sakka, Investigation of influence of hydrostatic pressure on double-pulse laser-induced breakdown spectroscopy for analysis of the composition of solids submerged at high pressures, Appl. Phys. Express 6 (2013) 042403.
[33] A. De Giacomo, A. De Bonis, M. Dell'Aglio, O. De Pascale, R. Gaudiuso, S. Orlando, A. Santagata, G.S. Senesi, F. Taccogna, R. Teghil, Laser ablation of graphite in water in a range of pressure from 1 to 146 atm using single and double pulse techniques for the production of carbon nanostructures, J. Phys. Chem. C 115 (2011) 5123–5130.
[34] J. Noack, A. Vogel, Laser-induced plasma formation in water at nanosecond to femtosecond time scales: calculation of thresholds, absorption coefficients, and energy density, IEEE J. Quantum Electron. 35 (1999) 1156–1167.
[35] B. Thornton, T. Ura, Effects of pressure on the optical emissions observed from solids immersed in water using a single pulse laser, Appl. Phys. Exp. 4 (2011) 022702–022703.
[36] S.M. Angel, J. Bonvallet, M. Lawrence-Snyder, W.F. Pearman, J. Register, Underwater measurements using laser induced breakdown spectroscopy, J. Anal. At. Spectrom. 31 (2016) 328–336.
[37] H. Hou, Y. Tian, Y. Li, R. Zheng, Study of pressure effects on laser induced plasma in bulk seawater, J. Anal. At. Spectrom. 29 (2014) 169–175.
[38] B. Thornton, T. Takahashi, T. Ura, T. Sakka, Cavity formation and material ablation for single-pulse laser-ablated solids immersed in water at high pressure, Appl. Phys. Express 5 (2012) 102402–102403.
[39] M. Dell'Aglio, R. Gaudiuso, R. Elnashedy, O. DePascale, G. Palazzo, A. De Giacomo, Collinear double pulse laser ablation in water for the production of silver nanoparticles, Phys. Chem. Chem. Phys. 15 (2013) 20868–20875.
[40] M. Dell'Aglio, A. Santagata, G. Valenza, A. De Stradis, A. De Giacomo, Study of the effect of water pressure on plasma and cavitation bubble induced by pulsed laser ablation in liquid (PLAL) of silver and missed variations of observable NPs features, Chem. Phys. Chem. (2017)http://dx.doi.org/10.1002/cphc.201601231.
[41] N. Takada, T. Nakano, K. Sasaki, Influence of additional external pressure on optical emission intensity in liquid-phase laser ablation, Appl. Surf. Sci. 255 (2009) 9572–9575.
[42] K. Sasaki, T. Nakano, W. Soliman, N. Takada, Effect of pressurization on the dynamics of a cavitation bubble induced by liquid-phase laser ablation, Appl. Phys. Express 2 (2009) 046501–046503.
[43] M. Lawrence-Snyder, J.P. Scaffidi, W.F. Pearman, C.M. Gordon, S.M. Angel, Issues in deep ocean collinear double-pulse laser induced breakdown spectroscopy: dependence of emission intensity and inter-pulse delay on solution pressure, Spectrochim. Acta Part B 99 (2014) 172–178.
[44] M. Dell'Aglio, R. Gaudiuso, O. De Pascale, A. De Giacomo, Mechanisms and processes of pulsed laser ablation in liquids during nanoparticle production, Appl. Surf. Sci. 348 (2015) 4–9.
[45] A. De Giacomo, R. Gaudiuso, M. Dell'Aglio, A. Santagata, The role of continuum radiation in laser induced plasma spectroscopy, Spectrochim. Acta Part B 65 (2010) 385–394.
[46] T. Sakka, T. Nakajima, Y.H. Ogata, Spatial population distribution of laser ablation species determined by self-reversed emission line profile, J. Appl. Phys. 92 (2002) 2296–2303.